

*Journal of*  
**Geophysical  
Research**

**VOLUME 66**

**DECEMBER 1961**

**NUMBER 12**

**PUBLISHED BY**

**THE AMERICAN GEOPHYSICAL UNION**

# Journal of Geophysical Research

*An International Scientific Publication*

## OFFICERS OF THE UNION

THOMAS F. MALONE, *President*  
GEORGE P. WOOLLARD, *Vice President*  
A. NELSON SAYRE, *General Secretary*  
WALDO E. SMITH, *Executive Secretary*

## OFFICERS OF THE SECTIONS

### Geodesy

FLOYD W. HOUGH, *President*  
CHARLES A. WHITTEN, *Vice President*  
BUFORD K. MEADE, *Secretary*

### Seismology

JAMES A. PEOPLES, JR., *President*  
JACK E. OLIVER, *Vice President*  
BENJAMIN F. HOWELL, JR., *Secretary*

### Meteorology

MORRIS NEIBURGER, *President*  
HENRY G. HOUGHTON, *Vice President*  
WOODROW C. JACOBS, *Secretary*

### Geomagnetism and Aeronomy

C. T. ELVEY, *President*  
E. H. VESTINE, *Vice President*  
J. HUGH NELSON, *Secretary*

### Oceanography

DONALD W. PRITCHARD, *President*  
ROBERT S. ARTHUR, *Vice President*  
ARTHUR E. MAXWELL, *Secretary*

### Volcanology, Geochemistry, and Petrology

HATTEN S. YODER, JR., *President*  
EDWARD D. GOLDBERG, *Vice President*  
DAVID R. WONES, *Secretary*

### Hydrology

WILLIAM C. ACKERMANN, *President*  
DAVID K. TODD, *Vice President*  
RALPH N. WILSON, *Secretary*

### Tectonophysics

LOUIS B. SLICHTER, *President*  
DAVID T. GRIGGS, *Vice President*  
IRIS BORG, *Secretary*

## BOARD OF EDITORS

Editors: PHILIP H. ABELSON and J. A. PEOPLES

## ASSOCIATE EDITORS

1959-1961

HENRI BADER	T. NAGATA
K. E. BULLEN	FRANK PRESS
CONRAD P. MOOK	A. NELSON SAYRE
WALTER H. MUNK	MERLE A. TUVE

JAMES A. VAN ALLEN

1960-1962

JULIUS BARTELS	L. A. MANNING
V. V. BELOUSSOV	TOR J. NORDENSON
E. G. BOWEN	E. N. PARKER
JOHN E. CHAPPELEAR	GEORGE P. RIGSBY
G. D. GARLAND	WALTER O. ROBERTS
GORDON J. F. MACDONALD	C. N. TOUTAT

JAMES R. WAIT

1961-1963

FRANKLIN I. BADGLEY	ROBERT O. REID
HENRY G. BOOKER	BRUNO ROSSI
JOSEPH W. CHAMBERLAIN	GEORGE H. SUTTON
HERBERT FRIEDMAN	DAVID K. TODD
MARK F. MEIER	VICTOR VACQUIER

ARTHUR H. WAYNICK

The Editors of the *Journal of Geophysical Research* welcome original scientific contributions on the physics of the earth and its environment.

Manuscripts should be submitted in triplicate to J. A. Peoples, Jr., Department of Geology, University of Kansas, Lawrence, Kansas. Authors' institutions in the United States or Canada, are requested to pay a publication charge of \$25 per page, which, if honored, entitles them to 100 free reprints.

Subscriptions to the *Journal of Geophysical Research* and *Transactions, AGU*, are included in membership dues.

Nonmember subscriptions, *Journal of Geophysical Research*, \$30 for back volume of 1959, \$42 for back volume of 1960, \$20 for the calendar year 1961.

Nonmember subscriptions, *Transactions, AGU*, \$4 per calendar year, \$1.25 per copy.

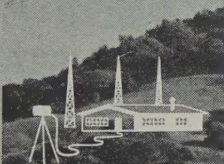
Subscriptions, renewals, and orders for back numbers should be addressed to American Geophysical Union, 1515 Massachusetts Ave., Northwest, Washington, D. C. Suggestions to authors are available on request.

Advertising Representative: Howland and Howland, Inc., 230 Park Ave., New York 17, N. Y.

Since January 1959 (Vol. 64, No. 1) the *Journal of Geophysical Research* has been published monthly by the American Geophysical Union, the U. S. National Committee of the International Union of Geodesy and Geophysics, organized under the National Academy of Sciences-National Research Council as the U. S. national adhering body. Publication of this journal is supported by the National Science Foundation and the Carnegie Institution of Washington. The new monthly combines the type of scientific material formerly published in the bi-monthly *Transactions, American Geophysical Union*, and the quarterly *Journal of Geophysical Research*. The *Transactions, American Geophysical Union*, continues as a quarterly publication for Union business and items of interest to members of the Union.

Published monthly by the American Geophysical Union from 1407 Sherwood Avenue, Richmond, Virginia. Second class postage paid at Richmond, Virginia.





## SPIN PRECESSION MAGNETOMETRY

For mapping magnetic fields in outer space • For monitoring geomagnetic micropulsations on earth • For investigating the ocean depths • For mineral and petroleum exploration.

Varian Associates has produced spin precession magnetometers that are the most rugged, accurate and reliable magnetometers available. Electron resonance instruments, with their high sensitivity, open new vistas for understanding the magnetic field. High accuracy proton free precession instruments provide data that is the recognized world standard.

Varian is prepared to measure any geomagnetic phenomena with existing products or to initiate development projects to solve new problems. For specifications, technical application data, sales and lease information, write the Instrument Division.



**VARIAN associates**  
PALO ALTO 43, CALIFORNIA



# SPRENGNETHER LONG PERIOD VERTICAL SEISMOMETER

## GENERAL SPECIFICATIONS:

- Period Range: 6 to 70 seconds.
- Magnification: Up to 15,000, depending on operating period.
- Damping: Electromagnetic.
- Transducer-moving coils in circular magnetic gaps.
- Boom centering adjustment visible through sealed windows to facilitate adjustment.
- Coils approximately 500 ohms. or to your specifications.
- Pendulum steady mass weight 22 lbs.
- Invar spring for thermal stability.
- Airtight metal cover is provided to prevent recording of microbarometric oscillations.

## PHYSICAL SPECIFICATIONS:

Length.....26"    Width.....14"    Height.....  
Net Weight.....120 lbs.    Shipping Weight.....175

*To compliment this instrument,  
a long period horizontal seismometer is also available.*

Internationally Known Mfrs. of Seismological, Geophysical Instruments.

**W. F. SPRENGNETHER INSTRUMENT CO., INC.**

4567 SWAN AVENUE

ST. LOUIS 10, MO.

WRITE FOR DETAILED  
INFORMATION ON THESE  
INSTRUMENTS.

## BULLETIN (IZVESTIYA), ACADEMY OF SCIENCES, U.S.S.R. GEOPHYSICS SERIES

Subscriptions for 1961 series now available

This monthly Russian publication, perhaps the leading journal of Geophysics of the U.S.S.R., is being translated and published in an English edition for the year 1961 by the American Geophysical Union. The twelve numbers in Russian cover about 2000 pages. Published with the aid of a grant from the National Science Foundation.

Send subscriptions now to

### AMERICAN GEOPHYSICAL UNION

1515 Massachusetts Avenue, N.W.

Washington 5, D. C., U.S.A.

*Subscription rates: \$25.00 for the volume of 12 numbers (\$20.00 to individual members of AGU subscribing for personal use)*  
Numbers will be mailed as issued.

The English edition of this publication for 1957 has been translated and published for the American Geophysical Union by Pergamon Press. This volume may be ordered through the American Geophysical Union at a price of \$25.00. The 1958, 1959, and 1960 series are available at a price of \$25.00 for each volume of 12 numbers. Titles and authors of the papers contained in the series have been published in recent issues of the *Transactions, AGU.*

Please mention JOURNAL OF GEOPHYSICAL RESEARCH, when writing to advertisers



## Only LaCoste & Romberg Geodetic Gravity Meter

**gives you thermal controlled accuracy in a 7-pound meter**

- world survey without resetting
- never requires recalibrating
- less than 0.5 mgl drift per month
- no "sets" or "tares" under normal operation

This new miniaturized Geodetic Gravity Meter retains all the accuracy and dependability of the standard model introduced by LaCoste & Romberg in 1956, yet it weighs only 7 pounds. Complete with battery and luggage-type carrying case, it weighs less than 17 pounds). With a world-wide range of over 6,000 mgl., this instrument has a repeatability of 0.01 mgl. Actual field tests over the complete gravity range have shown an accuracy better than 0.04 mgl. Exceptionally high sensitivity of the LaCoste & Romberg meter is attained by a zero length spring suspension (U. S. Patent No. 2,293,437). Calibration is stabilized by means of patented

lever systems that act on the main spring rather than on weak measuring springs. And by thermostating, drift is normally reduced to less than 0.5 milligal per month.

Rugged and dependable, the LaCoste & Romberg Geodetic Meter requires practically no maintenance in the field. Its gravity responsive system is completely suspended by springs and will therefore withstand any shock that will not damage the housing supporting it. It is specifically designed to provide a light-weight meter with higher accuracy and lower drift than can be attained in any other geodetic gravity meter. For complete information, write for *Miniature Geodetic Gravity Meter Bulletin*.



**LaCoste & Romberg**

6606 NORTH LAMAR

AUSTIN, TEXAS

Please mention JOURNAL OF GEOPHYSICAL RESEARCH, when writing to advertisers



## IMPROVED HIGH POWER PULSED OSCILLATOR, PG-650-C



The continued response of our clientele to the achievements of the PG-650-C model has led to further improvements. These include a  $\frac{1}{2}$   $\mu$ sec pulse with 3 cycles rise and fall, operation on C.W. and as a gated amplifier. This high powered pulsed oscillator has become standard equipment in leading laboratories in the United States and Europe for research in ultrasonics and nuclear magnetic resonance.

R. F. Output voltage  
(min) into 93 ohms ... 0-300 p. to p.  
0-600 Special order

Pulse length—continuous  $\frac{1}{2}$ —13  $\mu$ sec

Pulse droop ..... 5%

Noise output ..... Thermal noise from termination

Harmonic output  
(mostly third) ..... 10%

R. F. Leakage ..... Negligible

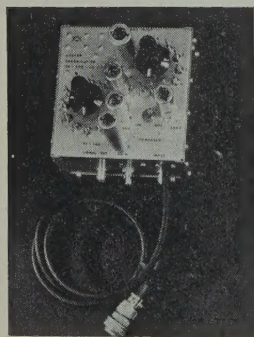
Calibrated delays ..... 120, 1100, 11000  $\mu$ sec

Gate Output available for intensifying and blanking purposes.

External modulation of r.f. oscillator

Special coils for coverage from .012 to 220 MC

## PREAMPLIFIER, PA-620



This Preamplifier is a general purpose device for matching ultrasonic transducers and cables with capacities as high as 100 pfd between 5 and 65 MC, and to provide a limited amount of gain with a good signal to noise ratio. Two of the three stages have variable bandwidth as well as center frequencies. An additional feature is a comparer stage with separate gain control.

### SPECIFICATIONS—

Input impedance ..... 93 to 3200 ohms

Bandwidths ..... 0.5—17 MC

Low noise cascode input with 6922 tube

### ACCESSORIES

A wide variety of accessories built for convenience and accuracy are available—resistors, capacitors and resistances, cable sets and balancing networks.

Single units or decade boxes are conveniently designed in series and parallel combinations.

For details and price list write to:

## ARENBERG ULTRASONIC LABORATORY, INC.

94 Green St., Jamaica Plain 30, Mass.

TEL. JAmaica 2-8640

Please mention JOURNAL OF GEOPHYSICAL RESEARCH, when writing to advertisers

## ARE YOU A MEMBER of AGU?

If you are a reader or user of either of the publications noted below, you should look into this matter.

Members regularly receive  
the monthly

## Journal of Geophysical Research

the quarterly

## Transactions American Geophysical Union

Members are entitled to special discounts on other publications of AGU such as

- **Geophysical Monograph Series**  
(Nos. 1 to 5 available)
- **Izvestiya of the Academy of Sciences, USSR; Geophysics Series**  
for the years 1957, 1958, 1959, and 1960
- **Geodesy and Cartography, USSR.**  
1959
- Annual meeting in Washington in late April or early May each year
- Regional meeting in the Pacific Northwest in autumn
- Regional meeting in the Pacific Southwest in winter
- National Western Meeting, December 1961

For application forms and other information regarding membership meetings, and other matters, write to

## AMERICAN GEOPHYSICAL UNION

1515 Massachusetts Ave., N.W.  
Washington 5, D. C.

(An application form is also inserted in the closing pages of this issue.)



# IONOSPHERIC PROPAGATION and HF COMMUNICATIONS



If you have the background, the imagination and the desire to contribute to important programs in these fields, you are invited to join a carefully selected team of outstanding scientists and engineers now contributing significantly to current knowledge through advanced research.

These programs are being conducted at our **ELECTRO-PHYSICS LABORATORIES** in the **SUBURBAN WASHINGTON, D. C.** area, ideally located from the viewpoint of advanced study which may be conducted at one of several nearby universities; for readily available housing in pleasant residential neighborhoods; and for the general amenities of living offered by this important Metropolitan center. All qualified applicants will receive consideration for employment without regard to race, creed, color or national origin.

#### OUR PRESENT NEEDS ARE FOR:

##### **SENIOR IONOSPHERIC**

**PHYSICISTS** Ph.D. preferred, with several years' experience in the study of Ionospheric phenomena. Should be familiar with present knowledge of upper atmosphere physics and possess an understanding of current programs using rockets and satellites for studies in F-region and beyond. Qualified individuals with supervisory abilities will have an exceptional opportunity to assume project leadership duties in HF projects already under way involving F-layer propagation studies, backed by a substantial experimental program.

##### **SENIOR DEVELOPMENT**

**PHYSICISTS** Advanced degree in Physics or E.E. preferred. Must be familiar with latest techniques in the design of advanced HF receivers and transmitters and possess working knowledge of modern HF networks employing ferrites and metallic tape cores. Strong theoretical background in modern linear circuit theory desired. Will carry out laboratory development and implementation of new HF communications systems.

##### **SENIOR ELECTRONIC**

**ENGINEERS** Advanced degree in E.E. preferred. Must be familiar with conventional pulse circuit designs and applications. Technical background should include substantial experience in data process and data recovery systems using

both analog and digital techniques. Knowledge of principles and application of modern information theory including correlation techniques helpful. Will be responsible for the design of sub-systems.

##### **JUNIOR ELECTRONIC**

**ENGINEERS** To assist Senior Engineers and Scientists in the development of HF communications and data process equipment. Should have formal electronics schooling and 2 years' experience in circuit design checkout or analysis of HF communications, Radar Pulse, Analog/Digital or Data Recovery equipment. Construction of prototypes of new and interesting equipment and design of individual components of communications and data processing systems will comprise the major efforts of selected applicants.

##### **FIELD STATION**

**ENGINEERS** B.S.E.E. or equivalent, consisting of combined civilian or military technical school, with work experience. Presently employed as a field engineer or project engineer with a valid 1st or 2nd Class FCC license and a good command of some of the following: Radar, preferably high power; HF long-distance communications systems; Tropospheric or Ionospheric scatter systems. Must be willing to accept assignments in areas where dependents are not permitted for periods of up to one year. Differential paid for overseas assignments.

For a prompt reply to your inquiry, please forward resume in confidence to: Dept. C-1, W. T. WHELAN, Director of Research & Development

**ACF ELECTRONICS**  
DIVISION

**ACF INDUSTRIES**

**HYATTSVILLE, MARYLAND**



# GEOPHYSICAL MONOGRAPH SERIES

## AMERICAN GEOPHYSICAL UNION

1515 MASSACHUSETTS AVENUE, N.W.

WASHINGTON 5, D. C., U.S.A.

**Antarctica in the International Geophysical Year**—Geophysical Monograph No. 1 (Publication No. 462, National Academy of Sciences—National Research Council); Library of Congress Catalogue Card No. 56-60071; 133 pp. and large folded map of the Antarctic, 1956, 7" x 10", \$6.00. Contains 16 pages by various American authorities on the Antarctic under the headings: General, Geographic and Meteorological, Geological and Structural, Upper Atmospheric Physics, and Flora and Fauna. Map (41" x 41") compiled by the American Geographical Society. Introduction by L. M. Gould.

**Geophysics and the IGY**—Geophysical Monograph No. 2 (Publication No. 590, National Academy of Sciences—National Research Council); Library of Congress Catalogue Card No. 58-60035; 210 pp., 1958, 7" x 10", \$8.00. Contains 30 papers by leading American authorities under the headings: Upper Atmospheric Physics, The Lower Atmosphere and the Earth, and The Polar Regions. Preface by Joseph Kaplan.

**Atmospheric Chemistry of Chlorine and Sulfur Compounds**—Geophysical Monograph No. 3 (Publication No. 652, National Academy of Sciences—National Research Council); Library of Congress Catalogue Card No. 59-60039; 129 pp., 1959, 7" x 10", \$5.50. Based on a symposium held jointly with the Robert A. Taft Sanitary Engineering Center of the U. S. Public Health Service in Cincinnati in November, 1957. Contains 23 papers (some as summaries) with discussion. Preface by James P. Lodge, Jr.

**Contemporary Geodesy**—Geophysical Monograph No. 4 (Publication No. 708, National Academy of Sciences—National Research Council); Library of Congress Catalogue Card No. 59-60065; 96 pp., 7" x 10", 1959, \$5.50. Based on a Conference held at Cambridge, Massachusetts, in December 1958 jointly by the AGU with the Smithsonian Astrophysical Observatory and the Harvard College Observatory. Contains 14 papers by leading authorities, with verbatim discussions on topics ranging from classical geodesy to trilateration by underwater sound to space navigation in the solar system. Edited by Charles A. Whitten and Kenneth H. Drummond.

**Physics of Precipitation**—Geophysical Monograph No. 5 (Publication No. 746, National Academy of Sciences—National Research Council); Library of Congress Catalogue Card No. 60-60010; 435 pp., 7" x 10", 1960, \$12.50. Based on a Conference held at Woods Hole, Massachusetts, in June 1959. Contains 48 papers by leading authorities, with verbatim discussions on topics ranging from planetary-scale phenomena to microanalysis including hail formation and precipitation control. Edited by Helmut Weickmann.

Postage is to be added to prices shown unless payment accompanies order. Quantity discounts (count each Monograph separately): 5-19 copies, 10%; 20-49 copies, 15%; 50 or more copies 20%.

### Purchase Order

### TO AMERICAN GEOPHYSICAL UNION

1515 Massachusetts Avenue, N.W., Washington 5, D. C., U.S.A.

Please enter our order for the following:

_____ copies of Geophysical Monograph No. 1, at \$6.00 *	\$ _____
_____ copies of Geophysical Monograph No. 2, at \$8.00 *	\$ _____
_____ copies of Geophysical Monograph No. 3, at \$5.50 *	\$ _____
_____ copies of Geophysical Monograph No. 4, at \$5.50 *	\$ _____
_____ copies of Geophysical Monograph No. 5, at \$12.50 *	\$ _____

☐ Payment of \$ \_\_\_\_\_ is enclosed.

☐ Please send invoice, adding postage charges.

☐ Enter our standing order for \_\_\_\_\_ copies of subsequent Geophysical Monographs at the special prepublication rates, e.g., prepublication rate for Monograph No. 4 for non-members was \$4.00, payment in advance, or \$4.75 (plus postage) on invoice.

\* List price is net for quantities up to four; see above for discounts on quantity purchases. Special discounts to members.

Typed name \_\_\_\_\_ Signature \_\_\_\_\_

Address \_\_\_\_\_

Please mention JOURNAL OF GEOPHYSICAL RESEARCH, when writing to advertisers



# *Journal of Geophysical Research*

## BACK ISSUES AVAILABLE

### **Volume 64, 1959**

**Total 2488 pages**

Complete Volume	\$30.00
January, 132 pp.	\$2.00
February, 138 pp.	\$2.00
March, 112 pp.	\$2.00
April, 106 pp.	\$2.00
May, 98 pp.	\$2.00
June, 110 pp.	\$2.00
July, 168 pp.	\$2.00
August, 268 pp.	\$4.00
September, 230 pp.	\$3.00
October, 284 pp.	\$4.00
November, 390 pp.	\$5.00
December, 452 pp.	\$6.00

### **Volume 65, 1960**

**Total 4248 pages**

Complete Volume	\$42.00
January, 384 pp.	\$5.00
February, 414 pp.	\$5.00
March, 284 pp.	\$4.00
April, 248 pp.	\$4.00
May, 314 pp.	\$4.00
June, 220 pp.	\$4.00
July, 348 pp.	\$4.00
August, 350 pp.	\$4.00
September, 462 pp.	\$6.00
October, 490 pp.	\$6.00
November, 344 pp.	\$4.00
December, 390 pp.	\$5.00

### **SYMPOSIA REPRINTED from JGR**

International Symposium on Electronic Distance-Measuring Techniques (144-page Symposium reprinted from the February 1960 issue)	\$3.50
Symposium on Sferics and Thunderstorm Electricity (102-page Symposium reprinted from the July 1960 issue)	\$3.50
Symposium on the Exosphere and Upper F Region (74-page Symposium reprinted from the September 1960 issue)	\$2.50
Scientific Effects of Artificially Introduced Radiations at High Altitudes (74-page Symposium reprinted from the August 1959 issue)	\$1.50
International Symposium on Fluid Mechanics in the Ionosphere (202-page Symposium reprinted from the December 1959 issue)	\$4.50

### **AMERICAN GEOPHYSICAL UNION**

**1515 Massachusetts Avenue, N.W., Washington 5, D. C.**

To obtain back issues for 1958 and earlier years, write to  
Walter J. Johnson, Inc., 111 Fifth Avenue, New York 3, New York.



43RD ANNUAL MEETING  
AMERICAN GEOPHYSICAL UNION  
APRIL 25 through 28, 1962  
WASHINGTON, D. C.

*your participation  
is welcomed*

If you want to present a paper  
send the abstract BEFORE DEADLINE DATE to

<i>Hydrology</i>	<i>before January 2, 1962, to Harry E. Schwarz, 315 Ladson Road, Silver Spring, Md.</i>
<i>Meteorology</i>	<i>before January 9, 1962, to William Hiatt, US Weather Bureau, Washington 25, D. C. (abstract plus comprehensive summary)</i>
<i>Geodesy</i>	<i>before February 1, 1962, to Erwin Schmid, US Coast &amp; Geodetic Survey, Washington 25, D. C.</i>
<i>Seismology</i>	<i>before February 1, 1962, to Benjamin F. Howell, Jr., Geophysical Laboratory, Mineral Sciences Bldg., Pennsylvania State Univ., University Park, Penna.</i>
<i>Oceanography</i>	<i>before February 1, 1962, to Arthur E. Maxwell, 5627 Potomac Avenue, N.W., Washington 16, D. C.</i>
<i>Volcanology, Geochemistry, and Petrology</i>	<i>before February 1, 1962, to David R. Wones, US Geological Survey, Washington 25, D. C.</i>
<i>Geomagnetism and Aeronomy</i>	<i>before February 1, 1962, to J. Hugh Nelson, US Coast and Geodetic Survey, Washington 25, D. C.</i>
<i>Tectonophysics</i>	<i>before February 1, 1962, to Mrs. Iris Borg, Box 579, Livermore, California</i>
<i>Planetary Sciences</i>	<i>before February 1, 1962, to Robert Jastrow, Goddard Institute for Space Studies, 475 Riverside Dr., New York 27, N. Y.</i>
<i>General Program</i>	<i>to Leroy R. Alldredge, 10500 Royal Rd., Silver Spring, Md.</i>

*Be sure to*

send 3 copies, including ribbon copy, of the abstract

double or triple space

make it concise—about 200 words

use correct format: John Doe (Physics Dept., Iowa State University, Ames, Iowa) Short-Period Micropulsations—The geographical extent,

see December *Transactions*, p. 465, for complete details on the meeting



# Journal of GEOPHYSICAL RESEARCH

VOLUME 66

DECEMBER 1961

No. 12

## Cosmic Ray Evidence for a Ring Current

P. J. KELLOGG AND J. R. WINCKLER

*School of Physics, University of Minnesota  
Minneapolis, Minnesota*

**Abstract.** Many observations show that low rigidity protons from solar flares are permitted entry at Minneapolis only during the main phase of magnetic storms. The measured energy is much below the normal Störmer cutoff at that time. This paper develops the idea that a ring current responsible for the main storm field reduces the Störmer cosmic-ray cutoffs. The model of the ring chosen is actually an azimuthal current on the surface of a sphere with current intensity proportional to  $\sin \theta$  where  $\theta =$  colatitude. It is shown that this mathematical form permits great simplicity in the analysis and leads to essentially the same result as a diffuse ring corresponding to the actual trapped radiation. The magnetic moment of the ring required to produce the cutoff change can be provided by reasonable intensities of very low energy trapped radiation. It is shown that the cosmic-ray data permit one to evaluate both the magnetic moment ( $M'$ ) and radius ( $R$ ) of the ring, whereas the surface magnetic measurements determine only the quantity  $M'/R^3$ . Since observation shows that the cosmic-ray cutoffs return to normal during the main phase, it must be assumed that the ring shrinks inward so that the surface field is maintained negative. Cosmic-ray evidence concerning the presence of a permanent ring current is discussed. Such a ring is measured directly by satellites during quiet times.

On several occasions during the past 3 years, cosmic-ray protons have been observed at balloon altitudes at Minneapolis (56°N geomagnetic latitude) that have energies much lower than those normally allowed by the earth's magnetic field (Peterson, Arnoldy, Hoffman, Peterson, and Winckler, 1959; Freier, Ney, and Winckler, 1961; Winckler, Bhavsar, and Peterson, 1961). During some of these events, protons of energies down to 75 Mev have been observed. At times it is clear that a cutoff is imposed by the earth's field and has a value of 250 to 300 Mev. The low rigidity protons are observed at Minneapolis only during magnetic storms, and an important step in the interpretation of these events was made when one of us (R.W.) noticed that the arrival of low energy protons coincided not with the beginning of the storm, but with the main phase of the storm, which is defined as the time when the horizontal component of the field at the equator

is decreased. In Figures 1 and 2, two examples of this correlation are presented. In one instance the positive, initial phase of the storm lasted only 20 minutes, and in the other it lasted nearly 9 hours. In each case, however, the arrival of the low energy protons coincided with the beginning of the main phase.

Table 1 gives a summary of all events observed by balloons at Minneapolis. In every case where a beam of sufficient intensity existed in space, and a storm occurred, protons below the normal cutoff at Minneapolis were observed.

For a long time [Schmidt, 1924] the main phase of a magnetic storm has been attributed to the formation of a ring current around the earth, but there has been little proof of this hypothesis. The effect of a ring current on cosmic rays has been discussed by Störmer [1955] and by Ray [1956]. We shall now apply their analysis to the events under discussion and show that the observed effects may be reasonably at-



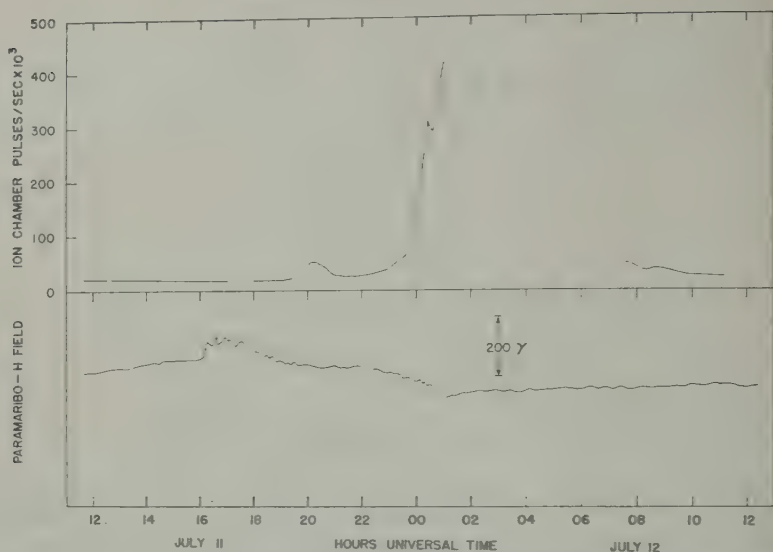


Fig. 1. Solar protons at Minneapolis and equatorial magnetic field for July 11-12. (For details see *Winckler, Bhavsar, and Peterson [1961].*)

tributed to a ring current, and, further, that observations at a northerly latitude like that of Minneapolis give new information on its size.

The ring current is presumably due, as was first suggested by *Singer [1957]*, to charged particles trapped in the earth's magnetic field in the same way that the Van Allen radiation belts are trapped. Trapped particles contribute to the earth's field in three ways: (1) their spiral

motion around lines of magnetic field gives them a magnetic moment  $W_{\perp}/B$ ; (2) the gradient of the field causes the particles to precess around the earth, giving an effective current which is in the westward direction if the earth's field is not seriously perturbed.  $W_{\perp}$  and  $W_{\parallel}$  are the perpendicular and parallel energies, and  $B$  is the magnitude of the magnetic field. The problem of solving for

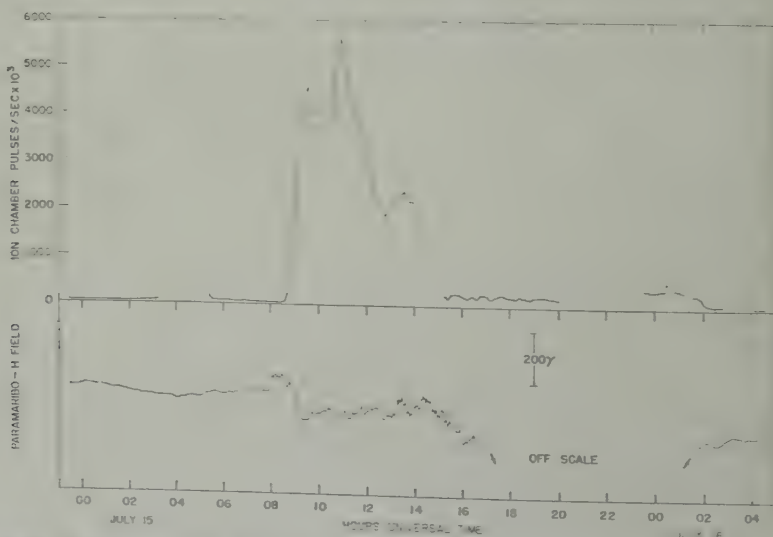


Fig. 2. Solar protons at Minneapolis and equatorial magnetic field for July 15-16. (For details see *Winckler, Bhavsar, and Peterson [1961].*)



g magnetic field is a complicated non-  
ne. We may discuss roughly the effects  
expected on the assumption that the  
field is not much perturbed by the trapped  
s. This assumption is a poor one but it is  
difficult to go further. On the assumption  
the trapping field is a dipole field, effects  
(3) give contributions to the magnetic  
t of the ring of (2)  $\frac{2}{3}W_{\perp}/B$  and (3)  
for particles at the equator. All three  
contributions to the magnetic moment of the

ring have the same direction. If the ring is large  
compared to the earth, then the fields produced  
at the earth are inversely proportional to the  
cube of the ring radius so the three fields are  
(1)  $W_{\perp}/B_0$ , (2)  $\frac{2}{3}W_{\perp}/B_0$ , and (3)  $2(W_{\parallel}/B_0)$   
where  $B_0$  is the magnitude of the earth's surface  
field at the equator. The field produced by the  
intrinsic magnetic moment (1) is opposite the  
fields (2) and (3), and the latter are opposed to  
the earth's own field. At the earth all three  
contributions to the field are of the same order

TABLE 1. Correlation of Cutoff Changes and Magnetic Field at Minneapolis

Cosmic Ray Flare		Related Sudden Commencement		Begin Negative Phase		Low-Energy Cosmic Ray Increase		Notes
Date	UT	Date	UT	Date	UT	Date	UT	
Mar. 23, 1958	0950	Mar. 25	1540	Mar. 26	1300	Mar. 26	1330	*Event includes evidence for trapping in solar cloud.
Aug. 22, 1958	1417	Aug. 24	0140	Aug. 24	0330	Undetected		Free space intensity probably too low to detect during main phase.
May 10, 1959	2055	May 11	2320	May 12	0430	May 12	0400-0500	Inferred from total difference between two flights.
July 10, 1959	0210	July 11	1623	July 11	2300	July 11	2330	
July 14, 1959	0325	July 15	0802	July 15	0830	July 15	0830	
July 16, 1959	2114	July 17	1638	July 17	1900	July 17	1900	
April 1, 1960	0843	Mar. 31	0800	Mar. 31	1600	April 1	0945	Main phase already in progress at time of cosmic ray flare.
April 5, 1960	0215	None		None		Undetected		Although free space rates high, no cosmic rays at Minneapolis.
April 28, 1960	0130	April 27	2000	April 27	2100	April 28	0315	Main phase in progress at time of cosmic ray flare.
April 29, 1960	0107	April 30	0130	April 30	0330	Apr. 30 before	0600	Very weak event in >100 Mev range.
May 4, 1960	1340	None		None		No low energy particles		All particles measured were above normal cutoff.
Sept. 3, 1960	0040	Sept. 4	0230	Sept. 4	0400	Sept. 4 about	0400	
Nov. 12, 1960	1322	Nov. 12	1348	Nov. 12	1740	Nov. 12 before	2000	*Main phase in progress at time of balloon ascent.
Nov. 15, 1960	0207	Nov. 15	1303	Uncertain	1400	Nov. 15	1400-1500	*Sudden commencement and storm from previous flare. Interpretation difficult.

Evidence indicates trapping in solar cloud, producing possible increases at time of sudden commencement associated with beam to space.

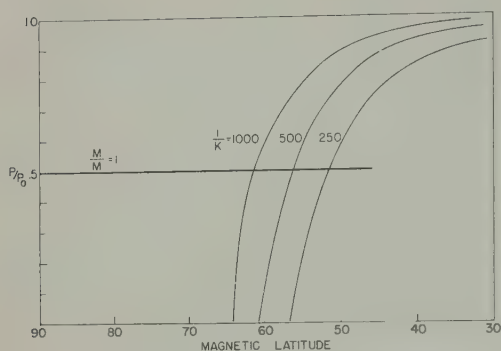


Fig. 3. Fractional reduction of cutoff rigidity due to ring currents with various parameters.

of magnitude. This is not true near the trapping region, however, since the field of a magnetic moment varies inversely as the cube of distance whereas that of a current element varies only inversely as the square. In the trapping region, the intrinsic magnetic moment produces most of the perturbation field, provided that the particle distribution is not too diffuse.

In spite of this we shall take as a model for the field of trapped particles the field produced by a simple ring current which cannot represent the intrinsic magnetic moment contribution. Great simplicity is gained, and the error introduced is probably not as large as might appear at first sight. It will turn out that the cosmic-ray effects depend only on the vector potential, and this, being the integral of the field, is not so strongly changed by the intrinsic moment field which is dominant in a fairly small region. Further, some of our results will be independent of the model.

In this rough approximation the ring current may be described by giving its radius and its magnetic moment. In an appendix, the theory of Störmer and of Ray is presented in a form that makes a close connection of the theory to the measured magnetic field in the equatorial plane. In Figure 3, results of calculations are presented for a model in which the current is not a ring but an azimuthal current on the surface of a sphere of radius  $R$ , the current being proportional to  $\sin \theta$  ( $\theta$  = colatitude). The effect of such a ring current on the cutoff rigidity for cosmic ray particles may be described as follows: The curve of critical rigidity versus latitude has two parts, depending on whether the Störmer pass closes inside or out-

side the ring current. The part of the curve pertaining to high latitudes corresponds to closing of the pass outside of the ring current. For this branch of the curve the cutoff rigidity is reduced from the Störmer value by a factor of  $(1 + M'/M)$

$$P = \frac{P_0}{1 + \frac{M'}{M}} \quad P_0 C = \frac{ZeM}{4R_E^2} \sin^4 \theta$$

where  $M'$  is the magnetic moment of the ring current and  $M$  is the magnetic moment of the earth. The branch of the curve that applies to middle and equatorial latitudes depends only on the parameter  $M'/R^3$  and has a more complicated form. As one proceeds southward from the intersection of the two curves the cutoff rigidity is reduced rapidly toward the Störmer cutoff  $P_0$ .  $2M'/R^3$  is just the magnetic field at the center of the ring current and is therefore the magnetic storm field. Thus at middle and low latitudes the reduction in cosmic-ray cutoff is a function of the storm field. This agrees with the observations of Yoshida and Wada [1959]. At higher latitudes the reduction of cutoff is not a function of the storm field, though we expect the two to be correlated.

Ray [1956] has calculated the effect of a current that flows in a ring. His results are similar to those for the model presented here. In the Appendix the general theory for the effect of a ring current which has previously been given by Störmer and Ray is presented in a form that allows one to see more clearly the effects of different ring currents.

We now show how this analysis can be used to determine the parameters of the ring. Suppose that during a magnetic storm the cutoff rigidity at Minneapolis is reduced by a factor of 2. Then (see Fig. 3) two things are necessary: the magnetic moment of the ring must be at least equal to or greater than the magnetic moment of the earth, and the parameter  $M'/R^3$  must also be sufficiently large. If we take the latitude of Minneapolis to be  $56^\circ$ , then  $M'/R^3 > 1/500 M/R_E^3$ . The parameters of the ring which give a cutoff at Minneapolis reduced by a factor of 2 are those with values in the shaded area on Figure 4. Additional information on ring parameters is given by observation of the earth's magnetic field, which determines the quantity  $M'/R^3$ . Suppose that the storm



at the equator has a value of 125  $\gamma$ . The parameters of the ring must then fall on the inner curve in Figure 4, and so the ring radius is larger than  $8R_E$  and its magnetic moment larger than  $M$ .

Calculating more accurately the parameters of the storm time ring, we are somewhat hindered because we do not know accurately what the magnetic cutoff at Minneapolis should be in the absence of a ring. Let us assume that about 530 Mev corresponding to the Quenby cutoff of 1.16 bev (Cogger, unpublished, 1960) for Minneapolis, and that this is reduced to 250 Mev by the quiet ring. For magnetic storms the cutoff at Minneapolis is reduced to below 75 Mev, and therefore the magnetic moment of the ring must increase to more than  $1.9M$ . However, there is evidence from neutron and gamma-ray production [Sar, 1961] by protons in the atmosphere that the cutoff is reduced to at least 40 Mev at Minneapolis which would require the ring to have a magnetic moment equal to  $3M$ . For this case the parameters of the ring must fall on the dotted boundary in Figure 4.

As has been mentioned, the cutoff at Minneapolis depends only on the magnetic moment of the ring, whereas the storm field at the equator depends on  $M'/R^3$ . Therefore we should not expect to find perfect correlation between the cutoff at Minneapolis and the storm field, even for a simple explanation. In real cases the ring current presumably has a structure that is described by an even larger number of parameters which further loosen the connection between cosmic-ray and magnetic observations. For example, it is possible to construct a ring current with a nonzero magnetic moment which produces a magnetic field at the center, which would then produce cosmic-ray cutoffs without producing observable magnetic effects. Another complexity which we have ignored concerns azimuthal asymmetry. We shall show that the energy of particles producing the ring may be quite low and so their drift time around the earth is comparable to the characteristic times of storms. There may be variations in the ring current with longitude, and perhaps a local time variation of cutoff.

In fact, it is observed that the cutoff at Minneapolis usually returns toward its usual value before the magnetic storm is over, and from

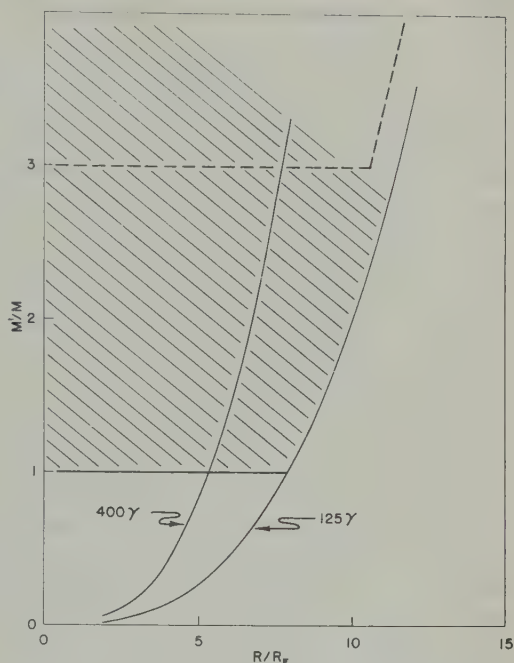


Fig. 4. Shaded area gives space of ring parameters which reduce cutoff rigidity at Minneapolis by more than a factor of 2. See text for further explanation.

this we can infer that during a magnetic storm the ring current must move inward. Suppose, for example, that the magnetic storm field remains constant while the cutoff at Minneapolis returns toward its normal value. Then the ring parameters must move along a curve line like the 125- $\gamma$  curve in Figure 4 and must move toward the origin and out of the region which represents a significantly lowered cutoff. The ring therefore shrinks in such a way that  $M'/R^3$  is constant but  $M'$  decreases, returning the cutoff at Minneapolis to normal. An example of this is shown in Figure 2. During the storm of July 14, the magnetic field at the equator was reduced by about 125  $\gamma$  for several hours, and then at about 1700 dropped further to about 400  $\gamma$  negative. The earth's field recovered slowly from the large decrease, and at 0300 on July 16, a  $D_{st}$  analysis communicated to us by Chapman and Akasofu shows that  $H$  at the equator is depressed by 200  $\gamma$ . At this time, solar protons were no longer arriving at Minneapolis, although measurements at Murmansk [Charakhchian, Tulinov, and Charak-

hchian, 1960] showed that there was still a strong beam in space. In Figure 4 we have drawn a curve for a ring current producing a field of 400  $\gamma$  (twice that observed, and corresponding to the maximum of the ring). It may be seen that even for such a large field, shrinkage of the ring to 4 earth radii would reduce its effect on cutoffs to small values.

*The possibility of a quiet ring.* The storm-time ring current discussed above appears quite reasonable in the light of the important evidence for a quiet time ring obtained by *Smith, Coleman, Judge, and Sonett* [1960]. They found that, at a distance of  $10R_E$ , the earth's field differs radically from the field produced in the earth's interior, and that the difference could be ascribed to a toroidal ring current having a major radius of  $10R_E$  and a magnetic moment  $\frac{1}{2}M_E$ . Their analysis used a ring current model and neglected the intrinsic magnetic moment contribution, so that their interpretation is not valid to high accuracy. Their results were obtained at magnetically quiet times and so indicate that a ring is a permanent feature of the earth's environment, which is intensified during storms.

There is also cosmic-ray evidence which may be interpreted as indicating the presence of a permanent ring current. Table 2 presents a number of measurements of cosmic-ray cutoff rigidities together with the values calculated according to the theory of Quenby and Webber by Cogger (unpublished, 1960). Figure 5 displays the ratio of the measured cutoff rigidity to the calculated values as a function of the effective latitude of Quenby and Webber's the-

ory. There is considerable scatter but it will be seen that at northern latitudes the measured value lies well below the calculated value. The curve gives the cosmic-ray cutoff to be expected in the presence of a ring current with a magnetic moment equal to one-half the earth's and a radius of  $8R_E$ . Thus the cosmic-ray cutoff at quiet times seems to indicate a ring current.

At present the whole question of cosmic-ray cutoffs at high latitudes is a vexing one, however, and the experimental situation is consistent with a permanent ring current, but does not require it. The measured cutoffs never appear to be sharp (Ney and Freier, private communication), and the reason for this is not clear. It may be due to penumbra effects, to time variations of the field, or to energy loss in comparison with the theoretical side, the calculation of the cutoff in the absence of a ring is uncertain. The Quenby and Webber value for Minneapolis is 1.16 bev, the Rothwell value is 0.88 bev, but machine calculations by one of us (P.J.K.) indicate a value greater than 1 bev.

*Trapped radiation intensity and ring current.* We now estimate the flux of charged particles which is required to give a ring current of magnetic moment  $\frac{1}{2}M_E$ . Since the magnetic moment of the ring depends on the total energy of trapped particles we need to know the average energy in order to calculate their flux. The radiation counters carried in Explorers IV, VI, and VII do not indicate much radiation in the region we are considering, so the average energy may be below their detectability threshold of about 20 kev. Rockets fired into auroras in the auroral

TABLE 2. Comparison of Cosmic Ray Cutoff Rigidities

Location		Reference	Cutoff, bev	Cutoff Q and W, bev	Q and Lat.?
32.1°N	95.5°W	Guss (1960)	5.00 ± 0.5	4.4	42.4
32.3°N	97°W	Freier, Ney, Waddington [1959a]	4.6 ± 0.2	4.4	42.6
38.6°N	95.5°W	McDonald [1959]	2.25 ± 0.15	2.35	50.6
45.75°N	96.5°W	McDonald [1959]	0.8 ± 0.1	1.24	58.2
42.6°N	88.1°W	McDonald [1957]	1.41 ± 0.08	1.31	56.0
44.6°N	92.7°W	McDonald [1957]	1.20 ± 0.04	1.30	57.7
45.5°N	8°E	Fowler, Waddington [1956]	4.7 ± 0.15	4.0	44.3
51.5°N	2.6°W	Waddington [1956]	2.6 ± 0.1	2.12	52.1
43.8°N	91.5°W	Fowler, Freier, Ney [1958]	< 1.14	1.31	57.0
46.1°N	88.4°W	Ney (Private communication)	0.6 ± 0.1	0.95	60.0



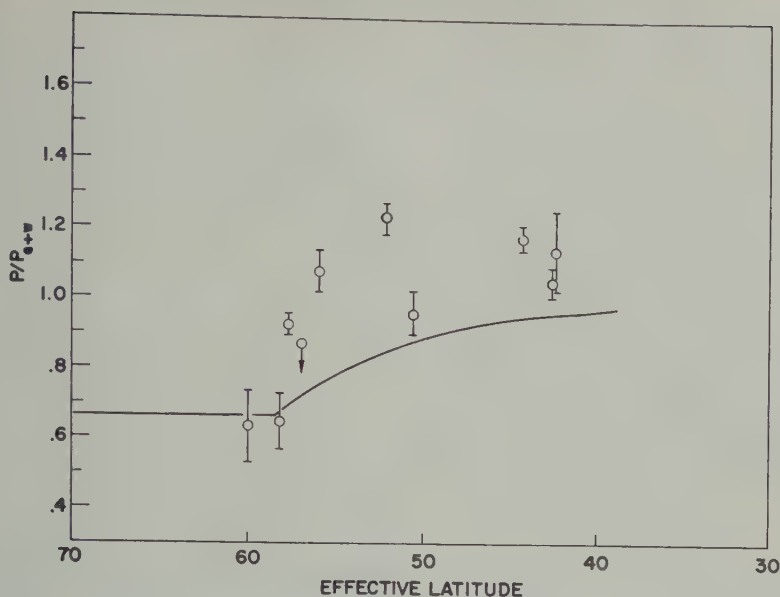


Fig. 5. Measured values of cutoff rigidity and calculated cutoff for a ring with  $M' = \frac{1}{2}M$ ,  $R = 8R_E$ .

have detected large fluxes of electrons of energy 5 kev [McIlwain, 1960], the energy in this case being not much above the threshold of detectability. Lines of force from the auroral region go through the trapping region we are considering, and so it seems reasonable to believe that the auroral electrons are samples of particles trapped in the ring current. This argument is somewhat strengthened by the observation that electrons that appear in the aurora over Minneapolis have energies comparable to those trapped along the same line of force, but it remains a weak argument nevertheless, and we must admit that we do not even know the kind of particle that produces the ring current.

We take the average energy to be 5 kev, therefore, but this may only represent an upper limit. If the center of gravity of the ring is at  $3R_E$  and we take the average contribution to the magnetic moment per particle to be  $2W/B$ , the total number of 5-kev particles required to give  $\frac{1}{2}$  the earth's moment is  $2.5 \times 10^{30}$ . If we take the ring to be a torus of minor radius  $3R_E$  and major radius  $8R_E$ , then the electron flux must be  $\approx 10^8$  electrons/sterad  $\text{cm}^2$  sec. This is comparable to the flux of higher energy electrons in the outer Van Allen zone. Thus we have evidence that low energy particles are trapped out to distances far beyond what is normally called

the peak of the outer Van Allen zone. If the trapped particles were protons of the same energy, their flux would be lower by a factor of  $(m/M)^{1/2} \approx 40$ . The trapped particles could also be protons of higher energy, corresponding to a still lower flux.

Recently, results from ion traps carried on Soviet space probes have become available. They find a flux of  $2 \times 10^8$  particles/ $\text{cm}^2$  sec of electrons of energy 200 —  $10^4$  ev. Their measurements were made on September 12–13, 1959, two of the 10 quiet days for that month. This flux seems lower than that required to give a significant quiet ring, but the volume of the ring and the energy spectrum of the particles are as yet too uncertain for a definite conclusion. In fact, Gringauz [1961] concludes that the flux he measured is consistent with the results of Smith, Coleman, Judge, and Sonett [1960]. We note also that the Soviet ion traps could not have measured a flux of the order of that calculated here as their instrument was nearly saturated at the level they did observe.

Changes in geomagnetic cutoffs have also been discussed by Obayashi [1959] and by Rothwell [1959]. In their theories, the earth's magnetic field is affected at large distances by a magnetic field carried by plasma clouds from the sun. These theories differ in end results from

the one presented here in that the cutoff at sufficiently far northern latitudes is reduced to zero, rather than to a finite fraction of the Störmer value.

Obayashi also discusses the effect of the compression of the earth's field by a plasma cloud which would be the effect expected on Chapman and Ferraro's model for the initial phase of a magnetic storm. The effect of such a compression is to increase the cutoff rigidity. Decreases in solar proton intensity corresponding to such increases in cutoff rigidity at the time of sudden commencement have been observed and these confirm the Chapman-Ferraro theory of the initial phase as the lowering of cutoff confirms the ring current theory of the main phase.

# APPENDIX

In this appendix we present the analysis of Störmer and of Ray in a different form which leads to an approximation which is often quite useful.

We proceed as usual with Störmer theory by writing down the equations of motion of a charged particle in a magnetic field with cylindrical symmetry. Such a symmetrical magnetic field can always be derived from a vector potential in the azimuthal direction,  $A_\phi$ . On account of the symmetry, the canonical angular momentum is conserved, and also the particle's speed. The angular momentum equation may be solved for the azimuthal component of velocity to give, in spherical coordinates,  $r, \theta, \phi$ :

$$\begin{aligned} \frac{v_\phi}{v} &= \frac{L}{pr \sin \theta} - \frac{e}{pc} A_\phi \\ &= \frac{2\gamma}{y \sin \theta} - \frac{\sin \theta}{y^2} \end{aligned} \quad (1A)$$

where  $e, p, v$  and  $L$  are the particles' charge, momentum, velocity, and angular momentum at infinity. The second part of the equation shows the usual form for this equation, with the dimensionless variables introduced by Störmer

$$R_{st}^2 = \frac{eM}{pc} \quad y = r/R_{st} \quad \gamma = \frac{L}{2pR_{st}}$$

and the vector potential for the earth's dipole field given by

$$A_\phi = + \frac{M \sin \theta}{r^2} \quad (2A)$$

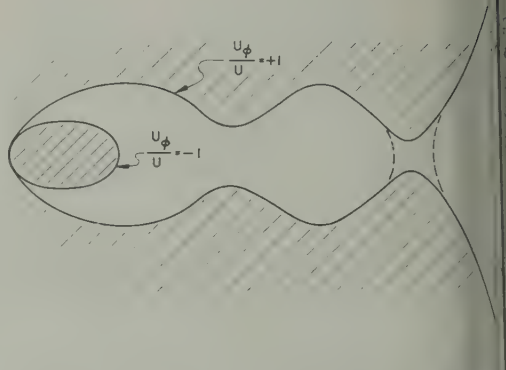


Fig. 6. Allowed and forbidden Störmer regions.

Clearly  $v_\phi/v$  must lie between  $-1$  and  $1$ , regions where this is not so, being forbidden.

The vector potential for the earth's dipole field is positive everywhere. The total vector potential will be positive everywhere, for a reasonable choice of ring current.

The two terms on the right-hand side of equation 1A represent respectively the effect of centrifugal force, and of the magnetic field in keeping the particle away from the axis. We are interested in particles that can reach the earth even though  $R_{st}$  is considerably greater than the radius of the earth, and for this to be possible the effects of centrifugal force and magnetic field must nearly balance, i.e., the two terms of equation 1A must be of opposite sign. Therefore  $L$  must be positive and, as we are interested in the smallest possible momentum which allows a particle to reach a given point on the earth, we need large values of  $L$  to compensate the second term. But the effect of centrifugal force extends to greater radii than that of magnetic field so that if  $L$  is too large, the particle is never allowed to approach close enough to the axis to feel the attractive effect of the magnetic field.

The general situation is illustrated in Figure 7 which the reader will recognize as a generalization of the well-known Störmer diagram. The solid lines bound the forbidden region for a value of  $L$  which is just sufficiently small to allow particles to enter the region where the magnetic field dominates. For a slightly larger value of  $L$ , the forbidden region would be bounded by the dotted curve, and particles would be repelled by centrifugal force before they could reach the earth, and we say that the pass is closed.



consider now a plot of the function  $v_\phi/v$  of on 1A for  $\theta = \pi/2$ . In the region near this function will come close to +1, not touching the line  $v_\phi/v = +1$  if the pass is, and rising slightly above it if the pass is. When the pass is just closed, we have a t with zero slope, therefore

$$\frac{e}{pc} A_\phi \left( r, \frac{\pi}{2} \right) = +1$$

$$-\frac{L}{pr^2} - \frac{e}{pc} \frac{\partial A_\phi}{\partial r} \left( r, \frac{\pi}{2} \right) = 0 \quad (3A)$$

two equations determine the critical value and the radius  $R$  at which the pass closes. s we have assumed that all passes close at equator. This assumption seems to be true asonable ring currents, but it implies that current is fairly diffuse.

y consider equation 1A evaluated at the e of the earth. Since  $L$  has been deter-, and  $A_\phi$  is known at the earth's surface, equation determines  $p$  as a function of le, and of  $v_\phi/v$ . This is the smallest  $p$  that a particle through the pass, and is, there- the cutoff momentum.

ave, then, a complicated set of three ions to solve in order to obtain the cutoff entum. In general this must be done rically in each case. For example, the r potential of a current flowing on the ce of a sphere of radius  $R$ , and having etic moment  $M'$ , is

$$A_\phi' = \begin{cases} \frac{M' \sin \theta}{r^2} & r > R \\ \frac{M' r \sin \theta}{R^3} & r < R \end{cases}$$

ng this function, equations 3A were solved rically to give Figure 3.

can, however, present an approximation is sufficiently good to allow one to see the effects of various ring currents.

assume that the actual vector potential of ing,  $A_\phi'$  is small compared to the vector tial of the earth. Equations 3A then e:

$$\frac{eM}{pcR^2} - \frac{e}{pc} A_\phi'(R) = +1$$

$$\frac{L}{pR^2} + 2 \frac{eM}{pcR^3} - \frac{e}{pc} \frac{\partial}{\partial r} A_\phi'(R) = 0 \quad (4A)$$

where we drop the argument  $\pi/2$  in  $A_\phi'$ , and these can be solved to give to first order in  $A_\phi'$

$$R^2 = R_{st}^2 - \frac{e}{pc} \left[ A_\phi'(R_{st}) + R_{st} \frac{\partial A_\phi'(R_{st})}{\partial r} \right]$$

$$= R_{st}^2 + \frac{e}{pc} B_\theta'(R_{st}) \quad (5A)$$

$$L = 2pR_{st} + \frac{e}{c} R_{st} A_\phi'(R_{st})$$

with  $R_{st}^2 = eM/pc$ .

We calculate only the vertical cutoff so that  $v_\phi/v = 0$ . Then equation 1A reads, when evaluated at the earth's surface,

$$0 = \frac{L}{pR_E \sin \theta} - \frac{eM \sin \theta}{pcR_E^2} - \frac{e}{pc} A_\phi'(R_E, \theta)$$

$$= \frac{2}{R_E \sin \theta} \sqrt{\frac{eM}{pc}} - \frac{eM \sin \theta}{pcR_E^2} \quad (6A)$$

$$+ \frac{e}{pcR_E \sin \theta} R_{st} A_\phi'(R_{st}) - \frac{e}{pc} A_\phi'(R_E, \theta)$$

If  $A_\phi'$  were zero, equation 6A could be solved for  $p$  to give the familiar dipole result

$$pc = \frac{eM}{4R_E^2} \sin^4 \theta, \quad R_{st} = \frac{2R_E}{\sin^2 \theta} \quad (7A)$$

for the cutoff momentum in the vertical direction at colatitude  $\theta$ . We put

$$pc = \frac{eM}{4R_E^2} \sin^4 \theta (1 + \delta) \quad (8A)$$

and find

$$\delta = -\frac{4R_E^2}{M \sin^4 \theta} A_\phi' \left( \frac{2R_E}{\sin^2 \theta}, \frac{\pi}{2} \right)$$

$$+ \frac{2R_E^2}{M \sin \theta} A_\phi'(R_E, \theta) \quad (9A)$$

where, for definiteness, we have inserted the angular argument in  $A_\phi$ . At northern latitudes (but not at the equator) and for reasonable ring currents, the second term is negligible.

In order to show the ease with which this theory may be applied, we use it to determine qualitatively the cutoff as a function of latitude due to a ring current of the kind calculated by *Apel* [1960]. In the topmost section of Figure 7 we show the sort of field which *Apel* obtains as due to trapped particles in the outer Van Allen

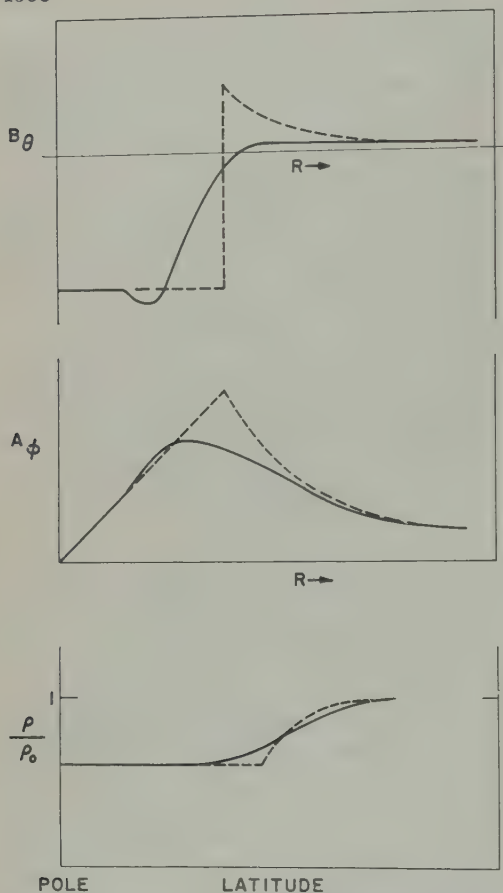


Fig. 7. Approximate cutoff calculation for a diffuse ring current.

Zone. The dotted curves show quantities given by our shell model which has been adjusted to give the same field at the center of the earth and at large distances. Apel's model gives a very small positive ring field as the current which he chooses is very diffuse and there is also a small pip at the inner part of the ring due to the diamagnetic effect. The center section of Figure 7 gives the vector potential computed from the formula

$$B_{\theta} = -\frac{1}{r} \frac{\partial}{\partial r} (r A_{\phi})$$

The principal effect of the diffuse ring is to round off the 'break' between the two curves. The small negative pip has very little effect on the vector potential. Changes in cutoff may be computed directly from the vector potential according to equation 9A. Note that a latitude near the poles

corresponds to a vector potential near infinity. At infinity the vector potential of the ring is just  $M'/R^2$  so that  $\delta = -(M'/M)$  and  $P/P_0 = 1 - M'/M$ . The exact result is  $P/P_0 = 1/(1 + M'/M)$  which is the same to the order calculated. This suggests that, for  $\delta$  given by equation 9A,  $P/P_0 = 1/(1 - \delta)$  is a better approximation than  $P/P_0 = 1 + \delta$  and numerical results seem to bear this out.

The bottom section of Figure 7 shows the cutoff  $P/P_0$ . This graph has been reversed in order to agree with Figure 3, so that cutoff at the left side of the graph near the pole corresponds to value of the vector potential at the right side of the upper two graphs.

*Acknowledgment.* This work was sponsored by the Office of Naval Research and the National Science Foundation.

#### REFERENCES

- Anderson, K. A., R. Arnoldy, R. Hoffman, Peterson, and J. R. Winckler, Observations of low-energy solar cosmic rays from the flare of 22 August 1958, *J. Geophys. Research*, **64**, 1133-1147, 1959.
- Apel, J. R., Geomagnetic field perturbations due to trapped particles, University of Maryland, Thesis 1960 (unpublished).
- Bhavsar, P. D., Gamma-rays from the solar cosmic ray-produced nuclear reactions in the earth's atmosphere, abstract, *J. Geophys. Research*, **66**, 2513-2514, 1961.
- Charakhchian, A. N., V. F. Tulinov, T. N. Charakhchian, Cosmic rays emitted by the sun, *Space Research*, edited by H. Kallmann, North-Holland Publishing Company, Amsterdam, pp. 649-661, 1960.
- Cogger, L. I., Magnetic cut-off rigidities according to the formulations of P. Rothwell and of J. Quenby and W. R. Webber, Atomic Energy, Canada, Ltd., Report AECL-1104, unpublished, 1960.
- Fowler, P. H., and C. J. Waddington, The energy distribution of cosmic ray particles over northern Italy, *Phil. Mag.*, **1**, 637, 1956.
- Fowler, P., P. S. Freier, and E. P. Ney, The primary alpha-particle spectrum over North America and geomagnetic cutoff energies, *Nuovoimento Suppl.*, **8**, 492-499, 1958.
- Freier, P. S., E. P. Ney, and C. J. Waddington, Flux and energy spectrum of cosmic ray particles during solar maximum, *Phys. Rev.*, **114**, 365-373, 1959.
- Freier, P. S., E. P. Ney, and J. R. Winckler, Balloon observation of solar cosmic rays on March 26, 1958, *J. Geophys. Research*, **64**, 685-686, 1959.
- Gringauz, K. I., V. V. Bezrukhikh, V. D. Ozer



- R. E. Rybchinskii, A study of the inter-  
etary ionized gas, high energy electrons, and  
uscular radiation from the sun by means of  
three-electrode trap for charged particles on  
second Soviet cosmic rocket, *Doklady 5*,  
364, 1960. Original ref: *Doklady Akad. Nauk*  
*R*, 131, 1301-1304, 1960.
- auz, K. I., and S. M. Rytov, Relationship  
between the results of measurements by charged-  
particle traps on the Soviet cosmic rockets and  
magnetic field measurements on the American  
allite "Explorer VI" and rocket "Pioneer VI,"  
*Doklady 5*, 1225, 1961. Original ref: *Doklady*  
*id. Nauk SSSR*, 135, 48-51, 1960.
- D. E., The primary cosmic ray alpha-particle  
energy spectrum in Texas at a time near solar  
maximum, Dept. of Physics, Washington Univer-  
sity, St. Louis (unpublished), 1960.
- Donald, F. B., Study of geomagnetic cutoff  
energies and temporal variation of the primary  
cosmic radiation, *Phys. Rev.*, 107, 1386-1395,  
1957.
- Donald, F. B., Primary cosmic-ray intensity  
near solar maximum, *Phys. Rev.*, 116, 462-463,  
1959.
- Swain, C. E., Direct measurement of particles  
producing visible auroras, *J. Geophys. Research*,  
65, 2727-2747, 1960.
- Hashi, T., Entry of high energy particles into  
the polar ionosphere, *Rept. Ionosphere and Space*  
*Research Japan*, 13, 201-219, 1959.
- Ray, E. C., Effects of a ring current on cosmic  
radiation, *Phys. Rev.*, 101, 1142-1148, 1956.
- Rothwell, P., Magnetic cutoff rigidities of charged  
particles in the earth's field at times of mag-  
netic storms, *J. Geophys. Research*, 64, 2026-  
2028, 1959.
- Schmidt, A., Das Erdmagnetische Aussenfeld, *Z.*  
*Geophysik*, 1 1-13, 1924-1925.
- Singer, S. F., A new model of magnetic storms and  
aurorae, *Trans. AGU*, 38, 175-190, 1957.
- Smith, E. J., P. J. Coleman, D. L. Judge and C. P.  
Sonett, Characteristics of the extraterrestrial  
current system; Explorer VI and Pioneer V,  
*J. Geophys. Research*, 65, 1858-1863, 1960.
- Störmer, Carl, *The Polar Aurora*, Clarendon Press,  
Oxford, 403 pp., 1955.
- Waddington, C. J., Observations on the multiply  
charged particles of the cosmic radiation, *Nuovo*  
*cimento*, 3, 930-955, 1956.
- Winckler, J. R., P. D. Bhavsar, and L. E. Peter-  
son, The time variations of solar cosmic rays dur-  
ing July 1959 at Minneapolis, *J. Geophys. Re-*  
*search*, 66, 995-1022, 1961.
- Yoshida, S. and M. Wada, Storm time increase of  
cosmic ray intensity, *Nature*, 183, 381-383, 1959.

(Manuscript received August 3, 1961.)







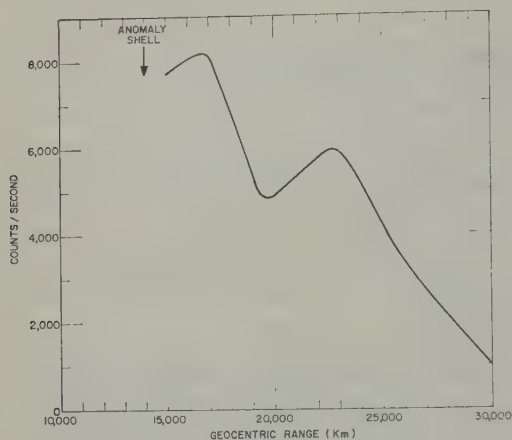


Fig. 1. Profile for the outer belt of the Geiger counter counting rate as if a pass went directly out the magnetic equator. The position of the anomaly affected trajectories is indicated.

about a 10 per cent decrease at the equator, approximately half the value observed. However, it has never been proven that the particles affected by the anomaly, assuming they had drifted on their magnetic shell to the longitude at which the experimental observations have been made, actually would pass through the position near the magnetic equator at which the minimum is observed. Such a construction can be made as follows:

The particles that would have mirror points below about 1300 km over the anomaly are of interest because at this altitude they begin to be rapidly scattered into the atmosphere. The locus of the mirror points of these particles must be followed as they drift in longitude around the earth to 148°E longitude. This gives the location of the affected mirror points at the longitude of experimental observation. Then the trajectories of the guiding centers must be found as the particles spiral out away from the earth to the place where they would cross the magnetic equator. This equatorial range is finally compared to the range at which the minimum in the outer belt is actually observed.

1. *Mirror point loci.* The locus of the mirror points of a trapped particle has been shown to be defined by two adiabatic invariants: (a) the magnetic moment, which defines the magnetic field strength  $B_m$  of the mirror point, and (b) the action integral,

$$I = \int_{B_m}^{B_m^*} \frac{V_{\parallel}}{V} dl = \int_{B_m}^{B_m^*} \left(1 - \frac{B}{B_m}\right)^{1/2} dl$$

which defines the magnetic line of force followed by the guiding center of the particle as it spirals out from  $B_m$ , across the magnetic equator, and back toward the earth to the field strength  $B_m^*$  [Welch and Whitaker, 1959]. Here  $V$  and  $V_{\parallel}$  are the total velocity and velocity component parallel to the field for the particle;  $dl$  is the arc length along the path of integration;  $B_m$ ,  $B_m^*$  are the conjugate mirror points; and  $B$  is the scalar field along the path of integration.

Jensen, Murray, and Welch [1960] have published tables of the geographic latitude, longitude, and altitude of the loci of mirror points as defined by various values of  $B_m$  and  $\ln I$ , using the 512 coefficient expansion of the earth's field in order to obtain a good fit near the Capetown anomaly.

In Figures 2a and 2b are plotted the loci of mirror points in the southern hemisphere defined by several values of  $B_m$  and  $\ln I$ . The particles having mirror points at the Capetown anomaly are slightly south of the  $\ln I = 9.5$  line in Figure 2a, but not nearly as far south as  $\ln I = 10.0$ . The tables of Jensen, Murray, and Welch [1960] do not have the locus of mirror points which pass directly through the anomaly. Figure 2b shows the altitude dependence of the mirror points as a function of longitude. The particles affected by the anomaly lie between the two lines. Any particle above the upper line never dips below 1300 km as it drifts around the earth. Any particle injected below the lower line, even at the maximum altitude of the line at 125°E will be almost immediately scattered into the atmosphere. The lines are for  $\ln I = 9.5$ ; the circled dots and squared dots give the minimum altitude of mirror points for  $\ln I = 10.0$  at the anomaly and the altitude at 148°E. Hence the four loci ( $\ln I = 9.5$ ,  $B_m = 0.18$  and 0.28; and  $\ln I = 10.0$ ,  $B_m = 0.20$  and 0.30) bracket the particles having mirror points affected by the anomaly. These four bracketed loci are shown in Figure 2c as the lower altitude and more southern latitude set of points when at the anomaly, and the higher altitude and more equatorial set when at 148°E longitude.

Hence we have found the approximate position of the particles having mirror points that would be affected by the anomaly when they have



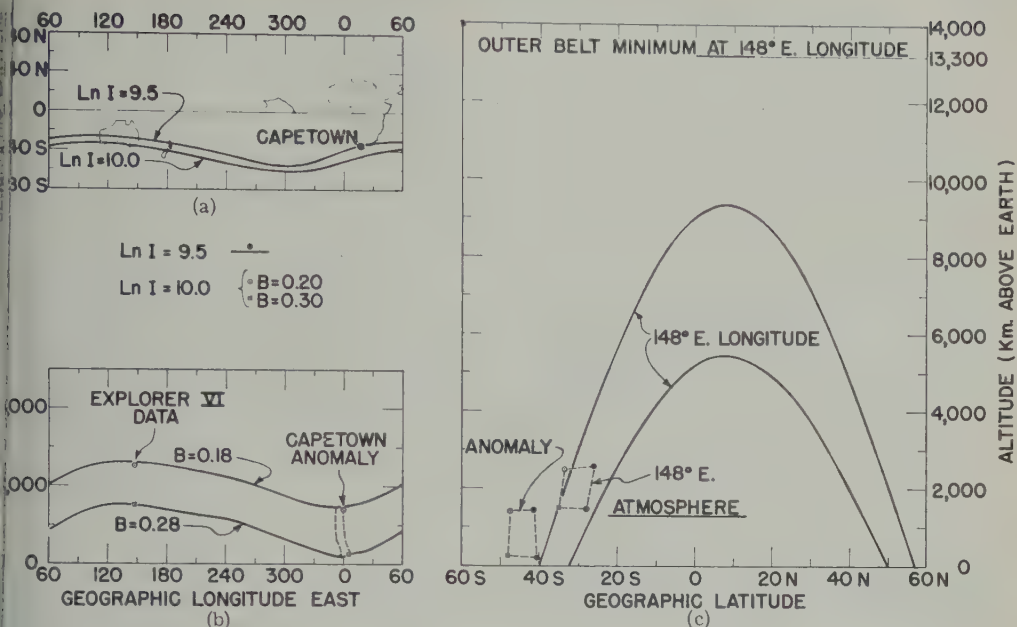


Fig. 2. *a*, *b*, and *c*. Construction to prove that any particles affected by the Capetown anomaly do not have trajectories that pass through the position of the outer belt minimum.

led to the longitude where the experimental observations have occurred. A typical particle has its mirror point at 148°E longitude at about 2000 km altitude.

**Guiding center trajectory.** The next step is to determine the altitude at which these affected particles will cross the magnetic equator at the longitude of experimental observations. *Jensen* [1959] has published tables of coordinates ( $\phi$ ,  $\lambda$ ,  $h$ ) of points defining the geomagnetic field lines intersecting the earth's surface at latitude  $\phi$  and longitude  $\lambda$ , appropriate at height  $h$ , using the 48 coefficient expansion. However, a line having  $\phi = 29^\circ$ S,  $\lambda = 148^\circ$ E, and  $h = 2,000$  km is required for the construction of a particle which has drifted from the anomaly. Such a line has not been published, so it is necessary to bracket the point of interest. Two such bracketing lines are plotted in Figure 2c, the lower one leaving the earth at  $\phi = 32^\circ$ S, and  $\lambda = 143^\circ 57'$  E, and the upper one leaving at  $\phi = 40^\circ 00'$  S, and  $\lambda = 150^\circ 00'$  E. Hence it is seen from Figure 2c that particles having mirror points affected by the anomaly cross the magnetic equator at about 148°E longitude somewhere between the altitudes of 9370 and 5450 km, perhaps at about 7500 km

altitude (14,000 km geocentric range). The minimum as experimentally observed has an altitude of 13,300 km, well above any anomaly-affected particles (see Fig. 1).

### C. DISCUSSION

The first conclusion resulting directly from the above discussion is that the Capetown anomaly is not an explanation for the minimum in the outer belt. This conclusion is based on the assumption that the primary magnetic data upon which *Jensen, Murray, and Welch* [1960] have based their analysis are correct. However, a comparison between the current United States' charts of total magnetic field and a recent magnetic survey of the area west of Capetown indicates that the field contours for 1955 could be moved east by as much as  $17^\circ$  [*Heirtzler and Hirshman*, 1960]. However, even such a large shift of the anomaly to the east would probably not move the anomaly-affected particles out of the four bracketing loci of mirror points, that is, south of the  $\ln I = 10.0$  line in Figure 2a. Therefore it is not likely that agreement can be reached between the actual position of the minimum and the equatorial range of the trajectories through the anomaly.

Dessler and Karplus [1960] and Hess [1960] have also used the theory of the anomaly causing the minimum as supporting evidence for the neutron albedo decay source of the outer belt. In order to cause the minimum in the equilibrium population of the particles, the local decrease in magnetic field strength at the anomaly would require an injection of particles that is strongly weighted toward the surface of the earth. Such a source is found in albedo neutrons, whose decay density falls off rather like  $R^{-4}$  [Hess, 1960]. A corollary to the first conclusion is that the minimum can no longer be considered as a piece of evidence in favor of the neutron source.

*Acknowledgments.* This work was supported by the National Aeronautics and Space Administration under contract NASw-56. I wish to thank my adviser, Dr. John R. Winckler, and my co-worker, Mr. Roger L. Arnoldy, for helpful discussions during the preparation of this paper.

#### REFERENCES

Arnoldy, R. L., R. A. Hoffman, and J. R. Winckler,

- Observations of the Van Allen radiation region during August and September 1959, Part 1, *J. Geophys. Research*, **65**, 1361-1376, 1960.
- Dessler, A. J., Effect of magnetic anomaly on particle radiation trapped in geomagnetic field, *J. Geophys. Research*, **64**, 713-715, 1959.
- Dessler, A. J., and R. Karplus, Some properties of the Van Allen radiation, *Phys. Rev. Letters*, **1**, 271-274, 1960.
- Heirtzler, J. R., and J. Hirshman, Measurements of the geomagnetic field near Capetown, *J. Geophys. Research*, **65**, 3016-3018, 1960.
- Hess, W. N., The radiation belt produced by neutrons leaking out of the atmosphere of the earth, *J. Geophys. Research*, **65**, 3107-3115, 1960.
- Hess, W. N., and J. Killeen, Densities of electrons from neutron decay trapped by the geomagnetic field, *Bull. Am. Phys. Soc.*, **5**, 260, 1960.
- Jensen, D. C., W. Murray, and J. A. Welch, Tables of adiabatic invariants for the geomagnetic field, 1955, *Air Force Spec. Weapons Center Albuquerque Rept. TN 60-8*, April 1960.
- Vestine, E. H., Geomagnetic field in space, *Radiation Corporation, Rept. L-4970*, 1959.
- Welch, J. A., and W. A. Whitaker, Theory of geomagnetically trapped electrons from an artificial source, *J. Geophys. Research*, **64**, 909-922, 1959.

(Manuscript received August 11, 1961;  
revised August 31, 1961.)



## Cosmic-Ray Knee in 1958

H. V. NEHER

*Department of Physics, California Institute of Technology  
Pasadena, California*

**Abstract.** During the International Geophysical Year, two series of balloon flights were made. One of these sampled the ionization due to cosmic rays over the range of geomagnetic latitudes from 38°N to 87°N. The other covered the range from 13°N to 79°S. In each case similar balloon flights from a base station were made to make possible an allowance for changes in the primary radiation. The second series of flights is used in this paper to determine the location of the knee of the latitude curve at atmospheric depths from 10 to 220 g cm<sup>-2</sup>. The results indicate that at this time of the solar cycle the knee moved toward the pole with decreasing amount of air overhead, reaching a geomagnetic latitude of 55° at 10 g cm<sup>-2</sup>. This movement of the knee becomes very slow at the lower pressures, however, suggesting that even at much lower pressures, the knee would not move appreciably farther toward the pole.

**Introduction.** When the ionization produced by cosmic rays in the atmosphere is measured as a function of geomagnetic latitude, keeping the depth in the atmosphere constant, there usually exists a latitude [Neher, Peterson, and Neher, 1953] beyond which, as one proceeds to lower latitudes, little or no change occurs. The same phenomenon exists when one measures the change in the nucleonic component only [Simpson, 1951]. This characteristic is usually referred to as the 'knee.'

The knee at sea level occurs at a geomagnetic latitude of about 40°. If the position of the knee is studied at different atmospheric depths, however, it is found to occur at higher latitudes when there is less air overhead. It is evident, therefore, that atmospheric absorption is at least partly responsible for the knee when measurements are made down in the atmosphere. To study the question whether the knee represents a abrupt change in the rigidity spectrum of the primaries, one must go to sufficient altitudes so that the primaries of the lowest rigidity can make themselves felt at the measuring instrument.

In the series of balloon flights carried out by the group at the California Institute of Technology in 1958, which covered a wide range of geomagnetic latitudes, considerable information was obtained on the position of the knee up to atmospheric depths corresponding to 0 g cm<sup>-2</sup>.

While these experiments were being carried

out, general solar activity was high and cosmic-ray intensity was near its minimum value for this particular solar cycle. However, no large solar flares or other large disturbances occurred during the two series of flights and no large change in ionizing radiation (except on one day) [Anderson, 1959] was observed. When geomagnetic effects and properties of the general solar modulation mechanism are to be studied, such fluctuations are undesirable and in this respect we were fortunate.

**2. Experiments and treatment of data.** During the first part of the period June and July of 1958, a base station was maintained at Bismarck, North Dakota. Simultaneous flights, using ionization chambers, were made from this base station and a mobile station, covering the geomagnetic range of 38°N to 57°N at a geographic longitude of about 100°W. Similar flights were made by the mobile station from 55° to 87° geomagnetic north. These latter were carried out at a mean geographic longitude of about 60°W. In like manner, while going toward the south pole by ship, a similar series of flights was made from shipboard from geomagnetic latitude 13°N to 79°S. In this case a base station was maintained at Invercargill, New Zealand, at geomagnetic latitude 52°S.

In using the data from the base station, to make corrections to the data from the mobile station, the following scheme was used. First, the two base stations were compared by making two simultaneous flights at Bismarck and Inver-

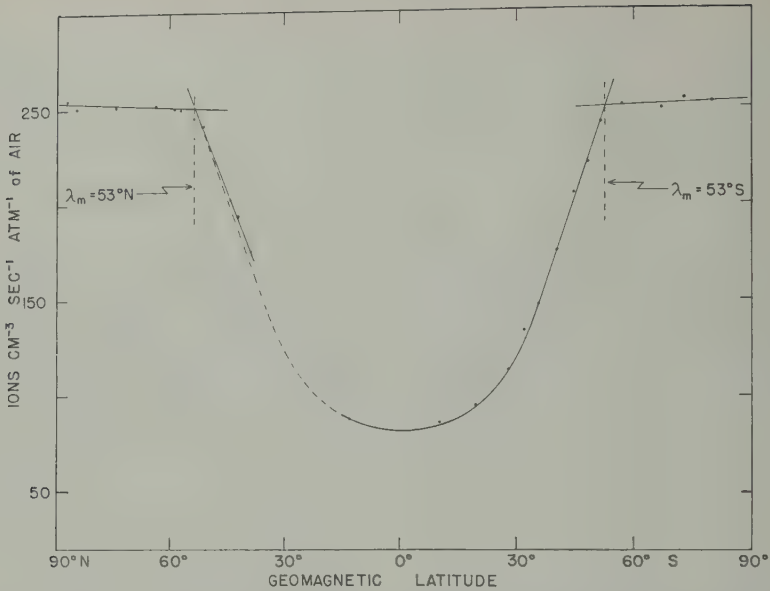


Fig. 1. The intensity of the ionization at the maximum of the ionization vs. atmospheric depth curves is here plotted as a function of geomagnetic latitude for the period June to December 1958.

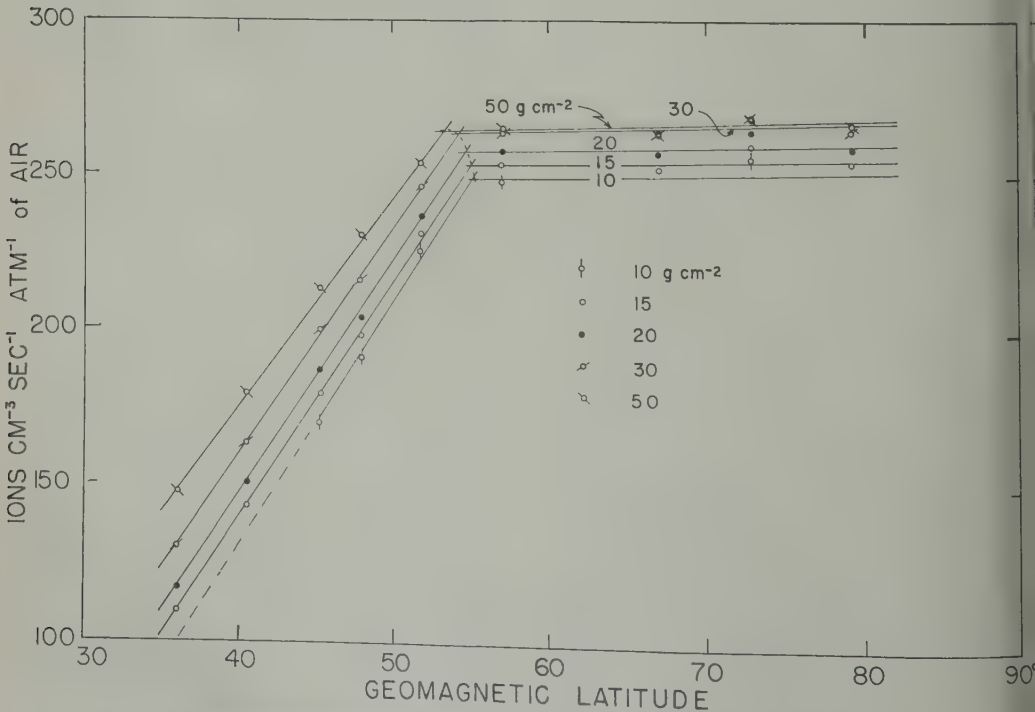


Fig. 2. For definite atmospheric depths the ionization vs. geomagnetic latitude shows an abrupt change over a small range of latitude. The location of the knee is defined as that latitude at which the two best straight lines above and below the knee intersect.



during October 1958. It was found that the 3-month interval between the series of measurements in the northern hemisphere and those in the southern, the average intensity of the radiation at the maximum of the depth-ionization curves had increased by 4.7 per cent at Bismarck. Some of this increase was due to particles which were able to get through the earth's magnetic field at Bismarck but not at Invercargill. The depth of 50 g cm<sup>-2</sup> in the atmosphere, where the maximum in the depth-ionization curves occurs, an estimate may be made of the correction which needs to be applied to the normalizing Invercargill flights to reduce them to the value that would have been obtained had the Invercargill correction been made in June and July when the series of flights was made at Bismarck. The correction thus found was -4 per cent.

To allow for the daily variations, a straight latitude correction was made to those flights taken at higher latitudes than the base station. The same procedure was also applied to the flights made at latitudes close to the base station. At latitudes near the equator, an estimate was made of the energy of the particles involved in the change on a particular day. This was done

by taking the difference between that day at the base station and the average value at the base station. The absorption curve for the particles involved was then compared with the difference curves found at various latitudes. For example, if the change was only in the low-energy particles that could not arrive at the mobile station, no correction was made.

It is convenient to have a definition for the location at which the knee of the cosmic ray latitude curve occurs. It will be noted that at the altitudes at which these data were taken, straight lines may be drawn through the experimental points, both below and above the knee. As was done at the Moscow Cosmic Ray Conference [Neher and Anderson, 1959], we here propose again that the knee be defined as occurring at that latitude where these two straight lines intersect (see Figs. 1, 2, and 3).

The values of the ionization taken at the maximum of the depth-ionization curves for both northern and southern hemispheres as a function of geomagnetic latitude thus obtained are given in Figure 1. As pointed out previously [Neher and Anderson, 1959] the knee occurs very close to the same northern and southern

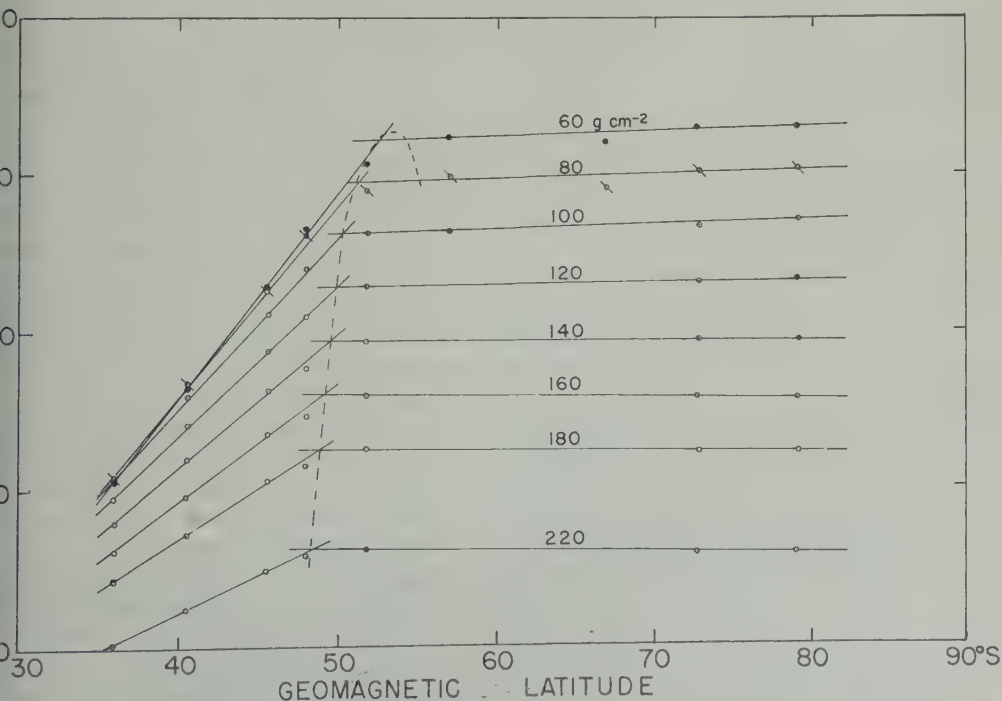


Fig. 3. A continuation of Figure 2 for greater atmospheric depth.

TABLE 1. Corrected Values of Ionization Due to Cosmic Rays at Definite Atmospheric Depths for Selected Latitudes in the Southern Hemisphere for the year 1958

Locations are given in terms of centered dipole geomagnetic latitudes. All data were taken close to 180° longitude.

g/cm <sup>2</sup>	Nov. 13 36°S	Nov. 14 40.5°S	Nov. 15 45.3°S	Nov. 23 48.0°S	Nov. 26 51.8°S	Nov. 28 57.0°S	Dec. 2 67.0°S	Dec. 3 72.8°S	Dec. 22 79.2°S
10	...	...	170.5	191.1	225.4	248.0	...	256.6	...
15	109.9	143.1	179.3	197.8	231.3	253.3	252.5	260.4	254.1
20	117.0	150.3	187.5	204.3	236.9	257.8	257.8	264.7	259.9
30	130.1	163.4	200.7	215.8	246.6	264.0	263.8	269.2	264.1
40	140.7	173.1	208.8	224.9	252.3	265.3	264.6	269.8	267.7
50	147.8	179.3	213.0	230.7	254.1	264.6	263.3	268.5	266.4
60	152.0	182.6	214.7	232.8	253.5	262.0	259.6	264.8	264.3
70	154.0	184.0	214.5	233.0	250.4	256.3	254.0	258.1	258.6
80	154.5	183.8	213.5	230.8	244.9	249.3	245.1	250.4	251.9
90	154.1	182.3	210.2	226.1	238.2	241.8	...	242.1	243.7
100	152.8	179.5	205.2	219.8	230.7	231.5	...	233.3	235.7
120	147.6	170.3	193.9	204.8	214.5	...	...	215.1	216.3
140	139.4	159.5	181.0	188.6	196.9	...	...	196.4	196.8
160	130.3	147.7	167.5	172.9	179.9	...	...	178.8	178.4
180	120.8	135.8	152.7	157.2	162.9	...	...	161.0	161.3
200	110.9	123.8	138.4	142.2	146.6	...	...	144.7	145.7
220	101.0	112.2	124.3	128.6	131.0	...	...	129.1	129.0
240	91.5	101.0	110.5	115.5	116.2	...	...	115.0	114.4
260	82.0	90.2	97.9	102.8	102.8	...	...	101.9	101.3
280	73.0	79.9	86.7	90.5	90.8	...	...	89.9	89.1
300	64.8	70.3	77.1	79.4	80.2	...	...	79.1	78.3
380	40.1	42.9	47.0	47.2	47.9	...	...	...	47.1
500	20.2	21.4	21.7	22.5	22.5	...	...	...	22.3

latitudes at the longitudes where these experiments were performed when centered dipole geomagnetic coordinates are used. Furthermore, it is noteworthy that the two hemispheres are symmetrical, at least to  $\pm 1$  or 2 per cent, at latitudes above the knee. In Figure 1 the dashed line in the northern hemisphere is the mirror image about the geomagnetic equator of the curve for the southern hemisphere. The experimental data between 38° and 57° in the northern hemisphere were taken at a different longitude. The difference in slopes is to be expected from the longitude effect.

As an example of a case where the change from one time to another was in the low-energy particles only, we may compare December 3 and December 22 at 72.8° and 79.2° geomagnetic south respectively. The data for these flights are given in Table 1. They have been corrected for changes at Invercargill. It is evident that the change in the primaries between these 2 days was in those particles that were absorbed in the first 50 to 60 g cm<sup>-2</sup>. For protons this corresponds to an energy of 300 Mev or a rigidity of 800

Mev and these would not be able to enter at Invercargill. There is thus no way to correct for this kind of change in the method here used. The corrections to the data taken by the mobile station were somewhat less for the second series of flights, i.e., for those data taken in the southern hemisphere. Consequently we here consider only those flights made by the two southern hemisphere stations from November 13 to December 22, 1958. For the 11 flights made at the southern base station during this time, the mean deviation from the average at the maximum of the ionization-depth curves was only 0.9 per cent.

Proceeding according to the method described above, the corrected data for the flights made from 36°S to 79.2°S are given in Table 1.

Because of the two-valued nature of the ionization vs. depth, the data given in Table 1 have been plotted in two figures, namely Figures 2 and 3. In Figure 2 considerably less weight was given to the data of the mobile station at 73°S than for the other stations for reasons mentioned above. Also, in drawing the line for 10 g cm<sup>-2</sup> pressure, some guidance was used from the



at higher pressures due to the incompleteness of the data at the lowest pressure. Figure 2 shows the geomagnetic latitudes of the intercepts of the two straight lines, which join points above and below the knee, as a function of air overhead.

Comparing these results with those obtained in a previous similar series of flights [Neher, Peterson, and Stern, 1953], we note (a) that in 1951 a 5 per cent increase in the ionization at  $15 \text{ g cm}^{-2}$  was found from the knee to the pole while the present flights show a 3 per cent increase at the same pressure; (b) the knee occurred at about  $56^\circ$  in 1951 compared with  $55^\circ$  in 1958; (c) the geomagnetic latitude for these experiments, both at  $15 \text{ g cm}^{-2}$ ; (d) at the higher pressures the ionization at a given depth in the atmosphere increases with increase of latitude. This is common to both sets of data and has been ascribed to a temperature effect [Neher, Peterson, and Stern, 1953].

**Discussion.** As one proceeds to higher latitudes at a given atmospheric depth, there are at least four effects that would produce a change in the intensity of cosmic rays in the atmosphere at latitudes higher than where the knee occurs. They may be listed as follows:

(1) Lower rigidity particles may be present in the primaries that cannot enter at the knee because of the earth's magnetic field.

(2) The earth intercepts particles that would not be at the point of observation if the earth were not present. The so-called shadow cones appear at the geomagnetic poles.

(3) The albedo particles that return to the atmosphere become fewer as one proceeds toward the poles.

(4) Meson decay in the lower atmosphere is more important at the higher latitudes than at lower latitudes in the summer. This is owing to the higher average temperature in the stratosphere and near the polar regions than in the intermediate latitudes.

These four effects will be discussed in reverse

order. The temperature effect, percentage-wise, will be most pronounced in the lower atmosphere and could be expected to become unimportant at higher altitudes where particles, in which we are here interested, would be present that would influence the position of the knee. We thus do not expect a difference in tempera-

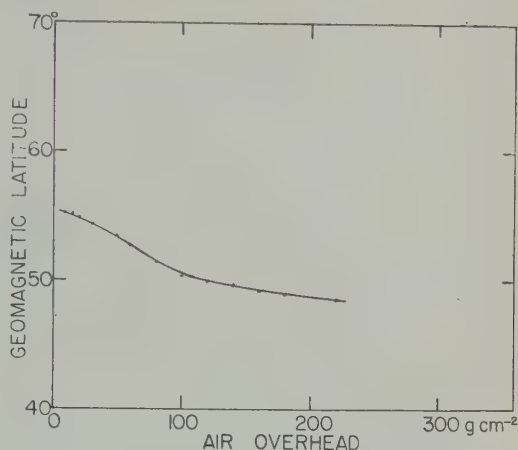


Fig. 4. The geomagnetic latitude at which the knee occurs moves toward the pole with decreasing air overhead, but appears to move very slowly at the lowest pressures.

ture of the air to result in a sharp knee at the lowest pressure that appears to go no farther toward the poles than  $56^\circ$  geomagnetic.

As to the albedo effect, it should result in less energy being dissipated in the atmosphere as one proceeds to higher altitudes. If this effect alone were present above the knee, the equipressure ionization-latitude curves of Figure 2 would slope downward as one went to higher latitudes. It would be expected, however, that no sudden break in the latitude curves would be found due to this cause.

Recent calculations by Kasper [1959] on the earth's shadow cones have led to a much smaller effect to be expected at the higher latitudes than was the case from the calculations of Schremp [1938]. As one proceeds to higher latitudes, positive particles are admitted near the eastern horizon that would have arrived at lower latitudes had they not been intercepted by the earth. One expects a gradual increase of ionization at the higher altitudes and latitudes due to this cause. Such behavior is opposite that expected from albedo particles.

All three effects discussed above are of a gradually changing nature and one does not expect a sudden change with latitude for any of them.

The abrupt change of slope of the latitude curve shown in Figure 2 occurs over a few degrees. Even with the omnidirectional characteristics of the detector here used, the change

seems to be completely over at  $57^\circ$  geomagnetic even at  $10 \text{ g cm}^{-2}$  pressure. A similar study of the data in the northern hemisphere confirms this conclusion.

It is here proposed, as an explanation of this phenomenon, that the sudden change in slope shown in Figure 2 at the low pressures is due to the absence or very near absence of particles with rigidities less than about 1.4 bev (corresponding to a proton energy of 0.73 bev or 0.23 bev per nucleon for particles with  $Z \geq 2$ ) in the primary cosmic radiation when these experiments were performed (1958).

That the knee at the lowest pressures is not due to atmospheric cutoff is evident from the fact that protons of 0.73 bev energy have a range in air of over  $200 \text{ g cm}^{-2}$ . Similarly,  $\alpha$ -particles of a corresponding rigidity have a range in air of  $30 \text{ g cm}^{-2}$ .

The reason for the absence or near absence of primary particles below a certain rigidity has long been sought. A discussion of some of the suggestions that have been made are reviewed by Neher, Peterson, and Stern [1953]. The most reasonable explanation at the present time appears to be that the cosmic-ray modulation mechanism resulting from the 11-year solar cycle so restricts the arrival at the earth of low rigidity particles that they are essentially eliminated. The sharp cutoff shown in Figure 2 is suggestive of the behavior to be expected from the action of static magnetic fields. This conclusion is probably not in conflict with that reached by Frier, Ney, and Fowler [1958] from flights they made in 1957. They drew the conclusion that the cutoff in 1957 was not sharp and hence could not be due to static magnetic fields. It should be pointed out however that they found only two  $\alpha$ -particles out of a total of 121 that had an energy less than the cutoff which the present data show, namely, 0.23 bev per nucleon. These two had

energies at the top of the atmosphere of 0.73 and 0.21 bev. Since the cosmic-ray intensity was only some 10 per cent higher in 1957 at high altitudes and latitudes compared with 1958, it is thought that there should be no significant difference in the numbers of low energy particles in these 2 years.

*Acknowledgments.* I wish to express my appreciation to the Office of Naval Research, the U. S. National Committee for the IGY, and to the National Academy of Science (through which the funds of the National Science Foundation were administered) for financial support. It is also a pleasure to thank the officers and personnel aboard the ice breakers, U.S.S. *Staten Island* and the U.S.S. *Atka* for their help and cooperation. I would also like to thank Dr. Hugh Anderson, M. Ralph Miles, Jr., Donald Barelli, and the personnel at both Bismarck and Invercargill, New Zealand for assistance in making the flights.

## REFERENCES

- Anderson, H. A., Sudden increase of cosmic-ray intensity, *Phys. Rev.*, **116**, 461, 1959.
- Frier, P. S., E. P. Ney, and P. H. Fowler, Primary  $\alpha$ -particle intensity at sunspot maximum, *Nature*, **181**, 1319, 1958.
- Kasper, J. E., The earth's simple shadow effect on cosmic radiation, *Nuovo Cimento (Suppl.)*, **1**, 1959.
- Neher, H. V., V. Z. Peterson, and E. A. Stern, Fluctuations and latitude effect of cosmic rays at high altitudes and latitudes, *Phys. Rev.*, **131**, 655, 1953.
- Neher, H. V., and Hugh R. Anderson, The knowledge of the latitude curve at balloon altitudes, *Proceedings of the Moscow Cosmic Ray Conference*, **4**, 105, 1959.
- Schremp, E. J., General theory of the earth's shadow effect of cosmic radiation, *Phys. Rev.*, **54**, 153, 1938.
- Simpson, J. A., Neutrons produced in the atmosphere by cosmic radiation, *Phys. Rev.*, **83**, 11, 1951.

(Manuscript received July 11, 1961.)



# The Magnetic Field of a Model Radiation Belt, Numerically Computed

SYUN-ICHI AKASOFU

*Geophysical Institute, University of Alaska, College*

JOSEPH C. CAIN

*Goddard Space Flight Center, National Aeronautics and Space Administration  
Greenbelt, Maryland*

SYDNEY CHAPMAN

*Geophysical Institute, University of Alaska, College  
High Altitude Observatory, University of Colorado, Boulder<sup>1</sup>*

**Abstract.** The magnetic field of a model ring-current belt encircling the earth symmetrically is numerically calculated, to a first approximation, for a particular model belt already discussed by Akasofu and Chapman [1961a]. They calculated the first approximation to the field only for points in the equatorial plane. The whole distribution of the field is here discussed, and for a particular intensity of the belt the calculation is carried to a second approximation. It is shown that over the earth's surface the field of the ring current is nearly uniform, though in auroral latitudes the diamagnetism of the belt produces an insignificant irregularity in the field disturbance. The model belt considered here is one whose center line is connected with the auroral zone by the dipole field lines of force; its particles have not yet been observed directly. Its existence is suggested by the quiet-day anomaly of the satellite-observed magnetic field at that distance. The known Van Allen radiation belts seem likely to contribute little to the ring current field, but during magnetic storms the radius of the belt mainly responsible for this field is probably less than 6 earth radii.

**Introduction.** Space observations by Van Allen and Frank [1959] and by Vernov, Chudakov, and Logachev [1959] have shown that the earth is encircled by 'radiation belts,' composed of charged particles trapped in the magnetic field  $F$  in the space around the earth [Van Allen, 1957].

A group of particles trapped in the earth's magnetic field, by their motions in this field  $F$ , produce a magnetic field  $\Delta F$ . The total field  $H$  is the vector sum of the intensities  $H_E$  of the earth's magnetic field  $F_E$  and the field  $\Delta F$  of the belt: thus

$$H = H_E + \Delta H \quad (1)$$

may be symbolically expressed by

$$F = F_E + \Delta F \quad (2)$$

The total field  $F$  and the precise distribution of the belt particles are interconnected in a complex way. One way of investigating

the problem is engaged in a program of research sponsored by the National Bureau of Standards and the U.S. Air Force Geophysical Research Directorate.

this interconnection is by successive approximation, as follows. The method is applied to a model belt whose particle content and general distribution are known or 'assumed.'

(a) Calculate the particle distribution and the magnetic field of the belt as if the total field present were simply the earth's field  $F_E$ . Let the belt field thus calculated be denoted by  $\Delta_1 F$ . Let the field  $F_E + \Delta_1 F$  be denoted by  $F_1$ .

(b) Calculate the particle distribution and the magnetic field of the belt as if the total field present were  $F_1$ . Let the belt field thus calculated be denoted by  $\Delta_2 F$ , and let  $F_2$  denote the field  $F_E + \Delta_2 F$ .

Continue this process, obtaining a series of values of the belt field  $\Delta_n F$ , and of the combined field  $F_n$ , given by

$$F_n = F_E + \Delta_n F \quad (3)$$

If  $F_n$  approaches a limiting value, it is to be expected that this is the true field  $F$  given by equation 1.

Akasofu and Chapman [1961a] have discussed the field  $\Delta_1 F$  analytically, for several model belts.

They treated  $F_E$  as the field of a point dipole of vector moment  $\mathbf{M}$  ( $8.31 \times 10^{25}$  gauss cm<sup>3</sup>) situated at a point  $O$  inside the earth (centered or eccentric). In this case the belt and its field  $\Delta F$ , hence also the total field  $F$ , have symmetry about the dipole axis and equatorial plane. Also, for a particular assumed model belt called  $V_8$ , they made numerical calculations of several of its properties, including the intensity  $\Delta_1 H$  of the field  $\Delta_1 F$ , for points in the equatorial plane of the dipole  $\mathbf{M}$ . They compared their results with the magnetic observations made by Explorer VI [Sonett, Smith, Judge, and Coleman, 1960].

Their model belt involves a parameter  $n_0 E$  (section 3) which, for the same distribution of the belt, determines its density everywhere. The field  $\Delta_1 F$  involves  $n_0 E$  as a factor; that is, its intensity everywhere is proportional to  $n_0 E$ . For a certain numerical value (150) of  $n_0 E$ , their calculated field  $F_1$  seemed to resemble the field indicated by Explorer VI, in the region up to about  $7a$  from the earth's center  $O$ ; here  $a$  denotes the radius of the earth ( $6.37 \times 10^8$  cm).

However, in the region between  $5a$  and  $7a$ , the observed field showed a notable proportionate departure from the earth's field  $F_E$ .

Hence the calculated field  $\Delta_1 F$  may not be a good approximation to the actual field  $\Delta F$  of the belt. As is stated by Akasofu and Chapman [1961a, section 5.21], 'further work on this problem is necessary to obtain a self-consistent system of current and field.'

In this paper we extend their numerical calculations for the model belt  $V_8$  so as to show the general character of the field  $\Delta_1 F$  in the whole space around the earth. We compare our results with the changes observed at the earth's surface during magnetic storms. We also draw some general conclusions that bear on theories of magnetic storms and on the planning of future satellite magnetic observations.

For a certain value (90) of the parameter  $n_0 E$  of the model belt, we have also calculated the second approximation ( $\Delta_2 F$ ) to its field in a region that includes the densest part of the belt. The difference between  $\Delta_1 F$  and  $\Delta_2 F$  suggests that, for this value of  $n_0 E$ , the field  $\Delta_2 F$  is a good approximation to  $\Delta F$ .

In later studies we propose to explore the problem further, in particular by calculating the potential of  $\Delta F$  (or at least of  $\Delta_1 F$ ) in terms

of zonal harmonic functions. In these calculations alternative values of  $\alpha$  and of the belt radius and thickness will be considered.

2. *Geometrical considerations.* The point  $P$  at which the dipole  $\mathbf{M}$  is located is taken as the origin of coordinate systems  $r, \theta, \lambda$  and  $x, y, z$  relative to a polar axis  $Oz$  antiparallel to  $\mathbf{M}$ .  $\lambda$  is measured parallel and  $x$  perpendicular to  $Oz$ .  $\lambda$  increases eastward,  $z$  northward.

In a magnetic field which, like  $F_E$  and  $\Delta F$ , is symmetrical with respect to  $Oz$  and the equatorial plane  $z = 0$ , it is convenient to substitute, for the coordinates  $r, \theta$  of any point  $P$ , the parameters  $r_e, s_1$ , where  $r_e$  denotes the distance from  $O$  to the point  $P_e$  where the line of force through  $P$  crosses the plane  $z = 0$ , and  $s_1$  denotes the length of the line of force from  $P_e$  to  $P$  (positive northward). Let  $\mathbf{h}, \mathbf{j}, \mathbf{k}$  denote a right-handed orthogonal triad of unit vectors with origin at  $P$ ,  $\mathbf{h}$  being the direction of  $\mathbf{H}$  at  $P$ , and  $\mathbf{k}$  along the eastward normal to the meridian plane through  $P$ ;  $\mathbf{j} = \mathbf{k} \times \mathbf{h}$ . An elemental area  $ds$  drawn from  $P$  can be thus expressed

$$ds = \mathbf{h} ds_1 + \mathbf{j} h_2 dr_e + \mathbf{k} h_3 d\lambda$$

Areal elements at  $P$  normal to  $\mathbf{h}, \mathbf{j}, \mathbf{k}$  may be denoted by  $dS_1, dS_2, dS_3$ :

$$dS_1 = h_2 h_3 dr_e d\lambda$$

$$dS_2 = h_3 ds_1 d\lambda$$

$$dS_3 = h_2 dr_e ds_1$$

Let  $H_e, H$  denote the (scalar) magnetic intensities at  $P_e$  and  $P$ . The constancy of the strength  $HdS_1$  of a tube of magnetic force along its length gives the relation

$$h_2 = r_e H_e / h_3 H \quad h_3 = r \sin \theta$$

Akasofu and Chapman [1961a] gave the spherical forms of  $h_2, r_e, H, H_e$ , and the radius of curvature ( $R_e$ ) of the line of force at  $P$ , for the field  $F_1$  of the dipole  $\mathbf{M}$ , in terms of  $r$  and  $\theta$ . These were used in evaluating  $\Delta_1 F$ . In equation 4 they wrote  $h_1 d\phi (= -h_1 d\theta)$  instead of  $ds_1$ , using  $\phi$  to denote geomagnetic latitude.

In addition to the general relations 4 to 6 we may note:

$$\nabla = \mathbf{h} \frac{\partial}{\partial s_1} + \mathbf{j} \frac{\partial}{h_2 \partial r_e} + \mathbf{k} \frac{\partial}{h_3 \partial \lambda}$$

$$\mathbf{H} \times (\mathbf{H} \cdot \nabla) \mathbf{H} = -H^3 \mathbf{j} / R_e$$



tion 8 refers to a field like  $F$ , symmetrical about  $z$ , whose lines of force lie in meridian planes.

*Model radiation belt.* The state of the belt can be specified at each point  $P$  (with position vector  $\mathbf{r}$  relative to  $O$ ) by the function  $F(\phi)$  expressing the distribution of particle speeds  $w$ . There is such a function for each particle in the belt;  $n(\mathbf{r}, \mathbf{w}) d\mathbf{w}$  denotes the number density of these particles, at  $\mathbf{r}$ , whose velocities lie in the small range  $d\mathbf{w}$  about  $\mathbf{w}$ . By symmetry,  $n$  is a function of  $r$  and  $w$ ; hence it can be written  $n(s_1, r_e, w)$ . The angle between  $\mathbf{w}$  and  $\mathbf{H}$  at  $P$  is called the pitch angle ( $\phi$ ). Except possibly at singular points of the field  $F$ , the distribution of the pitch angle of  $\mathbf{w}$  around  $\mathbf{H}$  is isotropic. Hence, for particles of this velocity group, the velocity distribution depends only on  $\phi$ . It may be expressed by a function  $F(\phi)$  such that  $F(\phi) d\phi$  is the fraction of all the particles of this velocity group whose pitch angles lie between  $\phi$  and  $\phi + d\phi$ . Thus

$$\int_0^\pi F(\phi) d\phi = 1 \quad (9)$$

The number density at  $P$ , of the particles of a particular kind (with speeds between  $w$  and  $w + dw$ ), can be denoted by  $n(s_1, r_e, w) dw$ .

$w) dw$

$$\int_0^\pi \int_0^\infty n(s_1, r_e, w) F(\phi) w^2 dw d\phi = 1 \quad (10)$$

Generally, as the particles move in the field  $F$ , their pitch angle distribution and number density vary from point to point. Parker [1957] showed that the pitch angle distribution given by

$$A(\alpha) \sin^{\alpha+1} \phi \quad (11)$$

satisfies (9), has the following remarkable properties: (a) If  $F(\phi)$  has this form at one point on a tube of force, this is its form, for the whole of  $\alpha$ , all along this tube; and (b) the number density varies as  $H^{-\alpha/2}$  along the tube, and we may write

$$n(s_1, r_e, w) = n(r_e, w) (H_e/H)^{\alpha/2} \quad (12)$$

where  $n(r_e, w) dw$  denotes the number density at  $P_e$  of particles with speeds between  $w$  and  $w + dw$ . Clearly the functional symbol  $n$  in (12) has different meanings in the two cases.

Following Akasofu and Chapman [1961a] we consider a model belt in which  $F(\phi)$  has the form (11), with the same value  $\alpha$ , throughout the whole field. Further, the density distribution in the equatorial plane  $z = 0$  is given by

$$n(r_e, w) = n_0(w) \exp \{ -q^2(r_e - r_{e0})^2 \} \quad (13)$$

Thus in this plane the radial distribution of density is gaussian for each particle speed. The factor  $q$  determines the radial spread of the belt. Conceivably it might be a function of  $w$ , but in this paper we consider only particles of a particular speed  $w$  or speed range  $w$  to  $w + dw$ . Thus our results should be integrated with respect to  $w$  if the distribution functions of the speed  $w$  (or energy  $E = \frac{1}{2}mw^2$ ) are known for the particles present.

The model belt considered by Akasofu and Chapman and here is specified by (11) and (13), with the particular values

$$r_{e0} = 6a \quad \alpha = -\frac{1}{2} \quad q/a = 1.517 \quad (14)$$

These parameters are chosen as an illustration of our numerical computation, and the same procedure can be applied to any set of these parameters. In our case, the dipole line of force that crosses the plane  $z = 0$  at  $6a$  meets the earth's surface in geomagnetic colatitude  $\theta = 24^\circ$ . The choice  $6a$  for  $r_{e0}$ , the radius of the center line of the belt distribution, is made because auroras often appear in about that colatitude during moderate magnetic storms. The value  $\alpha = -1/2$  corresponds to a pitch angle distribution that has more small pitch angles than would correspond to an isotropic distribution of the direction of  $\mathbf{w}$ . The chosen value of  $q$  corresponds to a reduction of density to a tenth of the maximum value (denoted by  $n_0(w) dw$  or simply by  $n_0$ ), at a radial distance  $a$  on either side of the center line of the belt, that is, at  $5a$  and  $7a$ .

4. *The current distribution corresponding to  $\Delta_1 F$ .* Let  $i$  denote the contribution to the equivalent electric current intensity in the belt, due to the particles of a particular kind, with the speed between  $w$  and  $w + dw$ . Let  $i_1$  denote the current intensity for the first approximation. Following

Parker [1957],  $i_1$  was expressed (substantially) as follows by Akasofu and Chapman [1961a, equation 51], for a belt having the pitch angle distribution (11):

$$i_1 = \frac{mcw^2}{H} \frac{dw}{dH} \left( \frac{H_e}{H} \right)^{\alpha/2} \cdot \left[ n(r_e, w) \frac{[1 - 6B(\alpha)]}{R_e} - \frac{dn(r_e, w)}{dr_e} \frac{2B(\alpha)}{h_2} \right] \quad (15)$$

Here

$$B(\alpha) = (\alpha + 2)/4(\alpha + 3) \quad (16)$$

The expression 15 is valid for the general field  $F$ . The current flows symmetrically round the axis  $Oz$ ; such a current distribution is here called a ring current.

Akasofu and Chapman<sup>2</sup> calculated the distribution of  $i$  for the model belt specified in section 3 when the total field present is taken to be the dipole field  $F_E$ . In this case  $i$  will be denoted by  $i_1$ . Then at any point  $P_0$  on the center line of the belt ( $z = 0$ ,  $r_e = r_{e0}$ ), the value of  $i_1$ , denoted by  $i_{10}$ , is given by

$$\begin{aligned} i_{10} &= 1.56 \times 10^3 mw^2 n_0(w) dw \quad \text{esu} \\ &= 1.66 \times 10^{-15} n_0(w) E dw \quad \text{amperes} \end{aligned} \quad (17)$$

Here  $E$  denotes the kinetic energy of the particle expressed in kev, so that

$$E = 3.12 \times 10^8 mw^2 \quad (18)$$

Akasofu and Chapman [1961a, Fig. 3c] illustrated the current distribution by a set of current isolines, for the current intensities

$$i_1/i_{10} = 12, 10, 8, 6, 4, 2, -2, -4, -6$$

Our Figure 1 reproduces some of these lines (10,  $\pm 6$ ,  $\pm 2$ ). Positive values correspond to westward current, negative to eastward; the eastward isolines are drawn in broken line. Their Figure 3c also shows by chain lines the dipole lines of force through the points  $r_e = 5a, 6a, 7a$ .

<sup>2</sup> Note that a factor  $(1 + \sin^2 \phi)$  should be added on the right of their equation 53, also that a factor  $\cos \phi$  is omitted from (29), and that in (51) the index of the factor  $H_e/H$  should be  $\alpha/2$ . The numerical factor  $1.66 \times 10^{-15}$  in (17) was written as  $1.61 \times 10^{-15}$ . These are errors only in the reproduction of the original text; the calculations were made from the correct formulas.

The current intensity changes sign near slightly nearer to  $O$ . The maximum westward and eastward current intensities slightly exceed  $12i_{10}$  and  $6i_{10}$ . Also they illustrated separately (Figs. 3a, 3b) the distribution of the parts given in (15); later they intend to illustrate the distribution of the parts of  $i$  that are attributed by the diamagnetism and drift current of the belt. The main contribution comes from the diamagnetism.

5. *The magnetic field  $\Delta_1 F$ .* Akasofu and Chapman [1961a] gave expressions (their equations 76 and 77) for the  $x$  and  $z$  components of the field  $\Delta_1 F$ . They calculated  $\Delta_1 H_x$  numerically at points in the equatorial plane  $z = 0$ , where  $\Delta_1 H_x = 0$  (see their Fig. 6). Using the same formulas, and their calculated values of  $i_1$  at a network of points  $P$  in a meridian half-plane, we have evaluated  $\Delta_1 H_x$  and  $\Delta_1 H_z$  at a large number of points  $P'$  in this half-plane. Figure 2 shows some of the results, by the vectors  $\Delta_1 F$  for points  $P'$  disposed along radii in latitude from  $0^\circ$  to  $70^\circ$  at  $10^\circ$  intervals, and mainly at intervals  $a$  of radial distance. Figures 2 to 5 illustrate these and other results in a different way. Their lower parts give graphs of the  $x$  and  $z$  components of the  $\Delta_1 F$  field on a linear scale along radii in latitude  $\phi_1$  from  $0^\circ$  to  $40^\circ$ , up to  $r = 8a$ , for a model belt such that  $n_0 E = 1$  where

$$n_0 = n_0(w) dw \quad (19)$$

This might correspond, for example, to a maximum number density  $1.5/\text{cm}^3$  of particles of energy 100 kev, or  $1/\text{cm}^3$  of particles of energy 150 kev, at points  $P_0$  on the center line of the belt. The upper parts of Figures 2 to 5 consist of graphs, on a logarithmic scale, of the intensities of the dipole fields  $F_E$  and of  $F_1$ . Figures 3 and 4 (upper) also show graphs of the  $x$  and  $z$  components of the field  $F_1$ .

For this value of  $n_0 E$  it is clear from Figures 2 to 5 that in certain regions, mainly near the center line of the belt,  $\Delta_1 F/F_E$  is not small. Hence for this belt intensity it is inadequate to ignore the distortion of the field  $F_E$  by  $\Delta_1 F$ . However, the graphs in the lower parts of the figures are valid for smaller values of  $n_0 E$ , where the scales of force proportionately reduced.

Figures 1 and 2 indicate that within a radius of about  $2a$  the field  $\Delta_1 F$  is nearly uniform. Beyond this  $\Delta_1 F$  becomes notably nonuniform.

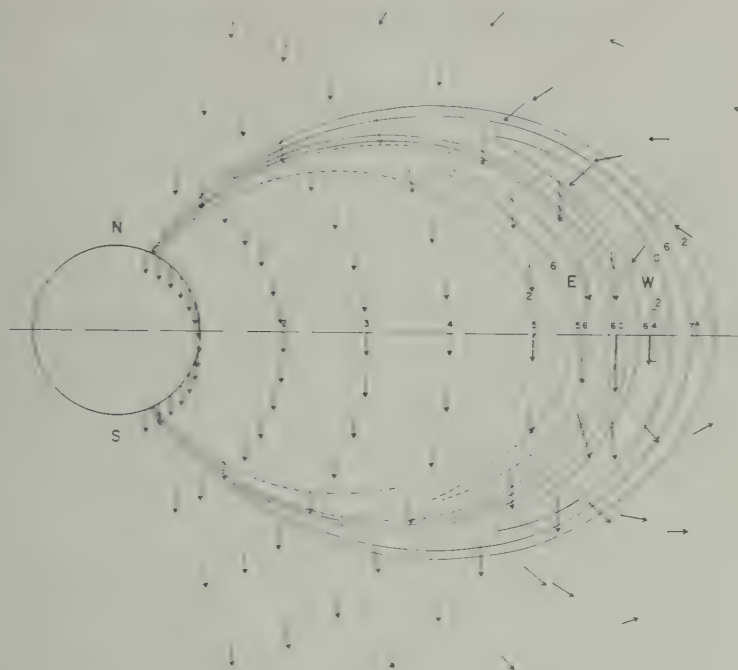


Fig. 1. The field vectors of  $\Delta F$ , the first approximation to the magnetic field of the model belt, in a meridian plane; and isolines of the equivalent current intensity in the belt (full lines indicate westward, broken lines eastward, currents). The vector scale of force, and the unit in which the current intensity is expressed, are proportional to the energy density  $n_0 E$  (kev/cm<sup>3</sup>) on the center line of the belt, at 6 earth radii from the earth's center.

shows considerable curl in the region of most current, centered about  $6.5a$  in the meridian plane. The field differs considerably, however, from that of a toroidal current. Outside the belt  $\Delta F$  tends, with increasing distance, to similarity with the dipole field, as theory would indicate.

Figures 2 to 5 may be useful for comparison with theory of the field of the model belt here compared with observations of the actual magnetic field around the earth. Clearly the net magnetic influence of the belt should be detected by satellites moving nearly in the meridian plane. For comparison with satellite observations, tables of  $\Delta F$  have been computed for many more points than are shown in the figures of this paper.

Figures 6 and 7 show some lines of force of the total field  $F_1 = F_E + \Delta F$ . These lines were computed approximately, taking steps of length  $a$  for the values  $n_0 E = 90, 150$ . These correspond, for example, to distributions of particles of energy 150 kev, of maximum number

densities 1/cm<sup>3</sup> and 0.6/cm<sup>3</sup>. Figures 6 and 7 show typical lines of force of the fields  $F_1$  (full lines) and  $F_E$  (broken lines). The distortion of the  $F_1$  lines is much greater for  $n_0 E = 150$  than for  $n_0 E = 90$ . Within the center line of the belt the ring current reduces the magnetic flux across the equatorial plane. Outside this line the flux is increased by an amount depending on the magnetic moment of the belt. Akasofu and Chapman gave a general formula for the magnetic moment of a belt of the type here considered (cf. their section 4.4).

6. *The ring-current magnetic disturbance of the earth's surface field.* As is shown particularly by Figures 1 and 2, the ring-current field at the earth's surface is nearly uniform and in the direction of  $\mathbf{M}$ , the dipole moment. Thus it decreases the horizontal component of the field and increases the numerical intensity of the vertical component. Such changes are observed during the major phase of magnetic storms. As the ring current grows during the early hours of the storm, its changing field induces electric



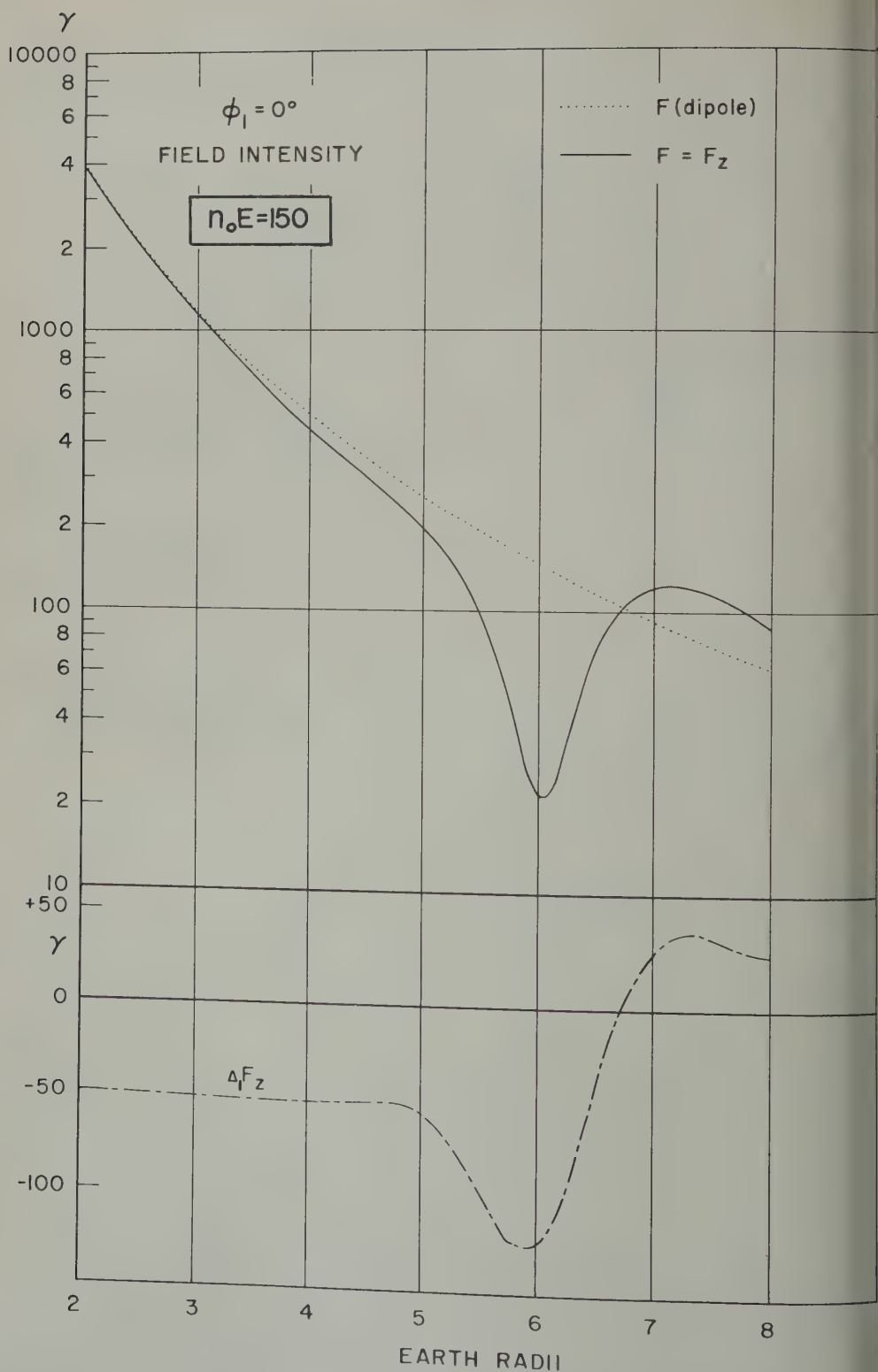


Fig. 2. For explanations of Figures 2 through 5 see text.

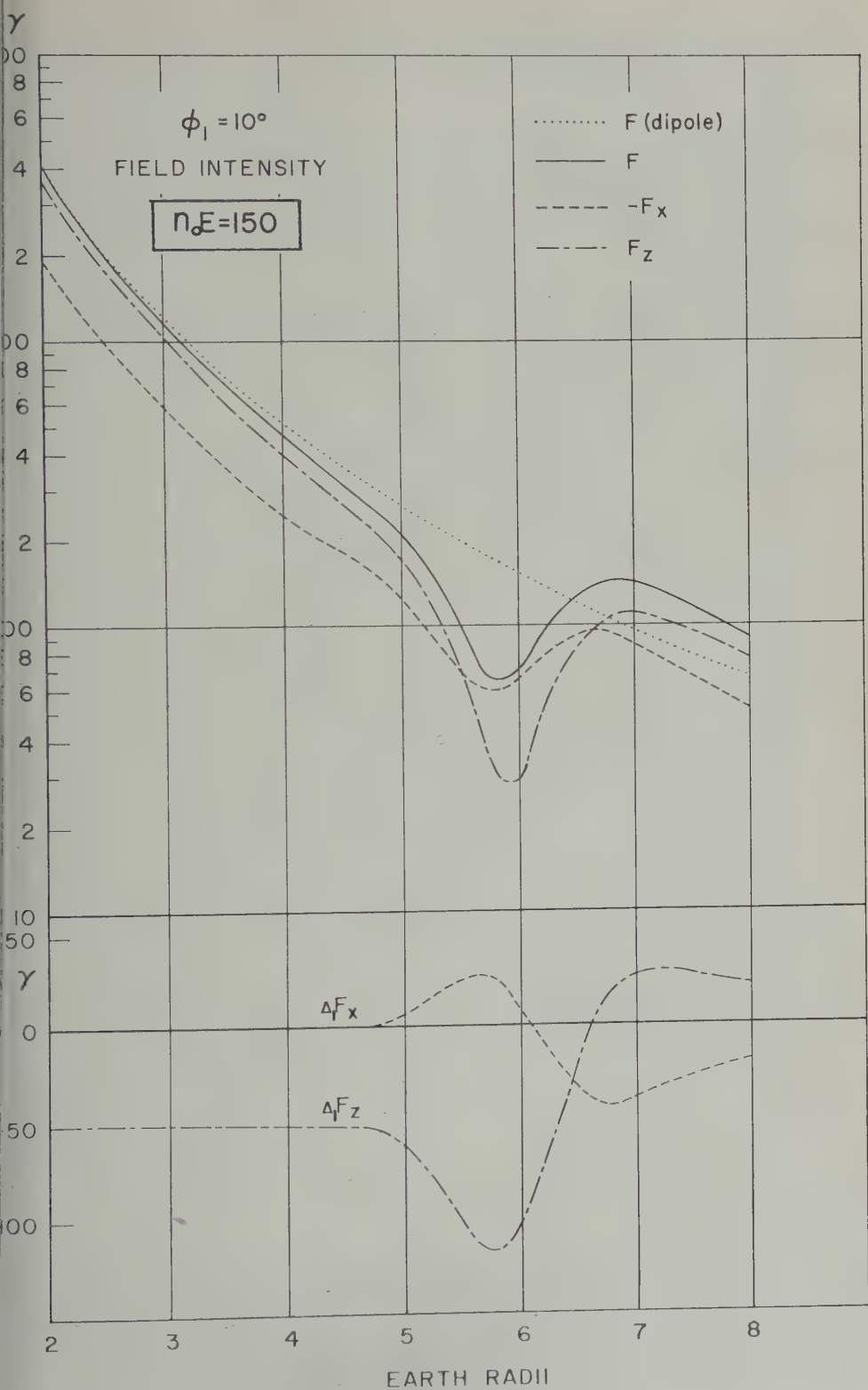


Fig. 3.

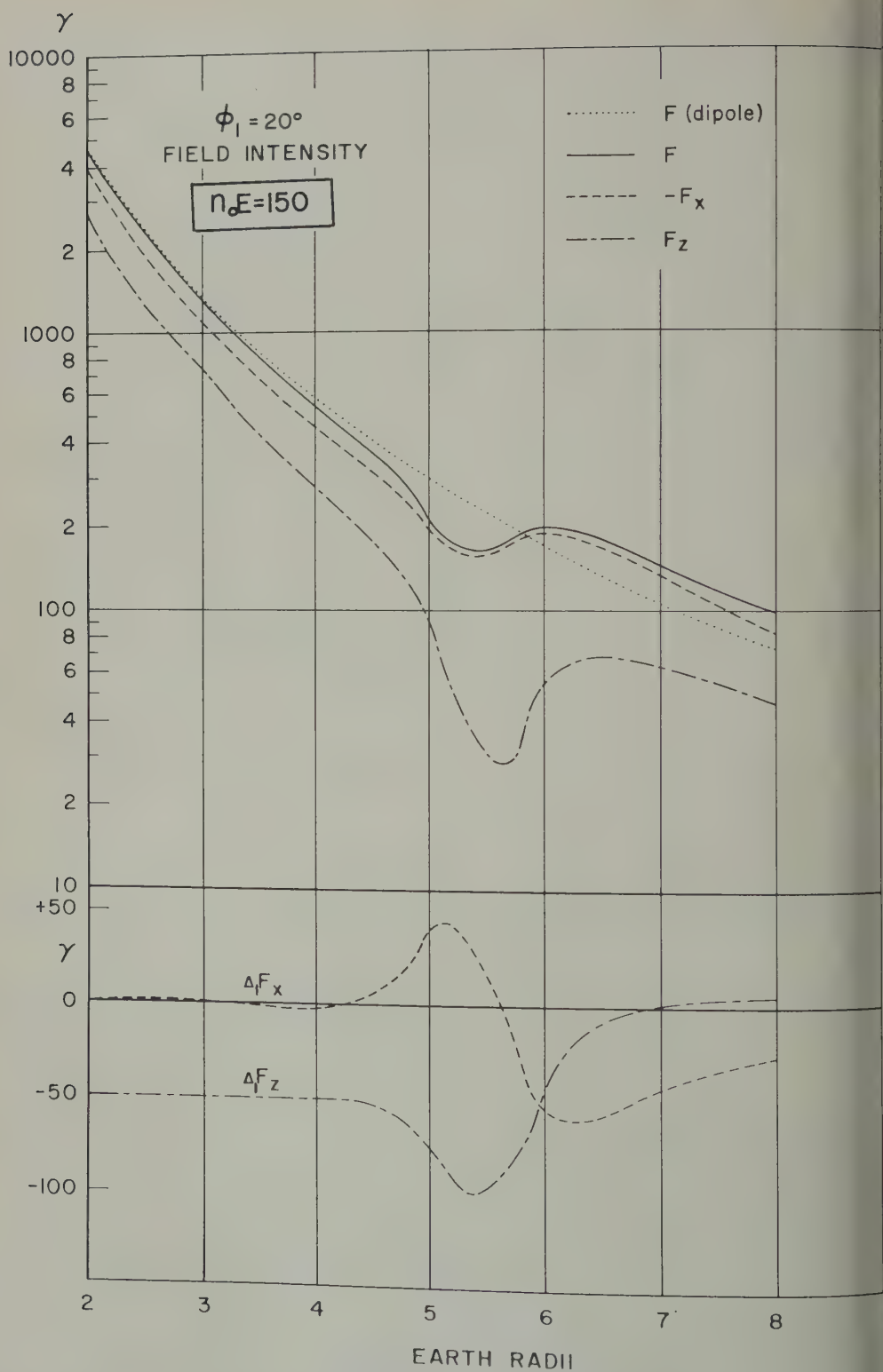


Fig. 4.



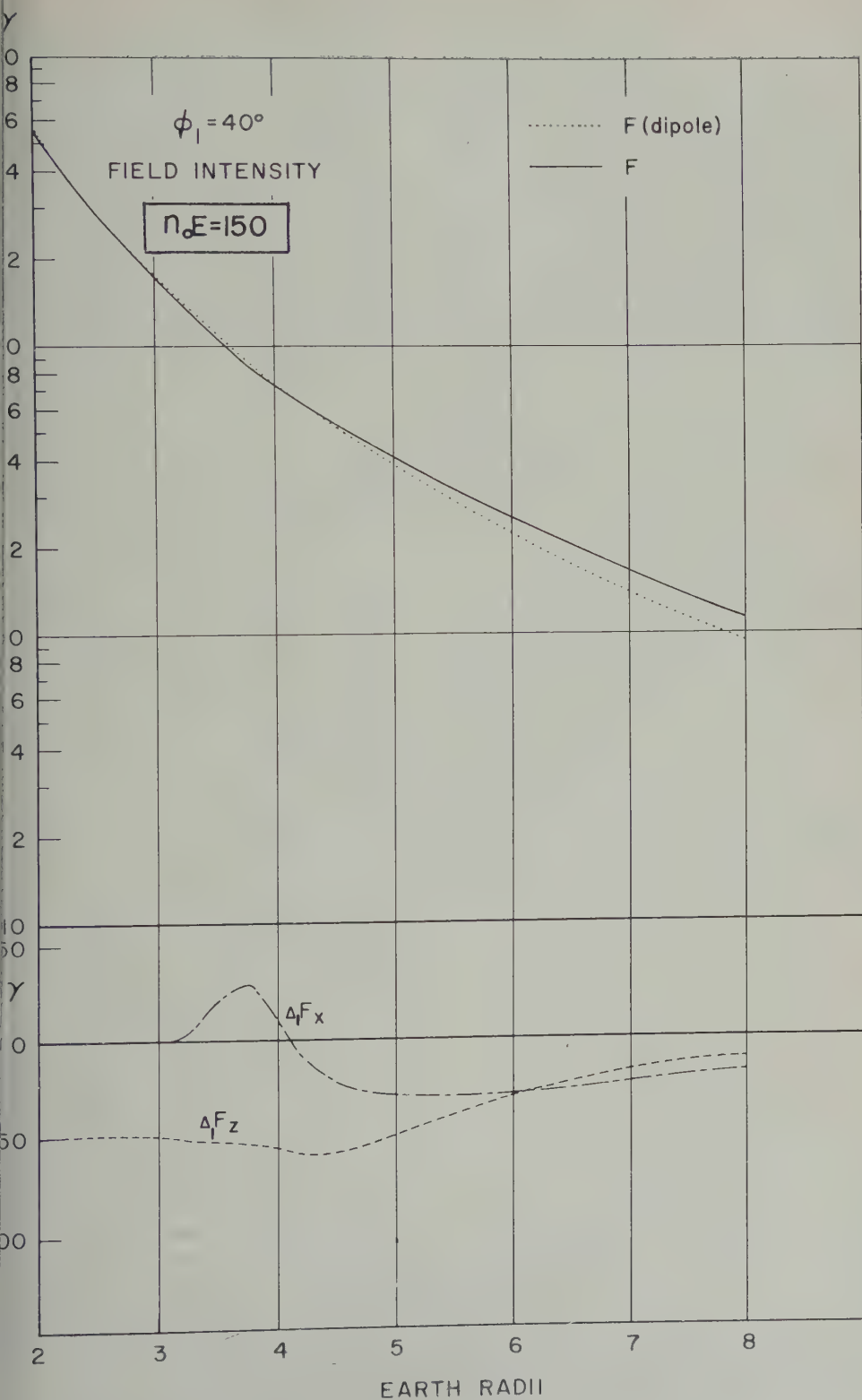


Fig. 5.

currents within the earth. These increase the change in the horizontal component and reduce that of the vertical component.

Figure 8 shows the ring-current change of the horizontal component (there denoted by  $H$ ) at the earth's surface, as a function of latitude up to  $70^\circ$ , for  $n_0E = 150$ . The curve is indistinguishable, on the scale shown, from a sine curve, corresponding to a uniform field, as suggested by Figure 1. The diagram also shows the graph of the vertical component  $V$  of the ring-current field at the earth's surface for the

same case  $n_0E = 150$ . Except near  $65^\circ$  latitude the curve is almost indistinguishable from a cosine curve corresponding to the sine curve of  $H$ . However, we made calculations of the field components of  $\Delta F$  at many points within and near the ring-current distribution (Fig. 1), and they revealed a small irregularity of the field in the current region, extending even to the earth's surface. This is to be attributed mainly to the diamagnetism of the belt. Figure 9 illustrates this feature in closer detail. It shows the variations of the total intensity  $\Delta_1 F$ , and

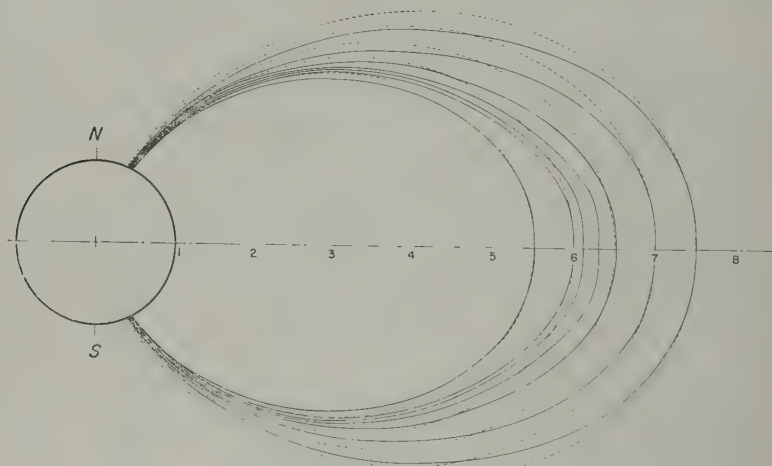


Fig. 6.  $n_0E = 90$ .

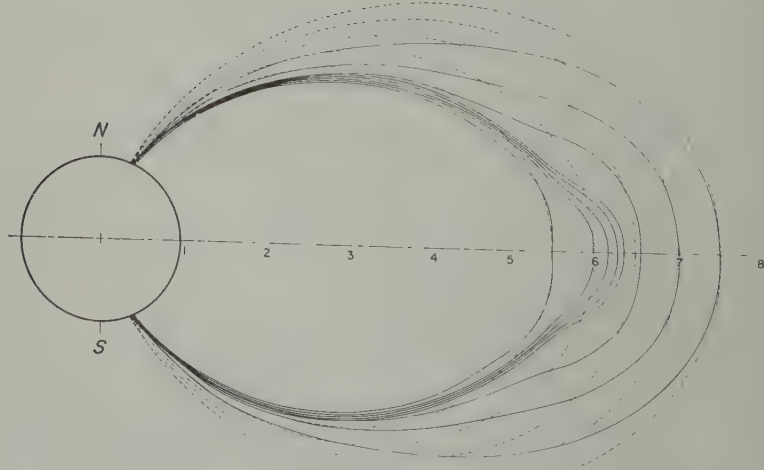
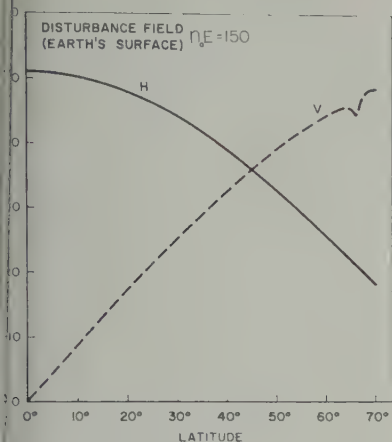


Fig. 7.  $n_0E = 150$ .

Figs. 6 and 7. The lines of force of  $F_1$ , the first approximation to the combined field of the geomagnetic dipole and the belt. The broken lines are lines of force of the dipole field.



8. The variations of the horizontal and vertical components ( $H$ ,  $V$ ) of the field of the belt, at Earth's surface, from the equator to latitude  $70^\circ$  (first approximation, for  $n_0 E = 150$ ).

horizontal and vertical components  $H$  and  $V$  at Earth's surface, between latitudes  $58^\circ$  and  $70^\circ$ . The irregularity mostly affects  $V$ , but its magnitude for  $n_0 E = 150$  does not exceed 5 gammas [Dessler and Parker, 1959, p. 2250]. The model belt would reduce the earth's horizontal magnetic intensity at the equator by 50 gammas. The induced earth currents increase this to about 90 gammas (and decrease the change in the vertical component). The observed decrease of the horizontal component at the maximum phase of the greatest magnetic storms is of the order of 600 gammas. The corresponding irregularity of the vertical component in the auroral zone will not exceed 10 gammas. This value may be contrasted with the changes of the vertical component that can be as great as 1000 gammas and somewhat more. In those latitudes the field of the belt, mainly diamagnetic, is insignificant by comparison, as was recognized by Dessler and Parker [1959]. This conclusion contrasts with the diamagnetic explanation of polar magnetic disturbances suggested long ago by Hulburt [1929], and used by Chapman [1930; see his section 10]. The second approximation ( $\Delta_2 F$ ) to the field of the ring current. For values of  $n_0 E$  such as considered in sections 5 and 6 the field of the ring current materially modifies the dipole field in the regions of greatest current intensity. Our calculation of  $\Delta_1 F$ , the first approximation to the ring-current field, needs correction

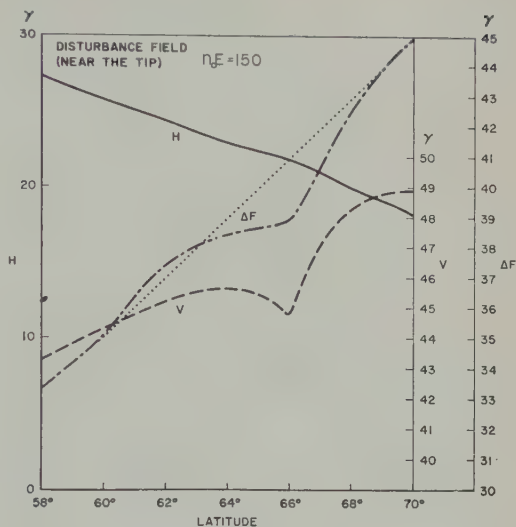


Fig. 9. Enlarged version, for the latitude range  $58^\circ$  to  $70^\circ$  (near the tip of the model belt), of the  $H$  and  $V$  curves of Figure 8; and the variation of  $\Delta_1 F$ , the corresponding total vector  $\sqrt{H^2 + V^2}$  (the dotted line shows the interpolated curve for  $\Delta_1 F$ , to indicate the slight irregularity due to the belt). Note the three different scales for  $H$  (left) and  $V$ ,  $\Delta_1 F$  (right).

for comparison with observed magnetic changes during storms.

Hence we have recalculated the current intensity at a network of points  $P_{m,n}$  (Fig. 10), for the model belt specified by equations 11, 13, and 14, in the presence of the field

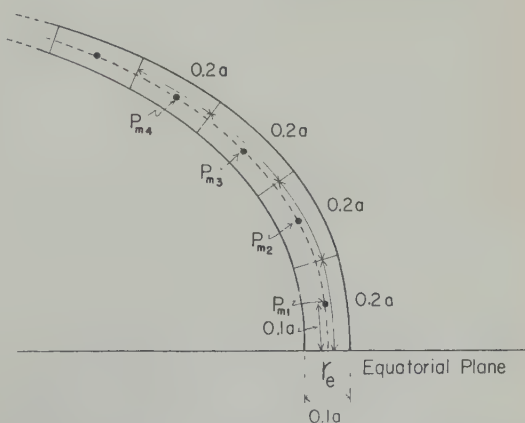


Fig. 10. The subdivision of the meridian plane used in computing  $\Delta_2 F$ , the second approximation to the field of the belt; the curved lines are lines of force of the field  $F_1$  (cf. Figs. 6 and 7).



$F_1 (= F_E + \Delta_1 F)$ . This calculation has been made for the case

$$n_0 E = 90 \quad (20)$$

The point  $P_{m,n}$  lies on the line of force for which

$$r_e = 4.8a + m \times 0.1a$$

and it is at the distance  $s_1$  along this line, from the plane  $z = 0$ ;  $s_1$  is given by

$$s_1 = 0.1a + n \times 0.2a$$

The values of  $m$  ranged from 0 to 27 (i.e., 28 lines of force), and the values of  $n$  ranged from 0 to 27 for  $m = 0$  and from 0 to 45 for  $m = 27$ .

The calculated current intensity at  $P_{m,n}$  is denoted by  $i_{2,m,n}$ , where the subscript 2 indicates that the value is a second approximation to  $i$ , corresponding to motion of the particles in the field  $F_1$ . The values of  $i_3$  were calculated from equation 15, using the values of  $H$ ,  $h_3$ ,  $R_c$  numerically computed for the field  $F_1$  and its lines of force.

The values of  $i_3$  at the points  $P_{m,n}$  having been obtained, the magnetic field  $\Delta_2 F$  was computed at another network of points  $P'_{m,n}$  using formulas 76 and 77 given by Akasofu and Chapman [1961a]. The current distribution was divided into filaments (Fig. 10) centered at the points  $P_{m,n}$  and of cross section  $h_2 dr ds_1$ ; the value  $i_{2,m,n}$  was taken to represent the mean current over this section. The number of points  $P_{m,n}$  in the two (northern and southern) halves of the meridian section of the belt exceeded 2000. The field  $\Delta_2 F$  was computed for points  $P'_{m,n}$  along radii in latitudes  $\phi_1 = 0^\circ, 10^\circ, 20^\circ$ , at radial distances  $a$  to  $8a$ . The radial interval was  $0.2a$  from  $r_e = 4.4a$  to  $r_e = 7.6a$ .

These results are embodied in numerical tables (not here reproduced). Figure 11 illustrates the variation of  $\Delta_2 F$  and  $F_3$  in the equatorial plane in the same way as Figure 2 does for  $\Delta_1 F$  and  $F_1$ ; Figure 2 refers to  $n_0 E = 150$ , and Figure 11 to  $n_0 E = 90$ . The second approximation corrects  $\Delta_1 F$  in this plane by a maximum amount of 15 gammas, at a point near  $P_0$ . The change from  $\Delta_1 F$  to  $\Delta_2 F$  scarcely alters the location (just within the center line of the belt) where  $\Delta_1 F$  is most intense, but it deepens this minimum by about 15 gammas, from 75 to 90. Except in this region, which produces a minimum of  $F_1$  and  $F_2$  near  $P_0$ , the second approximation makes a cor-

rection of less than 10 gammas; at the earth's surface the correction does not exceed 3 gammas. It seems likely that further approximations would produce little additional correction, so that  $\Delta_1 F$  and  $F_2$  nearly equal  $\Delta F$  and  $F$ .

The dip in the fields  $F_1$  and  $F_2$  between  $6a$  and  $7a$  are shown on a linear scale by an inset diagram in Figure 11. Near the center line of the belt, for  $n_0 E = 90$ , the estimated intensity of the true field  $F$  in the equatorial plane will be reduced to about 55 gammas.

For  $n_0 E = 150$ , the first approximation to the combined field is shown in Fig. 2; it reaches a minimum value of about 24 gammas. Because in the second approximation the minimum value is smaller than that for the first approximation, it may be expected that the above value of 55 gammas also becomes smaller.

If  $n_0 E$  is great enough to reduce the field to a low value near  $P_0$ , the guiding center approximation [Alfvén, 1950], used in obtaining equation 15, may cease to be valid near  $P_0$ . Paths of the particles there would be extremely complicated and the current intensity calculation must be modified. However, we notice that the dip near  $P_0$  is mainly produced by the strong eastward current and the westward current centered respectively at about  $5.5a$  and  $6.5a$ , where  $\Delta F$  is relatively small and the guiding center approximation will remain approximately valid.

In order to demonstrate this, we recalculate  $\Delta_2 F$  for  $n_0 E = 90$ , neglecting the contribution from the current in a region around  $P_0$ , limited by the lines of force  $r_e = 5.9a$  and  $r_e = 6.1a$  and by the radii between latitudes  $\pm 10^\circ$ . At 6.0 we found  $\Delta_2 F$  thus calculated to be 83.9 gammas. This may be compared with  $\Delta_2 F = 90.1$  gammas for the complete belt. Thus, more than 90 per cent of the field decrease near  $P_0$  is produced by the particles outside the above limits.

There is some doubt about what will happen if the value of  $n_0 E$  is further increased. We infer that beyond a certain value of  $n_0 E$  the field may be reversed near  $P_0$ . It is interesting to note that such reversals have been observed in the thermally driven nuclear reaction vessels (mirror machines) in which a very hot plasma is confined by a strong magnetic field [cf. Green, 1960]. Akasofu and Chapman [1961b] have attributed much importance to such a reversal in the formation of auroras.

the ring-current field beyond the belt. and Chapman [1961a] calculated the approximation  $\Delta_1 M$  to the magnetic moment model belt here considered (cf. their 4.4). Their value was  $1.17 \times 10^{23} n_0 E \text{ m}^3$ . Hence the equatorial field intensity and the belt will tend asymptotically with increasing distance to the value  $(M + \Delta_1 M)/r_e^3$ .

Table 1 gives the values of  $M/r_e^3$ ,  $(M + \Delta_1 M)/r_e^3$ , and the calculated values of  $F_1$ , from  $8a$  to  $15a$ , at intervals  $a$ , for the case  $n_0 E = 150$ . The values are expressed in gammas.

Table 1 shows that at  $15a$  the field approximates closely that of a dipole  $M + \Delta_1 M$ .

For  $n_0 E = 90$ , equatorial values of  $F_2$  have been calculated up to  $r_e = 8a$ . The values of  $F_1$

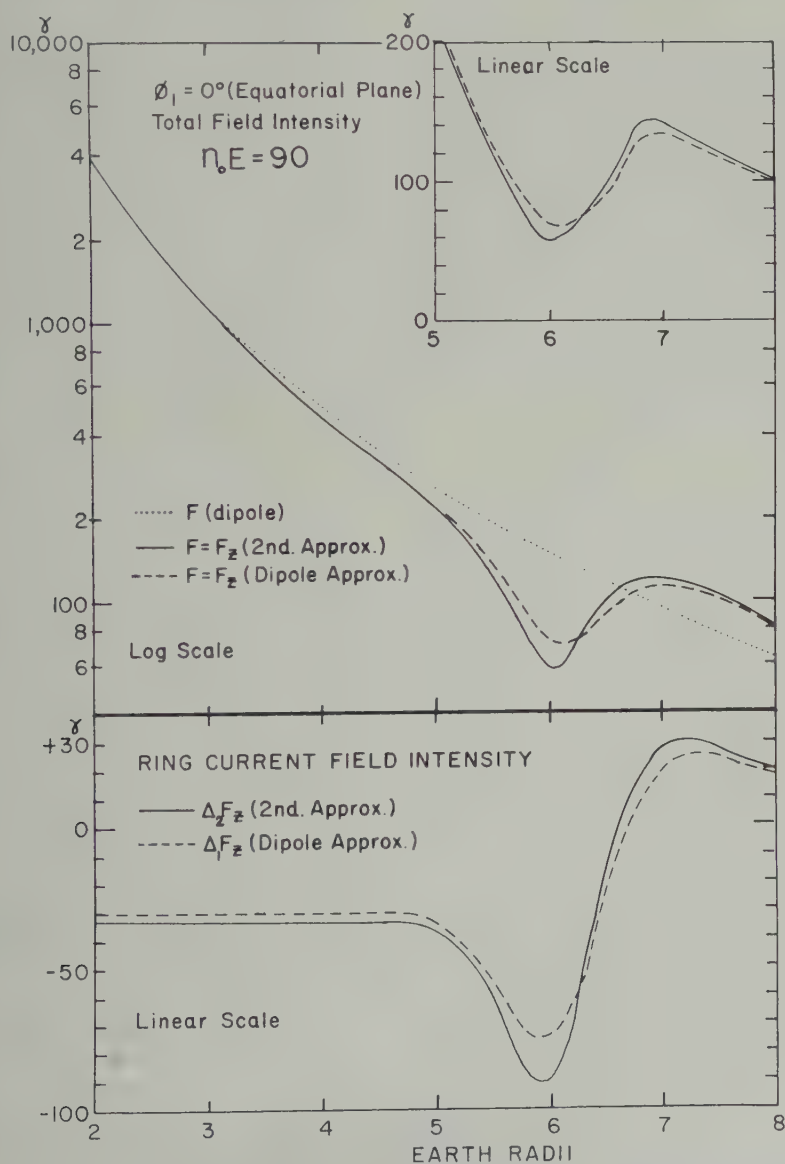


Fig. 11. Similar to Figure 2, but for  $n_0 E = 90$ , and with the addition of the second approximation to  $\Delta F$  (below) and to the combined field  $F$  (above). The broken line gives the first approximation, the full line the second. Top right: the variation of  $F_1$  (broken line),  $F_2$  (full line) on a linear scale, between  $5a$  and  $7a$ .

TABLE 1

	8a	9a	10a	11a	12a	13a	14a	15a
$r_e$								
$M/r_e^3$	62.5	43.9	32.0	24.0	18.5	14.6	11.7	9.5
$(M + \Delta_1 M)/r_e^3$	75.7	53.2	38.8	29.1	22.4	17.6	14.1	11.5
$F_1$	91.6	61.1	43.2	31.8	24.2	18.8	15.0	12.1

and  $F_2$  at 8a in this case are 80.0 and 81.7; at this distance  $(M_1 + \Delta_1 M)/r_e^3$  for  $n_0 E = 90$  is 70.4.

9. *The nonsteady state.* During a magnetic storm there are great changes in the number and distribution of the energetic particles in the region beyond the inner radiation belt. Akasofu and Chapman [1961a] have discussed these changes, as observed from satellites [Arnoldy, Hoffman, and Winckler, 1960], in connection with the magnetic variations during particular storms.

The formulas used to determine the field of the ring current of a steady radiation belt do not suffice, as they stand, for a changing belt. The corresponding changes in the field  $F$  introduce an electric field  $E$  such that

$$\partial \mathbf{H} / \partial t = -(1/c) \text{curl } \mathbf{E}$$

Assuming axial symmetry, and using cylindrical coordinates, this gives

$$\partial H_z / \partial t = -(1/cr) \partial(rE_\lambda) / \partial r$$

for the electric intensity  $E_\lambda$  in the direction  $\mathbf{k}$ . This electric field adds a term  $\mathbf{v}$  equal to  $(\mathbf{E} \times \mathbf{H})/cH^2$  or  $E_\lambda \mathbf{j}/cH_z$  to the velocity of the particles, and a term  $(nmc/H^2)\mathbf{H} \times d\mathbf{v}/dt$  to the current intensity  $\mathbf{i}$ . The velocity  $\mathbf{v}$  is directed outward or inward, in the meridian plane; it tends to distort the density distribution. A complete discussion of the ring current must take account of this electric field and of various loss processes in the belt.

*Acknowledgments.* The calculations described in this paper were made with the aid of the computing facilities at the Goddard Space Flight Center at Greenbelt, Maryland, and supported by a research grant from the National Aeronautics and Space Administration.

## REFERENCES

- Akasofu, S.-I., and S. Chapman, The ring current, geomagnetic disturbance, and the Van Allen belts, *J. Geophys. Research*, **66**, 1321-1350, 1961.
- Akasofu, S.-I., and S. Chapman, A neutral line discharge theory of the aurora polaris, *Philos. Trans. Roy. Soc. London, A*, **253**, 359-406, 1961.
- Alfvén, H., *Cosmical Electrodynamics*, Oxford University Press, 1950.
- Arnoldy, R. L., R. A. Hoffman, and J. R. Winckler, Observations of the Van Allen radiation region during August and September, 1959, part 1, *J. Geophys. Research*, **65**, 1361-1367, 1960.
- Chapman, S., On solar ultra-violet radiation as the cause of auroras and magnetic storms, *Monthly Notices Roy. Astron. Soc., Geophys. Suppl.*, **1**, 296-400, 1930.
- Dessler, A. J., and E. N. Parker, Hydromagnetic theory of geomagnetic storms, *J. Geophys. Research*, **64**, 2239-2252, 1959.
- Green, T. S., Evidence for the containment of a hot, dense plasma in a theta pinch, *Phys. Rev. Letters*, **5**, 297-300, 1960.
- Hulburt, E. O., On the ultraviolet light theory of auroras and magnetic storms, *Phys. Rev.*, **84**, 344-351, 1929.
- Parker, E. N., Newtonian development of the hydromagnetic properties of ionized gases of low density, *Phys. Rev.*, **107**, 924-933, 1957.
- Singer, S. F., A new model of magnetic storms and Aurorae, *Trans. Am. Geophys. Union*, **38**, 175-190, 1957.
- Sonett, C. P., E. J. Smith, D. L. Judge, and P. J. Coleman, Jr., Current systems in the vestigial geomagnetic field; Explorer VI, *Phys. Rev. Letters*, **4**, 161-163, 1960.
- Van Allen, J. A., and F. A. Frank, Survey of radiation around the earth to a radial distance of 107,400 kilometers, *Nature*, **183**, 430-434, 1959.
- Vernov, S. N., A. E. Chudakov, P. A. Vakulov, and Yu. I. Logachev, Study of terrestrial corpuscular radiation and cosmic rays during flight of the cosmic rocket, *Doklady Akad. Nauk SSSR*, **12**, 304-307, 1959.

(Manuscript received July 25, 1961;  
revised August 31, 1961.)



# Geomagnetically Trapped Electrons from Cosmic Ray Albedo Neutrons

A. M. LENCHEK<sup>1</sup>, S. F. SINGER, AND R. C. WENTWORTH<sup>2</sup>

*Physics Department, University of Maryland  
College Park, Maryland*

**Abstract.** The ability of the cosmic-ray neutron albedo mechanism to account for geomagnetically trapped electrons is investigated quantitatively. Injection as a function of energy, pitch angle, and altitude is computed from a reasonable neutron albedo model. Loss mechanisms (slowing down and pitch-angle diffusion) based on Coulomb interactions with the residual atmosphere are considered to act both independently and simultaneously. It is found that slowing down is generally dominant. The resulting electron belt has the following features: (a) an intensity whose energy spectrum shows a peak at  $\sim 200$  kev; (b) an angular distribution that is approximately isotropic up to the loss cone; and (c) an omnidirectional, integral intensity in the geomagnetic equatorial plane that is approximately constant vs. altitude. The absolute intensities depend directly on the atmospheric model used in the calculation; namely,  $r^{-2.7}$ , where atmospheric density is taken as  $\rho_0 r^{-2.7}$ . These results agree only poorly with spectrometer observations which show an energy spectrum with a peak at a much lower energy. However, the quantitative agreement as to intensity is good at energies  $\gtrsim 400$  kev. It is concluded that only a small fraction of the trapped electrons can be accounted for in terms of neutron albedo, essentially all trapped electrons  $> 400$  kev. An 'auroral' component of low-energy electrons is also present. The energy of this low-energy component probably derives from local acceleration, and ultimately from the sun. The effect of the Capetown magnetic anomaly is investigated and shown to produce a 'slot' of only 2 per cent in the equatorial plane in the vicinity of 2.7 earth radii.

## 1. INTRODUCTION

The possibility that the decay of cosmic-ray neutrons might contribute an electron component of the geomagnetically trapped radiation was first suggested by Kellogg [1959]. In a more recent paper, Kellogg [1960] has calculated the energy spectrum and flux of trapped electrons produced by albedo neutrons. This paper attacks the same problem. However, in addition, several more detailed features of the electron distribution are investigated explicitly, such as the angular distribution, the spatial distribution, and the dependence of the energy spectrum upon pitch angle. These latter results do not agree with Kellogg's.

Kellogg concludes that the cosmic-ray albedo mechanism cannot account for the observed electron flux, while Hess [1960], and more particularly Dessler and Karplus [1960], hold the

contrary view. Our aim here is to learn to what extent we can account for the observed electron component in terms of that produced by albedo neutrons, in view of the fact that there exists disagreement in the literature.

Throughout this calculation we explicitly assume a quiescent magnetic field that may be approximated closely by that of a dipole. We also consider a particular model of the outer atmosphere, although our results are easily re-derived for different models.

We are making use here of the guiding center approximation of Alfvén [1950]. This should be satisfactory since the radius of curvature of a trapped electron is very much less than the scale of magnetic field involved. Furthermore, we shall make the following assumptions which should hold reasonably well up to moderate altitudes and latitudes, i.e., in the region up to  $\sim 3$  earth radii where we compare theory with observations; namely, that not only the flux adiabatic invariant but also the longitudinal adiabatic invariant, and certainly the first adiabatic invariant, of magnetic moment are conserved.

The structure of the exosphere is not homoge-

<sup>1</sup> H. Goddard Memorial Fellow of the National Rocket Club, Washington, D. C. Part of this work was performed in partial fulfillment of the requirements for the Ph.D. degree at the University of Maryland.

<sup>2</sup> Present address: Lockheed Missiles and Space Company, Palo Alto, California.

neous, in the sense that the heavier components—oxygen and ionized oxygen—contribute primarily at altitudes below 1500 km, and also because of the eccentricity of the dipole field. We have considered a critical altitude at 1000 km below which the density is of such a high value that the lifetime of the electrons is too short for further consideration. It is realized, however, that the problem of the lower boundary of the electrons must be treated with considerably more caution. In particular, at the lower boundary the question of magnetic anomalies becomes of importance [Dessler and Karplus, 1960]. These factors are initially neglected but their effects are analyzed in the Discussion (Sec. 4).

The procedure which we shall follow is to assume, with Kellogg and Hess, an injection rate for the electrons derived from the decay density of neutrons at each point in space near the earth. We then proceed to calculate the injection spectrum of electrons, both in energy and in pitch angle. This distribution will be referred to the electrons as they cross the plane of the geomagnetic equator. We then consider the fate of the injected electrons under two different extreme assumptions: they are removed by pure energy loss; they are removed by pure scattering. The correct situation is intermediate and depends on certain factors which will be discussed. Finally, we compare the results of these calculations with observations.

## 2. INJECTION OF ELECTRONS

The starting point of our calculation is the neutron decay density in the space around the earth. Specifically, as was pointed out by Kellogg, it is the thermal neutrons which will be largely responsible for trapped electrons. His treatment makes use of data from cosmic-ray balloon observations on slow neutrons coupled with an analysis of their outward diffusion. He shows that the gravitational field of the earth must be considered in this problem [Kellogg, 1960]. Neutrons with energies less than 0.67 ev cannot escape from the earth's gravitational field. (Neutrons with energies  $< 1$  ev make up only  $\sim 0.5$  per cent of the albedo flux but are responsible for  $\sim 83$  per cent of the decays near the earth.) Kellogg gives results applying only to altitudes below about 3000 km. Hess, Canfield, and Lingenfelter [1961] have considered the neutron decay density in more detail

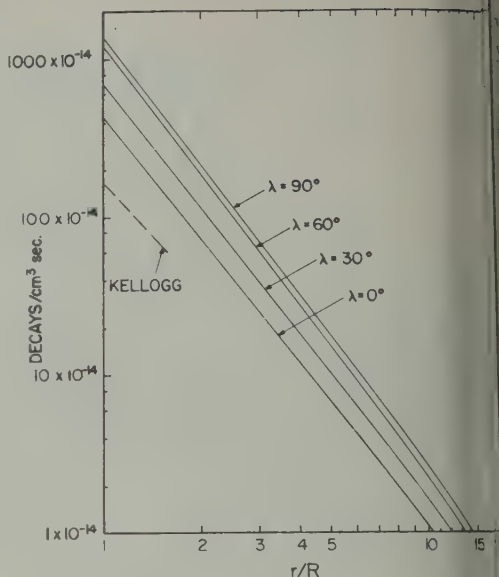


Fig. 1. Neutron decay density in space near the earth after Hess, Canfield, and Lingenfelter [1961] and Kellogg [1960].

and have based it largely on airplane measurements and a multigroup diffusion calculation. Their results apply out to several earth radii and include the latitude variation (Fig. 1).

The spatial distribution of neutron decay density near the earth obtained by Hess and his co-workers may be approximated analytically as follows:<sup>3</sup>

$$q(r, \lambda, E) = q_0(R/r)^{2.7}(3 - 2 \cos^2 \lambda)N_\beta(E)$$

Here  $r$  is the geocentric distance,  $R$  is the radius of the earth,  $\lambda$  is the geomagnetic latitude,  $q_0$  is  $3.7 \times 10^{-13}$ /cm<sup>2</sup>/ster/sec, and  $N_\beta(E)$  is the neutron  $\beta$  decay spectrum, normalized so that

$$\int_0^{780 \text{ keV}} N_\beta(E) dE = 1$$

The source density of injected electrons assumed to be isotropic at each point in space is

The  $\beta$ -decay energy spectrum is

$$N_\beta(E') = 1.2 \times 10^{-3}[E'(E' + 2)]^{1/2} \\ (E' + 1)(1.53 - E')^2$$

<sup>3</sup> This formula is in agreement with Kellogg's result and applies beyond 1000 km altitude. The  $r^{-4}$  dependence quoted by Dessler and Karplus [1960], and attributed to Hess, applies only to lower altitudes.

keV, where  $E' =$  kinetic energy/rest

now wish to average the injection rate  $q$  over the spiral path  $S$  and obtain the angular distribution  $\psi$  of the injected electrons as they cross the equatorial plane:  $\psi(\mu)$  is defined by

$$q(S) dS / \int dS = q_0(r_e/R)^{-2.7} \cdot N_\beta(E') \psi(\mu) \quad (3)$$

The integrations are carried out from the equatorial plane to the mirror point. We denote the line of the equatorial pitch angle by  $\mu$ . The line of force crossing the equatorial plane at  $r_e$  is described by

$$r/r_e = \cos^2 \lambda \equiv x \quad (4)$$

$$d\lambda/dx = -\frac{1}{2}(\cos \lambda \sin \lambda)^{-1}$$

be the arc length of the line of force (measured from the equatorial plane). Then

$$dZ^2 = dr^2 + r^2 d\lambda^2 \quad (5)$$

Using equations 4 and 5 we obtain

$$\frac{dZ}{dr} = -\frac{(1 + 3 \sin^2 \lambda)^{1/2}}{2 \sin \lambda} \quad (6)$$

The dimensionless arc length  $z$  is defined by

$$dZ/r_e = (1 + 3 \sin^2 \lambda)^{1/2} \cos \lambda d\lambda \quad (7)$$

It follows from (4) and (6). The dimensionless path length is

$$s = S/r_e \quad (8)$$

$ds$  and  $dz$  are related through the particle's pitch angle  $\alpha$ :

$$ds = dz / \cos \alpha \quad (9)$$

Using (7) and (9)

$$ds = \frac{(1 + 3 \sin^2 \lambda)^{1/2} \cos \lambda d\lambda}{\cos \alpha} \quad (10)$$

Using (4) and (10)

$$\frac{ds}{dx} dx = -\frac{(1 + 3 \sin^2 \lambda)^{1/2}}{2 \cos \alpha \sin \lambda} dx \quad (11)$$

Using (4)

$$ds = -\frac{(4 - 3x)^{1/2}}{2(1 - x)^{1/2} \cos \alpha} dx \quad (12)$$

Now,  $\cos \alpha$  is obtained as

$$\cos \alpha = [1 - (4 - 3x)^{1/2} x^{-3} \sin^2 \alpha_e]^{1/2} \quad (13)$$

from the adiabatic condition

$$\sin^2 \alpha / B = \sin^2 \alpha_e / B_e \quad (14)$$

and from the field variation along a line of force

$$B(\lambda)/B_e = (1 + 3 \sin^2 \lambda)^{1/2} / \cos^6 \lambda \quad (15)$$

Now, we may write the spatial part of  $q$  as

$$\begin{aligned} (R/r_e)^{2.7} (r_e/r)^{2.7} (3 - 2 \cos^2 \lambda) \\ = (R/r_e)^{2.7} x^{-2.7} (3 - 2x) \end{aligned} \quad (16)$$

Therefore the  $r_e$  dependence can be taken out of the integral equation 3, yielding

$$\bar{q}(r_e, \mu, E') = q_0(r_e/R)^{-2.7} \psi(\mu) N_\beta(E') \quad (17)$$

where

$$\begin{aligned} \psi(\mu) = \frac{1}{s(\mu)} \\ \cdot \int_{x_t}^1 \frac{(4 - 3x)^{1/2} (3 - 2x) dx}{2x^{2.7} (1 - x)^{1/2} [1 - (4 - 3x)^{1/2} (1 - \mu^2)x^{-3}]^{1/2}} \end{aligned} \quad (18)$$

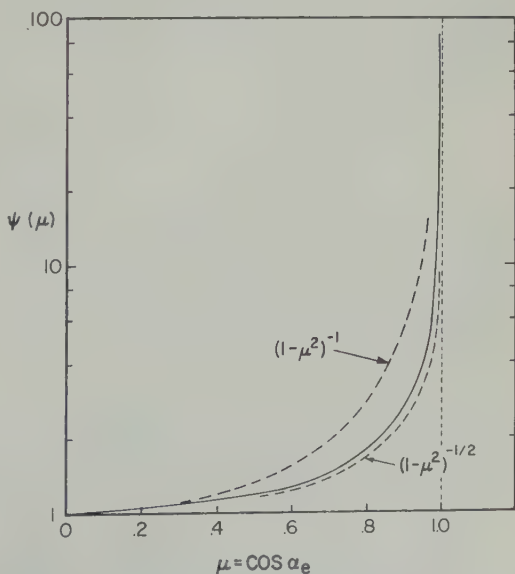


Fig. 2. Equatorial angular distribution of injected electrons,  $\psi(\mu)$ , calculated from a neutron decay density proportional to  $r^{-2.7} (3 - 2 \cos^2 \lambda)$ , is shown by a solid line. We see that  $\psi(\mu)$  can be approximated quite closely by  $1/\sin \alpha_e$ .



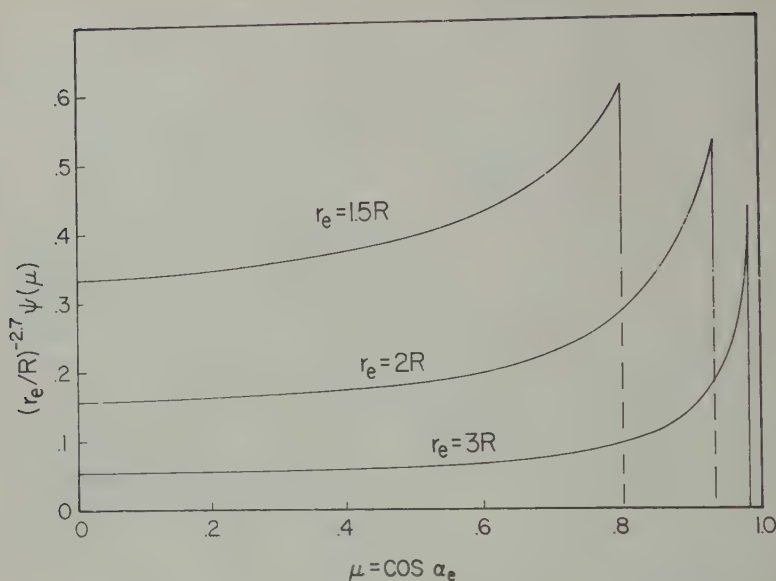


Fig. 3. Equatorial angular distributions of injected electrons (normalized by  $r_e^{-2.7}$ ) for various lines of force, characterized by  $r_e$ . We adopt a decay density proportional to  $r^{-2.7}$  ( $3-2 \cos^2 \lambda$ ) and a critical altitude 1000 km. Note that the area under each curve gives the total number of electrons injected along the line of force.

and  $\mu = \cos \alpha_e$ . Note that  $x_t$  refers to the turning point and depends on  $\alpha_e$ , being obtained from (14) and (15) by setting  $\alpha = 90^\circ$ . Here  $s(\mu)$  is obtained by substituting (13) into (12) and integrating between  $x = x_t(\mu)$  and  $x = 1$ . To a close approximation

$$s(\mu) \simeq 1.38 - 0.32[(1 - \mu^2)^{1/2} + (1 - \mu^2)^{1/4}] \quad (19)$$

Thus it can be seen that the (nondimensional) spiral path length (and therefore the bounce period between mirror points) varies only slowly with  $\alpha_e$  (and therefore with  $x_t$ ), namely, between 1.38 and 0.74. Note that  $s(\mu)$  does not depend on the particle's radius of gyration (or momentum).

$\psi(\mu)$  has been evaluated numerically and is shown in Figures 2 and 3. It is found that this function can be approximated quite closely by

$$\psi(\mu) \simeq \frac{1}{\sin \alpha_e} = \frac{1}{(1 - \mu^2)^{1/2}} \quad (20)$$

It is to be noted then that while the electrons are injected everywhere isotropically, the superposition along a line of force results in the rather nonisotropic distribution  $\psi(\mu)$  in the equatorial plane.

### 3. EQUILIBRIUM DISTRIBUTION OF ELECTRONS

The injected electrons are modified by the residual component of the earth's outer atmosphere. In collisions with ions and electrons and with the neutral atoms, small angle scattering and energy loss take place simultaneously. It has been shown that for protons, energy loss is dominant [Singer, 1958b]. Unfortunately, for the energies typical of  $\beta$ -decay electrons ( $\sim 30$  keV), both energy loss and scattering are of comparable importance. Nevertheless, considerable insight into the structure of the electron belt may be gained by considering the two effects independently; we will follow this procedure before attacking the combined problem.

**Atmospheric model.** The major constituents of the earth's exosphere above 530 km are neutral and ionized oxygen, and neutral and ionized hydrogen. The distribution of O is indicated from satellite drag data, the distribution of H is partly based on electron density measurements [Berning, 1960] and partly on the analysis of trapped proton intensities [Singer, 1960a].

The neutral hydrogen distribution in the exosphere has been determined by Öpik and Singer [1961], the relative distribution being calculated from theory, the normalization being

TABLE 1. Concentration of Major Constituents in the Terrestrial Exosphere (cm<sup>-3</sup>)

r/R	O	O <sup>+</sup>	H	H <sup>+</sup>
1.100	1.2 × 10 <sup>7</sup>	5 × 10 <sup>5</sup>	10 × 10 <sup>3</sup>	
1.200	2.7 × 10 <sup>4</sup>	2.5 × 10 <sup>4</sup>	6.6 × 10 <sup>3</sup>	9 × 10 <sup>3</sup>
1.300	1.7 × 10 <sup>3</sup>	1.7 × 10 <sup>3</sup>	4.4 × 10 <sup>3</sup>	6.6 × 10 <sup>3</sup>
1.400	1	1.3 × 10 <sup>3</sup>	3.1 × 10 <sup>3</sup>	5 × 10 <sup>3</sup>
1.500		11	2.3 × 10 <sup>3</sup>	3.7 × 10 <sup>3</sup>
1.75		< .1	1.25 × 10 <sup>3</sup>	2.1 × 10 <sup>3</sup>
2.00			8 × 10 <sup>2</sup>	1.3 × 10 <sup>3</sup>
3.00			2 × 10 <sup>3</sup>	3.5 × 10 <sup>2</sup>
4.00			82	1.5 × 10 <sup>2</sup>
5.00			43	85
6.00			25	51
7.00			16	33
8.00			12	23
9.00			9.1	17
10			6.5	11

by (day-time) Lyman- $\alpha$  observations [All and Tousey, 1960; Singer, 1960a]. The distribution is a subject of some controversy; the most extensive direct measurement is that of Smith and Helliwell [1960] by means of whistler observations.

The model which we adopt for the purpose of calculating trapped particle intensities is obtained from these sources and is shown in Table 1. The effective densities as defined in Appendix 1 are shown in Figure 4 and compared with results of Allcock [1959] and Pope [1961], together with a theoretical distribution calculated by Johnson [1960]. It should be pointed out explicitly that we are neglecting the rather large variations which certainly exist for all of the components. However, as the lifetime of the trapped particles is greater than 1 day, the mean distribution suggested in Table 1 may be used without making our calculations too unrealistic.

**Energy loss rate in the exosphere.** Assume for the moment that the electrons do not scatter; they retain their initial equatorial pitch angle throughout their lifetimes, but simply lose energy by interactions with particles in the atmosphere. The rate of energy loss is given by the following expression

$$-\frac{4\pi\rho_E r_0^2 c}{\beta} \ln (\lambda_D/b_{min}) [\text{sec}^{-1}] \quad (21)$$

The derivation of this important expression is given in Appendix 1. It is shown there that an effective density  $\rho_E$  can be calculated which depends on the composition and degree of ionization of the actual exosphere. Here  $r_0 = e^2/mc^2$

is the classical electron radius,  $\lambda_D = (kT/4\pi e^2 N_e)^{1/2}$  is the Debye shielding distance, where  $N_e$  is the density of free (plasma) electrons;  $b_{min}$  is the minimum impact parameter and

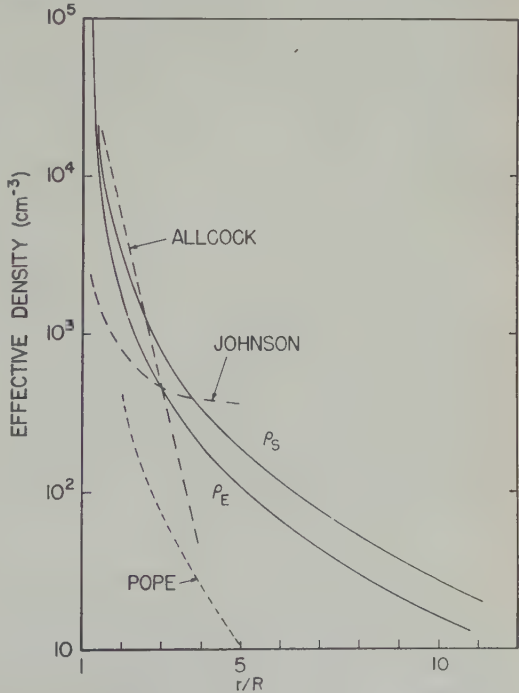


Fig. 4. Exospheric concentrations. Effective densities for energy loss,  $\rho_E$ , and for scattering,  $\rho_S$ , based on satellite observations [Öpik and Singer, 1961; Singer, 1960a] and on an ion distribution deduced from whistler observations [Smith and Helliwell, 1960]. Also shown are ion distributions reported by Johnson [1960], Allcock [1959], and Pope [1961].

depends on the electron's momentum  $p$  through  $b_{\min} = \hbar/p$ .

Since the trapped electron does not change its orbit in this model, we may average the atmospheric density over the spiral path, replacing  $\rho_E$  by  $\bar{\rho}_E$ . We can also express (21) in terms of  $E'$ :

$$\frac{dE'}{dt} = -3.0 \times 10^{-14} \bar{\rho}_E \frac{(E' + 1)}{[E'(E' + 2)]^{1/2}} \cdot \{22.9 + \log_{10} T - \log_{10} N_e + \log_{10} [E'(E' + 2)]\} \quad (22)$$

We have made use of the relations

$$\beta = \frac{[E'(E' + 2)]^{1/2}}{E' + 1}$$

$$\text{and } \frac{pc}{mc^2} = \beta\gamma = [E'(E' + 2)]^{1/2} \quad (23)$$

The log term varies very slowly with energy producing only a 3 per cent variation over the entire energy range of interest. It can be seen that  $dE'/dt$  is also fairly insensitive to the temperature of the exosphere. We therefore set the log term equal to 23 and use the following simplified expression

$$\begin{aligned} \frac{dE'}{dt} &= -6.9 \times 10^{-13} \bar{\rho}_E / \beta \\ &= -6.9 \times 10^{-13} \bar{\rho}_E (E' + 1) [E'(E' + 2)]^{-1/2} \end{aligned} \quad (24)$$

Before we proceed to determine the equilibrium distribution of trapped electrons as a function of energy and of spatial coordinates, we must evaluate  $\bar{\rho}_E$  as a function of orbit parameters  $r_e$  and  $\alpha_e$ .  $\bar{\rho}_E$  is the effective density seen by the trapped electron, averaged over its particular orbit, i.e.

$$\bar{\rho}_E(r_e, \alpha_e) = \int \rho_E ds / \int ds \quad (25)$$

It may be observed from Figure 4 that, in the range 2-8 earth radii, the effective energy loss density is (within a factor of 2)

$$\rho_E(r) \simeq \rho_0 (r/R)^{-\nu} \quad (26)$$

where  $\nu = 2.8$  and where  $\rho_0 = 10^4 \text{ cm}^{-3}$ . Equation 25 can now be evaluated using (9), (12), and (13). In Figure 5 we plot  $\bar{\rho}_E/\rho_{Ee}$ , the ratio of average density to equatorial density, as a

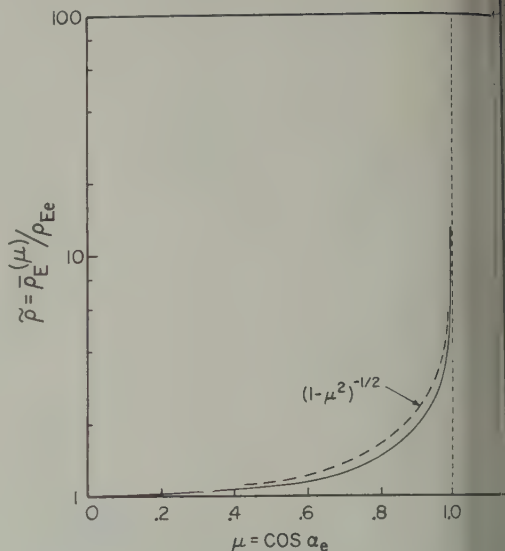


Fig. 5. Average effective density,  $\bar{\rho}_E$ , over spiral path in terms of equatorial value  $\rho_{Ee}$ . We assume  $\rho_E(r) \propto r^{-2.8}$ .

function of  $\mu = \cos \alpha_e$ . We also plot the function  $1/\sin \alpha_e$  which differs only slightly from  $\bar{\rho}_E/\rho_{Ee}$ . Within the range of uncertainty of exospheric densities the average density over a spiral orbit is therefore

$$\bar{\rho}_E \simeq \rho_{Ee} / \sin \alpha_e \quad (25')$$

and

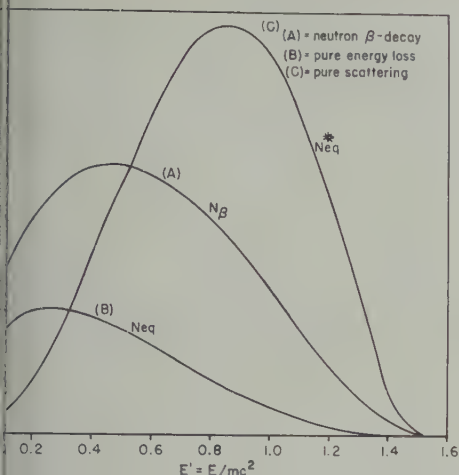
$$\begin{aligned} \frac{dE'}{dt}(r_e, \mu) &= -6.9 \times 10^{-13} \\ &\cdot \rho_0 (r_e/R)^{-\nu} [\beta \cdot \sin \alpha_e]^{-1} \end{aligned} \quad (24')$$

*Case 1: Pure energy loss approximation.* Now  $\bar{q}(E_i)$   $dE_i$   $d\Omega$  is the number of electrons injected per cubic centimeter per second having energy between  $E_i$  and  $E_i + dE_i$  and located (at the equator) within solid angle  $d\Omega$  at pitch angle  $\alpha$ . These electrons drift downward in energy at rate given by equation 24. In general, we can write an equation of continuity in 'E-space'

$$\begin{aligned} \frac{\partial n}{\partial t} + \text{div}_E \left( n \cdot \frac{dE}{dt} \right) \\ = \frac{\partial n}{\partial t} + \frac{\partial}{\partial E} \left[ n \frac{dE}{dt} \right] = \bar{q}(E) \end{aligned} \quad (27)$$

Under equilibrium conditions  $\partial n/\partial t = 0$ , and  $n(E)$  can be obtained in terms of the integral





6. Energy spectra of differential concentration for 3 cases: (A) injection spectrum, (B) equilibrium spectrum for pure energy-loss, and (C) equilibrium spectrum for pure scattering.

$d\Omega$  over all injection energies  $E_i > E$ .

$$n(E) = \frac{1}{|dE/dt|} \int_E^\infty \bar{q}(E_i) dE_i \quad (28)$$

$n(E) = n(E, r_e, \mu)$  is the differential concentration of electrons, i.e., electrons/cm<sup>3</sup> ster at the equatorial plane.

Substituting (17) and (24') into (28) and using numerical values we get

$$n_e, \mu = 6.4 \times 10^{-4} \cdot (r_e/R)^{-2.7} \frac{\psi(\mu)}{\bar{\rho}_{Ee}(\mu)} N_{eq}(E') \quad (29)$$

the equation for the  $\beta$  decay energy spectrum equation 2, we find the energy dependent part  $N_{eq}(E')$  (cf. Fig. 6):

$$N_{eq}(E') = \frac{[E'(E' + 2)]^{1/2}}{E' + 1} \int_0^{1.53} [u(u + 2)]^{1/2} (u + 1)(1.53 - u)^2 du \quad (30)$$

'angle dependent' part actually turns out nearly independent of  $\alpha_e$  since

$$\psi_{eq} \equiv \frac{\psi}{[\bar{\rho}_{Ee}(\mu)/\rho_{Ee}]} \cong \frac{1/\sin \alpha_e}{1/\sin \alpha_e} \quad (31)$$

last relation follows from (20) and (25') and that the equilibrium angular distribution

in the case of pure energy loss is approximately isotropic up to the critical angle,  $\alpha_c$ . For  $\mu > \mu_c = \cos \alpha_c$  the atmospheric density  $\bar{\rho}_{Ee}(\mu)$  is assumed to be infinite.

The differential directional intensity (electrons/kev cm<sup>2</sup> ster sec) is

$$j(E', r_e) = n\beta c = 1.9 \times 10^7 \frac{(r_e/R)^{-2.7}}{\rho_{Ee}(r_e)} j_1(E') \quad (32)$$

$j_1$  is shown in Figure 7. The counting rate of a spherical detector with threshold  $E'$  will be proportional to the integral omnidirectional flux

$$I(> E') = 4\pi \int_{E'}^\infty j(E') dE' \cdot \int_0^{\mu_c} d\mu [\text{electrons/cm}^2 \text{ sec}] \quad (33)$$

Assuming  $\mu_c \simeq 1$

$$I(> E') = \frac{1.9 \times 10^{11}}{\rho_{Ee}} (r_e/R)^{-2.7} I_1(E') \quad (34)$$

where

$$I_1(E') = \int_{E'}^{1.53} j_1(w) dw$$

$$I_1(0) = 0.40 \quad (35)$$

and

$$j_1(w) = \frac{w(w + 2)}{(w + 1)^2} \int_w^{1.53} [u(u + 2)]^{1/2} \cdot (u + 1)(1.53 - u)^2 du \quad (36)$$

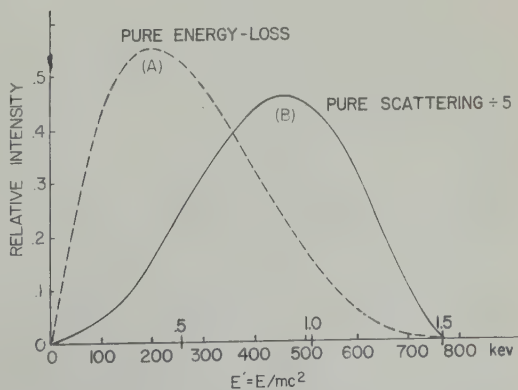


Fig. 7. Equilibrium energy spectra of intensity, assuming (A) pure energy-loss,  $j_1(E')$ , and (B) pure scattering,  $j_2(E')$ . Note that the pure scattering curve has been divided by 5.

TABLE 2. Lifetime for loss of 90 per cent of energy for 300 kev electron ( $\alpha_e = 60^\circ$ ).  $\bar{\rho}_E$  is effective density averaged over orbit.

$r_e/R$	$\bar{\rho}_E, \text{cm}^{-3}$	$T, \text{years}$
1.5	$\sim 10^5$	0.12
2	$2.1 \times 10^3$	6.7
3	$5.2 \times 10^2$	26.2
4	$2.3 \times 10^2$	59
5	$1.2 \times 10^2$	118

The integral omnidirectional flux  $I(>0)$  turns out to be (at the equator)  $10^7$  electrons/cm<sup>2</sup> sec, at 5  $R$  where  $\rho_{Ee} \sim 100 \text{ cm}^{-3}$  is assumed (see Fig. 4). Other estimates of the ion density in this region should be noted. *Johnson* [1960] deduces a density  $\sim 400 \text{ cm}^{-3}$  at this level.

Integrating equation 24 and using the exospheric densities given in Figure 4 we may calculate the lifetime (defined here as the time required to lose 90 per cent of its initial energy) of a 300-kev electron as a function of altitude. Typical lifetimes are given in Table 2. Inclusion of the effect of scattering will reduce these lifetimes, as will be discussed below.

Finally, it is noted that since the source density,  $\propto r_e^{-2.7}$ , and the atmospheric density,  $\propto r_e^{-2.8}$ , exhibit almost the same altitude dependence, the equilibrium flux will be almost constant in magnitude vs. altitude in the equatorial plane beyond  $\sim 3R$ .

Hence, insofar as we can approximate an atmospheric model by a power law in a certain range of  $r$ , we can easily rederive our results for any chosen atmospheric model.

**Case 2: Scattering without energy loss.** The assumption is now made that the electrons do not lose energy but only scatter in pitch angle (as would be the case if they scattered only from infinitely heavy particles). Each electron's velocity vector, always referred to the equatorial plane, executes a random walk in pitch angle. Although only ambient electrons are effective in absorbing energy, both electrons and nuclei are effective in the scattering process. Adding up the densities of each atmospheric component, each weighted according to its effectiveness relative to free electrons, we obtain the effective density of scattering centers,  $\rho_s$ . (For example, in fully ionized hydrogen  $\rho_s = \rho_{\text{electrons}} + \rho_{\text{protons}} = 2\rho_{\text{electrons}}$ . See Appendix 1, Table 1.1)

The random walk of the equatorial pitch angle

occurs with constant step size and at a rate determined by the equatorial density [*Wentworth* 1959, 1960]. The explanation of this last point is essentially that, because of the fundamental relation

$$\frac{\sin^2 \alpha}{B} = \frac{\sin^2 \alpha_e}{B_e}$$

a scattering event which occurs at some point along the line of force (where the pitch angle is  $\alpha$ ) and produces a change  $\Delta\alpha$  in the pitch angle at that point, only produces a change

$$\Delta\alpha_e = \frac{\tan \alpha_e}{\tan \alpha} \Delta\alpha \quad (3)$$

in the equatorial pitch angle. Note that  $\Delta\alpha_e/\Delta\alpha$  may be extremely small when the scattering occurs near the mirror point ( $\alpha \sim \pi/2$ ) and  $\alpha_e$  is small. The scattering rate depends on the average value of  $\rho_s(\Delta\alpha_e)^2$  over the orbit, or therefore upon  $\langle \rho_s \tan^2 \alpha_e / \tan^2 \alpha \rangle$ . When this average is computed, it is found that for wide variations in atmospheric models, the result is approximately equal to one-half the equatorial density of scattering centers  $1/2 \rho_{se}$  [*Wentworth* 1960]. Thus, while the energy loss rate is a function of equatorial pitch angle, the scattering rate is independent of  $\alpha_e$ .

The decay of  $n(\mu)$  from an initially injected distribution is governed by a diffusion equation of the form [*Walt and MacDonald*, 1961; *MacDonald and Wentworth*, 1961]

$$\frac{\partial n(\mu)}{\partial t} = -\frac{D}{\mu s(\mu)} \frac{\partial}{\partial \mu} \left[ \left( 1 - \mu^2 \right) s(\mu) \mu \frac{\partial n}{\partial \mu} \right] \quad (38)$$

where  $s(\mu)$  is defined in (19) and

$$D(E) = 1.73 \times 10^{-13} \rho_{se} \frac{E' + 1}{[E'(E' + 2)]^{3/2}} \quad (39)$$

The reciprocal of the diffusion coefficient is approximately the time it takes for the lowest eigenfunction of (38) to decay in amplitude by a factor  $1/e$ .  $(1/D)$  is also about equal to the time to random walk through  $90^\circ$  in simple one-dimensional diffusion [*Singer*, 1958a, 1958b; *Kellogg*, 1959; *Welch and Whitaker*, 1959].

It is shown in Appendix 1 (equations 1-10) that the mean square deflection of a fast electron moving through an ionized gas accumulates at a rate (per second) given by

$$= 8\pi\rho_s r_0^2 c \frac{(1 - \beta^2)}{\beta^3} \ln(\lambda_D p / \hbar) \quad (40)$$

$\rho_s$  is the effective (scattering) density, proportional to  $Z^2$ ,  $Z$  being the atomic number of the scatterer. Neglecting the variation of  $\beta$  with the process we may integrate equation (40) to obtain the mean time required to scatter through the angle  $\varphi$ :

$$= \frac{\varphi^2 \beta^3}{8\pi\rho_s r_0^2 c (1 - \beta^2) \ln(\lambda_D p / \hbar)} \text{ sec} \quad (41)$$

of the effect discussed in the previous paragraph we evaluate  $T_S$  using one-half the equatorial plane value of  $\rho_s$ , i.e.,  $1/2 \rho_{s_e}$ .

For  $\ln(\lambda_D p / \hbar) = 23$  the scattering time to

$$\approx 1.5 \times 10^{12} \frac{\varphi^2 \beta^3}{\rho_{s_e} (1 - \beta^2)} \text{ sec} \quad (42)$$

quoted in connection with the solution of equation 38,  $T_S(\pi/2)$  may be used as a measure of average lifetime.

We now calculate the equilibrium energy distribution as follows. The diffusion equation in the steady state is

$$= -\frac{D(E)}{\mu s(\mu)} \frac{\partial}{\partial \mu} \left[ (1 - \mu^2) s(\mu) \mu \frac{\partial n^*}{\partial \mu}(E, \mu) \right] \quad (43)$$

The starred quantities refer to the pure energy-loss case. Using equation 17 we see that equation 43 is separable, yielding

$$n^* = 2.6 \times 10^{-3} \frac{(r_e/R)^{-2.7}}{\rho_{s_e}} N_{eq}^*(E') \psi_{eq}^*(\mu) \quad (44)$$

The energy dependent part is

$$N_{eq}^*(E') = \frac{[E'(E' + 2)]^{3/2}}{E' + 1} N_B(E') \quad (45)$$

When plotted (in Fig. 6) we see that the peak of the flux is at a higher energy than the peak of the equilibrium flux for pure energy loss. The angular part of the solution of

$$\frac{\partial}{\partial \mu} \left[ s(\mu) \mu (1 - \mu^2) \frac{\partial \psi_{eq}^*}{\partial \mu} \right] = -\psi(\mu) \quad (46)$$

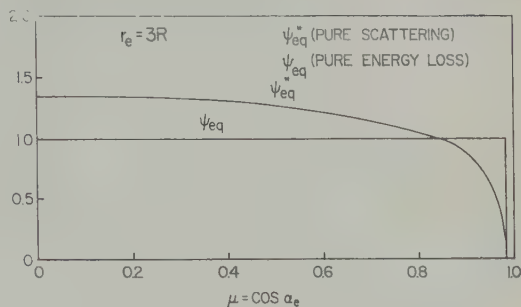


Fig. 8. Equilibrium angular distributions for the cases of (A) pure energy-loss and (B) pure scattering. Both distributions refer to  $r_e = 3R$ .

This is subject to the boundary conditions

$$\psi_{eq}^*(\mu_e) = 0; \quad \left. \frac{\partial \psi_{eq}^*}{\partial \mu} \right|_{\mu=0} = 0 \quad (47)$$

Equation 46 can be integrated exactly; a particular result is given in Figure 8.

The differential directional intensity is therefore

$$j^*(E', r_e, \mu) = \frac{7.8 \times 10^7}{\rho_{s_e}(r_e)} \psi_{eq}^*(\mu) (r_e/R)^{-2.7} j_2(E') \quad (48)$$

where we have multiplied  $N_{eq}^*$  by  $\beta c$ . Here

$$j_2(E') = \frac{[E'(E' + 2)]^{5/2} (1.53 - E')^3}{E' + 1} \quad (49)$$

and the integral omnidirectional flux in the equatorial plane is

$$I^*(> E') = \frac{7.8 \times 10^{11}}{\rho_{s_e}} (r_e/R)^{-2.7} \cdot \int_0^{\mu_e} \psi_{eq}^*(\mu) d\mu \int_{E'}^{1.53} j_2(u) du \quad (50)$$

As shown in Figure 7,  $j_2$  has a peak at 450 kev compared to the injection peak at  $\sim 300$  kev. This represents the fact that high-energy electrons scatter relatively less rapidly than low-energy electrons. It may be compared to the peak of  $j_1(E)$  at 200 kev for the pure energy loss case. The fluxes calculated on this basis are somewhat greater than those obtained from the pure energy loss model. Clearly the addition of another loss mechanism can only decrease the equilibrium flux; we must therefore regard the energy loss result as an upper limit to the actual flux.



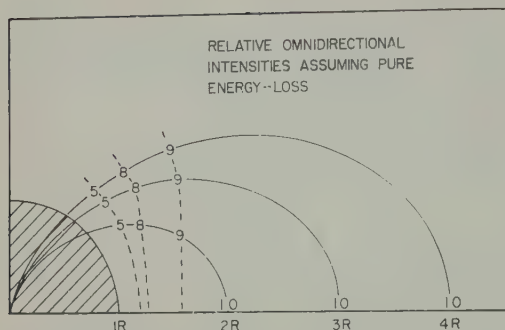


Fig. 9. Spatial distribution of omnidirectional intensity assuming pure energy-loss. This assumption is probably valid at low latitudes and altitudes. It should be noted, of course, that this spatial distribution applies only to the albedo component of trapped electrons.

#### 4. DISCUSSION OF RESULTS

The results of the preceding section give the differential directional intensity of the trapped electrons at the equatorial plane for the two extreme cases: (1) pure energy loss; (2) pure scattering. Here we shall calculate the spatial distribution of trapped electrons, and then approach the more difficult case of energy loss and scattering acting simultaneously in a qualitative analysis.

**Spatial distribution.** The altitude and latitude distribution of trapped particles is obtained from the equatorial values. In particular, the pitch-angle distribution gives the intensities along the line of force, using Liouville's theorem and geometry of the dipole field [Ray, 1960]. Since in our calculations of  $j(E', r_e, \mu)$  the variables are clearly separated, both differential and integral intensities will have the same spatial distribution.

In general, a completely isotropic distribution leads to constant omnidirectional fluxes along the line of force, but such a distribution does not exist. For example, in the pure energy loss case, the distribution is only *partly* isotropic; within the so-called 'loss cone' around  $\alpha_c = 0$ , extending to a critical angle  $\alpha_{ec}$ , there are no trapped particles. As a result, the omnidirectional differential flux  $i$  will decrease as we move away from the equator. The pure scattering case is similar, but tends smoothly to zero at  $\alpha_{ec}$  (Fig. 8).

We shall now calculate the omnidirectional flux  $i(\lambda)$  along a line of force in terms of the equatorial flux  $i_e$  for two cases: (1)  $j$  is 'isotropic'

(i.e., constant over a *range* of pitch angle, generally from  $\alpha_c$  to  $\alpha = \pi/2$ ); (2)  $j$  is a function of  $\alpha$ .

In general the omnidirectional flux is

$$i = 4\pi \int_0^{\alpha_{ec}} j(\alpha) d(\cos \alpha) \quad (5)$$

1. If  $j(\alpha)$  is 'isotropic' up to  $\alpha_c$ , then at latitude  $\lambda$

$$i(\lambda) = 4\pi j \cos \alpha_c(\lambda) \quad (5)$$

At the equatorial plane  $\alpha_c(\lambda = 0) = \alpha_{ec}$ . Hence

$$i(\lambda)/i_e = \cos \alpha_c(\lambda)/\cos \alpha_{ec} \quad (5)$$

Now  $\cos \alpha_{ec}$  is related to  $h$ , the critical altitude and  $r_e$ , the geocentric distance, through the adiabatic condition, equation 14, and the equations of the dipole field, equations 4 and 1. For the turning point

$$x_t = (R + h)/r_e = \cos^2 \lambda, \quad (5)$$

In (14) set  $\alpha = \alpha_t = \pi/2$  and  $B = B_t$ . Substitute (15) and (54) and obtain

$$\cos \alpha_{ec} = [1 - x_t^3(4 - 3x_t)^{-1/2}]^{1/2} \quad (5)$$

Write the adiabatic condition in the form

$$\cos \alpha_c(\lambda) = [1 - (B(\lambda)/B_e) \sin^2 \alpha_{ec}]^{1/2} \quad (5)$$

and express  $B(\lambda)/B_e$  by means of (15) and  $\sin^2 \alpha_{ec}$  with the help of (55). The result is

$$\cos \alpha_c(\lambda) = [1 - (4 - 3 \cos^2 \lambda)^{1/2} \cdot \cos^{-6} \lambda x_t^3(4 - 3x_t)^{-1/2}]^{1/2} \quad (5)$$

Equations 55 and 57 allow us to compute  $i(\lambda)/i_e$  from (53). The spatial distribution which then results is shown in Figure 9.

2. In cases where  $j(\alpha)$  is not 'isotropic,' a convenient technique for calculation of  $i(\lambda)$  is described in Appendix 2. We have evaluated a matrix which allows conversion from a given angular distribution into the corresponding spatial distribution, and vice versa.

**Effect of magnetic anomalies on spatial distribution.** The application of these formulas to observations is complicated by the fact that the geomagnetic field exhibits large departures from dipole symmetry. It has been suggested [Dessler and Karplus [1960]] that the Capetown anomaly (a region of reduced sea level field strength) accounts for the unusually low intensity

served on lines of force belonging to  $\sim 3R$ . The effect of an anomaly such as that at Cape Town is to lower mirror points on this line of force by some distance. This is roughly equivalent to raising the critical altitude by the same amount. For the Capetown anomaly this effect is  $\sim 1300$  km [Cladis and Dessler, 1961]. In this model we have computed the effect of the Capetown anomaly, assuming an 'isotropic' particle distribution, a normal critical altitude of 10 km and with  $r_e = 2.7R$ . In Figure 10 we plot the ratio of the omnidirectional fluxes in the presence of the anomaly and in its absence (for a near-by line of force). Note that the effect of the flux deficiency is a very sensitive function of altitude, as is pointed out by Dessler and Karplus [1960], and amounts to only 2% in the equatorial plane. (This result is insensitive to the form of the neutron decay curve above 1000 km.)

**Relative importance of energy loss and scattering.** In order to define the situations under which the contribution of scattering may be neglected we use the technique of comparing the two lifetimes [Karplus, 1958b]. We first integrate equation 21 to obtain the energy-loss lifetime for slowing down from an initial  $\beta_i$  to a final  $\beta_f$ :

$$[4\pi r_0^2 c \bar{\rho}_E \ln(\lambda_D/b_{\min})]^{-1} \int_{\beta_f}^{\beta_i} \beta dE' \quad (58)$$

where  $E' = \gamma - 1 = (1 - \beta^2)^{-1/2} - 1$  we have

$$dE'/d\beta = \beta(1 - \beta^2)^{-3/2} \quad (59)$$

$$[4\pi r_0^2 c \bar{\rho}_E \ln(\lambda_D/b_{\min})]^{-1} [g(\beta_i) - g(\beta_f)] \quad (60)$$

$$= \beta(1 - \beta^2)^{-1/2}$$

$$- \arcsin \beta = [E'(E' + 2)]^{1/2}$$

$$- \arcsin \{[E'(E' + 2)]^{1/2}(E' + 1)^{-1}\}$$

Integrating  $T_E$  by the scattering lifetime  $T_S$ , from equation 41, we obtain

$$T_S = [\rho_{Se}/\bar{\rho}_E(\mu)] 2\varphi^{-2} \cdot [g(\beta_i) - g(\beta_f)] (1 - \beta_i^2) \beta_i^{-3} \quad (61)$$

of  $E'$  this is

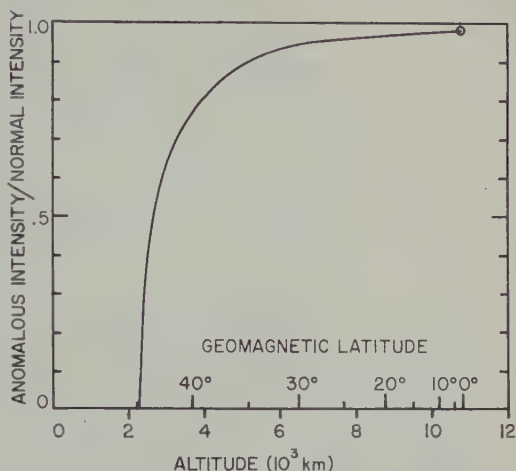


Fig. 10. Ratio of anomalous intensity to intensity which would exist in the absence of the magnetic anomaly at Capetown. The abscissa refers to the altitude and latitude of points lying on the line of force ( $r_e = 2.7R$ ) passing through the anomaly. The effect of the anomaly has been introduced schematically by raising the critical altitude from 1000 km to 2300 km. Note that the effect of the anomaly is pronounced only at latitudes above about  $40^\circ$ .

$$\begin{aligned} T_E/T_S &= \frac{\rho_{Se}}{\bar{\rho}_E(\mu)} \frac{2}{\varphi^2} \left\{ [E_i'(E_i' + 2)]^{1/2} \right. \\ &\quad - [E_f'(E_f' + 2)]^{1/2} \\ &\quad + \arcsin \left( \frac{[E_f'(E_f' + 2)]^{1/2}}{E_f' + 1} \right) \\ &\quad \left. - \arcsin \left( \frac{[E_i'(E_i' + 2)]^{1/2}}{E_i' + 1} \right) \right\} \\ &\quad \times \frac{E_i' + 1}{[E_i'(E_i' + 2)]^{3/2}} \quad (62) \end{aligned}$$

The energy-dependent portion of equation 62 is plotted in Figure 11 as a function of initial energy for various values of final energy. The remaining factor  $(\rho_{Se}/\bar{\rho}_E) (2/\varphi^2)$  is evaluated as 5.24 using a median value for  $\mu$  of 0.66 and for a line of force  $r_e = 4R$  ( $\mu_e = 0.99$ ).

Some important conclusions can be drawn from the examination of equation 61, and also from Figure 11.

(a) Evidently, the nature of the detector is of great importance in comparing experimental results with theory. For example, a detector sensitive to high-energy electrons only, but not to bremsstrahlung, e.g. a thin window coinci-

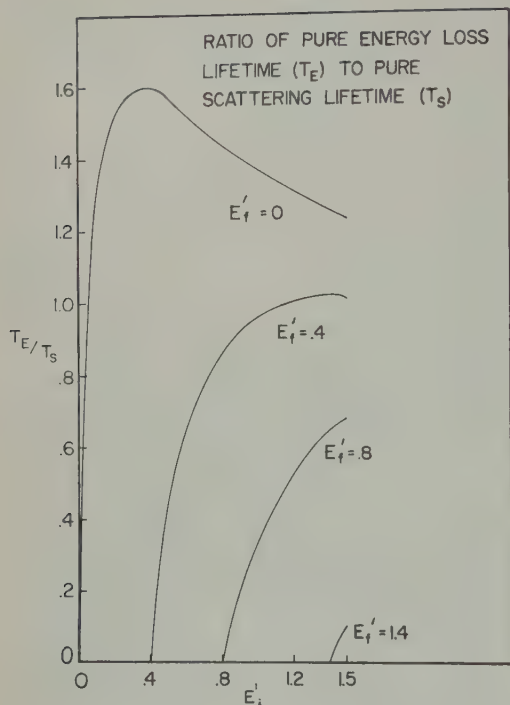


Fig. 11. Ratio of pure energy-loss lifetime ( $T_E$ ) to pure scattering lifetime ( $T_S$ ), as a function of initial energy  $E_i$  and for various final energies,  $E_f'$ . We have set  $(\rho_{SE}/\bar{\rho}_E)(2/\varphi^2) = 5.24$ , corresponding to  $\mu = 0.66$  at 4 earth radii.

dence telescope, covers such a small range of  $\beta$  that  $T_E/T_S \ll 1$ . A similar situation obtains for the case of a shielded counter where the response (efficiency) to bremsstrahlung (from electrons stopped in the shield) falls extremely rapidly with decreasing electron energy.

(b) For a detector that responds with very-high efficiency down to very low electron energies, scattering cannot be neglected. In practice however this case rarely concerns us: a comparison of albedo theory with experiment becomes difficult at very low electron energies ( $<100$  kev) because of the presence of a strong component of low-energy 'auroral' electrons (see sect. 5).

*Case 3. Simultaneous energy loss and pitch angle diffusion.* Where energy loss and diffusion are equally important, it is necessary to solve the Fokker-Planck equation in energy and pitch angle [Wentworth, MacDonald, and Singer, 1959; MacDonald and Walt, 1960]. Walt and MacDonald [1961] have solved this equation for

a source function isotropic in the equatorial plane. They use the Johnson [1960] atmosphere to derive a distribution matrix which is approximately diagonal. They neglect the off-diagonal elements in their solution and find that the equilibrium energy spectrum is a function of pitch angle, having peaks at higher energies at lower pitch angles. The error introduced by this approximation depends on the atmospheric model and becomes smaller for a more uniform atmosphere, the off-diagonal elements for a complete uniform atmosphere being identically zero. They found the error introduced by such an approximation to be small, however, and they conclude that the spectrum of trapped electrons gets harder at lower altitudes (low-pitch angles). This result they then explain on the basis of the qualitative argument that close to the loss cone (critical pitch angle) the low-energy particles, scattering faster, are relatively more quickly removed leaving the high-energy particles to dominate the spectrum in this region.

However, this result is a function of the form of the atmosphere. If the atmosphere is more dense near the mirror point, energy loss is enhanced, while pitch angle diffusion remains unaffected because of the ' $\tan^2 \alpha_e/\tan^2 \alpha$ ' effect. Indeed, it is possible to have an atmosphere that leads to the same pitch angle distribution for either pure energy loss or pure pitch-angle diffusion under an assumed source. This atmospheric model makes the Fokker-Planck equation separable, which implies that the energy spectrum is independent of pitch angle.

Consider the equation for simultaneous energy loss and scattering, in equilibrium,

$$-\frac{\partial}{\partial E} \left[ n \frac{\partial E'}{\partial t} \right] + D(E') \frac{1}{\mu s} \frac{\partial}{\partial \mu} \cdot \left[ (1 - \mu^2) \mu s \frac{\partial n}{\partial \mu} \right] + \bar{q} = 0 \quad (6)$$

Write

$$n(E', \mu) = M(E') \phi(\mu)$$

The assumption that  $\phi(\mu)$  satisfies both the pure energy loss and pure scattering equation implies

$$\phi(\mu) = \psi(\mu) [\bar{\rho}_E(\mu)/\rho_{Ee}]^{-1} \quad (7)$$

and

$$\frac{1}{\mu s} \frac{\partial}{\partial \mu} \left[ (1 - \mu^2) \mu s \frac{\partial \phi(\mu)}{\partial \mu} \right] = -\psi(\mu) \quad (8)$$



to the same boundary conditions given in equation 47.

Substitution of these last two into (63) yields an equation for  $M(E')$  which, upon integration,

$$= 6.4 \times 10^{-4} \frac{(r_e/R)^{-2.7}}{\rho_{Ee}(r_e)} N^\dagger(E'), \quad (66)$$

$$= e^{-\rho(E')}$$

$$u(u+2)(1.53-u)^2 e^{g(u)} du \quad (67)$$

$$\int_u^\infty \frac{1 + (\rho_{Se}/4\rho_{Ee})(w+1)}{w(w+1)(w+2)} dw. \quad (68)$$

Using  $\rho_{Se}/\rho_{Ee} = 2$ , (fully ionized hydrogen) the intensity energy spectrum,  $\beta N^\dagger$ , which is shown in Figure 12, with the pure energy loss spectrum for comparison. The combined energy loss and scattering spectrum shows the same shape, with a peak only a few percent higher than that of the pure energy loss spectrum.

The atmosphere which produces this separation in the equation depends, of course, upon the assumed angular distribution. With the injection distribution produced by neutron albedo, the atmosphere very similar to the real atmosphere in the altitude range  $\sim 1500$ – $3000$  km,  $r \propto \exp(-3r/R)$ , suffices.

We see that, under the assumption of a sharp cutoff at the critical altitude or pitch angle, the form of the atmosphere determines whether the energy spectrum gets harder or softer at low altitudes or small pitch angles. A uniform atmosphere leads to a hardening of the spectrum at low pitch angles, a special atmosphere leads to a constant energy spectrum for all pitch angles, and a steeper atmosphere would presumably lead to a softer spectrum at low pitch angles.

Another point needs to be considered, however, that can be expected of a diffuse boundary where the density of scattering centers increases rapidly at lower altitudes but does not remove particles off completely? In our original model a particle that reached the critical pitch angle was suddenly and catastrophically re-

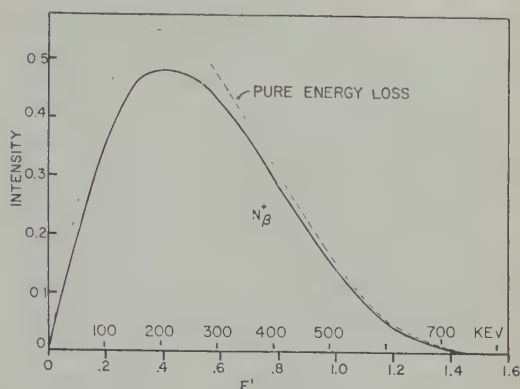


Fig. 12. Energy spectrum of the differential intensity,  $N^\dagger\beta$ , for the case of energy-loss plus scattering. The pure energy-loss and pure scattering angular distributions are taken to be nearly identical. The pure energy-loss spectrum is shown dotted for comparison. Note the remarkable similarity of the two.

moved. Now, that particle reaches the critical pitch angle, plunges into a relatively dense atmosphere at its mirror point, loses a relatively large amount of energy there, but lives to return to the equatorial plane. It can then be scattered back into the allowed region above the critical pitch angle. The spectrum of these particles will thus be determined essentially by the pure energy loss mechanism, and the resultant spectrum in the vicinity of the critical pitch angle will be softer than that calculated on the assumption of a sharp boundary.

Thus the relative hardness or softness of the energy spectrum of trapped electrons mirroring at low altitudes is fundamentally determined by the gradient in the atmospheric density at low altitudes, as well as its change in composition. This problem has not been satisfactorily solved up to the present. However, it is interesting to note the following: (1) The energy spectrum obtained by Walt and MacDonald under their assumption of a uniform atmosphere is, for all pitch angles, quite close to the pure energy loss spectrum. (2) The energy spectrum for our special atmosphere which leads to separation of the Fokker-Planck equation, is extremely close to the spectrum for pure energy loss. (3) Energy loss is relatively more important for high-energy electrons, which contribute most effectively to any Geiger counter experiment. Thus we may tentatively conclude that questions regarding the energy spectrum of the higher energy compo-

nents of the radiation belt produced by the decay of thermal neutrons may be fairly accurately solved by the application of the pure energy loss formulation.

### 5. COMPARISON WITH OBSERVATIONS

In the preceding sections we have discussed in some detail the injection and trapping of electrons generated by the decay of thermal cosmic ray neutrons. We have discussed quantitatively two major loss mechanisms, Coulomb scattering and energy loss in collisions in the exosphere, and have derived the properties of the equilibrium distribution of trapped electrons. In most practical cases the energy loss mechanism is the more important one, and therefore the results from that calculation are the ones which should be compared with experiments.

The results of such a comparison can then be used to decide whether neutron albedo does account for *all* of the trapped electrons (see *Dessler and Karplus*, 1960; *Hess*, 1960; and *Kellogg*, 1960, for conflicting views). Before a comparison is undertaken, however, it is well to remember that there may be other mechanisms which can remove the trapped electrons in addition to the ones which we have explicitly considered here. For example, scattering by hydromagnetic waves [*Welch and Whitaker*, 1959], radial drift due to field instabilities [*Gold*, 1959; *Parker*, 1960], or diffusion in the geomagnetic field [*Herlofson*, 1960], synchrotron radiation, and possibly others. Since these effects are not considered in our paper, our calculation represents the maximum values of electron intensities that can be accounted for from neutron albedo. As we shall see, our results are not able to account for all of the trapped electrons, and we therefore conclude that two separate sources are responsible for the geomagnetically trapped radiation.

We will make our comparison only with the two experiments in which energy and flux determinations of electrons have been performed.

*Walt, Chase, Cladis, Imhof, and Knecht* [1960] made magnetic spectrometer measurements of the electron flux at low altitudes on lines of force extending to  $\sim 2 - 2.5R$ . A flux of  $\sim 10^4$  electrons  $\text{cm}^{-2} \text{sec}^{-1} \text{keV}^{-1}$  is found at 200 keV. The energy spectrum is observed to cut off at a maximum energy of  $\sim 800$  keV. The

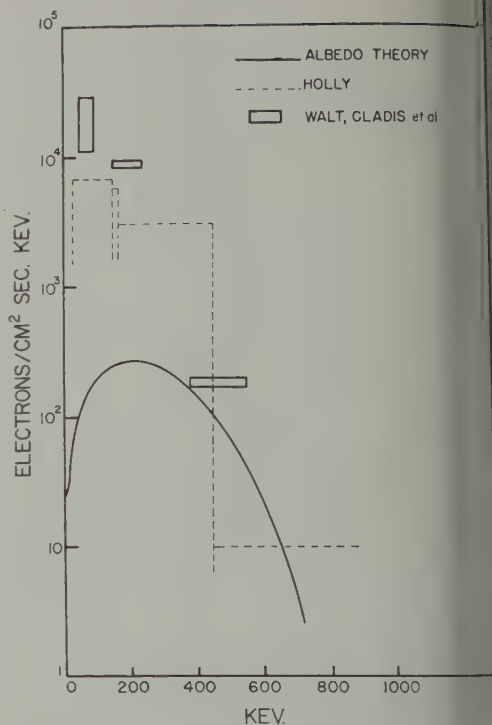


Fig. 13. Differential omnidirectional intensity of trapped electrons vs. energy. The solid curve is the result of the present work, calculated for the case of pure energy loss. The curve is normalized to the experimental data. It is calculated for an altitude of 1100 km on a line of force extending to  $1.5R$  using an average effective density of  $9.7 \times 10^4 \text{ cm}^{-3}$  computed from the exosphere model of Figure 4. The dashed curve is the spectrum at  $\sim 1100$  km on the line of force extending to  $1.5R$  [*Holly*, 1960]. The data points (rectangles) are observations at  $\sim 1000$  km on the line of force extending to  $\sim 2.3R$  [*Walt, Chase, Cladis, Imhof, and Knecht*, 1960; *Cladis, Chase, Imhof, and Knecht*, 1961].

slope of the spectrum decreases below 200 keV [*Cladis, Chase, Imhof, and Knecht*, 1961].

These results represent an integral flux of  $7 \times 10^6 \text{ cm}^{-2} \text{sec}^{-1}$  for  $E > 50 \text{ keV}$ ,<sup>4</sup> two orders of magnitude larger than the value calculated from the albedo theory.<sup>5</sup> However, if the observed differential spectrum and the a priori calculation

<sup>4</sup> The flux measured with the spectrometer (Walt) is three orders of magnitude smaller than *Van Allen's* [1959] measurement at a lower altitude and at  $\sim 3600$  km.

<sup>5</sup> Our calculated flux of  $10^7 \text{ [cm}^2 \text{sec}^{-1}]$  quoted earlier refers to  $r > 3R$  whereas for this low altitude experiment our theory gives  $\sim 10^5 \text{ [cm}^2 \text{sec}^{-1}]$ .

(for pure energy loss) are both plotted on a logarithmic basis, the two are in rough agreement above about 400 keV. At lower energies the observed spectrum contains about 100 times more particles (Fig. 13).

In a measurement, employing shielded Geiger tubes at  $\sim 1100$  km along lines of force extending to  $\sim 1.3 - 1.6R$  [Holly and Johnson, 1960] found an electron energy spectrum similar to the higher altitude spectrum above  $\sim 200$  keV (Fig. 13).

The spectrum which has been calculated for auroral purposes has been determined from a preliminary survey using the following steps: (1) The energy spectrum is fixed. (2) Its magnitude depends inversely on the particle density averaged over the spiral orbit. This orbit dips down into the oxygen and hydrogen regions near the mirror point. Using the  $\text{O}^+$  and  $\text{O}^{2+}$  distributions given in Table 2, it is assumed that the major contribution to  $\bar{n}_E$  comes from  $\text{O}^+$  and  $\text{O}^{2+}$ ; the  $\text{H}$  and  $\text{H}^+$  components contribute only  $\sim 10$  per cent of the total. The calculated contributions are: neutral oxygen  $0.4 \times 10^4 \text{ cm}^{-3}$ , ionized oxygen,  $3.4 \times 10^4 \text{ cm}^{-3}$ , hydrogen  $0.68 \times 10^4 \text{ cm}^{-3}$  and neutral hydrogen  $0.18 \times 10^4 \text{ cm}^{-3}$  (effective densities).

At least certain values are those for the auroral components. It is unfortunate that the measurements all refer to an altitude in which the importance of oxygen and hydrogen in the particle density are comparable. It would be desirable to perform a spectrometer experiment at a large enough altitude so that the contribution of oxygen can be completely determined.

Even so, there is a large measure of uncertainty in the magnitude of the calculated spectrum, and the shape of the spectrum is well known.

From these comparisons we arrive at the following conclusions; they are the same as those of Kellogg [1960] and similar to those of others [1960].

Cosmic ray neutron albedo cannot account for all of the observed trapped electrons. It is less than 5 per cent of the electrons observed in the Holly and Johnson experiment, and an even smaller fraction in the experiment of Kellogg and his co-workers. Although the calculated intensity could be increased by a factor of 10 if atmospheric density were lower than our

suggested values, it should also be remembered that our calculation purposely leads to a maximum value of the trapped electron intensity from albedo neutrons. The addition of other loss mechanisms, scattering by Coulomb collisions, hydromagnetic scattering, and other effects would all serve to reduce the calculated intensities. It can be seen that, even for the most favorable assumptions, the energy spectra agree only above 400 keV, or 200 keV at the most optimistic. Hence, one can argue that the neutron albedo contributes most, if not all, of the high energy electrons above 400 keV, possibly even above 200 keV.

2. At higher altitudes and latitudes corresponding to lines of force at 2 or more earth radii, an additional component is noticed which contributes electrons of lower energies, typically 20 to 50 keV, with a very steep spectrum and of very large intensity [McIlwain, 1960].<sup>6</sup> Since these low-energy electrons are responsible for many of the auroral phenomena, this would indicate that they are lost at a rapid rate and must therefore be replenished by processes capable of supplying a great deal of energy in a short time. Observations from Explorer VI (Arnoldy, Hoffman, and Winckler, 1960; Fan, Meyer, and Simpson, 1960; Rosen and Farley, 1961) which indicate the disappearance and reappearance of trapped electrons at very high altitudes would seem to bear out this conclusion.) Hence their energy is not derived from cosmic rays (or neutron  $\beta$  decay) but most likely from the sun through the medium of acceleration in the geomagnetic field.

*Acknowledgments.* It is a pleasure to acknowledge the many stimulating conversations we had with W. M. MacDonald and M. Walt. We thank J. B. Cladis for transmitting some of his results to us prior to their publication.

This research was supported in part by the USAF under contract AF-49(638)530 monitored by the AFOSR of the Air Research and Development Command.

<sup>6</sup> We have examined the production of a low-energy component of 'knock-on' electrons produced in large-angle scattering. The knock-ons are generated in a spectrum  $E^{-2}$  and the equilibrium concentration is  $\propto E^{-1/3}$ . The flux of these secondary electrons is therefore essentially flat ( $\lesssim 30$  keV) with a differential intensity  $\sim 10$  per cent of the average intensity in the fast component. This effect thus cannot be responsible for the large number of low-energy electrons that are observed.



## APPENDIX 1

## SCATTERING AND ENERGY LOSS OF A FAST ELECTRON

1. We wish to examine the scattering and energy loss of a fast electron moving through a plasma, particularly a fully ionized hydrogen plasma. Some ambiguity still exists in the literature concerning the relative effectiveness of protons vs. electrons in producing angular deflections of the incident particle; for example, Kellogg [1960] concludes that protons are more effective. In fact, in the deflection of thermal electrons in fully ionized hydrogen, protons are four times more effective [Öpik, 1961]. However, we emphasize that this applies to the deflection of thermal electrons only. We shall show that in the case of fast electrons ( $E \gg kT$ ), protons and electrons are equally effective in producing deflection.

We should like to compute the differential scattering cross section,  $(d\sigma(\theta))/d\omega$ , in the cases where the scattering centers are (a) protons and (b) electrons. Since we observe the deflection relative to a coordinate frame fixed in the lab, we need to compute  $d\sigma/d\omega$  in the lab frame. One way to do this is by first computing the cross section in the center of mass system, where it takes on a simple form, and then transforming to the lab system.

(a) For electrons scattered by protons we can regard the proton as being infinitely massive compared to the electron. Then the center of mass system coincides with the lab system. The cross section is, of course, the Rutherford cross section:

$$\frac{d\sigma(\theta)}{d\omega} = \frac{1}{4} \left( \frac{ZZ'e^2}{p\beta c} \right)^2 \frac{1}{\sin^4(\theta/2)} \equiv \sum_p \quad (1.1)$$

(b) We turn now to the case of fast electrons scattered by electrons at rest. Since the target electron recoils significantly during the encounter, it may be tempting to assume that the deflection is reduced compared to the electron-proton case. The correct cross section is, however, *not* obtained from the former case by merely replacing the incident particle's mass by the reduced mass. In fact, this leads to the cross section being *increased* by a factor of 4. Instead one must proceed as follows:

The center-of-mass cross section is given by (1.1) where now the momentum  $p$  is proportional

to the reduced mass,  $m/2$  here. Hence the CM cross section is  $4 \sum_p$ . This CM cross section must now be transformed into the corresponding lab cross section. The transformation consists of two parts. First the CM angle,  $\chi$ , must be transformed into the lab angle,  $\theta$ . For nonrelativistic velocities this yields  $\theta = \chi$ . Secondly, since the number of particles scattered into a given solid angle in one coordinate system must equal the number scattered into the corresponding solid angle in the other system, we require that

$$\frac{d\bar{\sigma}(\chi)}{d\omega} \sin \chi d\chi = \frac{d\sigma(\theta)}{d\omega} \sin \theta d\theta \quad (1)$$

(A barred quantity denotes CM.) Equation (1) leads directly to

$$\sum_e \equiv \frac{d\sigma}{d\omega}(\theta) = 4 \cos \theta \frac{d\bar{\sigma}}{d\omega}(2\theta) \quad (1)$$

where we have made use of  $\theta = \chi/2$  to eliminate  $\chi$ . For  $d\bar{\sigma}/d\omega$  we now substitute  $4 \sum_p$  (2). We find

$$\sum_e = 4 \left( \frac{ZZ'e^2}{p\beta c} \right)^2 \frac{\cos \theta}{\sin^4 \theta} \quad (1)$$

Now, for Coulomb scattering the predominant contribution to the mean deflection is made by small-angle scatterings. For  $\theta \ll 1$  both (1) and (1.4) reduce to the same result. Thus electrons and protons present the same cross section to the fast electron and therefore produce the same deflection.

2. The mean square deflection per second  $\langle(\Delta\theta)^2\rangle$ , may therefore be evaluated:

$$\langle(\Delta\theta)^2\rangle = 2\pi\rho\beta c$$

$$\cdot \int_{\theta_1}^{\theta_2} (\Delta\theta)^2 \frac{d\sigma}{d\omega}(\theta) \sin \theta d\theta \quad (1)$$

Here  $\rho$  is the density (number of scattering centers per unit volume). The minimum scattering angle,  $\theta_1$ , is set by the maximum impact parameter. In a plasma this is generally taken to be  $\lambda_D$ , the Debye shielding distance. The maximum scattering angle,  $\theta_2$ , is set by the minimum impact parameter,  $b_{\min}$ , which is limited by the uncertainty principle; i.e.,  $b_{\min} \gtrsim \hbar/p$ . For small  $Z$  and energies  $\gtrsim 5$  kev both angles are inversely proportional to their respective impact parameters (with the same coefficient of proportionality).

ity), yielding  $\theta_2/\theta_1 = \lambda_D p/\hbar$ . Assuming  $\theta \ll 1$ , we find

$$= 8\pi\rho Z^2 r_0^2 c \frac{(1 - \beta^2)}{\beta^3} \ln(\lambda_D p/\hbar) \quad (1.6)$$

$\beta = v/c$  and  $Ze$  is the charge of each scattering center.

dering from neutral or partly ionized atoms treated similarly. The maximum impact parameter is now the atomic radius. This reduces the factor somewhat.

multicomponent atmosphere we must add the effects of each component. It is convenient to express all densities in terms of the equivalent electron density. We therefore define an effective density of scattering centers,  $\rho_s$ , as

$$\ln(\lambda_D p/\hbar) = \sum_i \rho_i Z_i^2 \ln(\theta_2/\theta_1)_i \quad (1.7)$$

quantity  $\ln(\lambda_D p/\hbar)$  for exospheric densities and for electron energies from 1 to  $\sim 5$  Mev is 23. Table 1.1 summarizes the results for the major constituents of the atmosphere.

TABLE 1.1.

Multiply true density by following factors to obtain effective scattering densities,  $\rho_s$ .

Material	Conversion Factor
Fully ionized hydrogen	2.0
Neutral hydrogen	0.4
Fully ionized oxygen	16.2
Neutral oxygen	14.4

deflection rate may now be written

$$= 8\pi r_0^2 c \cdot 23 \cdot \rho_s \frac{(1 - \beta^2)}{\beta^3}$$

$$8 \times 10^{-12} \rho_s \frac{(1 - \beta^2)}{\beta^3} \text{ (radians)}^2 \text{ sec}^{-1} \quad (1.8)$$

The rate of energy loss of a fast electron is computed in a similar manner. Small-angle scattering is assumed. The momentum transferred to the target particle is computed in the small-angle approximation. The energy dissipated in the interaction is then inversely proportional to the mass of the target particle. It follows that electrons are much more effective in absorbing energy than protons. The energy given up in

each scattering may be expressed in terms of the deflection angle and the average energy-loss per second computed from the Rutherford cross section, considering collisions with electrons only. Thus

$$\frac{dE}{dt} = -2\pi\rho Z\beta c \int_{\theta_1}^{\theta_2} \Delta E(\theta) \frac{d\sigma}{d\omega}(\theta) \sin\theta d\theta \quad (1.9)$$

reduces to

$$\frac{dE}{dt} = -\frac{4\pi\rho Z r_0^2 m c^2}{\beta} \ln(\lambda_D p/\hbar) \quad (1.10)$$

Here  $\rho$  is the number of ions  $\text{cm}^{-3}$  and  $Z$  is the number of electrons per ion. In fully ionized hydrogen this reduces to equation 21. This result may also be derived on the basis of plasma dynamics [Gasirowicz, Neuman, and Riddell, 1956].

In neutral or partially ionized materials the log term is more complicated. The exact result is the Bethe-Bloch formula [Rossi, 1952].

As in the case of scattering we define an effective density for energy loss  $\rho_E$  through

$$\rho_E \ln(\lambda_D p/\hbar) = \sum_i \rho_i Z_i \ln(\theta_2/\theta_1)_i \quad (1.11)$$

Again,  $\ln(\lambda_D p/\hbar)$  is set equal to 23. In Table 1.2 we give conversion factors for several materials.

TABLE 1.2

Multiply true density by appropriate conversion factor to obtain effective energy loss density,  $\rho_E$ .

Material	Conversion Factor
Fully ionized hydrogen	1.0
Neutral hydrogen	0.47
Singly ionized oxygen	3.74
Neutral oxygen	3.22

## APPENDIX 2

### RELATION BETWEEN DIRECTIONAL AND OMNIDIRECTIONAL INTENSITIES

Nonisotropic angular distributions present a difficult problem. Ray [1960] has given concise expressions for deriving the directional intensities from the omnidirectional intensity measured along the line of force. We attack this problem, as well as the inverse problem, by means of a matrix method.

*Conversion Matrix.* In order to calculate the





Inversion Matrix for  $r_e = 3R$ ;  $(\Delta\mu)^{-1}$  $x_c = .3333, \mu_c = .9892$ 

1.0000	.9333	.8667	.8000	.7333	.6667	.6000	.5333	.4667	.4000
.0000	.5077	.6707	.7715	.8403	.8891	.9243	.9498	.9680	.9807
1	2	3	4	5	6	7	8	9	10
1.9695	-.6310	-.1830	-.0759	-.0371	-.0196	-.0108	-.0060	-.0032	-.0017
0	1.9659	-.6333	-.1828	-.0751	-.0361	-.0187	-.0100	-.0053	-.0027
0	0	1.9452	-.6259	-.1791	-.0725	-.0342	-.0172	-.0088	-.0044
0	0	0	1.9111	-.6108	-.1726	-.0686	-.0314	-.0152	-.0073
0	0	0	0	1.8659	-.5893	-.1636	-.0633	-.0279	-.0128
0	0	0	0	0	1.8109	-.5619	-.1525	-.0570	-.0239
0	0	0	0	0	0	1.7472	-.5291	-.1392	-.0496
0	0	0	0	0	0	0	1.6752	-.4908	-.1236
0	0	0	0	0	0	0	0	1.5948	-.4463
0	0	0	0	0	0	0	0	0	1.5060

## REFERENCES

- H., *Cosmical Electrodynamics*, Oxford University Press, London, 1950.
- McK., Electron density distribution in outer ionosphere derived from whistler data, *Atmospheric and Terrestrial Physics*, 14, 185, 1959.
- W. L., R. A. Hoffman, and J. R. Winckler, Observations of the Van Allen radiation region during August and September 1959, Part I, *J. Geophys. Research*, 65, 1361-1376, 1960.
- W. W., A sounding rocket measurement of electron densities to 1500 kilometers, *J. Geophys. Research*, 65, 2589-2594, 1960.
- J. B., L. F. Chase, W. L. Imhof, and D. J. Light, Energy spectrum and angular distribution of electrons trapped in the geomagnetic field, *J. Geophys. Research*, 66, 2297-2312, 1961.
- J. B., and A. J. Dessler, X rays from Van Allen belt electrons, *J. Geophys. Research*, 66, 150, 1961.
- A., and R. Karplus, Some properties of the Van Allen radiation, *Phys. Rev. Letters*, 4, 271, 1960.
- Y., P. Meyer, and J. A. Simpson, Trapped cosmic radiation measurements from Explorer VI, in *Space Research*, edited by H. Kall-Bijl, North-Holland Publishing Company, Amsterdam, 1960.
- wicz, S., M. Neuman, and R. J. Riddell, Dynamics of ionized media, *Phys. Rev.*, 101, 1956.
- C., Plasma and magnetic fields in the solar wind, *J. Geophys. Research*, 64, 1665-1674, 1959.
- on, N., Diffusion of particles in the earth's radiation belts, *Phys. Rev. Letters*, 5, 414, 1960.
- V. N., E. H. Canfield, and R. E. Lingenfelter, Cosmic ray neutron geodesy, *J. Geophys. Research*, 66, 665-677, 1961.
- V. N., The radiation belt produced by neutrons leaking out of the atmosphere, *J. Geophys. Research*, 65, 3107-3115, 1960.
- Holly, F. E., Radiation measurements to 1500 kilometers with Atlas Pods, *AFSWC Rept. TR-60-9*, 1960.
- Holly, F. E., and R. G. Johnson, Measurement of radiation in the lower Van Allen belt, *J. Geophys. Research*, 65, 771-772, 1960.
- Johnson, F. S., The ion distribution above the  $F_2$  maximum, *J. Geophys. Research*, 65, 577-584, 1960.
- Kellogg, P. J., Possible explanation of radiation observed by Van Allen at high altitudes in satellites, *Nuovo cimento*, 11, 48, 1959.
- Kellogg, P. J., Electrons of the Van Allen radiation, *J. Geophys. Research*, 65, 2705-2713, 1960.
- MacDonald, W. M., and M. Walt, Distribution function of magnetically confined electrons in a scattering atmosphere, *Ann. Phys.*, 15, 44, 1961.
- MacDonald, W. M., and R. C. Wentworth, Pitch angle diffusion in a magnetic mirror geometry, *Phys. Fluids*, in press, 1961.
- McIlwain, C. E., Direct measurement of particles producing visible auroras, *J. Geophys. Research*, 65, 2727-2747, 1960.
- Öpik, E. J., and S. F. Singer, Distribution of density in a planetary exosphere, *Phys. Fluids*, 2, 653, 1959; 3, 486, 1960; and 4, 221, 1961.
- Öpik, E. J., chapter in *Interaction of Space Vehicles with an Ionized Atmosphere*, edited by S. F. Singer, Macmillan Company, New York, 1961.
- Parker, E. N., Geomagnetic fluctuations and the form of the outer zone of the Van Allen radiation belt, *J. Geophys. Research*, 10, 3117-3130, 1960.
- Pope, J. H., An estimate of electron densities in the exosphere by means of nose whistlers, *J. Geophys. Research*, 66, 67-75, 1961.
- Purcell, J. D., and R. Tousey, The profile of solar hydrogen Lyman- $\alpha$ , *J. Geophys. Research*, 65, 370-372, 1960.
- Ray, E. C., On the theory of protons trapped in the earth's magnetic field, *J. Geophys. Research*, 65, 1125-1134, 1960.
- Rosen, A., and T. A. Farley, Characteristics of the

- Van Allen Radiation Belts as measured by the scintillation counter in Explorer VI, *J. Geophys. Research*, **66**, 2013-2028, 1961.
- Rossi, B., *High-Energy Particles*, Prentice-Hall, Englewood Cliffs, N. J., p. 27, 1952.
- Singer, S. F., Radiation belt and trapped cosmic ray albedo, *Phys. Rev. Letters*, **1**, 171, 1958a.
- Singer, S. F., Trapped albedo theory of the radiation belt, *Phys. Rev. Letters*, **1**, 181, 1958b.
- Singer, S. F., *Advances in Astronautical Sciences*, **4**, Plenum Press, Inc., New York, p. 335, 1959.
- Singer, S. F., Structure of the earth's exosphere, *J. Geophys. Research*, **65**, 2577-2580, 1960a.
- Singer, S. F., Latitude and altitude distribution of geomagnetically trapped protons, *Phys. Rev. Letters*, **5**, 300, 1960b.
- Smith, R. L., and R. A. Helliwell, Electron densities to 5 earth radii deduced from nose whistlers, *J. Geophys. Research*, **65**, 2583, 1960.
- Van Allen, J. A., The geomagnetically trapped corpuscular radiation, *J. Geophys. Research*, **64**, 1683-1689, 1959.
- Walt, M., L. F. Chase, J. B. Cladis, W. L. Imhof, and D. J. Knecht, Energy spectra and altitude dependence of electrons trapped in the earth's magnetic field, in *Space Research*, edited by H. K. Kallmann-Bijl, North-Holland Publishing Company, 1960.
- Walt, M., and W. M. MacDonald, Energy spectrum of electrons trapped in the geomagnetic field, *J. Geophys. Research*, **66**, 2047-2052, 1961.
- Welch, J. A., and W. A. Whitaker, Theory of geomagnetically trapped electrons from an artificial source, *J. Geophys. Research*, **64**, 909, 1959.
- Wentworth, R. C., W. M. MacDonald, and S. F. Singer, Lifetimes of trapped radiation belt particles determined by Coulomb scattering, *Phys. Fluids*, **2**, 499, 1959.
- Wentworth, R. C., Lifetimes of geomagnetically trapped particles determined by Coulomb scattering, Thesis, University of Maryland, 1961.

(Manuscript received June 27, 1961; revised September 20, 1961.)

# Solar Proton Impact Zones<sup>1</sup>

THOMAS KELSALL

*Theoretical Division, Goddard Space Flight Center  
National Aeronautics and Space Administration  
Washington, D. C.*

**Abstract.** The trajectories of charged particles moving in a magnetic dipole field have been calculated by numerical integration for application to data on the intensity variation of cosmic rays during recent solar events. All seasons and times of day have been covered by assuming a range of orientations of the incident particle beam with respect to the magnetic dipole axis. Points of impact with the earth have been determined for protons with energies from 0.05 to 50 bev. The computation includes 4000 trajectories and fills several gaps in previous investigations. In agreement with earlier calculations the results indicate that the protons strike in well-defined areas between 0 and 1200 hours local time, and are focused into small areas of impact at low energies. The investigation has revealed two points that are not new but have received relatively little attention in earlier work. First, the relative number of impacts in the northern and southern geomagnetic hemispheres is strongly dependent on season. Second, under certain conditions of season there is a class of trajectories, which may be called quasi-trapped, consisting of a set of paths resembling the trapped trajectories first discovered by Störmer but continuing to infinity. It is suggested that injection into trapped orbits from these quasi-trapped trajectories may make a contribution to the population of the Van Allen belts.

**Introduction.** In the past two decades five major solar flares associated with cosmic-ray increases have been reported. They occurred on May 28 and March 7, 1942; July 25, 1946; October 19, 1949; and February 23, 1956. (A cosmic-ray increase also accompanied the 3<sup>+</sup> flare of November 10–12, 1960.) The cosmic-ray increase usually began an hour after the optical flare had been sighted, rose sharply during a period of a few minutes, and decayed within a few hours. The increases were world-wide, and their amplitude and time of onset exhibited meridional dependence. The integral rigidity spectrum of the flare particles was much steeper than that of galactic cosmic rays.

Extensive investigations have been performed by Birkeland [1901], Lemaitre and Vallarta, 1936; Störmer, 1950; Schlüter, 1951; Firor, 1954; Lüst, 1955; and Katterbach, 1955; Jory, 1956; and [1957] in which Störmer trajectories were calculated for cosmic rays originating at the sun and moving in the earth's dipole field, in an effort to explain the ground-level pattern of the cosmic-ray increases observed during these solar flares. Laboratory models have also been con-

structed for this problem. Birkeland [1901] constructed the first such model, in which a phosphorescent coated magnetized sphere, called the terrella, was exposed to a stream of electrons in an evacuated chamber. The regions of electron impact phosphoresced and were photographed. More advanced experiments have been performed by Malmfors [1945], Brunberg and Dattner [1953], and Bennett [1956].

The present investigation extends the earlier theoretical studies on impact zones. The calculation includes orientations of the proton beam and dipole axis covering all possible conditions of season and time of day. Points of impact were determined for protons with energies ranging from 0.05 to 50 bev.

The results confirm earlier work indicating well-defined impact areas lying between 0 and 1200 hours local time, and diminishing in size with decreasing proton energy. Protons of relatively low energy, in the neighborhood of 1 bev and below, are strongly focused by the magnetic field into impact zones of very limited extent.

The calculations also demonstrate a strong seasonal dependence in the ratio of impacts in the northern and southern geomagnetic hemispheres. Finally, for certain conditions of season and time of day, trajectories appear to be com-

<sup>1</sup> This work was submitted to Georgetown University in partial fulfillment of the requirements for the degree of master of science.



mon in which the particle approaches the earth and makes several passes about it, in the manner of the Van Allen belt particles, before receding again to infinity. This class of quasi-trapped particles perturbed by scattering may be a source of protons for the Van Allen layers.

*Calculation of the trajectories.* The Lorentz force acting on a particle of charge  $q$  and velocity  $v$  in a magnetic field of strength  $H$  is

$$\mathbf{F} = (q/c)\mathbf{v} \times \mathbf{H} \tag{1}$$

For a dipole field

$$\mathbf{H} = [3\mathbf{rM} \cdot \mathbf{r} - Mr^2]/r^5 \tag{2}$$

where  $\mathbf{M}$  is the dipole moment and  $\mathbf{r}$  the position vector.

The magnetic force on a particle is transverse to its motion and can do no work; hence the energy and the magnitude of the velocity are constants of the motion. It is possible then to replace the increment in time by an increment in arc length,

$$dt = dS/v \tag{3}$$

Using equations 2 and 3 and taking  $z$  antiparallel to the dipole axis, expanding (1) gives

$$d^2x/dS^2 = x''$$

$$= Mq[(x^2 + y^2 - 2z^2)y' + 3yzz']/mcvr^5$$

$$d^2y/dS^2 = y''$$

$$= Mq[(2z^2 - x^2 - y^2)x' - 3xzz']/mcvr^5$$

$$d^2z/dS^2 = z'' = 3Mqz(xy' - yx')/mcvr^5$$

where  $m$  is the relativistic mass of the particle.

As  $Mq/mcv$  has the dimensions of (length)<sup>2</sup>, convenient to introduce the Störmer unit length,

$$S. U. = (Mq/mcv)^{1/2}$$

Since the dipole field is invariant for rotation about the  $z$  axis, the  $z$  component of the canonical angular momentum,  $h$ , is a constant [Morgery, 1949]

$$h = (xy' - yx') - (x^2 + y^2)/r^3$$

The final form of the equations used in integration is

$$x'' = [(x^2 + y^2 - 2z^2)y' + 3yzz']/r^5$$

$$y'' = [(2z^2 - x^2 - y^2)x' - 3xzz']/r^5$$

$$z'' = 3z[h/r^5 + (x^2 + y^2)/r^8]$$

The calculations refer to a stream of protons ejected from the sun during a flare. The protons in the beam are assumed to be moving parallel to the plane of the ecliptic when they reach earth's orbit, and to be without internal interactions. Each trajectory is designated by its coordinates in a plane, at right angles to the direction of the stream and with its center located 6 Störmer units from the center of the dipole geomagnetic longitude zero and colatitude nine degrees. This normal plane to the beam is labeled AB. Figure 1. Coordinates  $a$  and  $b$  in this plane are oriented in the ecliptic and perpendicular to it respectively. A trajectory is integrated numerically from a starting point in the plane.

The initial conditions for a proton striking the AB plane perpendicularly at a point  $P$  ( $a, b$ ) are, from Figure 1,

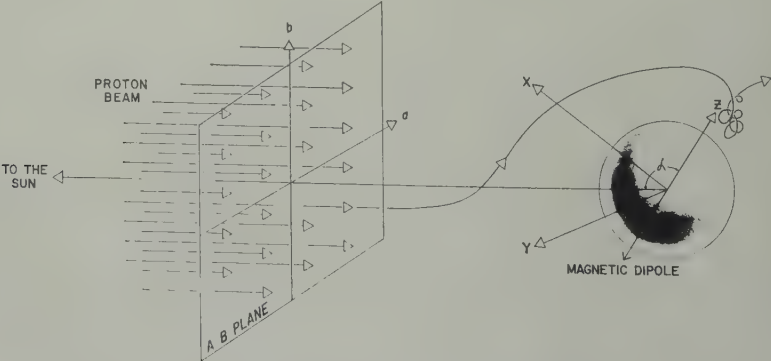


Fig. 1. Schematic of the problem's geometry.

$$\begin{aligned} x_0 &= 6 \sin \alpha - b \cos \alpha \\ y_0 &= -a \\ z_0 &= 6 \cos \alpha + b \sin \alpha \end{aligned} \quad (7)$$

$$\begin{aligned} x_0' &= -\sin \alpha \\ y_0' &= 0 \\ z_0' &= -\cos \alpha \end{aligned} \quad (8)$$

integration interval,  $\Delta S$ , is defined by

$$S = \begin{cases} 0.2 & \text{if } 0.2 \leq 0.02\bar{C}^{-1} \\ 0.02\bar{C}^{-1} & \text{if } 0.2 > 0.02\bar{C}^{-1} \end{cases}$$

is the curvature,

$$\bar{C} = [(x'')^2 + (y'')^2 + (z'')^2]^{1/2} \quad (9)$$

In a step of the integration the identity

$$E = 1 = (x')^2 + (y')^2 + (z')^2 \quad (10)$$

is checked; if  $E$  deviates from 1 by  $\pm 1.5$  per cent, the computation halts and an error check is initiated. The integration is usually terminated when  $\bar{C} \leq 10^{-2}$ , and is less than the previously determined  $\bar{C}$ . This condition on  $\bar{C}$  is intended to prevent the escape of the proton from the magnetic field.

The numerical integration of equation 6, using the fourth-order Runge-Kutta method, was done on the NORC at the Naval Proving Grounds in Dahlgren, Virginia, and the IBM 704 at the National Bureau of Standards.

The machine output consists of: (1) a first

TABLE 1. Corresponding Values of Energy, Velocity, S. U., and  $r_0$  for Protons

Rigidity, 10 <sup>9</sup> gauss cm	Velocity, 10 <sup>10</sup> cm/ sec	S. U. 10 <sup>9</sup> cm	Radius of Earth $r_0$ S. U.
170	3.00	0.69	0.922
86.5	3.00	0.97	0.658
36.4	2.96	1.49	0.427
19.6	2.96	2.04	0.313
11.0	2.88	2.71	0.235
5.65	2.62	3.78	0.168
3.64	2.27	4.72	0.135
2.43	1.84	5.77	0.110
1.48	1.28	7.40	0.086
1.03	0.94	8.85	0.072

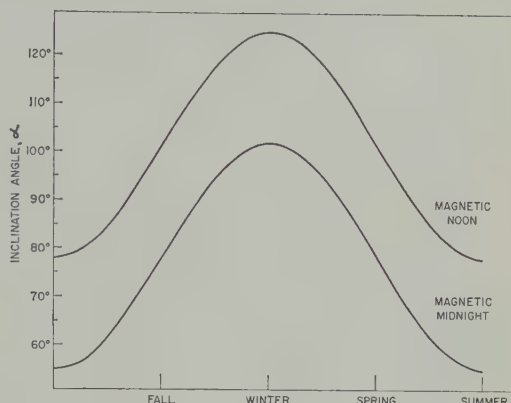


Fig. 2. Seasonal dependence of the extremes, magnetic noon and midnight, of the diurnal variation of the dipole's inclination angle.

line of  $a$ ,  $b$ ,  $\alpha$ , and  $h$ ; (2) lines of  $E$ ,  $S$ ,  $x$ ,  $y$ ,  $z$ ,  $r^2$ ,  $dS$ ,  $\bar{C}^2$ , where  $dS$  is the distance in Störmer units traversed between successive lines of printing; (3) a last line of  $E$ ,  $x$ ,  $y$ ,  $z$ ,  $x'$ ,  $y'$ , and  $z'$ . Since the Störmer unit is energy dependent, the earth's radius,  $r_0$ , differs for each proton energy (see Table 1). When in the integration a value of  $r$  is reached for the first time that is equal to an  $r_0$  for some proton energy the regular trajectory printing is interrupted by special function lines. These special lines give the cartesian coordinates and velocity components at the point of impact; the point's geomagnetic longitude ( $\Phi$ ) and colatitude ( $\Theta$ ); the angle of impact of the proton with respect to the local zenith ( $\Psi$ ). Special lines are printed for  $r$ 's representing protons with energies of 0.05, 0.10, 0.25, 0.5, 1.0, 2.5, 5, 10, 25, and 50 bev.

The field is represented by an earth-centered dipole, of moment  $8.1 \times 10^{25}$  gauss cm<sup>3</sup>, with its axis inclined to the axis of rotation by  $11.5^\circ$ . The dipole's angular orientation with respect to the earth-sun line varies with the time of day and of year. As the variation in the rotation axis' angular orientation with respect to the ecliptic is between  $90 \pm 23.5^\circ$  during a year, the dipole axis will vary between  $90 \pm 35^\circ$ . The envelopes of the extremes in the diurnal variation of the dipole's angle of inclination,  $\alpha$ , versus season are shown in Figure 2. Proton trajectory calculations are done covering the range in  $\alpha$  from  $90^\circ$  to  $125^\circ$  in five steps:  $\alpha = 90^\circ, 100^\circ, 110^\circ, 117^\circ$ , and  $125^\circ$ . The calculations are only for  $\alpha \geq 90^\circ$ , as equal variations of  $\alpha$  about  $90^\circ$  are

TABLE 2. Number of Trajectories Enclosed in the Net Area Used in Spanning the *AB* Plane for Proton Energies and Angles of  $\alpha$  of Interest

Proton Energy, bev	Number of Trajectories per Net Area, no./( <i>S. U.</i> ) <sup>2</sup>				
	$\alpha = 90$	$\alpha = 100$	$\alpha = 110$	$\alpha = 117$	$\alpha = 125$
50	$4/(0.1)^2$	$4/(0.1)^2$	$4/(0.1)^2$	$4/(0.1)^2$	$4/(0.1)^2$
25	"	"	"	"	"
10	$4/(0.05)^2$	$4/(0.05)^2$	$5/(0.05)^2$	$4/(0.05)^2$	$4/(0.05)^2$
5.0	"	"	"	"	"
2.5	$4/(0.025)^2$	$4/(0.025)^2$	"	"	"
1.0	"	"	"	"	"
0.50	"	"	"	"	"
0.25	"	"	"	"	"
0.10	"	"	"	"	"
0.05	"	"	"	"	"

equivalent from the equatorial and rotational symmetry of the dipole field. For example, the trajectory and associated impact points calculated for  $\alpha = 110^\circ$  equal those for  $\alpha = 70^\circ$  if the hemispheres are interchanged, i.e.,  $z \rightarrow -z$ .

Consideration of proton penetrability into the upper atmosphere limited the detailed analysis to protons with impact angle  $\leq 45^\circ$ .

The spacing of points required in the *AB* plane decreases with decreasing proton energy. Table 2 lists areas in the *AB* plane and the number of trajectory starting points enclosed within each area for the various proton energies and values of  $\alpha$ .

The centered dipole approximation appears to be good far above the surface from the form of the Van Allen belts and recent rocket-flown

magnetometer data. For a more accurate description near the surface, neutron monitoring experiments [Rothwell and Quenby, 1958; Kahl Meyer, and Simpson, 1958] indicate that the higher harmonics should be taken into account.

*Results.* The determined impact zones on the earth's surface are the product of 4000 separate trajectory calculations covering the five values of  $\alpha$ . The choice of parameters was intended to refer to protons, but the results can be applied to any charged particle. Table 3 lists three primary particles and the corresponding values of energy for which the results are valid. For negatively charged particles the hemisphere should be interchanged in all tabulations and figures presenting impact zones. The surface impact points for protons can be transformed

TABLE 3. Corresponding Energy Values for Protons, Electrons, and Alpha Particles for a Given Magnetic Rigidity and  $r_0$

Magnetic Rigidity, $10^6$ gauss cm	Earth's Radius, $r_0$ , <i>S. U.</i>	Proton Energy, bev	Electron Energy, bev	$\alpha$ -Particle Energy, bev
170	0.922	50.0	50.9	98.2
84.5	0.658	25.0	25.9	48.2
36.4	0.427	10.0	10.9	18.4
19.6	0.313	5.0	5.86	8.5
11.0	0.235	2.50	3.31	3.86
5.66	0.168	1.00	1.70	1.31
3.64	0.135	0.500	1.09	0.591
2.43	0.110	0.250	0.729	0.276
1.48	0.086	0.100	0.444	0.105
1.04	0.072	0.050	0.310	0.052

TABLE 4. Proton Energies that Transform the Impact Zones on the Earth to Specific Heights above the Surface

Proton Striking Energy, bev	Proton Energies for Specified Heights above the Surface, bev		
	50 km	100 km	250 km
50.0	49.2	48.3	46.1
25.0	24.6	24.2	23.1
10.0	9.84	9.66	9.1
5.00	4.92	4.84	4.5
2.50	2.44	2.41	2.2
1.00	0.970	0.948	0.8
0.500	0.487	0.474	0.4
0.250	0.241	0.234	0.2
0.100	0.096	0.093	0.0
0.050	0.049	0.047	0.0



at above the earth by an appropriate  
the proton energy. Table 4 lists the  
proton energy required to transform  
to altitudes of 50, 100, and 250 km.

3 shows lines, designated by a proton  
(beV), in the  $AB$  planes for the five  
 $\alpha$  enclosing the area from which pro-  
the specified energy come in and strike  
with impact angles ranging from  $0^\circ$   
the origin of the protons striking the  
predominantly the first and fourth  
of the  $AB$  plane, as the  $\mathbf{v} \times \mathbf{H}$  force  
twist the protons clockwise, looking  
the ecliptic plane. Since the measure  
in these plots is the Störmer unit, it is  
to estimate the actual contributing areas

for the various energies. The A columns of Table  
5 give the areas in the  $AB$  plane in square kilo-  
meters. The table shows that the contributing  
areas for protons with energies  $\geq 25$  beV de-  
crease with increasing  $\alpha$ , but for lower energies  
no clear relationship is obvious. The integrated  
area associated with striking low-energy protons  
( $\leq 10$  beV) peaks at  $\alpha = 107^\circ$ .

Rough estimates of the areas of the impact  
zones on the earth's surface are listed in the B  
columns of Table 5. C columns give the ratio of  
the  $AB$  area to the area of the impact zone. This  
ratio is a measure of the focusing of incoming  
protons by the geomagnetic field. The pronounced  
focusing at low energies was first noticed by  
Birkeland in his terrella experiments, and by

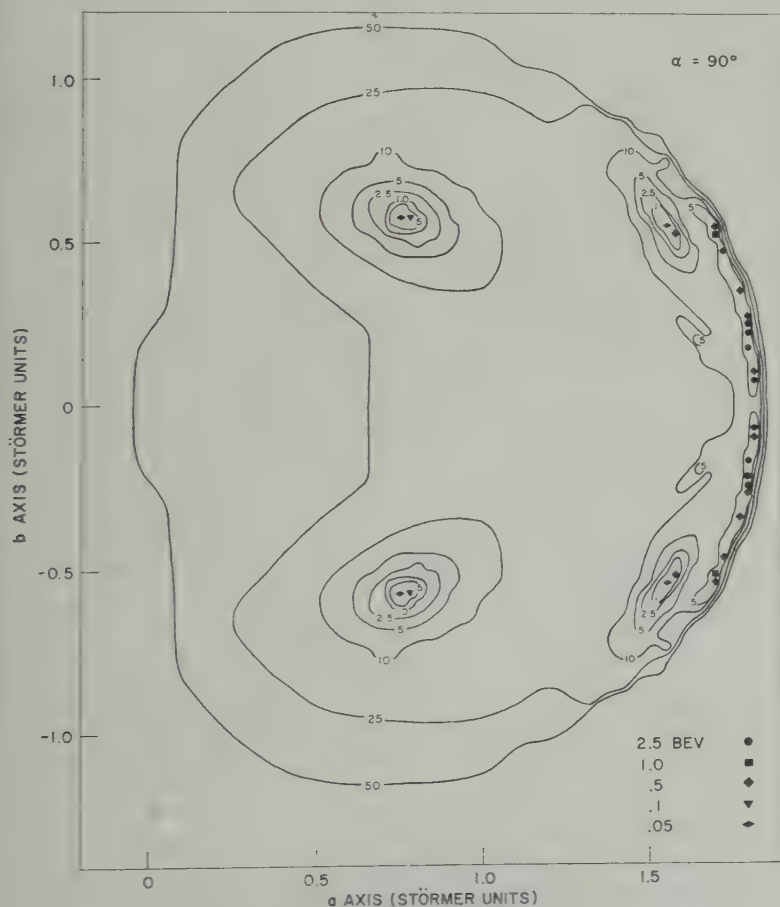


Fig. 3a.

Fig. 3 a-e. Lines designated by a proton energy (beV) enclose the  $AB$  areas that contrib-  
earth-striking protons with impact angles  $\leq 90^\circ$ . The origins of single low-energy trajec-  
s are shown as points.

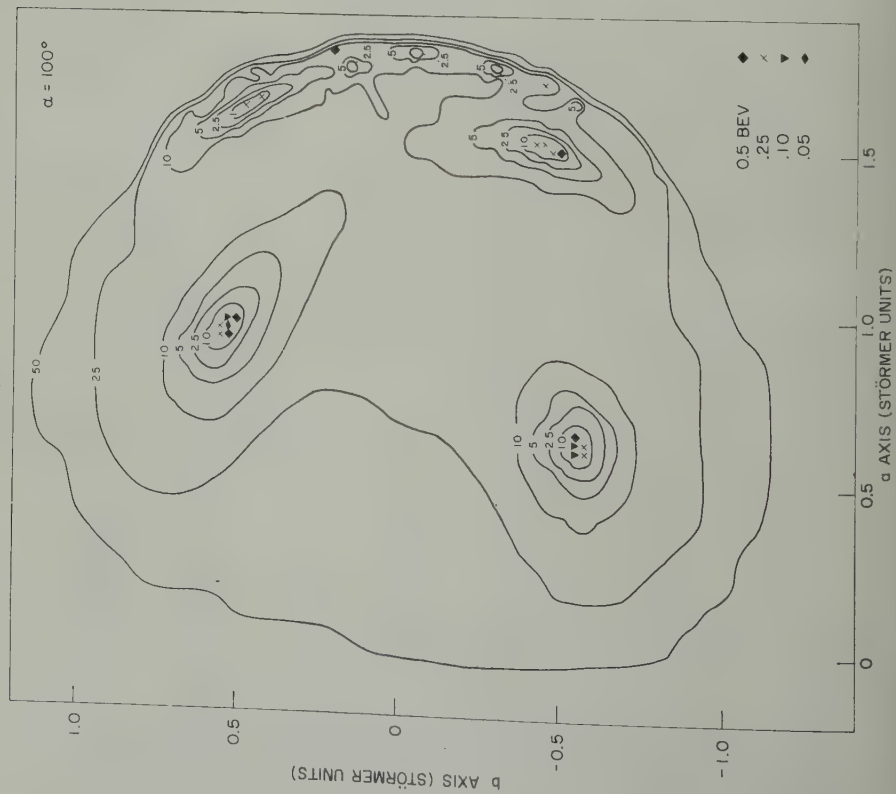


Fig. 3b.

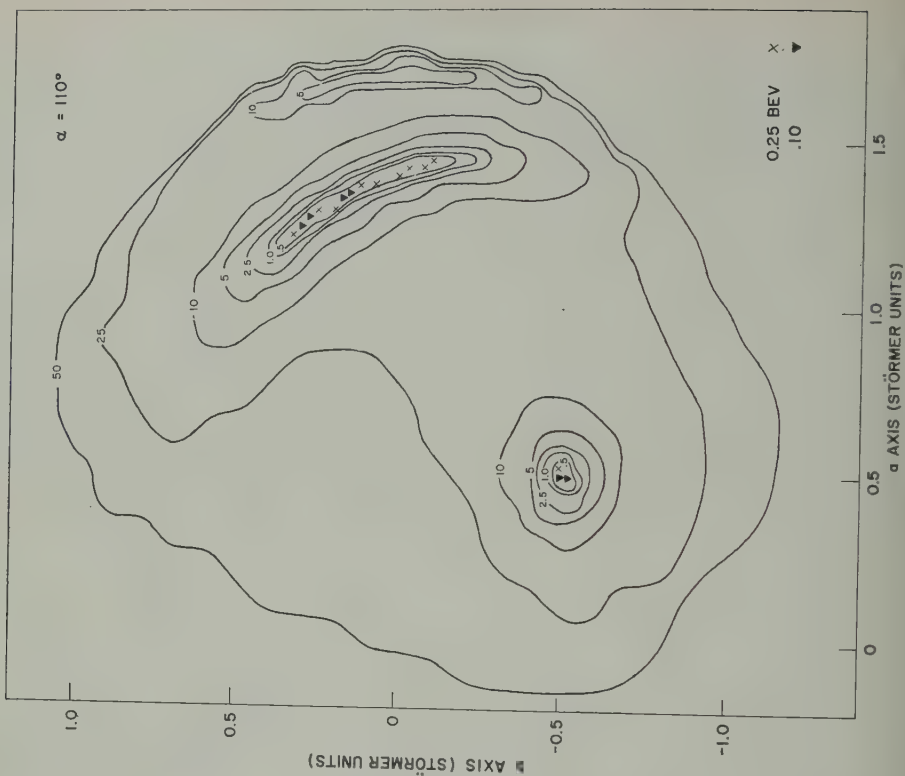


Fig. 3c.

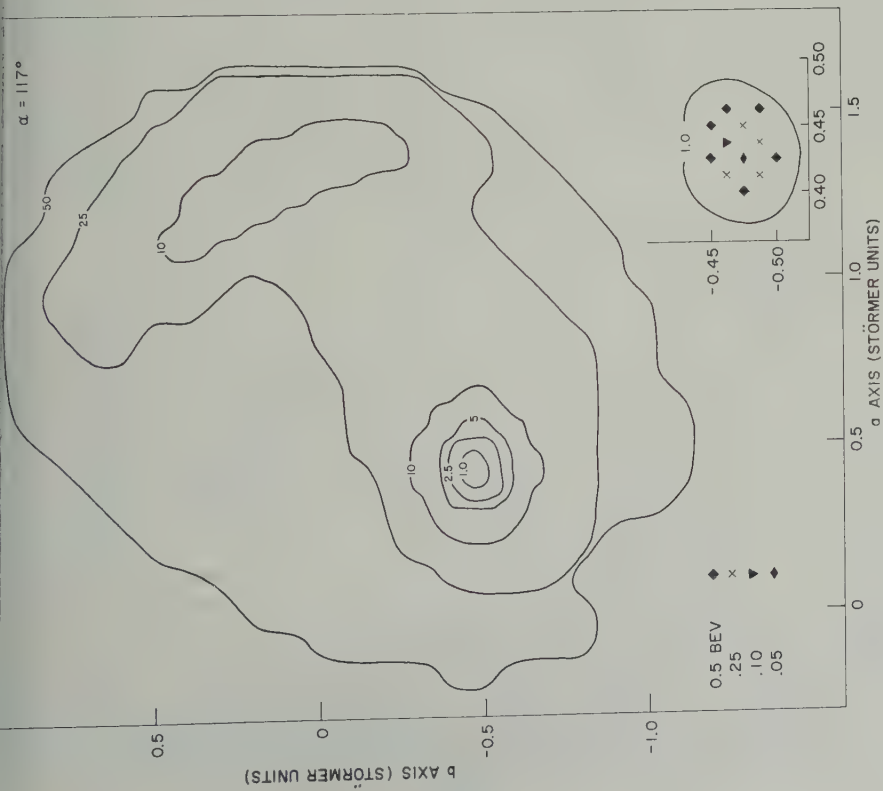


Fig. 3d.

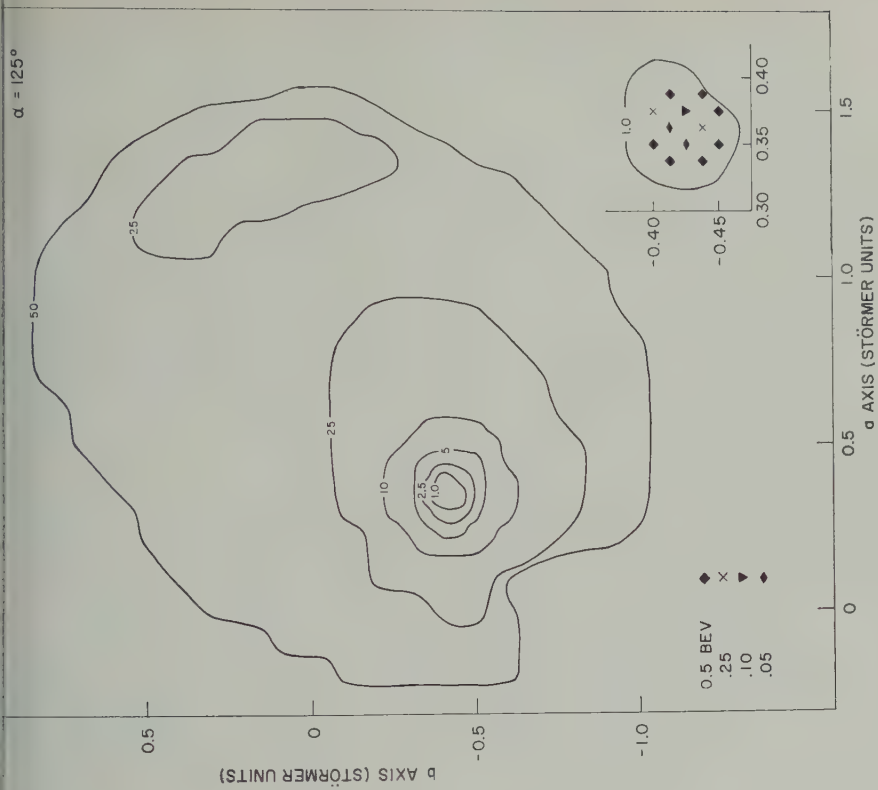


Fig. 3e.



TABLE 5. Areas Covered on the AB Plane and on the Earth by Protons with Impact Angles  $\leq 45^\circ$  for the Various Values

Proton Energy, bev	$\alpha = 90^\circ$			$\alpha = 100^\circ$			$\alpha = 110^\circ$			$\alpha = 117^\circ$			$\alpha = 125^\circ$	
	A	B	C	A	B	C	A	B	C	A	B	C	A	B
50	87	93	0.94	87	97	0.90	74	81	0.91	65	73	0.90	54	55
25	150	100	1.5	130	82	1.6	82	53	1.6	38	25	1.5	27	17
10	47	26	1.8	57	29	1.9	66	29	2.3	31	6.8	4.5	13	0.52
5.0	40	6.1	6.6	35	2.7	13	49	2.6	19	9.1	0.64	14	9.3	0.54
2.5	25	0.40	62	24	0.41	57	44	0.76	57	6.9	0.035	190	6.9	0.059
1.0	16	0.049	320	17	0.091	180	45	0.13	350	5.2	0.015	350	4.5	0.013
0.50	7.0	0.021	340	14	0.023	610	40	0.12	320	4.5	0.007	630	3.7	0.002
0.25	6.2	0.004	1600	8.3	0.012	680	18	0.052	350	3.6	0.004	830	2.9	0.003
0.10	6.8	0.002	3800	4.3	...	...	3.8	...	...	1.7	...	...	2.9	...
0.05	4.9	...	...	1.8	...	...	0.0	...	...	0.92	...	...	1.5	...

A, area in the AB plane ( $10^6 \text{ km}^2$ ). B, area on the earth ( $10^6 \text{ km}^2$ ). C, Ratio of A to B.

Lüst and Jory in their calculations. The focusing of the low-energy group is strongest for  $\alpha = 117^\circ$  and  $125^\circ$ . At other angles the low-energy contribution from areas along the edge and upper quadrant of the AB plane is scattered over a considerable region of the earth. When  $\alpha = 117^\circ$  and  $125^\circ$  the contributing area for the low energies is the lower left corner of the fourth quadrant, which exhibits particularly strong focusing. Two illustrative trajectories from this group are shown in Figure 4. A collection of such strongly focused spiraling trajectories may be a source of various local disturbances.

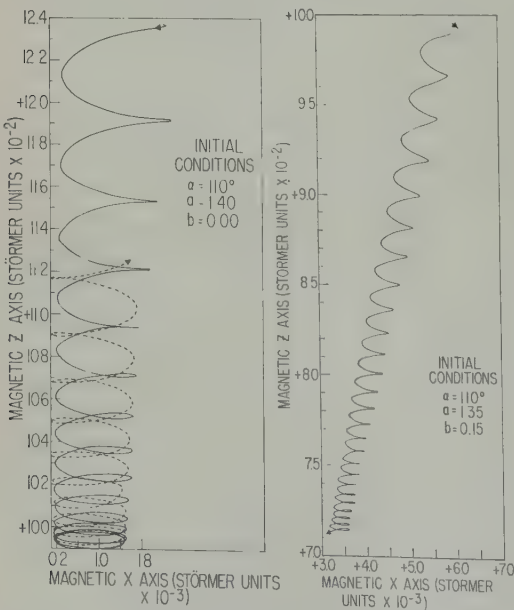


Fig. 4. Two examples of strongly focused protons spiraling about a line of force.

The systematic variation of the angle of impact for high-energy protons along a line of constant  $a$  or  $b$  is shown in Figure 5.

Figures 6 and 7 show the areas within which various energy groups will strike the earth's surface. All impact angles are included in the figures. Tables 6-A1 through 6-E1 list for five values of  $\alpha$  the counting rates of protons with impact angles  $\leq 45^\circ$ , in arbitrary units for the ten specified energies, in blocks on the earth's surface  $10^\circ$  geomagnetic colatitude by  $10^\circ$  geomagnetic longitude. In the construction of the tables all energies are given equal weight. In addition, the numbers have been normalized so that comparisons between different values of  $\alpha$  are permissible. For  $\alpha = 90^\circ$ , protons lying in the ecliptic plane, originating along  $b = 0$ , will

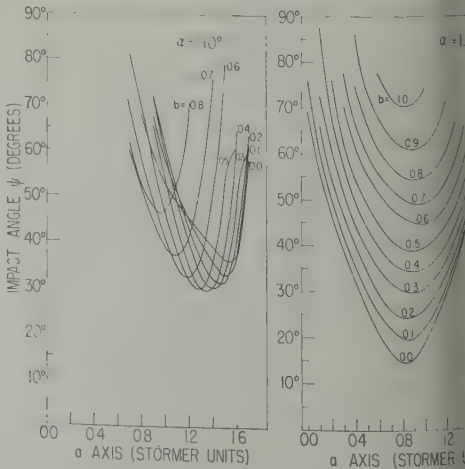


Fig. 5. The variation of impact angle with location in the AB plane for (left) 25-bev and (right) 50-bev protons.

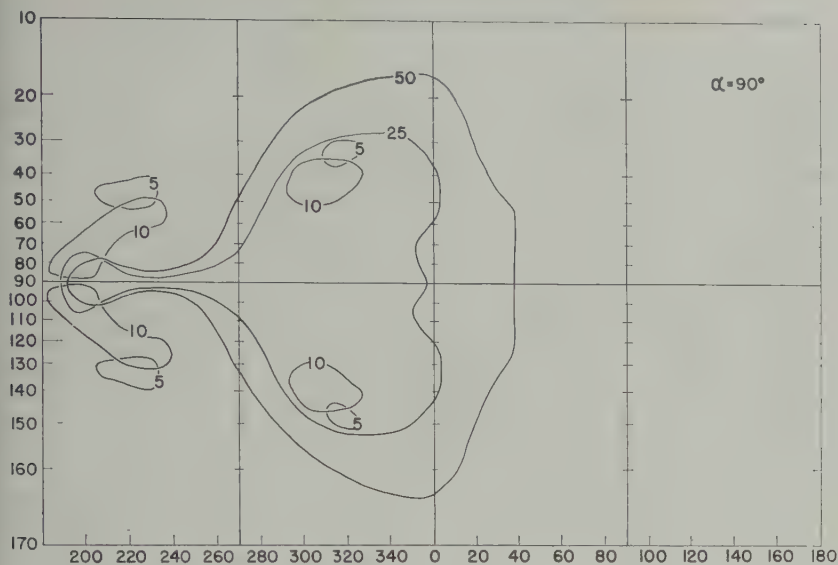


Fig. 6a.

Fig. 6 a-e. Impact zones on the earth's surface for 50-, 25-, 10-, and 2.5-bev protons with  $\alpha \leq 90^\circ$ ;  $0^\circ$  corresponds to local noon. The map is a Mercator projection with geomagnetic coordinates.

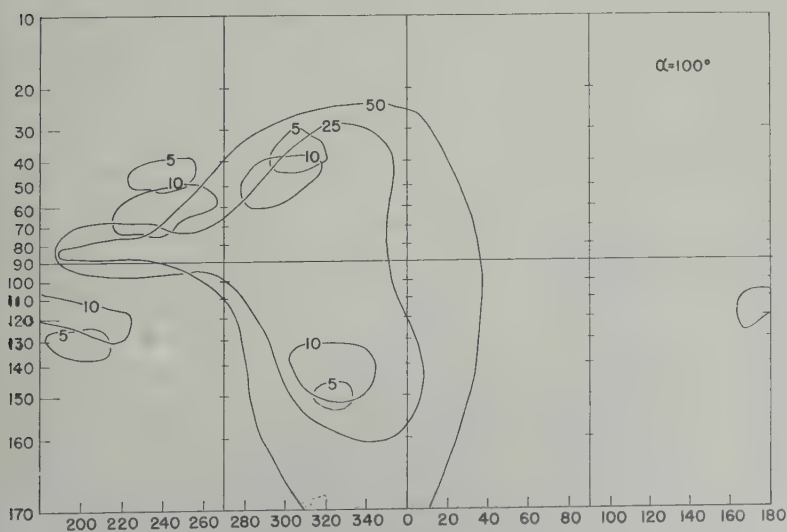


Fig. 6b.

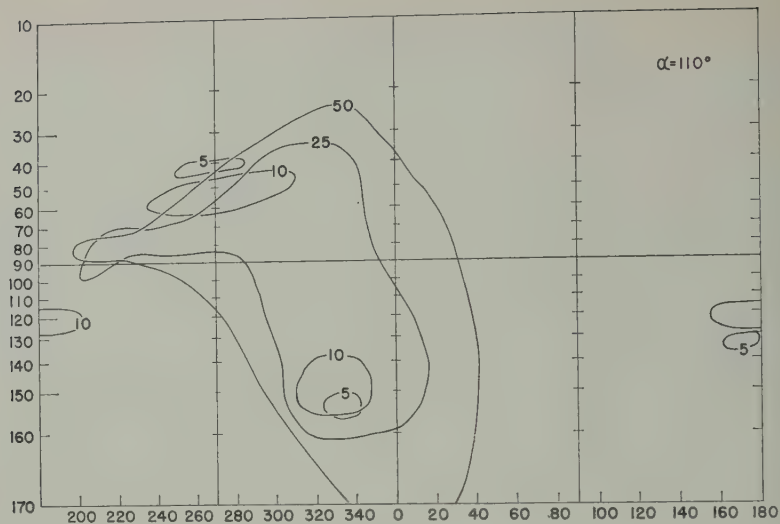


Fig. 6c.

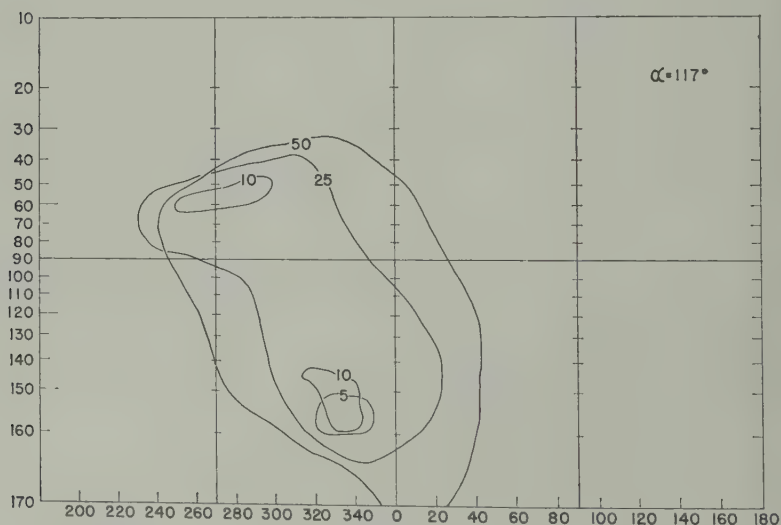


Fig. 6d.

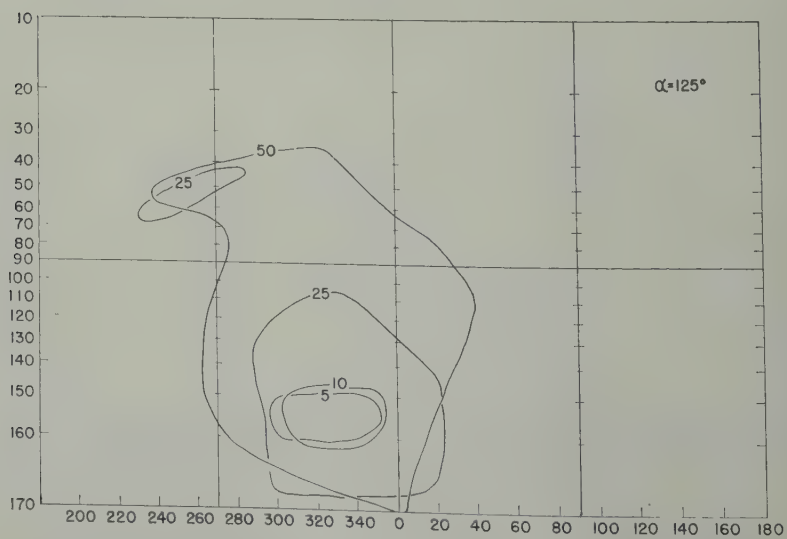
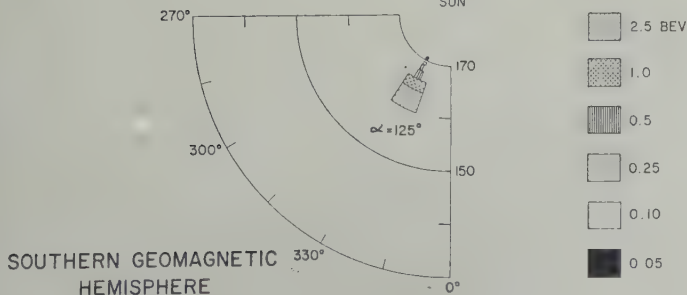
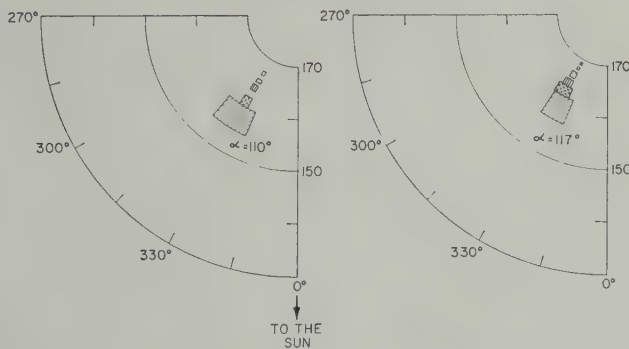
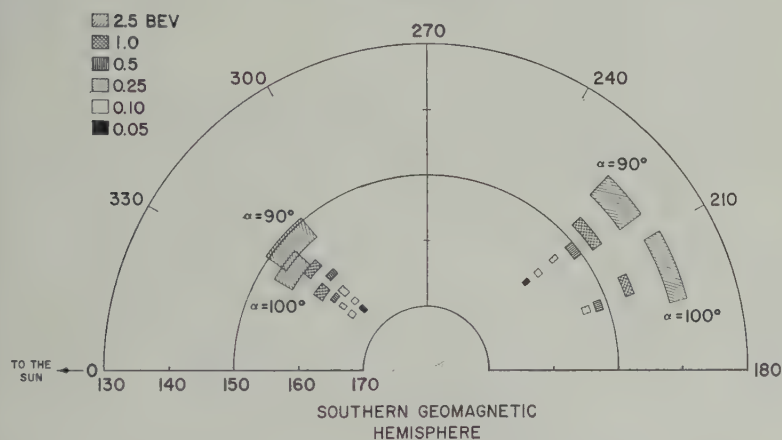
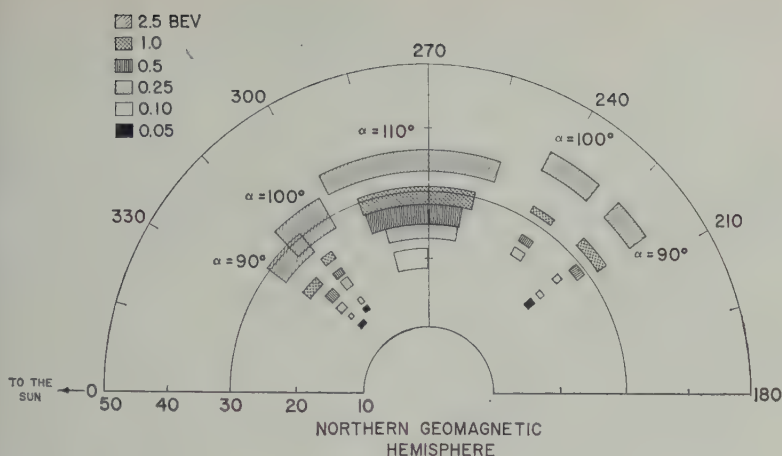


Fig. 6e.





7. Impact zones in the northern and southern geomagnetic hemispheres for 2.5 to 0.05-bev protons ( $\psi \leq 90^\circ$ ).

TABLE 6-A1

COUNTING RATES OF PROTONS WITH IMPACT ANGLES  $\pm 45^\circ$  AT THE EARTH'S SURFACE  
IN BLOCKS  $10^\circ$  GEOMAGNETIC LONGITUDE ( $\Phi$ )  $\times 10^\circ$  GEOMAGNETIC COLATITUDE ( $\Theta$ )  
FOR A FLAT ENERGY SPECTRUM BEAM INCIDENT ON THE AB PLANE

$$\alpha = 90^\circ$$

NORTHERN HEMISPHERE

$\phi$	$\theta$										Totals
	10	20	30	40	50	60	70	80	90		
0-10 50 Bev							3.0	3.0	6.0		
20-30 5 Bev				1.7	1.7					3.4	
30-40 10 Bev						3.6				3.6	
50-60 5 Bev				1.7	1.7					1.7	
70-80 5 Bev				2.9						2.9	
110-120 5 Bev					1.7					1.7	
130-140 10 Bev							3.6	3.6		7.2	
140-150 25 Bev									6.0	6.0	
150-160 5 Bev										1.7	
160-170 25 Bev										2.9	
170-180 25 Bev										5.7	
190-200 25 Bev										6.0	
210-220 10 Bev										3.6	
230-240 25 Bev										6.0	
250-260 25 Bev										6.0	
270-280 50 Bev										6.0	
290-300 50 Bev										6.0	
310-320 50 Bev										6.0	
330-340 50 Bev										6.0	
350-360 50 Bev										6.0	

$\phi$	$\theta$										Totals
	10	20	30	40	50	60	70	80	90		
280-290 50 Bev										10.7	
										17.5	
300-310 50 Bev										6.0	
310-320 50 Bev										17.8	
320-330 50 Bev										31.8	
330-340 50 Bev										8.8	
340-350 50 Bev										5.7	
350-360 50 Bev										18.0	
370-380 50 Bev										2.9	
390-400 50 Bev										24.3	
410-420 50 Bev										59.9	
430-440 50 Bev										3.4	
450-460 50 Bev										5.9	
470-480 50 Bev										11.4	
490-500 50 Bev										8.9	
510-520 50 Bev										27.4	
530-540 50 Bev										60.0	
550-560 50 Bev										33.4	
570-580 50 Bev										60.0	
590-600 50 Bev										60.0	
610-620 50 Bev										60.0	
630-640 50 Bev										60.0	
650-660 50 Bev										60.0	
670-680 50 Bev										60.0	
690-700 50 Bev										60.0	
710-720 50 Bev										60.0	
730-740 50 Bev										60.0	
750-760 50 Bev										60.0	
770-780 50 Bev										60.0	
790-800 50 Bev										60.0	
810-820 50 Bev										60.0	
830-840 50 Bev										60.0	
850-860 50 Bev										60.0	
870-880 50 Bev										60.0	
890-900 50 Bev										60.0	
910-920 50 Bev										60.0	
930-940 50 Bev										60.0	
950-960 50 Bev										60.0	
970-980 50 Bev										60.0	
990-1000 50 Bev										60.0	

TABLE 6-A2

COUNTING RATES OF PROTONS WITH IMPACT ANGLES  $\leq 45^\circ$  AT THE EARTH'S SURFACE  
IN BLOCKS  $10^\circ$  GEOMAGNETIC LONGITUDE ( $\phi$ )  $\times$   $10^\circ$  GEOMAGNETIC COLATITUDE ( $\theta$ )  
FOR A FLAT ENERGY SPECTRUM BEAM INCIDENT ON THE AB PLANE

$$\alpha = 90^\circ$$

## SOUTHERN HEMISPHERE

$\phi$	$\theta$	$\phi$	$\theta$
	90		90
	100		100
0-10 50 Bev	9.1	280-290 50 Bev 25	9.1 12.0
140-150 25 Bev	6.0	290-300 50 Bev 25	9.1 18.0
160-170 25 Bev	6.0	300-310 50 Bev 25	9.1 18.0
170-180 25 Bev	6.0	310-320 50 Bev 25	9.1 12.0
210-220 25 Bev	6.0	320-330 50 Bev 25	12.2 12.0
220-230 25 Bev	18.0	330-340 50 Bev 25	6.1 12.0
230-240 25 Bev	6.0	340-350 50 Bev	12.2
240-250 25 Bev	18.0	350-360 50 Bev	9.1
250-260 25 Bev	23.9		
260-270 25 Bev	29.9		
270-280 50 Bev 25	12.2 18.0		



TABLE 6-B1

COUNTING RATES OF PROTONS WITH IMPACT ANGLES  $\leq 45^\circ$  AT THE EARTH'S SURFACE  
IN BLOCKS  $10^\circ$  GEOMAGNETIC LONGITUDE ( $\phi$ )  $\times$   $10^\circ$  GEOMAGNETIC COLATITUDE ( $\theta$ )  
FOR A FLAT ENERGY SPECTRUM BEAM INCIDENT ON THE AB PLANE

$\alpha = 100^\circ$

NORTHERN HEMISPHERE

$\phi$	$\theta$									Totals
	10	20	30	40	50	60	70	80		
	20	30	40	50	60	70	80	90		
0-10 50 Bev							3.0	3.0		6.0
30-40 10 Bev							3.6			3.6
50-60 10 Bev							3.6			3.6
100-110 10 Bev					3.6					3.6
160-170 10 Bev						3.6				3.6
200-210 25 Bev							6.0			6.0
210-220 25 Bev 10						10.7	12.0	18.0		30.0 10.7
220-230 10 Bev 5				19.8	10.7	7.1				17.8 19.8
230-240 25 Bev 10 5 2.5 1.0 0.5				19.8 23.5 22.9	21.4	3.6	12.0	12.0		24.0 25.0 19.8 23.5 22.9 17.8
240-250 25 Bev 10 5 2.5 1.0				2.9 6.6 5.7	17.8		29.9	6.0		35.9 17.8 6.6 2.9 5.7
250-260 25 Bev 10				7.1	7.1		23.9			23.9 14.2

$\phi$	$\theta$									Totals
	10	20	30	40	50	60	70	80		
	20	30	40	50	60	70	80	90		
270-280 50 Bev 25						18.0	3.0 18.0	9.1 18.0		12.1 54.0
280-290 50 Bev 25				6.0	3.0 12.0	6.1 18.0	9.1 12.0	6.1 12.0		24.3 60.0
290-300 50 Bev 25			6.0	6.0	3.0 12.0	6.1 6.0	6.1 12.0	9.1 12.0		24.3 54.0
300-310 50 Bev 25 10 5 2.5 1.0 0.5 0.25 0.10 0.5				3.0 12.0 39.2	3.0 12.0	6.1 12.0	6.1 6.0	6.1 12.0		24.3 54.0 52.9 52.7 28.6 26.7 26.7 21.8 31.2
310-320 50 Bev 25 10 5 2.5			6.0 7.1 26.5 5.9	3.0 6.0 64.1	3.0 6.0	6.1 12.0	9.1 6.0	6.1 12.0		27.3 48.0 71.2 26.5 5.9
320-330 50 Bev 25				6.0	3.0 6.0	9.1 12.0	9.1 6.0	12.2 12.0		33.4 42.0
330-340 50 Bev					6.1	6.1	6.1	3.0		21.3
340-350 50 Bev				3.0	3.0	12.2	6.1			24.3
350-360 50 Bev 10						3.0 3.6	6.1	3.0		12.1 3.6

TABLE 6-82

COUNTING RATES OF PROTONS WITH IMPACT ANGLES  $\leq 45^\circ$  AT THE EARTH'S SURFACE  
IN BLOCKS  $10^\circ$  GEOMAGNETIC LONGITUDE ( $\phi$ )  $\times$   $10^\circ$  GEOMAGNETIC COLATITUDE ( $\theta$ )  
FOR A FLAT ENERGY SPECTRUM INCIDENT ON THE AB PLANE

$\alpha = 100^\circ$

SOUTHERN HEMISPHERE

$\theta$								Totals
90	100	110	120	130	140	150	160	
100	110	120	130	140	150	160	170	
9.1	6.1	6.1	3.0					24.3
		3.6						3.6
			3.6					3.6
	3.6							3.6
			3.6					3.6
			6.6	6.6 2.9	3.6 5.7		8.9	3.6 13.2 2.9 5.7 8.9
	3.6	3.6						7.2
		3.6	6.6	2.9				3.6 6.6 2.9
		10.7	6.6	13.2 5.9		5.7		10.7 19.8 5.9 5.7
			14.2	13.2 2.9	5.9 5.7		8.9 13.3	14.2 13.2 8.8 5.7 8.9 13.3
			10.7					10.7

$\phi$	$\theta$								Totals
	90	100	110	120	130	140	150	160	
	100	110	120	130	140	150	160	170	
270-280 50 Bev 25	6.1 6.0	3.0	3.0						12.1 6.0
280-290 50 Bev 25 2.5 1.0	9.1 12.0	6.1 18.0	12.2 6.0	6.1		2.9 5.7			33.5 36.0 2.9 5.7
290-300 50 Bev 25	6.1 12.0	6.1 18.0	6.1 12.0	6.1 12.0	6.1 12.0	6.0			30.5 72.0
300-310 50 Bev 25 5	9.1 12.0	6.1 12.0	9.1 6.0	6.1 12.0	6.1 6.0 6.6	6.1 6.0			42.6 54.0 6.6
310-320 50 Bev 25 5 2.5	9.1 12.0	9.1 6.0	9.1 12.0	6.1 12.0	6.1 6.0	3.0 12.0 6.6	6.0		42.5 66.0 6.6 2.9
320-330 50 Bev 25 10 5 2.5 1.0 0.5 0.25 0.10	6.1 6.0	6.1 12.0	9.1 6.0	9.1 12.0	3.0	3.0 89.0 6.6	46.3 41.0 28.6		36.4 48.0 89.0 52.9 41.0 28.6 33.6 26.6 21.8
330-340 50 Bev 25	6.1 6.0	12.1 6.0	6.1 6.0	6.1 6.0	6.1 6.0	6.1 6.0	6.0		42.6 42.0
340-350 50 Bev 25	12.2	6.1	6.1 6.0	3.0	6.1 6.0	6.1 6.0			39.6 18.0
350-360 50 Bev	6.1	6.1	9.1	3.0	6.1	3.0			33.4





COUNTING RATES OF PROTONS WITH IMPACT ANGLES  $\leq 45^\circ$  AT THE EARTH'S SURFACE IN BLOCKS  $10^\circ$  GEOMAGNETIC LONGITUDE ( $\Phi$ )  $\times$   $10^\circ$  GEOMAGNETIC COLATITUDE ( $\Theta$ ) FOR A FLAT ENERGY SPECTRUM BEAM INCIDENT ON THE AB PLANE

$$\alpha = 110^\circ$$

SOUTHERN HEMISPHERE

Φ	Θ										Totals
	90	100	110	120	130	140	150	160	170		
0-10 50 Bev	3.0	3.0	6.1	6.1	6.1	6.1	3.0			27.3	
10-20 50 Bev			3.0	3.0						6.0	
140-150 10 Bev			3.6							3.6	
150-160 10 Bev				3.6						3.6	
160-170 10 Bev 5			3.6	7.1	13.2					10.7 13.2	
170-180 10 Bev			3.6	21.4						25.0	
180-190 10 Bev			3.6	3.6						7.2	
190-200 10 Bev				10.7						10.7	
240-250 10 Bev				3.6						3.6	
280-290 50 Bev		12.2	3.0	6.1	6.1					27.4	
290-300 50 Bev 25	9.1	6.1	12.0	9.1	6.1	6.1	6.1	6.1	6.1	42.6 42.0	

Φ	Θ										Totals
	90	100	110	120	130	140	150	160	170		
300-310 50 Bev 25	9.1 6.0	6.1 6.0	9.1 18.0	6.1 6.0	6.1 12.0	6.1 12.0	6.1 12.0	6.0		42.6 66.0	
310-320 50 Bev 25 10	9.1 6.0	6.1 12.0	9.1 6.0	6.1 6.0	6.1 12.0	3.0 3.0	3.0 21.4	3.0 7.1		39.4 42.0 28.5	
320-330 50 Bev 25 10 5 2.5 1.0 0.5 0.25	9.1	6.1 12.0	6.1 6.0	9.1 6.0	6.1 12.0	6.1 12.0	6.1 21.4	3.0 28.5 33.1 75.1	3.0 6.0 49.0 34.3 17.8 26.6	45.6 54.0 49.0 33.1 75.1 34.3 17.8 26.6	
330-340 50 Bev 25 5 2.5	6.1	12.2	6.1 12.0	6.1 12.0	6.1 6.0	6.1 6.0	6.1 6.0	3.0 24.5 9.4		42.5 36.0 24.5 9.4	
340-350 50 Bev 25	9.1	6.1	9.1	3.0 6.0	6.1 6.0	6.1 6.0	6.1 6.0	6.0		39.5 24.0	
350-360 50 Bev 25	3.0	12.2	6.1	6.1	3.0 6.0	3.0 6.0	3.0 6.0	3.0 6.0		36.4 6.0	

COUNTING RATES OF PROTONS WITH IMPACT ANGLES  $\leq 45^\circ$  AT THE EARTH'S SURFACE IN BLOCKS  $10^\circ$  GEOMAGNETIC LONGITUDE ( $\phi$ )  $\times$   $10^\circ$  GEOMAGNETIC COLATITUDE ( $\theta$ ) FOR A FLAT ENERGY SPECTRUM BEAM INCIDENT OF THE AB PLANE

NORTHERN HEMISPHERE

[illegible]

$$\alpha = 117^\circ$$

SOUTHERN HEMISPHERE

$\phi$	$\theta$								Totals
	90	100	110	120	130	140	150	160	
0-10 50 Bev		3.0	6.1	3.0	6.1	3.0	3.0		24.2
10-20 50 Bev			3.0	3.0	6.1	3.0			15.1
280-290 50 Bev		3.0	3.0	6.1	3.0	6.1			21.2
290-300 50 Bev	3.0	6.1	9.1	6.1	6.1	3.0			33.4
300-310 50 Bev	9.1	6.1	9.1	6.1	3.0	6.1	6.1		45.6
25			6.0	18.0	6.0	12.0	6.0		48.0
310-320 50 Bev	9.1	9.1	9.1	6.1	9.1	3.0	3.0		48.5
25			6.0	12.0	6.0	12.0	12.0		48.0
320-330 50 Bev	9.1	6.1	6.1	9.1	3.0	3.0	3.0		39.4
25			12.0	12.0	6.0	6.0			36.0
10						3.6	3.6		3.6
5						23.2	11.7		23.2
2.5								7.0	18.7
1.0								18.3	18.3
0.5								7.1	7.1
0.25								21.3	21.3

$\phi$	$\theta$								Totals
	90	100	110	120	130	140	150	160	
330-340 50 Bev	3.0	12.2	6.1	6.1	9.1	6.1	3.0	3.0	48.6
25				6.0	12.0	6.0	6.0	6.0	36.0
10							85.4		85.4
5							34.7		34.7
2.5							46.9		56.3
1.0								9.4	36.6
0.5								42.7	42.7
0.25								21.3	21.3
0.10								34.9	34.9
0.05								25.0	25.0
340-350 50 Bev	12.2	3.0	9.1	6.1	6.1	3.0	3.0		39.5
25				6.0	6.0	6.0	6.0		18.0
350-360 50 Bev	3.0	9.1	6.1	9.1	3.0	6.1	3.0		39.4
25						6.0	6.0		12.0



TABLE 6-EI

COUNTING RATES OF PROTONS WITH IMPACT ANGLES  $\leq 45^\circ$  AT THE EARTH'S SURFACE  
IN BLOCKS  $10^\circ$  GEOMAGNETIC LONGITUDE ( $\phi$ )  $\times$   $10^\circ$  GEOMAGNETIC COLATITUDE ( $\theta$ )  
FOR A FLAT ENERGY SPECTRUM BEAM INCIDENT ON THE AB PLANE

$$\alpha = 125^\circ$$

SOUTHERN HEMISPHERE

$\phi$	$\theta$										Totals
	90	100	110	120	130	140	150	160	170	180	
0-10 50 Bev 25			9.1	3.0	9.1	3.0	6.1	6.0			30.3 6.0
10-20 50 Bev			3.0	6.1	3.0	6.1		3.0			21.2
20-30 50 Bev						3.0	3.0				6.0
280-290 50 Bev				3.0	3.0	6.1		3.0			15.1
290-300 50 Bev 25		3.0	6.1	9.1	3.0	3.0	6.1				30.3 12.0
300-310 50 Bev 25		9.1	6.1	9.1	3.0	6.1	3.0	12.0			36.4 36.0
310-320 50 Bev 25	6.1	9.1	6.1	6.0	9.1	3.0	6.1	6.0	3.0		48.6 24.0
320-330 50 Bev 25	9.1	6.1	12.2	6.1	3.0	3.0	3.0	6.0	6.0		42.5 36.0 3.3 2.5
				6.0	6.0	12.0	13.2	9.4			16.5 9.4

$\phi$	$\theta$										Totals
	90	100	110	120	130	140	150	160	170	180	
330-340 50 Bev 25	9.1	6.1	6.1	6.0	9.1	6.1	12.0				48.6 24.0 85.4
10											21.5
5											43.0
2.5											63.3
1.0											45.8
0.5											35.6
0.25											42.6
0.10											52.4
0.05											25.0
340-350 50 Bev 25	6.1	6.1	9.1	3.0	9.1	6.0	6.0				39.5 24.0
350-360 50 Bev 25		6.1	6.1	6.1	3.0	3.0	3.0				27.3 12.0

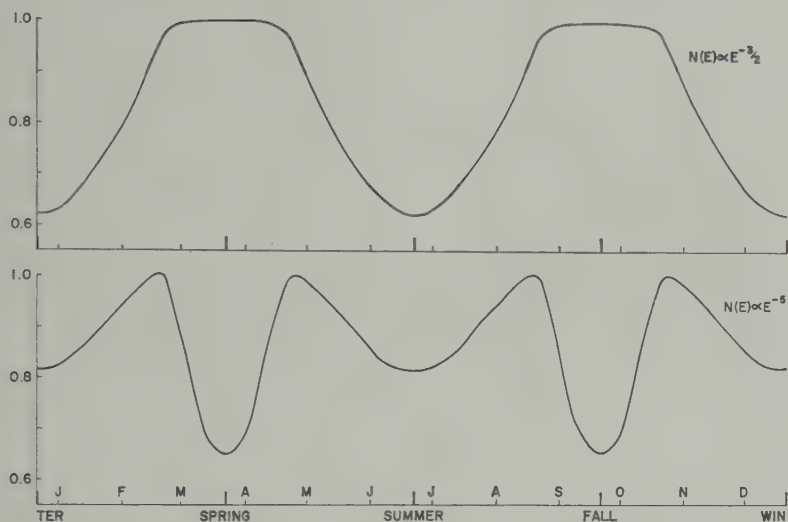


Fig. 8. The total incident daily flux integrated over the whole earth versus season for two energy spectra.

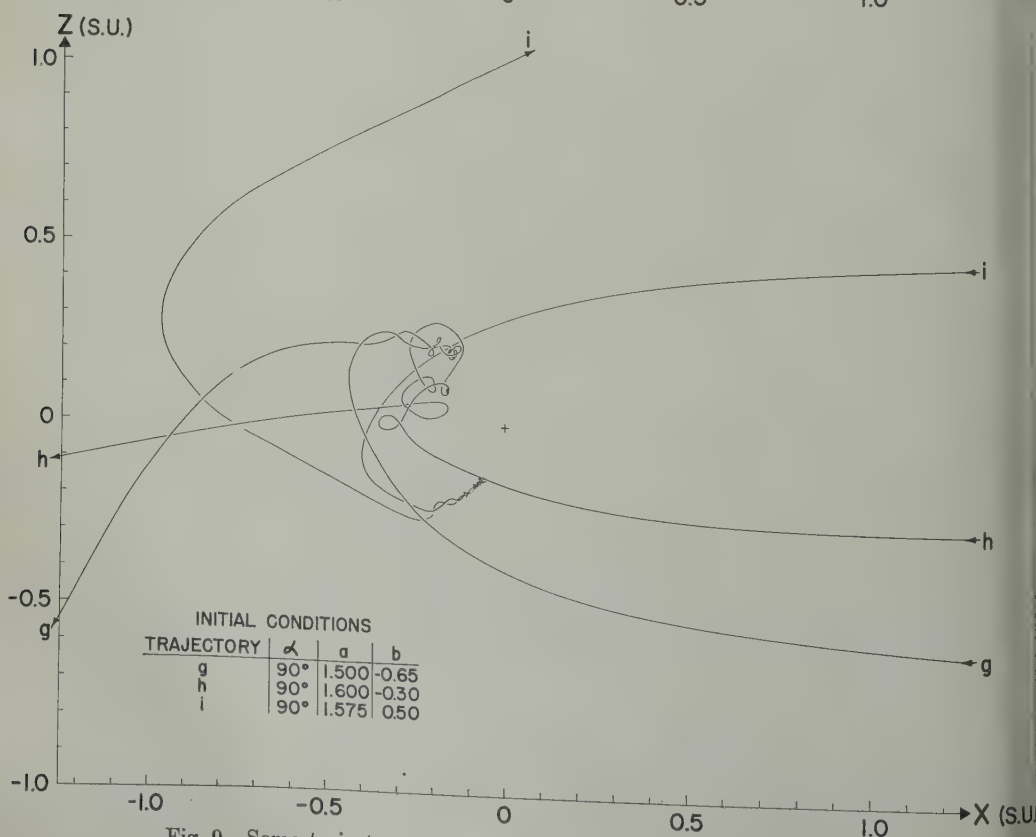
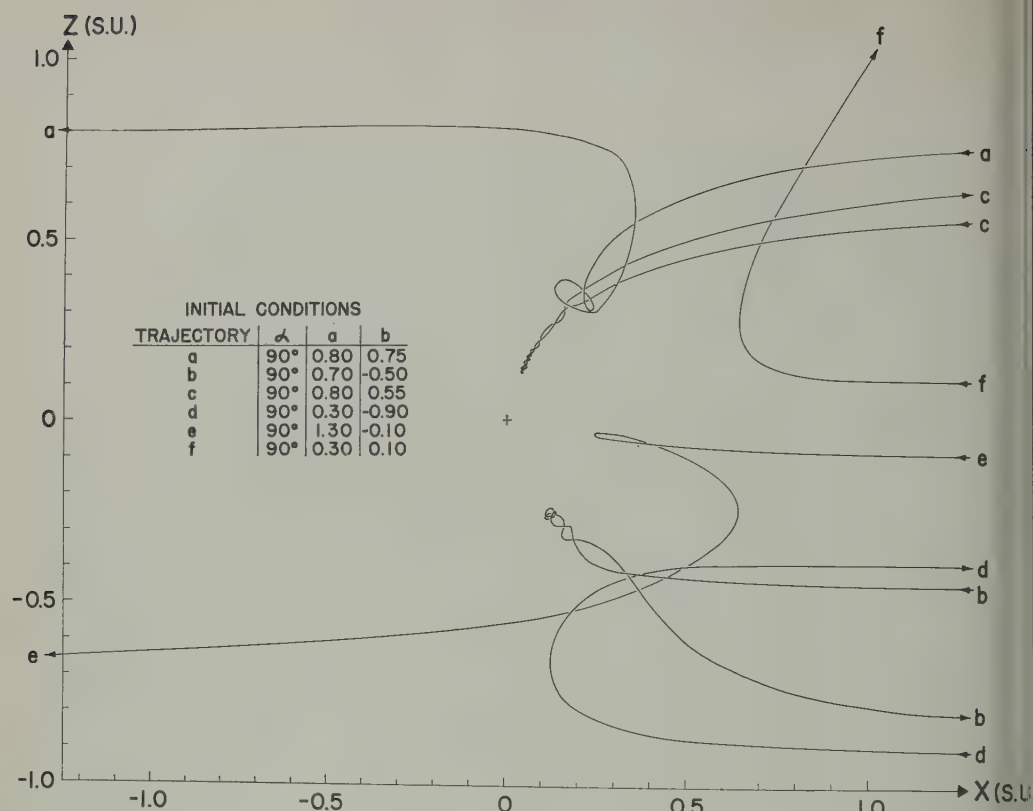


Fig. 9. Some trajectory examples: *above, day side, below, night side.*

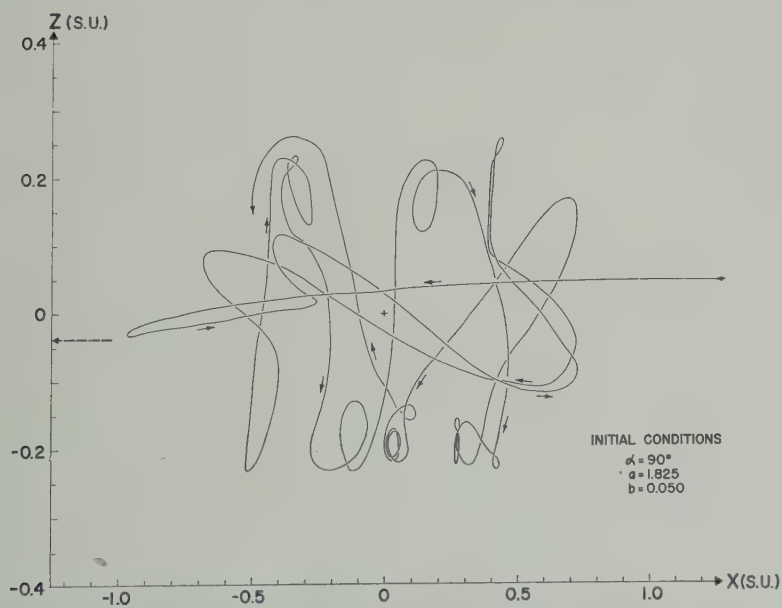
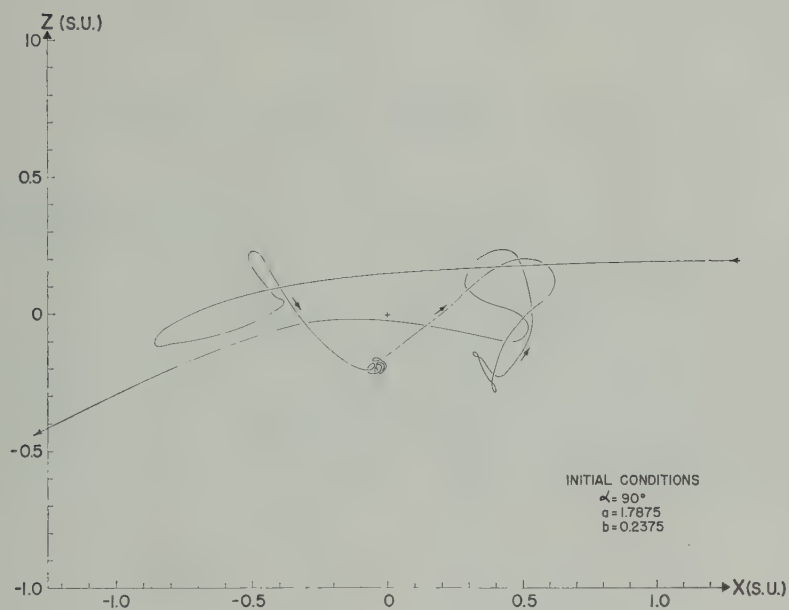


Fig. 10. Above, a simple, and below, a complicated, quasi-trapped trajectory.



strike along the magnetic equator; these have been counted as striking in the southern hemisphere. The number of equatorial impacts can be deduced from Table 6-A2, which lists the counting rates in the interval of colatitude  $90^\circ$  to  $100^\circ$  only.

Figures 6 and 7 and Table 6 indicate that ground observers would detect different counting rates, depending on their location.

In Figure 8 the daily flux integrated over the earth is plotted against season for two different energy spectra of the beam.

Figures 9 and 10 plot the three major groups of trajectories: (1) trajectories that approach the day side of the earth and return to infinity; (2) trajectories that approach the night side and return to infinity; (3) quasi-trapped trajectories, which stay in the vicinity of the earth for a number of close passes before returning to infinity.

*Acknowledgments.* I am grateful to Dr. Robert Jastrow for suggesting this investigation, and to Drs. Jastrow and C. A. Pearse for many stimulating discussions. I thank Mrs. L. Shapiro and Miss M. Pinker for preparing the machine programs that made these calculations possible. Much of the

work for this paper was done while I was at the Naval Research Laboratory, Washington, D. C.

#### REFERENCES

- Bennett, W. H., *J. Geophys. Research*, **61**, 3, 1956.  
 Birkeland, *Videnskapsselskapets-Skrifter, M naturv. Kl.*, no. 1, 1901.  
 Brunberg, E. A., and A. Dattner, *Tellus*, **5**, 1, 1953.  
 Dwight, K., *Phys. Rev.*, **78**, 40, 1950.  
 Firor, J., *Phys. Rev.*, **94**, 1017, 1954.  
 Jory, F. S., *Phys. Rev.*, **103**, 1068, 1956.  
 Katz, L., P. Meyer, and J. A. Simpson, *Nuovo cimento Suppl.*, **8**, 277, 1958.  
 Lemaitre, G., and M. S. Vallarta, *Phys. Rev.*, **719**, 1936.  
 Lüst, R., *Phys. Rev.*, **105**, 1827, 1957.  
 Lüst, R., A. Schlüter, and K. Katterbach, *Nachricht. Akad. Wiss. Göttingen*, no. 8, 1955.  
 Malmfors, K. G., *Arkiv. Fysik*, **32a**, no. 8, 1945.  
 Montgomery, D. J. X., *Cosmic Ray Physics*, Princeton University Press, Princeton, 317 p., 1949.  
 Rothwell, P., and J. Quenby, *Nuovo cimento Suppl.*, **8**, 249, 1958.  
 Schlüter, A., *Z. Naturforsch.*, **6a**, 613, 1951.  
 Störmer, C., *Astrophys. Norv.*, **1**, 1, 1936.

(Manuscript received August 21, 1961.)

# A Study of the Enhanced Ionization Produced by Solar Protons during a Polar Cap Absorption Event

G. C. REID

*Defence Research Telecommunications Establishment  
Shirley Bay, Ottawa, Canada*

**Abstract.** Polar-cap absorption of radio waves has been shown to be caused by an influx of fast particles emitted by the sun at the time of certain solar flares. The steady-state daytime and nighttime electron-density profiles produced in the lower ionosphere by such a particle flux are calculated, on the assumptions that the particles are protons and that their differential energy spectrum is of the form  $n(E) dE = KE^{-5} dE$ , with a sharp cutoff at the low-energy end. The shapes of the profiles are shown to be almost independent of the proton spectrum and low-energy cutoff, provided the latter is higher than about 10 Mev. The radio-wave absorption this ionization would produce is calculated for frequencies of 30 Mc/s and 60 Mc/s. Conditions during the twilight transition period are also examined, assuming that  $O_2^-$  is the only negative ion present. The photodetachment coefficient of  $O_2^-$  is calculated as a function of solar zenith angle, and corresponding electron-density profiles deduced. By comparing the absorption these profiles would produce with the observed variation of cosmic noise absorption during twilight, it is shown that the presence of  $O_2^-$  alone is insufficient to account for the observations.

## 1. INTRODUCTION

It is now generally recognized that following certain major solar flares the polar regions of the earth are subject to bombardment by fast-moving particles of solar origin, often for a period of several days. The ionization produced in the upper atmosphere by these particles gives rise to intense absorption of radio waves, and can completely disrupt radio communications in the HF band at high latitudes, giving rise to an ionospheric condition known as 'polar blackout'. Although these blackouts have been recognized for many years, their true nature was not understood until VHF measurements of cosmic noise and of signals propagated by ionospheric waves became available at high latitudes. As a result of these measurements, it was proposed [Bailey, 1959; Reid and Collins, 1959; Hultine, 1959] that the observed characteristics of this absorption could be explained if the sun emitted protons in the 10 to 100 Mev energy range following certain major flares. Anderson [1959] independently discovered such a proton flux during balloon flights of cosmic-ray equipment over Churchill, thereby confirming the hypothesis.

The name 'Type III absorption' originally used by Reid and Collins for these events has now been replaced by general agreement by

the term 'polar-cap absorption' (PCA) to distinguish them from the more frequent and more sporadic 'auroral absorption' events (previously referred to as 'Type II absorption'), which also give rise to polar blackouts in the HF band.

The purpose of this paper is to examine theoretically the electron-density height profile which would be expected from an influx of solar protons, with special emphasis on its variation with solar zenith angle at sunrise and sunset. Using published values for the electron collisional frequency in the lower ionosphere, the time variation of the cosmic-noise absorption that would be observed by an idealized riometer is computed and compared with observations. It is assumed throughout that the incident particle flux consists solely of protons. Recently there has been accumulating evidence that heavier particles, and in particular alpha-particles, are often present in appreciable numbers. However, there is general agreement that protons form the bulk of the flux, and our assumption of a pure proton flux is certainly justified in view of some of the other much more serious uncertainties in the calculation.

Bailey [1959] has attacked the problem of the day and night equilibrium electron-density profiles for the event of February 23, 1956, and as far as these profiles are concerned the present

analysis closely follows his work. However, better values of many of the atmospheric parameters have become available since the earlier work was carried out, and these values have been used in this paper. The author is indebted to D. K. Bailey (private communication) for pointing out the significance of some of this recent work.

It must be borne in mind that this analysis is based on a model which contains certain assumptions. The validity of these assumptions and their effect on the over-all picture will be discussed as they arise. It is felt, however, that the end result is a reasonably close approximation to the conditions that would exist in our model atmosphere during a moderately strong polar-cap absorption event.

## 2. THE SOLAR PROTON FLUX AND SPECTRUM

Several measurements have been made using balloon-borne instrumentation of the composition and spectrum of the solar particles responsible for PCA events. These measurements have shown, as mentioned above, that by far the largest proportion of the particles are protons, and that their spectrum is usually steeply inclined toward low energies. As a particular example, *Anderson and Enemark* [1960] found during a balloon flight over Resolute Bay in July 1959 that the integral proton spectrum in the energy range from 85 to 300 Mev was well represented by the relation

$$N(> E) = K(t)E^{-4} \quad (1)$$

where  $N(>E)$  is the number of protons with kinetic energy greater than  $E$ , and  $K(t)$  is a time-dependent proportionality factor. The corresponding differential proton spectrum is given by

$$n(E) dE = 4K(t)E^{-5} dE \quad (2)$$

where  $n(E) dE$  is the number of protons with energy between  $E$  and  $E + dE$ .

Unfortunately, measurements made from balloons are limited to protons which have enough energy to penetrate the residual atmosphere above the balloon (in the above example,  $E > 85$  Mev). The nature of the low-energy end of the spectrum can only be determined by rocket or satellite measurements, none of which were readily available when this work was carried out. In the present analysis it has been

assumed that the balloon-measured spectrum can be extrapolated down to some arbitrary lower energy limit, at which the flux is cut sharply. This is admittedly a somewhat artificial assumption, but it is difficult to improve upon in the current state of our knowledge. In order to test the effect of varying the low-energy cutoff, calculations were carried out for cutoffs of 40 and 20 Mev. Some justification for these values comes from some measurements of solar protons made by satellite-borne equipment as reported by *Rothwell and McIlwain* [1959]. They infer that during a particular event in August 1958 the spectrum measured by balloon could probably be extrapolated safely down to at least 30 Mev. The sharp cutoff we have assumed is not necessarily present in the particle flux in free space, but could be imposed by the geomagnetic field. Thus, at a geomagnetic latitude of  $68^\circ$ , for which the Störmer cutoff energy for protons is 40 Mev, a fairly sharp cutoff at this energy should be observed regardless of the form of the spectrum at lower energies.

The particle flux has been adjusted to correspond to the order of magnitude of the flux observed by *Anderson and Enemark* [1960] and their value of  $-5$  for the exponent of the differential spectrum has also been adopted. The final form of the assumed differential proton spectrum is then

$$n(E) dE = 2.24 \times 10^{10} E^{-5} dE \quad (3)$$

protons  $\text{cm}^{-2} \text{sec}^{-1}$

where  $E$  is measured in Mev. (This relation assumes that the protons are incident isotropically over the upper hemisphere. The directional flux per steradian is obtained by dividing by  $2\pi$ .) The function  $n(E)$  is shown in Figure 1.

The second important feature characterizing the proton flux is its directionality. If the protons traveled in direct paths from the sun to the earth, we would expect them to precipitate on the earth in fairly well-defined impact zones. Ground observations of the comparatively few events which have produced appreciable ground increases in cosmic radiation have shown some evidence that impact zones may exist during the early stages of an event. After a few hours, however, the particles appear to arrive at the earth isotropically from all directions, an observation which is confirmed by the remarkable



mity often evident in the polar-cap ab-  
 on measured by riometers over a wide  
 of latitudes [Reid and Leinbach, 1959].  
 ave assumed in the following analysis that  
 protons are incident at the top of the atmos-  
 with an angular distribution which is  
 pic over the upper hemisphere. The pro-  
 will spiral about the direction of the geo-  
 etic field, but as far as energy loss in the  
 sphere is concerned, a proton spiraling  
 with pitch angle  $\theta$  is equivalent to a pro-  
 traveling in a straight line with zenith angle  
 suming that the magnetic field is vertical  
 hat the pitch angle does not change in the  
 it region with which we are concerned. Both  
 these assumptions are sufficiently valid at  
 geomagnetic latitudes for our present pur-

### 3. RATE OF PRODUCTION OF IONIZATION

e rate of production of ionization in the  
 sphere by such an incoming proton flux can  
 be computed. In order to do this, a model  
 the atmosphere is required, and in this  
 ular case it has been assumed that the  
 position of the atmosphere throughout the  
 at region of interest is the same as that at  
 surface of the earth. It will be seen later  
 the region in question extends from about  
 o about 100 km, so that the major error in  
 above assumption probably lies in the neglect  
 e dissociation of oxygen at the higher levels.  
 ever, the inaccuracy introduced by this  
 ect is thought to be small. The variation of  
 ty with height reported by the *Rocket*  
*M* [1952] has been assumed in this part of  
 calculation.

Having assumed an atmosphere with sea-level  
 position, we can use the well-established  
 e-energy relations for protons in standard  
 o calculate the ionization rate. Curves of  
 on range versus energy and rate of energy  
 versus energy have been published by, for  
 ple, Bethe and Ashkin [1953]. The details  
 e calculations will not be presented here,  
 we shall merely outline the approach which  
 been followed.

ur discrete values of proton energy were  
 ed (10, 40, 100, and 200 Mev), and for  
 case the total energy lost by a vertically  
 ent proton in a certain height interval of  
 atmosphere was found. This calculation was

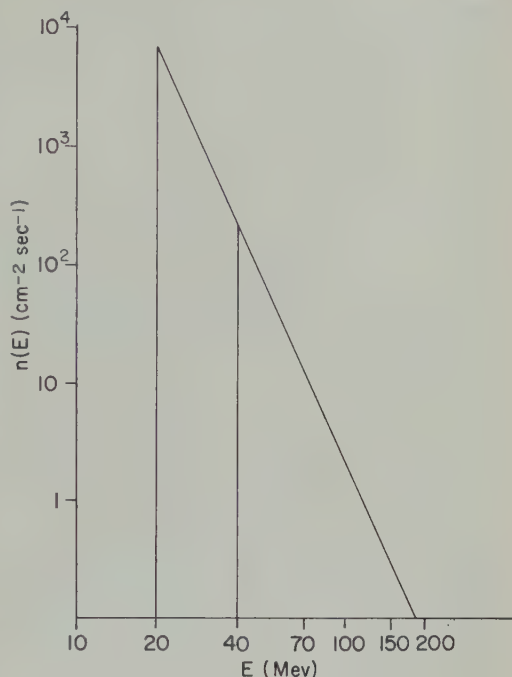


Fig. 1. Differential spectrum of incoming protons. The vertical lines correspond to low-energy cutoff values of 20 Mev and 40 Mev.

carried out for the 40 slabs of 2-km thickness  
 between 30 and 110 km and for the 8 slabs of  
 5-km thickness between 110 and 150 km. The  
 calculation was repeated for protons incident on  
 the atmosphere at zenith angles of 30°, 45°, 60°,  
 and 75°, and the energy loss at each zenith  
 angle was multiplied by an appropriate geo-  
 metrical factor to take account of the isotropic  
 properties of the flux to a close approximation.  
 These values were converted to energy loss per  
 unit volume per second at the height of the  
 center of the slab and summed for each proton  
 energy. The total energy loss at each height was  
 then normalized to arrive at a value for the total  
 energy loss per unit volume per second by a  
 flux of protons of unit intensity (1 proton per  
 cm<sup>2</sup> per second) isotropic over the upper hemi-  
 sphere. This quantity has been denoted by  $\epsilon$   
 $(E, h)$ . From curves of  $\epsilon(E, h)$  versus  $E$  for a  
 range of values of  $h$ , it is possible to determine  
 the rate of energy loss as a function of height  
 for any assumed isotropic proton flux.

The rate of energy loss can be converted into  
 the rate of electron production,  $q$ , by dividing  
 by the value for the average energy lost by a



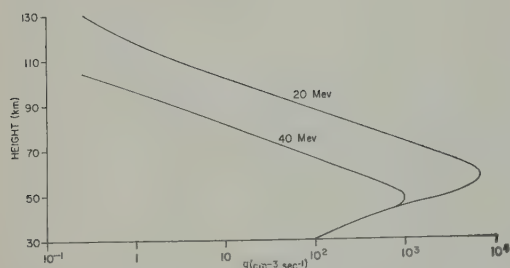


Fig. 2. Height profile of rate of electron production ( $q$ ) for low-energy cutoff values of 20 Mev and 40 Mev.

fast proton in producing an ion pair in air. This quantity is very nearly independent of proton energy and the value of 36 ev per ion used by Bailey [1959] has been adopted here.

Using the spectrum given by (3) above, based on the measurements of Anderson and Enemark [1960],  $q$  has been calculated as a function of height, assuming first a low-energy cutoff at 40 Mev and then at 20 Mev. The results are presented in Figure 2. It can be seen that in going from a cutoff of 40 to 20 Mev the height at which  $q$  reaches a maximum moves up from 47 to 55 km, since the protons that are added are of lower energy and stop at greater heights. The electron production rate itself increases by an order of magnitude at heights above 50 km because of the steep inclination of the spectrum toward low energies (the total number of protons with  $E > 20$  Mev is 16 times the number with  $E > 40$  Mev).

#### 4. THE STEADY-STATE ELECTRON-DENSITY PROFILES

The processes of electron production and removal which govern the steady-state electron density in the lower ionosphere have been dealt with by a number of authors, but for the sake of completeness we shall repeat the arguments here in a brief form. One of the major differences between the lower and upper ionospheres in this respect lies in the occurrence of negative ions in appreciable quantities in the former. We shall be assuming initially that the neutral constituents of the lower ionosphere are only  $O_2$  and  $N_2$ , i.e. all minor constituents such as ozone and the various oxides of nitrogen will be ignored. This assumption will be re-examined later when dealing with the twilight effects, but is probably

a safe approximation for steady-state day and night conditions. In such an atmosphere we can safely assume that the only negative ion is  $O_2^-$  since  $N_2^-$  has never been observed either in nature or in the laboratory. (We have mentioned above that the dissociation of oxygen, with the consequent possibility of forming  $O^-$  in the upper part of the region, has been ignored.)

Free electrons can be removed by becoming attached to  $O_2$  molecules to form  $O_2^-$ , and can be released by photodetachment by sunlight and by collisional detachment. In addition, direct recombination between electrons and positive ions and between negative ions and positive ions must take place. The best available information concerning the rates of these various processes is summarized below.

**Electron attachment.** Recent laboratory measurements by Chanin, Phelps and Bion [1959] have shown that electron attachment to  $O_2$  at low energies is predominantly a three-body process, the third body in the case of air being another  $O_2$  molecule. These measurements indicate that at lower ionosphere temperatures the attachment coefficient, which we shall denote by  $\alpha$ , is about  $1.5 \times 10^{-30} \text{ cm}^3 \text{ sec}^{-1}$ . The rate of occurrence of attachments in a region where the  $O_2$  concentration is  $n \text{ cm}^{-3}$  is then  $\alpha n^2 \text{ sec}^{-1}$  per electron.

**Photodetachment.** According to Phelps and Pack [1961] the electron affinity of  $O_2^-$  is about 0.46 ev. The limiting wavelength for photodetachment of electrons from  $O_2^-$  is therefore 2.7 microns, in the infrared portion of the spectrum. Hence the entire visible spectrum of sunlight possesses sufficient energy to detach electrons from  $O_2^-$ , and it is this process of photodetachment by sunlight which is assumed to account for the excess in daytime absorption over nighttime absorption during a PCA event. Smith, Burch and Branscomb [1958] have measured the photodetachment cross section for  $O_2^-$  as a function of wavelength, and their measurements give a value of about 0.44 sec for  $\rho$ , the rate of occurrence of photodetachment per negative ion in a sunlit atmosphere.

**Collisional detachment.** The rate at which this process takes place in the ionosphere is not yet well known. Bailey [1959] originally used a value of  $2.4 \times 10^{-37} \text{ cm}^3 \text{ sec}^{-1}$  for  $\kappa$ , the collisional detachment coefficient, and values as high as  $4 \times 10^{-37} \text{ cm}^3 \text{ sec}^{-1}$  have been quoted.

of measurements of the ratio of day-to-absorption during PCA events, *Bailey and Lomb* [1960] have revised this value to  $2 \text{ cm}^3 \text{ sec}^{-1}$ , and this value has been adopted in the present work. *Phelps and Pack* [1961], however, have carried out laboratory measurements that indicate the coefficient to be as low as  $10^{-20} \text{ cm}^3 \text{ sec}^{-1}$ . With such a low value for  $\alpha_d$  becomes very difficult to account for the enhanced nighttime ionization without invoking an alternative mechanism. The value of  $2 \times 10^{-20} \text{ cm}^3 \text{ sec}^{-1}$ , however, has the merit of being based directly on ionospheric observations, and is adopted here for that reason. The rate of occurrence of collisional detachments is then  $\kappa n'$  per ion in a region where the density of neutral particles is  $n' \text{ cm}^{-3}$ . In practice  $n'$  can be taken as the total neutral particle density, and a fair approximation  $n' = 5n$ , where  $n$  is the electron concentration, introduced above.

combination. Both dissociative recombination between electrons and positive ions and ion-ion recombination between positive and negative ions must be considered. The commonly used value of  $3 \times 10^{-8} \text{ cm}^3 \text{ sec}^{-1}$  has been used for  $\alpha_d$ , the dissociative recombination coefficient. For the ionic recombination coefficient, the value of  $10^{-7} \text{ cm}^3 \text{ sec}^{-1}$  quoted by *Nicolet and Aikin* [1960] has been adopted. Both of these values are subject to some uncertainty, and particularly the dissociative recombination coefficient should perhaps be somewhat higher, according to recent measurements of this coefficient by *St. Laurent*. However, the approximation is again probably good enough for the present purpose. We can now write down the familiar equations for the rate of change of electron density,  $N$ , positive and negative ion density,  $N^+$  and  $N^-$ ; these are given by

$$\frac{dN}{dt} = q + \kappa n' N^- - \alpha_i N N^+ \quad (4)$$

$$\frac{dN^+}{dt} = \alpha_i N N^+ - \kappa n' N^- - \rho N^- - \alpha_d N N^+ \quad (5)$$

and with the condition for charge neutrality

$$N^+ = N + N^- \quad (6)$$

the photodetachment term,  $\rho N^-$ , vanishes under nighttime conditions.

Under steady-state conditions, the time derivatives vanish, and by introducing the negative ion to electron density ratio,  $\lambda$ , we find

$$q = (1 + \lambda)(\alpha_d + \lambda \alpha_i) N^2 \quad (7)$$

by adding (4) and (5) and using (6). Once  $\lambda$  is known as a function of height we can use (7) to deduce the electron density profile from our previously determined profiles of  $q$ .

By introducing  $\lambda$  into (5) and again equating the time derivative to zero, we obtain another equation relating  $N$  and  $\lambda$ :

$$\alpha_i \lambda (1 + \lambda) N = \alpha_n^2 - (\kappa n' + \rho) \lambda \quad (8)$$

which can be written

$$\lambda = \frac{\alpha_n^2}{\kappa n' + \rho + \alpha_i (1 + \lambda) N} \quad (9)$$

Under conditions of full sunlight, the last term in the denominator can be shown to be negligible in comparison with either  $\kappa n'$  or  $\rho$ , depending on the level of the atmosphere in question. Ionic recombination, then, has little influence on  $\lambda$ , which becomes independent of  $N$ , and is given by

$$\lambda = \frac{\alpha_n^2}{\kappa n' + \rho} \quad (10)$$

Under nighttime conditions, however, when  $\rho = 0$ , this is no longer true as was pointed out to the author by *Bailey* (private communication). In this case a graphical solution for both  $N$  and  $\lambda$  was obtained from the two equations

$$N = \left[ \frac{q}{(1 + \lambda)(\alpha_d + \lambda \alpha_i)} \right]^{1/2} \quad (11)$$

obtained from (7), and

$$N = \frac{\alpha_n^2 - (\kappa n' + \rho) \lambda}{\alpha_i \lambda (1 + \lambda)} \quad (12)$$

obtained from (9).

Using (7) and (10) for daytime and (11) and (12) for nighttime conditions, steady-state electron-density profiles have been constructed for the production functions of Figure 2. The parameters  $a$ ,  $\kappa$ ,  $\rho$ ,  $\alpha_d$ , and  $\alpha_i$  were given the values discussed above, and the variation of  $n$  with height given by *Bates* [1954] was adopted.  $n'$  was assumed to be equal to  $5n$ .

The resultant electron-density profiles for day and night steady-state conditions are shown in

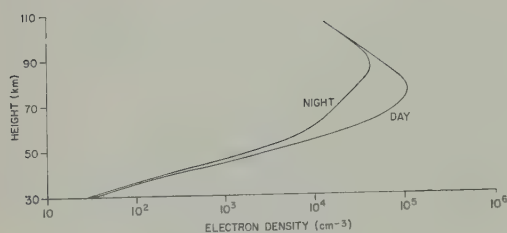


Fig. 3. Height profiles of electron density during daytime and nighttime steady-state conditions for a low-energy cutoff value of 20 Mev.

Figure 3 for a spectrum cutoff at 20 Mev and in Figure 4 for a spectrum cutoff at 40 Mev. It is interesting to note that, although in the case of the former value for the cutoff the total proton flux is some sixteen times greater than in the latter case, the forms of the profiles are remarkably similar. In particular, the daytime peak electron density occurs at 75 km and the nighttime peak at about 85 km in both instances. The actual peak value of the electron density and the total electron content are, of course, much greater for the 20 Mev cutoff.

The physical reason for this apparent invariance is of fairly fundamental importance and is worth closer examination. The explanation lies partly in the fact that, with the low-energy cutoffs we have assumed, practically all of the protons are being stopped at heights well below the maxima of the profiles of Figures 3 and 4 (even 20 Mev protons, if vertically incident, penetrate down to about 55 km). Since the atmospheric density decreases exponentially with height, this means that each proton loses only a fraction of its energy in passing through most of the region we are considering, and to a first approximation we can consider the proton velocity to be independent of height in the region above, say, 60 km.

The rate of loss of energy by an individual proton, and hence its rate of electron production,  $q$ , are both proportional to the air density and to some complicated function of the proton velocity. Since this latter function is approximately independent of height, the height dependence of  $q$  above 60 km is the same as that of the air density, or of  $n$ , the  $O_2$  molecular number density. This can be seen clearly in the semi-logarithmic plot of Figure 2, in which the curves above 60 km represent an exponential decrease

in  $q$  with height. Hence for each individual proton we can write for  $h > 60$  km.

$$q = fn$$

where  $f$  is independent of height.

The height of maximum  $N$  as a function of  $n$  can now be found by differentiating (11) with respect to  $n$  and equating to zero, having first substituted for  $q$  from (13). The result is

$$\frac{n\{\alpha_d + (1 + 2\lambda)\alpha_i\}}{(1 + \lambda)(\alpha_d + \lambda\alpha_i)} \frac{d\lambda}{dn} = 1$$

This equation is most easily dealt with under nighttime conditions ( $p = 0$ ), if we neglect the third term in the denominator of (9), which factor has little effect on the height of maximum  $N$ . Then

$$\lambda = \frac{an^2}{\kappa n'} = \frac{an}{5\kappa}$$

and hence

$$\frac{d\lambda}{dn} = \frac{a}{5\kappa}$$

Substituting this in (14) and solving for  $n$ , we find

$$n = \frac{5\kappa}{a} \left( \frac{\alpha_d}{\alpha_i} \right)^{1/2}$$

Inserting our adopted values of  $\alpha_d$ ,  $\alpha_i$ ,  $\kappa$  and we find  $n = 3.5 \times 10^{13} \text{ cm}^{-3}$ , which corresponds to a height of about 86 km, very close to the height of the computed night maxima of Figures 3 and 4.

Since we neglected the nonlinear effect of ionic recombination, the electron-density profiles due to all the protons present can be added and the resultant profile will also have its ma-

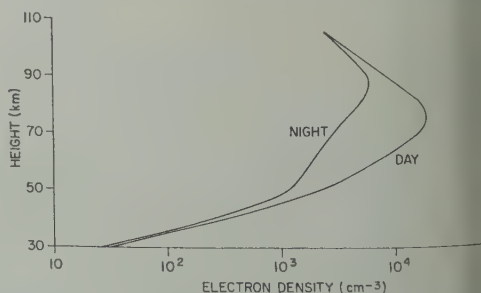


Fig. 4. Height profiles of electron density during daytime and nighttime steady-state conditions for a low-energy cutoff value of 40 Mev.



at 86 km. Thus we see that this height is independent of the proton spectrum, provided there are no protons present with energies less than 10 Mev, so that the assumption of constant proton velocity in the neighborhood of the peak is valid.

The height is also relatively insensitive to the values of the atmospheric parameters. For instance, to decrease the height to 80 km, where  $n = 10^{12}$  cm<sup>-3</sup>, we must either increase the ratio  $\alpha_d/\alpha_i$  by a factor of 3, or increase  $(\alpha_d/\alpha_i)$  by a factor of 9.

In the case of the daytime steady-state, when  $\rho$  does not vanish, is more complicated, and (14) becomes a sixth-degree equation of the form

$$Bn - Cn^2 - Dn^3 - En^4 - Fn^5 - Gn^6 = 0 \quad (18)$$

where the coefficients are functions of the atmospheric parameters. Graphical solution for the region of interest shows that this equation is satisfied at a height of 76 km, close to the maxima of Figures 3 and 4, and similar arguments about the insensitivity of the height to the proton spectrum and atmospheric parameters can be applied.

Thus the heights of the maxima in the electron density distribution during a PCA can be predicted, unless our knowledge of this part of the atmosphere is even more imperfect than presently appears. Although the above arguments are valid only when protons of less than 10 Mev energy are absent from the flux, it must be remembered that this restriction will be automatically applied by the Störmer cutoff at magnetic latitudes less than 72° under quiet geomagnetic conditions, even though the free-space flux does contain protons of lower energy. Alternative arguments show that if protons of higher energy were present, their effect would be to increase the height of the peak electron density, and at the heights we have been discussing are of lower limits.

The shape of the underside of the electron density profile, however, is more sensitive to the details of the incoming proton spectrum, since protons are reaching the ends of their paths in this region. As will be shown in the next section, this is the most important part of the problem from the point of view of absorption in the VHF bands, so that the specific ab-

sorption profiles in this frequency range might be expected to show some variation with proton spectrum.

### 5. RADIO-WAVE ABSORPTION

The effects of the ionized layers of Figure 4 (i.e. 40 Mev cutoff) on VHF cosmic noise will be examined. In particular, we shall compute the absorption which would be measured by an idealized riometer [Little and Leinbach, 1959] having a narrow-beam antenna pointing at the zenith. This will give an approximate indication of what would be measured on an actual riometer, which has a large antenna beamwidth and operates in the presence of thermal radiation from the ionosphere, the ground and the antenna cables.

The quasi-longitudinal approximation of the Appleton-Hartree formalism shows that the field-strength,  $E$ , of a vertically propagating plane radio wave arriving at the ground is related to the field strength above the ionosphere,  $E_0$ , by the relation

$$E = E_0 \exp \left( - \int_0^\infty k \, dh \right) \quad (19)$$

where  $dh$  is a height increment and  $k$  is given by

$$k = \frac{2\pi e^2}{mc} \frac{1}{\mu} \frac{N\nu}{\nu^2 + (\omega \pm \omega_L)^2} \quad (20)$$

Here  $N$  and  $\nu$  are the electron density and collision frequency,  $\mu$  is the refractive index,  $\omega$  is the operating angular frequency, and  $\omega_L$  is the longitudinal component of the gyrofrequency. We shall make the usual nondeviative approximation of assuming  $\mu = 1$ , and we shall also neglect  $\omega_L$  in comparison with  $\omega$ .

The ionized layer from 30 to 105 km was divided into 5-km slabs, and the electron density taken to be uniform in each slab, having the value appropriate to the center of the slab as shown in Figure 4. The values of electron collision frequency published by Nicolet [1959] have been adopted, and are shown in Figure 5. The contribution of each slab to the absorption was computed in decibels for frequencies of 30 and 60 Mc/s, and the total absorption found for both daytime and nighttime conditions. The results are presented in Table 1.

The ratio of day-to-night absorption is about 3.0 at 30 Mc/s and 2.5 at 60 Mc/s. Actual riometer



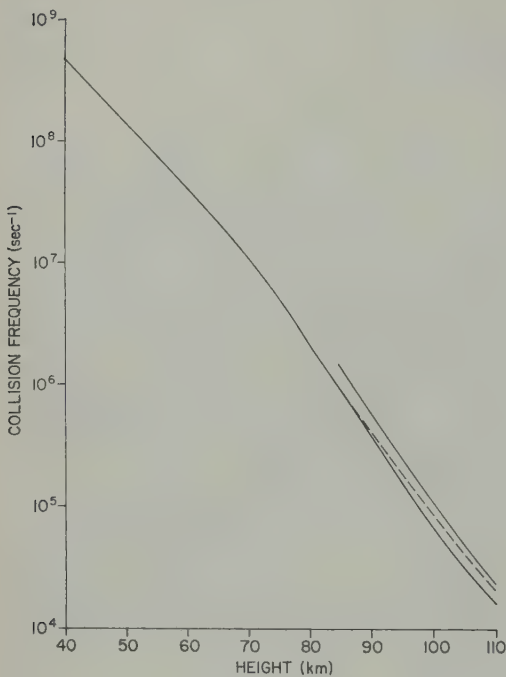


Fig. 5. Electron collision frequency in the lower ionosphere according to Nicolet [1959]. The two full lines above 85 km represent extreme values; the broken line indicates the values adopted here.

ter measurements at about 30 Mc/s during PCA events show that this is not unreasonable. The observed ratios often vary with time, which is to be expected since the nighttime and daytime electron-density profiles depend on  $q$  in rather different ways. The nighttime ionization is also dominated by collisional detachment, and, as we have seen above, the appropriate coefficient is not yet well known. However, the approximate agreement of the calculated day-night ratio with observation suggests that the adopted value for the effective collisional detachment coefficient is fairly good. If anything, the measured ratios at 30 Mc/s are somewhat higher than 3 on the average, and if we take 4 as a better value, crude arguments suggest that  $\kappa$  is probably closer to  $1.5 \times 10^{-17} \text{ cm}^3 \text{ sec}^{-1}$  than the adopted value of  $2 \times 10^{-17} \text{ cm}^3 \text{ sec}^{-1}$ .

The expression (20) for the absorption coefficient shows that if  $\omega \gg \nu$ , the absorption in decibels is inversely proportional to the square of the operating frequency, while if  $\omega \ll \nu$ , the absorption should be independent of frequency. Since our region extends on both sides of the

transition level at which  $\omega = \nu$  (about 45 km) we should expect the ratio of absorption at the two frequencies to be somewhere between the inverse square case (ratio of 4) and the independent case (ratio of 1). This is indeed the case, the daytime ratio of absorption at 30 Mc/s and 60 Mc/s being 3.5 and the nighttime ratio 2.9. Such frequency ratios have occasionally been interpreted in terms of an 'equivalent height,' defined as the height at which a theoretical absorbing region would show that particular frequency ratio. This method applied to our profile would give an equivalent height of 54 km during the day and 51 km during the night. It is interesting to note that although the height of the peak electron density moves up by about 10 km in going from day to night, the equivalent height for 30 Mc/s absorption actually moves down. This arises because of the decreased vertical gradient of electron density during the night in the 60- to 80-km region. The greater difference (20 to 35 km) between these equivalent heights and the actual height of the peak electron density is also worth noting.

Some of these features are illustrated in Figure 6, which shows the specific absorption in decibels per kilometer as a function of height for both frequencies and for both day and night. At 30 Mc/s the largest contribution to the absorption occurs at 58 km during the day and at 52 km during the night. The contribution from regions below 35 km and above 90 km is negligible.

The most direct method of determining specific absorption profiles experimentally is by means of radio propagation experiments employing rockets traveling through the region in question. The results of one such experiment have been published [Seddon and Jackson, 1958]. At about local noon on July 4, 1957, a rocket carrying a 7.75-Mc/s transmitter was fired into the ionosphere above Fort Churchill during a polar blackout, later found from riometer records

TABLE 1. Vertical Cosmic Noise Absorption (db) Produced by the Electron Density Profile of Figure 4

	Day	Night
30 Mc/s	9.7	3.2
60 Mc/s	2.8	1.1

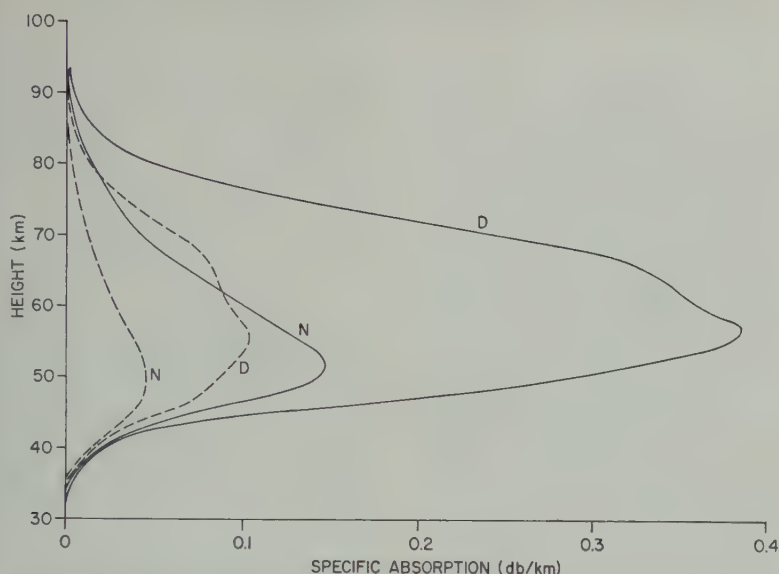


Fig. 6. Height profiles of specific absorption for vertical incidence. The full lines refer to frequency of 30 Mc/s and the broken lines to 60 Mc/s. *D* and *N* refer respectively to daytime and nighttime steady-state conditions.

been a moderately intense PCA event. The quantities measured on the ground are the differential absorption between the ordinary and extraordinary waves, i.e., the difference between the absorption (in decibels) of the two waves. This quantity has been calculated for our daytime profile of Figure 4 using equation 20 with  $\omega/2\pi = 7.75$  Mc/s and  $\nu = 1.5$  Mc/s. The resultant differential absorption profile is shown in Figure 7, together with the experimental results of Seddon and Jackson normalized to fit the theoretical curve. The agreement is fairly good, and is extremely good if the theoretical peak is shifted down by about 2 km. The experimental results then show an excess in absorption at the lower levels, which may be attributed to the influence of the normal *D* region. It must be remembered that the theoretical curve is based on a proton spectrum measured during a completely different and much more intense PCA event which occurred 2 years later than the Seddon and Jackson experiment. The very good agreement suggests that even the absorption characteristics of the PCA ionization differ very little from one event to another.

#### THE TWILIGHT TRANSITION PERIOD

The problem of the twilight transition between day and night conditions is of considerable im-

portance. As mentioned above, the entire visible spectrum of sunlight is capable of producing photodetachment of electrons from  $O_2^-$ . If  $O_2^-$  is the dominant negative ion, then, daytime conditions should prevail at any particular height until the sun is obscured by the solid earth (or by dense cloud in the lower atmosphere), and the nighttime steady state should be reached only when the solid earth shadow reaches the

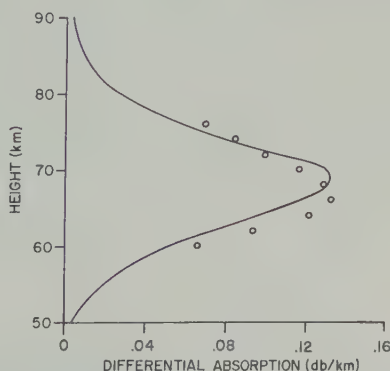


Fig. 7. Height profile of differential absorption between ordinary and extraordinary waves at 7.75 Mc/s. The curve represents theoretical values obtained from the daytime electron-density profile of Figure 4; the points are experimental values determined by Seddon and Jackson [1958]. The curve has been normalized to fit the experimental points near the maximum.

top of the absorbing region (neglecting the ionospheric time-constant for recovery of ionization). Reid and Collins [1959], however, noted the peculiar fact that during the PCA event of July 3-5, 1957, at Fort Churchill, a nighttime steady state was apparently reached despite the fact that the sun did not set at heights greater than 50 km. This peculiarity has since been noted during many other events, and these and similar observations by Eriksen, Holt, and Landmark [1960], together with rough calculations of the extinction of visible sunlight by the lower atmosphere, led Reid and Leimbach [1960] to suggest that the dominant negative ion during twilight was not  $O_2^-$ , but some ion with a much larger electron affinity, requiring ultraviolet light for efficient photodetachment. The effective screening region for ultraviolet light is the ozone layer, and when the solid earth shadow reaches 50 km, the shadow of the top of this layer is in the neighborhood of 85 km. Thus practically all the absorbing region we have been discussing in the previous sections is then in the ultraviolet shadow, and the establishment of the nighttime steady state becomes understandable.

Hultqvist and Ortner [1959], however, have suggested that the ionized layer is entirely below 50 km. If this view were correct, the assumption that  $O_2^-$  is the dominant ion would present no difficulty; it is, however, incompatible both with the earlier work of Bailey [1959] and with the results of the present calculations.

Donahue [1961] has pointed out that the controversy is analogous to that which existed concerning the interpretation of sodium twilight airglow results, which was resolved by carrying out detailed atmospheric extinction calculations. He suggests that such calculations might explain the observations, even if  $O_2^-$  were the dominant negative ion.

In an effort to clarify the situation, we have

carried out this calculation, and have obtained theoretical values for the photodetachment coefficient of  $O_2^-$  as a function of solar zenith angle in the range from  $90^\circ$  to  $102^\circ$  and of height in the range from 30 to 105 km. The methods and results of these calculations will be described briefly in the following section.

## 7. THE TWILIGHT PHOTODETACHMENT COEFFICIENT OF $O_2^-$

The calculation of the atmospheric extinction of visible sunlight was carried out using the method adopted by Hunten [1954] for the  $D$  lines in the twilight airglow. The difference, of course, lies in the fact that we are concerned here with the entire visible spectrum rather than with a narrow line. Three sources of atmospheric extinction were considered and are illustrated in Figure 8.

1. Extinction by Rayleigh scattering of sunlight reaching the point  $A$  along the path whose closest distance of approach to the earth is  $h_0$ .

2. Absorption of the visible sunlight by the diffuse Chappuis bands of ozone centered about 6000 Å.

3. Dilution of sunlight by refraction in the lower atmosphere. This is illustrated in Figure 8: the ray  $SB$  is bent more by refraction than is the ray  $SA$ , and the total energy is consequently spread out over a larger area. Refraction, also, of course, has the effect of reducing the height  $h$  illuminated by the sun for given values of  $\chi$ , the solar zenith angle, and  $h_0$ .

The details of the calculations will not be given here, and we shall merely outline the successive steps. Smith, Burch, and Branscomb [1958] have determined the differential photodetachment coefficient (in photodetachment ion per second per electron volt of energy) of  $O_2^-$  in sunlight as a function of photon v

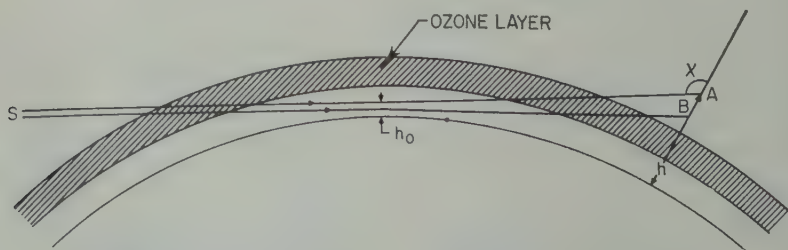
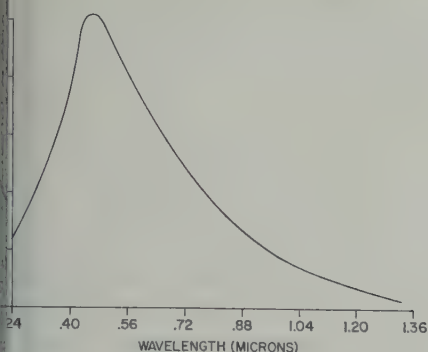


Fig. 8. Geometry of solar radiation at large zenith angles.





9. Differential photodetachment rate of  $O_2^+$  as a function of wavelength after *Smith, Burch, and Bransford* [1958].

1. Their resultant curve, transformed to a differential rate of photodetachments per ion per second per micron is shown in Figure 9. Integration of this curve gives the value of  $0.44 \text{ ion}^{-1} \text{ sec}^{-1}$  for the total photodetachment coefficient ( $\rho$ ) in full sunlight used in the previous electron-density calculations.

In order to calculate the twilight effect, the spectrum from 0.30 to 1.20 microns (1 micron =  $10^{-6}$  m) was divided into 0.04 micron intervals. The solar spectrum at wavelengths below 0.3 and above 1.2 microns was ignored as these regions apparently contribute little to the total photodetachment coefficient. For each wavelength, considering Rayleigh scattering alone, the intensity of sunlight received at point A in Figure 8 is related to the intensity at S by the relation

$$I = I_0 \exp(-\beta x) \quad (21)$$

where  $x$  is the equivalent path-length through air at standard atmospheric pressure and  $\beta$  is the extinction coefficient. *Hunten* [1954] has given an approximate formula for  $x$  as a function of  $h_0$ , assuming the lower atmosphere to have a constant scale-height of 7 km. This approximate formula assumes that the path-length between S and  $h_0$  is the same as that between  $h_0$  and A; this approximation is good for solar zenith angles appreciably greater than  $90^\circ$ , and the formula has been used here. The Rayleigh extinction coefficient,  $\beta$ , has been tabulated as a function of wavelength by *van de Hulst* [1951]. Using these values the Rayleigh scattering transmission was calculated for the center wavelength of each 0.04 micron interval for a range of values of the parameter  $h_0$  from 50 km (at which the extinction becomes negligible) to 0 km (corresponding to a ground-grazing ray). The resulting atmospheric transmission as a function of wavelength is shown in Figure 10 for selected values of  $h_0$ .

These transmission values were then multiplied by a refraction dilution factor also given in approximate form by *Hunten* [1954]. This factor is assumed to be independent of wavelength and to be a function of  $h_0$  only.

The transmission of visible sunlight of wavelength 5893 Å through the ozone layer has been calculated by *Blamont, Donahue, and Stull* [1958], assuming the layer to have a gaussian

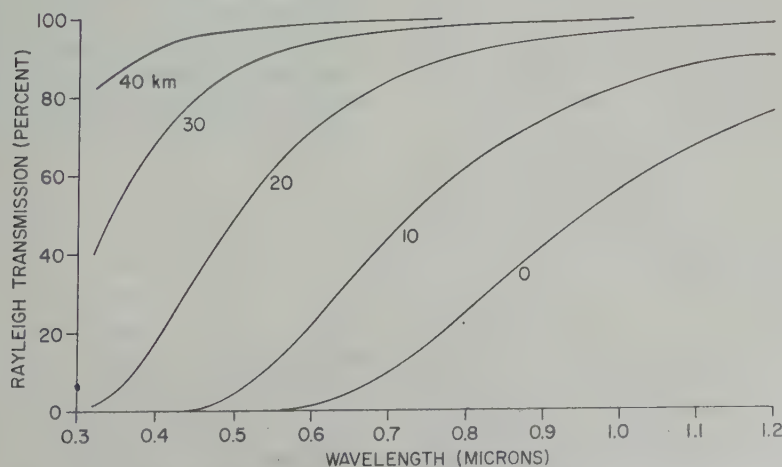


Fig. 10. Percentage transmission of the atmosphere allowing for Rayleigh scattering alone. The curves are for various values of the height parameter  $h_0$  of Figure 8.



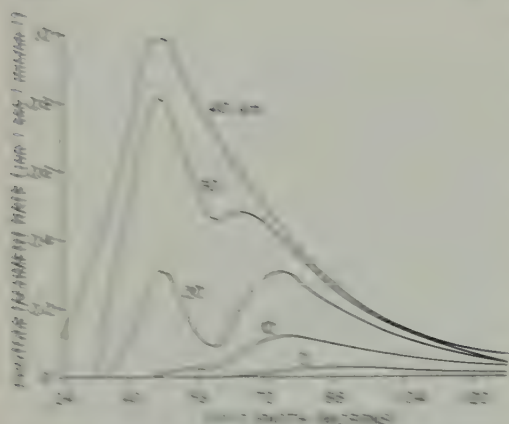


Fig. 8. Changing electrical permeability of the membrane of *A. niger* during growth of *A. niger*.

[illegible]

1. *Introduction*  
 2. *Background*  
 3. *Methodology*  
 4. *Results*  
 5. *Discussion*  
 6. *Conclusion*  
 7. *References*  
 8. *Appendix*  
 9. *Glossary*  
 10. *Index*  
 11. *Summary*  
 12. *Abstract*  
 13. *Keywords*  
 14. *Subject Headings*  
 15. *Notes*  
 16. *Footnotes*  
 17. *Tables*  
 18. *Figures*  
 19. *Equations*  
 20. *Formulas*  
 21. *Diagrams*  
 22. *Charts*  
 23. *Graphs*  
 24. *Tables*  
 25. *Figures*  
 26. *Equations*  
 27. *Formulas*  
 28. *Diagrams*  
 29. *Charts*  
 30. *Graphs*  
 31. *Tables*  
 32. *Figures*  
 33. *Equations*  
 34. *Formulas*  
 35. *Diagrams*  
 36. *Charts*  
 37. *Graphs*  
 38. *Tables*  
 39. *Figures*  
 40. *Equations*  
 41. *Formulas*  
 42. *Diagrams*  
 43. *Charts*  
 44. *Graphs*  
 45. *Tables*  
 46. *Figures*  
 47. *Equations*  
 48. *Formulas*  
 49. *Diagrams*  
 50. *Charts*  
 51. *Graphs*  
 52. *Tables*  
 53. *Figures*  
 54. *Equations*  
 55. *Formulas*  
 56. *Diagrams*  
 57. *Charts*  
 58. *Graphs*  
 59. *Tables*  
 60. *Figures*  
 61. *Equations*  
 62. *Formulas*  
 63. *Diagrams*  
 64. *Charts*  
 65. *Graphs*  
 66. *Tables*  
 67. *Figures*  
 68. *Equations*  
 69. *Formulas*  
 70. *Diagrams*  
 71. *Charts*  
 72. *Graphs*  
 73. *Tables*  
 74. *Figures*  
 75. *Equations*  
 76. *Formulas*  
 77. *Diagrams*  
 78. *Charts*  
 79. *Graphs*  
 80. *Tables*  
 81. *Figures*  
 82. *Equations*  
 83. *Formulas*  
 84. *Diagrams*  
 85. *Charts*  
 86. *Graphs*  
 87. *Tables*  
 88. *Figures*  
 89. *Equations*  
 90. *Formulas*  
 91. *Diagrams*  
 92. *Charts*  
 93. *Graphs*  
 94. *Tables*  
 95. *Figures*  
 96. *Equations*  
 97. *Formulas*  
 98. *Diagrams*  
 99. *Charts*  
 100. *Graphs*  
 101. *Tables*  
 102. *Figures*  
 103. *Equations*  
 104. *Formulas*  
 105. *Diagrams*  
 106. *Charts*  
 107. *Graphs*  
 108. *Tables*  
 109. *Figures*  
 110. *Equations*  
 111. *Formulas*  
 112. *Diagrams*  
 113. *Charts*  
 114. *Graphs*  
 115. *Tables*  
 116. *Figures*  
 117. *Equations*  
 118. *Formulas*  
 119. *Diagrams*  
 120. *Charts*  
 121. *Graphs*  
 122. *Tables*  
 123. *Figures*  
 124. *Equations*  
 125. *Formulas*  
 126. *Diagrams*  
 127. *Charts*  
 128. *Graphs*  
 129. *Tables*  
 130. *Figures*  
 131. *Equations*  
 132. *Formulas*  
 133. *Diagrams*  
 134. *Charts*  
 135. *Graphs*  
 136. *Tables*  
 137. *Figures*  
 138. *Equations*  
 139. *Formulas*  
 140. *Diagrams*  
 141. *Charts*  
 142. *Graphs*  
 143. *Tables*  
 144. *Figures*  
 145. *Equations*  
 146. *Formulas*  
 147. *Diagrams*  
 148. *Charts*  
 149. *Graphs*  
 150. *Tables*  
 151. *Figures*  
 152. *Equations*  
 153. *Formulas*  
 154. *Diagrams*  
 155. *Charts*  
 156. *Graphs*  
 157. *Tables*  
 158. *Figures*  
 159. *Equations*  
 160. *Formulas*  
 161. *Diagrams*  
 162. *Charts*  
 163. *Graphs*  
 164. *Tables*  
 165. *Figures*  
 166. *Equations*  
 167. *Formulas*  
 168. *Diagrams*  
 169. *Charts*  
 170. *Graphs*  
 171. *Tables*  
 172. *Figures*  
 173. *Equations*  
 174. *Formulas*  
 175. *Diagrams*  
 176. *Charts*  
 177. *Graphs*  
 178. *Tables*  
 179. *Figures*  
 180. *Equations*  
 181. *Formulas*  
 182. *Diagrams*  
 183. *Charts*  
 184. *Graphs*  
 185. *Tables*  
 186. *Figures*  
 187. *Equations*  
 188. *Formulas*  
 189. *Diagrams*  
 190. *Charts*  
 191. *Graphs*  
 192. *Tables*  
 193. *Figures*  
 194. *Equations*  
 195. *Formulas*  
 196. *Diagrams*  
 197. *Charts*  
 198. *Graphs*  
 199. *Tables*  
 200. *Figures*  
 201. *Equations*  
 202. *Formulas*  
 203. *Diagrams*  
 204. *Charts*  
 205. *Graphs*  
 206. *Tables*  
 207. *Figures*  
 208. *Equations*  
 209. *Formulas*  
 210. *Diagrams*  
 211. *Charts*  
 212. *Graphs*  
 213. *Tables*  
 214. *Figures*  
 215. *Equations*  
 216. *Formulas*  
 217. *Diagrams*  
 218. *Charts*  
 219. *Graphs*  
 220. *Tables*  
 221. *Figures*  
 222. *Equations*  
 223. *Formulas*  
 224. *Diagrams*  
 225. *Charts*  
 226. *Graphs*  
 227. *Tables*  
 228. *Figures*  
 229. *Equations*  
 230. *Formulas*  
 231. *Diagrams*  
 232. *Charts*  
 233. *Graphs*  
 234. *Tables*  
 235. *Figures*  
 236. *Equations*  
 237. *Formulas*  
 238. *Diagrams*  
 239. *Charts*  
 240. *Graphs*  
 241. *Tables*  
 242. *Figures*  
 243. *Equations*  
 244. *Formulas*  
 245. *Diagrams*  
 246. *Charts*  
 247. *Graphs*  
 248. *Tables*  
 249. *Figures*  
 250. *Equations*  
 251. *Formulas*  
 252. *Diagrams*

~~8 FOURTEEN EIGHTEEN NINE TWELVE~~

During the period of the first administration, the reference is a function of the second parameter  $\lambda$ , we are now in a position to define the second parameter of the  $\lambda$  as the first parameter  $\lambda$ , using the previous theory.

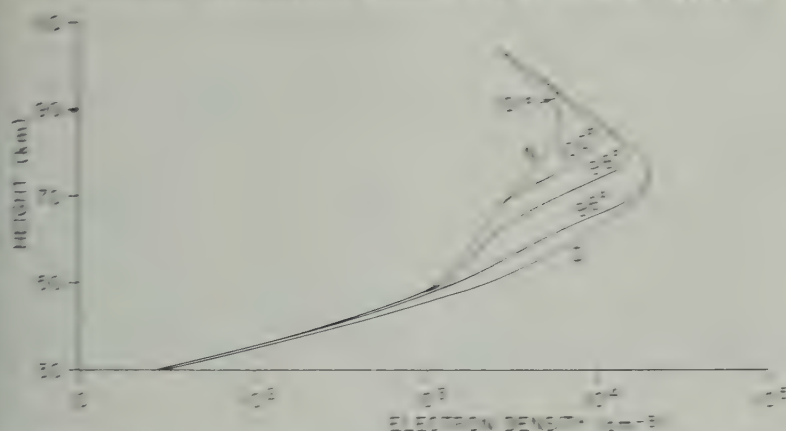


FIG. 16. Theoretical height profiles of electron density for various values of solar zenith angle.  $D$  and  $F$  refer respectively to daytime and nighttime steady-state conditions.

the theoretical curve shown in the figure the same shape as the curve of Figure 16, but along the vertical axis has been a different scaling so as to fit the observed ionospheric steady-state absorption. It shows another good comparison for Fort Churchill on April 11, 1958. Here the ion was evidently decaying throughout, and the theoretical curve has been scaled to allow for this decay. Figure 17 shows the Fort Churchill on October 25, 1958, with additional points being plotted at  $\chi = 90^\circ$ .

It is immediately obvious from these comparisons the agreement between theory and observation is very poor indeed, except possibly for small zenith angles. In particular at sunset the ionospheric first becomes evident at  $\chi = 90^\circ$ , whereas the theoretical curve shows some departure from daytime conditions at  $\chi = 85^\circ$ . In November at Fort

Churchill, this represents a time lapse of about 40 minutes. In the sunrise data of Figure 17, daytime conditions are apparently not fully established until  $\chi = 85^\circ$ , the difference between this value and the value of  $90^\circ$  for the corresponding turnover at sunset possibly being due to the time constant of the lower part of the ionosphere, which can certainly have values of the order of 15 minutes (Reid and Leinbach, 1960).

This lack of agreement between theory and observation appears to lend further justification to the suggestion of Reid and Leinbach (1960) that the dominant negative ion during the twilight period is not  $O_2^-$  but some ion that requires solar ultraviolet light for effective photodetachment. The effective screening region for light of wavelength less than 2000 Å is the ozone layer, and since the lower part of the ionized region is embedded in this layer, its screening

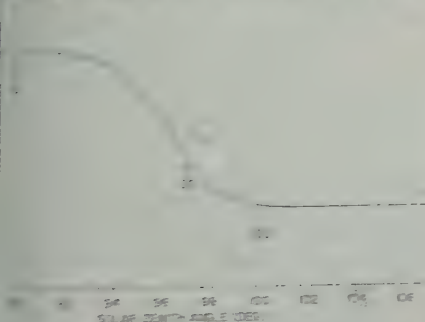


FIG. 17. Observed variation of vertical 30 Mc/s absorption with solar zenith angle.

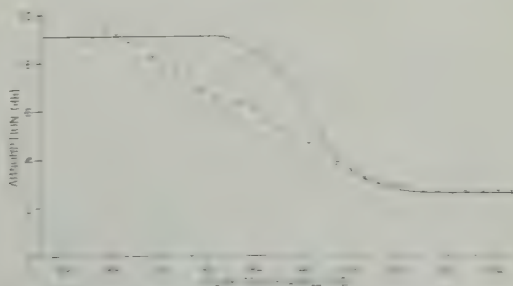


FIG. 18. Observed 30 Mc/s ionospheric absorption at Fort Churchill during sunset twilight on November 16, 1958.

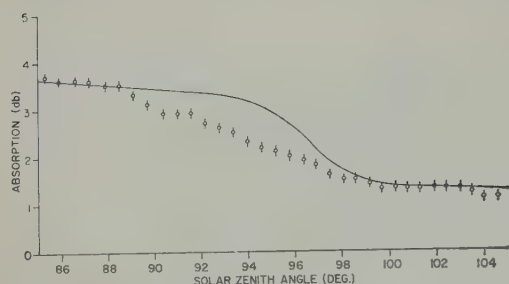


Fig. 16. Vertical 30 Mc/s cosmic-noise absorption at Fort Churchill during sunset twilight on April 11, 1958.

effect might be expected to become noticeable at solar zenith angles less than  $90^\circ$ . The ozone shadow effect would be completed roughly when the shadow of the peak of the ozone layer, at a height of about 25 km, reached the top of the absorbing region at about 80 km. The corresponding solar zenith angle is about  $97.5^\circ$  and it is indeed only at zenith angles greater than this that the observational points begin to show approximate agreement with the  $O_2^-$  theory.

The nature of the unknown negative ion will probably not be determined until direct rocket mass spectrometer data can be obtained from the region in question. At present it is only possible to forecast that its photodetachment coefficient in the visible spectrum must be unusually low. The attachment energy corresponding to the limit of the strong ozone ultraviolet absorption ( $\sim 2900$  Å) is over 4 eV. While the electron affinity of the ion may be less than this, its photodetachment cross section at energies less than 4 eV must certainly be very much less than that of  $O_2^-$ . Presumably the neutral molecule which forms the ion is a minor constituent of

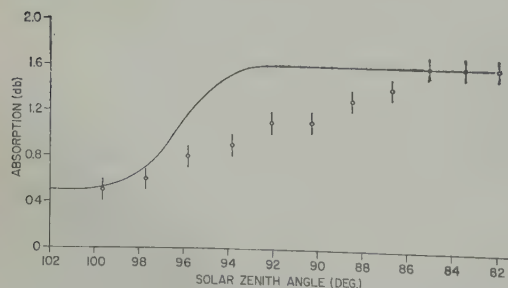


Fig. 17. Vertical 30 Mc/s cosmic-noise absorption at Fort Churchill during sunrise twilight on October 22, 1957.

the atmosphere, and during full daylight conditions when both  $X^-$  (the unknown ion) and  $O_2^-$  are suffering efficient photodetachment,  $X^-$  is probably the dominant negative ion by a large force of numbers of the neutral molecule. During sunset, however, at a level which is in the visible shadow but not yet in the visible shadow,  $X^-$  will have attained its nighttime concentration while  $O_2^-$  will still have its daytime concentration. The high attachment energy of  $X^-$  implies that collisional detachment is a very slow process so that the ratio of nighttime to daytime concentration might be very large. Thus, although  $X$  itself is a minor constituent compared with  $O_2$ , during twilight conditions  $X^-$  may become dominant over  $O_2^-$  simply because of the competition between the nighttime concentration of the former and the daytime concentration of the latter. If this unknown negative ion were also dominant during steady-state daytime and nighttime conditions, the previous calculations of electron density profiles would, of course, be invalidated, since the appropriate rate coefficients would be greatly altered.

Herzberg [1960] has put forward the alternative view that the concentration of NO might be enhanced during the PCA event, and that photoionization of NO by Lyman- $\alpha$  might be an appreciable factor. The quantitative importance of this effect is not yet certain, but must certainly be considered in any detailed investigation of conditions in the lower ionosphere during these events.

## 10. CONCLUSIONS

To summarize, we have examined the atmospheric ionization which would be produced by an incoming isotropic flux of protons with an energy spectrum which is steeply inclined toward low energies. The chief conclusions are:

1. The form of the electron-density profile under steady-state daytime conditions is not dependent on the value of the low-energy cutoff in the spectrum (provided it is higher than about 10 MeV) or on the exact shape of the spectrum. This is not so valid for steady-state nighttime conditions during intense events, when ionization combination affects the electron-negative ion equilibrium.

2. During the day, the peak in electron density occurs at about 75 km and during the night at about 85 km, with the same provisos as in



a frequency of 30 Mc/s the largest contribution to the absorption comes from the 10 to 55 km height range during the day, and from 35 to 85 km during the night; the entire absorption at this frequency. Detailed calculation of the variation of the detachment coefficient with solar zenith angle in the range from 90° to 102° has shown that the  $O_2^-$  hypothesis alone is apparently insufficient for explaining the observed twilight variation of absorption during a polar-cap event.

**Acknowledgments.** I wish to express my thanks to Bailey for helpful discussion in the specimens referred to in the text, and to H. Leinbach for much discussion of these events. I am indebted to many colleagues, especially to Dr. Herzberg for helpful discussion of the atmospheric processes. Thanks are extended to Mrs. S. who rendered assistance with many of the calculations.

# REFERENCES

Chapman, K. A., Ionizing radiation associated with auroral storm, *Phys. Rev. Letters*, **1**, 335-337, 1960.

Chapman, K. A., and D. C. Enemark, Observations of solar cosmic rays near the north magnetic pole, *J. Geophys. Research*, **65**, 2657-2671, 1960.

Chapman, D. K., Abnormal ionization in the lower atmosphere associated with cosmic-ray flux enhancements, *Proc. IRE*, **47**, 255-266, 1959.

Chapman, D. K., and L. M. Branscomb, Rate coefficient for  $O_2^-$  collisional detachment, *Bull. Am. Phys. Soc.*, (II) **5**, 123, 1960.

Chapman, J. R., The physics of the upper atmosphere, in *The Earth as a Planet* edited by G. Kuiper, University of Chicago Press, Chicago, 1960.

Chapman, J. A. and J. Ashkin, Passage of radiations through matter, Part II of *Experimental Nuclear Physics*, vol. I, edited by E. Segre, John Wiley & Sons, Inc., New York, 1953.

Chapman, J. E., T. M. Donahue, and V. R. Stull, Sodium twilight airglow 1955-1957, I, *Ann. Phys.*, **14**, 253-281, 1958.

Chapman, L. M., A. V. Phelps, and M. A. Biondi, Measurement of the attachment of slow electrons to oxygen, *Phys. Rev. Letters*, **2**, 344-346, 1960.

Chapman, T. M., A note on polar blackouts, *J. Geophys. and Terrest. Phys.*, **20**, 76-79, 1961.

Chapman, K. W., O. Holt, and B. Landmark, A note on the polar absorption event of 11-18 May, *J. Atmospheric and Terrest. Phys.*, **18**, 1-10, 1960.

Herzberg, L., The possible importance of nitric oxide formation during polar-cap ionospheric absorption events, *J. Geophys. Research*, **65**, 3505-3508, 1960.

Hultqvist, B., On the interpretation of ionization in the lower ionosphere occurring on both day and night side of the earth a few hours after some solar flares, *Tellus*, **11**, 332-343, 1959.

Hultqvist, B., and J. Ortner, Strongly absorbing layers below 50 km, *Planetary and Space Sci.*, **1**, 193-204, 1959.

Hunten, D. M., A study of sodium in twilight, I, Theory, *J. Atmospheric and Terrest. Phys.*, **5**, 44-56, 1954.

Inn, E. C. Y., and Y. Tanaka, Absorption coefficient of ozone in the ultraviolet and visible regions, *J. Optical Soc. Am.*, **43**, 870-873, 1953.

Little, C. G., and H. Leinbach, The riometer—a device for the continuous measurement of ionospheric absorption, *Proc. IRE*, **47**, 315-320, 1959.

Nicolet, M., Collision frequency of electrons in the terrestrial atmosphere, *Phys. Fluids*, **2**, 95-99, 1959.

Nicolet, M., and A. C. Aikin, The formation of the D region of the ionosphere, *J. Geophys. Research*, **65**, 1469-1483, 1960.

Phelps, A. V., and J. L. Pack, Collisional detachment in molecular oxygen, *Phys. Rev. Letters*, **6**, 111-113, 1961.

Reid, G. C., and C. Collins, Observations of abnormal VHF radio wave absorption at medium and high latitudes, *J. Atmospheric and Terrest. Phys.*, **14**, 63-81, 1959.

Reid, G. C., and H. Leinbach, Low-energy cosmic-ray events associated with solar flares, *J. Geophys. Research*, **64**, 1801-1805, 1959.

Reid, G. C., and H. Leinbach, Morphology and interpretation of the great polar cap absorption events of May and July, 1959, paper presented at meeting of AGARD Ionospheric Research Committee, Athens, 1960.

The Rocket Panel, Pressures, densities and temperatures in the upper atmosphere, *Phys. Rev.*, **88**, 1027-1032, 1952.

Rothwell, P., and C. McIlwain, Satellite observations of solar cosmic rays, *Nature*, **184**, 138-140, 1959.

Seddon, J. C., and J. E. Jackson, Rocket arctic ionospheric measurements, *IGY Rocket Rept. Ser. 1*, 140-148, 1958.

Smith, S. J., D. S. Burch, and L. M. Branscomb, Experimental photodetachment cross section and the ionospheric detachment rate for  $O_2^-$ , *Ann. geophys.*, **14**, 225-231, 1958.

van de Hulst, H. C., Scattering in the atmospheres of the earth and planets, Chap. 3 in *The Atmospheres of the Earth and Planets*, edited by G. P. Kuiper, University of Chicago Press, Chicago, Table 4, p. 55, 1951.





## Evidence of Low-Frequency Hydromagnetic Waves in the Exosphere

MASAHISA SUGIURA

*Geophysical Institute, University of Alaska  
College, Alaska*

**Abstract.** Damped waves of a period of several minutes with amplitude up to several hundred gammas are found in the geomagnetic field in the auroral zones. These damped waves occur simultaneously in magnetically conjugate regions in the northern and southern hemispheres. The waves are very nearly elliptically polarized in the plane approximately perpendicular to the magnetic field. Hence the damped waves are interpreted as low-frequency hydromagnetic waves generated in the exosphere at an altitude of several earth radii and transmitted to the earth along the lines of magnetic force in the longitudinal mode of propagation. The number of occurrences of these damped waves has a distinct local time variation that appears to vary with season.

**Introduction.** Since *Alfvén* [1942] theoretically predicted hydromagnetic waves, several experiments have demonstrated such waves in the laboratory using liquid mercury or sodium [e.g., *Quist*, 1949; *Lehnert*, 1954].

*Störmer*, *Ramm*, *Goldblatt*, and *Klemas* [1958] detected magnetic pulsations excited by high-altitude nuclear detonations in the Arctics. Experiments of 1958, and interpreted the pulsations as hydromagnetic waves. Postulating hydromagnetic waves at high altitudes are locally confined in ducts, they identified the observed two groups of waves as the modified Alfvén wave and the transverse wave on the basis of the transit times of the waves. A similar effect from the Johnston Island nuclear explosion has been reported by *Maeda and Ondoh* [1960].

The possibility that some of the geomagnetic pulsations observed on the earth's surface may be hydromagnetic waves in the ionosphere or in the exosphere has been theorized by many authors [*Dungey*, 1955, 1958; *Kato and Watanabe*, 1955; *Kato and Akasofu*, 1956; *Lehnert*, 1956; *Fejer*, 1958; *Obayashi and Jacobs*, 1958; *Veldert*, 1960; *Scholte*, 1960]; attenuation of hydromagnetic waves in the ionosphere has been considered theoretically [*Hines*, 1953; *Dungey*, 1955; *Akasofu*, 1956, 1960; *Dessler*, 1959; *Fejer*, 1958; *Francis and Karplus*, 1960].

However, precise identification of hydromagnetic waves in the observational record is difficult and has not been conclusive.

In a previous communication *Sugiura* [1961]

has presented a definite evidence of hydromagnetic waves generated in the exosphere and transmitted in the longitudinal mode along the lines of magnetic force to the northern and southern auroral zones. This paper presents more detailed discussions of the subject.

2. *Hydromagnetic damped waves observed in the auroral zones.* Quasi-sinusoidal magnetic field oscillations of amplitudes of several tens to several hundred gammas are occasionally observed in the auroral zones. Periods of truly great oscillations range roughly from 4 to 8 minutes. Amplitudes appear to decrease with decreasing period below this range, and outstanding oscillations of period longer than 10 minutes are not found.

Some of these oscillations take a distinct form of damped waves. It is this family of damped waves that we are concerned with in this paper.

These damped waves are confined to the auroral zone. This important characteristic is inferred from the comparison of the magnetic records taken at Point Barrow (geomagnetic latitude 68° 6'), College (64° 7'), and Kotzebue (63° 7') with the records from Sitka (60° 0'), a station in the subauroral zone.

The wave forms observed at College and Kotzebue are very similar. The amplitudes of the waves at Point Barrow are in some instances greater, and in others less, than at College. This may be interpreted as the position of the center of the wave packet differing slightly in different cases.

At Sitka the regular wave forms are partly

or nearly completely lost and the amplitudes much less than at College. Without knowing the occurrence of a damped wave in the higher latitudes, the wave would be in most instances overlooked at Sitka.

The second outstanding characteristic of the damped waves is their simultaneous occurrence at magnetically conjugate regions in the northern and southern hemispheres. According to the computation made by *Vestine and Sibley* [1959, 1960], the point conjugate to Macquarie Island (geomagnetic latitude  $61.^\circ$  IS), Australia, lies near Kotzebue, about  $15^\circ$  west of College.

From the comparison of records from College and Kotzebue it can be concluded that the longitudinal extension of the waves is greater than the separation of the two stations. Although Kotzebue is more nearly conjugate to Macquarie Island, the records from Kotzebue are less complete and are thought less reliable than the records from the permanent observatory at College. Thus the records from College were com-

pared with those from Macquarie Island for examination of simultaneity at a pair of magnetically conjugate points.

Two typical examples of damped waves observed simultaneously at College and Macquarie Island are shown in Figures 1 and 2. In each of these figures the left half is a reproduction of the (sensitive) magnetogram taken at the Coast and Geodetic Survey Magnetic Observatory at College, and the right half is reproduced from the magnetogram obtained at Macquarie Island; for this latter observation the traces were re-arranged for the ease of comparison with the traces of corresponding components for College. The damped waves to be analyzed in this paper are indicated by an arrow.

The wave shown in Figure 1 represents an example that occurred in a relatively quiet epoch and the one shown in Figure 2 an example from during a disturbed period. The occurrence of these damped waves does not appear to de-

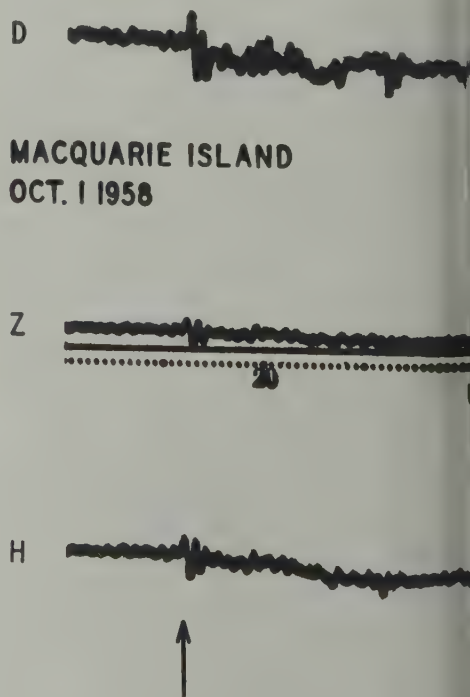
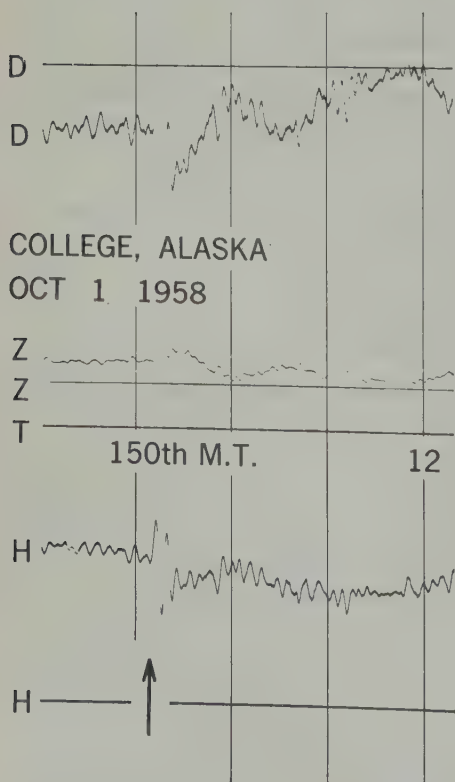


Fig. 1. A damped wave observed simultaneously at College and Macquarie Island. *D*, declination; *Z*, vertical component; *H*, horizontal component.

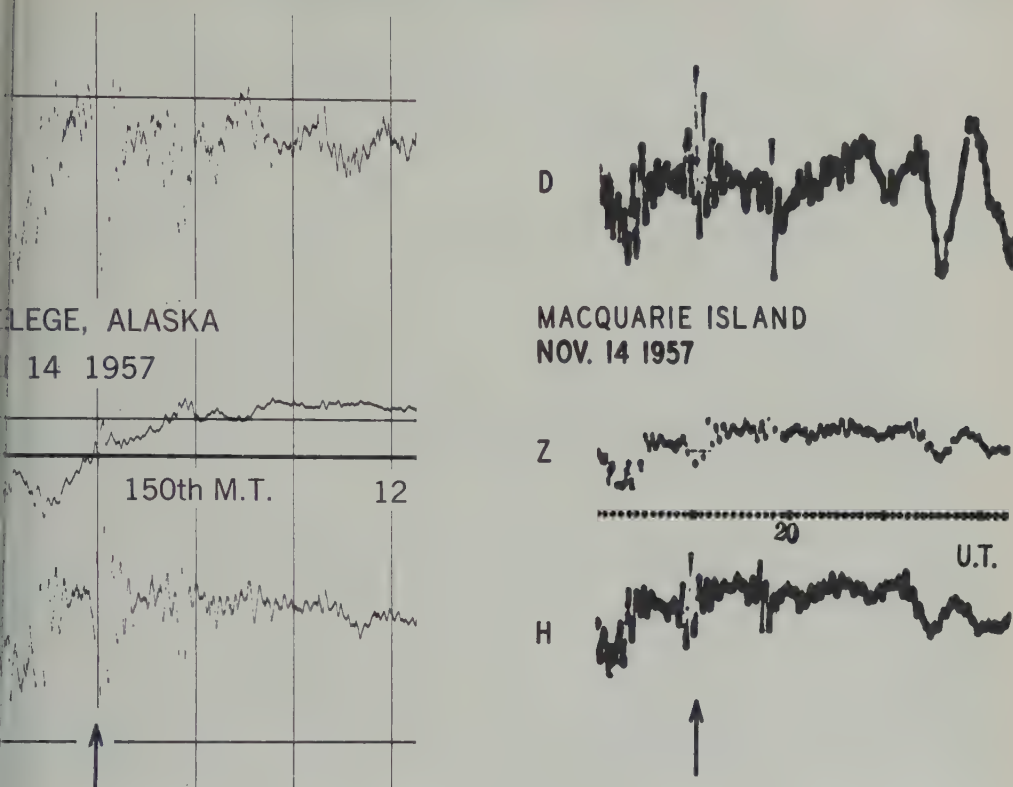


Fig. 2. A damped wave observed simultaneously at College and Macquarie Island.  $D$ , declination;  $Z$ , vertical component;  $H$ , horizontal component.

magnetic activity; this point will be discussed later.

Figures 1 and 2 the similarity of the waves at College and Macquarie Island is striking. In particular, the horizontal component  $H$  frequently shows a peak-to-peak correspondence at the two stations. The vertical component  $Z$  is small and its wave form is often irregular.

For a more detailed examination of the exact time of the onset of the damped waves and the wave forms at the two stations, the time resolution in the regular magnetograms is not adequate. For College, rapid-run magnetograms are available for this purpose. But unfortunately no records have not been taken at Macquarie Island.

*Identification of the damped waves as trans-hydromagnetic waves.* The simultaneous occurrence of the damped waves at both ends of the lines of magnetic force anchored in the northern and southern auroral zones suggests

that they are hydromagnetic waves generated in the exosphere at a geocentric distance of 5 or 6 earth radii and transmitted to the earth along the field lines in the longitudinal mode of propagation. Because of the anisotropic conductivity plane hydromagnetic waves of longitudinal mode are circularly polarized [Piddington, 1954, 1955]. Hence, if the observed waves are transverse waves, they must bear this polarization characteristic.

Since the vertical component of the waves is always much less than the horizontal component and declination, the damped waves in question are polarized very nearly in the plane perpendicular to the line of magnetic force.

Figure 3a shows the damped wave observed at College at about 0458 UT, April 4, 1960. By combining the variations in the horizontal component and declination the horizontal perturbation vector was constructed, and the locus of the end point of the vector is shown in Figure 3b. The attached numbers represent time reckoned



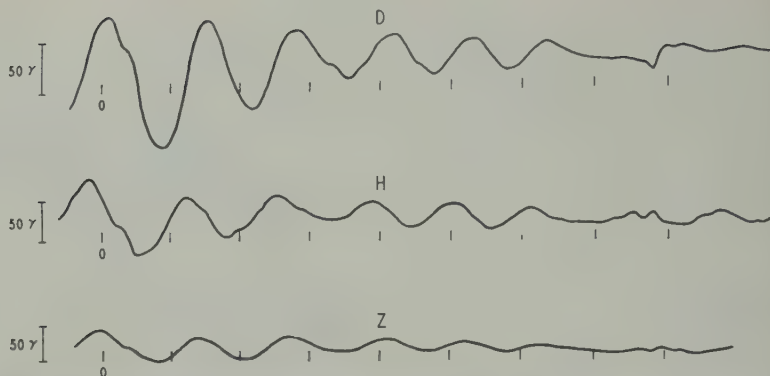


Fig. 3a. A damped wave observed at College at about 0458 UT April 4, 1960; curves traced from the rapid-run magnetograms taken by the Coast and Geodetic Survey Observatory. Time marks indicate 5-minute intervals.

in minutes from 0459 UT. The wave is nearly elliptically polarized. Considering the finite size of the wave packet and the complex boundary conditions, the polarization is remarkably regular, and the identification of the wave as a transverse hydromagnetic wave is justified.

The College rapid-run magnetograms for the two examples shown in Figures 1 and 2 are reproduced in the left half of Figures 4 and 5

respectively. The (horizontal) polarization diagrams based on these records are presented in the right half of the figures. Both diagrams clearly show that the polarization is nearly elliptical.

For the damped wave observed on October 1958, the traces in Figure 3a show that the wave is superposed on a slower change; this is manifested in the polarization diagram by a gradual

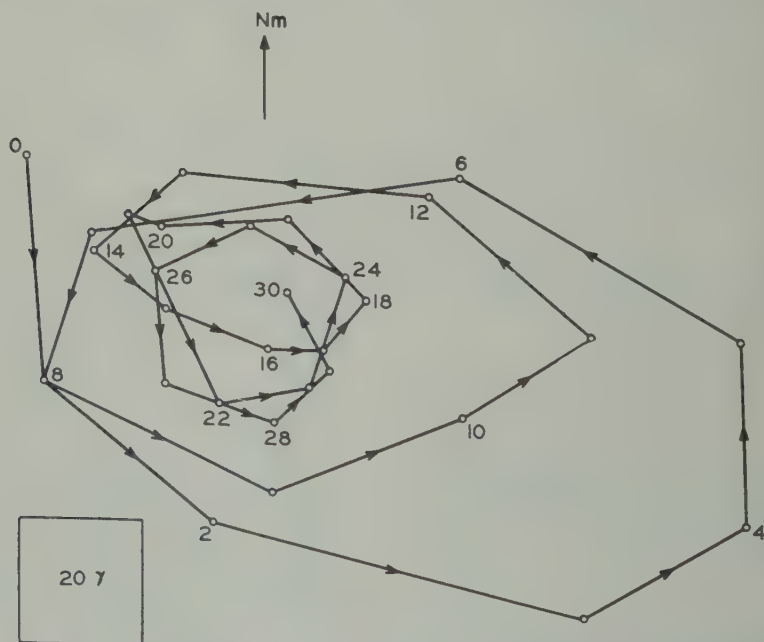


Fig. 3b. The polarization of the damped wave shown in Figure 3a. The polarization is represented by the locus of the end point of magnetic vector. The attached numbers indicate time lapse in minutes. The arrow on top shows the direction of the geomagnetic north.

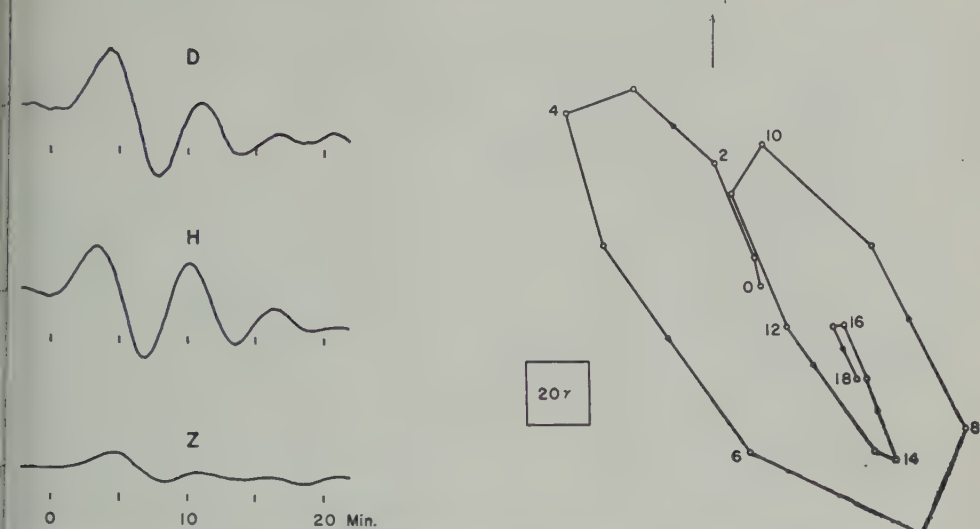


Fig. 4. The rapid-run magnetogram traces for the damped wave on October 1, 1958, and its polarization.

the origin of the magnetic vector for the Examples of this kind are frequently and when the slow variation on which ve is superposed is removed, the polariza- comes more regular and elliptical.

*Comparison of amplitude.* The amplitudes individual waves at College, Kotzebue, and arie Island were compared for the two

cases shown in Figures 1 and 2, and for four additional examples. For each of the examples the first four successive ranges, from peak to minimum, or from minimum to peak, were measured. For the wave on February 12, 1958, record for Kotzebue was not available. The scaled amplitudes and the ratios for pairs of stations are given in Table 1.

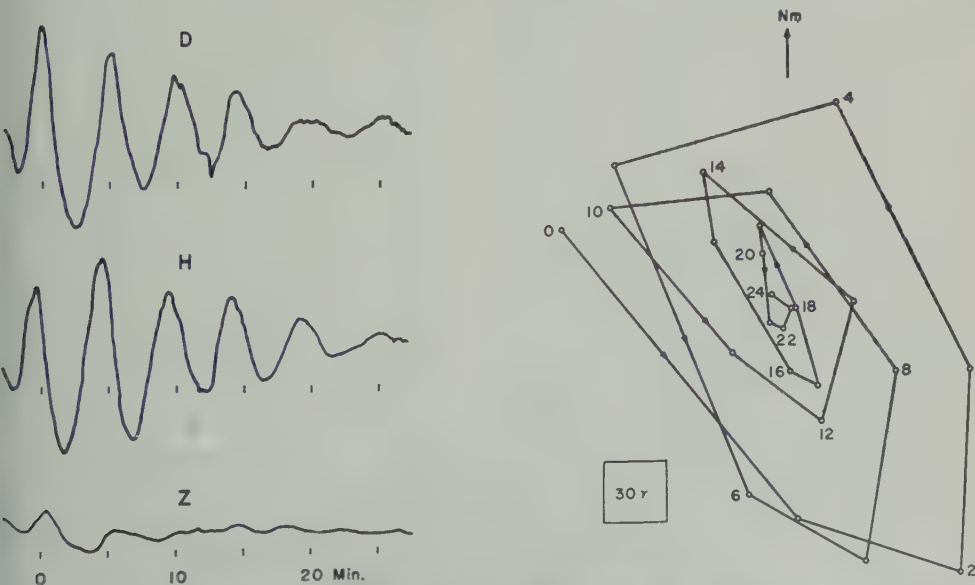


Fig. 5. The rapid-run magnetogram traces for the damped wave on November 14, 1957, and its polarization.

The amplitudes at College and Kotzebue are similar, but the ratio of College to Kotzebue is greater—or less—than unity, depending upon which station is nearer to the center of the disturbance; the longitudinal separation of the two stations is about  $15^\circ$ . This geometrical factor appears to be more important than the latitude difference of the two stations by  $1^\circ$ .

The amplitudes are, in general, considerably greater at Kotzebue than at Macquarie Island. The reason for this difference is not clear.

The ratio of the amplitudes at two stations remains, on the whole, constant throughout each event. This constancy of the amplitude ratio suggests a remarkably good correlation of the waves at the magnetically conjugate regions.

5. *Occurrence of damped waves.* It is of great interest to see how often these waves occur and if the occurrence depends on local time. The College rapid-run magnetograms for the horizontal

component for the 13 months, June 1957 to 1958, were inspected, and all the damped waves having amplitude exceeding 18 gammas were selected. There were 68 such waves of various amplitude; the monthly average occurrence was thus about 5.

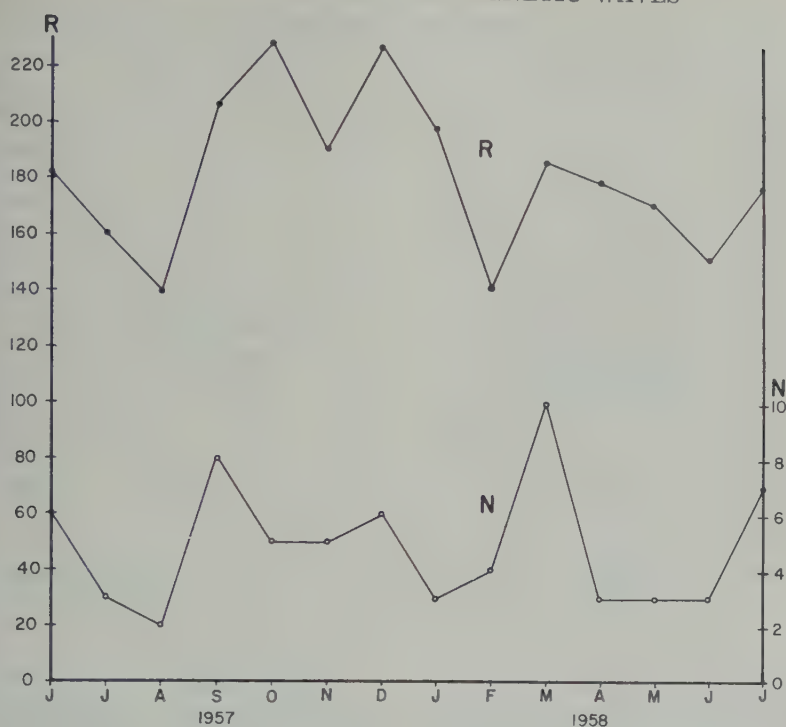
In order to see if the excitation of damped waves has any relation with solar activity, the number of monthly occurrences  $N$  is compared with the Zürich sunspot number  $R$  in Figure 1. The occurrence appears to be more frequent in months of high rather than in low sunspot number. We therefore expect the occurrence of damped waves to vary with sunspot cycle.

It might be speculated that the excitation of hydromagnetic waves in question might be more frequent in period of high than in low magnetic  $K$  indices. However, this is not the case; there is no indication that  $K$  indices are high in the 3-hour intervals in which damped waves are

TABLE 1. Amplitudes of Damped Waves at College, Kotzebue, and Macquarie Island

The numbers 1 to 4 in the second column refer to the first four successive ranges measured from peak to minimum, or from minimum to peak.

Date		College	Kotzebue	Macquarie Island	Ratio		
					Co/Mac	Co/Ko	Ko/M
Oct. 1, 1957 2153 UT	1	73 $\gamma$	131 $\gamma$	49 $\gamma$	1.5	0.6	2.3
	2	68	93	37	1.8	0.7	2.6
	3	49	56	37	1.3	0.9	1.4
	4	39	47	24	1.6	0.8	2.0
Oct. 21, 1957 0400 UT	1	76	75	85	0.9	1.0	0.9
	2	63	75	73	0.9	0.8	1.1
	3	30	47	37	0.8	0.6	1.3
	4	21	28	18	1.2	0.8	1.5
Nov. 10, 1957 2010 UT	1	166	205	98	1.7	0.8	2.1
	2	284	317	159	1.8	0.9	2.0
	3	239	280	134	1.8	0.9	2.0
	4	97	205	92	1.1	0.5	2.2
Nov. 14, 1957 1900 UT	1	232	...	113	2.1	...	...
	2	270	239	175	1.5	1.1	1.4
	3	253	227	163	1.6	1.1	1.4
	4	204	167	119	1.7	1.2	1.4
Feb. 12, 1958 2011 UT	1	203	Record missing	119	1.7		
	2	378		250	1.5		
	3	405		281	1.4		
	4	189		188	1.0		
Oct. 1, 1958 1909 UT	1	148	116	63	2.3	1.3	1.8
	2	129	96	56	2.3	1.3	1.8
	3	106	96	44	2.4	1.1	2.2
	4	50	58	19	2.6	0.9	3.0



6. The number  $N$  of occurrences of damped waves and the relative sunspot number  $R$  for the period June 1957 to July 1958.

The mean  $K$  index for the 68 cases is 3.0, the distribution of  $K$  indices for these 68 intervals has its peak at  $K = 2$ .

Another important feature of the occurrence of damped waves is its local time dependence. Figure 7 shows the local time variation of occurrence for the whole period of 13 months. There are distinct peaks at about 9 and 18 hours. The period is divided into three seasons,<sup>1</sup>  $E$  (April, September, October),  $D$  (November, December, January, February), and  $J$  (June, July, August), the distribution is to change with season; the diurnal variations in occurrences for these three seasons are shown in Figures 7b, c, and d. In winter there is a peak centered at 9 hours, and in summer this shifts to about 18 hours. In equinox the distribution is of a transitional character and has two peaks, as in the yearly mean.

**Discussion.** Since record with adequate resolution is not available for Macquarie Island it is not possible to investigate the

three seasons, namely, equinox, December and June solstice, are abbreviated as  $E$ ,  $D$ , and  $J$ , respectively.

polarization there. But if the waves are generated by some mechanism at an altitude of several earth radii and transmitted to the auroral zones in both hemispheres, the sense of (elliptical) polarization in the southern hemisphere would be opposite that in the northern hemisphere.

Not all the damped waves of our category show clear elliptical polarization because of the irregular changes on which the waves are superposed. But in no event was the polarization found unquestionably linear. This fact supports the hypothesis that the waves were transmitted along the magnetic field lines.

When the polarization is clearly elliptical at College, its sense is counterclockwise for all the cases so far analyzed. It is as yet uncertain whether or not the damped waves of the type discussed here are at times transmitted in the extraordinary mode, thus exhibiting a clockwise rotation at College.

The absence of large amplitude damped waves of the extraordinary mode, if proved real, may be accounted for in the following way. Piddington [1955] showed that in a medium in which



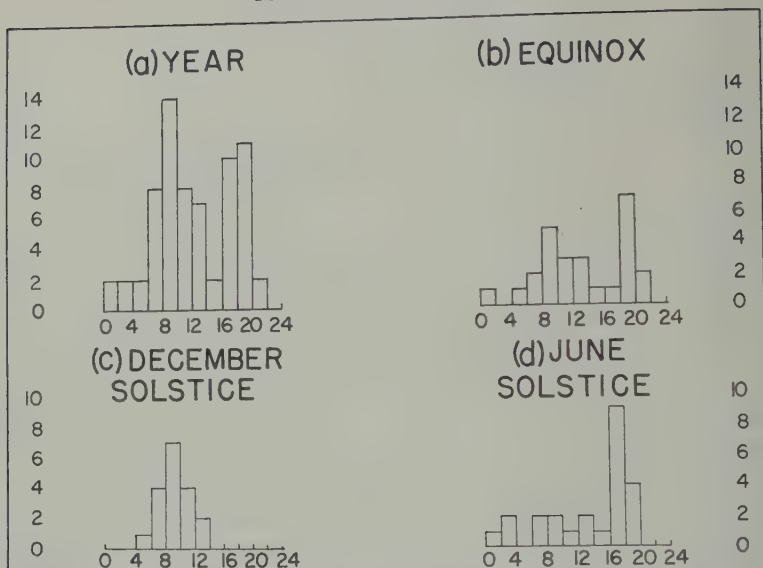


Fig. 7. The diurnal variation of the occurrence of damped waves for the period June 1957 to July 1958.

Alfvén wave velocity is much greater than sound velocity, the velocity of low-frequency waves is given by  $V \cos \psi$  for the ordinary wave and  $V$  for the extraordinary wave, where  $V$  is Alfvén wave velocity and  $\psi$  the angle between the direction of the magnetic field and the wave normal. Thus only for the ordinary waves the transmission of wave energy is confined to the narrow cones along the field line; whereas for the extraordinary waves the wave energy is transmitted in all directions without being focused by the magnetic field. However, it is not certain if such an argument is valid when the wavelength is greater than the radius of curvature of the curved wave fronts.

Numerous quasi-sinusoidal waves of shorter periods than the damped waves dealt with in this paper are found in College magnetograms. One example of such continuous waves, with a period of about 30 seconds, has been studied in detail. Though the waves appeared regular to the eye, their structure was found to have considerable complexity when the polarizations of the waves were analyzed. In a short time interval, such as several minutes, the sense of polarization changed twice, and the locus of the end point of magnetic vector was not at all as regular as might have been expected at first sight from the appearance of the waves in the magnetograms.

In such perturbations, therefore, the mode of propagation may be either ordinary or extraordinary. These magnetic pulsations have been interpreted as being resonant oscillations of magnetic field lines [e.g., *Dungey*, 1954, 1956; *Kato and Akasofu*, 1956; *Akasofu*, 1956; *Obayashi and Jacobs*, 1958; *Watanabe*, 1959]. A more careful analysis of the waves is needed to determine if they are actually continuous resonant oscillations of the field lines. The complicated structure of the waves may suggest that they are generated on the boundary surface of the magnetosphere and transmitted to the earth [Dungey, 1955; Parker, 1958; Dessler, 1959].

As has already been discussed in section 2, damped waves are confined to the auroral zone. The width along the meridian is probably very much greater than  $6^\circ$ . The longitudinal extension is more difficult to estimate. But from the distribution of occurrences it may be concluded that the extension is likely to be not equal to, or less than, the widths of the peaks in Figure 7a; the longitudinal extension is probably between  $30^\circ$  and  $90^\circ$ .

The present investigation thus suggests the existence of large-scale oscillations of gas in the exosphere at geocentric distances of several Earth radii.

**7. Conclusions.** A family of damped waves with periods of several minutes was found

oral zones. These waves occur simultaneously at magnetically conjugate areas in the northern and southern hemispheres.

The polarization of these damped waves is essentially elliptical; hence the waves are interpreted as low-frequency hydromagnetic waves generated along the lines of magnetic force in longitudinal mode.

The damped waves are generated more frequently in epochs of high rather than in low activity, but their occurrences are not directly correlated with magnetic activity.

The diurnal variation of occurrences of damped waves varies with season, and has a morning peak in summer solstice and an evening peak in winter solstice; the variation in equinoxes is seasonal, having both morning and evening

**Acknowledgments.** I wish to thank Mrs. Jean Fujian for her assistance in the analysis of data involved in this study. I am indebted to the Coast and Geodetic Survey and the Department of National Development, Bureau of Mineral Resources, Geology and Geophysics, Australia, for making the magnetic records available. The present study was supported by the Air Force Cambridge Research Laboratories, Office of Aero-Research, through contract AF 19(604)-7988, and by a grant from the National Science Founda-

## REFERENCES

- Fejer, S., On the geomagnetic micropulsations, *Int. Ionosphere Research, Japan*, **10**, 227-249, 1960.
- Fejer, S., On the ionospheric heating by hydromagnetic waves connected with geomagnetic micropulsations, *J. Atmospheric and Terrest. Phys.*, **10**, 160-173, 1960.
- Fejer, H., Existence of electromagnetic-hydrodynamic waves, *Nature*, **150**, 405-406, 1942.
- Fejer, H. A., W. J. Ramm, S. Goldblatt and V. Vasanas, Global hydromagnetic wave ducts in the ionosphere, *Nature*, **185**, 299-300, 1960.
- Francis, A. J., Large amplitude hydromagnetic waves above the ionosphere, *J. Geophys. Research*, **63**, 507-511, 1958.
- Francis, A. J., Ionospheric heating by hydromagnetic waves, *J. Geophys. Research*, **64**, 397-401, 1959.
- Dungey, J. W., The propagation of Alfvén waves through the ionosphere, *Pennsylvania State University Sci. Rept. No. 57*, 1954.
- Dungey, J. W., Electrodynamics of the outer atmosphere, *Proc. Ionosphere Conf. Phys. Soc. London*, 229-236, 1955.
- Dungey, J. W., *Cosmic Electrodynamics*, Cambridge University Press, 1958.
- Fejer, J. A., Hydromagnetic wave propagation in the ionosphere, *J. Atmospheric and Terrest. Phys.*, **18**, 135-146, 1960.
- Francis, W. E., and R. Karplus, Hydromagnetic waves in the ionosphere, *J. Geophys. Research*, **65**, 3593-3600, 1960.
- Hines, C. O., Generalized magnetohydrodynamic formulae, *Proc. Camb. Phil. Soc.*, **49**, 299-307, 1953.
- Kato, Y., and T. Watanabe, A possible explanation of the cause of giant pulsations, *Sci. Rept. Tohoku University*, (5) **6**, 95-104, 1955.
- Kato, Y., and S. Akasofu, Outer atmospheric oscillation and geomagnetic micropulsation, *Sci. Rept. Tohoku University*, (5) **7**, 103-123, 1956.
- Lehnert, B., Magneto-hydrodynamic waves in liquid sodium, *Phys. Rev.*, **94**, 815-824, 1954.
- Lehnert, B., Magneto-hydrodynamic waves in the ionosphere and their application to giant pulsations, *Tellus*, **8**, 241-251, 1956.
- Lundquist, S., Experimental investigations of magneto-hydrodynamic waves, *Phys. Rev.*, **76**, 1805-1809, 1949.
- Maeda, H., and T. Ondoh, Evidence of quasi-perpendicular propagation of hydromagnetic waves caused by nuclear explosions over Johnston Island, *Nature*, **188**, 1018-1019, 1960.
- Obayashi, T., and J. A. Jacobs, Geomagnetic pulsations and the earth's outer atmosphere, *Geophys. J., Roy. Astr. Soc.*, **1**, 53-63, 1958.
- Parker, E. N., Interaction of the solar wind with the geomagnetic field, *Phys. Fluids*, **1**, 171-187, 1958.
- Piddington, J. H., Electromagnetic field equations for a moving medium with Hall conductivity, *Monthly Notices Roy. Astron. Soc.*, **114**, 638-650, 1954.
- Piddington, J. H., Hydromagnetic waves in ionized gas, *Monthly Notices Roy. Astron. Soc.*, **115**, 671-683, 1955.
- Scholte, J. G. J., On the theory of giant pulsations, *J. Atmospheric and Terrest. Phys.*, **17**, 325-336, 1960.
- Sugiura, M., Some evidence of hydromagnetic waves in the earth's magnetic field, *Phys. Rev. Letters*, **6**, 255-257, 1961.
- Veldkamp, J., A giant geomagnetic pulsation, *J. Atmospheric and Terrest. Phys.*, **17**, 320-324, 1960.
- Vestine, E. H., and W. L. Sibley, Lines of force of the geomagnetic field in space, *Planetary Space Sci.*, **1**, 285-290, 1959.
- Vestine, E. H., and W. L. Sibley, Geomagnetic field lines in space, *Rand R-368*, 1960.
- Watanabe, T., Hydromagnetic oscillation of the outer ionosphere and geomagnetic pulsation, *J. Geomag. Geoelect.*, **10**, 195-201, 1959.

(Manuscript received July 28, 1961.)



# Hydromagnetic Interpretation of Sudden Commencements of Magnetic Storms

CHARLES R. WILSON AND MASAHISA SUGIURA

*Geophysical Institute, University of Alaska  
College, Alaska*

**Abstract.** Sudden commencements of magnetic storms observed during the IGY are analyzed using the rapid-run magnetograms taken at College, Sitka, Fredericksburg, Honolulu, Watheroo, and Marie Byrd. Most of the magnetic impulses of sudden commencements are found to be elliptically polarized at all these stations except at Honolulu; at this latter (low-latitude) station the polarization is usually linear. The following model is presented for sudden commencements. The impact of the solar gas stream upon the geomagnetic field creates a shock wave, which propagates over the earth as a longitudinal hydromagnetic wave in low latitudes. The compressional wave in the shock generates transverse hydromagnetic waves that propagate to high latitudes along the magnetic field lines. Since the field lines are firmly anchored in the conducting core of the earth, a strong shock may cause the field lines to oscillate for a considerable length of time. These oscillations are, in fact, observed in high latitudes as continuous waves following the sudden commencement. The frequent appearance of a reversed impulse, preceding the main impulse at geomagnetic latitudes above  $40^\circ$ , is due to the circumstance that at the time of the arrival of the transverse wave at the ionosphere the direction of the magnetic perturbation vector is south of the geomagnetic east-west, and that the vector subsequently rotates toward the north. Thus physically there is no essential difference between sudden commencements with a reversed impulse and those without it. The peculiar shape of sudden commencements in  $H$  observed during morning hours in latitudes above  $50^\circ$  can also be explained by a particular phase of the elliptically polarized wave at the time of arrival in these regions and the subsequent rotation of the magnetic vector. The picture of sudden commencements is thus greatly simplified.

## 1. INTRODUCTION

This paper presents the results of a new analysis of sudden commencements and our interpretation of the results. The sudden commencement (SC) of a magnetic storm is interpreted as an effect of the impact of a solar gas stream on the geomagnetic field, as was originally proposed by *Chapman and Ferraro* [1931; 1932] and discussed in detail by *Ferraro* [1952]. The impact effect is transmitted to the earth by hydromagnetic waves [*Dessler*, 1958; *Newton*, 1959; *Dessler and Parker*, 1959]. This paper shows that the perturbation generated by the impact of the solar stream is propagated over the earth primarily by longitudinal hydromagnetic waves in low latitudes, and by transverse hydromagnetic waves in high latitudes. These propagation modes are deduced from a study of the characteristics of the polarization of the SC magnetic field: in high latitudes the SC magnetic field is essentially elliptically polarized, whereas in low latitudes the polarization is linear.

## 2. BACKGROUND

The early important investigations of SC's were discussed by *Chapman and Bartels* [1940, pp. 296-299]. The more recent studies have been reviewed by *Akasofu and Chapman* [1960].

In the standard magnetograms an SC is typically a sudden increase in the horizontal component  $H$ . In moderate to high latitudes, SC impulses are often preceded by a smaller, and reversed, impulse. An SC characterized by such a precursor is usually marked by an asterisk as SC\* [e.g. *Newton*, 1948], or SC(- +) according to the symbols proposed by *Akasofu and Chapman* [1960] and *Matsushita* [1960]. *Ferraro*, *Parkinson*, and *Unthank* [1951], *Nagata* [1952], *Nagata and Abe* [1955], and *Abe* [1959] noted a local time dependence of the reversed impulse in SC\*'s.

Geometrical shapes of SC's in  $H$  have been studied by *Jackson* [1952], *Obayashi and Jacobs* [1957], *Matsushita* [1957, 1960], and *Akasofu and Chapman* [1960]; *Obayashi and Jacobs*, and *Matsushita* investigated the local time depend-



ence of occurrence of different types of SC's.

The magnitude of the main impulse of an SC varies with geomagnetic latitude; it is greatest in the auroral zone and decreases with decreasing latitude toward a minimum near  $30^\circ$  or  $20^\circ$ .

At the equator SC's are enormously enhanced during the hours of sunlight [Ferraro and Uthman, 1951; Sugiura, 1953]; at night the magnitudes of SC's at the equator are comparable with those at about  $50^\circ$ . On the basis of these glob

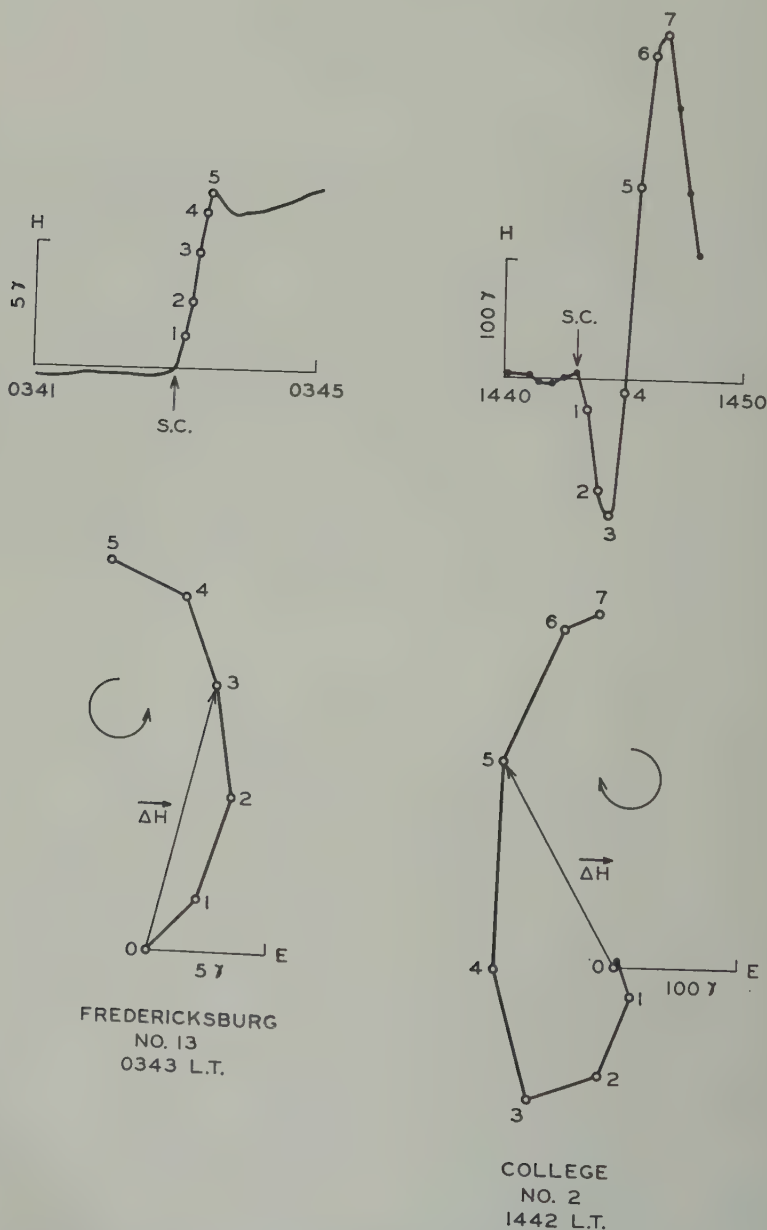


Fig. 1.  $H$  component of SC's at Fredericksburg and College and the corresponding vector diagrams, showing the locus of the end point of the total horizontal disturbance vector  $\Delta H$  as a function of time. The numbered points for the SC at Fredericksburg are 5 seconds apart, and those for the SC\* at College are 30 seconds apart. The arc with an arrow in each vector diagram indicates the sense of rotation of the magnetic vector.

teristics of SC's Vestine [1953] and Forbush Vestine [1955] suggested that SC's are due to the electric currents flowing in the there.

ata and Abe [1955] constructed a current for the reversed impulse of SC's and ed that such currents are generated in the here in the polar regions.

yashi and Jacobs [1957] divided the average d into two parts, Dst and DS, in the same r as the magnetic storm field is usually ed, and attempted to explain the DS part ionospheric dynamo mechanism.

sofu and Chapman [1960] proposed to te the magnetic field that would result he idealized Chapman-Ferraro mechanism the remaining field; the latter, being st in polar regions, was suggested to be o electric currents generated in the iono- e over these regions.

Z [1955] suggested that the SC of a magnetic is due to a shock wave propagated from n. Following Gold, Singer [1957] attributed C to a shock wave developed when a high- jet of gas is ejected from the sun. Singer esed that when the shock wave arrives near arth, it is focused by the geomagnetic field the auroral zones and gives rise to large nplitudes there.

their theory of the SC and the initial phase

of a magnetic storm, Chapman and Ferraro originally supposed the space between the front surface of the solar stream and the earth to be a void. In recent years the significance of the existence of a plasma around the earth was recognized. Dessler [1958], Piddington [1959], and Dessler and Parker [1959] pointed out that the magnetic impulse due to the impact of the stream on the earth's field must be transmitted through the plasma by hydromagnetic waves.

3. THE UNDERLYING IDEA OF OUR ANALYSIS

The impact of the solar stream on the earth's field will generate longitudinal hydromagnetic waves which will propagate to the earth essentially in that mode in low latitudes. At geocentric distances of several to 10 earth radii, the shock generates transverse hydromagnetic waves that are transmitted along the field lines to high latitudes in the northern and southern hemispheres. Thus the SC field is nearly circularly polarized in high latitudes. Figure 1 shows two typical examples of such SC's observed at College and Fredericksburg.

The above picture of SC's is the basis of our interpretation of the detailed analysis of SC's described in the following sections.

4. POLARIZATION OF THE SC FIELD

In all the papers on SC's referred to in section

TABLE 1. List of the Sudden Commencement Magnetic Storms Used in This Paper

GMT	Date	No.	GMT	Date
0016	Sept. 29, 1957	21	1212	Mar. 14, 1958
0042	July 5, 1957	22	1247	Apr. 26, 1958
0046	June 7, 1958	23	1300	Sept. 4, 1957
0048	June 25, 1957	24	1345	Sept. 22, 1957
0109	Nov. 28, 1958	25	1347	Aug. 9, 1957
0125	Feb. 11, 1958	26	1529	July 31, 1958
0315	Oct. 22, 1958	27	1540	Mar. 25, 1958
0408	Sept. 25, 1958	28	1557	Aug. 3, 1957
0508	Aug. 6, 1957	29	1637	July 21, 1958
0650	Oct. 28, 1958	30	1642	Feb. 16, 1958
0714	July 16, 1957	31	1742	June 28, 1958
0748	July 8, 1958	32	1812	Aug. 31, 1957
0843	Sept. 3, 1958	33	1817	Dec. 17, 1958
0857	July 2, 1957	34	1821	Nov. 6, 1957
0930	Sept. 16, 1958	35	1828	June 14, 1958
0931	Mar. 3, 1958	36	1920	Aug. 29, 1957
0937	Dec. 19, 1957	37	2022	Dec. 15, 1958
1005	Sept. 21, 1957	38	2241	Oct. 21, 1957
1005	Sept. 30, 1958	39	1652	May 31, 1958
1050	Jan. 25, 1958	40	0622	Aug. 17, 1958

TABLE 2. Geomagnetic Coordinates of Magnetic Stations

Station	Geomagnetic Latitude	Geomagnetic Longitude
College	64.7°N	256.5°
Sitka	60.0 N	275.4
Fredericksburg	49.6 N	349.9
Honolulu	21.0 N	266.4
Watheroo	41.7 S	185.8
Macquarie Island	61.1 S	243.1
Marie Byrd	70.6 S	336.0

2, discussions are substantially based on analyses of the *H* component alone. When declination *D* is taken into account, the amplitudes in *H* and *D* in their maximum phases are usually combined without careful examination of the simultaneity of these phases. Traces in the ordinary magnetograms do not warrant time resolution adequate for this purpose.

In polar regions the changes in *D* during SC's are, in general, of the same order of magnitude as those in *H*. Studies made without regard to *D*, therefore, may lead to seriously erroneous conclusions.

In comparison with relatively simple forms of variations in *H*, those in *D* are more complex. The latter often show an oscillatory nature, and it is not at all obvious if the maximum deviation in *D* coincides with that in *H*; nor does the component *D* vary proportionately with *H* throughout an SC. It is thus questionable if an SC can adequately be represented by a single current system.

It appears from the onset that the study of the behavior of the *total* magnetic vector through all phases of SC's is essential. Such a study is possible with the rapid-run magnetograms that have been taken in recent years at several observatories.

The changes during SC's in the vertical component *Z* are found to be small in comparison with the total horizontal component, namely the resultant of combination of *H* and *D*. Thus, in this paper the changes, in both magnitude and direction, of the total horizontal disturbance vector (here denoted by  $\Delta\mathbf{H}$ ) are examined. The characteristics of these changes show the nature of the polarization of the SC field.

Changes in the vector  $\Delta\mathbf{H}$  in the first few minutes of 40 world-wide SC's observed during

the IGY are examined for the magnetic observatories at College, Sitka, Fredericksburg, Honolulu, Watheroo, and Marie Byrd. These 40 SC's are listed in Table 1. The coordinates of the stations used in this paper are given in Table 2.

The *H* and *D* traces in the rapid-run magnetograms were scaled at 30 second intervals; values were reckoned from the pre-SC level. The locus of the end-point of the vector  $\Delta\mathbf{H}$  was drawn to represent the polarization graphically. When the variation in *H* or *D* is rapid, scaling was made with 15- or 5-second intervals.

Examples of polarization diagrams are shown in Figure 2: examples in the upper half of the figure illustrate typical cases where the rotation of the vector is counterclockwise, and those in the lower half are examples of clockwise rotation. The numbers under the station names are the serial numbers for the SC's in Table 1. The direction of the geomagnetic east and the scale in gammas are given for each SC. The numbers alongside each locus represent the time lag measured in minutes from the onset of the SC. The direction of rotation is shown in each diagram by the arc with an arrow.

The SC's were grouped into two types according to whether the polarization is or is not elliptical; the latter category includes both linear and irregular polarizations. This grouping is inevitably subjective to some extent, but it suffices for our qualitative discussions.

The number of SC's analyzed, and the percentage of occurrence of elliptically polarized cases of these SC's are listed in Table 3.

Table 3 shows that SC's are more frequently elliptically polarized in high than in low latitudes. The smaller percentage at College than at Sitka is probably due to our method of counting, according to which rapidly oscillating

TABLE 3. The Number *N* of SC's Analyzed and the Percentage *P* of Occurrence of Elliptically Polarized SC's

Station	Geomagnetic Latitude	<i>N</i>
College	64.7°N	24
Sitka	60.0 N	32
Fredericksburg	49.6 N	30
Honolulu	21.0 N	35
Watheroo	41.7 S	10
Marie Byrd	70.6 S	11

SC's are not included in the group of elliptically polarized SC's because of difficulty in determining the direction of rotation. Changes in azimuth of  $\Delta H$  in several examples are shown in Fig. 3 for College, Sitka, and Fredericksburg. In Figure 3 the azimuth is plotted against time; the time axis is taken from the beginning of the SC, and plots are made with 30-second intervals. The three traces on the left, for the stations of College, Sitka, and Fredericksburg, show examples of  $\Delta H$  rotating counterclockwise; in the three examples in the middle, for College and Sitka,  $\Delta H$  rotates clockwise.

All these examples represent elliptically polarized SC's. The three to the extreme right for the three stations show irregular polarization. The remarkably regular rate of change in azimuth for the elliptically polarized SC's is noteworthy. The linear nature of the polarization at Honolulu is demonstrated in Figure 4. The curves on the left-hand side show the loci of the end-point of the total horizontal magnetic vector and the curves on the right-hand side, the changes in the azimuth of the vector with time.

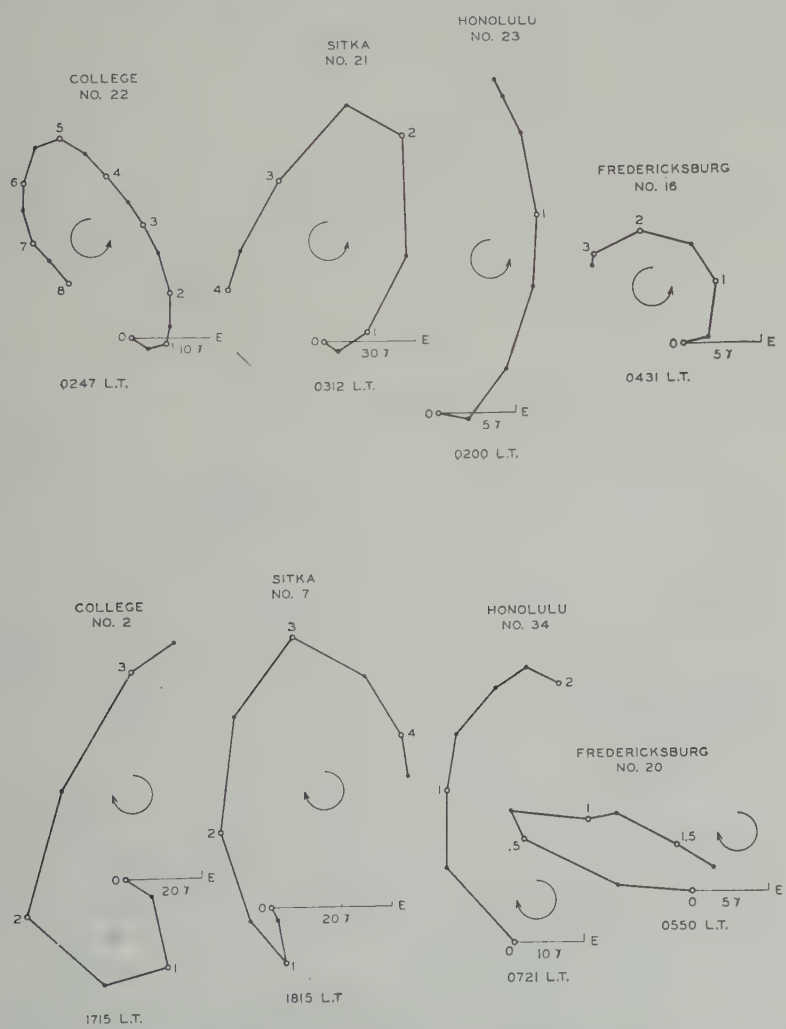


Fig. 2. Vector diagrams of elliptically polarized SC's for both clockwise and counterclockwise rotation of the magnetic vector. The local time for the onset of each SC, the scale in gammas, and the direction of geomagnetic east are indicated. The time intervals between the numbered points are 30 seconds. When projected onto the geomagnetic meridian plane, SC nos. 2 and 7 show a large reversed impulse at College and Sitka, respectively, and nos. 21, 22, 23 show a small reversed impulse at Sitka, College, and Honolulu, respectively.



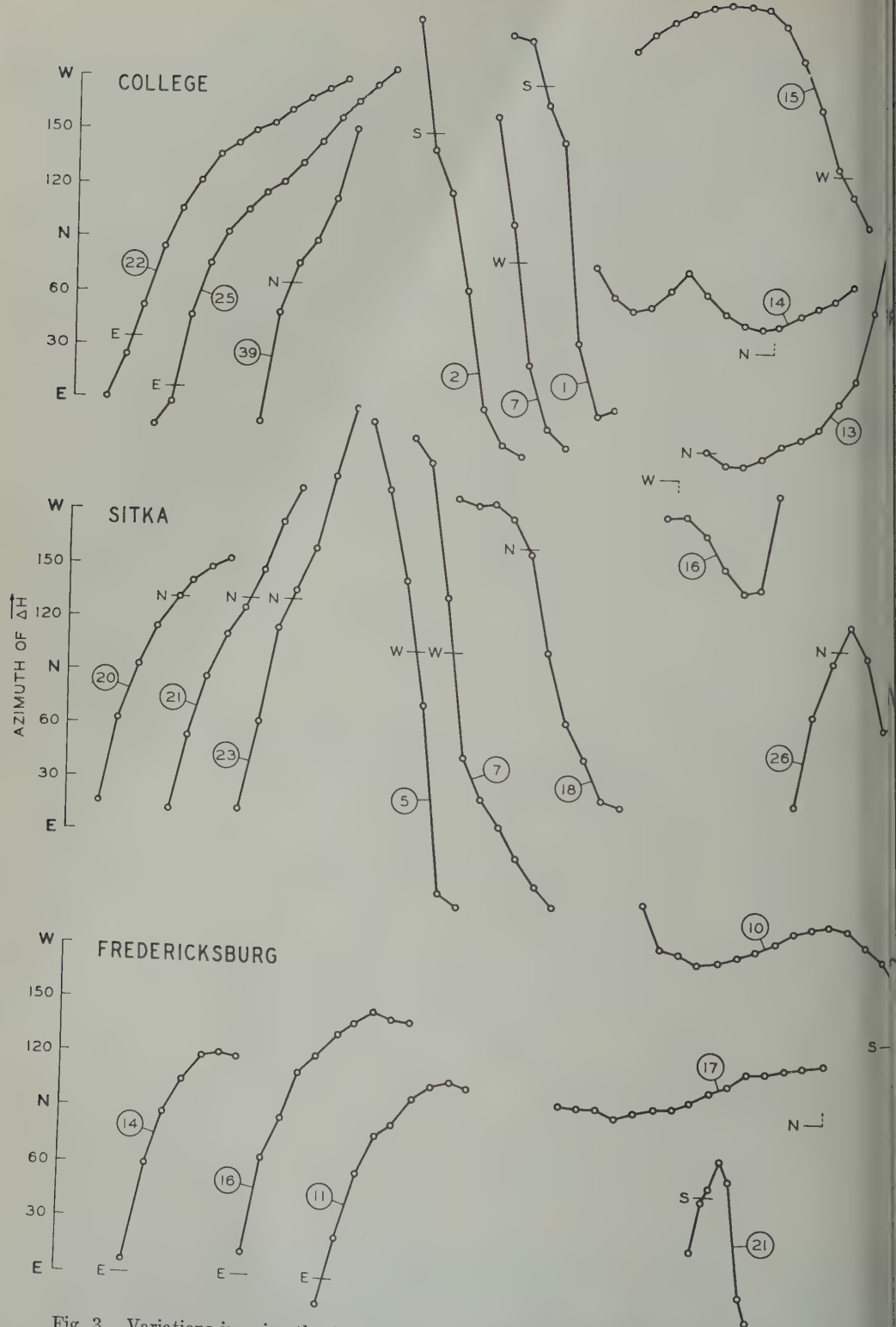


Fig. 3. Variations in azimuth of  $\Delta H$  with time. The reference azimuth is indicated for each curve. Plots are made with 30-second intervals. The serial number of each SC is given in a circle. Three examples of counterclockwise polarization are given to the left, those of clockwise polarization in the middle, and irregular ones to the right.

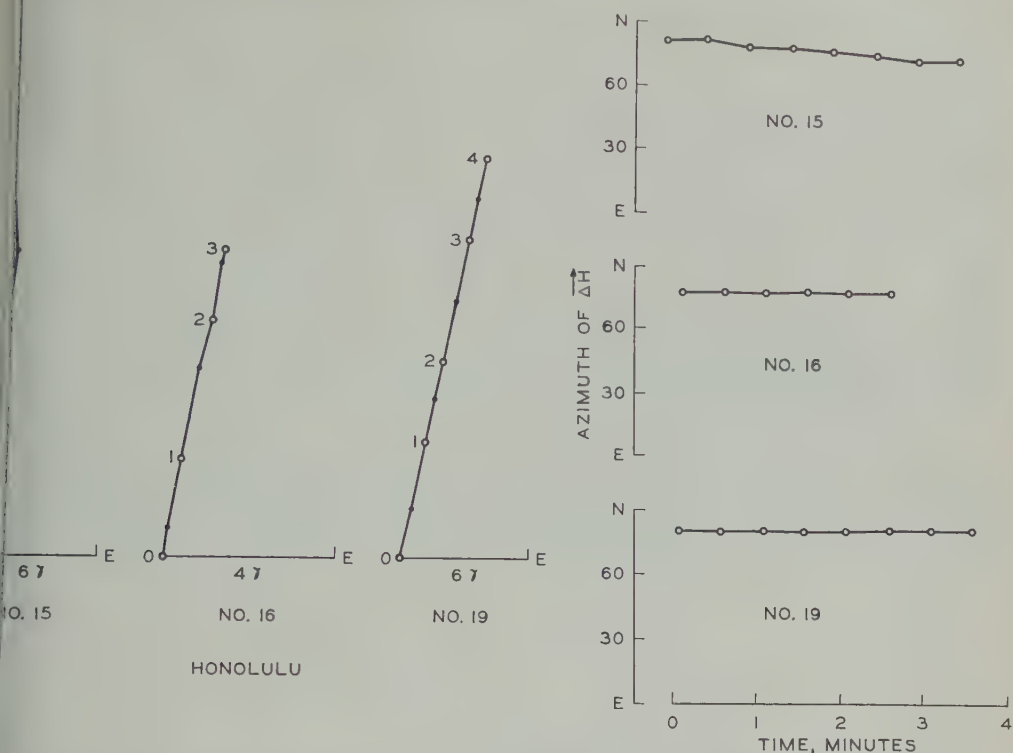


Fig. 4. Vector diagrams of  $\Delta H$  (on the left) and azimuth-time curves (on the right), showing linear polarization of SC's at Honolulu; intervals between numbered points are 1 minute.

## TWO RULES IN THE GLOBAL DISTRIBUTION OF THE SENSE OF ROTATION OF THE MAGNETIC VECTOR

**Local time dependence.** The sense of rotation of the vector  $\Delta H$  for elliptically polarized is found to depend on local time. In the northern hemisphere this rotation is clockwise only from 1000 to 2200 hours in local time, and counterclockwise from 2200 to 1000 hours. In the southern hemisphere the two zones of opposite senses of rotation are reversed. The pattern is fixed in orientation with respect to the sun. In this paper the sense of rotation, clockwise or counterclockwise, is always defined relative to the sense with which the total horizontal magnetic vector rotates at ground level when viewed from above.

Figure 5 shows the local time distribution of the sense of elliptically polarized SC's; those associated with clockwise rotation of the magnetic vector are indicated by open circles and those with counterclockwise rotation by black circles. These marks are placed in several con-

centric belts, each representing a station at which the SC's were observed.

There are transitional zones, centered at 1000 and 2200 hours, and with a width of several hours; in these zones the rotation of the magnetic vector may be in either sense.

It is remarkable that outside the transitional zones the 26 SC's for Sitka show no exceptions to the general pattern and that there is only one exception out of the 17 for College.

**5.2. Opposite sense of rotation in the southern hemisphere.** The sense of rotation of the magnetic vector during an SC is found to be opposite in the southern hemisphere to that in the northern hemisphere in each meridian. An example demonstrating this feature is shown in Figure 6 with the records for SC no. 22 from College in Alaska and Marie Byrd in Antarctica; the difference in geographic longitude between these stations is  $28^\circ$ . At the time of this SC both stations were within the 22 to 10 hour zone, in which the rotation is ordinarily counterclockwise in the northern hemisphere. Figure 6 shows that



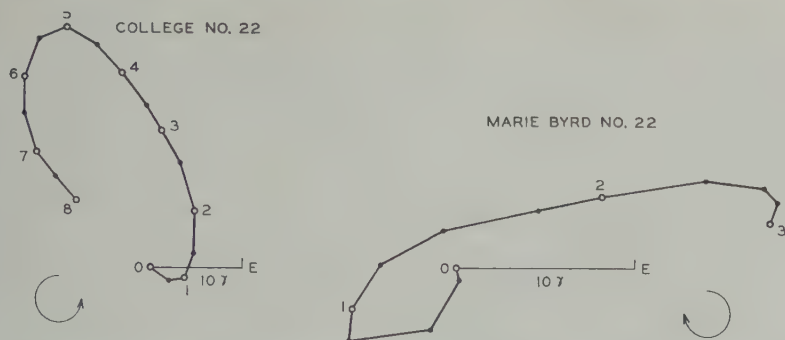


Fig. 6. Vector diagrams for  $\Delta H$  for SC no. 22, showing counterclockwise rotation of the magnetic vector at College, Alaska, and clockwise rotation at Marie Byrd, Antarctica.

in the northern and southern hemispheres. In the above discussion the division of the local time zones is made by a meridian plane through the earth's rotational axis. This division should be revised in the future as more data accumulate, since the surface of separation may depend on the actual configuration of the earth's magnetic field lines as well as on the geometrical factors with reference to its rotational axis and direction of the sun.

# 6. OSCILLATIONS FOLLOWING SUDDEN COMMENCEMENTS

Forty-one SC's of the 40 analyzed were accompanied by oscillations in the magnetic field which began at the time of the SC and continued 10 minutes to a few hours. Several examples of such SC's observed at College, Sitka, and Brooksburg are shown in Figure 8.

These SC oscillations occur more frequently at high than in low latitudes. This latitude effect and other data are shown in Table 4.

The period of the oscillations following SC's

varied from 2.5 to 10 minutes; the differences between the mean periods for different stations are probably due to the different cases included for different stations.

Column 6 of Table 4 gives, for each of the stations, the average size of all SC's with or without oscillations, and column 7 the ratio,  $A$ , of the average amplitude of SC's followed by oscillations to that of all SC's (i.e., the value given in the preceding column). These ratios indicate that oscillations are generated, on the average, by SC's of large amplitude. The difference in the ratios for different latitudes is probably due to statistical scatter.

The greater the amplitude of the SC oscillations the larger the area in which the oscillations are observed. For large oscillations the wave form is similar at stations that are close to each other. The similarity of the wave form at near stations is illustrated in Figure 10 with the records from College, Healy, and Big Delta for SC no. 22; all these stations are within 130 km from each other. Although the amplitude varies

TABLE 4. SC's Followed by Oscillations of the Magnetic Field

Station	Geomagnetic Latitude	No. SC's with Oscillations	Occurrence, %	Average Period Oscillations, min.	Average size of all SC's $\gamma$	Ratio,* $A$
College	64.7°N	19	81	4.2	135	1.35
	60.0 N	19	62	4.1	46	1.45
Brooksburg	49.6 N	8	47	6.1	37	1.86
Adulul	21.0 N	7	20	5.4	23	1.40
Marie Byrd	70.6 S	7	73	4.7	71	1.86

\* Ratio of amplitude of SC's followed by oscillations to the average of all SC's for the station.



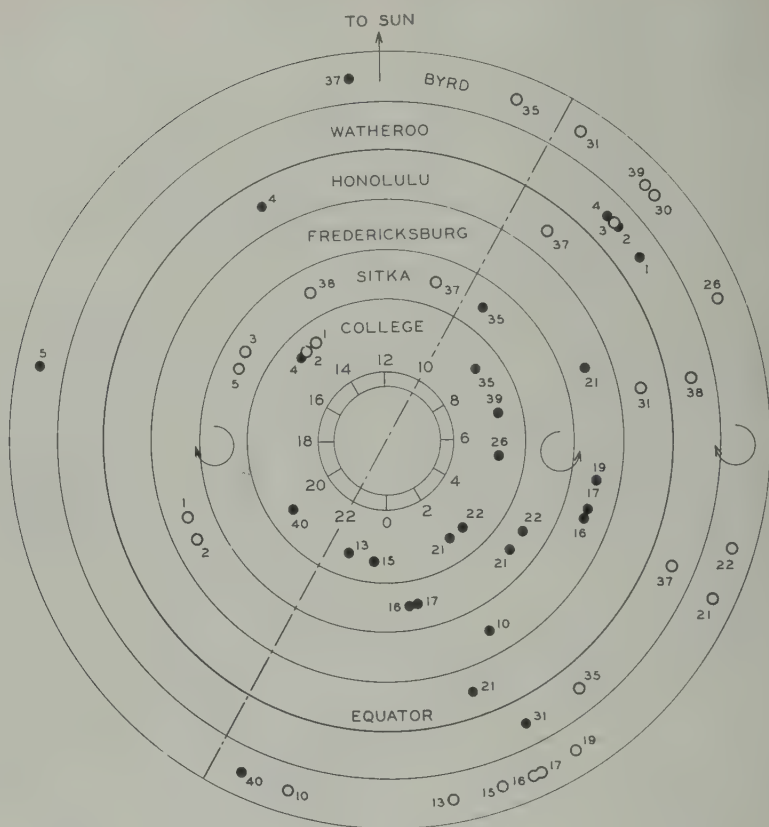


Fig. 7. Distribution of SC's with counterclockwise rotation (black circles) and clockwise rotation (open circles) of the magnetic vector. The sense of rotation of the vector is opposite in the southern hemisphere to that in the northern hemisphere in each of the local time zones into which the earth is divided by the meridian plane through 1000 and 2200 hours (see Fig. 5). The equator is represented by the heavy circle between the belts for Honolulu and Watheroo.

to some extent, the wave form and period are nearly the same at all these stations.

For oscillations that are especially regular, the period of the oscillations appears to be constant within the accuracy of the determination over a wide range of latitude; for instance, the period of the oscillations in SC no. 40 was: 3.2 minutes at College, 3.2 minutes at Big Delta, 3.1 minutes at Sitka, 3.0 minutes at Fredericksburg, and 3.2 minutes at Tucson.

In five SC's the oscillations were found remarkably similar at College and Macquarie Island; these stations lie in a pair of magnetically conjugate areas, one in the northern and the other in the southern hemisphere. Figure 11 shows such an example, namely, SC no. 40. Simultaneous SC oscillations have also been found at College and Marie Byrd.

The characteristics of the polarization of the oscillations following an SC are, in general, the same as those of the SC itself; thus the sense of rotation of the magnetic vector during oscillations usually follows the same local time pattern as that for SC's.

A few examples of the polarization diagrams for SC oscillations are shown in Figure 9.

## 7. DISCUSSIONS

In the previous sections we have shown evidence that at geomagnetic latitudes about  $40^\circ$  the SC magnetic field has characteristics of elliptical polarization (Figs. 2 and 3) and that at geomagnetic latitude of Honolulu, namely  $21^\circ$ , the polarization of the SC field is linear (Fig. 4). The elliptical nature of the polarization is most pronounced in high latitudes.

interpret these gross features of SC's in following manner. As the front of a solar gas advances into the geomagnetic field, it is a shock, because the speed of the stream is greater than the local Alfvén wave speed in the region of the impact. The longitudinal hydromagnetic shock wave propagates toward earth and is observed as a sudden increase in magnetic field in low latitudes. *Schneiders* [1961a, 1961b] has shown examples of transverse waves generated at a distance of several earth radii and transmitted along the magnetic field lines to the northern and southern auroral zones. This suggests that the compression wave created by the impact of the solar wind might generate transverse hydromagnetic waves that will propagate along the magnetic field lines to high latitudes. This mechanism has been suggested to the

authors by Dr. Eugene N. Parker whereby the rotation of the magnetic vector becomes opposite in the morning and evening sides of the earth. On these sides the equatorial portion of the field lines are initially blown by the shock toward the far side from the stream front. Thus, looking from above the north pole the initial motions of the field lines are clockwise in the morning side and counterclockwise in the evening side. When these perturbations are transmitted to the earth, the rotations of the magnetic vector at the surface of the earth, when viewed downward, are just as is depicted in Figures 5 and 7. This mechanism is shown schematically in Figure 12. When the shock is strong, the oscillation of the field lines continues in high latitudes for 20 minutes to 1 hour or longer after the sudden commencement. According to our detailed analysis, the transition from the transverse wave

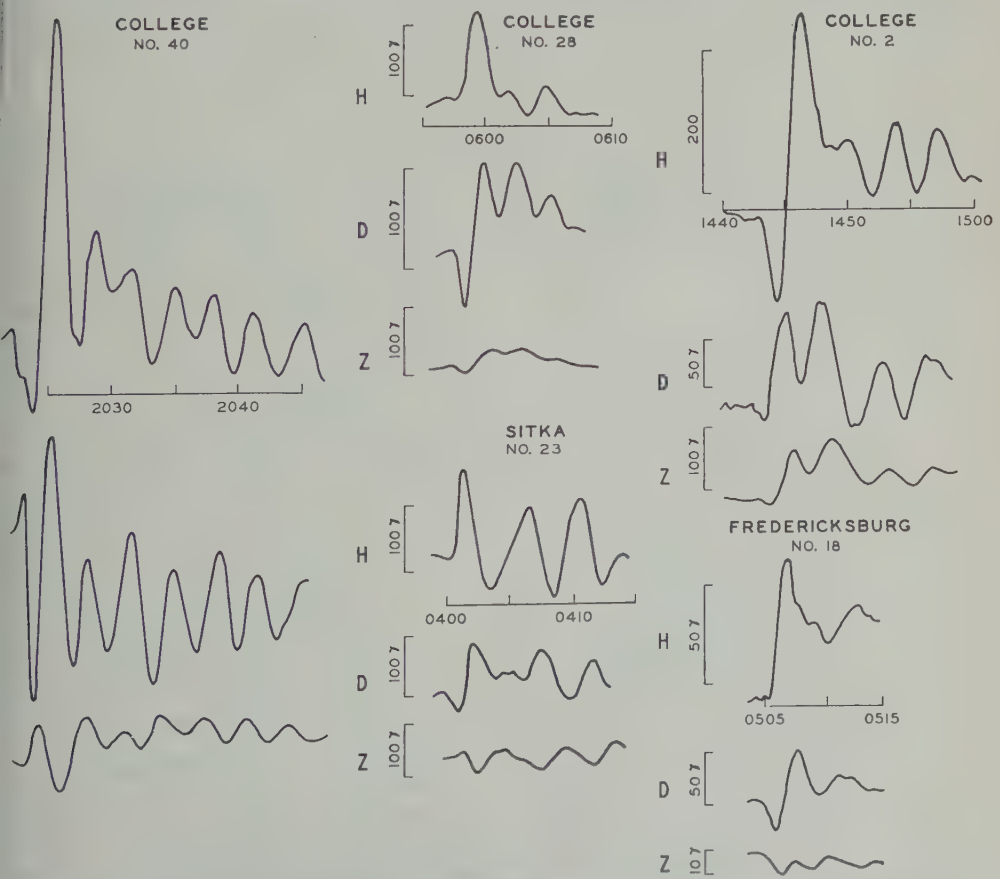


Fig. 8. Oscillations following SC's at College, Sitka, and Fredericksburg, for the three elements H, D, and Z.

of the sudden commencement itself to the succeeding oscillation is smooth and continuous. In fact, the whole of these variations should be considered as the vibration of the field lines excited by the sudden commencement shock wave.

The longitudinal shock waves, which propagate along the equatorial plane to low latitudes, may partly be transmitted to high latitudes. This may be the reason why the polarization in high latitudes is elliptical rather than perfectly circular, even if the increase in amplitude (with time) is taken into consideration.

In geomagnetic latitudes above about  $45^\circ$  a reversed impulse often precedes the main impulse

in  $H$ . This reversed impulse can be accounted for by the rotation of the magnetic vector in the transverse wave. If the azimuth of the initial direction of the magnetic perturbation vector is south of the geomagnetic east-west, and if the vector rotates toward the north either clockwise or counterclockwise, the  $H$  component will show an initial reversed excursion preceding the main northward change.

There is no evidence of discontinuous change either in the magnitude of the total field or in the rate of change in the direction of the field in the transition from the initial reversed impulse to the main impulse as seen in the  $H$  component.

The peculiar shape of SC's (in  $H$ ) in the

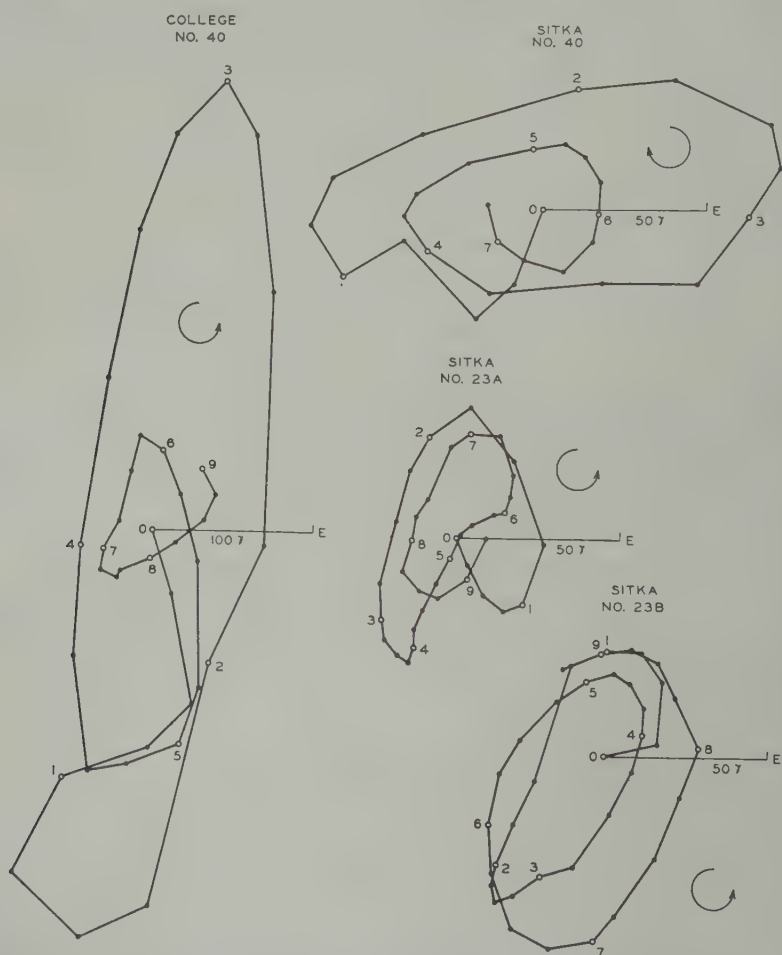


Fig. 9. Vector diagrams of  $\Delta H$  for SC oscillations at College and Sitka. Numbered points are plotted with 1 minute interval. For SC no. 23 for Sitka, the vector diagram 23A refers to the first 9 minutes of the SC, and the vector diagram 23B refers to the 9-minute interval which begins 30 minutes after the SC.

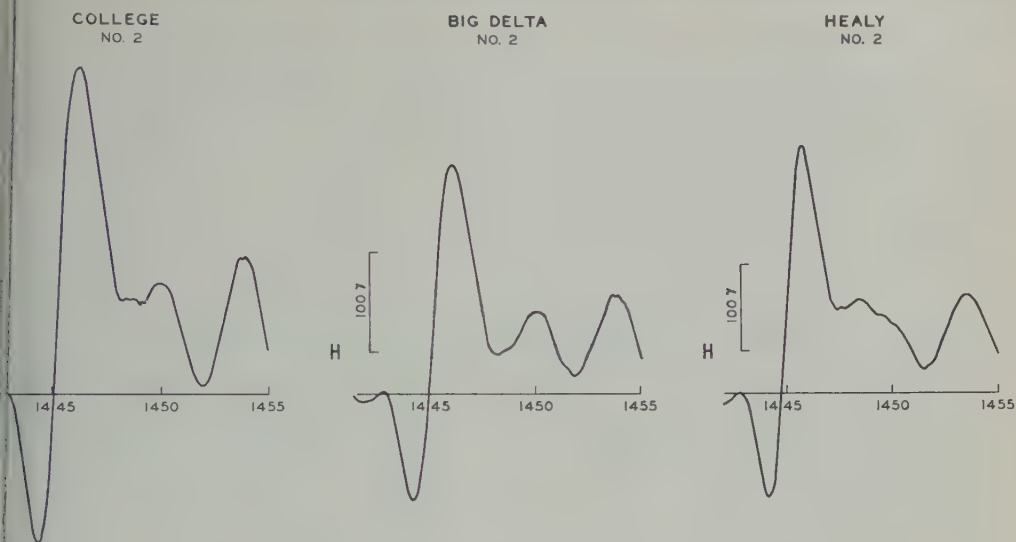


Fig. 10. Sudden commencement oscillations for SC no. 2 at College, Big Delta, and Healy, showing similarity in wave form at near stations; the three stations are within 130 km of each other.

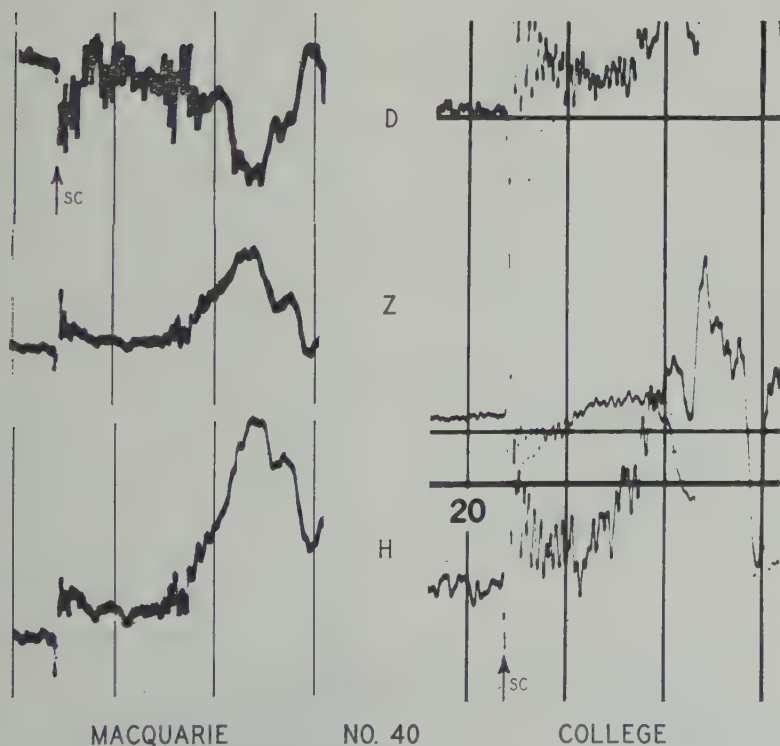


Fig. 11. Simultaneous sudden commencement oscillations in magnetically conjugate areas, represented by records from College and Macquarie Island.



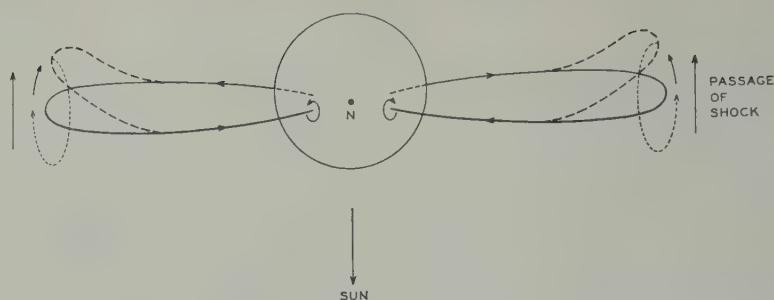


Fig. 12. Schematic picture describing the excitation of transverse hydromagnetic waves on the morning and evening sides of the earth.

morning hours observed at geomagnetic latitudes above about  $50^\circ$  [as noted, for instance, by Jackson, 1952] can also be explained by the rotation of the magnetic vector.

All these peculiarities in the shape of SC's, in  $H$  or  $D$ , can be interpreted as due to the difference in phase and sense of rotation of the magnetic vector in different latitudes and meridians. That is, because of different propagation modes and different path lengths the effect of the impact of the solar stream is transmitted to different parts of the globe in different ways and exhibit different shapes of pulse. There may also be modifications of the pulse form by the inhomogeneity of the upper atmosphere; but these are considered secondary.

Thus the physical picture of sudden commencements has been greatly simplified.

**Acknowledgments.** We wish to thank Dr. E. N. Parker for his valuable suggestion on the possible mechanism for the opposite polarization on the morning and evening sides. We are indebted to the U. S. Coast and Geodetic Survey, the Bureau of Mineral Resources, Geology and Geophysics of Australia, and the World Data Center A—Geomagnetism, for supplying the necessary records. We gratefully acknowledge the assistance of Mrs. Sharon Dean in the analysis involved in this work.

This project was supported by the Air Force Cambridge Research Laboratories, Air Force Office of Aerospace Research, through contract AF 19(604)-7988, and by a grant from the National Science Foundation.

#### REFERENCES

- Abe, S., Morphology of ssc and ssc\*, *J. Geomag. Geoelec.*, **10**, 153-163, 1959.
- Akasofu, S.-I., and S. Chapman, The sudden commencement of geomagnetic storms, *Vrania*, No. 250, Tarragona, Spain, 1960.
- Chapman, S., and J. Bartels, *Geomagnetism*, Clarendon Press, Oxford, 1940.
- Chapman, S., and V. C. A. Ferraro, A new theory of magnetic storms, *Terrestrial Magnetism and Atmospheric Elec.*, **36**, 77-97, 171-186, 1931; **37**, 147-156, 421-429, 1932; The theory of the first phase of a geomagnetic storm, *Terrestrial Magnetism and Atmospheric Elec.*, **45**, 245-268, 1940.
- Dessler, A. J., The propagation velocity of world-wide sudden commencements of magnetic storms, *J. Geophys. Research*, **63**, 405-408, 1958.
- Dessler, A. J., and E. N. Parker, Hydromagnetic theory of geomagnetic storms, *J. Geophys. Research*, **64**, 2239-2252, 1959.
- Ferraro, V. C. A., On the theory of the first phase of a magnetic storm: a new illustrative calculation based on an idealized (plane not cylindrical) model field distribution, *J. Geophys. Research*, **57**, 15-49, 1952.
- Ferraro, V. C. A., Theory of sudden commencements and of the first phase of a magnetic storm, *Rev. Mod. Phys.*, **32**, 934-940, 1960.
- Ferraro, V. C. A., W. C. Parkinson and H. W. Unthank, Sudden commencements and sudden impulses in geomagnetism: their hourly frequency at Cheltenham (Md.), Tucson, San Juan, Honolulu, Huancayo, and Watheroo, *J. Geophys. Research*, **56**, 177-195, 1951.
- Ferraro, V. C. A., and H. W. Unthank, Sudden commencements and sudden impulses in geomagnetism: their diurnal variation in amplitude, *Geofis. pura e appl.*, **20**, 27-30, 1951.
- Forbush, S. E., and E. H. Vestine, Daytime enhancement of size of sudden commencements at initial phase of magnetic storms at Huancayo, *J. Geophys. Research*, **60**, 299-316, 1955.
- Gold, T., *Dynamics of Cosmic Clouds*, North-Holland Publishing Company, Amsterdam, p. 10, 1955.
- Jackson, W., World-wide simultaneous magnetic fluctuations and their relation to sudden commencements, *J. Atmospheric Terrest. Phys.*, **160-172**, 1952.
- Matsushita, S., On sudden commencements of magnetic storms at higher latitudes, *J. Geophys. Research*, **62**, 162-166, 1957.
- Matsushita, S., Studies on sudden commencements of geomagnetic storms using IGY data from United States stations, *J. Geophys. Research*, **1423-1435**, 1960.
- Nagata, T., Sudden commencements preceded

- eliminary reverse impulse in a geomagnetic storm, *Nature*, 169, 446-447, 1952.
- T., and S. Abe, Notes on the distribution of magnetic storms in high latitudes, *Rep. Ionosphere Research*, 9, 39-44, 1955.
- H. W., Sudden commencements in the Greenwich magnetic records (1879-1944) and sunspot data, *Mon. Not. Roy. Astron. Soc., Phys. Suppl.*, 5, 159-185, 1948.
- Li, T., and A. J. Jacobs, Sudden commencement of magnetic storms and atmospheric ionospheric action, *J. Geophys. Research*, 62, 589-597, 1957.
- Sturrock, J. H., The transmission of geomagnetic disturbances through the atmosphere and interplanetary space, *Geophys. J. Roy. Astron. Soc.*, 2, 89, 1959.
- S. F., A new model of magnetic storms and aurorae, *Trans. Amer. Geophys. Union*, 38, 175-190, 1957.
- Sugiura, M., The solar diurnal variation in the amplitude of sudden commencements of magnetic storms at the geomagnetic equator, *J. Geophys. Research*, 58, 571-572, 1953.
- Sugiura, M., Some evidence of hydromagnetic waves in the earth's magnetic field, *Phys. Rev. Letters*, 6, 255-257, 1961a.
- Sugiura, M., Evidence of low frequency hydromagnetic waves in the exosphere, *J. Geophys. Research*, 66, 4087-4095, 1961b.
- Vestine, E. H., The immediate source of the field of magnetic storms, *J. Geophys. Research*, 58, 560-562, 1953.

(Manuscript received September 18, 1961;  
revised October 4, 1961.)



# Ionospheric Limitations on Attainable Satellite Potential

DAVID B. BEARD

*Lockheed Missiles and Space Division, Palo Alto, California  
and the University of California, Davis*

FRANCIS S. JOHNSON

*Lockheed Missiles and Space Division, Palo Alto, California*

**Abstract.** Artificial satellites orbiting in the ionosphere normally tend to acquire a slight negative charge due to the high velocity of the electrons relative to the ion and satellite velocities. (At very high altitudes where the ionospheric electron concentrations are small, and in the presence of solar radiation, satellites tend to have a small positive charge due to the photoelectric effect, which in this case predominates over the ionospheric effect.) If the attempt is made to change the potential of a satellite by ejecting energetic beams of electrons or positive ions, the ionosphere provides some rather stringent limitations on the potential that can be achieved, for a substantial potential on a satellite causes appreciable currents to flow between the satellite and the ionosphere, which is a highly conducting medium containing a large reservoir of charge. The physics of the ionospheric limitation on satellite charge is investigated, and it is shown how the satellite charge and potential depend on injection currents and ambient charge density for both intermittent and continuous injection currents.

**Introduction.** Artificial satellites, in general, are charged negatively [Jastrow and Pearce, 1960; Beard and Johnson, 1960], owing to the high velocity of ionospheric electrons compared with either the velocity of the satellite or the thermal velocity of the ambient ions. Although the charge of a large satellite is necessarily positive, motion across lines of force [Beard and Johnson, 1960], the entire satellite can be made negative only by ejecting a sizable current of energetic electrons, which occurs naturally at sufficiently high altitudes where the photoelectric effect due to solar radiation outweighs ionospheric effects. This paper investigates the possibility of producing high potentials on satellites by ejecting beams of electrons or positive ions, which may be required in some satellite missions. The study is relevant also to the possibility of artificially injecting measurable numbers of charged particles into the earth's radiation belts. Finally, the inquiry is of particular interest in its own right because it re-emphasizes various aspects of the high-altitude environment.

It is very difficult to establish and maintain a sizable satellite potential; a large amount of energy must be expended in withdrawing or injecting back into the environment the large number of electrons that results when there is

a sizable potential on the satellite. From an electrical standpoint, the most striking feature of the high-altitude environment is that it is a large reservoir of charge with high conductivity due to the small mass and consequent great mobility of electrons.

There is a much better possibility of producing a large negative potential on a satellite than of producing a positive potential. The neutralization current from the ionosphere in this case involves ions, not electrons. Owing to the low ion mobility compared with the electron mobility, the limitation on satellite potential is not as severe. The negative potentials due to ion currents are significantly lessened by secondary emission of electrons released as the ions strike the satellite surface. Even with this effect, however, large negative potentials should be producible.

Section 2 reviews the physics controlling the charge on passive satellites. Section 3 discusses the anticipated satellite potential and charge if a pulsed current of high-energy electrons is injected into the environment. Section 4 discusses the anticipated satellite potential and charge if a pulsed high current of energetic positive ions is ejected from the satellite; section 5, the anticipated satellite potential and charge for a continuous current of ejected electrons. Section 6



considers the possibility of developing a significant negative charge on the satellite if a beam of positive ions is ejected continuously. Several examples of interest to Van Allen layer studies are presented in section 7.

2. *Passive satellite.* Assuming a conducting sphere suspended stationary in the ionosphere, the electron current to it would initially exceed the ion current, owing to the greater velocity of electrons. The potential of the sphere would increase in a negative sense, and this potential on the sphere would repel electrons and reduce the electron current. It would also attract ions and increase the ion current, although in a less marked degree than in the case of the electrons. The negative potential attained in this way is just that which will reduce the electron current and slightly increase the ion current to the point where the two are equal. The potential can be calculated on the basis of either long or short mean free paths, with unchanged result. The effect of a magnetic field will be neglected in this section.

Suppose first that the mean free paths are short, and that the potential on the sphere is  $\varphi_0$ . Then, according to Chapman and Cowling, if diffusive equilibrium prevails, the electrons will be distributed according to a hydrostatic relationship

$$n_e = n_{e0} e^{-e\phi/kT} \quad (1)$$

where  $\varphi$  is the potential in space due to the sphere and  $n_{e0}$  is the undisturbed electron concentration, where  $\varphi = 0$ . The potential gradient does not affect the Maxwellian velocity distribution or the temperature. The electron current to the sphere is

$$\frac{1}{4} n_{e0} e^{-e\phi_0/kT} \left( \frac{8kT}{\pi m_e} \right)^{1/2} \text{ electron/m}^2 - \text{sec} \quad (2)$$

Similarly, the ion distribution is

$$n_i = n_{i0} e^{e\varphi/kT} \quad (3)$$

Near the sphere (within one mean free path), there will be some disturbance of these relationships, since the charged particles are not reflected by the wall but instead are neutralized. This situation was not considered by Chapman and Cowling; their expression applies rigorously only for particles that are not lost (or changed in character) at the boundary. The expression

is applicable as long as diffusion proceeds steadily. The solution would also be correct if the electrons and ions were reflected from the sphere without neutralization, in which case the potential on the sphere would have to be arbitrarily assigned.

If the mean free paths are long, again assuming a potential  $\varphi_0$  on the sphere, we must consider the detailed particle dynamics. Consider a fictitious spherical surface of radius  $R$  surrounding and concentric with the subject sphere, large enough so that the potential of the subject sphere is not felt at the outer sphere. Because of the shielding effects of the plasma, the outer sphere does not have to be much larger than the inner sphere in order to satisfy this condition. For ionospheric conditions, we may realistically assume the mean free paths to be larger compared with the size of the outer sphere. Consider particles entering the outer sphere at position  $S$ . (See Fig. 1.) If properly directed they will strike the inner sphere; to do this they must make an angle less than  $\alpha$  with the normal to the surface at  $S$ , where  $\sin \alpha = P_m/R$ .  $P_m$  is the impact parameter for a particle that just grazes the inner sphere, whose radius is  $a$ . From angular momentum considerations, it is easily shown that

$$P_m/a = (1 - 2e\varphi_0/mv^2)^{1/2}$$

The number of particles reaching the inner sphere is then

$$n_0 4\pi R^2 (m/2\pi kT)^{3/2} \cdot \int_0^{2\pi} \int_0^\alpha \int_{\sqrt{2e\varphi_0/m}}^\infty v^3 e^{-mv^2/2kT} \cdot \cos \theta \, dv \sin \theta \, d\varphi \, d\theta$$

Since

$$\int_0^{2\pi} \int_0^\alpha \cos \theta \sin \theta \, d\theta \, d\varphi = \pi \sin^2 \alpha = \pi (P_m/R)^2$$

the flux is

$$n_0 4\pi a^2 (m/2\pi kT)^{3/2} \cdot \int_{\sqrt{2e\varphi_0/m}}^\infty v^3 e^{-mv^2/2kT} \pi (1 - 2e\varphi_0/mv^2) \cdot \\ = n_0 \pi a^2 (2/\pi^{1/2}) (2kT/m)^{1/2} e^{-e\varphi_0/kT}$$

per unit area on the inner sphere is

$$(n_0/4)e^{-e\varphi_0/kT}(8kT/\pi m)^{1/2} \quad (7)$$

the same result obtained in the case mean free path if diffusion is assumed rapid. The independence of the result on concentration or collision frequency is, of course, well known. It is this property of the Maxwellian velocity distribution that gives rise to the validity of the hydrostatic equation in the atmosphere, as long as escape of atmospheric particles to space is unimportant.

In the case of a sphere moving at satellite velocity the ion current to the satellite is governed not only by the velocity of the sphere, not by the density of the ions. Consequently, the negative potential of the satellite, which must be maintained to limit the electron current to the same value as the ion current, is not the same as in the case of a stationary sphere. The ion current to a satellite at moderate altitudes ( $< 10^3$  km) is governed by the number of ions swept up by the forward motion of the satellite, and the satellite velocity greatly exceeds the ion thermal velocity. If the satellite were at plasma potential, the electron current to it would greatly exceed the ion current. Consequently, to balance the currents, the satellite must acquire a negative potential. At least in the nighttime, when photoelectron emission due to sunlight will not occur. This case was studied by *Jastrow and Pearce* [1960], ignoring the effect of magnetic field. *Johnson and Johnson* [1960] extended the treatment by taking into account the effect of the magnetic field, including the induction drag effect in addition to the charge drag. Although the result was derived by these authors entirely in reference to *Chapman and Cowling's* theory, we have just shown that a calculation in *Chapman and Cowling's* analysis leads to the same result even though, in general, *Chapman and Cowling's* theory for a static surface is not applicable when charged particles are swept upon reflection and also when the surface moves with respect to the plasma.

*Used electron sources.* We now consider the potential to be expected on a satellite when a intermittent electron beam is ejected. If an electron current of  $I$  amperes is maintained for a time  $\tau$ , a satellite orbiting in a vacuum would acquire a positive charge of  $I\tau$  coulombs. For a

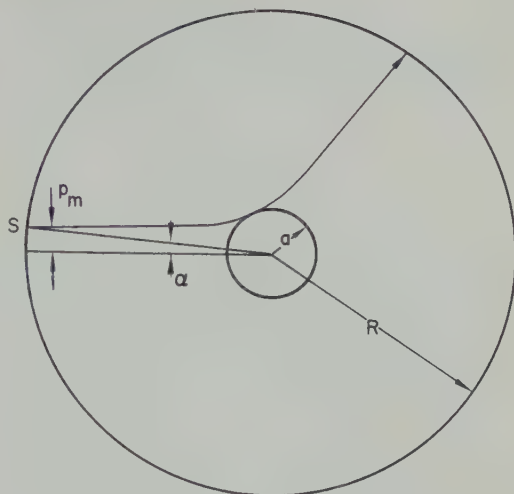


Fig. 1. Geometry for the approach of charged particles to a charged spherical satellite of radius  $a$ . Shown is the trajectory of a particle with impact parameter  $p_m$  which just grazes the satellite. The angle that the trajectory makes with the direction to the satellite at a distance  $R$  from the satellite is  $\alpha$ .

spherical satellite of radius  $a$  meters, this would result in a satellite potential of

$$\varphi = 9 \times 10^9 I\tau/a \quad (8)$$

This is the maximum voltage that would occur provided sufficient time elapses between pulses for the satellite to be neutralized (the time required would be infinite in the case of a perfect vacuum). If the electrons are to be ejected with an energy of  $\varphi_e$  volts, the radius of the satellite is limited by

$$a \geq 9 \times 10^9 I\tau/\varphi_e \quad (9)$$

otherwise the electrons could not all escape from the potential field of the satellite. For example, the limiting size is 36 meters if  $I = 100$  amperes,  $\tau = 4$   $\mu$ seconds, and  $\varphi_e = 10^6$  volts.

In a medium of charged particle density  $n_e$  electrons/m<sup>3</sup> and  $n_i$  ions/m<sup>3</sup> having a temperature of 1000°K, the ions will have an average velocity of  $10^3$  m/sec with respect to the medium,  $7 \times 10^3$  m/sec or  $3 \times 10^3$  m/sec with respect to the satellite at altitudes of  $10^3$  km and 5 earth radii respectively, and the electrons will have an average velocity of  $2 \times 10^5$  m/sec. Hence, because of their great mobility, the electrons will spiral along the magnetic field lines from both

sides, causing a negative counter current,  $I_e$ , to the charging current while the ions remain essentially immobile during the pulse time.

$$I_e = en_e 2\pi a^2 v_{th} \quad (10)$$

In order for  $I_e$  to equal  $I$ , however,  $a$  would have to be as large as  $\sqrt{50I}$  meters in the  $F$  layer, where  $n_e$  is a maximum, and even larger elsewhere. Thus a positive charge can be built up on the satellite during the pulse; however, this will attract more ambient electrons and thus increase the effective radius of the satellite for collection of electrons.

In order to compute the maximum charge on the satellite occurring at the end of a single pulse, we must compute the radial position at the end of the pulse time of all those electrons contained within a sphere of initial radius  $r_0$ , where  $r_0$  is the radius of the sphere containing a number of ambient electrons equal to the number of electrons ejected during the pulse. An electron at radius  $r_e$ , which was initially at  $r_0$ , will experience an acceleration due to the electric field (found from Gauss' law), given by

$$\frac{d^2 r_e}{dt^2} = -\frac{e}{m_e} \frac{1}{4\pi\epsilon_0 r_e^2} \cdot \left\{ It - \frac{4}{3} \pi en_e (r_0^3 - r_e^3 + 3r_e^2 \langle \frac{dr_i}{dt} \rangle t) \right\} \quad (11)$$

where  $\langle dr_i/dt \rangle$  is the effective radial velocity of the ions with respect to the satellite. The second term in the brace results because all the electrons initially within a sphere of radius  $r_0$  are within a sphere of radius  $r_e$  at time  $t$ , but the positive charge within a sphere of radius  $r_e$  is less by the amount of the second term in the brace than the positive charge within  $r_0$ , owing to the immobility of the ions.  $\langle dr_i/dt \rangle$  can be found by means of an equation similar to equation 11, but, because  $m_i \sim 30,000m_e$ , it is negligible compared with  $dr_e/dt$  and will be ignored. Because of the coefficient to the braces in equation 11, the electron acceleration is exceptionally high, again reflecting the high mobility of the electrons. The great mobility of the electrons suggests an approximation in which to zero order there is no charge separation (no electric field accelerating the electrons), and we can expand the solution in powers of  $m_e$ . Setting the brace of equation 11 equal to zero, we obtain the zero-order approximation to equation 11,

$$r_1^3 = r_0^3 - 3It/4\pi en_e = r_0^3(1 - t/\tau)$$

For the first-order approximation, let

$$r_e = r_0(1 - t/\tau)^{1/3} + x$$

$$\frac{dr_e}{dt} = -\frac{r_0}{3\tau} \frac{1}{(1 - t/\tau)^{2/3}} + \frac{dx}{dt}$$

$$\frac{d^2 r_e}{dt^2} = -\frac{2r_0}{9\tau^2} \frac{1}{(1 - t/\tau)^{5/3}} + \frac{d^2 x}{dt^2}$$

Substitution of equations 13 and 15 into equation 11 yields the next higher order approximation, the equation for  $x$ ,

$$\frac{d^2 x}{dt^2} = \frac{2}{9} \frac{r_0}{\tau^2} \frac{1}{(1 - t/\tau)^{5/3}} - \omega_p^2 x$$

where

$$\omega_p^2 = 4\pi e^2 n_e / 4\pi\epsilon_0 m_e$$

is the square of the plasma frequency. Expanding the particular solution of equation 16 in terms of the square of the reciprocal of the total number of plasma periods during the pulse and fitting the constants in the general solution to the conditions that, at  $t = 0$ ,  $r_e$  and  $dr/dt$  are both zero, we obtain

$$r_e = r_0 \left\{ \left( 1 - \frac{t}{\tau} \right)^{1/3} + \frac{1}{3\omega_p \tau} \sin \omega_p t + \frac{2}{9} \frac{1}{\omega_p^2 \tau^2} \left[ \frac{1}{(1 - t/\tau)^{5/3}} - \cos \omega_p t \right] \right\}$$

The expansion in  $\omega_p^{-2}$  is equivalent to an expansion in  $m_e$ . The oscillating terms are essentially small transient terms for  $\tau \gg \omega_p^{-1}$  resulting from initially turning on the electron beam, which sets up small plasma oscillations. (Their amplitude is less than 8.5 cm in the  $F$  layer for 100-ampere current lasting only 4  $\mu$ seconds.)

The last nonoscillatory term, which has been slightly overestimated, results from the charge separation and is the cause of the satellite potential and the accelerating electric field. Note that the inward velocity and acceleration of electrons are slowly varying in time, depending only on the inverse square and fifth powers respectively of the radial position (for constant charging current during the pulse). This is a consequence of the fact that, as soon as charge separation is sufficient to start the electron condensation, the charge within the condensation sphere of electrons varies slowly as the inverse



the radial position. The approximation is invalid if too large accelerations are obtained, as could result for low electron density, large charging currents, or small radii. The next approximation yields the result

$$r = r_1 \left[ 1 + \frac{2}{9} \frac{(r_0/r_1)^6}{\omega_p^2 \tau^2} - 20 \frac{(r_0/r_1)^{12}}{\omega_p^4 \tau^4} \right]$$

$r_1$  is defined by equation 12. For  $r_1$  too small for this asymptotic expansion to succeed, integrals for the particular solution to equation 11 may be evaluated numerically as long as  $r_1$  is not too small for particular problems. Otherwise equation 11 must be evaluated numerically for values of  $r$  for which the approximation fails. Alternatively, we may note that the approximation fails when  $r_1$  becomes sufficiently small that the correction term  $x$  to be comparable to  $r_1^2$ . A condition for the validity of the approximation may be expressed as

$$\begin{aligned} & [I^2 4\pi\epsilon_0 (m_e/e)/32(\pi n_e)^3]^{1/6} \\ & = 2.8 \times 10^5 I^{1/3} n_e^{-1/2} \end{aligned} \quad (18)$$

approximately equal to or less than this value, a simple upper value of the pulse voltage may be obtained by first finding the time at which an electron has the value of  $r_1$  if it was initially at  $r_0$ . The time will be called  $t_c$ . The electron's position at the end of the pulse time may then be estimated by assuming that it retains the velocity for the duration of the pulse as it has at the critical time  $t_c$ . In this way a slightly better approximation may be obtained for the number of electrons that have failed to reach the satellite at the end of the pulse time in order to have no charge on it.

Therefore, since

$$\tau = \frac{4}{3\pi n_e} r_0^3 / I \quad (19)$$

from equations 12, 18, and 19 we find that

$$\pi n_e (r_0^3 - r_1^3) / I = [1 - (r_1/r_0)^3] \tau \quad (20)$$

$$\tau - t_c = 0.0147 n_e^{-1/2} \quad (20a)$$

$$r \lesssim r_e(t_c) + \frac{dr_1(t_c)}{dt} \left[ \frac{r_1(t_c)}{r_0} \right]^3 \tau \quad (21)$$

$r_e(t_c)$  and  $dr_1(t_c)/dt$  are obtained from the terms on the right-hand side of equations 12 and 19.

Since no charge is created or destroyed within the plasma itself, the flux of electrons condensing from the plasma onto the satellite is nearly constant. That is,

$$4\pi r_e^2 \frac{dr_e}{dt} n_e = i \sim I \quad (22)$$

where  $i$  is the condensing electron current. Since  $r_e^2(dr_e/dt)$  is constant to very high order, as is readily deduced from equations 14 and 22,  $n_e$  is also constant down to about  $r_1(t_c)$  and is proportional to  $r_e^{-3}$  for  $r < r_1(t_c)$ ; thus the charge on the satellite at the end of  $\tau$  seconds is found to be

$$\begin{aligned} Q(\tau) &= \int_0^{r_e(\tau)} n_e(r_1(t_c)/r_e)^2 4\pi r_e^2 dr_e \\ &\sim 4\pi n_e r_e(\tau) (r_1(t_c))^2 \\ &= 2.0 \times 10^{-18} n_e r_e(\tau) (r_1(t_c))^2 \end{aligned} \quad (23)$$

The constant velocity approximation may be improved by solving equation 11 numerically or by assuming that  $t_c = \tau$ , which is nearly true.

$$r_e^2 \ddot{r}_e = k_1 I(\tau - t) - k_2 r_e^3 \quad (11a)$$

where

$$k_1 = (e/m_e)/4\pi\epsilon_0 = 1.58 \times 10^{18}$$

and

$$k_2 = 4\pi n_e k_1$$

Let  $\dot{r}_e = p$ . Then

$$\begin{aligned} p \frac{dp}{dr_e} &= \frac{k_1 I(\tau - t)}{r_e^2} - k_2 r_e \\ &< \frac{k_1 I(\tau - t_c)}{r_e^2} - k_2 r_e \end{aligned}$$

$$\begin{aligned} p^2 &= v_r^2(t_c) + 2k_1 I(\tau - t_c) \left[ \frac{1}{r_e(t_c)} - \frac{1}{r_e} \right] \\ &\quad + k_2 [r_e^2(t_c) - r_e^2] \end{aligned}$$

Assuming that  $t_c = \tau$ :

$$\begin{aligned} r_e &+ [2v_r^2(t_c)/k_2 - r_e^2(t_c) + r_e^2]^{1/2} \\ &= \{r_e(t_c) + [2v_r^2(t_c)/k_2]^{1/2}\} e^{\sqrt{k_2/2}(t_c - t)} \end{aligned}$$

For  $t \sim t_c$ ,

$$r_e(t) \sim r_e(t_c) - v_r(t_c)t$$



The neglect of the slight additional charge that leaves the satellite during the time  $t > t_c$  (which was done by assuming  $t_c \approx \tau$ ) is almost exactly balanced by neglecting the outward movement of the positive charge within the sphere  $r_e < r_e(t_c)$ .

It remains to show that negligible ions move out of a sphere of radius  $r_1(t_c)$ , where  $r_1(t_c)$  is given by equation 18, in time  $\tau$  seconds. The electric force on the positive ions at position  $r_i$  is equal and opposite to the force on the electrons at the same position; hence

$$\begin{aligned} \frac{d^2 r_i}{dt^2} &\leq \frac{2I^2/r_1^3}{r_1^2(4\pi en_e)^2} \frac{m_e}{m_i} \\ &= 1.7 \times 10^{31} I^2/n_e^2 r_1^5 \end{aligned} \tag{24}$$

If  $r_i$  is nearly constant for the duration of the pulse, the positive ions move a distance

$$\begin{aligned} \Delta r_i &\sim 8.5 \times 10^{30} I^2 \tau/n_e^2 r_i^5 \\ &= 3.8 \times 10^{-6} r_0^6/r_i^5 \end{aligned} \tag{25}$$

at the time  $\tau$ . In essence, since the positive ions are accelerated  $1/29,000$  as much as the electrons at the same radial position, their motion may indeed be neglected beyond  $r_1(t_c)$ , where the acceleration is used in the computation. Within  $r_1(t_c)$ , the electrons are conservatively treated as moving at constant speed with no acceleration. The ion mobility is related to the 'ion-plasma frequency,' which is  $6.13 \cdot 10^{-3}$  of the plasma frequency.

The maximum potential on the satellite which occurs at the time  $\tau$  can be estimated from equations 21 and 23. Since  $n_e$  remains constant everywhere in the vicinity of the satellite beyond  $r_1(t_c)$  the maximum electric field is always simply

$$\begin{aligned} E &= 0 \quad r \gg r_e(\tau) \\ E &= 2.8 \times 10^{-18} n_{e0} [r_e(\tau) - r] (r_1(t_c))^2 \\ &\quad r < r_e(\tau) \end{aligned} \tag{26}$$

and the electrical potential on the satellite is given by

$$\begin{aligned} \varphi(\tau) &\leq 1.8 \times 10^{-8} n_{e0} [r_1(t_c)]^2 \\ &\quad \cdot \left[ \frac{r_e(\tau)}{a} - 1 - \log_e \frac{r_e(\tau)}{a} \right] \end{aligned} \tag{27}$$

where  $a$  is the radius of the satellite.

4. Pulsed positive ion sources. A pulsed posi-

tive ion source has an effect on the medium very different from the effect of the electron source discussed in the previous section. Electrons, being highly mobile, are absent from any volume and at any time in which the movement of the positive charge is appreciable. Using Gauss' law, we again obtain the equation of motion for positive charges in the medium  $t$  times measured from the moment that electrons have been repelled from their vicinity and plasma ions experience attraction toward the satellite.

$$\ddot{r}_i = \frac{e/m_i}{4\pi\epsilon_0} \frac{It}{r_i^2}$$

Let

$$\begin{aligned} s &= [(e/m_i)I/4\pi\epsilon_0]^{1/3} t = 3.78 \times 10^4 I^{1/3} t \\ &\text{for oxygen ions} \end{aligned}$$

$$\frac{d^2 r_i}{ds^2} + \frac{s}{r_i^2} = 0$$

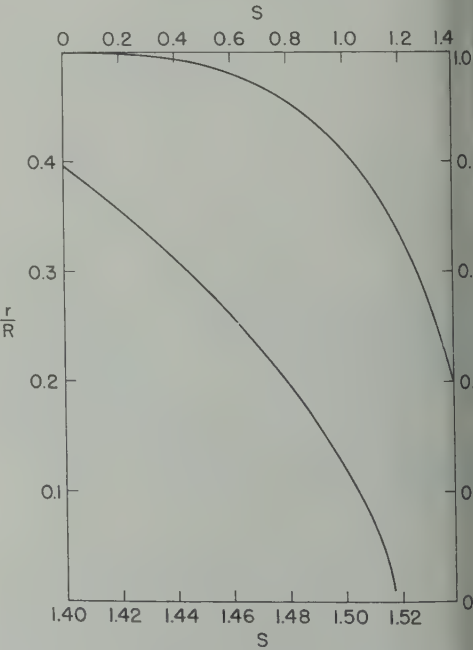


Fig. 2. Graph of particle position  $r/R$  as a function of  $S$ , where  $S$  is given as a function of time in equations 29 and 41 for positive ions and electrons, respectively.  $R$  is the initial characteristic particle position at  $t = 0$ . The ordinate scale for the upper curve is on the right of the figure, the abscissa for the upper curve is on the upper part of the figure. The lower abscissa and left-ordinate are for the lower curve.

TABLE 1. Charged Particle Radial Position and Radial Velocity as a Function of the Time (in appropriate units)  $s$  after the Particle Experiences the Electrostatic Attraction of a Charged Satellite

$S$	0	0.2	0.4	0.6	0.8	1.0	1.1	1.2	1.3
$R$	1	0.99867	0.98929	0.9635	0.9116	0.8205	0.7540	0.6680	0.5544
$S(r/R)$	0	0.02003	0.08070	0.1854	0.3444	0.5838	0.7532	0.9808	1.316
$\chi\varphi$	0	0.00013	0.00297	0.0165	0.0579	0.1797	0.2921	0.4887	0.8237
	1.35	1.40	1.42	1.44	1.46	1.48	1.50	1.51	1.515
	0.4827	0.3963	0.3560	0.3111	0.2601	0.2000	0.1234	0.07114	0.03483
	1.563	1.920	2.120	2.378	2.745	3.326	4.555	6.242	9.058
	1.179	1.799	2.202	2.781	3.696	5.394	10.02	19.09	40.93

ation 30 has been evaluated numerically; solution is presented as the graph in Figure 1. The condition for infinite time to be reached at  $s \sim 1.5$  or before, given by

$$5[(e/m_i)I/4\pi\epsilon_0]^{-1/3} = 4.0 \times 10^{-3} I^{-1/3} \text{ seconds} \quad (31)$$

oxygen ions.

charge on the satellite during the pulse is

$$= -It + \frac{4}{3}\pi r e_i (R^3(t) - a^3) = -I\tau + \frac{4}{3}\pi r e_i R^3(t) \quad (32)$$

$\tau$  is the duration of the pulse,  $t$  is measured from the start of the pulse, and  $R(t)$  is the initial position of the positive ions arriving at the satellite at time  $t$ . The ordinate of Figure 2 gives the value of the satellite radius to  $R(t)$  as a function of  $t$ . For example, at  $s = 1$ ,  $a/R(t) = R(t) = 1.22a$ .

result is very much affected by the presence of secondary electrons produced by the impact of the positive ions on the satellite surface. Space charge is unaffected, owing to the high energy of the emitted electrons, but the charge on the satellite is less than given in equation 32. If production of secondaries is included, equation 32 becomes

$$\frac{e/m_i}{4\pi\epsilon_0} \left[ -4\pi n_i \int_0^t \gamma(t) R^2(t) \frac{dR(t)}{dt} dt \right] \quad (28a)$$

the number of secondaries produced per

impacting ion; it is a function of time, since the energy of the impacting ions depends on the time after the pulse is initiated. A rough approximation to experimental observations for energies less than 100 kev is given by

$$\gamma(t) = 0.5E \text{ (kev)} \quad (33)$$

If the satellite radius is of the order of a meter or more, field emission is negligible for reasonable satellite potentials (anything less than  $10^8$  volts).

In general, if secondary electrons may be neglected, the charge within any sphere of radius  $A$  is given by equation 32. All times are measured from the time when the satellite charge is effective in attracting the ions, that is, from a time  $T$  after the pulse starts, given by

$$T = I^{-1} \frac{4}{3}\pi n_i A^3 \quad (34)$$

Therefore the voltage on the satellite (or at any point at radius  $a$ ) is given by (see equation 32):

$$\varphi = -\frac{1}{4\pi\epsilon_0} \int_a^{r_0} \frac{I\tau - \frac{4}{3}\pi n_i A^3 [R^3(t)/A^3]}{A^2} dA \quad (35)$$

where  $r_0$  is the radius of the sphere initially containing a charge  $I\tau$ .

$$\varphi = -\frac{1}{4\pi\epsilon_0} \left\{ I\tau \left[ \frac{1}{a} - \frac{1}{r_0} \right] - \frac{4}{3} \pi n_i \int_a^{r_0} A g(s) dA \right\} \quad (35a)$$

where  $g(s)$  is the reciprocal of the ordinate of Figure 2 and  $s$  is given by

$$s = I^{-1} \frac{4}{3}\pi n_i (r_0^3 - A^3) (eI/4\pi\epsilon_0 m_i)^{1/3}$$

The integration may be done numerically or by approximations to  $g(s)$

$$\begin{aligned} 1.48 < s < 1.52 & \quad g^{-1}(s) \sim 8.4 - 5.5s \\ 1.00 < s < 1.48 & \quad g^{-1}(s) \sim 2.71 - 1.71s \\ 0 < s < 1.00 & \quad g^{-1}(s) \sim 1 \end{aligned}$$

In many possible injection conditions, the pulse duration  $\tau$  is much less than the ion response time—the 'ion plasma frequency' ( $4\pi e^2 n_i / 4\pi\epsilon_0 m_i$ )<sup>1/2</sup>. For this condition, in which  $s < 1.5$ , the solution is given approximately by a series expansion in  $(t/r_0)^3$

$$r_i \approx R \left( 1 - \frac{e/m_i}{6(4\pi\epsilon_0)} \frac{It^3}{R^3} \right)$$

$$\varphi(a, \tau) = -\frac{1}{4\pi\epsilon_0} \quad (36)$$

$$\int_a^{r_0} \frac{I\tau - \frac{4}{3}\pi(r_i^3 - a^3)en_i}{r_i^2} dr$$

where

$$r_0 = (I\tau / \frac{4}{3}\pi en_i)^{1/3}$$

$$\varphi(a, \tau) \sim \frac{-I\tau}{4\pi\epsilon_0 a} \left( 1 - \frac{3}{2} \frac{a}{r_0} \right) \quad (37)$$

5. *Continuous electron sources.* If a steady continuous current of high-energy electrons is ejected from a satellite, it must be compensated by a cylinder of negative charge spiraling along magnetic field lines into the region of the vehicle. The effective cross-sectional area of the satellite to the electrons incident with thermal velocities from opposing sides of the vehicle is required by charge conservation to be

$$2\pi r_0^2 = I/v_{th}en_e \quad (38)$$

whence  $r_0$  is found to be

$$r_0 = 2.2 \times 10^6 \sqrt{I/n_e} \quad (39)$$

where the thermal velocity of the electrons is taken to be  $2 \times 10^5$  m/sec appropriate to an ambient temperature of about 1000°K.

In order to maintain an attractive field sufficient both to dominate the magnetic force and to deflect a 0.1-ev electron at a distance  $r_0$  from the satellite, the shielding effect of the condensing electron current must be exceeded for this distance. Throughout most of the volume within the sphere of radius  $r_0$  the potential energy of

the positive ions exceeds their kinetic energy; hence they are excluded. The problem is similar to that treated in the previous section which electrons were swept out of the volume of interest. If time is measured from the moment an electron enters the attractive unshielded field of the satellite, an equation of motion for the electron while in this attractive field resembles similar to equation 28.

$$\ddot{r}_e = -\frac{e/m_e}{4\pi\epsilon_0} \frac{It}{r_e^2}$$

Let

$$s = 1.165 \times 10^6 I^{1/3} t$$

and obtain

$$\frac{d^2 r_e}{ds^2} + \frac{s}{r_e^2} = 0$$

The charge on the satellite is simply the charge that accumulates during the time  $t_0$  for an electron to travel from  $r_0$  to the surface of the satellite. That is,

$$Q_0 = It_0$$

Thus, for any particular set of conditions found by means of equation 39. The satellite radius divided by  $r_0$  is located on the ordinate of Figure 2. The graph then yields a value for  $t_0$  that can be used in equation 41 to find  $t_0$ , and finally  $Q_0$  from equation 42. If the charge within a sphere of radius  $r$  is desired, the same procedure will give this charge if  $r$  is substituted for the satellite radius  $a$ . (These simple relationships unfortunately do not apply to the time-dependent pulsed problems treated in earlier sections.)

The voltage at radius  $r$  may be found by numerically evaluating the integral for the voltage given by

$$\varphi(r) = -\frac{I}{4\pi\epsilon_0 r_0} \int_1^{r/r_0} \frac{t dr'}{(r')^2}$$

Table 1 gives values for this integral as a function of  $(r/r_0)$ . For attraction times greater than  $s = 1.50$  [ $r/r_0 < 0.1234$ ]

$$\begin{aligned} \varphi(r) &= \frac{(I/4\pi\epsilon_0 r_0)(1.5r_0/r - 2.14)}{1.165 \times 10^6 I^{1/3}} \\ &= 7.72 \times 10^3 I^{2/3} \left( \frac{1.50}{r} - \frac{2.14}{r_0} \right) \end{aligned}$$

continuous positive ion source. In the case of continuous ejection of positive ions, electrons are ejected from the sphere in which the ions are attracted to the satellite and the equations of section 5 apply if equation 38 is substituted for equation 41,  $m_i$  replaces  $m_e$ , equation 40, and the satellite velocity  $V$  replaces  $v$  in equation 38, so that equation 39

$$\sqrt{I/\pi n_i} V \sim 1.6 \times 10^7 \sqrt{I/n_i} \quad (39a)$$

at a factor of 2 has disappeared in the case for  $r_0$ , since the positive ions are incident on only one side of the satellite.  $V$  has been taken to be  $8 \cdot 10^3$  m/sec.

The effect of the production of secondary electrons on the satellite surface is easy to include in the steady-state problem. Equation 39a be-

$$= 1.6 \times 10^7 \sqrt{I/n_i(\gamma + 1)} \quad (39b)$$

The efficiency for secondary electron production is given roughly by equation 33 for ions impinging on a light metal such as aluminum. If this value for  $r_0$  is substituted in the calculation or into equation 44 if equation 44 is valid, a better value for the voltage is obtained. In most circumstances in which equation 45 (given below) may be used, however, the efficiency may change a great deal, but the dependence of the potential on  $r_0$  is so weak that it is affected very little under the conditions of interest for equation 45.

$$s > 1.5 \quad r/r_0 < 0.1234$$

$$\frac{I(1.5/r - 2.14/r_0)}{4\pi\epsilon_0 3.78 \times 10^4 I^{1/3}} = 2.38 \times 10^5 I^{2/3} \left( \frac{1.5}{r} - \frac{2.14}{r_0} \right) \quad (45)$$

In this section and the previous sections questions of conservation of angular momentum have been neglected because the initial angular momentum due to the electron's thermal motion is much smaller than the product of their final angular momentum and a satellite radius of as little as 1 m. That is, the electrical potential increases much faster with decreasing  $r$  than is needed to conserve the angular momentum and yet cause the electrons to intersect a satellite. Similarly, the

electric field at the effective radius of the satellite's attractive field is greater than that needed to dominate the magnetic force causing the electrons to spiral along the geomagnetic field lines.

7. *Conclusions and examples.* It has been shown [Jastrow and Pearse, 1957; and Beard and Johnson, 1960] that, because of the great mobility of electrons, a conductor moving in the tenuous plasmas between a planetary atmosphere and interplanetary space will normally acquire a slight negative potential. If the conductor is made a source of high-energy electrons injected into the exosphere, however, a positive potential will develop due to the enormous mobility of the ambient electrons. It is difficult to induce a large positive potential in such an environment, as is well demonstrated for the separate cases of a pulsed and continuous high-energy electron source in sections 3 and 5, respectively, so that for most cases of interest the energy of the injected electrons at distances far from the satellite will not be appreciably affected by the positive potential they induce on the satellite.

For example, suppose that it is desired to produce a pulse of 100 amperes of 1-Mev electrons for 4  $\mu$ seconds in an environment of  $10^{14}$  electrons/m<sup>3</sup>, corresponding to the  $F$  layer. The sphere of electrons surrounding the satellite containing a number of electrons equal to the number of ejected electrons during the pulse has a radius,  $r_0$ , given by equation 19, of 18.1 m. The plasma frequency is  $1.70 \cdot 10^7$  radians/sec. The approximations used in this section are valid for electron positions greater than  $r_1$ , given by equation 18 to be 4.1 m. The first-order approximation is 10 per cent of the zero-order term in  $m_e$  at  $r_1 = 6$  m. The outermost electrons needed to neutralize the sphere which were initially at  $r_0 = 18.1$  m are at  $r_0(\tau)$  m at the end of the pulse, found by equation 21 to be  $6.2 - 2.0 = 4.2$  m. Hence at the end of the pulse there will result a maximum charge on the satellite, from equation 22, of  $3.0 \cdot 10^5$  c. Therefore, if the satellite has a radius of 1 m, it will have a retarding potential of less than  $1.7 \cdot 10^5$  volts at the end of the pulse time. A 1-Mev electron source will thus produce electrons of energy greater than 0.8 Mev at infinity under these conditions. The total charge neutralized will be  $4 \cdot 10^4$  c, and since the electron density is that of undisturbed space beyond  $r_1(t_e)$ , the small



charge of  $3 \cdot 10^{-8}$  c is quickly neutralized in the time following the pulse.

As a second example consider a continuous source of 1 ma of 1-Mev electrons in an environment of  $10^8$  electrons/m<sup>3</sup> corresponding to the exosphere at several earth radii. A satellite 1 m in radius will attract electrons from a distance given by equation 39 to be 6.96 m. From the value of the ordinate  $6.96^{-1} = 0.144$ , Figure 2 gives a value of  $s_0$  of 1.495 which by equation 41 corresponds to a time  $t_0$  of  $1.283 \cdot 10^{-8}$  sec. The charge on the satellite is  $+1.283 \cdot 10^{-8}$  c (equation 42). Equation 44 gives a satellite voltage of 92.7 volts. The difference between this result and that for the previous example is due to the current (a factor of  $\sim 10^{-5}$ ) inasmuch as the pulse time is long for both examples; the over-all power output is about the same.

A negative potential far in excess of the fraction of a volt expected on passive satellites will result, on the other hand, if the satellite is made a source of high-energy positive ions injected into the exosphere. Although the medium limits the potentials that can be obtained in this case also, the attainable negative potentials are very much higher than the attainable positive potentials, owing to the much more limited mobility of the environmental positive ions that carry the return current in this case.

A pulsed positive ion source injecting under conditions similar to the electron source in the first example would have an  $s_0$  (equation 29) of 0.70, which leads from Figure 2 to an  $r_0$  of only 1.06 m. Under these conditions equations 36 and 37 are valid, and therefore the potential on the

satellite at the end of the pulse would be  $-10^8$  volts. So few positive ions arrive at the satellite surface during this time that secondary electrons do not appreciably change this result. A longer pulse time would result in higher voltages. Field emission would not occur until the potential became of the order of  $10^8$  volts. Ionization of any environmental neutrals would greatly increase the conductivity of the medium and thereby slightly reduce the potential attainable on the satellite.

A continuous positive ion source in circumstances similar to the electron source in the second example would have an effective radius for attracting positive ions of 51 m (equation 32a).  $1/r_0 \sim 0.02$ , so that  $t \sim 1.52$ . Equation 45 is valid, and thus  $\phi = -3.47 \cdot 10^8$  volts. Secondaries are included (equations 33 and 39).  $r_0$  becomes 30 m, but the potential is essentially unchanged.

*Acknowledgments.* This material stems in part (sections 3 and 5) from a project sponsored by the Advanced Research Projects Agency, Department of Defense.

It is a pleasure to thank Dr. David Elliot for several interesting and helpful discussions.

#### REFERENCES

- Beard, D. B., and F. S. Johnson, Charge and magnetic field interaction with satellites, *J. Geophys. Research*, 65, 1-9, 1960.
- Jastrow, R., and C. A. Pearce, Atmospheric drag on the satellite, *J. Geophys. Research*, 62, 41423, 1957.

(Manuscript received July 3, 1961.)

## Effects of the Earth's Magnetic Field on the Orbit of a Charged Satellite

I. I. SHAPIRO AND H. M. JONES

*Lincoln Laboratory,<sup>1</sup> Massachusetts Institute of Technology  
Lexington 73, Massachusetts*

**Abstract.** The changes in the orbital elements of a charged satellite due to the  $\mathbf{v} \times \mathbf{B}$  force have been examined. We conclude that the ascending nodes of the Project West Ford dipoles may be detectably perturbed by it.

There has been considerable discussion in the literature of direct electromagnetic effects on satellite orbits. However, no such influences have yet been observationally established. In this note we examine the interaction of a charged satellite with the earth's magnetic field, and show that the orbit of the belt of 1-mil diameter fiber fibers (recently proposed as a passive wide communication system [Morrow, 1959]) may be observably perturbed by this interaction.<sup>2</sup> In particular, if these fiber satellites maintain a potential of about 10 volts, the right ascension of their ascending nodes will thereby be changed by approximately .0008 deg/day. For a positively charged fiber the node will regress; for a negatively charged fiber, it will progress.) This motion of the nodal position may be detectable after several months. The difficulty involved in observing the change in the spreading (dispersion) of the fiber may obscure this relatively small average motion of the nodes of the individual fibers. However, if the fibers are in polar orbits, the regression of their nodal positions may be considerably smaller than .0008 deg/day—at least in the first 200 days. The change in the argument of perigee is comparable to that of the node, but is more difficult to detect. The changes in the other orbital elements are much smaller.

We also examine briefly the effect of this magnetic field interaction on the orbits of charged meteoroids that may possibly be in circum-earth orbits.

**Models for satellite potential.** It has been suggested that the Project West Ford dipoles were generated with support from the U. S. Air Force. Several cases of this interaction have been considered previously [Fain and Greer, 1959; Westerbom, 1960].

It has been established in the last few years that close-in earth satellites become charged while orbiting the earth. The magnitude and sign of this natural electrostatic potential and their dependence on time and the orbit parameters are not well known. In order to make explicit calculations, we shall consider two models for the potential. In the first we assume that the charge on the satellite remains essentially constant during an orbital period, whereas in the second we assume that the charge varies sinusoidally over this period. Our results are quite sensitive to the particular model used; these models have been chosen primarily for convenience in calculation. However, we feel that the orbit perturbations derived from them provide reasonable bounds on the behavior to be expected from this magnetic interaction.

For any potential model, the concomitant acceleration,  $\mathbf{A}$ , of the center of mass of the satellite is

$$\mathbf{A} = \frac{q}{M} \frac{\mathbf{v}}{c} \times \mathbf{B} \quad \text{cm/sec}^2 \quad (1)$$

where  $q$  is the satellite charge in esu,  $M$  its mass in grams,  $(\mathbf{v}/c)$  its velocity relative to that of light, and  $\mathbf{B}$  the magnetic field of the earth in gauss. We neglect the contribution to  $\mathbf{A}$  of the electric field created by the time variations of the magnetic field which are caused mainly by the earth's rotation. Our results are therefore valid only for close-in satellites whose periods are short compared with 24 hours.

If we denote the colatitude measured from the south magnetic pole (which is located near the north geographic pole) by  $\Phi (0 \leq \Phi \leq \pi)$ , then the components of the magnetic field in

the radial and  $\Phi$  directions, respectively, are given approximately by

$$B_{\Phi} = -\frac{m}{r^3} \sin \Phi \quad (2)$$

$$B_r = -\frac{2m}{r^3} \cos \Phi \quad (3)$$

where  $r$  is the distance from the center of the earth ( $r \geq R_0$  = radius of earth), and  $m$  is the magnetic dipole moment of the earth ( $m \simeq 8.2 \times 10^{25}$  gauss/cm<sup>3</sup>).

For each model of the satellite charge, we calculate the changes in the orbital elements due to equation 1 by integrating the set of first-order differential equations relating the elements to the components of this perturbing acceleration [Moulton, 1914]. The usual components chosen are along the radial direction ( $\hat{r}$ ), along the direction ( $\hat{s}$ ) in the orbit plane perpendicular to the radial direction (and making an acute angle with  $\mathbf{v}$ ), and along the direction ( $\hat{w}$ ) perpendicular to the orbit plane chosen so that  $\hat{r} \times \hat{s} = \hat{w}$ . In terms of these unit vectors,  $\mathbf{A}$  can be written as

$$\mathbf{A} = \frac{qm\mu^{1/2}}{cMp^{1/2}r^3} \left[ f(i, \Omega, \Omega_m) \cdot [-(1 + e \cos \theta)\hat{r} + e \sin \theta \cdot \hat{s}] \right]$$

$$\Delta a = 0$$

$$\Delta e = -2\pi\lambda\psi(1 + e - e^2) \sin i_m \sin i \sin (\Omega_{mo} - \Omega)$$

$$\Delta \omega = 2\pi\lambda \{ 3 \cos i \cos i_m + [3 \sin i - (\sin i)^{-1}] \sin i_m \cos (\Omega_{mo} - \Omega) \}$$

$$\Delta \Omega = -2\pi\lambda \{ \cos i_m - \cot i \sin i_m \cos (\Omega_{mo} - \Omega) \}$$

$$\Delta i = -2\pi\lambda \sin i_m \sin (\Omega_{mo} - \Omega)$$

$$\begin{aligned} &+ \left\{ f\left(i + \frac{\pi}{2}, \Omega, \Omega_m\right) [2(1 + e \cos \theta) \right. \\ &\quad \cdot \sin (\theta + \omega) + e \sin \theta \cos (\theta + \omega)] \\ &- f\left(\frac{\pi}{2}, \Omega + \frac{\pi}{2}, \Omega_m\right) \\ &\quad \cdot [2(1 + e \cos \theta) \cos (\theta + \omega) \\ &\quad \left. - e \sin \theta \sin (\theta + \omega)] \right\} \hat{w} \end{aligned} \quad (4)$$

where

$$f(i, \Omega, \Omega_m) = \cos i \cos i_m + \sin i \sin i_m \cos (\Omega_m - \Omega)$$

and where  $p = a(1 - e^2)$ . The quantities  $a$ ,  $\omega$ ,  $\Omega$ , and  $i$  are the usual set of satellite orbital elements with  $a$  given in centimeters.  $\theta$  is the true anomaly of the satellite;  $\mu$  is the product of the gravitational constant and the mass of the earth in cgs units; and  $\Omega_m$ ,  $i_m$  represent the position of the (time dependent) node and inclination of the magnetic equator. (For the purposes of this paper, we have assumed that the geographic center of the earth coincides with that of the magnetic dipole field. We also note that, owing to the rotation of the earth,  $\Omega$  increases by at least  $20^\circ$  during each orbital period. The value of  $i_m$  is approximately  $10^\circ$  and the south magnetic pole is located at approximately  $280^\circ$ E longitude.)

*Satellite with constant charge.* For a satellite that maintains a constant charge during each revolution, we have calculated the changes per revolution in the orbital elements, due to the magnetic interaction, to the lowest nonvanishing order in  $\psi$ , the satellite's period in sidereal days. (In view of that statement following equation 1, the inclusion of higher order terms in  $\psi$  is inconsistent with our approximation.) These changes are:

where

$$\lambda = \frac{qm}{cMp^{3/2}\mu^{1/2}}$$

$$\psi = \frac{\omega_e a^{3/2}}{\mu^{1/2}}$$

and where  $\omega_e$  is the angular velocity of the earth and  $\Omega_{mo}$  is the longitude of the node (corresponding to  $i_m \approx 10^\circ$ , measured in the usual sense of the magnetic equator at the time the satellite last passed through perigee. In deriving the results it was assumed that the changes

elements (due to all perturbations) are during one revolution.

parameter  $\lambda$  is (to within about a factor the ratio of the magnitude of the average perturbation due to the magnetic interaction to that due to the earth's gravitational field.  $\psi$  is the ratio of the period of the satellite to that of the earth's rotation about its axis.

Since  $\Omega_m$  has a 24-hour period, all terms in equation 6 of the form  $\sin(\Omega_{mo} - \Omega)$  or  $\cos(\Omega_{mo} - \Omega)$  will lead to relatively very small perturbations over times long compared to a day. Provided, of course, that the satellite period is short compared with 24 hours. Under these conditions, the largest long-term effects are in  $\Omega$  and  $\omega$ :

$$\left. \begin{aligned} \dot{\Omega} &\approx -3 \cos i \cdot \Delta\Omega \\ \dot{\omega} &\approx -2\pi\lambda \cos i_m \approx -2\pi\lambda \text{ rad/rev} \end{aligned} \right\} \quad (9)$$

if orbital inclination is not too small.

*Satellite with sinusoidally varying charge.* If the charge on the satellite were to vary sinusoidally during each revolution, then the changes in the elements for close-in near-earth satellite orbits would be given to zero order in  $\psi$  by

$$\left. \begin{aligned} \dot{\Omega} &= 0 \\ \dot{\omega} &= -\pi\lambda(1 - e^2) \cos(\alpha + \omega) \cdot f(i, \Omega, \Omega_{mo}) \\ \dot{i} &= -\frac{\Delta e}{e} \left( \frac{1 + e^2}{1 - e^2} \right) \tan(\alpha + \omega) - \cos i \cdot \Delta\Omega \\ \dot{\alpha} &= \frac{\pi\lambda e}{4 \sin i} \left\{ [2 \cos \alpha \sin \omega + 3 \sin(\alpha + \omega)] f\left(i + \frac{\pi}{2}, \Omega, \Omega_{mo}\right) \right. \\ &\quad \left. - [2 \sin \alpha \sin \omega - \cos(\alpha + \omega)] f\left(\frac{\pi}{2}, \Omega + \frac{\pi}{2}, \Omega_{mo}\right) \right\} \\ \dot{\omega} &= \frac{\pi\lambda e}{4} \left\{ [2 \cos \alpha \cos \omega + \cos(\alpha + \omega)] f\left(i + \frac{\pi}{2}, \Omega, \Omega_{mo}\right) \right. \\ &\quad \left. - [2 \sin \alpha \cos \omega + 3 \sin(\alpha + \omega)] f\left(\frac{\pi}{2}, \Omega + \frac{\pi}{2}, \Omega_{mo}\right) \right\} \end{aligned} \right\} \quad (10)$$

$$q(t) = q \sin[\alpha + \omega + \theta(t)] \quad (11)$$

where  $\alpha$  is an (arbitrary) phase angle.

In contrast to the model treated in the last section, we note here that (for small eccentricities) the motion of the node is smaller by a factor of  $e$ , whereas the motion of  $\omega$  is increased by approximately  $e^{-1}$ . In addition, for nonpolar orbits, the eccentricity is subject to much larger long period variations.

For both models,  $\Delta a$  vanishes identically ( $da/dt = 0$ ). Since the  $\mathbf{v} \times \mathbf{B}$  force does no work, and since the satellite is moving under the influence of the conservative gravitational field of the earth, we see immediately that there is no change in energy, and hence that  $\Delta a$  vanishes. (Since eddy current and/or hysteresis losses are quite negligible compared with the orbital energy, and since the motion with respect to the center of mass is only weakly coupled to that of the center of mass, these losses have virtually no effect on  $a$ .)

*Numerical estimates.* To estimate the magnitude of the element changes described in equations 6 and 10, we have only to calculate  $\lambda$  (equation 7). For a given orbit,  $\lambda$  depends solely on the charge-to-mass ratio of the satellite. Hence, for a given potential on the satellite,  $\lambda$  will be determined by the capacity-to-mass ratio ( $C/M$ ). For a sphere, this ratio is given by

$$\frac{C}{M} = \frac{4\pi\epsilon_0\rho}{M} \text{ farads/g} \quad (12)$$

where  $\epsilon_0 = 10^{-11}/36\pi$  farads/cm, and  $\rho$  is the



sphere radius in centimeters. For a thin wire, we have

$$\frac{C}{M} \approx \frac{2\pi\epsilon_0 l}{M \log_e \left( \frac{l}{\rho} \right)} \quad (13)$$

where  $l$  and  $\rho$  are the length and radius, respectively, in centimeters.

The pertinent quantities for Vanguard I, Echo I, and a possible fiber design are given in Table 1.

TABLE 1

Vanguard I	Echo I	Fiber
$\rho = 8 \text{ cm}$ $M = 1.5 \times 10^3 \text{ g}$	$\rho = 1.5 \times 10^3 \text{ cm}$ $M = 6.5 \times 10^4 \text{ g}$	$l = 1.8 \text{ cm}$ $\rho = 1.3 \times 10^{-3} \text{ cm}$ $M = 8. \times 10^{-5} \text{ g}$

Assuming that each satellite is charged to the same potential, one gets

$$\frac{\lambda_{\text{fiber}}}{\lambda_{\text{Echo I}}} = 7 \times 10^4$$

$$\frac{\lambda_{\text{fiber}}}{\lambda_{\text{Vanguard I}}} = 3 \times 10^5 \quad (14)$$

It is clear that the fiber satellites are much more sensitive to this  $\mathbf{v} \times \mathbf{B}$  interaction.

If the fibers maintain a potential of  $-10$  volts and are in near-circular orbits at a mean altitude of  $3500 \text{ km}$ , one finds

$$\lambda = -3 \times 10^{-7} \quad (15)$$

hence the ascending node would progress at  $\approx 8 \times 10^{-4} \text{ deg/day}$ . The line of apsides in this case will retrogress at a rate  $3 \cos i$  times as great. If the charge varies sinusoidally, then for a near-circular orbit the largest variation will be a precession of the apsidal line at a rate of  $\approx 4 \times 10^{-4} e^{-1} \sin(\alpha + \omega) \cos i \text{ deg/day}$ .

We note that for a near-polar orbit and a constant potential on the satellite,  $\omega$  changes at a much slower rate than  $\Omega$ . For a sinusoidally varying potential,  $\omega$  changes more rapidly than  $\Omega$  by a factor of  $\approx e^{-2}$  (provided that  $e^2 \ll \cos i$ ).

Let us now discuss the possibility of observing these motions of the fiber satellites. For detectability it is necessary that they be at least comparable in magnitude to the dispersion of the

fiber belt, and larger than the uncertainties of the similar motions caused by other perturbing forces. If the belt is near-polar, then (excepting the contribution due to dispensing) the dispersion in  $\Omega$  [Shapiro and Jones, 1961] increases at the average rate of  $\approx 10^{-4} \text{ deg/day}$  for the first 200 days of its life. This dispersion is primarily due to the interaction of the effects of sunlight pressure with those of the second harmonic of the earth's gravitational field. If the maximum separation speeds of the dipoles from the dispensing package are as much as  $\pm 3 \text{ m/sec}$  in directions perpendicular to the orbital plane of the dispenser, then the dispersion in  $\Omega$  (due to the spread in inclination angles caused by dispensing) will be approximately twice  $8 \times 10^{-4} \text{ deg/day}$ . Hence, the effects of a constant potential of  $\pm 10$  volts may be observable if accurate measurements of the plane of the belt orbit are made over an extended period of time. If the potential is only of the order  $\pm 1$  volt, detection of this  $\mathbf{v} \times \mathbf{B}$  effect will be extremely difficult.

Observing the effect through the change in  $\omega$  is more doubtful, since an accurate determination of this belt parameter is considerably more difficult. However, if the orbit is not near-polar but is near-circular and if the potential were to vary sinusoidally, then the change in  $\omega$  might be detectable.

If an otherwise unexplained motion of the ascending node of the belt is observed, then the possibility that this motion is due to the  $\mathbf{v} \times \mathbf{B}$  effect should be seriously considered. (Other possibilities which our analysis ignores include, for example, the possible influences of plasma effects on the nodal motion. A discussion of recent work in this field, together with an extensive bibliography, can be found in Chopt [1961].) Assuming that the motion is caused by this effect, we can obtain a lower bound estimate of the minimum possible magnitude which the potential of the fibers must have exceeded during some portion of their orbits. Of course, in any event, from the motion of the node alone it is impossible to determine rigorously whether (to what extent) the charge on the fibers varies during an orbital period.

*Effect on micrometeoroid orbits.* Data obtained from Explorer I led Hibbs [1961] to conclude that some micrometeoroids may be in circumterrestrial orbits. The orbits of such dust particles will also be influenced by the earth's magnetic

Assuming that the micrometeoroids are spherical, and considering the effects of solar radiation pressure, we note that the minimum possible radius for these particles to have been found in the solar system is  $\rho_m \approx .6/d \times 10^{-4}$  where  $d$  is the micrometeoroid density in g/cm<sup>3</sup>.

For illustrative purposes, we consider a spherical particle of radius  $.8 \times 10^{-4}$  cm which corresponds to an iron sphere with radius  $10 \rho_m$ . This particle is in orbit about the earth at an altitude of about 3000 km and maintains an electrically constant potential of  $-1$  volt, then due to the  $\mathbf{v} \times \mathbf{B}$  force its node will progress at a rate of approximately  $.2$  deg/day while its line of nodes will precess at  $\approx .6 \cos i$  deg/day. The charge on the dust particle varies sinusoidally, then for small eccentricities the elements most strongly affected are  $\omega$  and  $e$ : With a constant potential of  $1$  volt,  $\omega$  will change at a maximum rate of approximately  $.1/e$  deg/day and  $e$  at a maximum rate of  $.002/\text{day}$ . While all these perturbations are quite large, their direct experimental verification is obviously impossible at present. (We also note that the effects on the other elements of sunlight pressure is even smaller.)

The models we have considered above for the effects of charge on satellites are probably inadequate representations of the actual

physical situation. Therefore our results should not be taken literally. They are primarily intended to show the type and order of magnitude of the orbit perturbations that may be expected from the interaction of a charged satellite with the earth's magnetic field. Any other (more physically meaningful) charge variation can be treated in the same manner.

#### REFERENCES

- Chopra, K. P., Interactions of rapidly moving bodies in terrestrial atmosphere, *Rev. Mod. Phys.*, **33**, 153-189, 1961.
- Fain, W. W., and B. J. Greer, Electrically charged bodies moving in the earth's magnetic field, *ARS J.*, **29**, 451-453, 1959.
- Hibbs, A. J., The distribution of micrometeorites near the earth, *J. Geophys. Research*, **66**, 371-378, 1961.
- Morrow, W. E., Orbital scatter communication, presented at the XIII General Assembly of the International Scientific Radio Union, London, England, 1960.
- Moulton, F. R., *Introduction to Celestial Mechanics*, The Macmillan Company, New York, 1914.
- Shapiro, I. I., and H. M. Jones, Lifetimes of orbiting dipoles, *Science*, **134**, 973-979, 1961.
- Westerman, H. R., Perturbation approach to the effect of the geomagnetic field on a charged satellite, *ARS J.*, **30**, 204-205, 1960.

(Manuscript received August 3, 1961.)



## A 'Layered' Exponential Model of Radar Refractivity

F. L. MARTIN AND C. G. WALDRON<sup>1</sup>

*U. S. Naval Postgraduate School  
Monterey, California*

**Abstract.** A 'layered' exponential model for the vertical distribution of refractivity in the form

$$N = N_i \exp [-c_i (z - z_i)]$$

is investigated. Here  $N_i$  and  $z_i$  are the refractivity and height, respectively, at a mandatory pressure level. The parameter  $c_i$  is the 'best fit' when  $N = N_{i+1}$  is the value at the next level where  $z = z_{i+1}$ . A formula for  $c_i$  is derived and is found to give good agreement, layer by layer, with the above model. This model appears to have particular merits for the case of air-to-air radar tracking.

**Introduction.** Recently, revised standards of the vertical distribution of refractivity have been proposed by several investigators. Among foremost among these proposals have been the CRPL reference atmosphere-1958 [see, for example, *Bean and Thayer*, 1959] and the C model atmosphere proposed by *Campen, Ingham, and Plank* [1957]. Both models make it possible to express the distribution of refractivity  $N = (n - 1) \times 10^6$ , where  $n$  is the index of refraction, by means of empirically determined relationships of the form

$$N = N_s \exp (-\bar{c}z) \quad z \leq 9 \text{ km} \quad (1)$$

where  $N_s$  is the surface-mean value of the refractivity,  $z$  is the height above the earth's surface, and  $\bar{c}$  is the mean value of a so-called 'refractivity factor.' The parameter  $\bar{c}$  is the best-fit constant in the exponent of (1). *Bean and Thayer* [1959] gave values for  $\bar{c}$  lying in the range 0.1062 to 0.1540 (km)<sup>-1</sup> as  $N_s$  ranges from 0 to 450  $N$  units, respectively. A value of 0.1218 corresponds to  $N_s = 313$ , a representative mid-latitude surface value of refractivity. However, above 9 km, *Bean and Thayer* give  $N$  by the formula

$$N = 105 \exp [-0.1424(z - 9)] \quad z \geq 9 \text{ km} \quad (2)$$

where the value of  $\bar{c}$  is, in general, somewhat larger above 9 km than below.

<sup>1</sup> Present address, Fleet Weather Central, Guam.

The values of  $N$  and  $N_s$  are determined from meteorological data by use of the Smith-Weintraub expression

$$N = 77.6(p/T) + 3.73 \times 10^5(e/T^2) \quad (3)$$

where  $p$  is the atmospheric pressure and  $e$  is the water-vapor pressure, both in millibars, and  $T$  is the absolute temperature.

The main purpose of model investigations of  $N$ , based upon climatology, has been to determine reasonable values of the *average ray bending* as a function of the initial ray direction and the height above the transmitter. The earliest standard for this purpose, the 4/3 earth, suffers from the defect [*Bean and Thayer*, 1959] that 'at low heights it gives too little bending, while at high altitudes it gives too much bending.'

One may write Snell's law for a spherically homogeneous atmosphere in the form

$$n(z + a) \cos \theta = n_I(z_I + a) \cos \theta_I \quad (4)$$

where  $\theta$  is the elevation angle at any height  $z$  along the ray trajectory and  $a$  is the radius of the earth. The subscript  $I$  on the right side of (4) indicates known initial conditions along the ray. Using (4), *Bean and Thayer* [1959] gave essentially the following result for the total bending angle  $\tau_{1,2}$  along a ray passing through arbitrary points 1 and 2:

$$\tau_{1,2} = - \int_{z_1}^{z_2} \frac{10^{-6} (dN/dz) dz}{\tan \theta} \quad (5)$$



It must be recalled that  $\tan \theta$  is known as a function of height through (4), provided that  $n = 1 + 10^{-6} N$  is known for all  $z$ . In the use of (4) and (5), horizontal variations of  $N$  have been neglected; however, on the average, horizontal gradients of  $N$  are small compared with those in the vertical.

In the study presented here, a *layer-by-layer* determination of an exponential model was undertaken. This was done by representing the value  $N_{i+1}$  at the  $(i+1)$ th mandatory radiosonde level in terms of that at the  $i$ th level,  $N_i$ , by means of the equation

$$N_{i+1} = N_i \exp [-c_i(z_{i+1} - z_i)] \quad (6)$$

where  $z_{i+1}$  and  $z_i$  are the heights at the  $(i+1)$ th and  $i$ th mandatory levels, respectively. The parameter  $c_i$ , called the decay factor, may be obtained directly by taking natural logarithms of both sides of (6), leading to

$$c_i = \frac{\ln N_i / N_{i+1}}{z_{i+1} - z_i} \quad (7)$$

Once  $c_i$  has been obtained an exponential formula

$$N = N_i \exp [-c_i(z - z_i)] \quad (8)$$

may be interpolated over the height-range  $z_i$  to  $z_{i+1}$ .

Values of  $c_i$  computed according to (7) may be based upon individual daily radiosonde data, or upon *climatological data* if a model atmosphere for a given locality is desired.

In section 3, it will be shown empirically that  $c_i$  varies with elevation. However, for purposes of computational convenience one may wish to obtain a bulk-exponential model in the form of (1), valid for the entire layer 0 to 9 km, or some comparable layer. This is possible if successive functions in the form of (6) are known. By repeated multiplication of such functions, one obtains

$$\begin{aligned} N_{i+1} &= N_s \exp [-(c_i \Delta z_i + \dots \\ &\quad + c_2 \Delta z_2 + c_1 \Delta z_1)] \\ &= N_s \exp [-\bar{c}(z_{i+1} - z_s)] \end{aligned} \quad (9)$$

where  $\Delta z_i = z_{i+1} - z_i$  is the thickness of the  $i$ th layer, and  $\Delta z_1 = z_2 - z_s$  is the thickness of the first layer. Note that  $\bar{c}$  is simply the weighted mean of the  $c_i$  in the layer  $z_s$  to  $z_{i+1}$ . Moreover,

an  $N$  distribution in the form of (9) may be applied to any sublayer of the layer  $z_s$  to  $z_{i+1}$ , for example  $z_j$  to  $z_{i+1}$ , with  $j < i+1$ .

In section 2 an alternative formula (equation 14) is derived, relating  $c_i$  to the vertical lapse rate, temperature and of humidity in the  $i$ th layer. In section 3, values of  $c_i$  are computed first by (7) and then by (14). Comparisons are made on the basis of mean data for the winter season 1958-1959 at several climatologically diverse stations.

2. *An alternative formula for  $c_i$ .* The refractivity  $N$  of (3) may be written in the form

$$N = N_d + N_w$$

where  $N_d = 77.6p/T$ , and  $N_w$  is the term involving water vapor on the right side of (3). Figure 1 illustrates the average magnitudes of  $N_d$  and  $N_w$  as functions of height, after *Campe, Cunningham, and Plank* [1957]. Taking the partial derivative of  $N$  with respect to  $z$  leads to

$$\begin{aligned} \frac{\partial N}{\partial z} &= \frac{77.6}{T} \frac{\partial p}{\partial z} - \frac{77.6p}{T^2} \frac{\partial T}{\partial z} \\ &\quad + \frac{3.73 \times 10^5 e}{T^2} \left( \frac{1}{e} \frac{\partial e}{\partial z} - \frac{2}{T} \frac{\partial T}{\partial z} \right) \end{aligned} \quad (10)$$

Making use of the hydrostatic equation and the equation of state, we have

$$\frac{\partial p}{\partial z} = -\frac{gp}{R_d T} = -\frac{\gamma_A p}{T} \quad (11)$$

where  $\gamma_A = g/R_d = 34.14^\circ\text{K/km}$  is the 'autoconvective' lapse rate. In (11), virtual temperature has been replaced by absolute temperature with very slight error. Combining (10) and (11), and using the notation  $\gamma = -\partial T/\partial z$ ,  $N_d = 77.6p/T$  and  $N_w = 3.73 \times 10^5 e/T^2$ , we obtain

$$\frac{\partial N}{\partial z} = -N_d \left( \frac{\gamma_A - \gamma}{T} \right) + N_w \left( \frac{1}{e} \frac{\partial e}{\partial z} + \frac{2\gamma}{T} \right)$$

Then, with  $N_d = N - N_w$ , the last equation becomes

$$\begin{aligned} -\frac{1}{N} \frac{\partial N}{\partial z} &= \left\{ \left( \frac{\gamma_A - \gamma}{T} \right) \right. \\ &\quad \left. - \frac{N_w}{N} \left[ \frac{1}{e} \frac{\partial e}{\partial z} + \frac{\gamma + \gamma_A}{T} \right] \right\} \end{aligned} \quad (12)$$

Using finite differences in all derivatives of  $N$  in the  $i$ th layer, we may express (12) in the form

$$\frac{-\ln N_{i+1}}{1 - z_i} = \left\{ \left( \frac{\gamma_A - \gamma_i}{T_i} \right) \right. \\ \left. \left( \frac{N_w}{N} \right)_i \left[ \frac{1}{e_i} \left( \frac{\partial e}{\partial z} \right)_i + \frac{\gamma_i + \gamma_A}{T_i} \right] \right\} \quad (13)$$

$\gamma_i$  represents the mean lapse rate, while the symbols  $1/T_i$ ,  $1/e_i$ ,  $(N_w/N)_i$  represent the mean value of the corresponding element in the  $i$ th layer. Combining (7) and (13), we

$$\frac{\gamma_A - \gamma_i}{T_i} - \left( \frac{N_w}{N} \right)_i \left[ \frac{1}{e_i} \left( \frac{\partial e}{\partial z} \right)_i + \frac{\gamma_i + \gamma_A}{T_i} \right] \quad (14)$$

second term on the right side of (14) indicates the effect of a strong lapse of vapor pressure increase  $c_i$ .

To simplify the computations resulting from we have used values of  $1/T_i$ ,  $(N_w/N)_i$ , and at the base of each layer (rather than layer  $i$ s). The value of  $(N_w/N)_i$  may be approximated by the empirical expressions for  $N_w$  and from the model atmosphere of *Campen, Cunningham, and Plank* [1957]:

TABLE 1. Proposed Values of  $N_w/N$  at Various Levels, from Equation 15

$p$ , mb	$z_p$ , km	$N_w/N$
1013.3	0	0.1361
850	1.46	.1080
700	3.01	.0789
500	5.57	.0238
$p \leq 400$	$z_p \geq 7.18$	.0000

$$\frac{N_w}{N} = 1 - 0.8639 \exp (.00668z) \quad z \leq 25 \quad (15)$$

where  $z$  is in thousands of feet. Equation 15 leads to the values of  $N_w/N$  up to 400 mb given in Table 1. In this table only non-negative values of  $N_w/N$  have been considered.

3. *Comparison of computations of  $c_i$ .* For eight climatologically diverse stations (Adak, Denver, Kodiak, Lake Charles, Ship 'N,' Ship 'P,' Tatoosh, Washington, D. C.), mean values of refractivity were computed for each mandatory level, except for the 1000-mb level (for which the surface value was substituted), using (3). The data period was December 1, 1958, through February 28, 1959, and for this

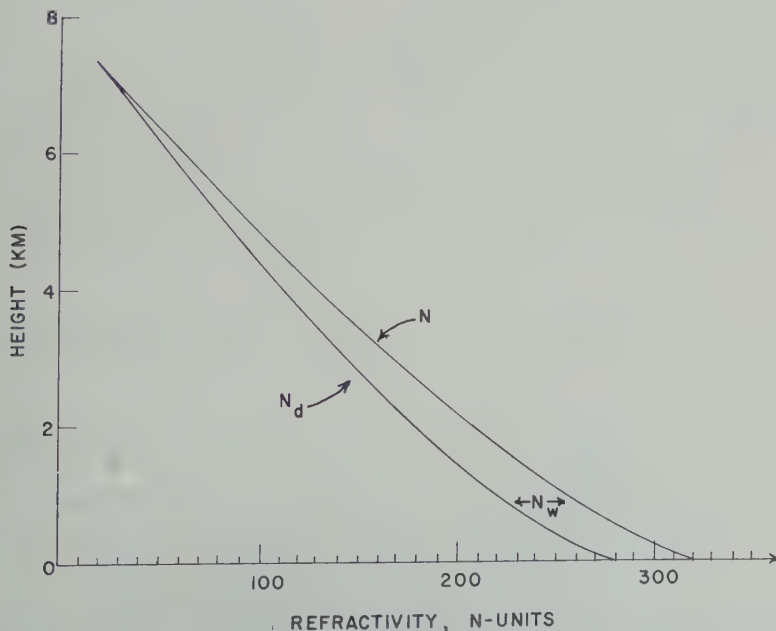


Fig. 1. Variation of standard refractivity with height, after *Campen, Cunningham, and Plank* [1957].

TABLE 2. Three-Month Mean Values of  $N_i$  at Indicated Pressure Levels, in  $N$  units

Pressure, mb	Station							
	Adak 3 Meters*	Denver 1611 Meters	Kodiak 8 Meters	Lake Charles 5 Meters	Ship N 6 Meters	Ship P 6 Meters	Tatoosh 31 Meters	Washington D.C. 88 Meters
Surface	312.8 (1002.7 mb)	254.3 (831.7 mb)	311.3 (1002.8 mb)	328.0 (1021.1 mb)	344.6 (1020.1 mb)	314.0 (992.6 mb)	322.8 (1014.8 mb)	309.5 (1009.7 mb)
850	261.6		262.3	267.6	271.8	261.1	265.8	261.3
700	215.6	211.9	216.7	217.1	215.5	214.3	217.1	217.4
500	161.1	157.0	160.9	155.6	153.5	158.5	159.0	157.9
400	133.5	130.5	133.1	127.6	127.6	131.3	131.4	130.4
300	104.9	102.8	104.6	100.1	100.8	103.0	103.8	102.5
250	87.6	88.4	88.2	86.6	86.8	87.3	88.8	87.8
200	70.5	71.6	69.8	71.9	71.2	69.9	71.2	71.4
150	52.0	53.7	51.9	55.0	54.7	51.8	53.0	53.6
100	34.6	36.4	34.7	38.0	37.8	34.8	35.6	36.5
50	17.3	18.1	17.4	18.5	18.3	17.2	17.8	18.1
25	8.6	9.0	8.7	9.0	8.9		8.9	8.9

\* Surface height is listed under each station; mean station pressure is enclosed in parentheses.

period 180 checked radiosonde reports were extracted for each specified station and mandatory level in the northern hemisphere data tabulations [U. S. Dept. of Commerce, 1958-1959]. To reduce the amount of computation, 90-day mean temperatures and humidities were computed for each station and level, and then mean  $N_i$  values were obtained (Table 2). The humidity contribution to  $N$  was slightly overestimated by the technique employed in this paper: the mean humidity was obtained using only those reports having no motorboating. However for

$p \leq 700$  mb, motorboating occurred at least one-third of the time. A test of the humidity overestimate was conducted for the period January 1-15, 1959, at Washington, D. C. leading to the following results:

	700 mb	400 mb
(1) $\bar{\epsilon}$ , all reports	$\bar{\epsilon} = 1.39$ mb	$\bar{\epsilon} = 0.116$ mb
(2) $\bar{\epsilon}$ , motorboat- ing excluded	$\bar{\epsilon} = 2.12$ mb	$\bar{\epsilon} = 0.165$ mb
(3) $N$ error, using (2)	$\Delta N = 3.9 N$ units	$\Delta N = 0.3 N$ units

TABLE 3. Three-Month Mean Values of  $c_i$  in  $(\text{km})^{-1}$ , Computed from Equation 7, Sample Means of Each Layer, and Their Standard Deviations

Pressure, mb	Station									
	Adak	Denver	Kodiak	Lake Charles	Ship 'N'	Ship 'P'	Tatoosh	Washing- ton, D.C.	Sample, $\bar{c}_i$	Std. Dev. of Mean
Surface-										
850	0.1349		0.1300	0.1344	0.1557	0.1250	0.1380	0.1209	0.1341	0.0111
850-700	0.1286	0.1255	0.1277	0.1317	0.1454	0.1395	0.1328	0.1218	0.1316	0.0072
700-500	0.1174	0.1201	0.1215	0.1261	0.1389	0.1207	0.1213	0.1240	0.1238	0.0066
500-400	0.1206	0.1165	0.1190	0.1195	0.1114	0.1184	0.1226	0.1229	0.1189	0.0034
400-300	0.1261	0.1240	0.1258	0.1194	0.1169	0.1226	0.1211	0.1197	0.1220	0.0030
300-250	0.1437	0.1261	0.1441	0.1194	0.1223	0.1377	0.1208	0.1328	0.1315	0.0090
250-200	0.1614	0.1480	0.1627	0.1296	0.1371	0.1571	0.1677	0.1328	0.1496	0.0138
200-150	0.1701	0.1571	0.1624	0.1466	0.1458	0.1593	0.1625	0.1691	0.1591	0.0083
150-100	0.1482	0.1541	0.1514	0.1608	0.1551	0.1482	0.1513	0.1510	0.1525	0.0044
100-50	0.1510	0.1541	0.1523	0.1666	0.1622	0.1548	0.1592	0.1645	0.1581	0.0050
50-25	0.1554	0.1665	0.1652	0.1676	0.1728		0.1544	0.1599	0.1631	0.0061

results from all reports, it was necessary to convert motorboating reports into probable humidities, using Table 18 of the *Journal of Radiosonde Observations* [WBAN, 1958]. Using the Washington test sample as a basis for all stations, we found that the climatological values of  $c_i$  computed by (7) are high by 3.1 per cent in the layer 700 to 900 mb.

In vapor pressures at levels higher than 900 mb were missing at all stations used except at 'N,' where occasionally 300-mb reports were available. Hence for  $p \leq 300$  mb, only the term of (3) was considered.

Values of  $c_i$  computed according to (7) are given in Table 3. For this computation, the values of  $\ln(N_i/N_{i+1})$  formed from Table 2 are multiplied by the 90-day mean thicknesses of each layer, which were also determined from the data of [U. S. Dept. of Commerce, 1958-1959]. The values of  $c_i$  in Table 3 were used to plot

mean values  $\bar{c}_i$  (over all eight stations) versus height at the layer center in Figure 2. Note that the logarithm of pressure has been introduced as a secondary ordinate. Note also that the mean value  $\bar{c}$  over the layer from the surface to 9 km is close to 0.1300, a value reasonably consistent with that proposed in CPRL-1958 model.

The climatological value of  $\bar{c}_i$  decreases with height up to the 500 to 400-mb layer and then increases abruptly to the 200 to 150-mb layer, above which a reasonably constant value appears to be maintained. These features may be explained qualitatively by reference to (14). The first term on the right side of (14) indicates that where  $\gamma_i$  is largest (smallest),  $c_i$  tends to be smallest (largest). In addition, the humidity correction, which is generally proportional to  $(N_w/N)_i$ , tends to be close to zero at levels of 6 to 8 km where  $\gamma_i$  is also a maximum. At elevations above the tropopause, the value of  $\gamma_i$

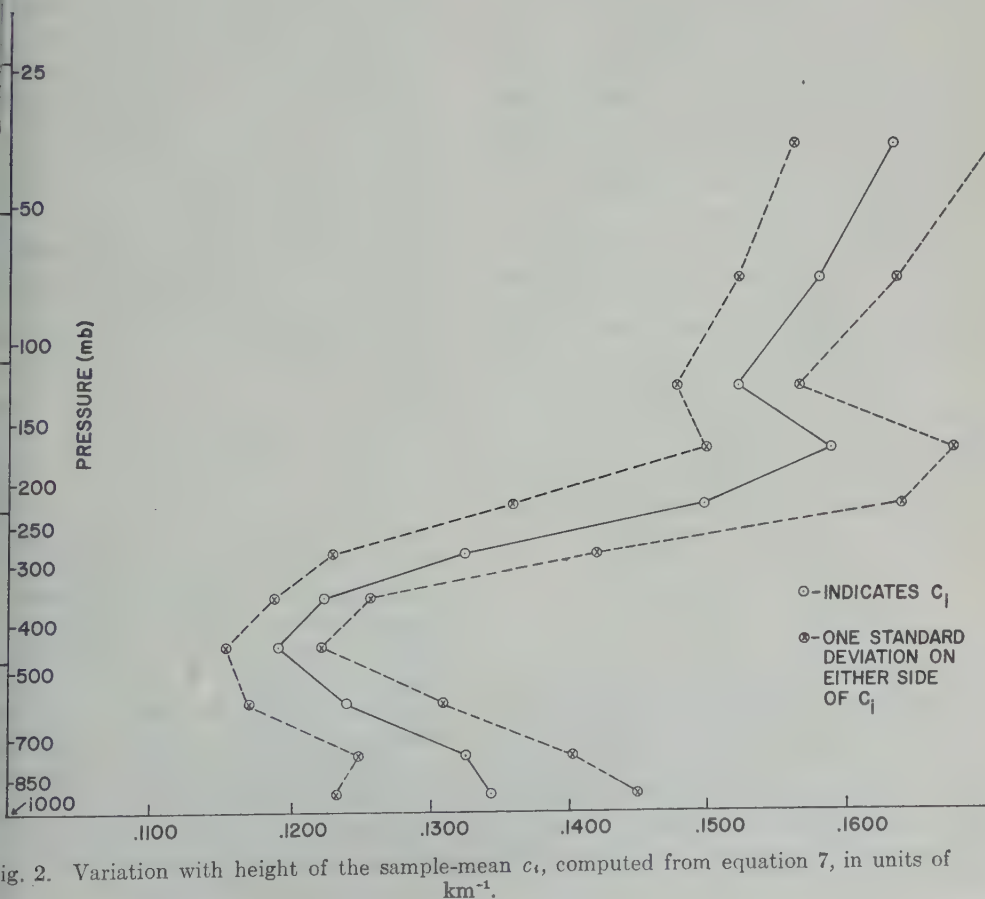




TABLE 4. Three-Month Mean Values of  $c_i$  in (km)<sup>-1</sup> Calculated by Equation 14, but Omitting Moisture Correction above 400 mb. Mean error is Computed Relative to the Sample  $\bar{c}_i$  of Table 3.

Pressure, mb	Station								Sample, $\bar{c}_i$	Mean Error
	Adak	Denver	Kodiak	Lake Charles	Ship 'N'	Ship 'P'	Tatoosh	Washing- ton, D.C.		
Surface-										
850	0.1507		0.1239	0.1324	0.1267	0.1400	0.1316	0.1226	0.1322	-0.00
850-700	0.1393	0.1384	0.1507	0.1221	0.1311	0.1362	0.1330	0.1157	0.1348	0.00
700-500	0.1187	0.1121	0.1208	0.1133	0.1171	0.1180	0.1168	0.1207	0.1172	-0.00
500-400	0.1237	0.1165	0.1243	0.1148	0.1085	0.1223	0.1213	0.1197	0.1189	0.00
400-300	0.1217	0.1147	0.1213	0.1083	0.1078	0.1193	0.1151	0.1150	0.1156	-0.00
300-250	0.1431	0.1241	0.1432	0.1153	0.1124	0.1383	0.1322	0.1258	0.1299	-0.00
250-200	0.1616	0.1425	0.1632	0.1268	0.1318	0.1531	0.1538	0.1416	0.1468	-0.00
200-150	0.1628	0.1586	0.1576	0.1472	0.1438	0.1593	0.1538	0.1563	0.1549	-0.00
150-100	0.1523	0.1514	0.1514	0.1462	0.1459	0.1500	0.1519	0.1518	0.1501	-0.00
100-50	0.1526	0.1607	0.1521	0.1734	0.1729	0.1545	0.1571	0.1616	0.1606	0.00
50-25	0.1540	0.1619	0.1548	0.1709	0.1698		0.1563	0.1664	0.1630	-0.00

tends to be negative and  $T_i$  is relatively low, both factors contributing to highest values of  $c_i$ .

The dashed curves of Figure 2 denote one standard deviation (for all eight stations) relative to the mean  $\bar{c}_i$ . Figure 2 illustrates that the 250 to 200-mb layer, in which the greatest interdiurnal and geographic variability of tropopause height occurs, is also the seat of the greatest standard deviation of  $c_i$ .

Next, values of  $c_i$  have been computed using equation 14 and are listed in Table 4. In this connection, it was again necessary to make use of the 90-day mean temperature and humidity data. The values of  $N_w/N$  have been taken from Table 1, although more appropriate values for specific areas could be assigned if area climatological studies of the type depicted in Figure 1 were available. Finite-difference methods for each layer were employed in using (14). Thus, for example, a typical term of (14) is

$$\frac{1}{e_i} \left( \frac{de}{dz} \right)_i = \frac{1}{e_i} \frac{e_{i+1} - e_i}{z_{i+1} - z_i}$$

As a check on the accuracy afforded by (14), the mean value of  $c_i$  obtained from (7) has been subtracted from that obtained from (14). The mean algebraic difference in each layer has been entered in the last column of Table 4. The mean difference is -0.0020, representing a percentage difference of 1.4. However the mean absolute difference between Tables 3 and 4 is approxi-

mately 5 times as large. These larger differences are induced primarily by the time-averaging and finite-differencing procedures employed.

Equation 7 affords, in principle, a more precise model representation of  $c_i$  in the  $i$ th layer than is given by (14). The latter represents an approximation owing to the use of the expression for  $N_w/N$  from (15), which will not apply everywhere, nor in all seasons. However the rather close agreement between the results afforded by equations (7) and (14) indicates the usefulness of the latter in making *semiquantitative assessments* of the ray curvature relative to the horizontal. This can be done, for example, by means of

$$\frac{\Delta \theta}{\Delta s} \doteq \left[ \frac{1}{a} + 10^{-6} \left( \frac{N_{i+1} - N_i}{z_{i+1} - z_i} \right) \right] \cos \theta \quad (1)$$

which is a finite-difference approximation to (5).

4. *Summary.* Table 3 presents some mean values for eight widely separated stations during the winter season of 1958-1959. These results permit extension of previous refractivity models to other geographic areas and give an added fine-structure detail with height. However, it must be re-emphasized that the computation of  $c_i$  by (7), or more qualitatively by (14), need not be restricted to mandatory levels or to climatological studies, but may be applied to arbitrary layers of an individual sounding. The use of (14) in conjunction with (4) and (5) would th

the computation of ray trajectories in an area having negligible horizontal gradient

computation of ray trajectories is frequently carried out [see, for example, *Bean and 1959*] using a simple mean decay factor 'troposphere,' which for approximate heights extends from 0 to 9 km. However, the fact that  $c_1$  varies with height suggests that in research from an elevated source, say from an aircraft, one might achieve somewhat better results by using a mean decay factor  $\bar{c}$  for the 3- to 9-km range with a model

$$N_3 \exp [-\bar{c}(z - 3)]$$

$$3 \text{ km} \leq z \leq 9 \text{ km} \quad (17)$$

where  $N_3$  is the  $N$ -value at 3 km. The refractivity for heights  $z \geq 9$  km would presumably be unaffected.

*Acknowledgment.* Appreciation is expressed to CDR Leo C. Clarke, USNR, for his reading of the manuscript and for his helpful comments.

#### REFERENCES

- Bean, B. R., and G. D. Thayer, Models of the atmospheric radio refractive index, *Proc. IRE*, **47**, 740-755, 1959.
- Campan, C. F., Jr., R. M. Cunningham, and V. G. Plank, Electromagnetic wave propagation in the lower atmosphere, chap. 13, sec. 1, of *Handbook of Geophysics*, Geophysics Research Directorate, Air Force Cambridge Research Center, Bedford, Mass., 1957.
- U. S. Department of Commerce, *Northern Hemisphere Data Tabulations Daily Bulletin*, Washington, D. C., Dec. 1, 1958 through Feb. 28, 1959.
- WBAN, *Manual of Radiosonde Observations (Circular P)*, 7th ed., Govt. Printing Office, Washington, D. C., 1957.

(Manuscript received July 10, 1961;  
revised September 28, 1961.)



# Polar Ionospheric Spread Echoes and Radio Frequency Properties of Ice Shelves

S. EVANS

Scott Polar Research Institute  
Cambridge, England

**Abstract.** Records from three stations in the Antarctic and one Arctic drifting station show that downward radiation from an ionosonde aerial is reflected from sea water under the ice on which the station is built. As the ice is several wavelengths thick, an interference pattern is established which makes it possible to derive (a) the thickness and dielectric constant of the ice and (b) the direction from which ionospheric spread echoes arise. Spread *F* frequently occurs at vertical incidence in the polar regions.

## INTRODUCTION

As pointed out by Piggott and Barclay (1954) that dry snow and ice are transparent to radio waves in the frequency range used in ionospheric sounding. They showed that the 'ground' loss at Royal Society base, Halley Bay, was accounted for by assuming the principal reflection to be at the sea water under the ice on which the ionosonde was built.

In this paper we shall consider in more detail the behavior of the wave is to be expected in these circumstances and what is observed at three ionosonde stations in the Antarctic and at one Arctic drifting station. The results show that range spread-ionospheric *F* echoes frequently occurs at vertical incidence in the polar regions. A value for the dielectric constant of snow in the range 1.5 to 2.0 Mc/s is derived as a by-product. The possibility of applying these ideas to snow depth measurement is discussed.

## A SIMPLE MODEL

Consider a uniform layer of snow of depth *d* having dielectric constant  $\epsilon'$  lying on sea water, as shown in Figure 1. The notation used is  $\epsilon'$  for the real part and  $\epsilon''$  for the imaginary part of the relative permittivity. Let us dispose of the properties of sea water first. For frequencies below 1 Mc/s,  $\epsilon' = 81$ , and for the lowest salinity only found the conductivity  $\sigma$  falls to approximately 1 mho/meter [Dorsey, 1940]. Thus  $\epsilon''$  is unity for a frequency *f* of the order of 1 Mc/s, which means that it behaves as a perfect conductor at frequencies much lower than

In snow,  $\epsilon'$  and  $\epsilon''$  vary over a wide range with frequency, temperature, and density [Kuroiwa, 1954; Yoshino 1961], but the power factor  $\epsilon''/\epsilon'$  is much less than unity for frequencies greater than 1 Mc/s under all conditions. Thus the electric field strength reflection coefficient versus frequency, when a plane wave is incident on the top snow surface, may be derived by analogy with a terminated transmission line. The 'ground

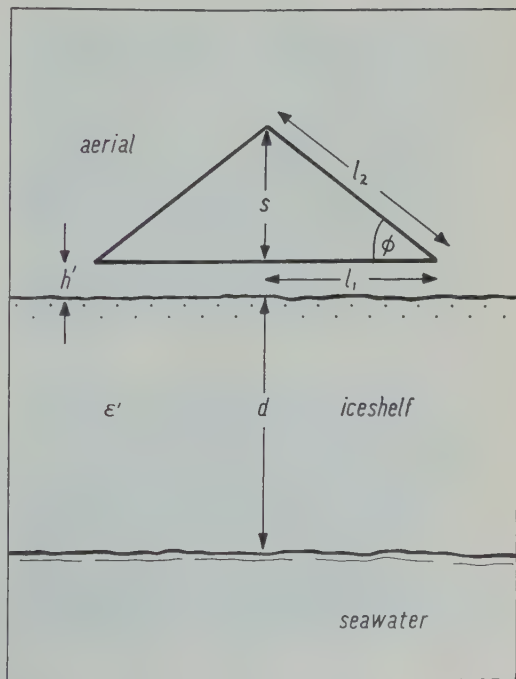


Fig. 1. The dimensions of a delta aerial on an ice shelf.



TABLE 1. Station List

Station	Position	$S$ , meters	$\sin \phi$	Periods Analyzed 1958
Ellsworth	78S 41W	18.9	0.690	March, June Sept., Dec.
Little America V	78S 162W	18.9	.690	March, June Sept., Dec.
Halley Bay	76S 36W	21.0	.414	Jan., April, Aug.
Fletcher's ice is.	81N 104W	18.9	.690	March, June Sept., Dec.

loss' derived from the strength of multiple ionospheric echoes by *Piggott and Barclay* [1961] must be attributed to a loss in propagation through the snow, not to reflection from the top surface.

At the ionosonde stations considered (see Table 1) delta aerials are used, for which the theoretical far field strength has been given by *Bailey* [1951]. The aerial dimensions are shown in Figure 1;  $h'$  is small, and  $h$  is equal to  $d\sqrt{\epsilon'}$  in

our case. The field is the resultant of two vectors whose phase rotates with periods of  $2\pi h/\lambda$  and  $(S + 2h)\pi/\lambda$ , the first derived from the horizontal limbs of the aerial and their image, the second from the sloping limbs and their image. It is not assumed that the value of  $h$  is large compared with the dimensions of the aerial, but it is found in the examples given in this paper that these do not affect the result beyond the effect on the free space polar diagram.

ANALYSIS OF IONOGRAMS

*Ellsworth.* Ionograms for all seasons frequently show gaps, corresponding to minimum upward radiated power, in  $E$  and  $F$  traces at certain fixed frequencies separated by an approximately constant frequency interval. Examples are shown in Figure 2, and the analysis separately for four seasons, in Figure 3. The width of each block covers the extreme range over which any narrow gaps were observed in an otherwise continuous echo. At least ten occurrences were counted in each block before the existence was considered established, but at Ellsworth only the strongest ionospheric echoes obscure the

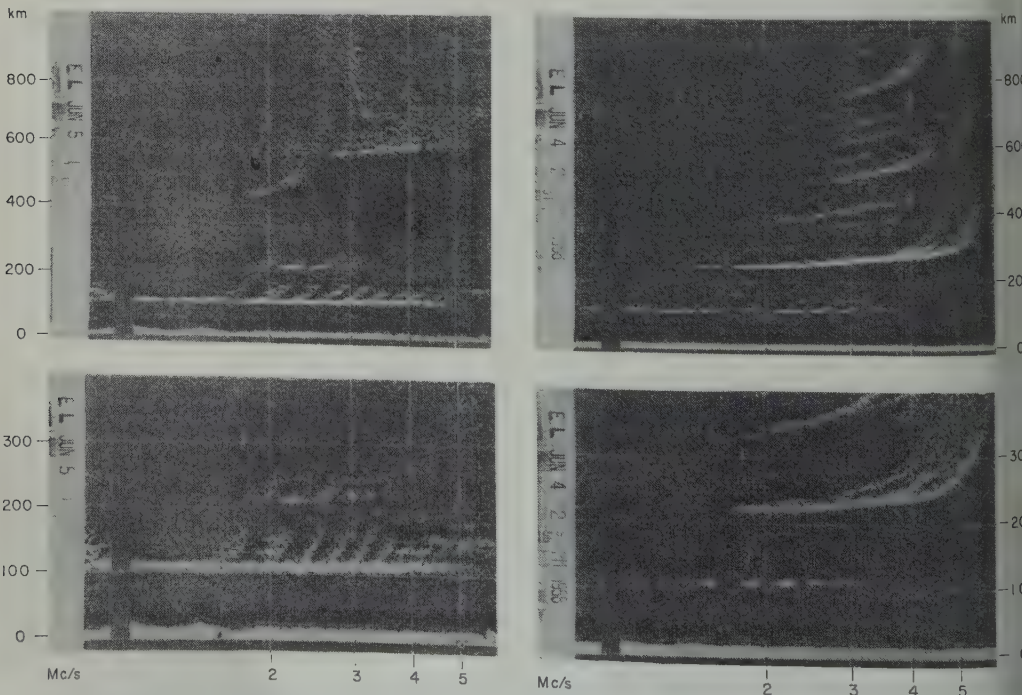


Fig. 2. Sample ionograms from Ellsworth, the left-hand pair showing range spread and the lower pair having an extended height scale.

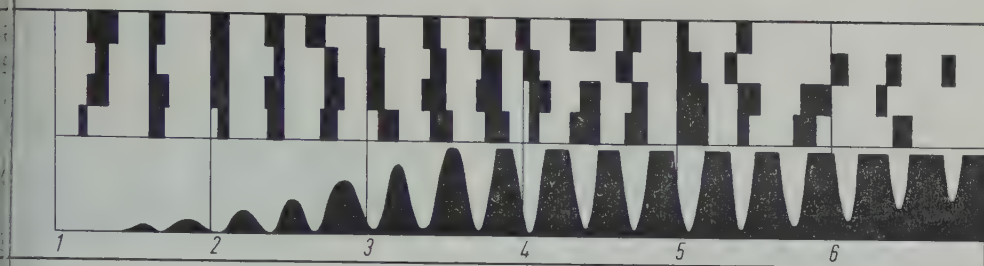


Fig. 3. At the top, analysis of Ellsworth ionograms for four different seasons. Each block shows the range of frequencies in which a narrow gap might be observed in an otherwise continuous echo. Below is plotted the power radiated vertically according to Bailey's equation with  $h = 440$  m.

The difference between the seasons is considered significant.

At the bottom of Figure 3, for comparison, is plotted the power radiated vertically according to Bailey's equation with  $h = 440$  meters. The model of the ice shelf, and the use of the far field are clearly adequate to explain the features of the aerial polar diagram at Ellsworth.

*Little America V.* The minima are much more regular than at Ellsworth, and it is possible to identify with certainty here. This we can explain by supposing that the bottom of the ice shelf has a lower reflection coefficient due to ice. A characteristic scale size for the irregularities of the bottom dimension of the irregularities would explain why certain orders are consistently missing from the observed interference pattern shown in Figure 4. We also find that the spacing between the minima is not nearly so constant that we can be sure of the best value of  $h$ , but a computed curve is given for  $h = 490$  m.

*Little America Bay.* In Figure 5 an earlier, independent analysis by W. R. Piggott (private communication) precedes the three seasonal analyses by the author. It is clear that most of the minima agree but that they cannot be fitted

into a single, equally spaced series. However, they do fall into two series, one of which has the expected minimum when extrapolated to zero frequency. The spacing of both series considered separately is  $0.60$  Mc/s, which corresponds to the computed result for  $h = 254$  m, plotted below. No explanation of the second series can be offered. It implies the existence of a downward wave having a constant phase difference (not a constant time delay) from the expected wave. There should be no upward wave in this displaced phase. Further observations are to be made at Halley Bay with a single dipole aerial in a different position on the ice shelf.

*Fletcher's ice island.* From glaciological studies it is known that the thickness of the ice here is comparable with the height of the aerial. Two series of minima having different spacings are found as shown in Figure 6; both have minima when extrapolated to zero frequency. It is quite possible that the narrower spacing is produced by a longer path length within the ice allowed by the shape of the bottom surface. A computation for  $h = 130$  m which agrees well with the more widely spaced series is shown for comparison.

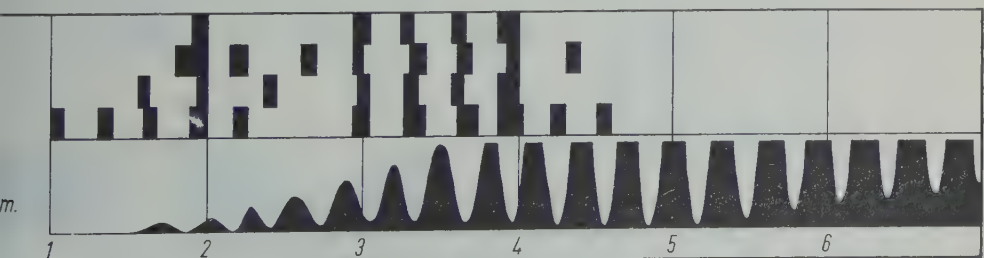


Fig. 4. Frequencies of low power observed at Little America V at the top. Below, the power radiated vertically computed for  $h = 490$  m.

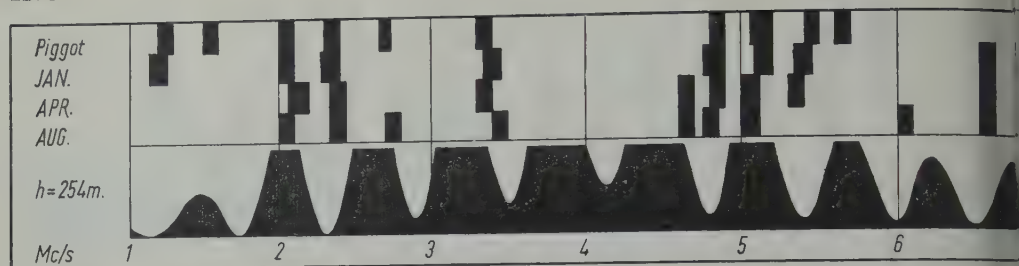


Fig. 5. Frequencies of low power observed at Halley Bay at the top. Below, the power radiated vertically computed for  $h = 254$  m.

### SPREAD ECHOES

*E region.* Figure 2 shows an example from Ellsworth of flat  $E_s$  echoes spread in virtual range. It will be observed that the radio frequencies for which the  $E_s$  echo power is a minimum vary with virtual range in a manner which suggests that the range spread is due to echoes arising at some angle to the vertical from the station. If we assume a horizontal ionospheric layer, of the same virtual height for a range of radio frequencies (small group retardation) as in Figure 2, and if  $f$  is the frequency of a minimum of order  $n$ , then the ratio of height  $H$  to slant range  $R$  is given by simple geometry from the equation for the optical path difference in a parallel-sided film:

$$(H/R)^2 = (c/2d)^2(n/f)^2 + (1 - \epsilon') \quad (1)$$

A total of 55 values of  $(H/R)$  versus  $(n/f)$  has been taken from flat  $E_s$  echoes at Ellsworth and the best straight line fitted by least squares on an electronic computer. From the gradient of the line we find  $d = 265 \pm 3$  m for the true thickness of the ice shelf at Ellsworth. From the intercept we find  $\epsilon' = 2.78 \pm .05$  for the ice shelf material below the immediate surface layers. It can be shown that if the dielectric constant of the snow increases with depth (due

to compaction) over a depth  $\delta$ , then the correction required to the value of  $\epsilon'$  at the bottom of the ice shelf is  $\lesssim \epsilon'/100$  if  $\delta \lesssim d/10$ . According to Kuroiwa [1955] solid ice has  $\epsilon' = 3.2$  at high frequencies, and our figure corresponds to isotropic crystalline snow of specific gravity 0.78, which is reasonable.

The slope of the minima is the same in the second  $E_s$  echo as in the primary echo. This surprising result means that wide-angle scattering occurs in the  $E_s$ , and specular reflection in the ground vertically below. Flat  $E_s$  echoes with range spread have not been observed at any of the other stations, so a separate determination of  $\epsilon'$  has not been possible. Values of the actual snow thickness at other stations may be derived using the Ellsworth value of  $\epsilon'$  and the suggested values of  $h$ , except at Fletcher's island where the snow is likely to contain water or be of different composition.

*F region.* On the same example (Fig. 2) we can see that the power minima in spread  $F$  remain at constant frequency with increasing virtual range, and from equation 1 we can estimate that the range spreading occurs within 1° of vertical incidence. The spread could be produced by a minimum time echo which arises from angles of incidence rather near the vertical, to

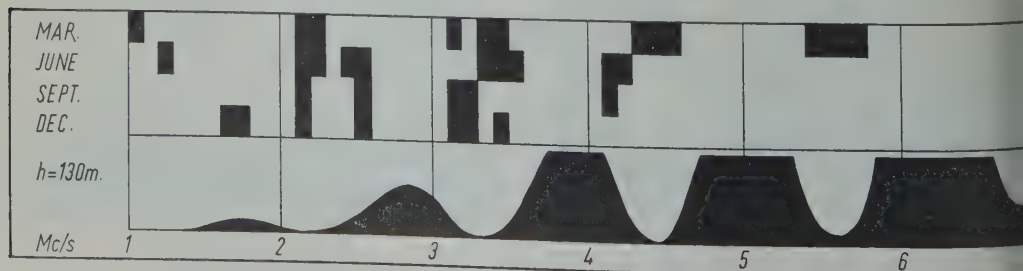


Fig. 6. Frequencies of low power observed at Fletcher's ice island at the top. Below, the power radiated vertically computed for  $h = 130$  m.



ing reflected by irregularities with vertical ion. This produces a sharp minimum of small retardation. The vertical incidence suffers large group retardation and produces a sharp maximum range as in Figure 2. These effects are observed regularly at polar stations [Wright, Knecht, and Davies, 1957]; the result shows that the minimum time echo is at a few degrees of the vertical.

### CONCLUSIONS

The radiation pattern of the ionosonde aerial is worth may be accounted for by assuming it is supported at a considerable height above the reflecting surface which we identify as the sea ice below the ice. The interference pattern observed is not so easily visible at other stations but the effect is clearly present. The structure of the radiation pattern enables us to recognize echoes which arise at some angle to the vertical, and it is suggested that ionospheric layers should bear this in mind when analyzing data from polar stations. A weak effect may be found in permafrost, according to the properties given by Cook [1960] and Hatherton [1960]. The value of  $\epsilon'$  derived, and the low value of  $\epsilon''$  which is implied, agree with laboratory measurements. This is clearly not the best frequency range when searching for air gaps, i.e., crevasses, in the surface of the snow. By using frequencies of a few hundred cycles and exploring the static electric field, advantage is taken of the large ratio of the dielectric constants of ice to air (about 81) in this range [Cook, 1957]. However, for exploring the bottom topography, it is likely that higher frequencies will be useful. A resolution of the order of 5 m could be achieved with the 40-Mc/s sweep frequency modulation system used in radio altimeters working at 440 Mc/s. Tests of the less accurate pulsed altimeter have been made by Waite

and Schmidt [1961], and we hope to use the method further. At higher frequencies, higher resolution can be attained, but the roughness of the reflecting surface, its reflection coefficient, and scattering within the medium are expected to reduce the echo.

**Acknowledgments.** This work was carried out at the Scott Polar Research Institute with continual encouragement from the Director, G. de Q. Robin. It is a pleasure to thank W. R. Piggott for calling my attention to the phenomenon, T. R. Kaiser for helping discussions, R. W. Knecht for details of the American aerials, the Cavendish Laboratory for the loan of records, and the Director of the Mathematical Laboratory for the use of its facilities.

### REFERENCES

- Bailey, R., Aperiodic aerials, *Wireless Engineer*, **28**, 208-214, 1951.
- Cook, J. C., The design of a crevasse detector for polar exploration, *J. Franklin Inst.*, **241**, 361-377, 1957.
- Cook, J. C., RF properties of salty ice and frozen earth, *J. Geophys. Research*, **65**, 1767-1772, 1960.
- Dorsey, N. E., *Properties of Ordinary Water Substance*, Reinhold Publishing Corporation, New York, 1940.
- Hatherton, T., Electrical resistivity of frozen earth, *J. Geophys. Research*, **65**, 3023-3024, 1960.
- Kuroiwa, D., Dielectric property of snow, *U.G.G.I. Association Internationale d'Hydrologie Scientifique, Assemblée General de Rome, Tome IV*, p. 52, 1954.
- Piggott, W. R., and L. W. Barclay, The reflection of radio waves from an iceshelf, *J. Atmospheric and Terrest. Phys.*, **20**, 289-299, 1961.
- Waite, A. H., and S. J. Schmidt, Gross errors in height indication from radar altimeters operating over thick ice or snow, to be published in *Proc. IRE*, 1961.
- Wright, J. W., R. W. Knecht, and K. Davies, Ionospheric vertical soundings, *Ann. IGY*, **3**, part 1, 88-108, 1957.
- Yoshino, T., Radio wave propagation on the ice cap, *Antarctic Record*, **11**, 228-233, Ministry of Education, Tokyo, Japan, 1961.

(Manuscript received August 9, 1961;  
revised September 25, 1961.)





# Solar Activity Effect and Diurnal Variation in the Upper Atmosphere

W. PRIESTER<sup>1</sup>

*Institute for Space Studies  
New York 27, New York*

**Abstract.** It has been shown that the relation between density variations in the upper atmosphere derived from satellite drag measurements and the solar flux in the decimeter range can be written by  $\rho \sim S^m$  where  $\rho$  is the density,  $S$  the solar flux, and the exponent  $m$  is a function of altitude and local time. This function has been derived for the altitudes 350, 650, and 1300 km (Figs. 1, 2, and Table 1). Further, the temperature variation at 650 km as function of solar activity, measured by the 20- or 10.7-cm flux, has been calculated for the diurnal maximum (14 h LT) and minimum (5 h LT). To explain the calculated temperature-variation, it is suggested that in addition to the heating of the  $F$  layer by solar extreme ultraviolet radiation, another important energy source must be present that also increases toward the maximum of the solar cycle.

Comparison of the fluctuations in the orbital period of the satellite 1957 $\beta$  (Sputnik 2), given by Jacchia [1958], with the fluxes of the solar radiation, measured by the Heinrich Institute, Berlin, revealed a striking correlation (Priester, 1958, 1959), which was brilliantly confirmed by Jacchia [1959a, b] in satellites 1957 $\beta$ , 1958 $\beta_2$  and 1958 $\delta_1$ , using the 10.7-cm flux measured at Ottawa, and by Priester and Martin [1960] in satellites 1958 $\beta_2$ , 1958 $\alpha$ , and 1958 $\delta_1$ . The perigee heights of these satellites are in the range of 200 to 660 km above earth's surface. The correlation was later also confirmed for higher altitudes (1000 to 1600 km) from the observations of the orbital elements of the satellite Echo I by Roemer [1961], Zadunaisky, and Jones [1961], and by R. Bryant (unpublished data). The fluctuations occur aperiodically, having periods of between 24 and 27 days. This variation is commonly referred to as the '27-day period.' As early as 1958 Jacchia suggested that the cause of the fluctuations might be a variable radiation from the sun (Jacchia and Briggs, 1958). In addition, a close correlation between the fluctuations of satellite period and the sunspot numbers was found by Priest [1959].

The fluctuations of these periods are obviously caused by density variations in the upper atmosphere. Of course, it was clear in advance that solar decimeter radiation could not be the physical cause for the fluctuations in the atmospheric density, but should merely be considered as an index of it. In our first paper on this matter [Priester, 1958, 1959], it was pointed out that the cause of the fluctuations in density could be seen in the heating of the atmosphere by variable X radiation of the sun, which, according to Elwert [1956] is mainly absorbed in the ionospheric  $E$  layer. During the Symposium on Space Research held in Nice, January, 1960, it became clear from a paper by Hinteregger, Damon, Hiroux, and Hall [1960], who have measured the extreme ultraviolet spectrum of the sun, that the major source of the heating of the upper atmosphere is the absorption of EUV radiation, which mainly occurs in the altitude range 150 to 250 km. Most important seems to be the 304 Å line of ionized helium. For theoretical reasons, we can expect a very close correlation between the so-called 'slowly varying component' of the solar radiation in the 3- to 30-cm range, which, according to Waldmeier and Mueller [1950], is due to thermal emission by coronal condensations and both the X rays and the 304 Å line that should also originate in these condensations.

From the first rough analysis [Priester and Martin, 1960] it turned out that this correlation between air density and the solar decimeter

<sup>1</sup> National Academy of Sciences, National Research Council Research Associate with National Aeronautics and Space Administration, on leave from University Observatory.

radiation [3–30 cm], which we called the ‘solar activity effect,’ is, as a first approximation, represented by  $\rho \sim S$ , where  $\rho$  is the density and  $S$  the flux of the 20-cm or the 10.7-cm radiation. This proportionality between density and flux was also used and confirmed by *Jacchia* [1960]. It is the main concern of the present paper to give a more sophisticated relation between density and solar flux.

But first we have to consider another strong effect in the upper air densities, which is closely related physically to the ‘solar activity effect’: the diurnal variation of density. This reaches its peak at about 14 h local time, followed by a decline until sunset. During the night, the density continues to decline, though more slowly. After sunrise, the curve begins to rise steeply until it reaches the peak. The amplitude of the variation increases with increasing altitude. At 200 km, it is only a few per cent, contrary to the solar activity effect which yields quite pronounced density variations even at this altitude. But at about 300 km the diurnal variations become the most important characteristic of the density fluctuations, which reach an amplitude of about a factor of 10 at 650 km. This effect was found nearly at the same time and separately by *Wyatt* [1959], *Jacchia* [1959b], *Priester and Martin* [1960] and *Paetzold and Zschoerner* [1960]. Detailed results for the heights 210, 562, and 660 km were given by *Priester, Martin, and Kramp* [1960] and by *Jacchia* [1960].

There are three further effects causing density variations in the upper atmosphere. One of these, correlated with large magnetic storms, was found by *Jacchia* [1959c]. He confirmed this result by analyzing the changes of period of seven satellites during the November 1960 event [*Jacchia*, 1961]. It was also confirmed by *Jastrow and Bryant* [1961] on the data of Echo I. This effect is believed to result from the solar corpuscular radiation. A possible mechanism, proposed by *Dessler* [1959], consists of heating the upper atmosphere by means of hydromagnetic waves. They arise at heights between  $3 \times 10^4$  and  $6 \times 10^4$  km as a result of instability, which occurs when the stream of solar particles interacts with the earth’s magnetic field. The dissipation of the energy of these waves would occur at a height of approximately 150 to 200 km and heat the  $F_1$  layer. From this we might

expect that in general the quiet-day solar wind makes a nonnegligible contribution to the heating of the  $F$  layer.

The second effect has a semiannual period was found by *Paetzold and Zschoerner* [1961]. This phenomenon is characterized by a general decrease in density during the months June, July and January. A similar effect exists in the frequency of occurrence of auroras and in the general variation of the geomagnetic indices when they are averaged over many years [*Bartels*, 1932]. This supports the suggestion that the semiannual effect is also due to solar corpuscular streams.

The third effect was recently found by *Rasool* [1961]. It is a correlation between density variations in the upper atmosphere and the occurrence of large meteor showers. But this effect is generally small and therefore not very significant. It yields density increases of about 5 per cent which last for a few days, as a statistical analysis of the density data obtained during the occurrence of fifteen showers has shown. In this study *Rasool* used the density data derived by *Martini* [1961]. These data are reduced to a standard level of solar activity (solar 20-cm flux  $S = 170 \cdot 10^{-22} \text{ w/m}^2 \text{ c/s}$ ) and also reduced to the mean perigee height. Further, the required density scale heights for the individual local times of perigee were taken from the atmospheric model of *Priester, Martin, and Kramp* [1960]. The orbital elements were mainly taken from the papers by *Jacchia* [1959] and *Zadunaisky* [1960]. As the magnetic storm effect and the meteor shower effect, however, are rather transient, they do not influence our statistics on the solar activity effect and on the diurnal variation, since the disturbed days can simply be omitted.

During the course of the investigation of the solar activity effect it turned out that the density variation can be given by

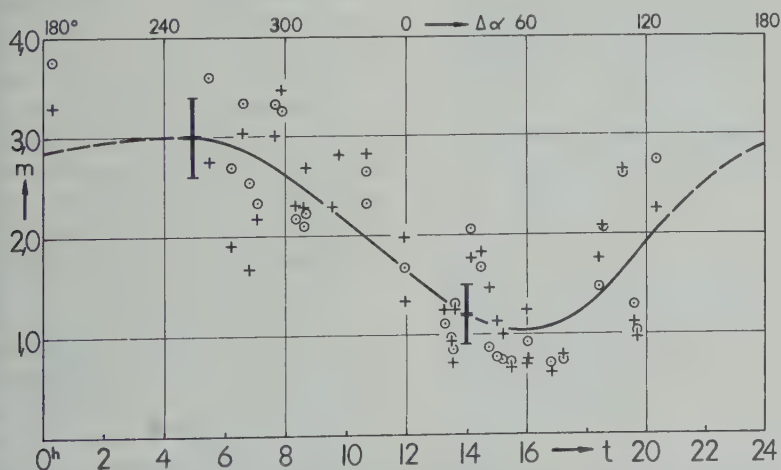
$$\rho \sim S^m$$

where  $\rho$  is the density and  $S$  the solar flux. The empirical quantity  $m$  is derived from the satellite drag measurements. Preliminary values of  $m$  as a function of height were previously given by *Martin, Neveling, Priester, and Rasool* [1961]. *Paetzold and Zschoerner* [1961] give the variation of the solar activity effect with heights up to 650 km. Their numerical

in satisfactory agreement with our present knowledge of the heat- upper atmosphere owing to absorp- solar extreme ultraviolet radiation and of heat conduction in the thermo- and exosphere, we are led to suppose exponent  $m$  is not only a function that with altitude but also depends on the . In order to derive these functions, the atmospheric densities calculated by for the altitudes 350 and 650 km and the obtained by Roemer [1961] and by R. (unpublished data, 1961) from the or- nents of satellite 1960<sub>u</sub> (Echo 1) for between 1000 and 1600 km. The suc- axima and minima of the 27-day den- ation were correlated with the corres- extremes of the 20-cm and the 10.7-cm . In order to avoid the possible in- f other effects that also change the t at a given height, the amplitude of each was calculated by taking the differ- between the maximum density and the of the two adjacent minimum values, versa, for determining the amplitude minimum. The same procedure was fol- determining the amplitudes for the of the solar flux. In this way the ex- were calculated using the formula

$$m = \frac{\log \rho_{\max} - \log \rho_{\min}}{\log S_{\max} - \log S_{\min}} \quad (2)$$

The results for 650 km, derived from Vanguard I, and for 350 km, derived from Explorer I, are plotted in Figures 1 and 2 as functions of local time. Despite the fact that we used the best satellite data available at present, the scattering of the values of  $m$  is very large, because  $m$  has to be derived as a quotient of two small numbers. Plotted are only those values for which the denominator in formula 2 was larger than 0.100. In order to see how much scatter is the result of the uncertainty in the radio fluxes, we used both the 10.7-cm and the 20-cm fluxes. For the altitude range between 1000 and 1600 km, data from satellite Echo I were only available for the interval of local time between 12 and 20 h. For this reason only an average value of  $m$  can be given for this time interval. We found for 1300 km  $m = 2.0 \pm 0.4$ . Despite the large scatter in Figure 1, a diurnal variation of  $m$  at an altitude of 650 km can be seen, with  $m = 1.2 \pm 0.3$  at 14 h local time and  $m = 3.0 \pm 0.4$  at about 5 h local time. A preliminary curve has been drawn to fit the points considering their individual accuracy. It turns out that the relative amplitude of the density variations due to the solar activity effect is greater at dawn than



1. Variation of the exponent  $m$  with local time  $t$  for an altitude of 650 km, derived from satellite Vanguard I;  $m$  is defined by  $\rho \sim S^m$  where  $\rho$  is the atmospheric density and  $S$  the flux. In deriving  $m$  we used the 20-cm flux (circles) and the 10.7-cm flux (crosses) in order to finish the uncertainty of the results due to the scatter of the radio data. The upper line gives  $\alpha_\pi - \alpha_s$  where  $\alpha_\pi$  is the right ascension of the satellite perigee,  $\alpha_s$  the right ascension of the Sun. The large crosses at 14 hours and 5h 20m mark the values used in the further calculations (Table 1).



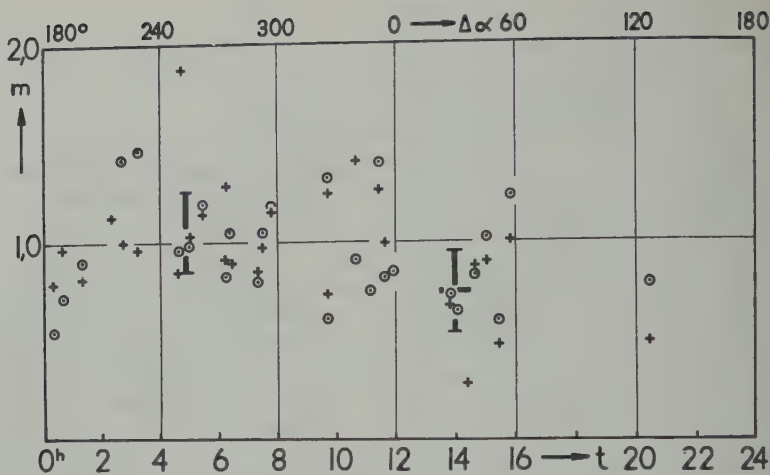


Fig. 2. Variation of the exponent  $m$  with local time for an altitude of 350 km, derived from the satellite Explorer I. The scales and the symbols are the same as in Figure 1.

early in the afternoon. Obviously this is caused by the combined effects of the heating owing to absorption of solar EUV radiation during daytime and the heat conduction. It would be of interest to derive the temperature variation in this part of the lower exosphere as a function of local time and solar activity. To do this we need a model of the upper atmosphere that fits the satellite data and gives the physical properties as a function of height, local time, and solar activity. We used a model whose main characteristic is a linearly increasing pressure-scale-height  $H_p$ . In this model the gradient  $dH_p/dh$ , where  $h$  is the altitude, is a function of local time and solar activity; this dependence was derived from the satellite data. A model of this kind was calculated by Nicolet [1960]. A similar model, which we have now derived (Priester, unpublished data, 1961) has been shown to give an

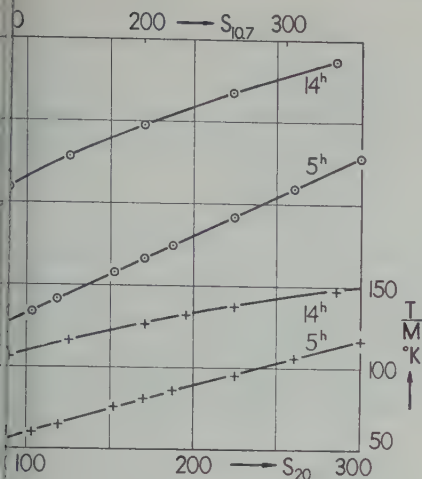
excellent representation of the densities derived from satellites in the range from 350 to 1600 km.

Using this model and the two  $m$  values calculated for 650 km for 14 h and 5 h LT we were able at first to derive  $m$  as a function of local time and altitude and to check these results with the findings plotted in Figure 2 for 350 km with the result for 1300 km described above. We found a satisfactory agreement between calculated and observed  $m$  values (see Table 1).

Furthermore, it was easy to calculate the variation of  $T/M$  as a function of local time and solar activity, where  $T$  is the temperature and  $M$  the mean molecular weight. The data for an altitude of 650 km are plotted in Figure 3. Unfortunately it is not possible to derive the variation of  $T$  only, because the absolute values of the mean molecular weight and its variation with time and solar activity are not known with accuracy. But from the fact that the atmosphere is shifted upward during the daytime, yielding a bulge near the subsolar point, we can make some reasonable estimates of the variation of  $T/M$ . We used a linear relation between  $M$  and  $dH_p/dh$  where  $M$  varies from 13.8 at just before dawn and at minimum solar activity to 16.0 at 14 h local time and maximum solar activity. With this estimate, it was possible to derive a preliminary representation of the temperature variation as a function of solar activity, indicated by the 20- or the 10.7-cm flux, for the diurnal maximum at 14 h local time and the diurnal minimum at about 5 h local time.

TABLE 1. The Exponent  $m$  as Function of Altitude and Local Time

Altitude	14 h LT	5 h LT	Remarks
km			
350	$m = 0.55$	$m = 1.05$	Calculated
350	$m = 0.75 \pm 0.2$	$m = 1.05 \pm 0.2$	Observed
650	$m = 1.2 \pm 0.3$	$m = 3.0 \pm 0.4$	Observed
1300	$m = 2.2$	...	Calculated
1300	$m = 2.0 \pm 0.4$	...	Observed



Variation of temperature  $T$  (upper two curves) and  $T/M$  (lower two curves) with solar activity measured by the 20-cm solar flux (lower scale) and the 10.7-cm flux (upper scale). Both  $T$  and  $T/M$  are expressed in units of  $10^{-23}$  w/m<sup>2</sup> c/s.  $M$  is the molecular weight. The data refer to an altitude of 650 km and the two curves show the variation at 14 h and 5 h local time, respectively.

are plotted in the upper part of Figure 3. One can see the expected increase of temperature with solar activity for both diurnal maximum and minimum. But from the viewpoint of energy balance, conduction and absorption of EUV radiation, it is difficult to understand why the temperature is almost constant, or is even decreasing with increasing solar flux. This can also be seen from the  $T/M$  values and holds for any reasonable variation of the variation in  $M$ . The most plausible explanation seems to be to assume an additional heating process which is available during day and night and which also increases with solar activity. It is reasonable to suppose that this mechanism involves the solar wind, also in order to explain the seminannual variation and the magnetic storm effect. Only very rough estimates can be given from the temperature variation in Figure 3. We should expect that this mechanism is able to maintain the exosphere temperature at night at a temperature level of about 100 K during maximum solar activity when the solar activity is greater than 250 in the usual units. At solar minimum the contribution of the solar wind effect to the temperature should be less than 300°. When we compare the den-

sity variations in the upper atmosphere calculated from formula 1 using the  $m$  values derived from the 27-day variations with the mean densities given by King-Hele and Walker [1961] for 1958, 1959, 1960, we find a slightly larger variation in the latter data. This perhaps can also be explained by the additional heating process mentioned above.

The conclusions must be considered as very preliminary, but investigation of the solar activity effect and the diurnal variation during the present solar cycle seems to offer a possibility of getting better insight into the energy balance of the upper atmosphere. For this, however, it is necessary to have very accurate satellite data.

**Acknowledgments.** I am grateful for support of this research provided by the Theoretical Division of Goddard Space Flight Center. Further I am grateful to Mr. Stephen Maran for helpful discussion.

#### REFERENCES

- Bartels, J., Terrestrial magnetic activity, *Terrestrial Magnetism and Atmospheric Elec.*, **37**, 29, 1932.
- Dessler, A. J., Upper atmospheric density variation due to hydromagnetic heating, *Nature*, **184** (Suppl.), 261, 1959.
- Elwert, G., Roentgenstrahlung Koronaler Kondensationen *Z. Astrophys.*, **41**, 67, 1956.
- Hinteregger, H. E., K. R. Damon, L. Hiroux and I. A. Hall, Telemetering monochromator measurements of solar 304Å radiation and its attenuation in the upper atmosphere, COSPAR Symposium, Nice 1960, in *Space Research*, edited by H. Kallmann-Bijl, North-Holland Publishing Company, Amsterdam, 615-627, 1960.
- Jacchia, L. G., Basic orbital data for satellite 1957  $\beta$ , *Smithsonian Astrophys. Observatory Spec. Rept.* 9, 1958.
- Jacchia, L. G., Atmospheric fluctuations of solar origin revealed by satellites, Harvard Observatory Announcement Card 1423, 1959a.
- Jacchia, L. G., Solar effects on the acceleration of artificial satellites, *Smithsonian Astrophys. Observatory Spec. Rept.* 29, 1959b.
- Jacchia, L. G., Corpuscular radiation and the acceleration of the artificial satellites, *Nature* **183**, 1662-1663, 1959c.
- Jacchia, L. G., A variable atmospheric-density model from satellite accelerations, *Smithsonian Astrophys. Observatory Spec. Rept.* 39, 1960.
- Jacchia, L. G., The atmospheric drag of artificial satellites during the November 1960 events, COSPAR Symposium, Florence, 1961.
- Jacchia, L. G., and R. E. Briggs, Orbital acceleration of satellite 1958  $\beta_2$ , *Smithsonian Astrophys. Observatory Spec. Rept.* 18, 1958.

- Jastrow, R., and R. Bryant, Effects of a severe solar storm on the orbit of Echo I, *IGY Bull.* 44, 6, 1961.
- King-Hele, D. G., and D. M. C. Walker, Upper atmosphere density during the years 1957 to 1961 determined from satellite orbits, COSPAR Symposium, Florence, 1961, *Nature*, 191, 114, 1961.
- Martin, H. A., W. Neveling, W. Priester, and M. Roemer, Model of the upper atmosphere from 130 through 1600 km derived from satellite orbits, *Mitt. Sternwarte Bonn* 35, COSPAR Symposium, Florence, 1961.
- Nicolet, M., Les variations de la densité et du transport de chaleur par conduction dans l'atmosphère supérieure, in *Space Research*, edited by H. Kallmann-Bijl, North-Holland Publishing Company, Amsterdam, 46-89, 1960.
- Paetzold, H. K., Observations of the Russian satellites and the structure of the outer terrestrial atmosphere, *Planetary Space Sci.*, 1, 115-124, 1959.
- Paetzold, H. K., and H. Zschoerner, Bearings of Sputnik III and the variable acceleration of Satellites, in *Space Research*, edited by H. Kallmann-Bijl, North-Holland Publishing Company, Amsterdam, 24-36, 1960.
- Paetzold, H. K., and H. Zschoerner, The structure of the upper atmosphere and its variations after satellite observations, COSPAR Symposium, Florence, 1961.
- Priester, W., Sonnenaktivitaet und Abbremsung der Erdsatelliten, *Mitt. Univ. Sternwarte Bonn* 24, 1958; *Naturwiss.* 46, 197, 1959.
- Priester, W., and H. A. Martin, Solare und zeitliche Effekte in der Hochatmosphäre, Beobachtungen Kuenstlicher Erdsatelliten, *Mitt. Univ. Bonn*, 29, 1960; English translation: Royal Aircraft Establishment Farnborough Library Translation 901.
- Priester, W., H. A. Martin, and K. Kramp, Diurnal and seasonal density variations in the upper atmosphere, *Nature*, 188, 202, 1960.
- Rasool, S. I., Effect of major meteoric showers on the densities of the upper atmosphere, *Science*, 134, 385-386, 1961.
- Roemer, M., Modell der Exosphaere im Höhenbereich 1000-1700 km berechnet aus den Beobachtungen des Satelliten Echo 1, *Mitt. Univ. Sternwarte Bonn*, 37, 1961; *Nature* 191, 238, 1961.
- Waldmeier, M., and H. Mueller, Die Sonnenstrahlung im Gebiet von  $\lambda = 10$  cm, *Z. Astrophys.*, 58, 1959.
- Wyatt, S. P., Solar effects in the motion of Vanguard I, *Nature* 184 (Suppl.), 351, 1959.
- Zadunaisky, P. E., The orbit of satellite 195 (Explorer I) during the first 10,500 revolutions, *Smithsonian Astrophys. Observatory Spec. Rep.* 50, 1960.
- Zadunaisky, P. E., I. I. Shapiro, and H. M. Jorgensen, Experimental and theoretical results on the orbit of Echo I, *Smithsonian Astrophys. Observatory Spec. Rep.* 61, 1961.

(Manuscript received August 9, 1961.)

## The Seasonal Anomalies in the $F$ Region

G. A. M. KING

*Geophysical Observatory, D.S.I.R.  
Christchurch, New Zealand*

*Abstract.* The seasonal anomaly in  $f_oF_2$ , whereby the winter noon values are greater than summer, is shown to be accompanied by a difference in the  $F$  region division into  $F_1$  and  $F_2$ . The main cause of the anomaly seems to be a seasonal change in the rate of electron loss. The seasonal change is related to the behavior of traveling disturbances, and a theory of the anomalies is used to propose a connection with the atmospheric tides below 80 km.

*Introduction.* At middle and high latitudes, the critical frequency of the  $F_2$  layer is lower in winter than in summer [Kirby, Berkut, 1934]. This anomaly was at first attributed to a seasonal variation in atmospheric temperature at  $F$ -region heights [Appleton, 1951], but the effect of the temperature, although present, is not enough to explain the observations. A 'dynamic' theory based on atmospheric heating [Hulburt, 1951] is the forerunner of the 'tidal' theory of the anomalies [Martyn, 1947], in which the variations of tidal flow at ionospheric heights and Earth's magnetic field cause large vertical displacements of the ionization in the  $F_2$  layer. This tidal theory has been moderately successful in explaining the diurnal behavior at middle and low latitudes, and it is commonly felt that a more complete theory of  $F$ -region anomalies will be expected in the future. However, the present contribution to the subject [Rishbeth, 1961] departs radically from the present approach, invoking a seasonal variation in the composition, which affects the rate of electron loss and 'observable' properties. The present paper discusses a particular example of the seasonal anomaly in  $f_oF_2$ , and, by giving also the extent of  $F$ -region stratification between  $F_1$  and  $F_2$ , presents evidence that the cause of the anomaly is a seasonal variation in the rate of electron loss. Further study of the anomaly discloses a connection with ionospheric traveling disturbances, and the discussion is shifted to the seasonal variation in these disturbances. A theory of these disturbances [Hines, 1960] is then used to support

a proposal that the atmospheric tides below 80 km can affect indirectly the rate of electron loss in the  $F$  region. The seasonal anomalies therefore arise from the change in tidal flow which must result from the seasonal change in atmospheric temperature profile between 50 and 80 km at high latitudes [Stroud, Nordbery, Bandeen, Bartman, and Titus, 1960].

The author believes that this theory need not be antithetical to that of Martyn; more study is needed to assess the relative importance of tidal flows in the  $F$  region and in the lower atmosphere.

*The seasonal variation of  $\beta$ .* The nature of the seasonal anomaly can be seen readily by a study of Figure 1; this is a daily plot of the noon critical frequency of the  $F_2$  layer at Campbell Island (52°33'S, 169°09'E) from the beginning of February to the end of April 1960.

Of the values in the first half of the plot, up to March 16, none is above 9 Mc/s, whereas in the second half two-thirds of the values are above 9 Mc/s. At this southern hemisphere station February is a 'summer' month and April a 'winter,' so that the higher critical frequencies after the middle of March are contrary to expectation based on the seasonal change in solar zenith angle.

The noon values of  $K$  index at Amberley are plotted in the lower part of Figure 1, and it is clear that the anomalous behavior is not due to persistently high magnetic activity in summer; in fact, the average  $K$  is slightly—although not significantly—higher in the second half of this 3-month period.

Six of the ionograms that contributed  $f_oF_2$  values to Figure 1 are reproduced in Figure 2.



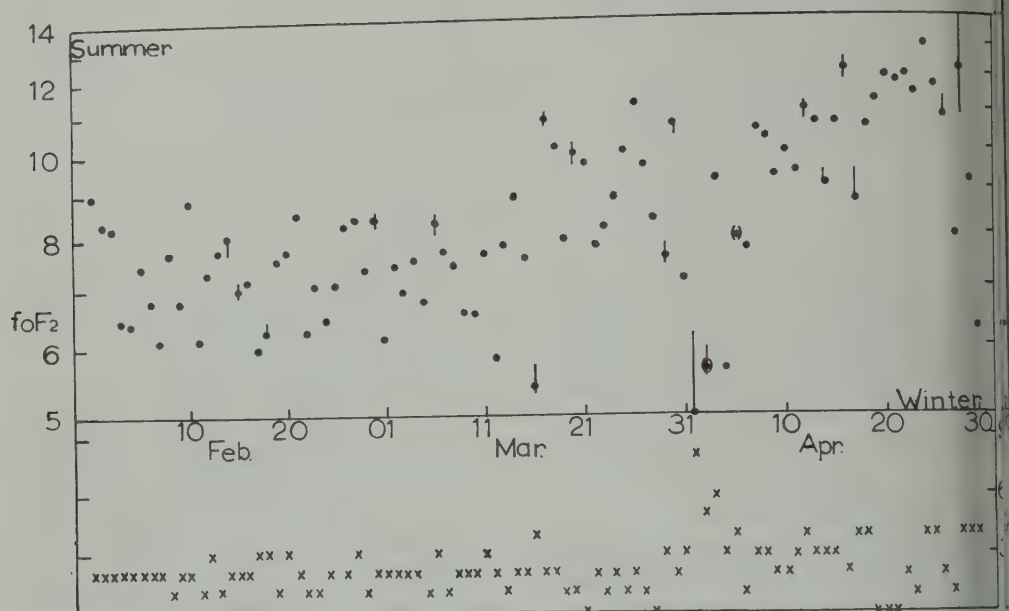


Fig. 1. The noon critical frequency of the  $F_2$  layer at Campbell Island for February, March, and April, 1960. Lower part of figure, Amberley  $K$  index.

The lower three tracings have  $F_2$  critical frequencies close to the median value of the 'winter' half of Figure 1, and the upper three have  $F_2$  critical frequencies close to the median value of the 'summer' half; notice, though, that one of the upper three is actually taken from the 'winter' period (see later).

Figure 2 illustrates the fact, well known to those who read ionograms routinely, that the lower values of  $f_oF_2$  are associated with a greater stratification of the  $F$  region into  $F_1$  and  $F_2$ .

The degree of  $F$ -region stratification can be measured [King, 1961] by the parameter  $G$ :

$$G = \frac{\beta_0^2}{q_0 \alpha} \quad (1)$$

where  $q_0$  and  $\beta_0$  are the rates of electron production and of atom-ion interchange at the height of maximum production, and  $\alpha$  is the rate coefficient for electron loss by dissociative recombination. Because full analysis is tedious and often rendered difficult by traveling disturbances and 'valley' errors in the  $N(h)$  analysis,  $G$  is estimated here by a simple model method. Figure 3 shows the virtual height curves ( $h'$ ,  $f$ ) expected at Campbell Island for different values of  $\log_{10} G$ . For preparing these curves, the  $E$  layer and  $E$ - $F$  valley deduced by  $N(h)$  analysis

from the ionogram, 10.15 on February 2, 1961, were attached to models of the  $F$  region [King, 1961] with an assumed scale height of 40 km, the maximum of electron production; the refinement of a variable gradient of scale height [Cummack, 1961] was incorporated.

Comparison of Figures 2 and 3 gives for 'summer' type of  $F$  region  $\log G \doteq 0.7$ -0.8, for the 'winter' type  $\log G \doteq 0.1$ -0.2. 'summer'/'winter' ratio in  $G$  is therefore about 10.

The factors that affect  $G$  are (equation 1)

1. Change in  $q_0$  with solar activity.
2. Change in  $q_0$  with atmospheric scale height.
3. Change in  $q_0$  with solar zenith angle,  $\chi$ .
4. Change in  $q_0$  with atmospheric composition.
5. Change in  $\beta_0$  with solar zenith angle.
6. Change  $\beta_0$  with atmospheric composition.

The changes with solar zenith angle, (3) (5), arise because  $G$  is defined at the maximum of the electron production function and not at a virtual maximum for overhead conditions. The connection between  $q_0$  and scale height,  $H_0$ , is given by the constant  $q_0 H_0 / \cos \chi$  [Nicolet, 1951].

Of these various factors, the first two are obviously incapable of producing a four-fold change. The seasonal progression of the

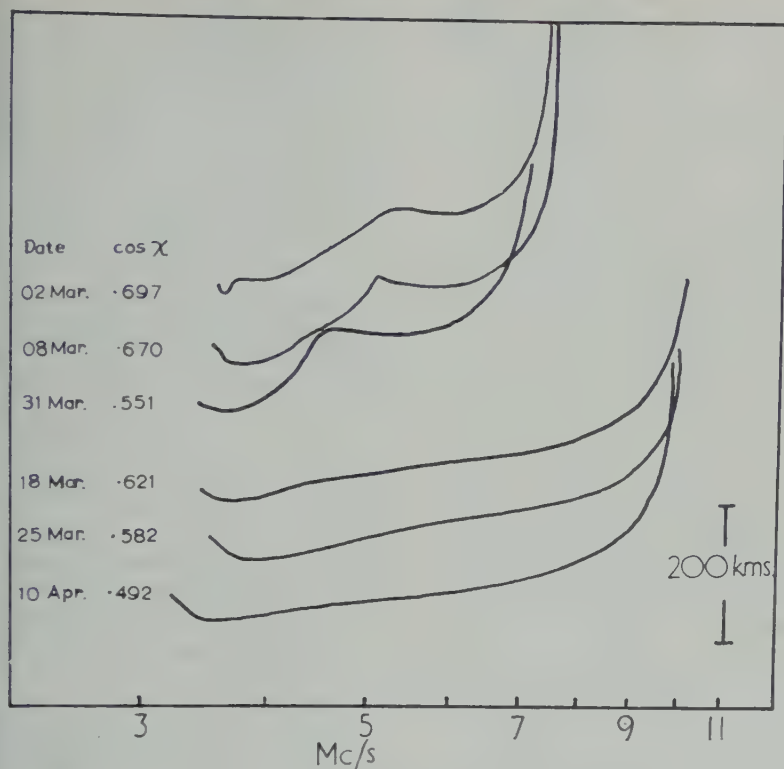


Fig. 2. Tracings of six ionograms at Campbell Island. See text.

gle certainly affects  $G$ , decreasing its winter through the term,  $\beta_0$ , and its value through  $q_0$ , although the  $\beta_0$  mostly predominates. However, two considerations indicate that this steady progression is the main cause of the seasonal change in ionization. One is the abrupt nature of the change in the middle of March (see Fig. 1). Another is the fact that 'summer' type records are far more common during the 'winter' period. An example of this, shown in Figure 2;  $\cos \chi$  for March 31, is lower than for two of the 'winter' records in the lower part of the figure. The factors responsible are the changes of  $q_0$  and  $\beta_0$  with time and ionospheric composition—changes suggested by *and Setty* [1961].

It appears to the second power and  $q_0$  is the first in the expression for  $G$  (equation 1). It is likely that the main contribution to the seasonal change comes from  $\beta_0$ . The likelihood is increased by noting that changes in  $q$  and  $\beta$  are seasonal to those at the height of maximum ionization, and are expected at all greater heights in the F region, and in particular at  $h_{\max} F_2$ .

Assuming equilibrium conditions [*Rishbeth and Barron*, 1960] the 'summer'/'winter' ratio in  $f_o F_2$  from Figure 2, 0.74, requires a 'summer'/'winter' ratio in  $\beta/q$  of 1.82 ( $=1/0.74^2$ ); combined with a ratio of 4 in  $G$ , this means a ratio of 2.2 in  $\beta_0$ —enough to account for all the change in  $G$  without any contribution from a change in  $q_0$ .

These results, although needing support from the analysis of a large body of data, indicate that the seasonal anomalies in  $f_o F_2$  and in the stratification of the F region are due to a seasonal change in  $\beta$ , the rate of atom-ion interchange.

*Traveling disturbances.* Another obvious difference between the 'summer' and 'winter' ionograms at Campbell Island is in the nature of traveling disturbances. In summer, the disturbances are frequent, so that the lower part of  $F_1$  is continually distorted; in winter, on the other hand, disturbances are few and slight. It is profitable to inquire if there could be a connection between this seasonal change and the change in  $\beta$ .

Immediately, an observational difficulty arises:

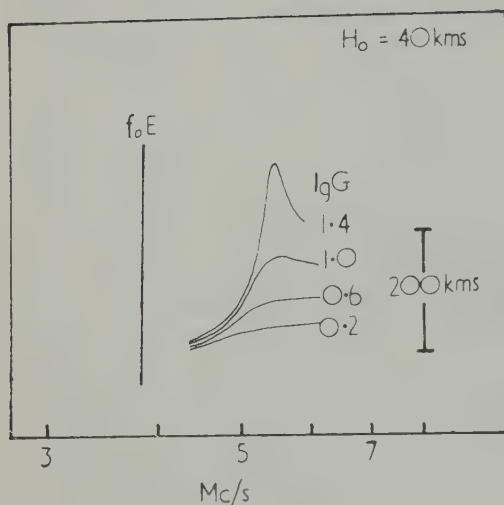


Fig. 3. Change in shape with  $\log_{10} G$  of the virtual height curves near  $f_o F_1$  at Campbell Island.

in winter, the effects of disturbances are too nebulous to study, whereas, in summer, it is hard to find periods when individual disturbances can be isolated. One relatively quiet period at Campbell Island was on the afternoon of February 16, 1960; tracings from the ionograms at 5-minute intervals between 15.40 and 16.40 are shown in Figure 4.

The irregularities on the  $h'f$  traces in Figure 4 are of two types. For example, at 15.50 there are sharp discontinuities near 4 Mc/s and a smoother inflection, like a normal  $F_1$  cusp, near 5 Mc/s. The discontinuities are the immediate effect of a traveling disturbance in the form of an atmospheric wave [Hines, 1960] while the inflection can be regarded as the normal  $f_o F_1$ ; its value varies with time and is raised above that expected from Figure 3 because the ionization is not in equilibrium between production and loss.

Although the idea of a  $G$  value for the division into  $F_1$  and  $F_2$  cannot be applied strictly to non-equilibrium stratifications, it is useful for a qualitative discussion of this figure. Thus, the 15.40 ionogram is free from disturbance and  $G$  is low. At 15.45 a traveling disturbance appears and  $G$  starts to rise, reaching a maximum value between 15.50 and 15.55 and then dropping again until 16.10. At 16.15, another traveling disturbance coincides with the beginning of another surge in  $G$ . The pattern illustrated in this sequence, once recognized, is easy to find in

quite complicated series of records, especially with the aid of a movie projector.

The conclusion seems inevitable that a traveling disturbance causes a temporary increase in  $G$ , and, as  $\cos \chi$ ,  $q$  and  $H$  are unlikely to be noticeably affected in so short a time, this may be interpreted as a temporary increase in  $\beta$ .

The seasonal anomalies discussed in the previous section now receive a ready explanation. In summer the overlapping effects of many traveling disturbances maintain a high value of  $\beta$ , with consequent low  $F_2$  critical frequencies and marked division into  $F_1$  and  $F_2$ ; in winter the disturbances are absent,  $\beta$  is therefore low so that  $F_2$  critical frequencies are high and the division into  $F_1$  and  $F_2$  is absent.

*Discussion of the experimental results.* The foregoing inspection of ionograms from Campbell Island has suggested that the value of the 'linear' loss coefficient,  $\beta$ , depends on the incidence of traveling disturbances. This suggestion seems very reasonable provided two assumptions are made:

1. The basic motion of a traveling disturbance is an internal gravity wave in the atmosphere (Theoretical paper by Hines [1960].)

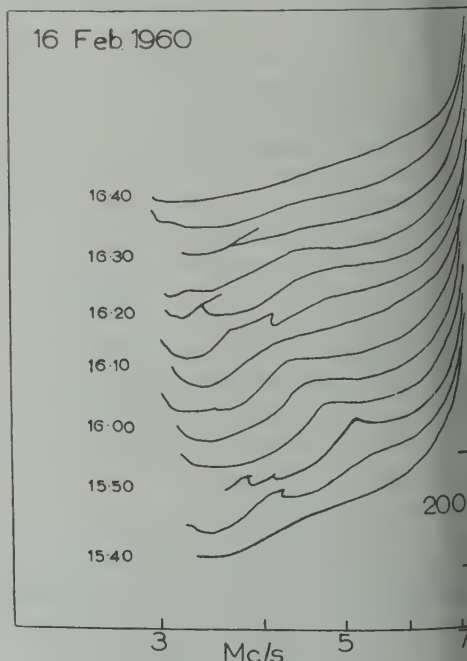


Fig. 4. A sequence of ionograms at Campbell Island, showing the effects of traveling disturbances.

atmospheric constituents are in diff-equilibrium under gravity starting at a low the  $F$  region. (Rocket observations *Howe and Townsend* [1958].)

Second assumption means that the molec-constituents, which determine the value of  $\beta$  [*Howe and Massey*, 1947], fall off faster with height than the atomic. Therefore, if there were to occur in the lower  $F$  region, involving the diffusive equilibrium over a height range, the molecular concentration at greater heights would be raised, and the value of  $\beta$ . If the first assumption required such mixing must occur, as the following considerations show.

According to Hines, gravity waves propagating upward undergo an increase of amplitude in that the energy flux remain constant in spite of the decreasing gas density. This means that at some height, determined by the characteristic wavelengths, the amplitude becomes so large that the motion severely nonlinear. Further mixing is prevented by degradation of the waves into shorter wavelength modes, which are rapidly dissipated by molecular viscosity. At a certain height the waves suddenly break, and the atmosphere in this region is filled with turbulence. (An analogy may be drawn with the breaking of sea waves on a beach; the line of breakers occurs at a certain finite depth of water.) From inspection of Figure 4 it is apparent that, in summer at Johnston Island, this height lies in the lower  $F$  region since the sharp discontinuities are not observed above 4.3 Mc/s. Therefore, the passage of a traveling disturbance is associated with turbulence in the lower  $F$  region, which causes the anomalies postulated in the last paragraph.

Third assumption made at the beginning of this discussion carries the implication that the atmosphere is predominantly atomic; the height of maximum electron production number density of atomic oxygen is three times that of molecular nitrogen. Furthermore, at 304 Å, the wavelength of the He II line is probably the main contributor to the spectrum, the absorption cross section of atomic oxygen is roughly twice that of molecular oxygen [*Dalgarno and Parkinson*, 1960]. Nitrogen, on the other hand, absorbs only a small fraction of the incident radiation. When mixing of traveling disturbances doubles this fraction,

there is a decrease in  $q$  through an increase in the 'unobserved' ionization [*Bates*, 1951]; but the change in  $q$  is small. And the rather crude experimental data given earlier agree with this theoretical conclusion.

*Proposed connection with atmospheric tides.* It is now necessary to consider why there should be a seasonal variation in incidence of the gravity waves associated with traveling disturbances. In the present state of knowledge, it is not possible to do more than suggest a mechanism to be tested by further study.

It is clear from Hines' analysis that the energy for these particular gravity waves propagates upward, indicating a source below the ionospheric atmosphere. Hines proposed two sources—tidal oscillations and low-level wind systems. Although the operation of the latter source has not been established, the diurnal and semidiurnal tidal oscillations are known to have large amplitudes below 100 km [*Greenhow and Hall*, 1960], and the nonlinear generation of the smaller scale gravity waves from them appears inevitable. For this discussion the tidal source is assumed.

The semidiurnal tidal oscillation owes its amplitude to the existence of a resonant mode in the earth's atmosphere [*Thomson*, 1882], the upper boundary being provided by the region of decreasing temperature between 50 and 80 km; if this mesodecline were not present, the tidal amplitude would be extremely small.

Now recent determinations of mesospheric temperatures at Fort Churchill have shown that the mesodecline practically disappears at high latitudes in winter [*Stroud, Nordberg, Bandeen, Bartman, and Titus*, 1960; see their Figs. 13 and 14]. One expects therefore, that the semidiurnal tidal oscillation would not extend to high latitudes in winter. At middle and low latitudes, the tidal flow should suffer hardly any change, but the summer high-latitude cap, on the other hand, should show increased tidal amplitude over that expected on the basis of an atmosphere uniform in latitude.

On this qualitative picture, the seasonal variations of traveling disturbances, and with them the seasonal anomalies in the  $F$  region, could well be due to changes in the global tidal flow below 80 km.

*Acknowledgments.* This work is part of the research program of the Geophysical Observatory of the New Zealand Department of Scientific and



Industrial Research (Superintendent, Mr. J. W. Beagley). It has benefitted from discussions with colleagues in the Observatory and at the U. S. National Bureau of Standards while I was supported by grant 50.4 through the National Academy of Sciences. The C4 ionosonde at Campbell Island was made available by the United States Government. Refractive indices used in preparing Figure 3 were computed by Mrs. R. Mason, and other computations and drawings were made by Misses C. Berryman and E. Currie.

## REFERENCES

- Appleton, E. V., *Nature*, **136**, 52, 1935.  
 Bates, D. R., *Proc. Phys. Soc.*, **64B**, 805, 1951.  
 Bates, D. R. and H. S. W. Massey, *Proc. Roy. Soc.*, **192A**, 1, 1947.  
 Cummack, C. H., *J. Geophys. Research*, **66**, 1961.  
 Dalgarno, A., and D. Parkinson, *J. Atmospheric and Terrest. Phys.*, **18**, 335, 1960.  
 Greenhow, J. S., and J. E. Hall, *J. Atmospheric and Terrest. Phys.*, **18**, 203, 1960.  
 Hines, C. O., *Canad. J. Phys.*, **38**, 1441, 1960.  
 Hulburt, E. O., *Phys. Rev.*, **46**, 822, 1934.  
 King, G. A. M., *J. Geophys. Research*, **66**, 1961.  
 Kirby, S. S., L. V. Berkner, and D. M. Stettin, *Proc. Inst. Rad. Eng.*, **22**, 481, 1934.  
 Lepechinsky, D., *J. Atmospheric and Terrest. Phys.*, **1**, 278, 1951.  
 Martyn, D. F., *Proc. Roy. Soc.*, **189A**, 241, 1945.  
 Meadows, E. B. and J. W. Townsend, *J. Geophys.*, **14**, 80, 1958.  
 Nicolet, M., *J. Atmospheric and Terrest. Phys.*, **141**, 1951.  
 Rishbeth, H., and D. W. Barron, *J. Atmospheric and Terrest. Phys.*, **18**, 234, 1960.  
 Rishbeth, H., and C. S. G. K. Setty, *J. Atmospheric and Terrest. Phys.*, **20**, 263, 1961.  
 Stroud, W. G., W. Nordberg, W. R. Bandeen, F. L. Bartman, and P. Titus, *J. Geophys. Research*, **65**, 2307, 1960.  
 Thomson, W., *Proc. Roy. Soc. Edinburgh*, **11**, 27, 1882.

(Manuscript received July 15, 1961.)

# Ionospheric Currents Responsible for Sudden Commencements Observed at the Geomagnetic Equator

TADANORI ONDOH

*Geophysical Institute, Kyoto University, Kyoto, Japan*

**Abstract.** The intensities and altitudes of ionospheric currents responsible for sudden commencements at the geomagnetic equator are calculated by using the horizontal and vertical disturbance vectors of the sc's observed simultaneously at the Jarvis and Fanning Island stations, on the assumption either that these currents are line currents or that they are uniform current sheets. The result shows that the total intensity of the current responsible for the sc is of the order of  $10^4$  amperes at the geomagnetic equator, and that there is no relation between the altitude of the current responsible for the sc and the local time of the occurrence. It seems likely that this current is caused by the arrival of hydromagnetic waves generated by the impact of the solar plasma cloud on the geomagnetic field. Possible explanations for the daytime enhancement of the amplitude of the sc at the geomagnetic equator are discussed.

**Introduction.** The daytime enhancement of the amplitude of the sc observed at the geomagnetic equator has been studied by many researchers since Ferraro and Unthank [1951]. Ratios of the amplitudes of the horizontal magnetic component of the sc's for Huancayo to Cheltenham, located on nearly the same magnetic meridian as Huancayo, reach as high as between 0.8 and 1.3 hours local time, with a maximum around 11 hours, and decrease toward evening, remaining constant (approximately 1) throughout the night.

In this fact Sugiura [1953] suggested that the immediate source of the main part of an sc occurs during sunlit hours at the geomagnetic equator is within the upper atmosphere of Earth. Forbush and Vestine [1955], using statistical tests, confirmed Sugiura's suggestion. Findings are as follows: (1) The average amplitude of sc's and the initial phase of the geomagnetic storm are both significantly greater during daylight hours at Huancayo. (2) The average amplitude of sc's is greater for days with larger variation  $S_q$  at Huancayo. (3) The initial phase of sc size, with  $S_q$ , at Huancayo is the same whether the average size of the same sc at San Juan and Honolulu is large or not. (4) The diurnal variation of sc's at San Juan and Honolulu is practically negligible, and so the sc at San Juan and Honolulu are useful to determine the size of sc's at other stations.

From the above facts Forbush and Vestine concluded that the current system responsible

for the sc is closely associated with the electrojet effect responsible for the large diurnal variation in the horizontal magnetic component at Huancayo, that is, with a narrow belt of high electrical conductivity around the  $E$  layer near the geomagnetic equator, and that this current may be driven by emf's originating mainly in the polar region.

Matsushita [1960] showed that the daytime enhancement of the sc is also seen at Koror and Jarvis stations, using the ratios of the amplitude of the horizontal magnetic component of sc's for Koror and Jarvis stations to those for Guam and Honolulu stations. He suggested that hydromagnetic waves or shock fronts generated by the impact of the solar plasma on the geomagnetic field bring eastward currents in the ionosphere, and the fact that the sc enhancement is 6 to 10 times greater in the magnetic equatorial region whereas the daily variation in that region is 2 to 3 times larger than that in lower latitudes could be explained by assuming double layers in the equatorial electrojet in which the direction is usually reversed. Maeda and Yamamoto [1960], using the ratios of the amplitudes of sc's for stations within  $\pm 45^\circ$  in geomagnetic latitude around the geomagnetic equator to those at Honolulu, also showed that the daytime enhancement of the amplitude of the sc occurs at stations less than about  $20^\circ$  in dip, that an abnormally large amplitude appears at stations very close (within about  $3^\circ$  in dip) to the dip equator, and that the magnitude of sc's at night

is almost the same for all equatorial stations. They suggested that the daytime enhancement of sc's is due to an electric current flowing in the  $S_q$  current layers and that the nighttime enhancement follows the Chapman-Ferraro model.

Hirono [1952] gave a theoretical explanation for the presence of the locally enhanced conductivity in the  $E$  region near the geomagnetic equator. Singer, Maple, and Bowen [1951], by means of total field magnetometer carried in rockets, established the existence in the  $E$  region of a current system, called the equatorial electrojet, which is responsible for the diurnal variation of the geomagnetic field at sea level near Huancaayo. Cahill [1959] has also found the equatorial electrojet, which consists of at least two layers of electric current, one layer near an altitude of 100 km and the other 20 to 25 km higher, by magnetometer flights near Jarvis Island, at the geomagnetic equator. From the above results we can understand that the daytime enhancement of the amplitude of sc's at the geomagnetic equator is closely correlated with the equatorial electrojet, that is, with locally enhanced effective conductivity in the equatorial ionosphere.

The above studies of the daytime enhancement of sc's at the geomagnetic equator treat the ionospheric currents responsible only qualitatively. In this paper we calculate the intensities and altitudes of ionospheric currents responsible for typical sc's at the geomagnetic equator, using the horizontal and vertical disturbance vectors of sc's observed at the Jarvis and Fanning stations, and discuss causes of the daytime enhancement of sc's at the geomagnetic equator.

## 2. Altitudes of ionospheric currents responsible

for sc's at the geomagnetic equator calculated the assumption of line current. Altitudes of ionospheric currents responsible for sc's observed at the Jarvis and Fanning stations are above 100 km under the assumption of line current. The altitude of the ionospheric current responsible for the sc seems to be independent of the time of the occurrence.

We first treat the ionospheric current for sc observed at the geomagnetic equator as a line current and calculate its altitude using the horizontal and vertical magnetic field of the sc observed at the Jarvis and Fanning stations. Rake and Yokoyama [1953] pointed out that an anomalously large amplitude of the vertical component of transient geomagnetic variations caused by the magnetic field originating in the earth. Such anomalies have never yet been observed near Jarvis and Fanning Islands. Therefore we do not need to consider such anomalies in analyzing magnetic data observed at these stations.

The Jarvis station (geomag. lat.  $00^{\circ}30'$ , geomag. long.  $269^{\circ}00'$ ) is approximately geomagnetic south of the Fanning station (geomag. lat.  $05^{\circ}20'$ ; geomag. long.  $276^{\circ}10'$ ). We project these two stations on the geomagnetic meridian plane (geomag. long.  $272^{\circ}35'$ ) as shown in Figure 1. In this figure  $V$  and  $P$  denote the vertical and horizontal disturbance vectors of the external field, respectively;  $h$ , the altitude of the ionospheric current;  $\theta$ , the angle between the directions of vectors  $V$  and  $P$ ;  $I$ , the total intensity of this current;  $D$ , the distance between projections of the stations (650 km); and subscripts  $J$  and  $F$  refer to these stations, respectively.

The ionospheric current considered here flows

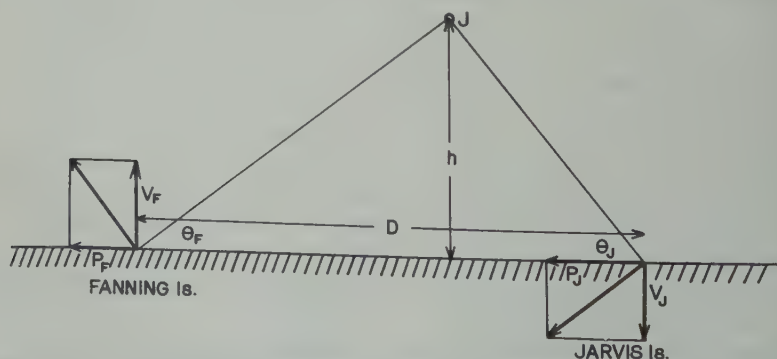


Fig. 1. Geometry determining an altitude of current responsible for a sc at the geomagnetic equator.

TABLE 1. Altitudes of Ionospheric Currents Responsible for Sudden Commencements Observed at Jarvis and Fanning Stations

sal Time	Local Time	$H_J, \gamma$	$Z_J, \gamma$	$H_F, \gamma$	$Z_F, \gamma$	$h, \text{ km}$
g. 29 1957	0920 Aug. 29	84.4	-10.5	43.3	10.4	590
pt. 13	1446 Sept. 12	98.6	-17.8	82.6	13.9	620
pt. 29	1416 Sept. 28	56.9	-10.7	31.5	8.7	470
v. 06	0821 Nov. 06	95.4	-14.5	51.1	14.4	500
p. 04 1958	0304 Feb. 04	15.3	-1.9	15.7	1.7	930
p. 11	1525 Feb. 10	130.5	-26.9	59.0	7.0	660
ar. 03	2331 Mar. 02	7.6	-1.9	7.9	3.4	320
ar. 05	1937 Mar. 04	15.2	-3.8	11.8	3.4	400
ar. 14	0212 Mar. 14	26.6	-3.8	15.7	10.1	270
ar. 25	0540 Mar. 25	30.3	-7.6	27.5	3.4	580
ar. 26	0247 Apr. 26	7.8	-2.0	7.5	1.6	460
ne 07	1446 June 06	58.9	-4.2	28.5	14.0	380
ne 14	0828 June 14	55.0	-8.3	32.6	3.5	840
ne 15	1909 June 14	27.5	-4.2	24.4	1.7	970
ly 08	2148 July 07	85.4	-16.5	84.5	10.3	690
ly 18	1621 July 18	11.6	-4.1	12.1	3.4	340
g. 17	2022 Aug. 16	46.6	-8.2	44.8	7.2	640
g. 22	1627 Aug. 21	81.5	-16.5	52.9	14.4	460
g. 24	1540 Aug. 23	93.2	-12.4	57.0	18.0	480
g. 27	1703 Aug. 26	31.1	-4.1	28.5	5.4	670
pt. 03	2243 Sept. 02	15.7	-4.2	24.4	7.2	380
pt. 16	2330 Sept. 15	23.6	-4.2	24.4	7.2	460
pt. 25	1808 Sept. 24	35.4	-4.2	28.5	7.2	580
pt. 30	0005 Sept. 30	27.5	-4.2	24.4	7.2	480
ov. 28	1509 Nov. 27	46.6	-8.2	20.3	3.6	610
ec. 15	1022 Dec. 15	69.9	-8.2	36.6	3.6	1010
ec. 17	0817 Dec. 17	120.4	-12.4	73.3	14.4	720

rd. The altitude of an ionospheric current  
the current is

$$h = \frac{D}{\cot \theta_J + \cot \theta_F}$$

$\cot \theta_J = V_J/P_J$  and  $\cot \theta_F = V_F/P_F$ .

calculate  $h$  for  $V = 2Z$ ,  $P = 2/3 \cdot H$ ,  $Z$  and  
ating respectively the vertical and horizon-  
turbance components of the magnetic  
served at the ground.

results of calculations of altitudes of cur-  
responsible for sc's observed at the Jarvis  
anning stations are given in Table 1. It is  
at most of the currents are at a height be-  
300 km and 1000 km, and that the am-  
s of corresponding sc's are generally  
at the Jarvis than at the Fanning station.  
mer fact is very different from the sug-  
by *Forbush and Vestine* [1955]. But we  
remember that the assumption of a line  
as the current responsible for the sc  
geomagnetic equator is an idealization.  
ter fact suggests that the currents re-

sponsible for sc's observed simultaneously at the  
two stations must be closer to the Jarvis than to  
the Fanning station.

Next we plot the data of Table 1 as a graph  
of the altitude of ionospheric current responsible  
for the sc against the local time of the occurrence.  
This is shown in Figure 2, from which we can  
deduce that there is no relation between the alti-  
tude of the current responsible for the sc and the  
local time of the occurrence.

3. *The intensity of an ionospheric current re-  
sponsible for an sc at the geomagnetic equator.* It  
is deduced from the next calculations that the  
total intensity of an ionospheric current respon-  
sible for an sc at the geomagnetic equator is of  
the order of  $10^4$  amperes. The total intensity of  
an ionospheric current  $I$  responsible for an sc at  
the geomagnetic equator is given by

$$I = \frac{D[(P_J^2 + V_J^2)(1 + \cot^2 \theta_J)]^{1/2}}{2(\cot \theta_J + \cot \theta_F)} \quad (1)$$

assuming a line current.

Rocket observations [*Cahill*, 1959] have in-



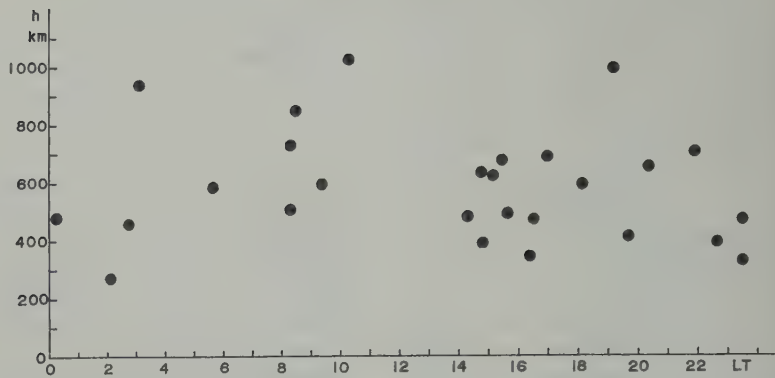


Fig. 2. A relation between the altitude of the current responsible for the sc calculated on line-current assumption and the local time of the occurrence.

indicated that the equatorial electrojet has the finite lateral extent of the layers (these widths being greater than 300 km) and a small vertical dimension. We next treat the current responsible for the sc at the geomagnetic equator as a uniform current sheet. The current density of  $J$  of a uniform current sheet with width  $2w$  is then given by

$$J = \frac{P}{2 \tan^{-1} \frac{(2w/h)}{[1 + (L/h)^2 - (w/h)^2]}} \tag{2}$$

where  $h$  is the height of the layer,  $L$  the horizontal distance from the center of the layer, and  $P$  the horizontal disturbance component of the external field [Chapman, 1951].

The results of calculation of  $I$  and  $J$  for the sc's occurring at 0016 UT Sept. 29, 1957 (1446 LT Sept. 28), 0140 UT Aug. 24, 1958 (1540 LT

Aug. 23), and 0005 UT Sept. 30, 1958 (0005 LT Sept. 30) are given in Table 2.

Baker and Martyn [1952] have indicated that the effective conductivity has only a single narrow maximum near 100 km in height. Forbush and Vestine [1955] have suggested that the normal augmentation of sc, initial phase, and those at Huancayo are associated with a narrow band of high electrical conductivity near the geomagnetic equator. Therefore we have adopted the values deduced from the line-current assumption and the most probable one of 120 km as  $h$  in the calculation of  $J$  in Table 2.

In equation 2 the values of  $L$  are obtained from the geometry of line-current assumption and those of  $P$  are taken as  $2/3 \cdot H$ . When  $P$ ,  $w$ , and  $L$  are constant,  $J$  attains a minimum at  $L = (L^2 - w^2)^{1/2}$  in equation 2 where  $L > w$ . Therefore the current height at which the effect of  $J$  on  $H$  is largest is dependent on  $L$  and  $w$  which

TABLE 2. Intensities of Ionospheric Currents Responsible for Sudden Commencements Observed at Jarvis and Fanning Stations (1 emu = 10 amperes)

Local Time of sc Occurrence	$H_J, \gamma$	$Z_J, \gamma$	$I, \text{emu}$	$J, \text{emu/cm}$	$J, \text{emu/cm}$
1416 Sept. 28, 1957	56.9	-10.7	$1.06 \times 10^4$	$3.10 \times 10^{-4}$	$3.48 \times 10^{-4}$
				$h$ 190 km; $L$ 260 km; $w$ 150 km	$h$ 120 km; $L$ 260 km; $w$ 150 km
1540 Aug. 23, 1958	93.2	-12.4	$1.19 \times 10^4$	$3.64 \times 10^{-4}$	$3.42 \times 10^{-4}$
				$h$ 190 km; $L$ 190 km; $w$ 150 km	$h$ 120 km; $L$ 190 km; $w$ 150 km
0005 Sept. 30, 1958	27.5	-4.2	$3.99 \times 10^3$	$1.23 \times 10^{-4}$	$1.25 \times 10^{-4}$
				$h$ 190 km; $L$ 220 km; $w$ 150 km	$h$ 120 km; $L$ 220 km; $w$ 150 km

constant. The total current intensity re-  
le for the sc on Sept. 30, 1958, is calcu-  
s  $3.8 \times 10^4$  amperes by the assumption  
form current sheet; it is calculated as 4.0  
amperes by the assumption of line cur-  
nce these values of total current intensity  
the same order, the line current must be  
good approximation to the current re-  
le for the sc at the geomagnetic equator.  
urrent densities responsible for sc's at the  
netic equator are calculated by means of  
in 2 for the probable values of  $P$ ,  $L$ ,  $w$ ,  
that are deduced from the average of ob-  
values on the line-current assumption;  
results are given in Table 3.

in  $L = 250$  km and  $w = 150$  km, the cur-  
eight at which the effect of  $J$  on  $H$  is  
it is estimated as 200 km. It is shown in  
3 that the ionospheric current density re-  
le for the sc observed at the geomagnetic  
r is of the order of  $10^{-8}$  amp/cm. This may  
pared with the auroral electrojet of 5.6  
amp/cm [Akasofu, 1960], the equatorial  
jet of  $7.86 \times 10^{-4}$  amp/cm [Onwumechilli,  
and the equatorial noon current density  
( $S_e$  of  $1.9 \times 10^{-4}$  amp/cm [Chapman  
rtels, 1940]. From Table 3 we can deduce  
he effect of the width of the current layer  
current density is greater than the effect  
current height.

on the horizontal distance from the center  
current layer to the Jarvis station,  $L$ , is  
190 km,  $w = 150$ , and  $P$  is given, the cur-  
density of a uniform current sheet attains a  
um at a height of about 120 km. The ef-  
electrical conductivity of the ionosphere  
a maximum at about 120 km. Therefore,  
the ionospheric current whose center lies  
190 km from the Jarvis station in the  
ntal distance flows at a height of 120 km,  
eatest effect of the current  $J$  on  $H$  will be  
ed at the Jarvis station ( $w = 150$  km).

discussion of the daytime enhancement of  
plitude of the sc at the geomagnetic equator.  
ial electrical conductivity  $\sigma_s$  applies to  
s flowing parallel to the electric field and  
erse to the magnetic field when Hall  
is prevented from flowing. At the geomag-  
equator Hall conductivities  $\sigma_{xy}$  and  $\sigma_{yz}$   
and  $\sigma_s (= \sigma_{yy})$  is considered to be effective.  
electric current flowing eastward in the  
ere at the geomagnetic equator is given by

TABLE 3. Ionospheric Current Densities  
Responsible for sc's at the Geomagnetic  
Equator Calculated by the Assumption  
of Uniform Current Sheet  
(1 emu/cm = 10 amp/cm)

$H, \gamma$	$P, \gamma$	$J$ , emu/cm
When $h = 120$ km, $L = 250$ km, and $w = 150$ km		
120	80	$6.84 \times 10^{-4}$
90	60	$5.13 \times 10^{-4}$
60	40	$3.42 \times 10^{-4}$
30	20	$1.71 \times 10^{-4}$
When $h = 210$ km, $L = 250$ km, and $w = 150$ km		
120	80	$6.22 \times 10^{-4}$
90	60	$4.67 \times 10^{-4}$
60	40	$3.11 \times 10^{-4}$
30	20	$1.56 \times 10^{-4}$
When $h = 510$ km, $L = 250$ km, and $w = 150$ km		
120	80	$8.48 \times 10^{-4}$
90	60	$6.36 \times 10^{-4}$
60	40	$4.24 \times 10^{-4}$
30	20	$2.12 \times 10^{-4}$
When $h = 120$ km, $L = 250$ km, and $w = 200$ km		
120	80	$4.37 \times 10^{-4}$
90	60	$3.28 \times 10^{-4}$
60	40	$2.18 \times 10^{-4}$
30	20	$1.09 \times 10^{-4}$

$$J = KE \tag{3}$$

where  $E$  is an eastward electric field and  $K$  is  
the height integral of  $\sigma_s$  in the  $E$  layer ( $K = \int_E \sigma_s$   
 $dh$ ). The value of  $K$  at noon is about 10 times  
that at midnight ( $4.0 \times 10^{-8}$  emu) [Hirono and  
Maeda, 1955]. Therefore if the approximately  
uniform eastward electric field exists in the  
ionosphere along the geomagnetic equator at  
the time of sc, the daytime enhancement of the  
amplitude of sc at the geomagnetic equator may  
be explained by means of equation 3. The  
electric fields responsible for sc's having distur-  
bance fields of 120 and 30 gammas are of the  
order of 10 and 0.5 volt/km in the  $E$  layer,  
respectively.

Francis, Green, and Dessler [1959] have pro-  
posed that the sudden commencement is caused  
by the arrival of hydromagnetic waves generated  
by the impact of the solar plasma cloud on the  
geomagnetic field. Matsushita [1960] has sug-

gested that these hydromagnetic waves bring the eastward currents in the ionosphere. It is shown in Table 1 that the currents corresponding to the sc's with large amplitude are at a height between 450 and 700 km. But there is no evidence that the current flows at such a high altitude. Therefore we cannot precisely determine the altitudes of ionospheric currents responsible for the sc's at the geomagnetic equator. Piddington [1959], Francis and Karplus [1960], and Tamao [1961] have shown that theoretically the hydromagnetic waves responsible for the sc's do not propagate in the lower ionosphere.

Combining the Maxwell's equations of rot  $\mathbf{E} = -\partial\mathbf{B}/\partial t$ ,  $\text{div } \mathbf{B} = 0$ ,  $\mathbf{B} = \mu\mathbf{H}$ ,  $\mathbf{J} = \sigma\mathbf{E}$ , and  $\text{rot } \mathbf{H} = 4\pi\mathbf{J}$ , we have

$$\frac{\partial\mathbf{H}}{\partial t} = \frac{1}{4\pi\sigma\mu} \nabla^2\mathbf{H} \quad (4)$$

where  $\mu$  is the magnetic permeability,  $\sigma$  the electrical conductivity,  $\mathbf{J}$  the current density,  $\mathbf{E}$  the electric field strength, and  $\mathbf{H}$  the magnetic field strength.

Equation 4 shows that the magnetic field caused by the ionospheric current diffuses through to the ground. It seems likely that the large absorption of the hydromagnetic waves in the ionosphere may support the existence of ionospheric currents responsible for sc's and that the magnetic field thus produced by the current may diffuse to the ground.

The altitudes of ionospheric currents responsible for the sc's at the geomagnetic equator may be determined by detailed consideration of the distribution of the electrical conductivity and the absorption of the hydromagnetic waves.

The world-wide distribution of the maximum electron density in the  $F_2$  layer has been studied by Maeda, Uyeda, and Shinkawa [1942], Appleton [1946, 1950], Bailey [1948], Uyeda [1948], and Aono [1953]. Their results have indicated that, for noon conditions, there is a belt of low values for maximum electron density in the  $F_2$  layer along the geomagnetic equator, the center lying roughly at the geomagnetic equator, and that the maximum values of maximum electron density in the  $F_2$  layer are attained at about 20° north and south geomagnetic latitudes, the belt of the maximum electron density in the  $F_2$  layer being abnormally high at the geomagnetic equator.

Hirono and Maeda [1955] have suggested that

this anomaly is caused by the vertical drift of electrons in that layer. The vertical drift affects the positive ions as well as the electrons. Therefore it seems likely that the number density of positive ions in the  $F_2$  layer at the geomagnetic equator is also low for noon conditions. These facts suggest that the hydromagnetic waves propagating from the outer boundary of the earth's exosphere may be locally refracted toward the geomagnetic equator when they pass through the increase in height of the maximum positive ion density of the  $F_2$  layer at the geomagnetic equator, and that such hydromagnetic waves refracted into the  $F_2$  layer may be less attenuated at the geomagnetic equator than at other latitudes because of the low density of the positive ions in the noon  $F_2$  layer there. This reasoning might explain the statement by Maeda and Yamamoto [1960] that the daytime enhancement of the amplitude of the sc occurs at stations less than about 20° in dip, and an abnormally large amplitude of the sc appears at stations very close to the dip equator.

*Acknowledgments.* I wish to express my sincere thanks to Professor Y. Tamura and Dr. H. Maeda for their kind suggestions and advice, and also to Mr. T. Kitamura for his valuable discussions.

## REFERENCES

- Akasofu, S., Large-scale auroral motions and polar magnetic disturbances, I, A polar disturbance about 1100 hours on 23 September 1957, *J. Atmospheric and Terrest. Phys.*, **19**, 10-25, 1960.
- Aono, Y., On world-wide distributions of  $f_oF_2$ , *Rep. Ionosphere Research Japan*, **6**, 69-78, 1952.
- Aono, Y., Regional anomalies in  $f_oF_2$  of the ionosphere, *Rept. Ionosphere Research Japan*, **30**-33, 1953.
- Appleton, E. V., Two anomalies in the ionosphere, *Nature*, **157**, 691, 1946.
- Appleton, E. V., *J. Atmospheric and Terrest. Phys.*, **1**, 106, 1950.
- Bailey, D. K., The geomagnetic nature of the  $F_2$  layer longitude-effect, *Terrest. Magnetism and Atmospheric Elec.*, **53**, 35-39, 1948.
- Baker, W. G., and D. F. Martyn, Conductivity of the ionosphere, *Nature*, **170**, 1090-1092, 1952.
- Cahill, L. J. T., Jr., Investigation of the equatorial electrojet by rocket magnetometer, *J. Geophysical Research*, **64**, 489-503, 1959.
- Chapman, S., *Arch. Meteorol. Wien*, **4**, 368, 1950.
- Chapman, S., and J. Bartels, *Geomagnetism*, Oxford University Press, 1940.
- Ferraro, V. C. A., and H. W. Unthank, *Geophys. Res. appl.*, **20**, 27, 1951.
- Forbush, S. E., and E. H. Vestine, Daytime enhancement of size of sudden commencement

- initial phase of magnetic storms at Huan-  
*J. Geophys. Research*, *60*, 299-316, 1955.
- , W. E., M. I. Green, and A. J. Dessler,  
 omagnetic propagation of sudden com-  
 ements of magnetic storms, *J. Geophys. Re-*  
*h*, *64*, 1643-1645, 1959.
- , W. E., and R. Karplus, Hydromagnetic  
 s in the ionosphere, *J. Geophys. Research*,  
 3953-3600, 1960.
- , M., A theory of diurnal magnetic varia-  
 in equatorial regions and conductivity of  
 ionosphere *E* region, *J. Geomag. Geoelect.*  
*o*, *4*, 7-21, 1952.
- , M., and H. Maeda, Geomagnetic distur-  
 of the *F*<sub>2</sub> region on the magnetic equator,  
*ophys. Research*, *60*, 241-255, 1955.
- , K., H. Uyeda, and H. Shinkawa, *Rept.*  
*arch Phys. Inst. Rad. Waves*, nos. 1, 2, and  
 42.
- , H., and M. Yamamoto, A note on daytime  
 ncrement of the amplitude of geomagnetic  
 in sudden commencements in the equatorial  
 n, *J. Geophys. Research*, *65*, 2538-2539, 1960.
- shita, S., Studies on sudden commencements  
 geomagnetic storms using IGY data from  
 ed States stations, *J. Geophys. Research*, *65*,  
 1435, 1960.
- Onwumechilli, C., The relation between *H* and *Z*  
 variations near the equatorial electrojet, *J. At-*  
*mospheric and Terrest. Phys.*, *16*, 274-282, 1959.
- Piddington, J. H., The transmission of geomagnetic  
 disturbances through the atmosphere and inter-  
 planetary space, *Geophys. J.*, *2*, 173-189, 1959.
- Rikitake, T., and I. Yokoyama, Anomalous rela-  
 tions between *H* and *Z* components of transient  
 geomagnetic variations, *J. Geomag. Geoelect.*  
*Kyoto*, *5*, 59-65, 1953.
- Singer, S. F., E. Maple, and W. A. Bowen, Jr.,  
 Evidence for ionosphere currents from rocket ex-  
 periments near the geomagnetic equator, *J. Geo-*  
*phys. Research*, *56*, 265-281, 1951.
- Sugiura, M., The solar diurnal variation in the  
 amplitude of sudden commencements of mag-  
 netic storms at the geomagnetic equator, *J.*  
*Geophys. Research*, *58*, 558-559, 1953.
- Tamao, T., Lecture at the Society of Terrestrial  
 Magnetism and Electricity of Japan, Tokyo,  
 May 1961.
- Uyeda, H., *Rept. Research Phys. Inst. Rad. Waves*,  
 no. 8, 1948.

(Manuscript received July 24, 1961;  
 revised September 29, 1961.)





## A Metastable Helium Magnetometer for Observing Small Geomagnetic Fluctuations

A. R. KEYSER, J. A. RICE, AND L. D. SCHEARER

*Texas Instruments Incorporated  
Dallas, Texas*

**Abstract.** A metastable helium magnetometer using the principle of optical pumping has been constructed. The operating principles of the device are discussed together with some of the design considerations. The application of the magnetometer to the direct recording of variations in the magnitude of the earth's magnetic field in the milligamma range is presented. Records of the commencement and ending of a magnetic storm are shown.

**Introduction.** The application of optical pumping techniques [Kastler, 1954; Dehmelt, 1955; Hawkins, 1955] to the precise measurement of weak magnetic fields has led to the development of several magnetometers [Skillman and Bender, 1958; Unterberger, 1960; Bell and Rice, 1957; Rice, 1961] capable of measuring the magnitude of the earth's field. The chief advantages of the optically pumped magnetometer over other types lie in (1) their ability to measure extremely small changes in total field (gamma), (2) the absolute character of the measurements involved, and (3) the nature of the output signal which permits continuous observation of the field without calibration.

Rubidium vapor magnetometers have been successfully used to monitor field variations [Skillman and Bender, 1958; Unterberger, 1960]. The Rb devices have, however, several undesirable features. All alkali atoms possess a nuclear spin which further splits the atomic energy levels. The signal in the case of Rb<sup>87</sup> consists of a complex of six resonance lines; consequently, unnecessary confusion can result in an automatic recording device. This is particularly true for lower field values where the lines are less well resolved. The presence of the nuclear spin introduces nonlinearities in the relationship between the magnetic field and magnetometer output. The pumping process additionally requires that the absorption cell be temperature controlled.

We have recently developed an optically pumped, highly sensitive, absolute magnetometer which utilizes helium atoms in their metastable states. The use of helium atoms as the

working substance does not have the disadvantages associated with the Rb magnetometer, although the performance of the two instruments is similar.

**Optical pumping in helium.** Optical pumping is a technique for orienting free atoms by the action of a specially prepared beam of light. The orientation in helium [Colegrove and Franken, 1960; Schearer, 1961] is accomplished by passing a beam of circularly polarized resonance radiation along the axis of the magnetic field and through an ensemble of helium atoms in their metastable state. In a weak magnetic field the 2<sup>3</sup>S<sub>1</sub> metastable state is split into three Zeeman sublevels. The energy separation between the sublevels is directly proportional to the magnetic field. The principle of operation of the helium magnetometer depends upon the ability of resonance radiation of wavelength 1μ to orient the magnetic moments, or populations of the triplet metastable helium atom, by the process of optical pumping. The polarization thus produced can be destroyed by the application of a radio-frequency magnetic field at right angles to the constant magnetic field and at a frequency

$$\nu_0 = eH/2\pi mc \approx 28 \text{ cps}/\gamma \quad (1)$$

corresponding to the Zeeman splitting of the sublevels. The resonance condition can be observed because the amount of pumping light removed from the beam depends upon the population ratios (and hence on the magnitude of the magnetic moment) of the Zeeman sublevels.

The resonance signal is obtained by monitor-

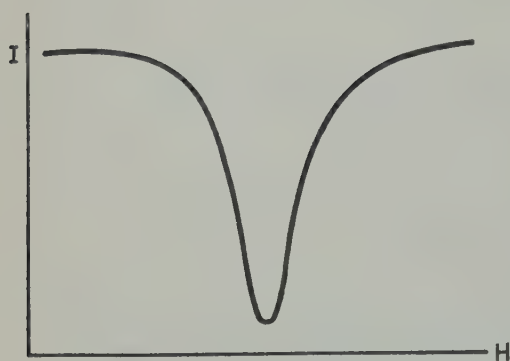


Fig. 1. Resonance signal.

ing the light passing through the ensemble of metastable helium atoms. In general, the atoms in each of the three magnetic sublevels absorb light at different rates, which results in unequal populations of the three levels. The signal is the difference between the light absorbed under these conditions and the light absorbed when an RF magnetic field restores equal populations of the levels. The amount of light transmitted through the absorbing atoms decreases when the RF resonance field is applied because more atoms have been placed in the more highly absorbent states. Figure 1 shows the light intensity as a function of the magnetic field. At the resonance frequency the transmitted light intensity becomes markedly smaller.

*Description of resonance device.* Figure 2 is a schematic diagram of the helium resonance

device. Resonance radiation is obtained from a 6-mm capillary tube filled with helium to a pressure of 8 mm Hg. The lamp is excited from a 50 Mc/s 5-watt RF power supply. Pure helium gas at a pressure of 0.2 mm Hg in a 60-ml pyrex absorption cell is excited to the  $2^3S_1$  state by the application of a weak RF electric field. Light from the lamp is linearly polarized with a Polaroid type HR infrared polarizer. A 3-mil thick polyethylene sheet is used as a quarter-wave plate for radiation of wavelength  $1\mu$ . Several turns of wire with a diameter of 1 inch provide the required 200- $\gamma$  RF magnetic field when connected to the RF resonance oscillator. The signal produced by passage through resonance is detected by a PbS photocell sensitive to the  $1.08\text{-}\mu$  resonance radiation.

*The magnetometer.* A small magnetic field of 200  $\gamma$  modulated at several hundred cycles per second is applied collinearly with the external field to be measured. This magnetic modulation in turn modulates the light reaching the photodetector. The voltage output of the photocell is fed to a phase sensitive amplifier along with a reference voltage at the modulation frequency. The output of the phase detector is a voltage proportional to the derivative of the resonance curve. Figures 3a and 3b illustrate the manner in which the derivative is obtained. The phase detector output is then applied to a voltage-variable resonance oscillator so that the frequency of the oscillator is maintained at the center of the resonance condition determined

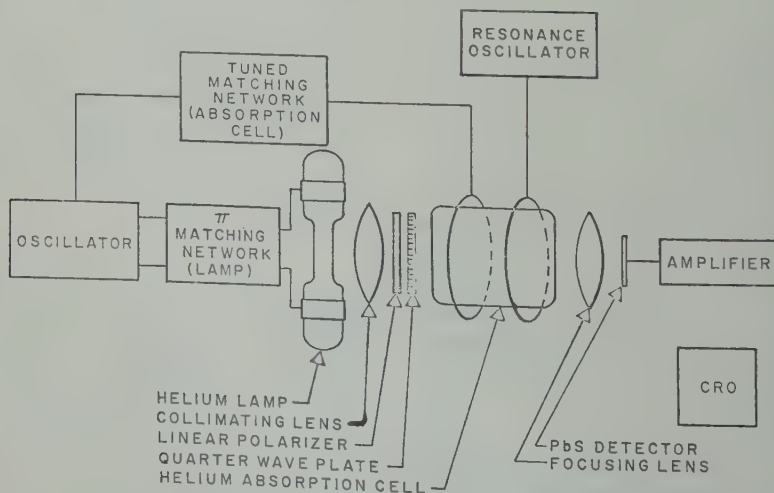


Fig. 2. Schematic diagram of the helium magnetometer.

). The voltage output of the photocell is sent to a servomotor which integrates the cumulative slow-drift error inherent in the all-electronic loop. The mechanical integrator, however, possesses considerable inertia due to starting friction, and hence its frequency response and resolution are limited. The use of an all-electronic loop gives the advantages of both. The electronic loop provides fast response and high resolution while the integrating mechanical loop corrects the oscillator for long-term drifts of either frequency or amplitude. This latter correction is necessary because the frequency output of the control oscillator is error dependent and the static error must be kept small if high accuracy is desired for the measurement of absolute fields or in relative measurements at very low frequencies. As the earth's field changes the oscillator automatically tracks the resonance frequency.

In a field of 50,000  $\gamma$  the frequency output of the resonance oscillator is about 1.4 Mc/s. A crystal mixer is used to provide a beat frequency which is frequency modulated by the magnetic field variations. A Hewlett-Packard Model 500B frequency meter and discriminator are used to demodulate the carrier and provide an analog of the field variations. The analog signal output of the discriminator was then recorded. Direct digital readout of the resonance oscillator is used to provide an absolute measure of the field. Digital readout and recording equipment may be obtained commercially or built-in cycle counters. A count to the next cycle represents a resolution of 0.03  $\gamma$ .

*Results.* The limiting sensitivity of the instrument is determined primarily by the signal-to-noise ratio and the width of the resonance. The signal-to-noise ratio is typically 10,000 in a 2-cps bandwidth. The resonance half-width is of the order of 0.03  $\gamma$ . This permits the automatic setting of the oscillator to better than 1 cps.

Various typical geomagnetic behavior patterns have been observed and recorded at Grapevine, Texas, using the metastable helium magnetometer. Figure 4 shows the dramatic ending of a magnetic storm as indicated by micropulsations in the frequency range of 0.03 to 0.3 cps. Note the characteristic 'beads of pearl' effect in the decaying micropulsations. The sensing and recording conditions remain constant as indicated throughout the recording. A micropulse, although somewhat less dramatic, decay

of micropulsation activity is shown in Figure 5. Note the variation of the periodicity of the activity. A well-documented sudden commencement of a magnetic storm is shown in Figure 6. Figure 7 is an 8-hour record of total field. Figure

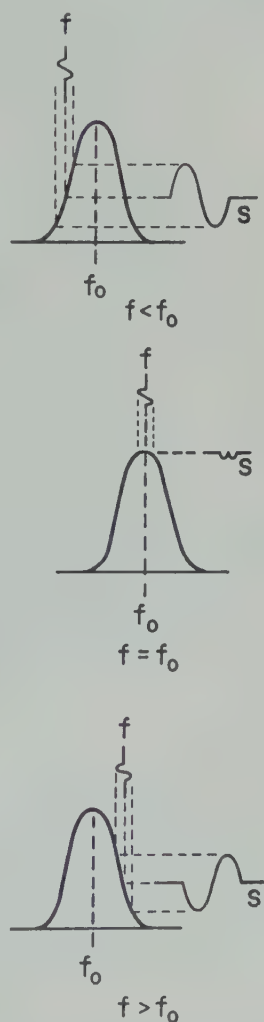


Fig. 3a. Photodetector output with small amplitude field modulation.

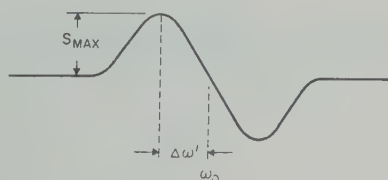


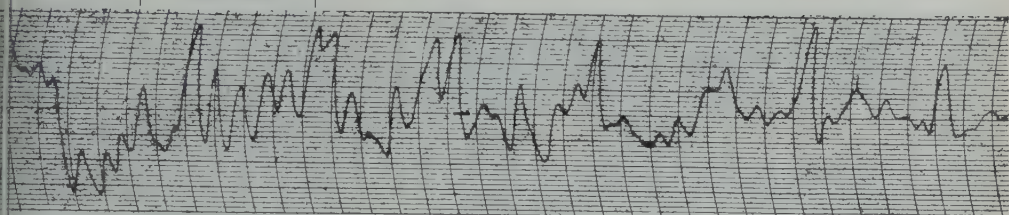
Fig. 3b. Signal after phase detection and demodulation.



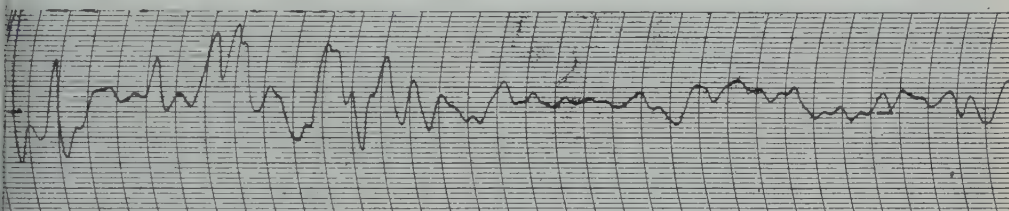


Fig. 4. Geomagnetic fluctuations: death of a storm observed March 24, 1961.

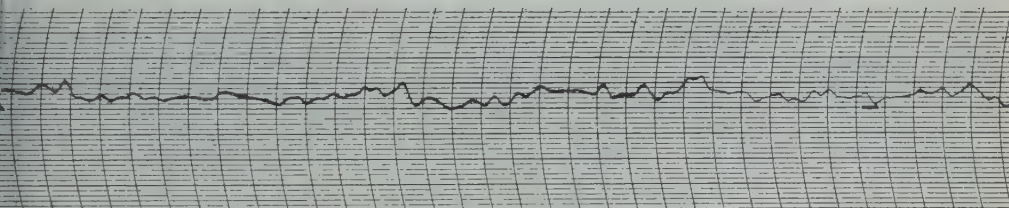
← 30 SECONDS →



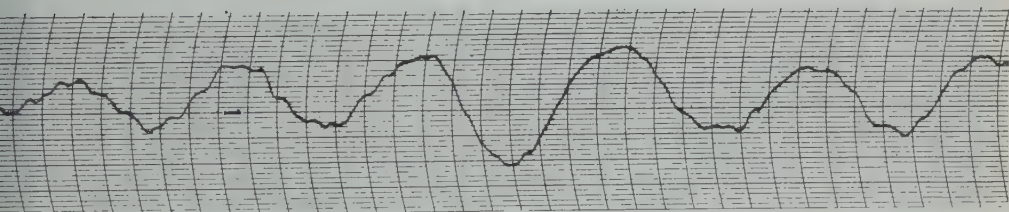
21:30 GMT 27 JANUARY 1961



21:45 GMT



22:30 GMT



23:00 GMT

TEXAS INSTRUMENTS GRAPEVINE, TEXAS OBSERVATORY  
BANDPASS 0.03 TO 0.3 (-3 db)  
SENSITIVITY  $\approx 33$  MILLIGAMMA/MINOR DIVISION, CHART SPEED = 1 MM/SECOND

Fig. 5. Geomagnetic fluctuations observed January 27, 1961.

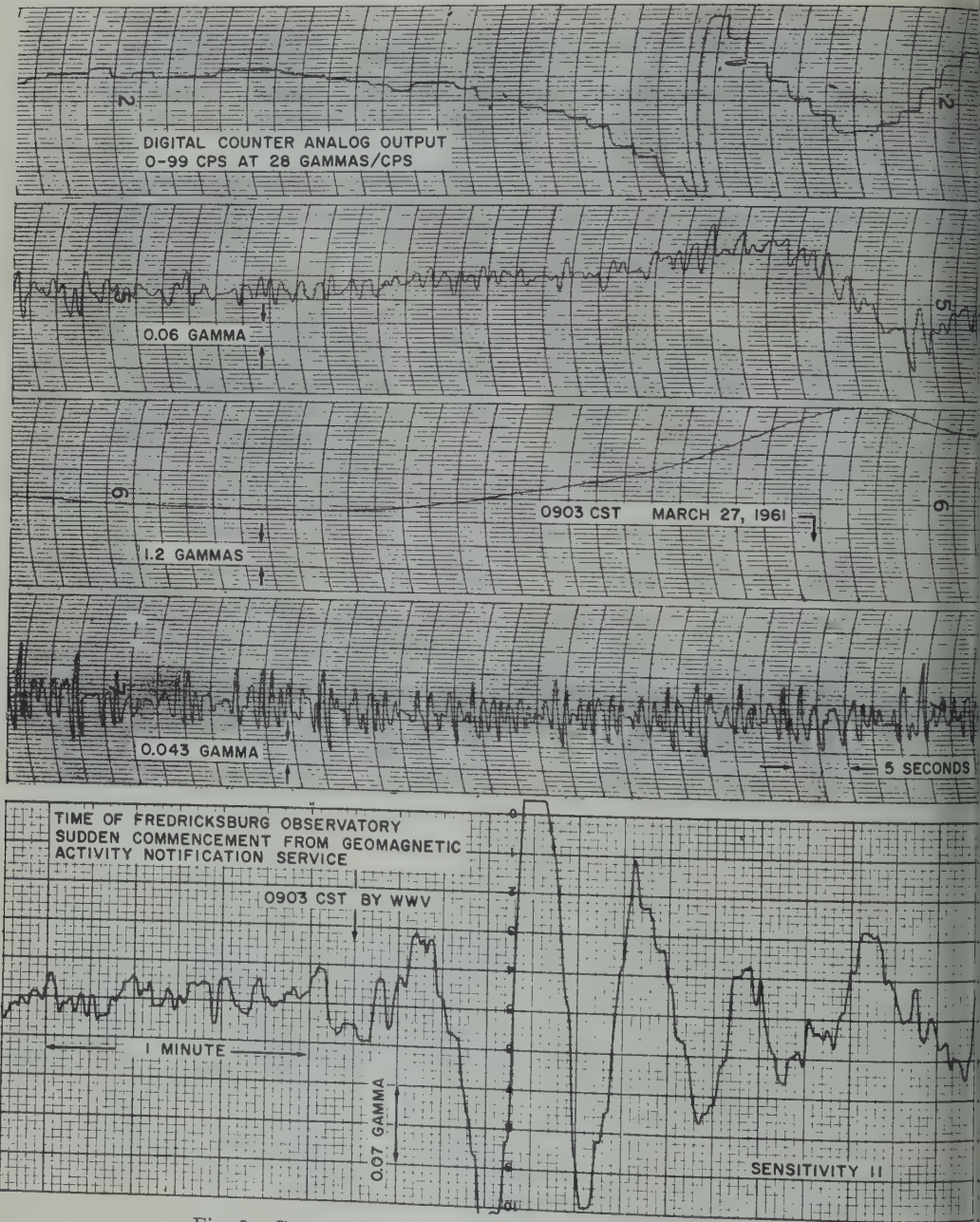
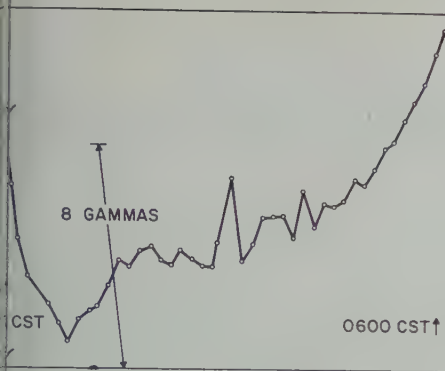
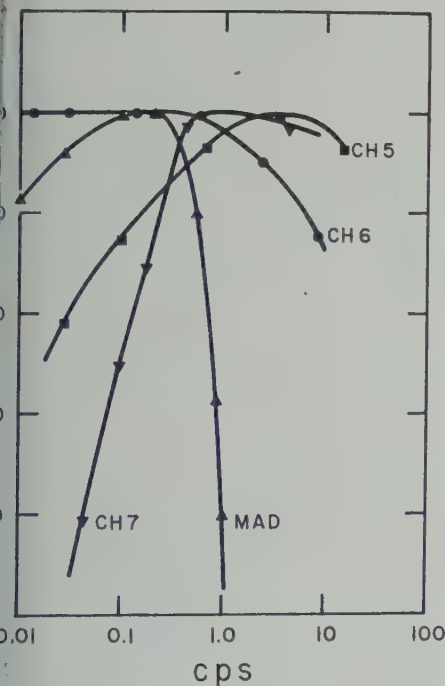


Fig. 6. Geomagnetic fluctuations: commencement of a storm.





Geomagnetic fluctuations: 8-hour night activity observed June 29, 1961.



Frequency response curves of recording channels.

8 gives response characteristics for geomagnetic data not otherwise indicated; channel numbers corresponding to those in this figure are shown on appropriate recordings in block numerals.

Instrument noise evaluated in a magnetically quiet period such as is shown at the end of Figure 4 would suggest that micropulsations considerably less than the  $0.01 \gamma$  reported by Unterberger [1960] can be resolved by the metastable helium magnetometer.

*Conclusion and comment.* The simplicity of construction and operation of the helium magnetometer and the sensitivity and absolute character of its measurements make the instrument ideally suited for operation as a station magnetometer. The device suffers no environmental problems which are not also inherent in the electronic equipment; it offers reliability and long operating life.

We wish to express our appreciation to J. Chivian and D. Eden for their part in recording the magnetic data presented.

#### REFERENCES

- Bell, W. E., and A. L. Bloom, Optical detection of magnetic resonance in alkali vapor, *Phys. Rev.*, **107**, 1559, 1957.
- Colegrove, F. D., and P. A. Franken, Optical pumping of helium in the  $^3S_1$  metastable state, *Phys. Rev.*, **119**, 680, 1960.
- Dehmelt, H. G., Slow spin relaxation of optically polarized sodium atoms, *Phys. Rev.*, **105**, 1487, 1957.
- Hawkins, W. B., Orientation and alignment of sodium atoms by means of polarized resonance radiation, *Phys. Rev.*, **98**, 478, 1955.
- Kastler, A., Les méthodes optiques d'orientation atomique et leurs applications, *Proc. Phys. Soc. London A*, **67**, 853, 1954.
- Rice, J. A., *Record of IRE Intern. Conv.*, 1961.
- Scheerer, L. D., *Advances in Quantum Electronics* (to be published).
- Skillman, T. L., and P. L. Bender, Measurement of the earth's magnetic field with a rubidium vapor magnetometer, *J. Geophys. Research*, **63**, 513, 1958.
- Unterberger, R. R., Direct recording of small geomagnetic fluctuations, *J. Geophys. Research*, **65**, 4213, 1960.

(Manuscript received August 10, 1961.)





# The Effects of Atmospheric Refraction on Angles Measured from a Satellite

A. C. HOLLAND

*Baird-Atomic, Inc., Cambridge 38, Massachusetts*

**Abstract.** The refraction at a satellite is defined as the angle subtended at a satellite by the actual line of sight and the vacuum line of sight from the satellite to a point on the earth. If the satellite is assumed to be above the sensible atmosphere and if the well-known expression for astronomical refraction is accepted, the equations for the satellite refraction and the first order error coefficients can be derived. Results of computations show that the refraction at the satellite is always less than 1.0 per cent of the total or astronomical refraction and that the sensitivity to changes in the independent variables is small. It is also shown that changes in the astronomical refraction have very little effect on the refraction at the satellite.

**Introduction.** The use of artificial earth satellites for mapping and surveillance has increased interest in the error in angular measurements made at a satellite due to atmospheric refraction in the visible spectrum.

Atmospheric refraction causes an apparent change in the zenith distance of an observed object (Fig. 1). If a spherical earth and a constant atmosphere are assumed, refraction is defined to a plane defined by geocentric radii to the observer and to the target. The refraction is the angle between the lines of sight to objects at the observer's zenith and may be as much as 35 minutes of arc at the observer's zenith.

The refraction at the ground  $\Delta\phi_o$  is defined as the angle at the ground, between the apparent line of sight to a satellite  $T$  and the true or vacuum line of sight. The refraction at the satellite  $\xi$  is defined as the angle subtended at the satellite by the apparent and vacuum lines of sight. For objects at heights that are small compared with the radius of the earth, the refraction at the satellite is zero, and the refraction at the ground is equal to the astronomical refraction. However, for satellites near the earth, the satellite refraction can become appreciable. When satellites are used for geodetic measurements, in which an accuracy of 1 to 2 seconds of arc is required, a good estimate of the magnitude of the satellite refraction is needed. In this paper, equations for the magnitude of the refraction and its sensitivity to changes in the independent variables are derived.

**Refraction.** The integral of the curvature of the light path between the observer and the

target is defined as the refraction  $\xi$  by the well-known equation [Smart, 1956]

$$\xi = \mu_o R_o \sin \phi_o$$

$$\cdot \int_{\mu(R_T)}^{\mu(R_o)} \frac{d\mu}{\mu(\mu^2 R^2 - \mu_o^2 R_o^2 \sin^2 \phi_o)^{1/2}}$$

where  $R$  is the geocentric distance to a point on the light path, and  $\mu(R)$  is the index of refraction at that point.  $R_o$  and  $R_T$  are the geocentric distances to the observer and target, respectively, and  $\phi_o$  is the apparent zenith angle from the observer to the target. If the Gladstone-Dale relation  $\mu = 1 + c\rho$  [McLeod, 1919] is used and some model atmosphere is assumed, the integral can be evaluated.

When the target is within the atmosphere, the integral  $\xi$  must be evaluated for every target height of interest. However when the target is outside the atmosphere,  $\mu(R_T) = 1.0$  and the integral  $\xi$  is independent of target height. Here we consider only the case in which the target is

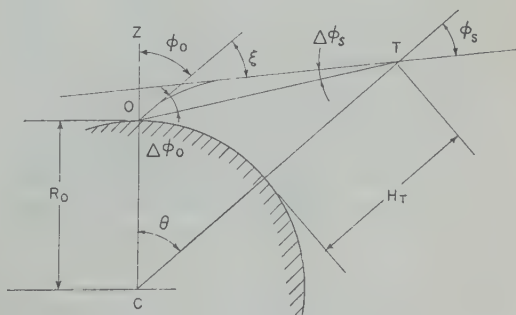


Fig. 1. Geometrical relationships.

outside the earth's atmosphere; the integral  $\xi$  is then the astronomical refraction.

For moderate zenith angles ( $\phi_o < 75^\circ$ ) the astronomical refraction is given to a good approximation by the expression [Smart, 1956]

$$\xi = \eta_o(1 - \sigma) \tan \phi_o - \eta_o \sigma \tan^3 \phi_o + \frac{1}{2} \eta_o^2 \tan^5 \phi_o$$

where  $\eta_o = (\mu_o - 1)$  is the refractive modulus and  $\sigma = L/R_o$ . Here  $L$  is defined as the height of a homogeneous atmosphere having the same density as that at the ground observer, and giving the same atmospheric pressure. For mean sea-level conditions  $L$  is approximately 8 km and  $\sigma$  is then roughly  $1/800$ . The refractive modulus at the observer is approximately  $3 \times 10^{-4}$  so that the term  $\eta_o^2/2$  is approximately  $4 \times 10^{-8}$  and is neglected. The astronomical refraction can then be expressed as

$$\xi = (\mu_o - 1) \tan \phi_o - (\mu_o - 1) \sigma \tan \phi_o (1 + \tan^2 \phi_o)$$

For standard sea-level conditions ( $P = 30$  in Hg,  $T = 50^\circ\text{F}$ ) the mean astronomical refraction is  $\xi = 58.2'' \tan \phi_o - 0.0668'' \tan^3 \phi_o$ .

The flat earth approximation for astronomical refraction is [Smart, 1956]

$$\xi = (\mu_o - 1) \tan \phi_o$$

which differs from the general form by less than 0.5 seconds of arc when  $\phi_o$  is less than  $60^\circ$ . In this treatment we shall use the flat earth approximation for the astronomical refraction since it gives a simple functional relation between  $\xi$  and the variables  $\phi_o$  and  $\mu_o$ .

Neglecting the second term in the equation for the refraction is conservative, since that term reduces the refraction and hence reduces both  $\Delta\phi_o$  and  $\Delta\phi_s$ . Later we shall examine the effects of changes in the astronomical refraction on both  $\Delta\phi_o$  and  $\Delta\phi_s$ .

The variation of the mean astronomical refraction with temperature and pressure can be expressed as the variation of the index of refraction with temperature and pressure [Handbook of Geophysics for Air Force Designers, 1957]:

$$10^6 \times \eta_o = (\mu_o - 1) \times 10^6 \\ = 77.6 P_o / T_o + 0.584 P_o / \lambda^2 T_o$$

where  $P_o$  is the ambient pressure in millibars,  $T_o$  is the ambient temperature in degrees Kelvin, and  $\lambda$  is the wavelength of the light in microns. The *Handbook of Geophysics for Air Force Designers* states that this equation is accurate to 1  $n$  unit (i.e. 1 millionth part of  $\mu_o$ ) for dry air and that, without corrections for water vapor, an additional error of 3  $n$  units is possible.

*Selection of independent variables.* In general it takes only two variables to specify a point in the plane. We could specify the position of the satellite  $T$  with respect to the center of the earth by the two independent variables  $R_T = (R_o + H_T)$  and  $\theta$ . However  $\theta$  depends on  $\phi_o$  and  $\xi$ , and  $\xi$  is a function of  $\phi_o$  and  $\mu_o$ . The position of the observer with respect to the earth center is specified by  $R_o$ . We could take  $R_o$  as a constant and then specify the position of the satellite with respect to the observer in terms of a constant  $R_o$  and the three independent variables  $\phi_o$ ,  $\mu_o$ , and  $H_T$ . However, in this treatment we consider the satellite refraction to be a function of the four independent variables ( $\phi_o$ ,  $\mu_o$ ,  $R_o$ ,  $H_T$ ). Here  $\phi_o$  is the apparent zenith angle from the observer to the satellite and  $\mu_o$  is the index of refraction at the observer.  $R_o$  is the distance of the observer from the center of coordinates and  $H_T$  is the height of the satellite above the observer.

*Equation for satellite refraction.* The sum of the refraction angle at the observer  $\Delta\phi_o$  and the refraction angle at the satellite  $\Delta\phi_s$  is  $\xi$  (Fig. 1). Applying the law of tangents to triangle  $OT$  we obtain

$$\frac{R_T + R_o}{R_T - R_o} = \frac{\tan \frac{1}{2}[180 - (\phi_o + \Delta\phi_o) + \phi_s - \Delta\phi_s]}{\tan \frac{1}{2}[180 - (\phi_o + \Delta\phi_o) - \phi_s + \Delta\phi_s]}$$

or

$$\Delta\phi_s = \theta/2 + \phi_s - \tan^{-1} [A \cdot \tan \theta/2] \\ = \Delta\phi_s(\phi_o, \mu_o, R_o, H_T) \\ \Delta\phi_o = \theta/2 - \phi_o + \tan^{-1} [A \cdot \tan \theta/2] \\ = \Delta\phi_o(\phi_o, \mu_o, R_o, H_T)$$

where

$$R_T = R_o + H_T \\ A = 1 + 2R_o/H_T$$

$$\theta = \phi_o - \phi_s + \xi$$

$$\phi_s = \sin^{-1} \left( \frac{\mu_o R_o}{R_T} \sin \phi_o \right).$$

first order in the independent variables  $R_o, H_T$ )

$$= \frac{\partial(\Delta\phi_s)}{\partial\phi_o} d\phi_o + \frac{\partial(\Delta\phi_s)}{\partial\mu_o} d\mu_o \\ + \frac{\partial(\Delta\phi_s)}{\partial R_o} dR_o + \frac{\partial(\Delta\phi_s)}{\partial H_T} dH_T$$

partial derivatives or 'error coefficients'

$$= \bar{Q}[1 + (\mu_o - 1) \sec^2 \phi_o] + Q \frac{\tan \phi_s}{\tan \phi_o}$$

$$= \bar{Q} \tan \phi_o + \frac{Q \tan \phi_s}{\mu_o}$$

$$= \left( \frac{H_T}{R_o + H_T} \right)$$

$$Q \tan \phi_s - \frac{(R_o + H_T)(2Q - 1) \sin \theta}{H_T(2R_o + H_T)} \Big]$$

$$= -\frac{R_o}{H_T} \cdot \frac{\partial(\Delta\phi_s)}{R_o}$$

$$= \frac{1}{2} \left[ 1 - \frac{A \sec^2 \theta/2}{1 + A^2 \tan^2 \theta/2} \right]$$

$$= 1 - \bar{Q}$$

equations can be derived for the derivation of  $\Delta\phi_o$  with respect to the independent variables.

Results. Values of the refraction corrections and  $\Delta\phi_s$  and their derivatives or 'sensitivity coefficients' for several representative values of the zenith angle and height are given in Table 1. In all cases the value of  $\mu_o$  was 1.0002817, corresponding to a temperature of 50°F, a pressure of 1013.23 mb, and a wavelength of 0.72  $\mu$ . The radius of the earth was taken as 6370.00 km. Calculations were carried out on a Recomp II computer. Original angle results were in degrees and minutes and showed errors of 1 or 2 in the seventh decimal place.

Section of Table 1 shows that the refraction correction  $\Delta\phi_s$  is small for all cases computed. In particular, in the worst case computed (100 km) the satellite refraction  $\Delta\phi_s$  is

never more than 1 per cent of the astronomical refraction  $\xi$ . For satellite heights above 1600 km the satellite refraction is negligible.

The satellite refraction is insensitive to variations in  $\phi_o$  or  $\mu_o$ . If we assume that the maximum uncertainty in  $\phi_o$  is  $\pm 1$  min of arc, then the maximum possible error in  $\Delta\phi_s$  is  $\pm 0.004$  sec of arc for the worst case computed. Also if 10  $n$  units is the maximum error in  $\mu_o$ , then the maximum error in  $\Delta\phi_s$  is 0.139 sec of arc. For satellite heights greater than 800 km, errors in  $\phi_o$  and  $\mu_o$  have no appreciable effect on  $\Delta\phi_s$ .

The satellite refraction is insensitive to variations in  $R_o$  or  $H_T$ . The largest 'sensitivity coefficient' calculated ( $H_T = 100$  km,  $\phi_o = 75^\circ$ ) is only  $1.85 \times 10^{-2}$  sec of arc per km. Hence, errors in satellite refraction caused by errors in  $R_o$  or  $H_T$  can be neglected.

The satellite refraction is also insensitive to variations in  $\xi$ , the astronomical refraction. Errors in  $\xi$  can arise in two ways: first, through discrepancies between the flat earth approximation used here and tabulated values of refraction; second, through discrepancies between tabulated values of mean refraction and the actual refraction experienced by an observer. As we have seen, the first case amounts to less than  $1/2$  sec of arc for zenith angles less than  $60^\circ$ .

The discrepancies between mean and actual refraction are due to differences between the model atmosphere used in integrating  $\xi$  and the actual atmosphere. Fletcher [1952] estimated that the primary discrepancies are due to (1) tilting of atmospheric layers (i.e. the layers of constant optical properties are not truly spherical and concentric with the earth) and (2) the seasonal variation of temperature gradients in the lower atmosphere, including inversions. Strand [1953] estimated that the differences between mean and actual refractions can be as high as 8 per cent from one night to the next. This would imply a maximum variation in  $\xi$  of approximately  $\pm 8$  sec of arc for a zenith angle of  $60^\circ$ .

The sensitivity of the satellite refraction  $\Delta\phi_s$  to changes in the astronomical refraction  $\xi$  can be expressed as

$$\frac{\partial(\Delta\phi_s)}{\partial\xi} = \frac{\partial(\Delta\phi_s)}{\partial\phi_o} \cdot \frac{\partial\phi_o}{\partial\xi}$$

or

$$= \frac{\partial(\Delta\phi_s)}{\partial\mu_o} \cdot \frac{\partial\mu_o}{\partial\xi}$$



TABLE 1. Refraction Corrections and Their Sensitivity to Changes in the Independent Variables

$\phi_0$ , deg	$\xi$ , sec	$\Delta\phi_0$ , sec	$\Delta\phi_0$ , sec	$\partial(\Delta\phi_0)/\partial\phi_0$ , sec/deg	$\partial(\Delta\phi_0)/\partial\phi_0$ , sec/deg	$\partial(\Delta\phi_0)/\partial\mu_0$ , sec/n-unit	$\partial(\Delta\phi_0)/\partial\mu_0$ , sec/n-unit	$\partial(\Delta\phi_0)/\partial R_0$ , sec/km	$\partial(\Delta\phi_0)\partial H_T$ , sec/km
$H_T = 100$ km									
0	0	0	0	1.014	0.00	0	0	0	0
15	15.569	15.560	0.009	1.085	0.002	0.055	0.000	$1.47 \times 10^{-6}$	$-0.94 \times 10^{-4}$
30	33.547	33.547	0.075	1.344	0.008	0.119	0.000	$1.18 \times 10^{-6}$	$-0.75 \times 10^{-4}$
45	58.105	57.842	0.263	2.010	0.018	0.204	0.002	$0.41 \times 10^{-4}$	$-0.26 \times 10^{-4}$
60	100.641	99.950	0.691	4.014	0.042	0.352	0.005	$1.06 \times 10^{-4}$	$-0.67 \times 10^{-4}$
75	216.853	214.866	1.987	14.960	0.279	0.756	0.014	$2.86 \times 10^{-4}$	$-1.82 \times 10^{-4}$
$H_T = 800$ km									
0	0	0	0	1.014	0	0	0	0	0
15	15.569	15.568	0.001	1.087	0.004	0.055	0.000	$1.81 \times 10^{-7}$	$-1.46 \times 10^{-6}$
30	33.547	33.537	0.010	1.351	0.010	0.119	0.000	$1.46 \times 10^{-6}$	$-1.18 \times 10^{-6}$
45	58.105	58.071	0.034	2.025	0.003	0.206	0.000	$0.51 \times 10^{-6}$	$-0.41 \times 10^{-6}$
60	100.641	100.544	0.097	4.050	0.006	0.357	0.000	$1.35 \times 10^{-6}$	$-1.09 \times 10^{-6}$
75	216.853	216.508	0.345	15.100	0.039	0.767	0.013	$4.1 \times 10^{-6}$	$-3.29 \times 10^{-6}$
$H_T = 1600$ km									
0	0	0	0	1.014	0	0	0	0	0
15	15.569	15.569	0.000	1.087	0.000	0.055	0.000	$0.92 \times 10^{-7}$	$-0.36 \times 10^{-6}$
30	33.547	33.542	0.005	1.352	0.000	0.119	0.000	$0.74 \times 10^{-6}$	$-0.29 \times 10^{-6}$
45	58.105	58.087	0.018	2.027	0.001	0.206	0.000	$0.26 \times 10^{-6}$	$-0.10 \times 10^{-6}$
60	100.641	100.588	0.053	4.053	0.003	0.357	0.000	$0.71 \times 10^{-6}$	$-0.28 \times 10^{-6}$
75	216.853	216.648	0.205	15.114	0.015	0.768	0.002	$2.37 \times 10^{-6}$	$-0.94 \times 10^{-6}$
$\lim H_T \rightarrow \infty$									
0	0	0	0	1.014	0	0	0	0	0
15	15.569	15.569	0	1.087	0	0.055	0	0	0
30	33.547	33.547	0	1.352	0	0.119	0	0	0
45	58.105	58.105	0	2.028	0	0.206	0	0	0
60	100.641	100.641	0	4.056	0	0.357	0	0	0
75	216.853	216.853	0	15.139	0	0.770	0	0	0

Sensitivity of the Refraction Corrections in the Astronomical Refraction

$\partial(\Delta\phi_s)/\partial\xi$ , sec/sec	$\partial(\Delta\phi_o)/\partial\xi$ , sec/sec
0	0
0.002	0.998
0.006	0.994
0.009	0.991
0.011	0.989
0.012	0.988

interval of interest ( $0 < \phi_o < \pi/2$ ),  $\xi$  is a monotonically increasing function of  $\phi_o$  and  $\mu_o$ , and its partial derivatives with respect to  $\phi_o$  and  $\mu_o$  are continuous functions of  $\phi_o$  and  $\mu_o$ . Then it follows that

$$\frac{\partial\phi_o}{\partial\xi} = 1.0 \quad \text{and} \quad \frac{\partial\xi}{\partial\mu_o} \cdot \frac{\partial\mu_o}{\partial\xi} = 1.0,$$

$$= \frac{\partial(\Delta\phi_s)}{\partial\phi_o} \bigg/ \frac{\partial\xi}{\partial\phi_o} = \frac{\partial(\Delta\phi_s)}{\partial\mu_o} \bigg/ \frac{\partial\xi}{\partial\mu_o}.$$

Equations (1) and (2) hold for  $\Delta\phi_o$ .

Table 2 summarizes results for the most cases calculated (i.e.  $H_T = 100$  km). In Table 2, the sensitivity of the satellite refraction to changes in astronomical refraction is

less than 2 per cent. So a maximum error in  $\xi$  of  $\pm 8$  sec implies an error in refraction at the satellite of less than 0.16 sec of arc.

*Summary.* The satellite refraction is small for all satellite altitudes above 100 km and zenith angles less than  $60^\circ$ . The sensitivity of the satellite refraction to variations in the independent variables is certainly small enough so that reasonable errors in determining the variables should not affect the required geodetic accuracy of 1 to 2 sec of arc. It further appears that for zenith angles up to  $75^\circ$ , corrections calculated on the basis of the equations presented here should prove sufficient for geodetic purposes.

## REFERENCES

- Fletcher, A., Astronomical refraction at low altitudes in marine navigation, *J. Inst. Navigation*, 5 (4), 307, 1952.  
*Handbook of Geophysics for Air Force Designers*, U. S. Air Force, Cambridge Research Directorate, Macmillan Co., New York, 1961.  
 McLead, A. R., On terrestrial refraction, *London Phil. Mag.*, 38, 546, 1919.  
 Smart, W., *Text Book on Spherical Astronomy*, Cambridge University Press, chap. 3, 1956.  
 Strand, K., Investigation of atmospheric refraction at low altitudes, *Arctic, Desert, Tropic Inform. Center Publ. A102*, Air University, Maxwell Air Force Base, Feb. 1953 (Astia Doc. AD-6452).

(Manuscript received April 27, 1961.)



## Numerical Errors in the Time Integration of Advective Processes

JOSEPH B. KNOX

*Lawrence Radiation Laboratory, University of California  
Livermore, California*

**Abstract.** A series of numerical experiments with the one-dimensional linearized advection equation are used to explore and to compare the properties of two methods of time integration: (1) an uncentered explicit time integration scheme with parabolic space interpolation of the advected field; (2) the well-known centered explicit scheme. Initial configurations of the advected field are single wavelike disturbances of length  $8\Delta x$  and  $16\Delta x$ . The computational results of the single disturbance of length  $8\Delta x$  are particularly interesting. The uncentered explicit scheme with parabolic space interpolation is shown to be superior to the centered explicit scheme with regard to the following effects of truncation: (a) the error in the displacement of the advected field; (b) the dispersion of the initial configuration, both upstream and downstream. With the introduction of a suitable artificial diffusion coefficient, the amplitude of the parasitic waves dispersing from a single disturbance of length  $8\Delta x$  and  $16\Delta x$  can be significantly reduced. In some parts of the computational region used in the numerical experiments, the amplitude of the parasitic waves can be reduced by one or more orders of magnitude. In addition, numerical experiments relevant to short-range numerical predictions are described in which a suitable artificial diffusion coefficient is selected for the control of parasitic waves arising from the dispersion from a single wavelike disturbance in the uncentered explicit finite difference solutions.

## INTRODUCTION

The application of numerical methods to the prediction of weather is discussed by Thompson and Gates [1957], [1960], Cressman and Hubert [1957], and others have discussed errors in numerical models and have classified them into three categories: (a) physical errors resulting from truncation of the hydrodynamical set of equations for the weather prediction problem, (b) errors in the description of the initial atmospheric state resulting from either observation or model techniques, (c) mathematical errors, including truncation effects and boundary errors. The physics of prediction models is improved and it is more desirable to find a finite difference analog to advection and a method of introducing artificial diffusion to reduce these truncation effects and, if possible, to suppress data errors. In this paper we shall be concerned with the effects of truncation errors, the error in the displacement of the advected field and the artificial dispersion of the initial configuration of the advected field through the generation of unphysical parasitic waves. We shall describe numerical experiments, relevant to short-range numerical prediction. These are directed toward the selection of a suitable artificial

diffusion coefficient that is a function of the non-dimensional ratio  $\mu = -U\Delta t/\Delta x$ , so that parasitic waves are suppressed over an interesting range of  $\mu$ .

The literature contains several studies related to the expressed goals. One possibility for reducing the truncation effects associated with the centered explicit scheme is to explore other kinds of finite difference approximations. The truncation error, computational stability, and convergence of various finite difference solutions of the linearized barotropic vorticity equation have been examined by Gates [1959], who compared the centered explicit difference solution with an implicit difference solution. The result of Gates' comparison is that the implicit scheme he used, while having the advantage of unconditional stability and avoiding problems associated with a false root to the finite difference equation, had a truncation error of the same general character as the centered explicit scheme. Since efforts to reduce truncation effects by the use of implicit finite difference analogs have so far been unsuccessful, it was suggested by C. E. Leith (private communication, 1960) that explicit schemes might be improved through better space interpolation of the advected field. In the next



section, parabolic space interpolation is explored as one means of improving explicit schemes.

In 1955, Charney suggested the possibility of control of the 'unmeteorological' behavior of numerically predicted fields through the introduction of viscosity or the use of suitable smoothing techniques [Charney, 1960]. In this regard, the study by Obukhov [1957] of differential difference solutions to the one-dimensional linearized advection equation,

$$\partial F / \partial t = -U \partial F / \partial x$$

showed that the introduction of artificial diffusion (analogous to the introduction of viscosity) can control the parasitic waves forming upstream from a blocklike configuration of the advected field. Obukhov suggested an optimal value of the artificial diffusion coefficient for suppressing parasitic waves that disperse upstream from a blocklike, or frontlike, configuration of the advected field. Obukhov's success in suppressing parasitic waves for frontlike disturbances naturally suggested the use of an artificial diffusion process to suppress the unwanted short-wave noise that arises in numerical prediction of large-scale meteorological fields. In exploring this latter possibility, Phillips [1960] showed that the introduction of Obukhov's optimal diffusion coefficient into the centered explicit difference approximation (suitable for the prediction of large-scale meteorological fields) corresponded to the uncentered space and time difference analog, which damped the meteorologically interesting scale too heavily.

As was pointed out by Platzman [1961], the success of prediction by numerical methods will be limited by noise appearing in the numerical solution. This noise could be real or it could arise as a truncation effect like the parasitic waves described by Obukhov [1957] or from a nonlinear computational instability [Phillips, 1959]. To suppress the unwanted noise, whatever its origin, Platzman [1961] explored the use of harmonic smoothing. However, he concluded that, unless the integration program were suitably formulated in expansion coefficients, harmonic smoothing would not be an efficient scheme for this purpose. Still another possibility of controlling noise is through the successive application of smoothing operators, as discussed by Shuman [1957] and Platzman [1961].

In the present paper, we suggest a form of an

artificial diffusion coefficient which can be suitably adjusted so that the parasitic waves arising in large-scale numerical weather prediction can be suppressed without adversely affecting the prediction of the long, sinusoidal waves of meteorological interest.

Thompson [1957] discussed the manner in which data errors excited short-wavelength disturbances, which, under favorable atmospheric conditions, grew in a two-parameter model such an amplitude during the 120-hour forecast period as to render the numerical prognosis essentially useless. It may very well be that the introduction of a suitable artificial diffusion coefficient will aid in the suppression of the errors in short-range numerical predictions without adversely damping the meteorological disturbances.

#### ONE-DIMENSIONAL ADVECTION

Consider the one-dimensional initial distribution of an advected field  $F(x, 0)$ , defined in the interval  $-\infty < x < \infty$  and transported by the fluid in the  $x$  direction at a constant speed  $U$ . The partial differential equation for this advection process is

$$\partial F / \partial t = -U \partial F / \partial x$$

The true solution to (1) [Phillips, 1960] is

$$F(x, t) = F(x - Ut, 0)$$

A finite difference approximation to (1), frequently used in the integration of meteorological prediction models, is the centered explicit scheme

$$F_i^{n+1} = F_i^{n-1} + \mu(F_{i+1}^n - F_{i-1}^n)$$

where

$$\mu = -U \Delta t / \Delta x$$

The computational stability, truncation error, and the solution of this finite difference (3) have been discussed by Phillips [1960] and need not be reproduced here.

An alternative finite difference analog to the one-dimensional advection equation is suggested by the form of the true solution (2).

To describe this alternative finite difference scheme, we let the independent space and time variables,  $x$  and  $t$ , be made discrete as follows:  $x_i = i\Delta x$  and  $t_n = n\Delta t$ . The value of the advected field  $F_i^n$  (at the time  $t_n$ ) is interpolated as

$U\Delta t$  upstream of the position designated Fig. 1). This value of the advected field ( $-U\Delta t$ ) arrives at  $x_i$  at the time  $t_{n+1}$ . In this scheme, parabolic interpolation is used in the interval of  $(x_i - \Delta x) \leq (x_i - U\Delta t) \leq (x_i + \Delta x)$ , so that

$$F_i^n = F^n(x_i - U\Delta t) - \frac{U\Delta t}{\Delta x} \left( \frac{F_{i+1}^n - F_{i-1}^n}{2} \right) + \frac{(U\Delta t)^2}{2(\Delta x)^2} \left( \frac{F_{i+1}^n - 2F_i^n + F_{i-1}^n}{2} \right) \quad (5)$$

the introduction of the nondimensional parameter  $\mu = -U\Delta t/\Delta x$  into (5), the finite difference analog to the one-dimensional advection equation becomes

$$F_i^n = F_i^{n-1} + \mu \left( \frac{F_{i+1}^{n-1} - F_{i-1}^{n-1}}{2} \right) + \mu^2 \left( \frac{F_{i+1}^{n-1} - 2F_i^{n-1} + F_{i-1}^{n-1}}{2} \right) \quad (6)$$

The finite difference approximation to the one-dimensional advection equation is subject to a restriction for computational stability, namely that  $|\mu| \leq 1$ , as is discussed in the Appendix. It should be noted that the  $\mu^2$  term in the finite difference analog (6) has the effect of an artificial diffusion term.

In performing numerical experiments with the finite difference analogs (3) and (6), certain appropriate initial conditions and boundary conditions are required. We now consider the initial conditions and boundary conditions used in each of the methods of time integration.

*Centered explicit scheme (equation 3).* The initial configuration of the advected field is specified as

$$\frac{1}{2} \left[ 1 + \cos \frac{\pi}{m} (i - f) \right] \quad \text{for} \quad -m \leq \left( i - \frac{p}{2} \right) \leq m \quad (7)$$

the constant  $f$  is so fixed that the maximum value  $F_i^0 = 1$  occurs at  $i = p/2$ . For  $|i - p/2| > m$ , the initial value of the advected field is zero. In addition to this initial information at  $t = 0$ , the centered explicit scheme (3) requires knowledge of the advected field 1 time unit earlier (at  $t = -\Delta t$ ). From the analytical

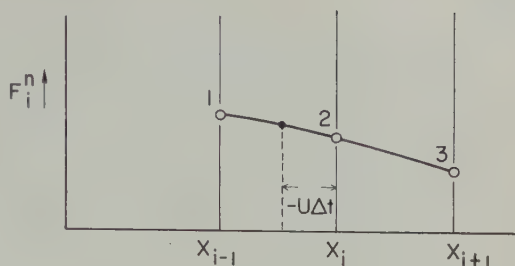


Fig. 1. Diagram illustrating the uncentered explicit scheme with parabolic space interpolation. The points 1, 2, and 3 represent values of  $F_i^n$  at three equally spaced  $x$  coordinates. A parabola fitted to these points specifies the value of the advected field at the point  $x_i - U\Delta t$ .

solution to the one-dimensional advection problem it can readily be seen that this additional initial information can be obtained from the following expressions:

$$F_i^{n-1} = \frac{1}{2} \left[ 1 + \cos \frac{\pi}{m} (i + \mu - f) \right] \quad \text{for} \quad -m \leq \left( i + \mu - \frac{p}{2} \right) \leq m \quad (8)$$

and

$$F_i^{n-1} = 0 \quad \text{for} \quad \left| i + \mu - \frac{p}{2} \right| > m$$

The boundary conditions used in the calculation of the finite difference solution are

$$F_0^n = 0 \quad (9)$$

and

$$F_p^{n+1} = F_p^n + \mu(F_p^n - F_{p-1}^n) \quad (10)$$

These boundary conditions are similar to those used by Platzman [1954] to eliminate a secondary instability introduced by the use of certain approximate boundary conditions.

*The uncentered explicit scheme with parabolic space interpolation (equation 6).* The computation of finite difference solutions to one-dimensional advection using (6) requires, of course, the initial information  $F_i^0$ , described by (7); however, the additional initial information at  $t = -\Delta t$  is unnecessary for the uncentered finite difference scheme. The boundary conditions used in this scheme with parabolic interpolation are the same as those discussed above (equations 9 and 10).



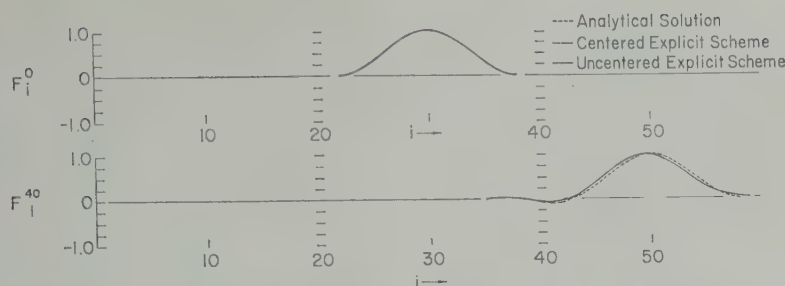


Fig. 3. Experiment 2, showing the effects of truncation for a single-wave disturbance whose initial configuration is specified by  $m = 8$ ,  $f = -2$ ,  $p = 60$ , and  $\mu = -0.5$ .

the following section we describe the numerical experiments performed with both the centered explicit scheme (3) and the uncentered difference analog (6).

### COMPARISON OF TRUNCATION EFFECTS

**Experiment 1.** In the first experiment in the simulation of one-dimensional advective changes we consider the initial configuration  $F_i^0$  described by (7), where  $p = 50$ ,  $f = 1$ ,  $m = 4$ , and  $\mu = 0$ . The upper part of Figure 2 shows the initial configuration  $F_i^0$ . The analytical solution and the two finite difference solutions are presented in the diagrams (Fig. 2) for  $n = 20, 40, 60$ . (The centered explicit solution is shown as a broken curve; the uncentered solution is shown in a solid curve.) An examination of Figure 2 and a comparison of the two finite difference solutions yield the following salient facts:

- For  $n = 20$ , it is evident that the forward displacement of the initial configuration is about 10 per cent less (in magnitude) for the uncentered scheme than for the centered explicit scheme.
- For  $n = 40$ , it is evident that the error in the displacement of the maximum value of  $F$  is increased by about 25 to 30 per cent for the centered difference scheme.
- For  $n = 40$ , the upstream dispersion of the initial configuration is much less in the uncentered difference solution; for instance, at  $i = 38$  and  $39$  the amplitude of the parasitic wave in the uncentered difference solution is about 60 per cent of that associated with the centered explicit solution. Farther upstream, at  $i = 18$  and  $19$ , the amplitude of the parasitic wave is decreased by a factor of  $10^4$  in the uncentered difference solution.
- At  $n = 60$ , a time at which the actual

configuration of the advected field has moved outside of the computational region, irrelevant noise contaminates the computational region in both difference solutions. However, as we have already noted at  $n = 40$ , the uncentered difference solution is clearly superior.

**Experiment 2.** The second experiment shows the manner in which the three undesirable truncation effects on advective changes (illustrated in experiment 1) decrease with an increase in the longitudinal length of the disturbance. Consider the initial configuration  $F_i^0$  described by (7), where  $p = 60$ ,  $m = 8$ ,  $f = -2$ , and  $\mu = -0.5$ . Figure 3 shows the initial configuration  $F_i^0$ , the analytical solution to the advected field, and the two finite difference solutions at  $n = 40$ . The only difference discernible in this figure between the two finite difference solutions is that the amplitude of the parasitic waves is reduced by about 30 per cent immediately to the rear of the disturbance, and, for  $i \leq 30$ , their amplitude is reduced by a factor between  $10^1$  and  $10^2$ .

The results of experiments 1 and 2 indicate that the uncentered explicit scheme with parabolic space interpolation is superior to the centered explicit scheme in regard to the following truncation effects: (1) the error in the displacement of the advected field and (2) the upstream (and downstream) dispersion of unmeteorological parasitic waves. It should be mentioned that the selection of a finite difference scheme that suppresses parasitic waves is of some importance in the integration of prediction models. In this regard, the physical argument that follows is similar to that given by J. von Neumann and reported by Blair and Metropolis [1958] in connection with the uncentered solution of the two-dimensional flow of two inviscid incompressible fluids of different density in a gravitational field.



Consider one possible example. If fictitious behavior of a finite difference scheme falsifies some of the computed densities, then at subsequent time steps some of the accelerations and finally the computed velocities will be falsified. Once velocities are falsified the transfer processes are affected and are in error. This kind of physical reasoning indicates the desirability of selecting the uncentered explicit scheme with parabolic space interpolation in preference to the centered explicit scheme.

#### SUPPRESSION OF PARASITIC WAVES

We shall now illustrate a method of selecting a suitable artificial diffusion coefficient so that the amplitude of the dispersed unmeteorological waves is further reduced without damping the meteorologically interesting scale too seriously.

Consider the simple but illustrative problem of one-dimensional advection of vorticity, where the vorticity  $\zeta$  replaces  $F$  in the finite difference analog (equation 6), in the initial configuration (equation 7), and in the boundary conditions (equations 9 and 10). At each time step, the  $y$  component of the wind,  $v(x)$ , is obtained from the vorticity (defined as  $\zeta = \partial v / \partial x$ ) at each  $x$ , by the application of the trapezoidal rule to the following integral for  $v$ :

$$v(x) - v(0) = \int_0^x \zeta \, dx$$

At  $x = 0$ , the boundary condition  $v(0) = 0$  is used in the  $v(x)$  computation. For this specific problem, we introduce the form of an artificial diffusion coefficient,

$$A(\mu) = (C_1 \mu^2 / 2) + C_2 \quad (11)$$

into the finite difference analog (6) as the coefficient of the second difference term. The form of  $A(\mu)$  proposed in (11) is suggested by the presence of the  $\mu^2$  term in the finite difference analog (6), and by some preliminary numerical experiments. It could very well be that the inclusion of terms involving  $|\mu|$  or terms of higher order than  $\mu^2$  in  $A(\mu)$  might afford a better control of the parasitic waves than (11) over a considerable range of  $|\mu|$ ; however, a simple form, such as (11), will probably suffice to illustrate the principle in this initial investigation.

In selecting values of  $C_1$  and  $C_2$  in (11), it is

desirable to choose these constants in such a way that the unphysical behavior of the finite difference solution is suppressed over a range of  $\mu$  normally used in the numerical integration of the vorticity equation. Phillips [1960] has estimated that the magnitude of  $\mu$ , for numerical analogs currently in use, is at most about 0.5 for large systems. It therefore appears that a pertinent and typical range of  $|\mu|$  is  $0 < |\mu| \leq 0.5$ . The method used in the solution of (11) and  $C_2$  suitable for this range of  $|\mu|$  is outlined below.

(a) Experiment 2 is repeated several times with  $\mu = -0.5$  and with several different values of  $A(\mu)$ . A suitable value of  $A(\mu)$  for  $\mu = -0.5$  is selected by inspection of the degree of suppression of the undesirable features of the finite difference solution to (6).

(b) A limited number of experiments are performed for  $\mu = -0.1$  with several different values of  $A(\mu)$ , which permit the selection of a second value of  $A(\mu)$  for  $\mu = -0.1$ .

(c) With these two selected values of  $A(\mu)$ ,  $A(-0.1)$  and  $A(-0.5)$  determined from experiments, a pair of algebraic equations is solved for constants  $C_1$  and  $C_2$ .

(d) The final step is to perform a series of experiments for  $\mu = -0.1, -0.2, -0.4$ , and  $-0.5$ , to confirm that constants  $C_1$  and  $C_2$  define a suitable artificial diffusion coefficient for control of the undesirable parasitic waves without unduly damping disturbances of meteorological interest.

Table 1 summarizes the results, shown graphically in Figure 4, of suppressing the parasitic waves arising from a single wavelike disturbance.

From these data it is possible to select a value of  $A(\mu)$  so that  $R$  reflects a suppression of parasitic waves without introducing a larger error than necessary in the predicted  $v(x)$ . Using this criterion, it is possible to select a value of  $A(\mu)$  of 0.175 from Table 1. In a similar manner, a series of experiments for  $\mu = -0.1$  is performed, the above criterion is applied to their results, and a value of  $A(\mu)$  is selected, such as 0.015 (or possibly, 0.025). By means of these two values of  $A(\mu)$ ,  $A(-0.5) = 0.175$  and  $A(-0.1) = 0.015$ , the two constants  $C_1$  and  $C_2$  are found to be  $4/3$  and  $1/12$ , respectively. We shall now perform a series of calculations with  $A(\mu)$  as defined by the selected values of  $C_1$  and  $C_2$  in order to ascertain whether

TABLE 1. Summary of Results on Suppression of Parasitic Waves

$m = 4, p = 50, f = 1, \mu = -0.5, n = 40$

$a_p(38)$	$a_m$	$E_{\max}$	$r$	$R$
0.12	0.79	0.12	0.92	0.33
0.09	0.72	0.12	0.84	0.24
0.08	0.68	0.12	0.78	0.23
0.05	0.65	0.12	0.75	0.14
0.03	0.63	0.125	0.73	0.09
0.01	0.61	0.130	0.71	0.03

The column headings in this table are defined as:

$a_p(38)$  = the value of the artificial diffusion coefficient.

$a_m$  = the amplitude of the parasitic wave at  $i = 38$ .

$E_{\max}$  = the maximum value of  $\zeta$ ; for the single-wave disturbance in the finite difference solution.

$r$  = the ratio of the maximum error in the predicted  $v$  field to the maximum value of  $v$  (from analytical solution).

$R$  = the ratio of  $a_m$  for the uncentered explicit scheme to  $a_m$  for the centered explicit scheme.

$a_p(38)$  = the ratio of  $a_p(38)$  for the uncentered explicit scheme to  $a_p(38)$  for the centered explicit scheme.

The value of  $a_p$  so specified, is suitable for suppressing parasitic waves in the range of  $0.1 \leq |\mu| \leq 0.5$  for  $n \leq 40$ .

In this second series of experiments we consider an initial configuration prescribed by (7) with  $m = 4, p = 50$ , and  $f = 1$ , and the parameter  $\mu$  is set equal to  $-0.1, \dots, -0.5$ . The constants  $C_1$  and  $C_2$ , specifying the diffusion coefficient  $A(\mu)$ , are those cited above. For sake of comparison, the corresponding centered explicit solutions are calculated without a diffusion coefficient, and the two numerical solutions are

compared at  $n = 40$ . Figure 5 shows the initial vorticity and  $v$  fields, the uncentered solution with the specified diffusion coefficient at  $n = 40$ , and the centered explicit solution at  $n = 40$ . An examination of this figure indicates that the uncentered scheme with artificial diffusion is successful in suppressing the parasitic waves immediately upwind of the disturbance by a factor of 2 to 10, depending on  $\mu$ . Farther upwind of the disturbance, the suppression of the parasitic waves is much more effective. Table 2 summarizes some of the pertinent results of this series of experiments; columns 2, 3, and 4 give  $R$  (same as for Table 1) at  $i = 38$ , and  $E_{\max}$  for the uncentered and centered solutions. In this series of experiments it is quite possible to reduce or suppress the parasitic waves significantly without causing an undesirable effect on the predicted  $v$  field. A close examination of the last pair of curves in Figure 5 shows that the error in the displacement of the vorticity maximum is about twice as small in the uncentered scheme as in the centered explicit scheme.

We must now determine to what extent the introduction of an artificial diffusion coefficient into the finite difference analog (6) has adverse effects on the prediction of either the advected field  $\zeta$  or the  $v$  field for disturbances somewhat larger in scale than the  $m = 4$  disturbance. To obtain the relevant information, calculations were performed for an initial configuration computed from (7) with  $m = 8, p = 60$ , and  $f = -2$ , for  $\mu = 0.1, \dots, -0.5$ . Table 2 also shows the maximum amplitude of the parasitic wave, the maximum error in the  $v$  field as represented by  $E_{\max}$ , and the ratio of  $a_m$  of the disturbance

TABLE 2. Summary of Results on the Suppression of Parasitic Waves by the Introduction of the Artificial Diffusion Coefficient  $A(\mu)$

$$A(\mu) = (C_1 \mu^2/2) + C_2, \text{ where } C_1 = 4/3 \text{ and } C_2 = 1/120$$

For  $m = 4$  and  $n = 40$

$\mu$	$R$	Uncentered Explicit	Centered Explicit	For $m = 8$ and $n = 40$		
		$E_{\max}$	$E_{\max}$	$a_p$	$E_{\max}$	Ratio $a_m$ 's
-0.1	0.5	0.04	0.05	0.025	*	0.95/0.96
-0.2	0.4	0.09	0.10	0.025	0.02	0.95/0.96
-0.3	0.29	0.11	0.11	0.03	0.025	0.94/0.96
-0.4	0.2	0.12	0.12	0.03	0.03	0.91/0.96
-0.5	0.1	0.14	0.13	0.01	0.04	0.87/0.96

\* Not measurable in graph.

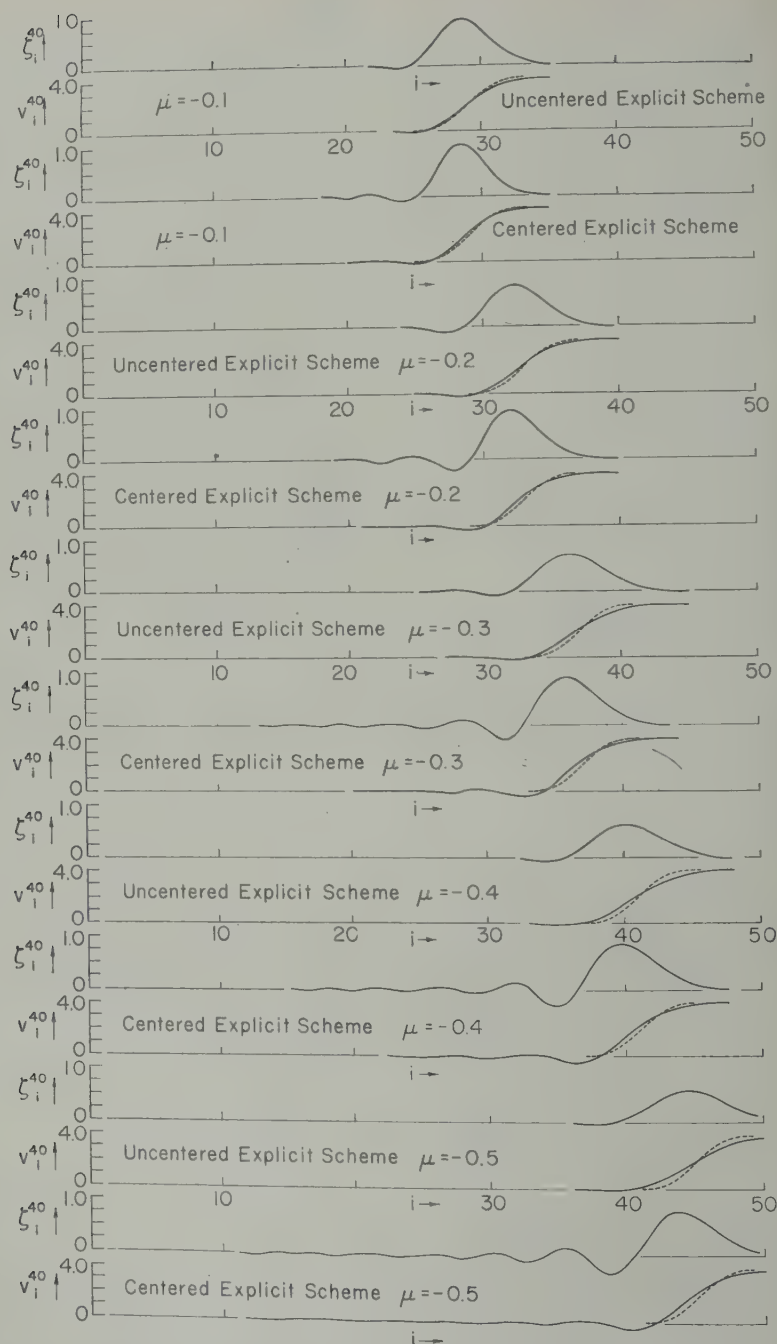


Fig. 5. Experiments 9 to 13, showing the suppression of parasitic waves by the introduction of the artificial diffusion coefficient  $A(\mu) = (C_1\mu^2/2) + C_2$  for various values of  $\mu$  from  $-0.1$  to  $-0.5$ . The initial configuration of the single-wave disturbance is the same as in Figure 4. (See also Table 2 for summary of results of Experiments 9 to 13, as well as of Experiments 14 to 18 for  $m = 8$  and  $n = 40$ .)

finite difference solution to  $a_m$  in the analytical solution. The damping of the advected field by the finite difference solution, for  $0 < \mu < 0.5$ , is at most about 13 per cent after 40 time steps. This degree of damping compares reasonably well with the damping ( $\sim 4$  per cent) of the vorticity field for a viscously damped gravity wave on a nonrotating earth,

$$\exp [(i2\pi/L)(x - Ut)] \cdot \exp [-\nu 4\pi^2 t/L^2]$$

For appropriate values of time and wavelength and an eddy viscosity equal to  $10^6$  m<sup>2</sup>/sec in the above equation.

### CONCLUDING REMARKS

The results of this investigation on the one-dimensional advection equation indicate that:

(1) The uncentered explicit scheme with parabolic interpolation is, at least for short time intervals, superior to the centered explicit scheme with respect to the displacement of the advected field.

(2) The introduction of an artificial diffusion coefficient of the form  $(C_1\mu^2/2) + C_2$  into the one-dimensional linearized vorticity equation can suppress the unmeteorological parasitic waves by a factor between 2 and 10 over a range of  $\mu$  of  $0.1 \leq |\mu| \leq 0.5$ . The suppression of this undesirable characteristic of the finite difference solution is achieved after 40 time steps without unduly damping the waves of meteorological interest.

(3) Parasitic waves may arise in the numerical solution of problems involving advection in other fields of geophysics. The initial conditions for these problems may be (a) 'frontlike' disturbances similar to those considered by *Obukhov*, (b) 'pulselike' disturbances of finite extent, or (c) a single sinusoidal disturbance of small longitudinal extent. It is probably desirable to suppress the parasitic waves, or unwanted noise, in these geophysical problems to improve the prediction of the physically interesting features of the advected field are not adversely affected by the technique of noise suppression. The uncentered finite difference approximation of the advective process and/or the technique of introducing an artificial diffusion for the control of unwanted noise, discussed herein, may have applications not only in meteorology

but also in other fields such as magnetohydrodynamics or ground-water hydrology for the numerical simulation of the movement and dispersion of ion species in water-bearing porous material.

### APPENDIX

In this appendix we shall derive the restrictions on  $\mu$  necessary for computational stability of the uncentered finite difference scheme with parabolic interpolation (equation 6). The substitution of  $A\omega^m \exp(ikj\Delta x)$  for  $F_{i,j,n}$  in (6) gives the following expression for the growth factor  $\omega$ :

$$\omega = 1 - \mu^2(1 - \cos k\Delta x) + i\mu \sin k\Delta x \quad (\text{A-1})$$

where  $k$  is the wave number in the  $x$  direction. The magnitude of the growth factor is  $|\omega|^2 = [1 - \mu^2(1 - \cos k\Delta x)]^2 + \mu^2 \sin^2 k\Delta x$ , which, upon rearrangement, becomes  $|\omega|^2 = 1 - (\mu^2 - \mu^4)(1 - \cos k\Delta x)^2$ .

From (A-1) it is readily seen that  $1 \geq |\omega|^2 \geq 0$ , if

$$1 \geq \mu^2(1 - \mu^2)(1 - \cos k\Delta x)^2 \geq 0 \quad (\text{A-2})$$

The replacement of  $(1 - \cos k\Delta x)^2$  by its maximum value, 4, in (A-2) results in the inequality;

$$1 \geq g(\mu) \geq 0 \quad (\text{A-3})$$

where  $g(\mu) = 4\mu^2(1 - \mu^2)$ . Analysis of  $g(\mu)$  shows that (A-3) is satisfied if  $0 \leq \mu^2 \leq 1$ . The result is that the magnitude of the growth factor is less than or equal to 1, provided  $0 \leq \mu^2 \leq 1$ , and the finite difference analog is stable [*Richtmyer*, 1957].

*Acknowledgments.* I wish to thank Mr. Roger Fulton for the programming of the problem for the IBM 709, and Mrs. Florence Sullivan for the plotting of machine output.

The work reported in this paper was done under the auspices of the U. S. Atomic Energy Commission.

### REFERENCES

- Blair, A., and N. Metropolis, A study of a numerical solution to a two-dimensional hydrodynamical problem, *LA-2165*, Los Alamos Scientific Laboratory, University of California, 81 pp., 1958.  
 Charney, J., Numerical prediction and the general circulation, in *Dynamics of Climate* (Proceedings of a conference on the application of numerical



- integration techniques to the problem of the general circulation held October 26-28, 1955), Pergamon Press, New York, 1960.
- Cressman, G. P., and W. E. Hubert, A study of numerical forecasting errors, *Monthly Weather Rev.*, **85**, 235-242, 1957.
- Gates, W. L., On the truncation error, stability and convergence of difference solutions to the barotropic vorticity equation, *Sci. Rept. 1*, Dynamical Weather Prediction Project, University of California, Los Angeles, 1959.
- Obukhov, A. M., The accuracy of computation of advective variations of fields in quantitative forecasting of weather, *Bull. Acad. Sci. USSR, Geophys. Ser.*, no. 9, 63-72, 1957 (AGU translation).
- Phillips, N. A., An example of nonlinear computational instability, *The Rossby Memorial Volume*, Rockefeller Institute Press, New York, 1959.
- Phillips, N. A., Numerical weather prediction, in *Advances in Computers*, vol. 1, Academic Press, New York, pp. 43-90, 1960.
- Platzman, G. W., The computational stability of boundary conditions in numerical integration of the vorticity equation, *Arch. Meteorol., Geophys. u. Bioklimatol., Ser. A* **7**, 29-40, 1954.
- Platzman, G. W., An approximation to the product of discrete functions, *J. Meteorol.*, **18**, 31-32, 1961.
- Richtmyer, R. D., *Difference Methods for Initial Value Problems*, Interscience Publishers, New York, 1957.
- Shuman, F. G., Numerical methods in weather prediction, 2, Smoothing and filtering, *Monthly Weather Rev.*, **85**, 357-361, 1957.
- Thompson, P. D., Uncertainty of initial data as a factor in the predictability of large-scale atmospheric flow patterns, *Tellus*, **9**(3), 275-295, 1957.
- Thompson, P. D., and W. L. Gates, A test of numerical prediction methods based on the barotropic and two-parameter baroclinic models, *Meteorol.*, **13**, 127-141, 1957.

(Manuscript received June 22, 1961;  
revised September 25, 1961.)

# Further Evidence of Hysteresis as a Factor in the Evaporation from Soils

LARRY G. KING AND RICHARD A. SCHLEUSENER

Civil Engineering Department, Colorado State University  
Fort Collins, Colorado

**Abstract.** Evaporation studies were conducted on a fine sand which was in contact with a water table and was subjected to diurnal cyclic atmospheric conditions. Previous studies under steady atmospheric conditions showed that an inverse relation between the rate of evaporation from soils and the rate of evaporation from a free-water surface occurred under certain conditions. These studies also showed that this inverse relationship was produced by decreased evaporativity as the depth to the water table was increased. A theoretical explanation of this phenomenon was presented on the basis of a hysteresis in the functional relation between permeability and saturation of soils. The data presented in the present paper show that this phenomenon also occurs under cyclic atmospheric conditions. The conclusion is that the inverse relationship could occur in soils under field conditions, and therefore it could be a significant consideration in predicting evaporation from soils.

**Introduction.** Results reported by Schleusener and Corey [1959] show that an inverse relationship sometimes exists between evaporation rate from a 'free-water surface' and evaporation rate from soil having a water table at a constant depth below the surface. Figure 1 is taken from a paper by Schleusener and Corey. This figure is a plot of the results for various soils; that is, for low water tables and low evaporativity, the rate of evaporation from the soils was approximately the same as from the free-water surface. For deeper water tables and higher evaporativity, however, the soils exhibited a maximum value of evaporation rate, so that increased evaporativity produced a decreased evaporation rate from the soils. This result was contrary to previous theory which predicted a limiting evaporation rate from the soils with increasing evaporativity. The existence of this inverse relationship was explained by Schleusener and Corey [1959] on the basis of a hysteresis phenomenon. The study was conducted under steady atmospheric conditions. The question arose whether the inverse relation would also occur under cyclic atmospheric conditions similar to those found in the field where the high evaporativity exists for a short part of a 24-hour period. Experiments have been conducted to study this ques-

$e_f$ : Evaporation rate from free-water surface expressed in inches per day. Subscript refers to the period of time for which evaporation was measured; i.e.,  $e_{f,1.2}$  refers to the evaporation rate as measured over the 1.2-hour period of maximum evaporation.

$e_s$ : Evaporation rate from soil expressed in inches per day.

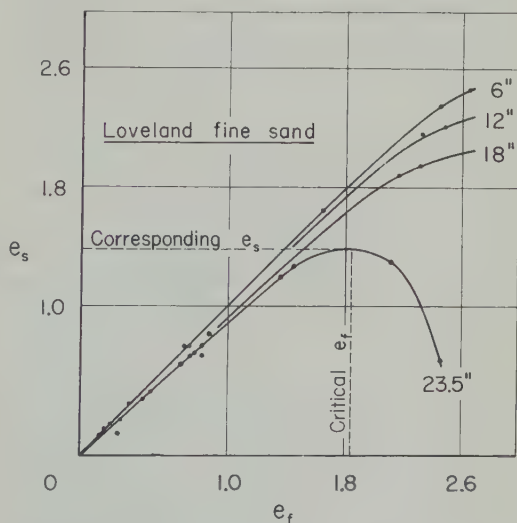


Fig. 1. Evaporation rate from Loveland fine sand ( $e_s$ ) as a function of evaporation rate from free-water surface ( $e_f$ ), for water-table depths of less than 23.5 inches. (Evaporation rates are expressed in inches per day and are measured over a 24-hour period of constant atmospheric conditions.)

itions.

**Free-water surface:** A column of sand in which the water table was maintained at the surface.

TABLE 1. Ranges of Ambient Variables and Methods Used for Increasing  $e_r$  during Studies of the Effect of Cyclic Variation of Ambient Conditions on Evaporation from Soils in Contact with a Water Table

Run No.	Temp. Range, °F	RH Range, %	Radiation Level	Wind Velocity
8	75-105	10-20	Increasing	Approx. 10 fps at $e_{r, 1.2} = 3.0$ and 4.37 in/day
9	50-80	25-50	Increasing	Approx. 10 fps at $e_{r, 1.2} = 2.2$ and 3.62 in/day
10	65-95	20-40	Increasing	Approx. 10 fps at $e_{r, 1.2} = 2.7$ and 3.84 in/day
11	Increasing from 45-75 to 75-105 in 5° increments	25-50	Constant	None
12	Decreasing from 75-105 to 50-80	25-50	Constant	None
13	60-90	25-50	Constant	Increasing from 0 to 20 fps
15*	60-90	25-50	Increasing	Approx. 10 fps at $e_{r, 1.2} = 2.8$ and 4.08 in/day
16	60-90	25-50	Constant	Increasing from 0 to 25 fps

\* Water-table depths for run 15 were 24, 25, and 26 inches. For all other runs the water-table depths were 18, 24, and 27 inches.

Critical  $e_r$ : Value of  $e_r$  at which  $e_s$  begins to decrease with increasing  $e_r$  (see Fig. 1).

Corresponding  $e_s$ : Value of  $e_s$  when critical  $e_r$  occurs (see Fig. 1).

Evaporativity: The potential rate of evaporation produced by ambient conditions (measured by  $e_r$ ).

*Apparatus and procedure.* The study was conducted in an environmental chamber with controls modified so that the temperature, relative humidity, and radiation automatically underwent a diurnal cyclic variation as described by Schleusener and King [1960]. A fine sand was placed in 3½-inch-i.d. Lucite containers which were placed upon a rotating table at equal radii. Water was supplied to the base of each column at a constant pressure from a Mariotte-siphon bottle. Measurements of evaporation rate were taken for a 1.2-hour period of highest evaporativity and for a 24-hour period (one full cycle). After the rate of evaporation was determined for one set of cyclical conditions, the cycle was changed and measurements were taken for the new conditions. The range of the ambient variables and the method used for increasing the rate of evaporation from the free-water surface

$e_r$  are shown in Table 1. (For example, Table 1 shows that for run 16 the ambient temperature range was 60° to 90° F, the range of relative humidity was 25 to 50 per cent, and the radiation was held constant. The evaporativity was increased by increasing the wind velocity from 0 to 25 ft/sec.

*Experimental results.* The results for the 1.2-hour period are shown in Figure 2. The curves for the 24-hour period are not shown, but they were of similar shape. From examination of Figure 2 it can be seen that, for some conditions an increase in  $e_r$  did result in a decrease in  $e_s$ ; that is, the inverse relationship mentioned above did exist for some conditions. The value of  $e_r$  for which this phenomenon occurred is called the 'critical  $e_r$ .' These critical values of  $e_r$  for the 27-inch water-table depth and related data are shown in Table 2. The critical values of  $e_r$  and  $e_{r, 24}$  occurred during the same cycle of ambient variables.

From examination of Figure 2 and Tables 1 and 2, several factors may be noted:

1. A critical value of  $e_{r, 1.2}$  was reached only for water-table depths greater than 24 inches.
2. The inverse relation between  $e_s$  and  $e_r$  was noted only for conditions of increasing radi-

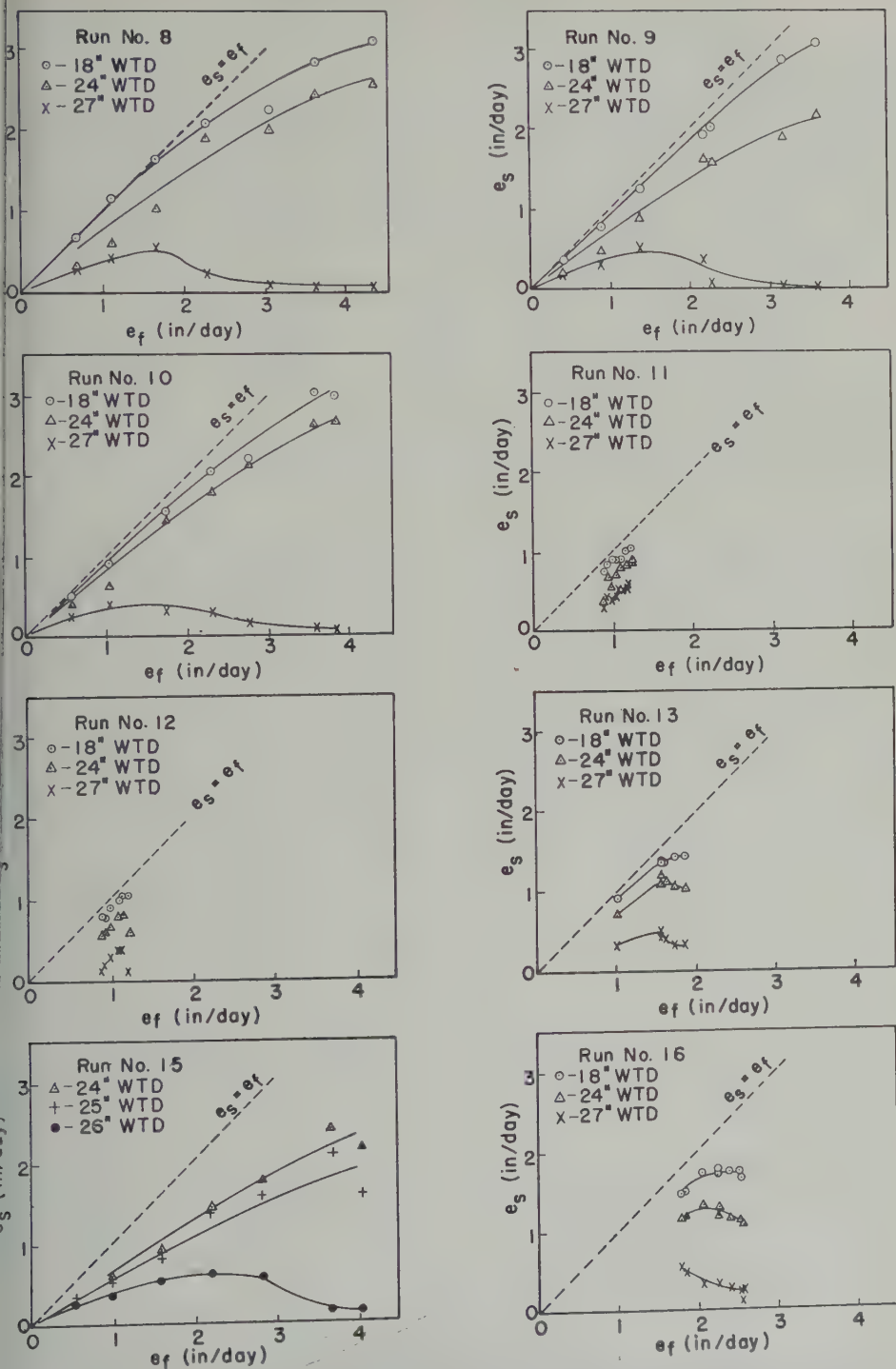


Fig. 2. Evaporation rate from Loveland fine sand ( $e_s$ ) as a function of evaporation rate from free-water surface ( $e_f$ ), for various water-table depths. (The cyclic ambient conditions and method of changing  $e_f$  are specified in Table 1. All rates are expressed for the 12-hour period of highest evaporativity.)



TABLE 2. Critical Values of  $e_f$  and Related Data

Run No.	Critical $e_{f\ 1-2}$ , in/day	Corresponding $e_{s\ 1-2}$ , in/day	Critical $e_{f\ 24}$ , in/day	Corresponding $e_{s\ 24}$ , in/day	Critical $\frac{e_{s\ 1-2}}{e_{f\ 1-2}}$	Critical $\frac{e_{s\ 24}}{e_{f\ 24}}$	Temperature of Soil Surface, °F	Temperature of Free-Water Surface, °F
8	1.6	0.55	0.9	0.4	0.34	0.44	127	115
9	1.5	0.5	0.7	0.3	0.33	0.43	110	106
10	1.5	0.4	0.7	0.3	0.27	0.43	104	102
11	*	*	*	*	*	*	*	*
12	*	*	*	*	*	*	*	*
13	1.5	0.5	0.7	0.3	0.33	0.43	92	79
14	*	*	*	*	*	*	*	*
15	2.3†	0.6†	1.0†	0.4†	0.26†	0.40†	138†	119†
16	1.8 or less	0.5 or more	0.9	0.3	0.28 or more	0.33	135	121

\* Inverse relation between  $e_s$  and  $e_f$  was not observed during these runs (see Fig. 2).

† Depth to the water table was 26 inches.

energy (runs 8, 9, 10, and 15) or for conditions of increasing wind velocity (runs 13 and 16). In each of these runs,  $e_{f\ 1-2}$  exceeded about 1.5 in/day and  $e_{f\ 24}$  exceeded about 0.7 in/day. The inverse relationship was not noted for conditions such that  $e_{f\ 1-2}$  did not exceed about 1.2 in/day (runs 11 and 12), or when  $e_{f\ 24}$  did not exceed about 0.5 in/day. This result appeared to be independent of whether the ambient temperature range was increased or decreased with time.

3. The critical value of  $e_{f\ 1-2}$  was approximately 1.5 in/day for the 27-inch depth to the water table. The corresponding value of  $e_{s\ 1-2}$  was about 0.5 in/day.

4. The critical value of  $e_{f\ 24}$  was approximately 0.7 in/day for the 27-inch depth to the water table. The corresponding value of  $e_{s\ 24}$  was about 0.3 in/day.

5. The critical values of  $e_{s\ 24}/e_{f\ 24}$  were larger than  $e_{s\ 1-2}/e_{f\ 1-2}$  in each run for which a critical  $e_f$  occurred, the values being approximately 0.4 and 0.3, respectively.

6. Soil-surface temperature and the temperature of the free-water surface were erratic and appeared to follow no consistent pattern in relation to critical values of  $e_f$ .

7. An inverse relation between  $e_s$  and  $e_f$  can be produced under cyclic ambient conditions.

*Discussion of results.* Both Figure 2 of Schleusener and Corey [1959] and Figure 2 of this paper show that the inverse relation between the rate of evaporation from a free-water surface and the rate of evaporation from soils in contact

with a water table is produced by smaller and smaller evaporativity as the depth to the water table is increased. This trend is also predicted by the theoretical considerations presented in detail by Schleusener and Corey [1959].

Let us consider a saturated soil in contact with a water table at a constant depth. As long as the rate of evaporation from the surface does not exceed the rate at which water can be conducted upward from the water table,  $e_s$  should be proportional to  $e_f$ . Whenever the rate of evaporation from the surface exceeds the rate at which water can move upward through the soil, the surface must dry out. Subsequent to such drying of the surface, the water to be evaporated must be imbibed by the drier surface layer. At this time, the inverse relation occurs because of hysteresis in the functional relation between permeability and saturation as discussed in detail by Schleusener and Corey [1959]. For the same evaporativity, as the water table becomes deeper the gradient for upward flow becomes smaller and as a result the rate of movement of water upward from the water table decreases. Hence a smaller evaporativity is required to produce the inverse relation as the water table becomes deeper.

The conditions reported here are probably more severe than would be encountered in the field. However, water tables in the field are often much deeper than 27 inches. Thus, the inverse relationship may exist under certain conditions in the field.

results given in this paper are noteworthy they are compatible with the hysteresis presented earlier. Further, they support implications given by Schleusener and [1959]: (1) that measurements from evaporation pans are unreliable as an estimate of evaporation from bare soils and (2) that conditions which cause rapid initial drying of the soil surface should conserve soil moisture under most conditions.

## REFERENCES

- Schleusener, R. A., and A. T. Corey, The role of hysteresis in reducing evaporation from soils in contact with a water table, *J. Geophys. Research*, *64*, 469-475, 1959.
- Schleusener, R. A., and L. G. King, Modification of bridge controls to simulate diurnal cyclic variation of temperature, humidity, and radiation, *Agr. Eng.*, *41*, 450-451, 1960.

(Manuscript received July 8, 1961;  
revised September 19, 1961.)



# Neutron Measurement of Surface Soil Moisture<sup>1</sup>

C. H. M. VAN BAVEL

*United States Water Conservation Laboratory  
Tempe, Arizona*

**Abstract.** A neutron probe design for the measurement of surface soil moisture is described. The probe consists of a single  $\text{BF}_3$  tube, a Ra-Be source in a gamma shield and a plastic shield which serves also as a standard. Adequate accuracy and sensitivity are reported when surface soil is homogeneous. When surface soil is stratified the interpretation of measurements is uncertain.

## INTRODUCTION

Belcher, Cuykendall, and Sack [1952] described a surface neutron probe based upon GM counting of a neutron-activated silver foil, the foil being enveloped in a paraffin shield. Factory calibration was reported, but no examination of performance took place. Subsequently, Van Bavel, Underwood, and Swanwick [1956] suggested a surface probe design consisting of a solid B-10 neutron counter with an attached neutron source. The device could be factory calibrated but showed low counting efficiency. No hydrogenous shield was used, complete performance characteristics were not given.

Phillips, Jensen, and Kirkham [1960] published a test report concerning a neutron surface probe using  $\text{BF}_3$  counters with an attached neutron source. No data were supplied on counting rate and calibration. Good agreement was obtained between indicated and directly determined soil moisture content. However, all tests were carried out on one level of soil moisture and for an uneven distribution of moisture with depth. The surface probe used in the studies by Phillips, Jensen, and Kirkham was a rather complicated device containing ten  $\text{BF}_3$  neutron counters. A hydrogenous shield was not used.

The purpose of the present report is to describe a simple surface probe based upon the design of Belcher, Cuykendall, and Sack [1952], to give data on its characteristics, and to evaluate the usefulness of the method in the field.

## EQUIPMENT AND PROCEDURE

The neutron surface probe is assembled from a standard neutron depth probe. The latter is described in detail by Van Bavel and Nielsen [1961]. Briefly, the depth probe consists of a  $\text{BF}_3$  tube, 4.7 cm in diameter, to one end of which a Ra-Be source is attached. The entire depth probe is 30 cm long. In adapting it for surface measurement, the source is detached and placed beside the counter in a plastic shield<sup>2</sup> as shown in Figure 1. Thus, source and counter are placed in almost direct contact with the soil surface but separated from the air by a hydrogenous shield. The neutron counting rate may be determined with any suitable scaler or rate meter. The counting device should provide about 1300 volts and an adjustable input sensitivity around 0.1 volt, and it should be able to count up to 50,000 cpm without appreciable coincidence loss. The counting rate depends, of course, upon the strength of the source and the moisture content of the soil, but it will never be less than the counting rate with the probe suspended in air. This counting rate is caused by the shield and can conveniently be used as a standard to verify instrument performance. Thus, probe and standard are one and the same.

In the present studies, we used a 5-mc Ra-Be source resulting in a standard, or 'shield,' counting rate of 9300 cpm. The counting rate was about 28,000 cpm when the probe was placed upon soil containing 0.30 moisture by volume.

The assembled surface probe weighs about 8.5

<sup>1</sup> Contribution from Soil and Water Conservation Research Division, Agricultural Research Service, U. S. Department of Agriculture.

<sup>2</sup> Both the neutron probe and the plastic shield were obtained from Troxler Electrical Laboratories, Box 5253, Raleigh, N. C. This information does not constitute endorsement or preference.



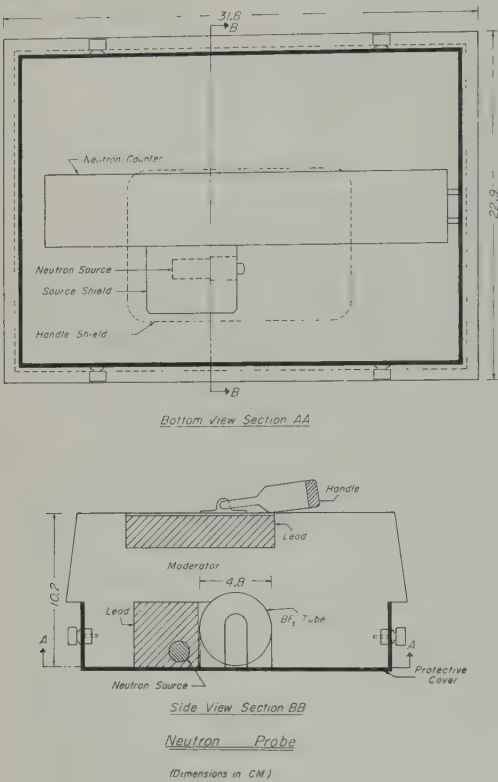


Fig. 1. Schematic drawing of surface neutron probe.

kg, which permits carrying by hand. In using the surface probe, care must be taken that it conforms closely to the soil surface. The significance of this point will be discussed further on. Tests

of performance and calibration were carried out using wooden boxes 60 × 60 cm in area and 30 cm deep, filled with soil at the desired moisture content. The soil was carefully packed and its moisture content on a weight basis ascertained in the usual manner. The entire box was then weighed, and, from the weight, the dimensions and the moisture content by weight, the moisture content by volume was found to the nearest 0.001. During measurements, surface evaporation was prevented by a thin polyethylene film cover.

EXPERIMENTS AND RESULTS

**Calibration.** Measurements were made on homogeneous soil masses at nine different moisture contents ranging from 0.05 to 0.50 by volume. Counting was done for 5 minutes, resulting in a minimum of 100,000 total counts. The counting rate is reported in Figure 2 as counts per minute. Within the range of measurements the calibration is linear, and the deviations from an eye-fitted straight line imply an estimated precision of 0.01 moisture by volume, equivalent to 400 cpm, when moisture content is derived from observed counting rates.

A maximum standard error of 400 cpm with the present equipment requires a least counting time of 1/4 of a minute. Consequently, a source of 5/4 millicurie should give sufficiently precise results if a 1-minute counting time is adopted for routine measurements.

The sensitivity of the apparatus is about 400 cpm per 0.01 moisture by volume as may be cal-

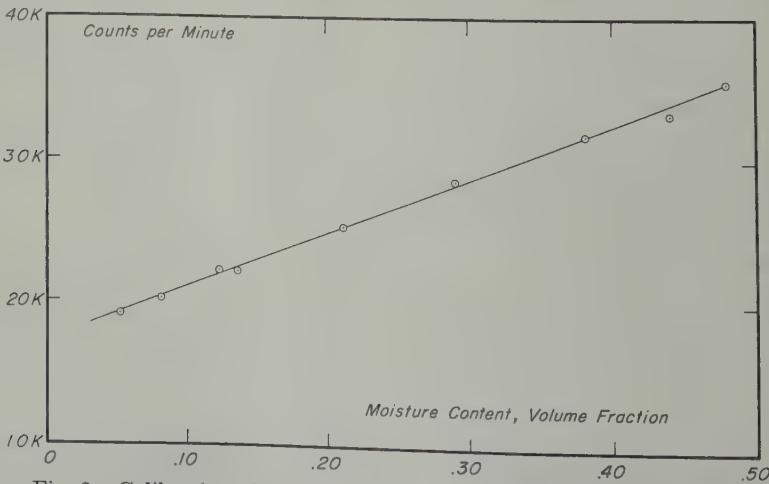
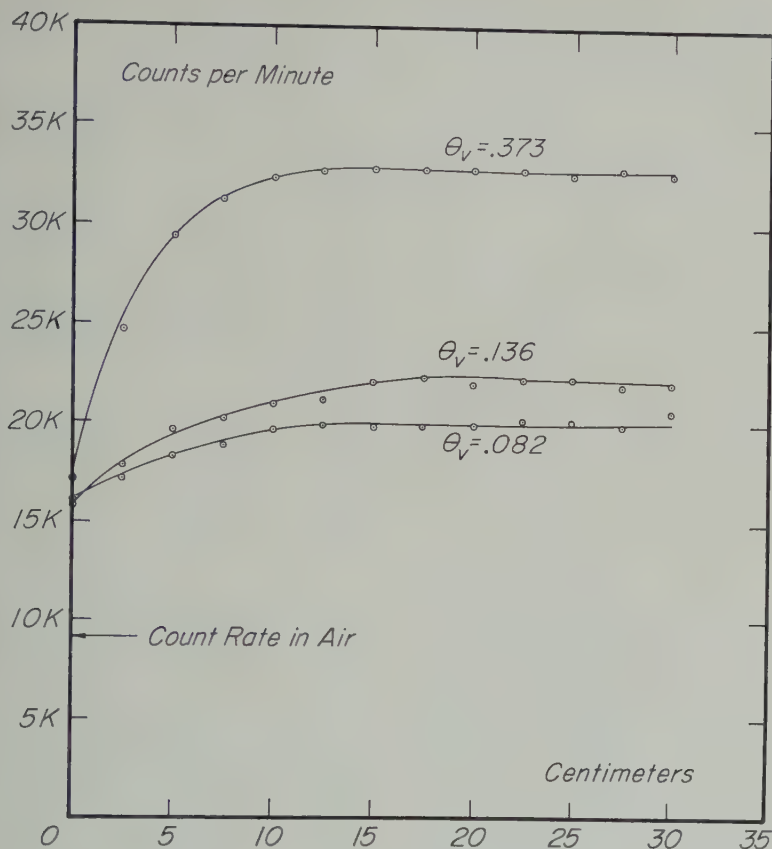


Fig. 2. Calibration of surface neutron probe with 5-mc Ra-Be source.



g. 3. Effect of thickness of soil layer with uniform moisture content upon counting rate with a 5-mc neutron surface probe. Moisture content ( $\theta_v$ ) in volume fraction.

from the data in Figure 2. By comparison, the sensitivity of the original depth is approximately the same if a 5-mc probe is used [Van Bavel and Nielsen, 1961]. In the latter case, however, counting rates are lower for corresponding moisture contents, and the error of the counting rate therefore increases more favorably with the sensitivity than in the case with the surface probe. Therefore, for both types of probes, a 1-mc source should give adequate precision. The use of a 2-mc source practically eliminates counting statistics as a possible source of instrument error.

**Thickness of measurement.** In order to find the thickness of soil that contributes significantly to the counting rate the following experiment was done. Homogeneous soil bodies of dimensions  $100 \times 60 \times 30$  cm were prepared at three different moisture contents. A surface count was

made and then 2.5 cm of soil was removed for the next counting rate observation. This was done in 12 successive steps until the entire soil body, originally 30 cm thick, was reduced to zero thickness.

In Figure 3 the effect of soil thickness upon counting rate is shown at three moisture contents. Evidently, the thickness of soil must be less than 15 cm before a measurable effect on the counting rate is obtained. The 'residual' counting rate at zero thickness is caused by the wooden bottom of the soil container.

**Effect of moisture stratification.** It would be erroneous to conclude from the previous section that the surface probe measures the moisture content of the top 15 cm of soil. Only in a soil with evenly distributed moisture content would this be the case. In order to find the effect of stratification of moisture upon counting rate, two experiments were done.

TABLE 1. Effect of Moisture Stratification in a 15-Centimeter Layer upon Surface Neutron Probe Count Rate and Indicated Moisture Content

Thickness, cm		Moisture Content		Counts per Minute	Indicated Moisture	Actual Moisture
Top Layer	Lower Layer	Top Layer	Lower Layer			
Dry Soil over Wet Soil						
2.5	12.5	0.038	0.417	23,300	0.155	0.354
5.0	10.5	.037	.238	19,200	.050	.171
7.5	7.5	.077	.404	21,600	.115	.240
10.0	5.0	.048	.367	19,200	.050	.154
12.5	2.5	.036	.441	18,800	.040	.104
Wet Soil over Dry Soil						
2.5	12.5	.441	.036	26,800	.250	.104
5.0	10.0	.367	.048	30,600	.350	.154
7.5	7.5	.404	.077	31,400	.375	.240
10.0	5.0	.238	.037	26,700	.245	.171
12.5	2.5	.417	.038	32,800	.410	.354

In the first, two layers of soil with different moisture content were placed upon each other, each being homogeneous within itself. The total thickness was 15 cm in all cases. The case of dry soil over wet soil was considered as well as the reverse situation. In Table 1, the various combinations are given, together with the moisture contents of the individual layers, the counting rates, the indicated moisture contents, and the average moisture content of the entire

15-cm layer. The indicated moisture contents were obtained from the calibration line in Figure 2.

In the second experiment, a 30-cm layer of soil, originally homogeneously wet, was left to dry in the air. Periodically, a measurement was made with the surface neutron probe, and, at the same time, the moisture distribution was measured by direct sampling through the sides of the container. The container size was, again, 60 × 60 cm in area and 30 cm deep. Moisture samples were taken every 2.5 cm.

TABLE 2. Effect of Surface Drying upon Moisture Distribution and Moisture Content, the Latter as Measured by a Surface Neutron Probe

Days of Drying	2	7	11	28
Depth in cm	Moisture by Volume			
2.5	0.096	0.068	0.054	0.057
5.0	.201	.164	.119	.093
7.5	.216	.208	.189	.139
10.0	.228	.216	.212	.165
12.5	.223	.224	.218	.186
15.0	.235	.228	.219	.199
Counts per minute	24,200	22,900	22,100	22,100
Indicated moisture	0.180	0.150	0.130	0.120
Actual moisture	0.200	0.185	0.168	0.140

In Table 2, the moisture distribution in the top 15 cm is shown 2, 7, 11, and 28 days after the soil was placed in the box. Also given are the counting rates at each date and the indicated moisture content, derived again from Figure 2, as well as the average moisture content of the top 15 cm.

The data of Tables 1 and 2 demonstrate that when moisture is stratified in the top 6 inches the surface neutron probe indicates a moisture content very different from the average for the top 15 cm of soil. It is obvious that the effect of the top 2.5-cm layer predominates over the next 2.5-cm layer, and so on. The moisture conditions at depths beyond 7.5 cm hardly influence the neutron meter readings.

When the moisture distribution is gradual, in the case of a drying soil layer, the error in the neutron meter indication is not as large when abrupt changes occur in moisture con-

he latter would be typical if a small of rain were to fall upon a dry soil. data of Table 1 and of Figure 2 suggest od of estimating the moisture content e neutron counting rate in which surface re given more weight than deeper layers. mple schemes can be employed, and none generally satisfactory because a super- et layer has a relatively greater effect superficial dry layer. As a compromise rage moisture content of the top 7.5 cm mpared with the indicated moisture con- s shown in Table 3. It appears that the e content of the 7.5-cm surface layer is mated by the surface neutron probe. six cases in Table 3 is agreement satis- l, four of these pertaining to instances he top 10 or 12.5 cm of soil is homogene-

t of surface irregularity. Previous data ll obtained with surfaces that had been y smoothed. In practice, such a condi- not always found or realized and the f an irregular surface is easily surmised. xperiments were done. In the first, the e was corrugated with furrows and ridges 3 cm apart and with elevation differences 1.8, and 2.4 cm, respectively. Counting ere then obtained from a soil of uniform

TABLE 3. Comparison of Moisture Content asured with Surface Neutron Probe with tual Values for the Top 7.5 Centimeters

	Indicated Moisture	Actual Moisture	Differ- ence
	0.155	0.290	-0.135
	.050	.104	-.054
er wet soil	.115	.077	+.038
le 1	.050	.048	+.002
	.040	.036	+.004
	.250	.238	+.012
	.350	.367	-.017
er dry soil	.375	.404	-.029
le 1	.245	.238	+.007
	.410	.417	-.007
ing at	.180	.141	+.039
urface	.150	.147	+.003
le 2	.130	.121	+.009
	.120	.096	+.024

TABLE 4. Effect of Surface Corrugation and of Tilting of Surface Neutron Probe on Counting Rate and Indicated Soil Moisture Content as Volume Fraction

Corrugations Size, cm	Counts per Minute	Indicated Moisture	Fractional Deviation
0.0	26,800	0.240	...
1.2	24,000	.165	0.31
1.8	23,000	.140	.42
2.4	22,400	.120	.50
Tilt Height, cm			
0.0	26,800	.240	...
1.1	25,200	.200	.17
2.2	23,200	.140	.42
3.3	21,000	.090	.63
4.4	19,200	.040	.93

moisture content in a container  $60 \times 60 \times 30$  cm (Table 4).

In the second experiment the surface probe was tilted at one corner so that the latter would, at one point, be above the surface by 1.1, 2.2, 3.3, and 4.4 cm, respectively (Table 4). The results of both experiments clearly illustrate the need for making surface neutron measurements on a smooth surface. By scraping and/or pressing it should be possible to obtain reproducible and meaningful readings.

#### CONCLUSION

The work reported here agrees with that of others in showing that a workable surface neutron moisture probe can be constructed and operated without difficulty. In particular, it is shown that such a probe may be simply and inexpensively adapted from a depth probe. The key design factor is the use of a hydrogenous shield over the source-counter assembly. The shield prevents the complete escape of fast neutrons emanating from the source in an upward direction and thereby increases the efficiency. Also, it may decrease the depth of measurement somewhat, as inferred from work by *Mortier, De Boedt, and De Leenheer* [1960], in which embedding the source in a lucite capsule was shown to improve resolution of a depth probe.

The calibration of the device described here is linear and its sensitivity to changes in soil moisture content is as good as or better than that of



a depth probe. Satisfactory results can be had with currently available fast neutron sources as small as 1 mc of Ra-Be.

In further agreement with previous work [Van Bavel, Underwood, and Swanson, 1956], it is found that for uniform moisture content the depth of measurement is about 15 cm, substantially independent of moisture content. It is very important that the surface be flat and that it conform closely to the probe. Errors resulting from a lack of close fit are quite large.

On the other hand, the readings of a surface neutron probe are not simply related to the moisture content of the top 15 cm of soil when moisture content is not evenly distributed. The stratification of moisture and the moisture content itself can result in widely varying readings for the same average moisture content of the surface layer of soil. Consequently, readings obtained on soil surfaces that have been superficially wetted or dried can be used only as crude estimates of the soil moisture in the top 10- to

15-cm layer. This limits the utility of a neutron surface probe.

#### REFERENCES

- Belcher, D. J., T. R. Cuykendall, and H. S. Sack, Nuclear meters for measuring soil density and moisture in thin surface layers, *Civil Aeronaut. Admin. Tech. Develop. and Evaluation Center, Tech. Develop. Rept. 161*, 1952.
- Mortier, V. P., M. De Boodt, and L. De Leenheer, Über das Auflösungsvermögen der Neutronendifusionsmethode für Feuchtigkeitsbestimmungen im Boden, *Z. Pflanzenernähr., Düng., u. Bodenk.*, 87, 244-250, 1959.
- Phillips, R. E., C. R. Jensen, and Don Kirkham, Use of radiation equipment for plow-layer density and moisture, *Soil Sci.*, 89, 2-7, 1960.
- Van Bavel, C. H. M., and D. R. Nielsen, Calibration and characteristics of two neutron moisture probes, *Soil Sci. Soc. Am., Proc.*, 25, 1961.
- Van Bavel, C. H. M., Newton Underwood, and R. W. Swanson, Soil moisture measurement by neutron moderation, *Soil Sci.*, 82, 29-41, 1956.

(Manuscript received May 15, 1961;  
revised September 1, 1961.)

# An Evaluation of Uranium as a Tool for Studying the Hydrogeochemistry of the Truckee Meadows Area, Nevada

PHILIP COHEN

*U. S. Geological Survey, Carson City, Nevada*

**Abstract.** Forty-seven water samples collected in the Truckee Meadows, an alluviated Tertiary basin in western Nevada, were analyzed for uranium and for the principal dissolved constituents. Some of the relationships between uranium and other chemical constituents described by other writers are verified in the study of the hydrogeochemistry of the Truckee Meadows area; others are not. The following relationships between uranium and bicarbonate-plus-carbonate content, uranium and chloride content, and uranium and sulfate content were observed in the waters of the Truckee Meadows area. (1) Uranium content tends to increase as the bicarbonate-plus-carbonate content increases, (2) thermal, chloride-rich waters of the Steamboat Springs area are relatively deficient in uranium, (3) some waters high in sulfate content are relatively rich in uranium; others are not. Because of the variability in concentration and the complex interrelationships between the bicarbonate, carbonate, sulfate, and chloride anions, and because uranium content appears to be dependent upon these variables, uranium has little value as a tool for studying the hydrogeochemistry of the area.

## INTRODUCTION

**Purpose and scope of the report.** The occurrence of uranium in the waters of the Truckee Meadows area is discussed, and the use of uranium as a tool for studying the hydrogeochemistry of the area is evaluated. The study is a contribution to an investigation of the waters of the Truckee Meadows area which is presently being made by the U. S. Geological Survey in cooperation with the Nevada Department of Conservation and Natural Resources. This report is based in large part on a study of chemical and radiochemical analyses of 47 water samples.

**Previous investigations.** Barker and Scott (1957) have discussed the potential value of uranium as a tool for studying the geochemistry of ground water and have shown a theoretical mathematical relationship between uranium and bicarbonate content, and between uranium and dissolved-solids content. Their report is the work upon which the present study is based. Scott encouraged the use of radiochemical analyses in the study of the hydrogeochemistry of the Truckee Meadows area and arranged for the analysis of all but one of the samples included in this report.

Thompson, Fix, Gianella, and White [1948] and White [1957a, b] have developed several

important geochemical concepts relative to the Steamboat Springs area in the southern part of the Truckee Meadows area. Thompson [1956] has discussed some aspects of the geochemistry of the area. His geologic maps have been significant aids in the present study.

## GEOGRAPHIC SETTING

Truckee Meadows is an alluviated Tertiary basin in western Nevada. The valley is drained by two perennial streams, Steamboat Creek and the Truckee River. The Truckee River heads in the Sierra Nevada and follows a meandering course eastward through Reno and across Truckee Meadows. It leaves the valley through a bedrock gorge in the Virginia Range. Steamboat Creek enters the valley from the south and joins the Truckee River near the railroad siding of Vista (see Fig. 1).

## GEOLOGIC FEATURES

Truckee Meadows is at the western margin of the Great Basin section of the Basin and Range physiographic province. The valley is bordered by maturely eroded fault-block mountains and is partially filled with unconsolidated and partly consolidated alluvial deposits.

The bordering mountains are composed of

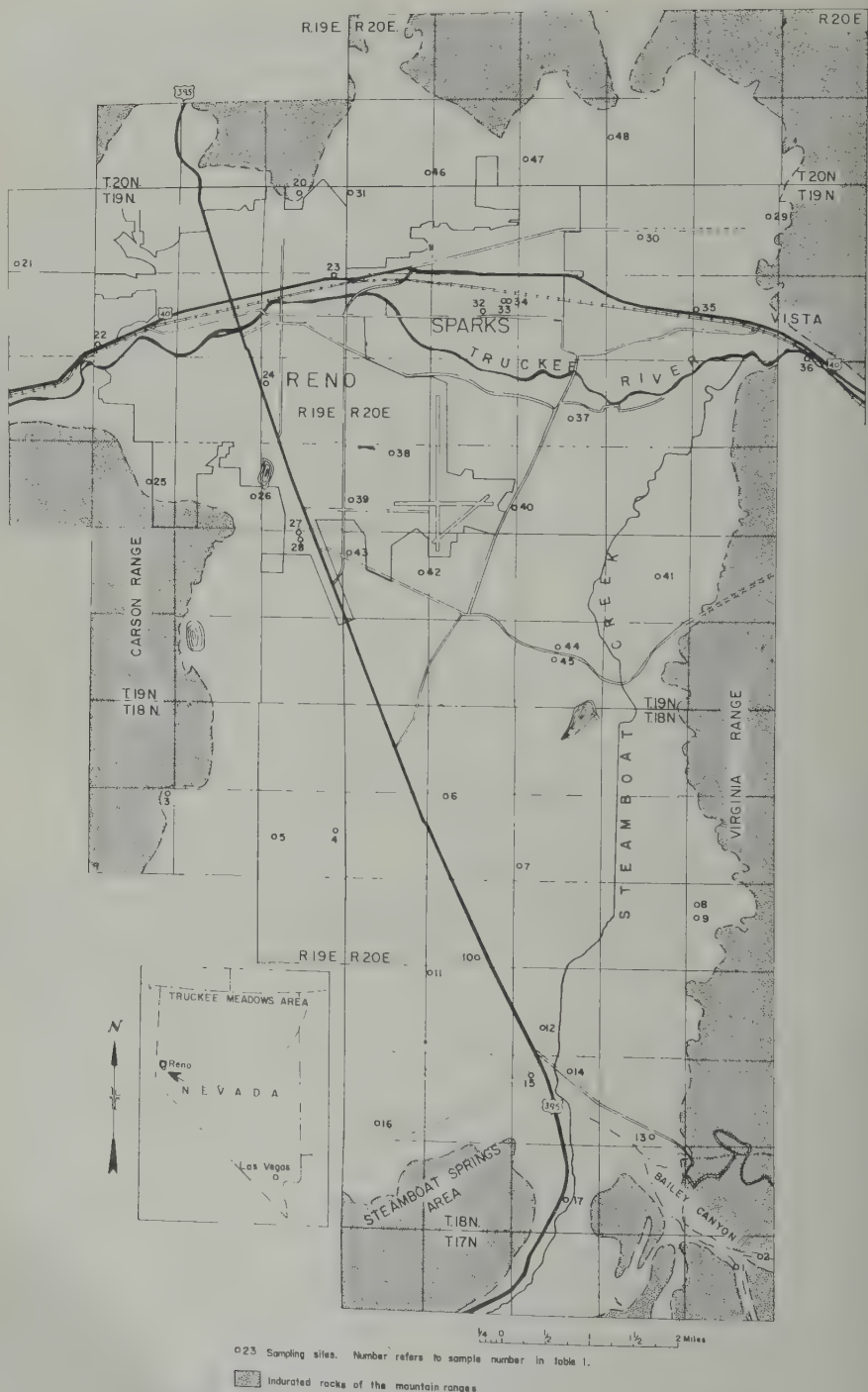


Fig. 1. Map of the Truckee Meadows area showing the location of sampling sites.

metamorphic, and sedimentary rocks range in age from Mesozoic(?) to Quaternary. The Carson Range consists in large part of igneous rocks of Cretaceous(?) age that were intruded into a complex sequence of metamorphic rocks of Triassic(?) age. Pyroclastic rocks, and lake beds cover much of the older igneous and metamorphic rocks. The Virginia Range is composed predominantly of volcanic rocks of intermediate to basic chemical composition. Granodiorite of Miocene(?) age has intruded, and, in part, hydrothermally altered the igneous rocks. The ore bodies of the famous Black Rock lode, which is about 20 miles south of Reno, are associated with this intrusive. Alluvial deposits of the valley fill, which probably are more than 3500 feet thick, range in age from Pliocene to Recent. The predominantly fine-grained deposits of the Truckee formation are of recent age and consist of relatively impermeable diatomite and partly cemented gravel, silt, clay, and tuff. Moderately permeable alluvial sediments of late Pliocene, Pleistocene, and Recent age overlie the Truckee formation. A pronounced angular unconformity separates the rocks of pre-Tertiary age have been involved in folding and thrust-faulted. Younger, normal faults have broken the mountain ranges into distinct structural troughs and ridges which trend roughly northward. Normal faults also have deformed and cut much of the alluvium and form the valley fill.

#### HYDROLOGIC FEATURES

Essentially all the economically recoverable groundwater in Truckee Meadows occurs in alluvial deposits of the valley fill. The principal source of recharge to the aquifers of the valley fill is the Truckee River. Recharge occurs by infiltration directly from the Truckee River and also by seepage from irrigation ditches and infiltration of excess water diverted from the Truckee River for irrigation. Lesser amounts of groundwater recharge occur as a result of infiltration of precipitation and seepage loss from ephemeral streams flowing across the alluvial valley. The principal means of ground-water discharge include seepage directly into the Truckee River and Steamboat Creek, seepage into irrigation and drainage ditches in the lower parts of the valley, and evapotranspiration. Lesser

amounts of ground water are discharged by wells and springs.

#### CHEMICAL QUALITY OF THE WATERS

*Location of sampling sites.* The location of most of the water sampling sites is shown in Figure 1. Two sites are outside of Figure 1; sample 18 was collected from Lawton's Hot Springs, and sample 19 was collected from the Truckee River near the hot springs. Lawton's Hot Springs is in the canyon of the Truckee River, in sec. 13, T. 19 N., R. 18 E., about 2 miles west of the northwest corner of the map.

*Classification of the waters.* Some of the more important factors considered in evaluating the geochemistry of the waters of the Truckee Meadows area are enumerated below.

1. The complex chemical composition of the sediments of the valley fill and the rocks of the bordering mountains.
2. The complex stratigraphy and structural deformation of the aquifers.
3. Exchange between ions in the waters and those in the rocks in which the waters occur.
4. Mixing of highly mineralized waters from hot springs and areas of bleached rock with relatively dilute irrigation waters.

Partly because of these factors, a chemical classification system of the waters of the area was needed. The classification adopted is based solely upon the major anions sulfate, chloride, bicarbonate, and carbonate. Each water sample is shown on a trilinear diagram in which the vertexes of the triangle represent a composition of 100 per cent equivalents per million of sulfate, chloride, or bicarbonate-plus-carbonate. (See Fig. 2.) The diagram is subdivided into three fields as follows: (1) Waters in which the percentage of chloride is greater than the percentage of sulfate, and the percentage of bicarbonate plus carbonate is less than 80 per cent of the sum of the major anions. Waters of this composition are plotted in field I on Figure 2 and are classified as chloride waters. (2) Waters in which the percentage of sulfate is greater than the percentage of chloride, and the percentage of bicarbonate plus carbonate is less than 80 per cent of the sum of the major anions. Waters of this composition are plotted in field II and are classified as sulfate waters. (3) Waters in which the percentage of bicarbonate plus carbonate is greater than 80 per cent of the



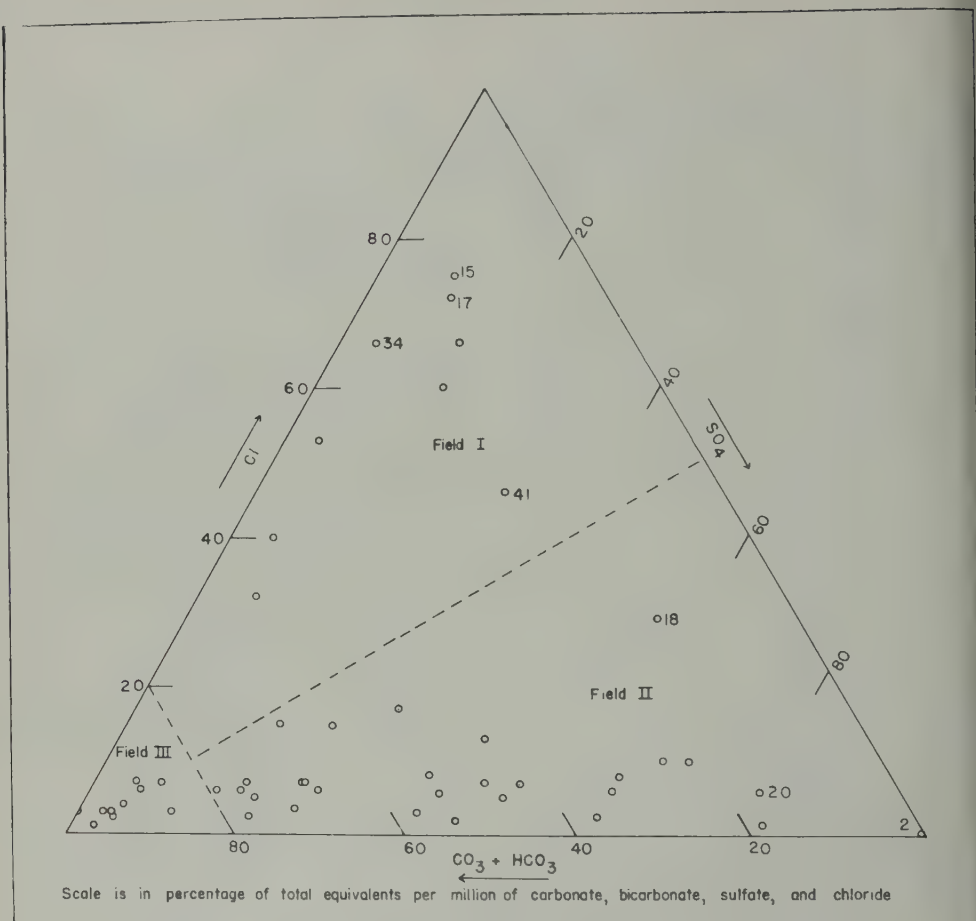


Fig. 2. Classification of the waters of the Truckee Meadows area.

sum of the major anions. Waters of this composition are plotted in field III and are classified as bicarbonate-carbonate waters.

*Mixtures and sources of the waters.* It is convenient to use the terms 'high bicarbonate-carbonate waters,' 'high chloride waters,' and 'high sulfate waters' to describe some of the waters of the Truckee Meadows area. High bicarbonate-carbonate waters are relatively rich in bicarbonate (or bicarbonate plus carbonate), have a low dissolved-solids content, and are indicative of waters from the Truckee River and some of the smaller streams in the area. High chloride waters are rich in chloride, have a high dissolved-solids content, and are associated with the thermal waters of the Steamboat Springs system. High sulfate waters are rich in sulfate, have a high dissolved-solids content, and are associated with bleached rocks.

Most of the samples shown in Figure 2 are mixtures of either high sulfate or high chloride waters and high bicarbonate-carbonate waters. Samples 18 and 41 are exceptions. They are mixtures of high chloride and high sulfate waters. Samples 15 and 17 are considered to be typical high chloride (predominantly sodium chloride) waters. Sample 15 is from a relatively deep well, and sample 17 is from a hot spring. Both sample sources are in the Steamboat Springs area. Samples 2 and 20 are considered to be typical of the high sulfate waters of the area. Sample 2 is from the stream in the north branch of Bailey Canyon, and sample 20 is from a shallow well in hydrothermally altered andesite.

All the samples in field I, except sample 15, are associated with or are downgrade from the Steamboat Springs. Sample 34 was taken from an 18-foot-deep dug well adjacent to a railroad.

Much of the ground near the well is saturated with sodium chloride, which was used to transport railroad cars. Presumably, the chloride in the sample was derived from leaching of the surrounding rock.

Altered rocks are the principal source of uranium in the waters that are plotted in field II. Mineral assemblages of most of the rocks in the Truckee formation have been altered to some degree by hydrothermal alteration. Pyrite ( $\text{FeS}_2$ ) was introduced into the formation, and, as a result of the near-surface oxidation of pyrite and the formation of sulfurous acid, almost all the hydrothermally altered rocks exposed to weathering have been bleached. The products of the bleaching are dominantly clay and some quartz and opal.

Like the chloride waters that are mostly derived from a single source (Steamboat Springs), sulfate waters are found throughout the area. Samples having the greatest percentage of sulfate are found in areas of bleached rock. The relationship between bleached rock and high sulfate content is illustrated by samples of water from Bailey Canyon. Sample 1, containing 3.98 epm (equivalents per million) sulfate, was obtained from the small stream in the south branch of Bailey Canyon. This stream drains an area underlain by rock that, for the most part, is not bleached. Sample 2, containing 53.51 epm sulfate, was obtained from a stream of similar size in the north branch of Bailey Canyon. This stream drains an area underlain for the most part by bleached rock.

**Uranium.** The uranium content of 47 samples collected in the Truckee Meadows area ranged from less than 0.1 to 43 ppb (parts per billion); the median was 1.7 ppb. This compares with a range of 0.9 to 12 ppb and a median of 2 ppb for 47 samples of the ground waters in the Ogallala formation of Texas and New Mexico, and a range of less than 0.1 to 22 ppb and a median of 1.6 ppb for 67 random samples in alluvial deposits throughout the United States [Barker and Scott, 1958, p. 462].

The uranium content of the waters of the Truckee Meadows area tends to increase as the bicarbonate-plus-carbonate content increases. (Fig. 3.) This verifies the findings of Barker and Scott (p. 463), who state that this relationship is a function of the increased solubility of

uranium as the bicarbonate content increases, presumably because uranium and bicarbonate form relatively soluble uranyl carbonate complexes.

Other relationships involving uranium are suggested by comparing Figures 2 and 3. Most of the analyses that are plotted in field II of Figure 2 tend to fall to the left or above the curve in Figure 3, indicating that most of the sulfate waters sampled tend to contain relatively more uranium than the chloride or bicarbonate-carbonate waters having the same concentration of bicarbonate plus carbonate. Sample 20, which had the third highest percentage and second largest concentration of sulfate, was richest in uranium, containing 43 ppb. All points in field I, except sample 34 whose anomalous chloride content is explained above, fall to the right or below the curve, suggesting that the chloride waters contain less uranium than either sulfate or bicarbonate-carbonate waters of comparable concentrations of bicarbonate plus carbonate. Samples 15 and 17, which contained the highest percentages and highest concentrations of chloride, fall farthest to the right of the curve in Figure 3. Thus, although the amount of uranium in the waters of the Truckee Meadows area appears to be a function of bicarbonate-plus-carbonate content, it also appears to be related to the chloride and sulfate contents.

The waters studied by Barker and Scott [1958, pp. 463-464] showed a tendency toward an increasing concentration of uranium with an increase in dissolved solids. Barker and Scott observed that, in general, waters at successive downgrade sampling sites were relatively richer in uranium than those at upgrade sites. They state, 'The downgradient increase in uranium content probably is a result of the water at successive downgradient locations having been in the aquifer longer than water obtained from upgradient sources.'

Figure 4 relates uranium content in parts per billion against dissolved-solids content in parts per million. According to the method used by Barker and Scott (p. 464), two groups of points are shown in Figure 4—one group in which bicarbonate plus carbonate is greater than 50 per cent (open circles), and one group in which bicarbonate plus carbonate is equal to or less than 50 per cent of the principal anions (solid circles). There appears to be a slight indication

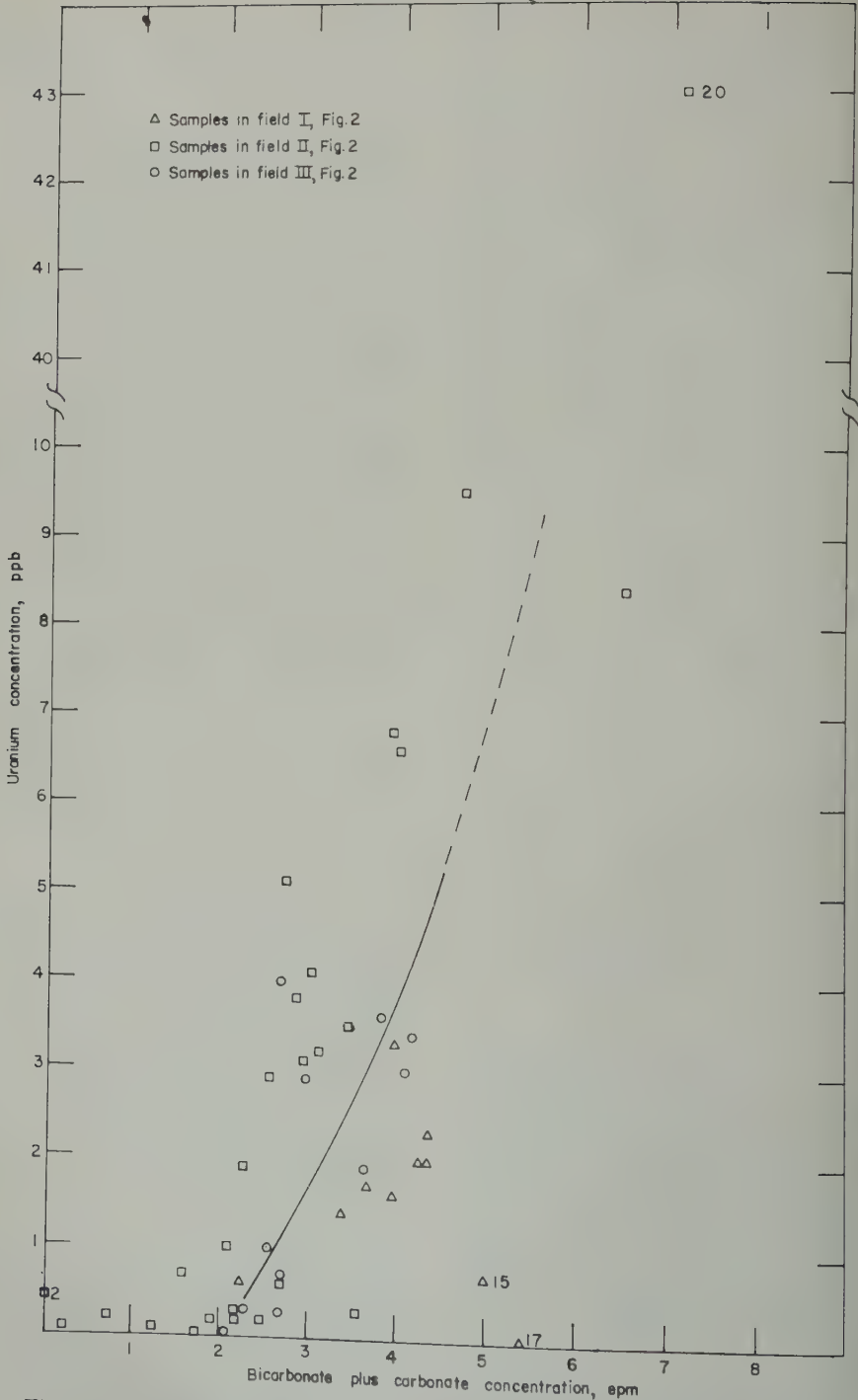


Fig. 3. Relationship between uranium concentration and bicarbonate-carbonate concentration in the waters of the Truckee Meadows area.

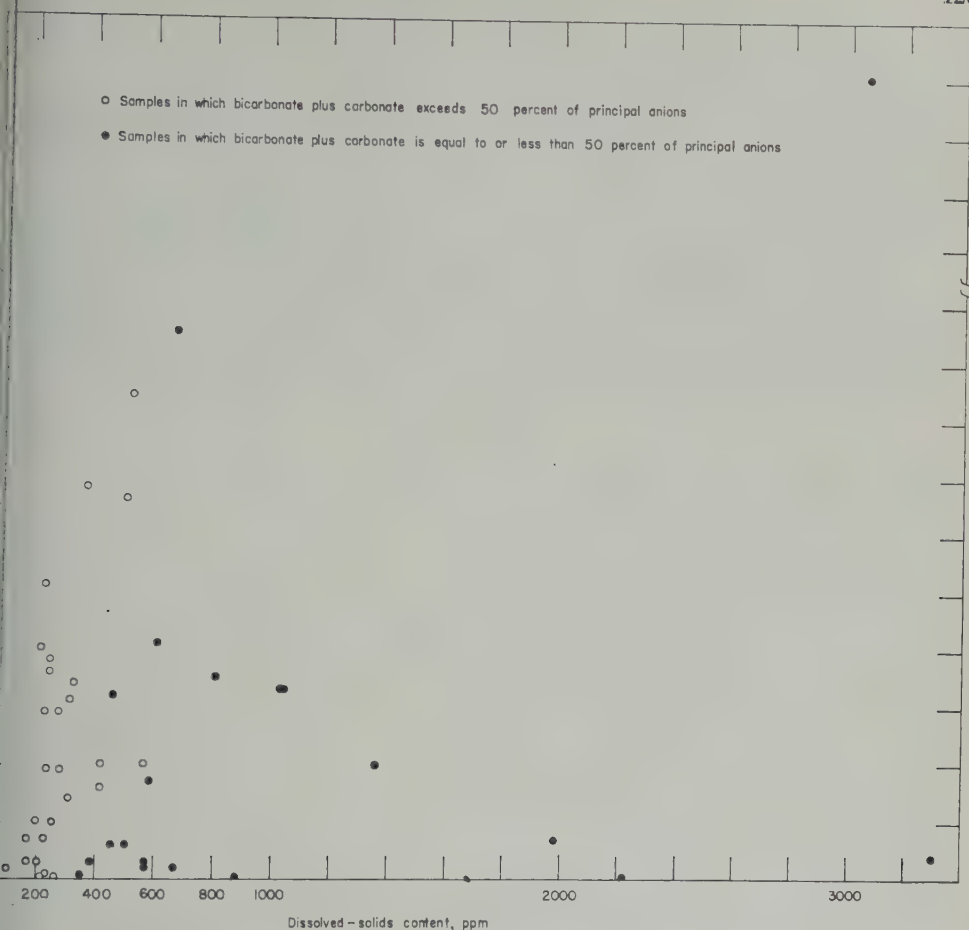


Fig. 4. Relationship between uranium concentration and dissolved-solids content in the waters of the Truckee Meadows area.

relation between uranium content and dissolved-solids content in the former group but the latter group. Barker and Scott decided that there was a correlation between uranium and dissolved-solids content in both groups. However, the correlation was better in the latter group.

probable reasons for the relatively poor correlation between the uranium and dissolved-solids content of the waters of the Truckee Meadows area are as follows: (1) Chloride waters tend to have a high dissolved-solids content and are relatively deficient in uranium. (2) Sulfate waters of high dissolved-solids content are relatively rich in uranium, but chloride waters are not. (3) The uranium content of the waters of the area is probably extremely

## CONCLUSIONS

The uranium content of the waters of the Truckee Meadows area is not a significant aid in itself for evaluating the hydrogeochemistry of the area. It is inferred, therefore, that uranium alone will not be very useful for evaluating the hydrogeochemistry of similar alluviated intermontane basins in the Basin and Range physiographic province. However, uranium may be useful for evaluating the hydrogeochemistry of monolithologic or near-monolithologic terranes. In addition, an evaluation of uranium in the waters of an area, if closely related to a study of the geology of the area, may result in a better understanding of the hydrologic factors that control the occurrence, movement, and chemical quality of those waters.



*Acknowledgments.* O. J. Loeltz, district engineer in charge of U. S. Geological Survey groundwater investigations in Nevada, in the course of his collaboration with the writer on the investigation of the water resources of the Truckee Meadows area, has provided valuable guidance in the preparation of this report.

Publication authorized by the Director, U. S. Geological Survey.

#### REFERENCES

- Barker, F. B., and R. C. Scott, Uranium and radium in the ground water of Llano Estacado, Texas and New Mexico, *Trans. Am. Geophys. Union*, 39(3), 459-466, 1958.
- Brannock, W. W., P. F. Fix, V. P. Gianella, and D. E. White, Preliminary geochemical results from Steamboat Springs, Nevada, *Trans. Am. Geophys. Union*, 29(2), 211-226, 1948.
- Thompson, G. A., Geology of the Virginia City quadrangle, *U. S. Geol. Survey Bull.* 1042-C, 47, 1956.
- White, D. E., Thermal waters of volcanic origin, *Bull. Geol. Soc. Am.*, 68(12), 1637-1657, 1957.
- White, D. E., Magmatic, connate, and metamorphic waters, *Bull. Geol. Soc. Am.*, 68(12), 1637-1682, 1957b.

(Manuscript received July 9, 1961; revised August 30, 1961.)

# Laminar Flow in Rough Rectangular Channels

DAH-CHENG WOO AND ERNEST F. BRATER

*University of Michigan, Ann Arbor*

**Abstract.** The results of an investigation of open channel flow in the laminar and transition ranges are presented. This type of flow is encountered during runoff from rainfall. Values of the friction factor were determined for two roughnesses and for 11 slopes varying from 0.001 to 0.01. It was found that for laminar flow the values departed significantly from the theoretical values derived for smooth surfaces and that for very rough surfaces the variations depended on slope. The results for both the laminar and transition ranges are presented graphically to compare with theoretical values and with results obtained by other investigators. It is believed that these data will prove useful in studies of overland flow and particularly for investigations of soil erosion.

## NOMENCLATURE

channel width.  
 $f_e N_R$ .  
 coefficient of friction.  
 gravitational acceleration.  
 length along bottom surface from upper end of the flume.  
 Manning's coefficient of roughness.  
 Reynolds number =  $VY/\nu$ .  
 pressure gradient.  
 discharge per unit width.  
 slope of energy gradient.  
 slope of bottom surface.  
 temperature of water ( $^{\circ}\text{C}$ ).  
 velocity component in the direction of flow.  
 average velocity.  
 horizontal distance perpendicular to and from the center line of the flume.  
 vertical distance from water surface.  
 water depth.  
 absolute viscosity.  
 kinematic viscosity.  
 density.

## INTRODUCTION

Data which form the basis of this paper were obtained as part of an investigation of variability in thin sheets of water over rough surfaces. The results of the tests of steady uniform flow are presented here. It is expected that the results of the studies of spatially variable flow from artificial rainfall will be presented in a later date. The investigation was undertaken to obtain a better understanding of the sheet flow pro-

duced by rainfall. Evidence obtained from runoff plots [Wisler and Brater, 1959] indicates that such flow may be in the laminar range or in the transition range between laminar and fully developed turbulent flow. To study spatially variable flow produced by rain it was first necessary to establish the flow characteristics of steady uniform flow for the same range of Reynolds numbers and roughnesses.

The law of laminar flow in pipes of circular section was first published by Hagen in 1839 and by Poiseuille in 1840 from experimental results, and it was derived analytically by Wiederman in 1856. Since then by numerous experiments with various fluids flowing in circular pipes of different sizes, materials, and relative roughnesses the law has been closely verified. Among the better known are the work of Stanton and Pannell [1914], Nikuradse [1933], and Freeman [1941]. Boussinesq [1868] derived the equation of laminar flow in a pipe of rectangular section of any ratio of width to depth. It was proved correct by experiments on smooth surfaces by Davis and White [1928], Cornish [1928], Nikuradse [1933], Schiller [1932], and Allen and Grunberg [1937]. The lack of experimental data on rough surfaces leaves the question of the validity of this equation for these conditions unanswered. Laminar flow in open channels has been explored even less. Whether Boussinesq's analytical equation for flow in rectangular pipes can be applied to open channels has not been proved.

It is the purpose of this paper to present the results of a series of tests made by the authors as well as results obtained by other investigators

in such a manner as to check their agreement with analytical equations for laminar flow and to provide friction factors for use in the transition range.

#### REVIEW OF PAST LITERATURE

The earliest researcher on this subject probably was *Hopf* [1910]. His experimental work was carried out on three kinds of smooth surfaces (polished and unfinished brass, and glass) with four different slopes (1/125, 1/50, 1/25, and 3/50) and by using three different fluids (water and sugar solution, 12 and 25 per cent.) The results show that for small Reynolds numbers they follow the theoretical relationship closely. The upper limits of laminar flow was in the range of Reynolds numbers from 300 to 330 for water and 250 to 280 for sugar solutions.

*Jeffreys* [1925] did his experimental work on a rectangular flume and found that his results generally agreed with *Hopf's*. His tests showed the upper limit of laminar flow to be at a Reynolds number of 310. *Horton, Leach, and Van Vliet* [1934] published their results on a rectangular channel with a smooth bottom surface of white pine, and their results also checked closely with the theoretical values within the laminar region. *Allen* [1934] reported in his work that introducing a different degree of turbulence in the approaching channel would affect the flow characteristics in the testing section. He found the upper limit of true laminar flow to be about Reynolds number 300. Although he used both smooth (painted wood) and rough (paint intermixed with sand) surfaces, all but a few points for the smooth surface were for Reynolds numbers larger than 500. From tests in a rectangular channel *Parsons* [1949] found that on a smooth surface of troweled mortar the measured depths checked perfectly with the theoretical ones, but on a rough surface of a mixture of sand and cement the measured depths were larger and the measured velocities were smaller than the theoretical ones. The discrepancies increased with increasing surface slopes. *Chow* [1959] also indicated that the experimental data in open channels of both smooth and rough surfaces showed the same general relationship between  $f_o$  and  $N_R$  as in the pipe flow. He noted that the value of  $C$  in  $f_o = C/N_R$  (Equation 12) is generally higher for rougher

channels and that this value changes with channel shape, being higher for rectangular than for triangular channels.

*Owen's* [1954] results on surfaces of polished brass checked very well with the theoretical values. Again *Straub, Silberman, and Nelson* [1958] experimental results with rectangular channels with smooth surfaces, constructed rolled structural shapes, checked theoretical values, but those obtained from a 90° triangular channel, with a rough surface of sand close showed clear differences from the analytical equation for triangular channels. This later paper also includes information from an earlier paper by *Straub* [1939] concerning flow in the transition region in open channels.

#### THEORETICAL ANALYSIS

*The basic equation.* The following equation for laminar flow in rectangular pipes having a width  $b$  and depth of  $2Y$  was first derived analytically by *Boussinesq* [1868].

$$v = -\frac{Y^2}{2\mu} \frac{dp}{dz} \left[ 1 - \frac{y^2}{Y^2} - \frac{32}{\pi^3} \sum_{n=0}^{\infty} \frac{(-1)^n}{(2n+1)^3} \frac{\cosh \frac{2n+1}{2} \frac{\pi x}{Y}}{\frac{2n+1}{4} \frac{\pi b}{Y}} \cdot \cos \frac{2n+1}{2} \frac{\pi y}{Y} \right]$$

in which  $x$  and  $y$  are the coordinates, with respect to the center of the pipe, of a point where the velocity is  $v$ . By substituting  $g S_o/\nu$  for  $-(dp/dz)(1/\mu)$ , equation 1 becomes

$$v = \frac{g S_o Y^2}{2\nu} \left[ 1 - \frac{y^2}{Y^2} - \frac{32}{\pi^3} \sum_{n=0}^{\infty} \frac{(-1)^n}{(2n+1)^3} \frac{\cosh \frac{2n+1}{2} \frac{\pi x}{Y}}{\frac{2n+1}{4} \frac{\pi b}{Y}} \cdot \cos \frac{2n+1}{2} \frac{\pi y}{Y} \right]$$

the flow pattern in a rectangular pipe symmetrical about the horizontal center line, be applied to a rectangular channel of width  $b$  and depth  $Y$  to obtain the following equation for average velocity:

$$\frac{S_0 Y^2}{3\nu} \left[ 1 - \frac{384}{\pi^5} \frac{Y}{b} \sum_{n=0}^{\infty} \frac{1}{(2n+1)^5} \cdot \tanh \frac{2n+1}{4} \frac{\pi b}{Y} \right] \quad (3)$$

channel of infinite width, (3) reduces to

$$V = g S_0 Y^2 / 3\nu \quad (4)$$

basic equation to be used in this paper is equation 4. A much simpler derivation of this equation was presented by Horton, Leach, and Met [1934]. It was based on the equilibrium of the component of weight, in the direction of flow, and the shearing resistance of the bottom. The assumption of zero shearing resistance at the free water surface was imposed. The equation for velocity at any distance  $y$  from the channel bottom is

$$v = \frac{g S_0}{\nu} \left( Y y - \frac{y^2}{2} \right) \quad (5)$$

average velocity, it has the form of (4), or

$$S_0 = 3 V \nu / g Y^2 \quad (6)$$

The Reynolds number in the open channel is defined by

$$N_R = V Y / \nu \quad (7)$$

Equation 6 can be rearranged as follows:

$$S_0 = \frac{6\nu}{V Y} \frac{1}{Y} \frac{V^2}{2g} = \frac{6}{N_R} \frac{1}{Y} \frac{V^2}{2g} \quad (8)$$

Replacing  $6/N_R$  with  $f_c$

$$S_0 = f_c \frac{1}{Y} \frac{V^2}{2g} \quad (9)$$

Equation 9 corresponds to the general energy equation for pipe flow. The theoretical relationship between  $f_c$  and  $N_R$  (equation 10) has been derived for wide smooth surfaces:

$$f_c = 6/N_R \quad (10)$$

The effect on this relationship of finite width and surface roughness is one of the purposes of this study.

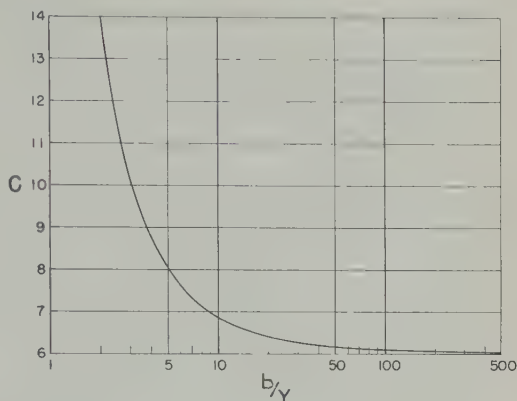


Fig. 1. Variation of  $C$  with  $b/Y$ .

*Consideration of side wall effect.* The importance of the side wall effect for a rectangular channel of finite width was investigated analytically in order to evaluate its importance in the interpretation of the test data. For this purpose, equation 3, which includes the effect of side walls, was compared with equation 4 as follows. Through rearrangement, (3) can also be written as

$$S_0 = \frac{6}{N_R K} \frac{1}{Y} \frac{V^2}{2g} \quad (3a)$$

where

$$K = 1 - \frac{384}{\pi^5} \frac{Y}{b} \sum_{n=0}^{\infty} \frac{1}{(2n+1)^5} \cdot \tanh \frac{2n+1}{4} \frac{\pi b}{Y} \quad (11)$$

Equating (3a) and (9) gives

$$f_c = 6/N_R K = C/N_R \quad (12)$$

and

$$C = 6/K \quad (13)$$

$C$  is then computed for various values of  $b/Y$  and plotted against  $b/Y$  in Figure 1, from which the effect of side walls can be estimated. Figure 1 shows, for example, that, for  $b/Y = 25$ , values of  $C$  differ from 6 by less than 5 per cent.

#### EXPERIMENTAL WORK

*Experimental arrangement.* The experimental work presented here was a portion of a research project to determine water surface profiles during spatially variable flow [Woo, 1956].



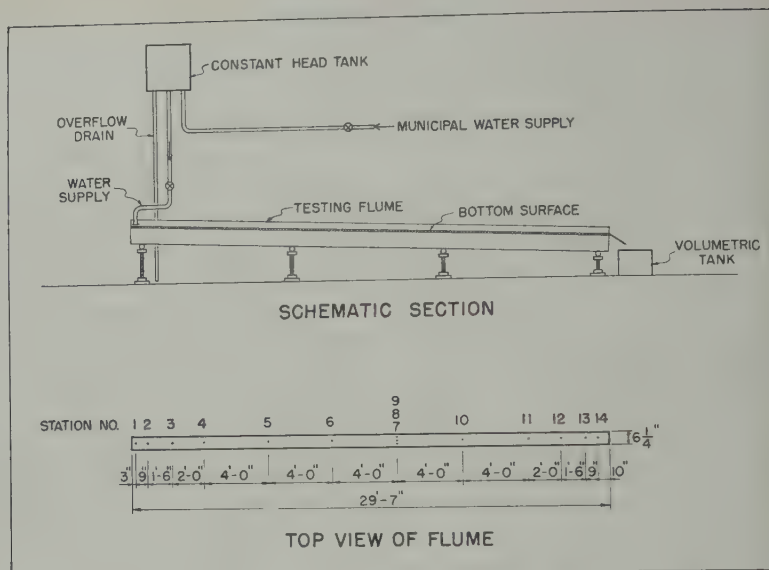


Fig. 2. Experimental arrangement.

The tests were run in a wooden flume 29 feet 7 inches long by  $6\frac{1}{4}$  inches wide. It was supported on a wooden frame which, in turn, rested on four supports of which three were attached to threaded bars for adjusting transverse flatness as well as longitudinal slope. Two bed materials were used to represent rough and very rough surfaces. The former was made of masonite board with the rough side turned up and with a thin coating of floor sealer applied for water-proofing. The latter was formed by gluing sand with an average size of 1 mm (or 0.04 inch) on the masonite surface. The fabrication of this surface closely followed that of the rough pipes in Nikuradse's experimental work in 1933, and the size of sand was also selected within the sizes used by Nikuradse, thus permitting a more direct comparison of the two sets of results.

The water surface profile along the center line of the flume was measured at twelve locations, called stations in this paper, through the holes in the bottom surface (see Fig. 2). They were connected to a manometer board inclined at such an angle that the water depth could be read to 0.005 inch. A 10-gallon volumetric tank was used to measure the discharge from the flume. Eleven slopes were used for each surface; they were 0.001, 0.002, 0.003, 0.004, 0.006, 0.008, 0.010, 0.015, 0.020, 0.040, and 0.060.

*The test procedure.* At the beginning of a

series of tests on a new surface the flume was adjusted to a horizontal position, and the manometers were tested for accuracy. In all cases manometer errors were found to be more than 0.005 inch.

Water was introduced from a constant head tank to the upper end of the flume. The amount of supply was controlled by a gate valve. Usually after the control valve was turned on, an interval of 2 minutes or more for small discharges was required to allow the condition of steady uniform flow to be established. Since the water depths were small and the flume was long, no tail gate was used for creating uniform flow in the flume. Constant water depths were always recorded at the middle section of the flume (stations 6, 8, and 10) for each run. From these the average value was used as the depth of uniform flow. Room and water temperatures were taken for each run.

A relationship given by Goldstein [1938],

$$lv/Y^2 V = 0.16 \quad (1)$$

was used to insure that the boundary layer was fully developed at the beginning of the test section (station 6). Equation 14 may be rearranged to yield the following expression for the ratio of the required distance from the entrance,  $l$ , to the depth in the channel,  $Y$ :

$$l/Y = 0.16N_R \quad (15)$$

assumed to be 1000, then, for the maximum  $l$  used in any of the tests, 0.35 inch,  $l$  would be 56 inches. Because stations were located 130 inches from the entrance, it was concluded that normal flow conditions were established at this location.

**Results.** The results of all tests are presented in Tables 1 and 2. Columns 1 through 4 give test conditions and the measured values, columns 5, 6, and 7 show the computed values of Reynolds number, the friction coefficient, and Manning's  $n$ , respectively. The water depths for the sand surface are the measured depths from the water surface to the average height of the tops of the sand grains plus one-half the average size of the sand grains. A correction (0.01 inch) was added to take into account the voids between sand particles. The friction coefficients  $f_o$  were computed from (9). The  $f_o$  are plotted with respect to  $N_R$  for the smooth surface in Figure 3 and for the rough surface in Figure 4.

Test results which fall within the laminar range for the masonite surface are plotted in Figure 3. However, for the turbulent transition range, plotting was restricted to four selected values of  $S_o$  to make it easier to visualize the data. It may be noted that values in the

laminar range follow a trend roughly parallel to the theoretical line for very wide channels represented by (12), with  $C$  equal to 6. However, it may also be seen from Figure 3 that the experimental values may be quite well represented by a line having a slope of  $-1.0$  and  $C$  equal to 7.7. The deviation from the theoretical value of  $C$  is far more than can be explained by the fact that the channel used in the tests was of finite width (6.25 inches). This conclusion was reached by noting that in columns 3 and 5 of Tables 1 and 2 the largest depth for which flow was laminar was 0.31 inch, which corresponds to a value of  $b/Y$  of 20. Figure 1 shows that the theoretical value of  $C$  for  $b/Y = 20$  is 6.4. Thus, it would be expected that all points would lie to the left of the line  $f_o = 6.4/N_R$  if the only cause for deviation were the channel width.

All test results for the sand surface are plotted in Figure 4. It may be seen that for this rougher surface the values of  $C$  are larger than those for the smooth channel (Fig. 3) and that  $C$  increases with the slope of the channel for slopes greater than 0.003. Again, the points follow trends which can very well be represented by lines parallel to the line  $f_o = C/N_R$ . These lines were drawn in locations which appeared to best represent the trends for various slopes. Values of  $C$  read from the various straight lines shown in Figure 4 are tabulated in Figure 4 and plotted in Figure 5.

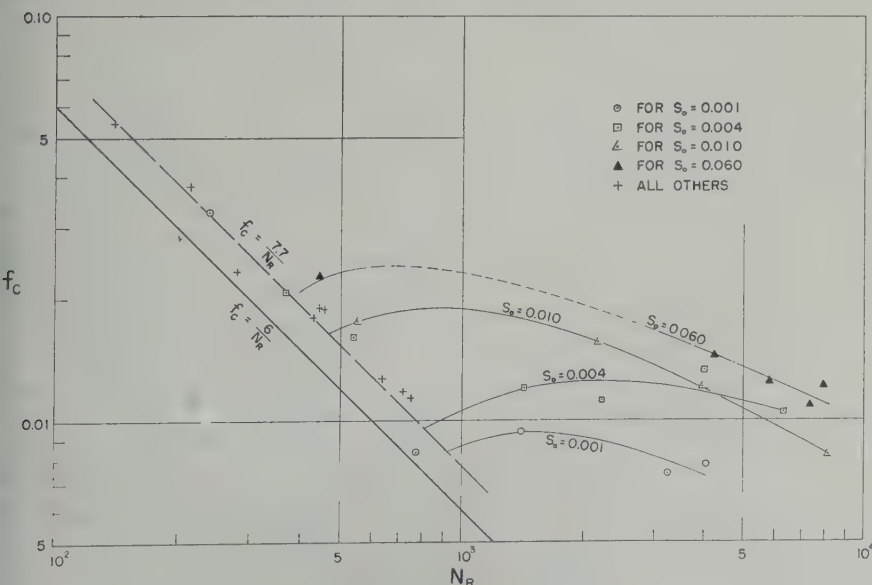


Fig. 3. Test results for masonite surface.

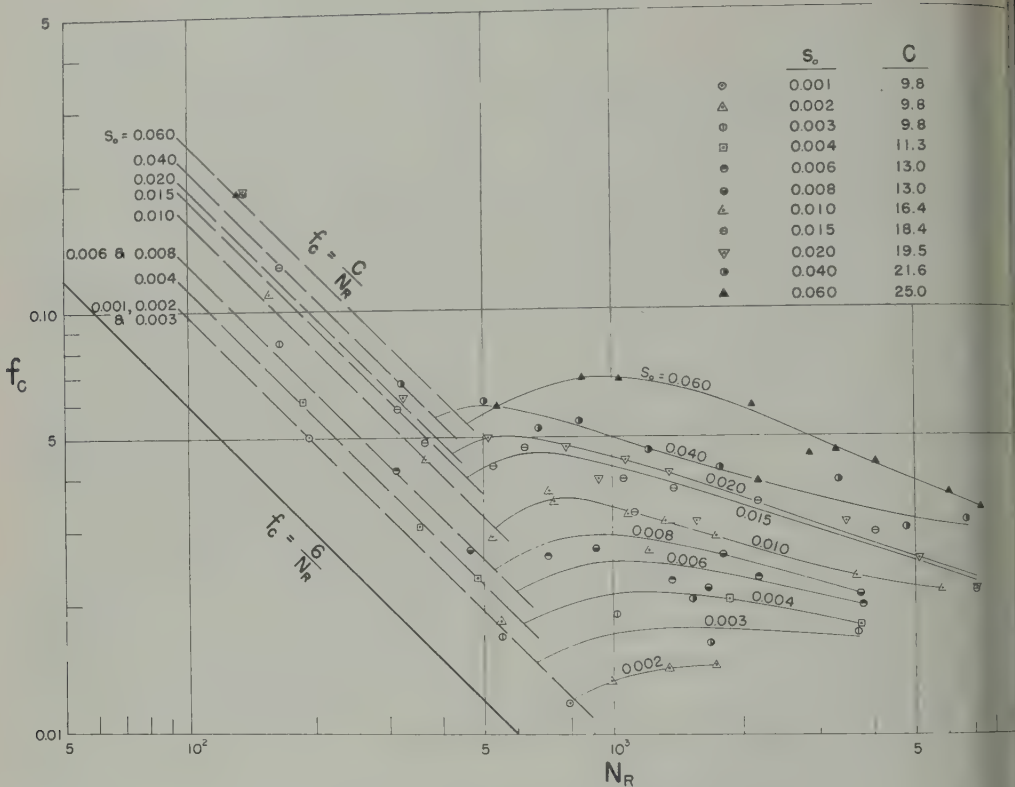


Fig. 4. Test results for sand surface.

For slopes from 0.003 to 0.060 there appears to be an orderly relationship between  $C$  and the slope.

VICKSBURG DATA

It is of interest to determine whether other types of channel surfaces will provide relationships between  $f_c$  and  $N_R$  similar to those reported in this paper. The authors computed  $f_c$

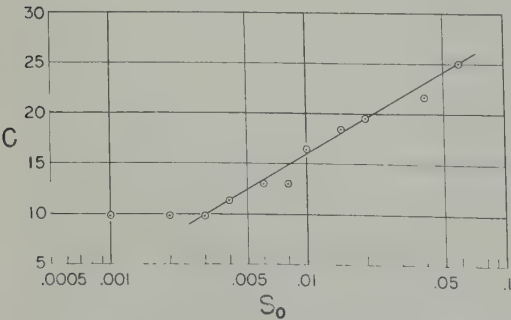


Fig. 5. Variation of  $C$  with bottom slope  $S_0$  for sand surface.

for ten sets of open channel tests reported in *U. S. Waterways Experiment Station Paper* [1935]. These experiments were conducted in flume 40 feet long and 2.313 feet wide. One of tests was run on a 'cement' surface, and the remainder were made with sands varying in average size from 0.0081 to 0.161 inch. The slopes used at Vicksburg varied from 0.0005 to 0.0020 for all the tests except for the coarse sand, in which case slopes up to 0.0045 were used. Because the writers' tests included slopes varying from 0.001 to 0.060, the Vicksburg results provide a comparison for only a small portion of the total range of slopes.

It should be noted that the sand surfaces were movable and that, although there was probably very little movement in the laminar range, the nature of the packed sand surface may have been different from the glued sand surface used by the writers. Values of  $f_c$  and  $N_R$  for cement surface are plotted in Figure 6, and values of  $C$  derived by the authors from Vicksburg data, as well as from their own tests

TABLE 1. Test Results on Masonite Surface

Discharge $q$ , ft <sup>3</sup> /sec/ft	Depth $Y$ , in.	Temp., °C	Reynolds No. $N_R$	Coeff. of Friction $f_c$	Manning's $n$
(2)	(3)	(4)	(5)	(6)	(7)
0.002683	0.185	18.8	239	0.0328	0.0161
.00889	.26	17.5	768	.00829	.0094
.0163	.405	17.4	1403	.00933	.0094
.0374	.645	17.5	3230	.00716	.00848
.0463	.765	17.8	4030	.00776	.00889
.00471	.175	19.2	424	.018	.01195
.01275	.28	17.1	1091	.00981	.00941
.03075	.515	17.3	2640	.0108	.0103
.0457	.66	17.8	3980	.01028	.01015
.07	.87	16.9	5950	.01	.01015
.001538	.105	19.0	138	.0547	.02
.00748	.185	17.0	638	.01265	.0101
.01495	.30	17.1	1280	.01353	.01095
.0464	.555	17.4	4000	.00888	.00939
.0733	.805	16.9	6240	.01086	.01054
.0042	.135	18.1	368	.0208	.01255
.00627	.165	17.3	539	.01705	.01162
.01653	.28	17.4	1425	.012	.0126
.02607	.37	16.9	2220	.01113	.01015
.0469	.58	17.0	4000	.01323	.01147
.0746	.73	16.7	6320	.01042	.0103
.003096	.10	19.0	277	.02335	.01305
.0084	.155	16.9	715	.01178	.00961
.02356	.34	16.6	1990	.0159	.01205
.0482	.545	17.2	4130	.0156	.01242
.0761	.685	16.5	6410	.0124	.0112
.00238	.09	18.9	213	.0383	.0167
.01123	.205	16.8	953	.0204	.01293
.0472	.465	17.2	4050	.01345	.0114
.0668	.585	16.7	5660	.0134	.01153
.0883	.69	16.8	7500	.0126	.01128
.00266	.10	17.3	229	.0527	.0196
.00643	.125	17.1	551	.0176	.01015
.02545	.30	17.0	2170	.01555	.01176
.0461	.41	17.1	3950	.01207	.01072
.0923	.57	18.0	8075	.0081	.00896
.002323	.065	17.6	201	.0284	.01312
.00865	.115	17.3	744	.01136	.00906
.01994	.19	17.1	1705	.00966	.00877
.0471	.34	16.9	4010	.00991	.00954
.0936	.50	17.2	8030	.00797	.0088
.00536	.09	17.1	459	.0189	.0117
.015	.155	17.2	1285	.01235	.00984
.02825	.215	17.3	2430	.00928	.00879
.0471	.315	17.5	4075	.0105	.00969
.099	.47	17.5	8550	.00792	.00875
.00521	.07	16.7	441	.019	.011
.04515	.245	16.5	3805	.01075	.00954
.05395	.295	16.3	4520	.01315	.0108
.0805	.36	16.5	6775	.01078	.00998
.00519	.065	17.2	445	.0228	.01175
.0492	.25	17.1	4215	.0144	.01105
.068	.295	17.0	5800	.01245	.0105
.0861	.33	17.1	7380	.01083	.01088
.09275	.36	17.4	7980	.01215	.0106



are given in Table 3. The values of  $C$  shown in the table were determined by selecting a straight line having the slope ( $-1.0$ ) which provided the best fit for the points in the laminar range, as

illustrated in Figures 3, 4, and 6. It may be noted from the table and the figure that the values of  $C$  and the behavior of the plot at points are much the same for the cement surfa

TABLE 2. Test Results on Sand Surface

Slope $S_0$	Discharge $q$ , ft <sup>3</sup> /sec/ft	Depth $Y$ , in.	Temp., °C	Reynolds No. $N_R$	Coeff. of Friction $f_c$	Manning's $n$
(1)	(2)	(3)	(4)	(5)	(6)	(7)
0.001	0.000786	0.145	16.5	66	0.184	0.037
	.002345	.195	16.0	195	.0502	.02
	.0097	.31	15.2	789	.0118	.0103
0.002	.00614	.21	18.8	547	.0183	.01215
	.01198	.295	15.8	992	.0133	.01085
	.0166	.375	14.8	1340	.01425	.0145
	.02165	.45	14.4	1730	.0145	.0118
0.003	.002017	.145	15.6	166	.084	.025
	.00673	.19	15.5	553	.0169	.0115
	.0126	.30	15.1	1025	.01905	.013
	.02097	.40	14.7	1687	.0163	.01235
	.04655	.695	14.2	3695	.01735	.01325
0.004	.002323	.13	15.0	188	.0608	.0208
	.00446	.16	14.2	354	.0308	.0153
	.00611	.18	13.9	482	.0233	.0135
	.02397	.43	13.6	1870	.0207	.01405
	.0477	.65	13.5	3720	.018	.0135
0.006	.003834	.14	15.0	311	.0418	.01755
	.0089	.21	14.2	707	.0262	.0145
	.01747	.315	14.1	1384	.023	.01435
	.02756	.43	13.9	2188	.0234	.01495
	.0485	.595	13.7	3795	.0201	.01415
0.008	.0058	.145	14.9	469	.027	.01415
	.0115	.23	14.4	919	.0274	.01505
	.02106	.32	14.1	1670	.022	.0141
	.02295	.36	14.0	1811	.0264	.0156
	.0481	.55	13.7	3768	.0214	.0146
0.010	.00213	.11	11.4	157	.1095	.0269
	.00506	.145	10.9	367	.0445	.0182
	.00724	.16	10.7	523	.0291	.0149
	.00997	.215	10.6	718	.0374	.01735
	.00921	.20	14.2	732	.0351	.01675
	.01492	.27	10.7	1080	.0329	.0168
	.01558	.26	13.7	1221	.027	.0151
	.01825	.305	11.0	1330	.0318	.01675
	.0224	.34	13.4	1740	.0292	.0164
	.0472	.52	13.3	3664	.0235	.0152
0.015	.0741	.685	13.8	5820	.0218	.0149
	.002256	.105	11.6	167	.1275	.0287
	.00433	.125	11.1	316	.0582	.0203
	.00445	.12	16.6	367	.0488	.01825
	.00731	.16	10.8	530	.0429	.01805
	.00868	.185	10.6	626	.047	.0192
	.01483	.25	10.6	1070	.0398	.01835
	.01437	.23	13.8	1130	.033	.0165
	.01904	.29	11.1	1393	.0376	.0182
	.02665	.355	13.5	2178	.0352	.018
	.0521	.525	13.6	4075	.0298	.01715
	.0921	.69	13.1	7100	.0217	.01485

TABLE 2. (Continued)

Discharge $q$ , ft <sup>3</sup> /sec/ft	Depth $Y$ , in.	Temp., °C	Reynolds No. $N_R$	Coeff. of Friction $f_e$	Manning's $n$
(2)	(3)	(4)	(5)	(6)	(7)
.001824	.095	11.8	136	.193	.0344
.004275	.115	11.2	313	.062	.0204
.0071	.15	10.9	516	.05	.01945
.0108	.195	10.9	785	.0475	.0194
.01177	.195	13.9	928	.04	.0178
.01477	.235	11.0	1076	.0443	.01925
.01835	.265	11.6	1360	.0412	.01865
.02033	.26	13.1	1570	.0317	.0164
.0456	.445	12.8	3490	.0316	.0174
.0668	.535	12.8	5110	.0256	.0166
.0948	.64	12.3	7160	.0217	.0148
.001812	.075	12.1	136	.1915	.0334
.00437	.095	11.3	321	.0671	.0203
.0069	.125	11.0	503	.0611	.0208
.0093	.145	10.9	676	.0527	.0198
.01158	.17	10.8	840	.0547	.0205
.01666	.205	11.1	1220	.0464	.01925
.0197	.175	13.4	1530	.0207	.0127
.0235	.25	12.4	1780	.0422	.0189
.04425	.36	12.3	3340	.0356	.0181
.0635	.435	12.3	4800	.0305	.017
.0895	.555	11.9	6690	.0318	.01775
.001795	.065	10.9	131	.1905	.0366
.00759	.115	10.0	538	.0592	.0199
.01208	.165	10.0	857	.0689	.0288
.01618	.20	10.0	1048	.0683	.0234
.0296	.285	10.2	2110	.0592	.0226
.02808	.24	13.1	2165	.0392	.0182
.03924	.315	11.2	2880	.0455	.0202
.0437	.34	12.3	3300	.0461	.0205
.05435	.385	12.1	4080	.0432	.02
.0808	.475	11.8	6020	.0368	.0189
.0991	.53	11.8	7380	.0339	.0183

as for the masonite surface tested by  
ors (Fig. 3).

nce to Table 3 shows that the finest  
d as a very smooth surface having a  $C$   
6.0, whereas the values of  $C$  for the  
sand surfaces were larger than 6.0, the  
values of  $C$  being obtained from the  
surface. The values of  $C$  for the in-  
e sands were of the same order of  
e as those determined by the authors  
masonite and glued sand surfaces for the  
es.

thors' tests on the glued sand surface  
ery little relation between  $C$  and slope  
as small as those used at Vicksburg  
Therefore, it may be surmised that  
large but haphazard variations of  $C$

shown in Table 2 for the intermediate and  
coarse sands were caused to some extent by  
movement or rearrangement of the sand.

#### DISCUSSION OF EXPERIMENTAL RESULTS

*Comparison of measured and theoretical values of  $f_e$ .* The experimental results will be discussed separately for three categories of roughness—smooth, rough, and very rough. These categories are defined in terms of the surfaces which were tested. Although distinctive differences have been observed for these three categories, it is very likely that future research will disclose other variations or borderline situations.

Smooth surfaces. Although the authors have not experimented with smooth surfaces, results obtained by other investigators indicate that the



laminar open-channel flow can be defined by the value of  $N_R$  at which the relation between  $f_0$  and  $N_R$  starts to deviate from  $C/N_R$ . Figures 4 and 5 indicate that the value of  $N_R$  is not a constant but changes from  $N_R = 400$  to 900. The test results indicate that it varies inversely with the roughness seemed to have no consistent results. The authors' tests gave a range of critical  $N_R$  from 400 to 900 for the masonite surface and 400 to 900 for the sand surface. The Vicksburg tests show that this point varies from  $N_R = 400$  to 900. Other reported values vary from 400 to 900. For larger values of  $N_R$  flow is in a range in which it is quite common. As values of  $f_0$  increase as  $N_R$  increases. For values of  $N_R$  greater than those in the transition range, flow becomes fully turbulent and the reduction of  $f_0$  values begins. The upper limit of the transition range is not clearly defined. It is not unusual for  $N_R$  at this point to change its value at the end of the laminar

## CONCLUSION

Experimental results are presented which will be useful in determining the characteristics of flow in thin sheets over rough surfaces. The results showed that values of the friction factor  $f_0$  are determined from the relationship  $f_0 = C/N_R$  at that  $C$  is larger than the theoretical value of  $C$  which applies to smooth surfaces. For rough surfaces (sand) the magnitude of  $C$  is determined by the slope. The range of critical Reynolds number, at which flow ceases to be laminar, varied from 400 to 900. This indicates that there is a need for additional experimentation with other forms of roughness.

## REFERENCES

- Streamline and turbulent flow in open channels, *Phil. Mag.*, 7th Series, 17, 1081-1112, 1934.
- and N. D. Grunberg, The resistance to flow of water along smooth rectangular passages and the effect of a slight convergence or divergence of the boundaries, *Phil. Mag.*, 7th Series, 23, 490-503, March 1937.
- de Saint Venant, M. J., Mémoire sur l'influence des rugosités dans les mouvements réguliers des fluides, *J. Math., pures et appl.*, Série II, XIII, 1868.
- and T. J. T., *Open-Channel Hydraulics*, McGraw-Hill Book Co., New York, 7-14, 1959.
- Cornish, R. J., Flow in a pipe of rectangular cross-section, *Proc. Roy. Soc. London A*, 120, 691-700, 1928.
- Davis, S. J., and C. M. White, An experimental study of the flow of water in pipes of rectangular section, *Proc. Roy. Soc. London A*, 119, 92-107, 1928.
- Freeman, J. R., *Flow of Water in Pipes and Pipe Fittings*, American Society of Mechanical Engineers, New York, 1941.
- Goldstein, S., *Modern Developments in Fluid Dynamics*, Vol. I, Clarendon Press, London, England, 309-310, 1938.
- Hopf, L., Turbulenz bei einem flusse, *Ann. Physik*, 337, Vierte Folge, 32, 777-808, 1910.
- Horton, R. E., H. R. Leach, and R. Van Vliet, Laminar sheet flow, *Trans. Am. Geophys. Union*, Part II, 393-404, 1934.
- Jeffreys, H., The flow of water in an inclined channel of rectangular section, *Phil. Mag.*, 6th Series, 49, 293, 793-807, 1925.
- Nikuradse, J., Stromungsgesetze in rauen Rohren, *VDI-Forschungsh. Beil. Forsch. Gebiete Ingenieurw.* Ausgabe B Band 4, July/August 1933. (English translation, *Tech. Mem. 1292*, National Advisory Committee for Aeronautics, Washington, 1950).
- Owen, W. M., Laminar to turbulent flow in a wide open channel, *Trans. Am. Soc. Civil Engrs.*, 119, 1157-1164, 1954.
- Parsons, D. A., Depths of overland flow, *SCS-TP-82*, Soil Conservation Service Research, U. S. Department of Agriculture, July 1949.
- Schiller, L., *Wein-Harms: Handbuch der Experimentalphysik*, IV, 4 Teil—Hydro- und Aerodynamik, Akademische Verlagsgesellschaft M.B.H., Leipzig, 138-154, 1932.
- Stanton, T. E., and J. R. Pannell, Similarity of motion in relation to the surface friction of fluids, *Phil. Trans., Roy. Soc. London A*, 214, 199-224, 1914.
- Straub, L. G., Studies of the transition-region between laminar and turbulent flow in open channels, *Trans. Am. Geophys. Union*, 20, part IV, 649-653, 1939.
- Straub, L. G., E. Silberman, and H. C. Nelson, Open-channel flow at small Reynolds' numbers, *Trans. Am. Soc. Civil Engrs.*, 123, 685-714, 1958.
- U. S. Waterways Experiment Station paper 17, Studies of river bed materials and their movement, with special reference to the lower Mississippi River, Vicksburg, Mississippi, January 1935.
- Wisler, C. O., and E. F. Brater, *Hydrology*, 2nd ed., John Wiley & Sons, New York, 240-245, 1959.
- Woo, D. C., Study of overland flow, an unpublished dissertation for Ph.D. submitted to University of Michigan, Ann Arbor, Michigan, January 1956.

(Manuscript received April 14, 1961;  
revised September 5, 1961.)





# A Partial Duration Series for Low-Flow Analyses

JOHN B. STALL AND JAMES C. NEILL

*Illinois State Water Survey Division  
Urbana, Illinois*

**Abstract.** A partial series of low-flow events is described which is particularly useful in the design of an impounding reservoir in Illinois. An important feature of this series is the introduction of the duration of the low flow as a parameter. A number of low-flow series are developed for durations varying from 1 month to 60 months. As compared with the more easily interpreted annual series, one of the principal advantages of this partial series is its suitability to use with low-flow periods longer than 12 months. A recurrence interval is assigned to each low flow in the series, and coordinates are presented for its representation. The flow in terms of runoff from the watershed expressed in inches is plotted on a logarithmic scale versus the recurrence interval for the extreme-value law.

## REQUIREMENTS FOR IMPOUNDING RESERVOIR DESIGN

The low-flow series described in this paper was devised to aid in the hydrologic design of a water supply impounding reservoir and is based on a pending publication, 'Low Flows of Streams for Impounding Reservoir Design'. Since the critical period for reservoir design may exceed 1 year, it was required that the low-flow series distribution be applicable to periods longer than 12 months. Such a series was developed by utilizing a rational approach to provide the information needed. The following factors are important: (1) duration of low flow; (2) magnitude of low flow; (3) frequency of low

**Selection of low flow.** The length or duration of the critical period for a reservoir is a function of the relative magnitudes of (a) the draft rate from the reservoir and (b) the rate of runoff from the drainage area feeding the reservoir. Experience has indicated that in Illinois, during severe droughts, the duration of the critical period during which the draft rate from the reservoir exceeds the rate of inflow may be from 12 to 48 months. However, it is desirable to have knowledge of the low-flow probability for a wide range of durations in order that the critical duration can be found for each design. In the current study, low-flow series have been derived for durations from 1 month to 60 months. Assigning various values to the duration in this manner makes it possible to

evaluate the influence of the duration in the reservoir design.

**Magnitude and frequency.** The other factors involved in the design of an impounding reservoir are the magnitude of the low flow and the frequency of occurrence. The next two sections of this paper discuss the generation of the low-flow series and the determination of the corresponding recurrence intervals. With this information, the reservoir can readily be designed by methods similar to the traditional mass curve analysis. The actual reservoir design procedure is not included in this paper, but it can readily be carried out provided the proper low-flow data are available.

## SELECTION OF THE SERIES

**Data.** The flow data analyzed in this example were obtained from a stream-gaging station located on the Sangamon River at Monticello, Illinois. The drainage area is 550 square miles. A 45-year continuous record from October 1914 through September 1959 was available. These data have been published by the *U. S. Geological Survey* [1961]. Runoff information expressed as inches of runoff from the drainage area during each month of the record served as basic data.

A separate series of low-flow events was derived for each of 36 different time periods or durations. These durations were multiples of 1 month from 1 through 12 months and multiples of 2 months from 14 through 60 months. Thus, the duration of the low-flow period was a pa-

TABLE 1. Thirty-Month Low-Flow Series for Sangamon River at Monticello

Runoff in inches for the ten driest 30-month periods on record based on 45-year flow record for water years 1915-1959. (Mean flow for this period = 0.31 inches per month or 24.30 inches in 30 months)

Rank of Event	30-Month Flow, Inches	Dates Low-Flow Period Occurred			
		Beginning Month	Year	Ending Month	Year
1	6.43	Aug.	1952	Jan.	1955
2	6.63	June	1930	Nov.	1932
3	11.72	Apr.	1939	Sept.	1941
4	13.95	July	1933	Dec.	1935
5	14.40	June	1916	Nov.	1918
6	17.41	May	1919	Oct.	1921
7	18.07	June	1955	Nov.	1957
8	18.64	July	1944	Dec.	1946
9	21.43	June	1947	Nov.	1949
10	23.62	July	1936	Dec.	1938

parameter because it was assigned each of these 36 values. Using the same basic data, similar low-flow series were developed for each of the 36 durations.

As an example, the selection of the low-flow series for a duration of 30 months will be described. A duration of this length was chosen in order to illustrate the suitability of the series for durations longer than 12 months.

*Selection procedure.* The basic monthly flow data were converted to running totals for the duration under consideration. In this case the 30-month running totals were computed for the 45-year period of record. These 511 running totals were then inspected and the lowest 30-month flow was selected. It was found for the Sangamon River at Monticello that the lowest 30-month flow was 6.43 inches and that it occurred from August 1952 through January 1955.

After the lowest ranking flow value for a 30-month period had been selected, all the remaining running totals which included any of the 30 months included in this lowest total were excluded from further consideration. This procedure voided 29 running totals preceding the one selected and 29 running totals following the one selected. The remaining 30-month totals were inspected to locate the second most severe 30-month low-flow period. This was found to be the 30 months from June 1930 through November

1932, during which the total runoff was 6.43 inches. This period was similarly excluded from further consideration. In like manner, the fourth, fifth, and successive low flows from record were selected. The process was continued until (1) the number of periods selected was approximately equal to one-half of the years of record, (2) all data were eliminated, (3) the selected flow value was greater than the mean. In this example, only 10 low flows were selected, as is explained below. This series of flows is presented in Table 1.

Figure 1 is an illustration of the magnitude of each event in this low-flow series and the period of occurrence of each event. In this figure the horizontal scale denotes the 45-year period from October 1914 through September 1959 for which the flow record was available. The first selected low flow of 6.43 inches is shown in Figure 1 for the period August 1952 through January 1955. It is labeled (1) because it is the lowest-ranking 30-month low-flow event found at this gaging station. The remaining events in the series are shown similarly. Figure 1 illustrates an important feature: the selection procedure does not permit the individual events in the series to overlap in time.

*Termination of the series.* Every series is terminated when the selected flow for the duration in question reached an amount equal to the mean flow. This is illustrated in Table 1, and the series of 30-month low flows as devised by the method described are also listed. Only 10 values appear in this series, the highest one showing a flow of 23.62 inches in 30 months. It was found that the eleventh value was 25.38 inches, which exceeded the mean 30-month flow of 24.30 inches at the gaging station.

#### RECURRENCE INTERVAL

The recurrence interval is the average length of time between exceedances of an extreme event of selected severity. This recurrence interval is computed as follows:

$$R = T/m$$

where

$R$  = recurrence interval in years.

$T$  = number of years of data available.

$m$  = rank of the event, rank 1 being the most extreme (in this case the rank 1 event was the lowest flow).

SANGAMON RIVER AT MONTICELLO  
30-MONTH LOW FLOW EXCEEDANCES

RANK SHOWN THUS: (7)

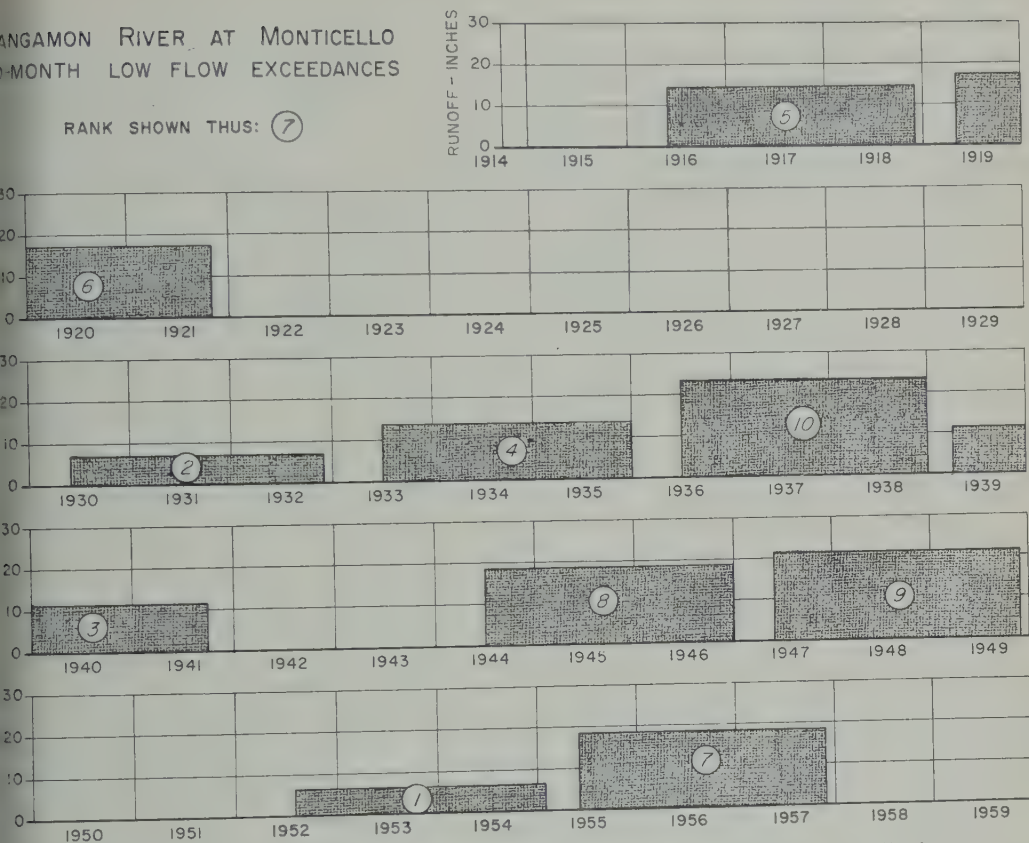


Fig. 1. The 30-month low-flow exceedances, Sangamon River at Monticello, Illinois.

The use of this equation for computing the recurrence interval of a series of annual exceedances has been described by *Hudson and Roberts* [1955], by *Chow* [1953], and by *Gumbel and von Schelling* [1950].

According to this equation, the most extreme event is expected to occur once in 45 years and is therefore assigned a recurrence interval of 45 years. The second ranked event is expected to occur twice in 45 years and is assigned a recurrence interval of 22.5 years. Succeeding computations are made in like manner.

## CHARACTERISTICS OF THE SERIES

**Partial nature.** The ten low-flow events presented in Table 1 form an example of the basic series utilized in this study. Since we are interested in low flows only, the mean flow at the station was selected as the base or upper limit. The resulting series is partial; only events below a particular base are retained in the series.

The 45-year period of data contains a total of 540 months. During this 540-month period, 18 consecutive periods of 30 months each could occur. The ten 30-month periods included in this series thus represent 300 months of the total 540 months of basic data or ten of a possible eighteen 30-month periods. The resulting series contains more than half of the basic data in this case. In this sense it contains considerably more of the basic data than is included in a partial series in its normal connotation.

**Annual series versus partial series.** Several writers have discussed the differences between the annual series and the partial series of exceedances. These writers include *Chow* [1953] and *Langbein* [1949]. As described by Chow, a series of annual extreme events is usually obtained by selecting the single most extreme event which occurred during each year of record. The number of extreme events is equal to the number of years of record. Another series, partial in



nature, can be devised as follows: the total number of events which occurred during the entire period of record are ranked without regard to the year in which they occurred and the top-ranking values are selected. The number included in such a series is equal to the number of years of record. These events are labeled 'annual exceedances.'

The extreme events which make up this latter partial series of exceedances are selected in such a manner that more than one may occur in one year. Some years may not be represented at all. Two extreme events occurring during the same year are included in the exceedance series, but the lesser one is excluded from the annual series for the reason that the two events may be dependent.

In interpreting these two events it can be said that the combination of the many climatic and physical factors which caused the event of primary severity may have influenced the event of secondary severity in the same year.

It is important to note that the combination of factors which produces an extreme event and the associated probability of occurrence are governed very strongly by their being a part of the 12-month solar cycle. It is the established strength of this cycle which justifies the difference in interpretation between a series of annual extremes and a partial series of exceedances. The presence of this cycle justifies the exclusion of secondary events from the annual series and is the underlying factor in the conception that these events are dependent.

*Independence.* In the above discussion the important differences between a series of annual maximum events and a partial series of exceedances are briefly reviewed. It helps in the proper interpretation of the events included in the series presented in this study. Consider, for example, the ten 30-month low-flow events shown in Table 1. The selection procedure insures that the events are independent chronologically. If two of these events were to be considered dependent in any other sense, it would be necessary to show that two 30-month events were the result of at least a portion of the same combination of causative climatic factors. In this exceedance series, the dependence of a secondary 30-month low-flow event on a more extreme 30-month low-flow event could be caused by the presence of a multi-year cycle in the causative

climatic factors. Although multi-year cycles have been shown by various authors to exist to some degree, the magnitude of these cycles is not as pronounced as that of the 12-month solar cycle. Consequently, current evidence of multi-year cycles is hardly justification for assuming that any particular 30-month low-flow event could be associated with the same factors which produced another 30-month low-flow event.

In the selection of the ten 30-month periods to form the partial series as devised in this study, no constraint is put on the selection procedure because of the strength of the 12-month cycle. Even if two 30-month periods were adjacent and continuous in time, each 30-month period spans  $2\frac{1}{2}$  solar cycles. The presence of the solar cycle is therefore not likely to cause any important degree of dependence between the two events.

In this series there is no strong tendency for extreme events to be clustered together at any one period of years. This is illustrated in Figure 1 for the 30-month series and was also found to be true generally for other durations. However, this tendency is not completely absent, and for durations less than 6 months the tendency is noticeable. Figure 2 shows the series of 6-month low-flow events. For this series, two of the 6-month low-flow events occurred in direct time sequence on one occasion in the 22 values. These were the first and twentieth ranked values. In this case the occurrence in direct time sequence is considered to exert only a negligible effect on the series.

*Recurrence of events.* The group of ten 30-month flows shown in Table 1 and their assigned recurrence intervals furnished an estimate of the average length of time in years that can be expected to elapse between the beginnings of the various 30-month events. For example, the third ranking event in this series has a recurrence interval of 15 years. On the basis of the past 4 years, it can be said that the probability is 1 in 15 that we will enter sometime this year a 30-month period during which the total flow will be as low as 11.72 inches. According to Table 1 the 30-month low-flow periods began during the months from April to August. The above probability applies to the extreme 30-month low-flow event regardless in which month of the year begins. Moreover, one of the principal features of the use of the partial series of low-flow events

# MON RIVER AT MONTICELLO TH LOW FLOW EXCEEDANCES

RANK SHOWN THUS: (7)

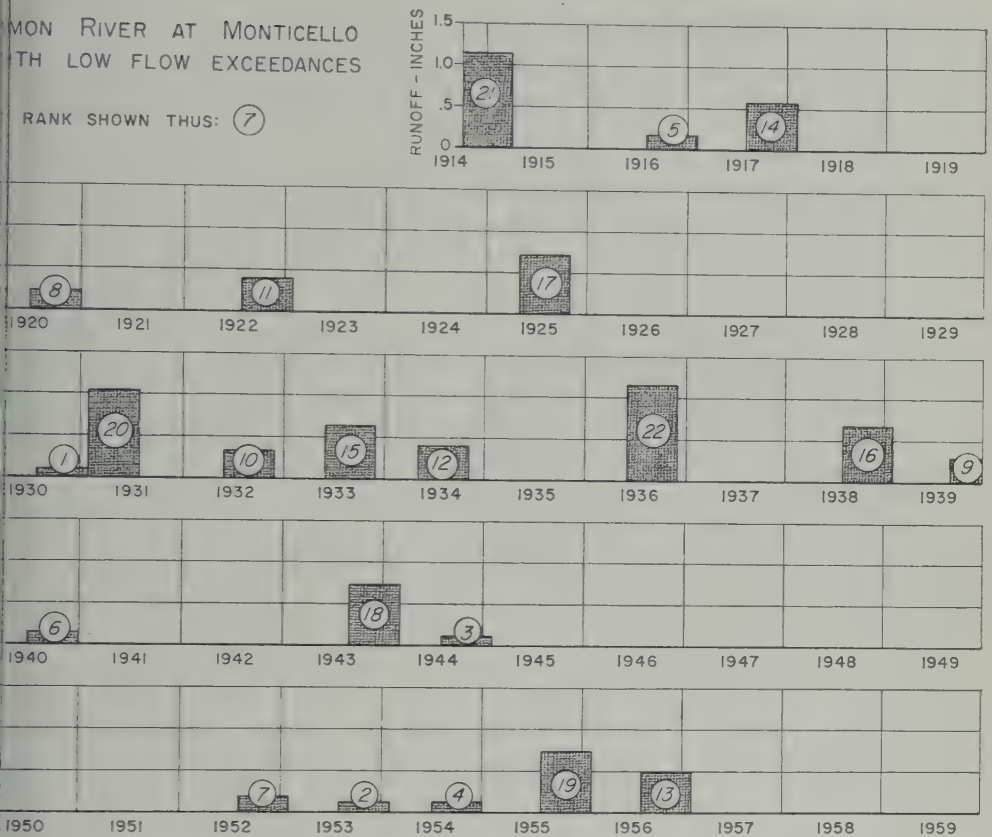


Fig. 2. The 6-month low-flow exceedances, Sangamon River at Monticello, Illinois.

the selection procedure puts no restraint beginning or ending time of the event.

## GRAPHICAL REPRESENTATION

After considerable experimentation of coordinates was found which seemed to portray the family nature of the series in this study. In these plots the ordinate is logarithmic and the abscissa follows the value law. Figure 3 shows a plot of a series of the type derived in this study for the Sangamon River at Monticello. Series shown in solid lines are for durations of 6 to 60 months at duration intervals of 6 months; the dashed lines show the same series for durations of 4 months.

It should be noted that the horizontal scale in Figure 3 shows the recurrence interval in years. As a result of the selection procedure, the recurrence interval was longer than 2 years, and for the series shown on the horizontal scale in Figure 3 between 2 and 6 years.

The use of this particular set of coordinates for the representation of low flows is not new. These coordinates have been used by Hudson and Roberts [1955], by Gumbel [1958], and by Velz and Gannon [1960] to show the shape of low-flow curves.

## CONCLUSIONS

1. A basic series of low-flow events has been derived. This series is particularly appropriate for use in the design of an impounding reservoir in Illinois.

2. The duration of each low-flow event in the series is considered a parameter in that a separate series is derived for low-flow periods having various selected durations.

3. The resulting series furnishes meaningful results for low-flow durations longer than 12 months; in this case the duration has been extended as far as 60 months.

4. The resulting series is free of any major constraint due to the presence of the annual

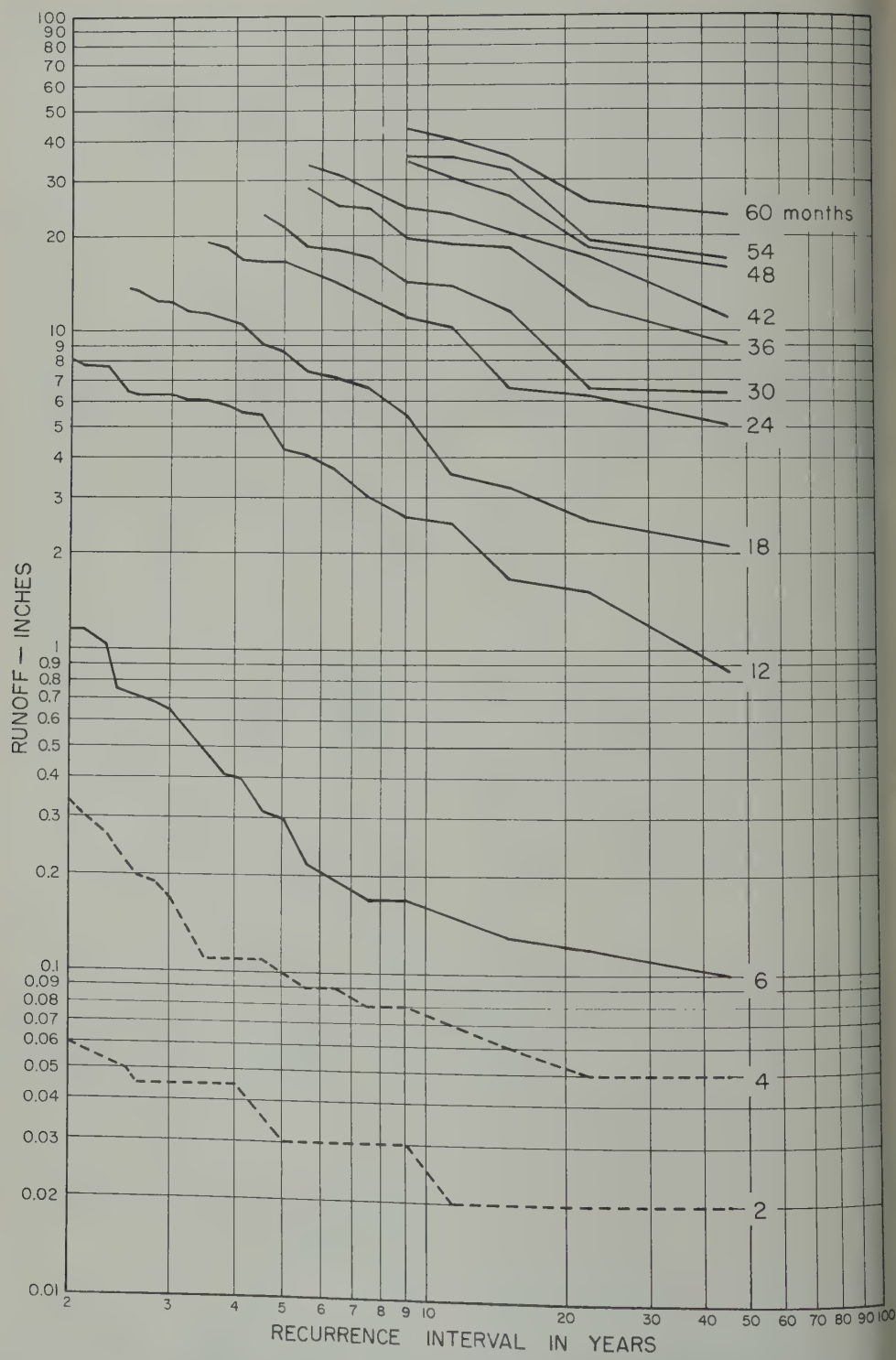


Fig. 3. Low-flow series, Sangamon River at Monticello, Illinois, for durations of 2 to 60 months.

le. It is subject only to a very minor at due to a multi-year cycle. The strength multi-year cycle is so weak in comparison strength of the annual cycle that the re considered to be independent of any ar cycle.

e events in this series are considered to endent to the extent that each is the re- e separate combination of the complex e climatic and physical factors which ream flow.

e events in this series are considered to esult of so many causative factors that urrence is distributed in accord with the chance. The events are thus randomly ed. No significant departure from this ion was noted except in the case of du- of less than 6 months.

e recurrence interval assigned to each this series is considered to be the aver- interval between occurrences of similar Because of their random distribution it ed that future events can be expected to hese average recurrence intervals.

nowledgments. The work described in this as carried out by the authors as a part of gular work at the Illinois State Water

Survey, under the guidance of William C. Ackermann, Chief, and H. F. Smith, Head of the Engineering Section. The low-flow series were developed utilizing the University of Illinois digital computer, the Illiac, programmed by Dr. Neill.

#### REFERENCES

- Chow, Ven Te, Frequency analyses of hydrologic data with special application to rainfall intensities, *Univ. Illinois Eng. Exp. Sta. Bull.* 414, 1953.
- Gumbel, E. J., *Statistics of Extremes*, Columbia University Press, New York, p. 301, 1958.
- Gumbel, E. J., and H. von Schelling, The distribution of the number of exceedances, *Ann. Math. Statistics*, 21(2), 247-262, 1950.
- Hudson, H. E., Jr., and W. J. Roberts, 1952-55 Illinois drouth with special reference to impounding reservoir design, *Illinois State Water Survey Bull.* 43, 1955.
- Langbein, W. B., Annual floods and the partial-duration flood series, *Trans. Am. Geophys. Union*, 30(6), 879-881, 1949.
- U. S. Geological Survey, Surface water supply of the United States 1959, 5, Hudson Bay and upper Mississippi River basins, *Water Supply Paper 1628* (and others in this series) Washington, D. C., 1961.
- Velz, C. J., and J. J. Gannon, *Drought Flow Characteristics of Michigan Streams*, Water Resources Commission, State of Michigan, Lansing, 1960.

(Manuscript received May 31, 1961;  
revised September 27, 1961.)





## Local Scour in Rivers

L. J. TISON

*Department of Hydraulics and Fluid Mechanics, University of Ghent  
Braamstraat 61, Gentbrugge, Belgium*

**Abstract.** It has been found that the scour in rivers is influenced not only by water velocities but also by the curvature of streamlines. An obstacle with an arbitrary shape placed in a stream produces curvatures, which are the origin of a scour and which have an intensity expressed in terms of the velocity at the surface, the velocity in the neighborhood of the bottom, and the radius of curvature of the streamline. Integrals are taken along a line tangent to each point to the principal normal of the streamlines. Some applications of the relationship are presented.

**Development of sediment near piers.** An obstacle as a pier with an arbitrary shape, placed in a stream parallel to the bottom, produces (1) a first curvature with a center  $O_1$  and radius  $\rho_1$ , followed by a second curvature  $O_2$ , in the neighborhood of the bank of the river, which exerts no action on the direction of the streamlines. In the region of the first curvature, such as  $AB$ , tangent at each point to the principal normals of the streamlines in the neighborhood of the surface, leads to the rela-

$$z + \frac{p_B}{\gamma} + \frac{1}{g} \int_A^B \frac{v^2}{\rho_1} ds = z_A + \frac{p_A}{\gamma} \quad (1)$$

where  $z$  is the vertical height,  $p$  is the pressure,  $v$  the velocity, and  $\gamma$  is the specific weight of the fluid.

In the neighborhood of the bottom another relationship of the same nature gives

$$\frac{p_{B'}}{\gamma} + \frac{1}{g} \int_{A'}^{B'} \frac{v'^2}{\rho_1} ds = z_{A'} + \frac{p_{A'}}{\gamma} \quad (2)$$

where  $B$  and  $B'$  are on the same line, perpendicular to the bottom, and  $v'$  is the velocity near the bottom. The variation of the pressure between  $B$  and  $B'$  follows the hydrostatic law, so

$$z_B + \frac{p_B}{\gamma} = z_{B'} + \frac{p_{B'}}{\gamma} \quad (3)$$

From these three relationships

$$\begin{aligned} & \frac{p_A}{\gamma} - \left( z_{A'} + \frac{p_{A'}}{\gamma} \right) \\ &= \frac{1}{g} \left[ \int_A^B \frac{v^2}{\rho_1} ds - \int_{A'}^{B'} \frac{v'^2}{\rho_1} ds \right] \quad (4) \end{aligned}$$

greater than  $v'$ .

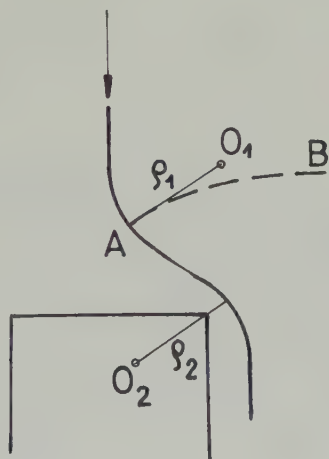


FIG.1

An immediate consequence of (4) is that the motion cannot be parallel to the bottom; the trajectories must dive. Diving motion will have as another consequence a local attack on the bottom near the influence of the first curvature,  $O_1$ ,  $\rho_1$ .

Evidently, the importance of scour depends upon the value of the vertical component of the diving motion, and this component depends upon the value of the second term of (4). For example, small values of  $\rho_1$  will increase the second term and therefore the depth of scour.

Experiments in a laboratory with different models of piers having the same lengths, discharges, and heights gave a confirmation of this result. Rectangular piers (with reduced values of  $\rho_1$ ) produced a scour of 113 mm with a discharge of 30 liters per second in a flume with a breadth of 70 cm and a water depth of 10.5 cm.

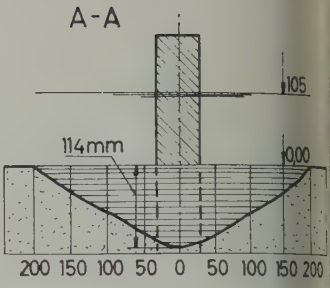
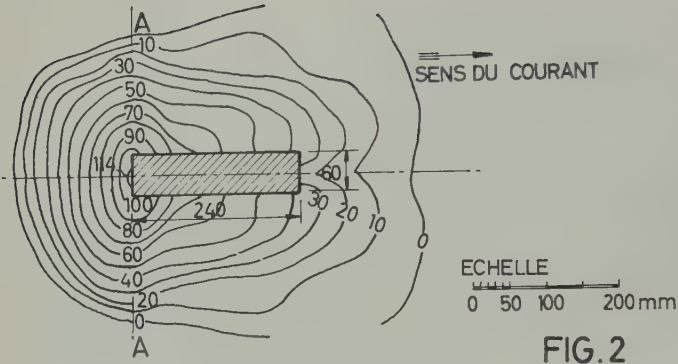


FIG.2

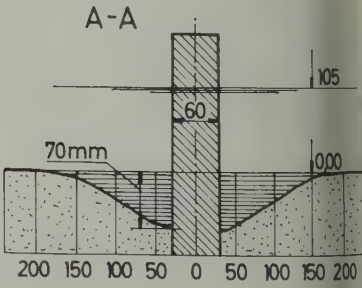
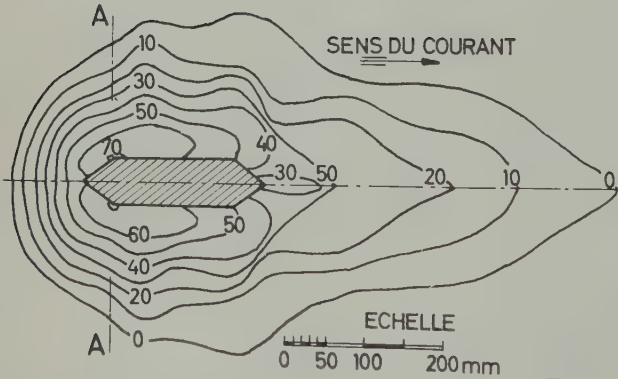


FIG.3

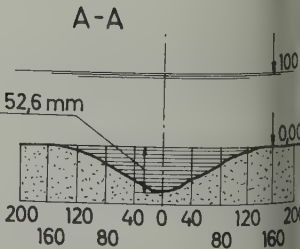
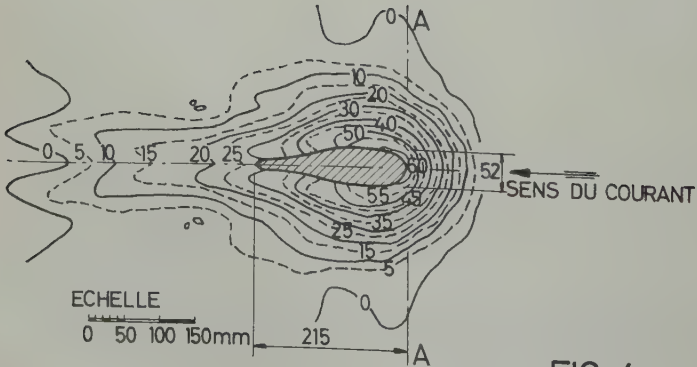


FIG.4

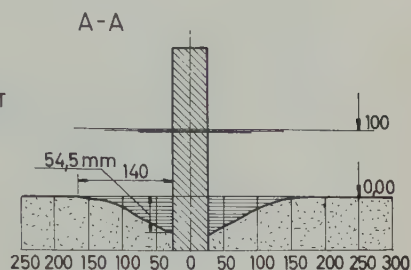
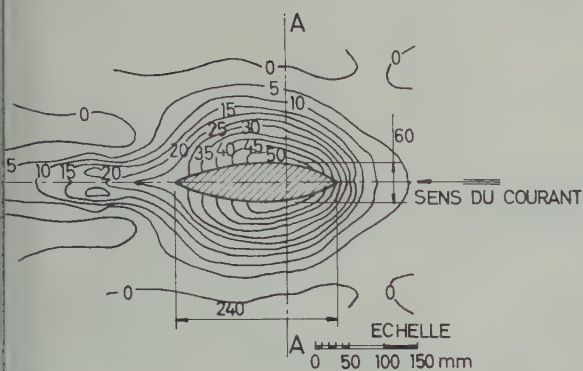


FIG. 5

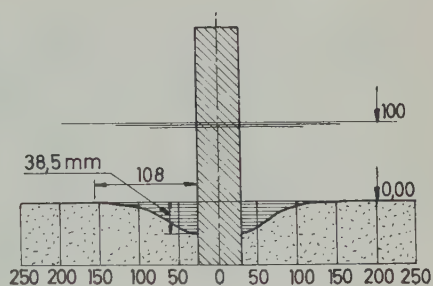
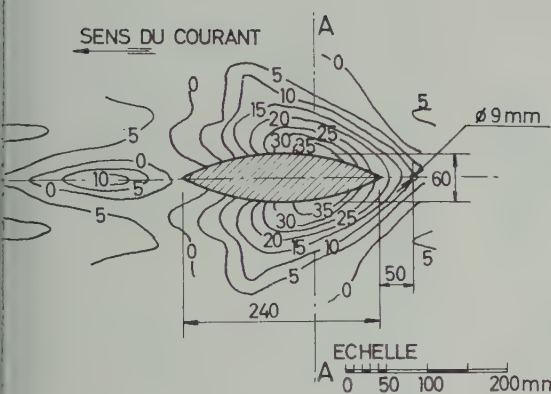


FIG. 6

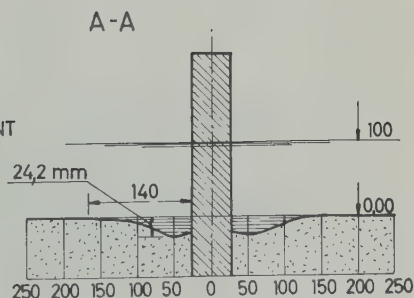
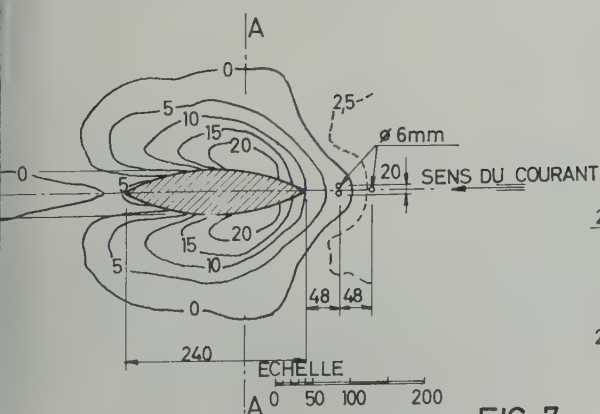


FIG. 7



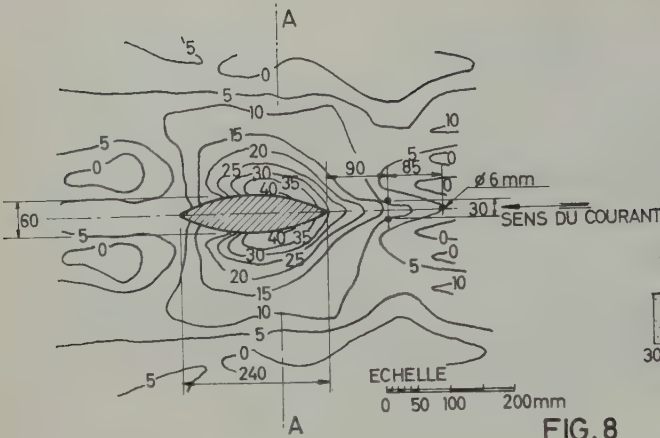


FIG. 8

The length of the pier was 24 cm and the breadth was 6 cm (Fig. 2). The simple rounding of the edges of the pier reduced the scour to 91 mm, whereas the triangular shape reduced it to 70

mm (Fig. 3). An aerodynamic shape gave further reduction (Fig. 4), but a lens shape produced a reduced scour of 54 mm under the influence of the large values of  $\rho_1$  (Fig. 5). The protection of a simple pile before the lens-shaped pier reduced the scour to 38 mm; this pile produced larger values of  $\rho_1$  and worked as a reduction of the breadth-length ratio (Figs. 6 and 7). However, when the distance between the pier and the pile became too great, the stream flowed around the pile and produced no reduction of the scour (Fig. 8).

A change in the velocity distribution will have an influence on the second term of (4) and therefore on the values of the scour. A greater roughness of the bottom at a distance upstream of the pier (obtained in the model with pebbles instead of sand) reduced  $v'$  but increased the scour (Fig. 9), and it was concluded that erosion would increase. Measurements showed an increase of 71 mm with gravel and a lens-shaped

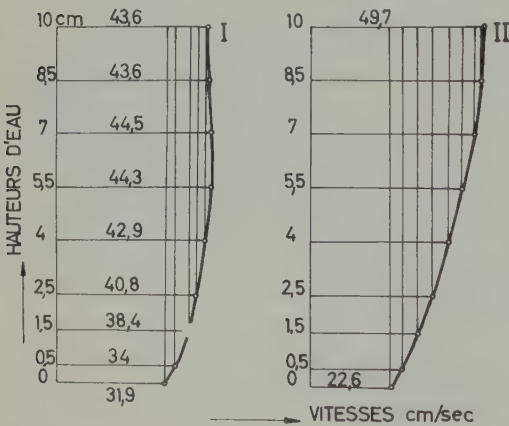


FIG. 9

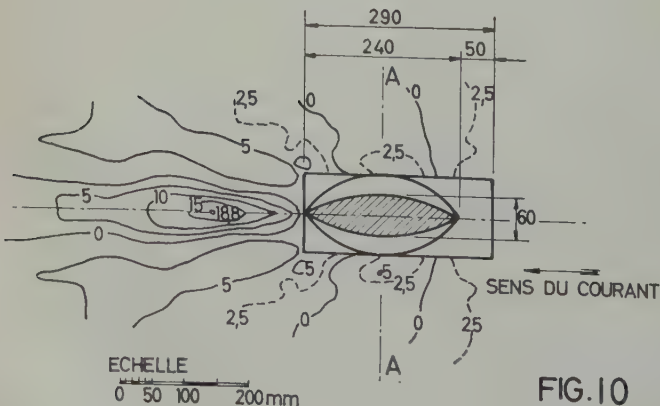
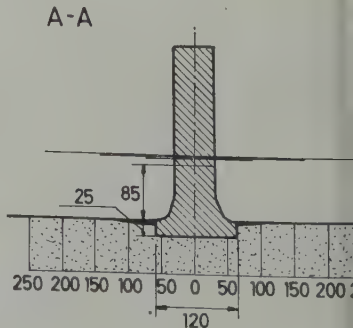


FIG. 10



, but only 54 mm with fine sand. Consideration of (4) shows that it would be possible considerably reduce erosion by adapting the variation of the radius with that of  $v^3$ . Therefore, the velocity distribution from the bottom to the surface was measured and the lens-shaped pier with given variable radii of curvature corresponding to values of  $v^3$  (Fig. 9). The result was a nonprismatic pier with a larger base. Erosion behind this new model was reduced to 5 mm (Fig. 10).

It is easy to see that the second curvature  $\rho_2$  will give a relation in (4) having a negative second term. A rising motion will therefore follow the first diving motion. This was observed in all the models. For the rectangular pier the first radii of curvature around the upstream face produced a quasi-vertical rising motion. The rising motion gave a rising bottom in the direction of flow. Behind the obstacle with the lens-shaped section, the type 2 curvature was followed by type 1 curvature, and the formation of a secondary smaller scour was observed behind the pier (Fig. 5). This secondary scour did not appear with the rectangular pier; that is, the streamlines did not follow the pier behind the pier but left it. There was no curvature of type 2 and therefore no scour. The diving motion initiated by the first curvature  $O_1, \rho_1$  was not only the origin of the scour but the reaction of the river bed and of the bottom of the scour reflecting the diving streamlines so that they formed a

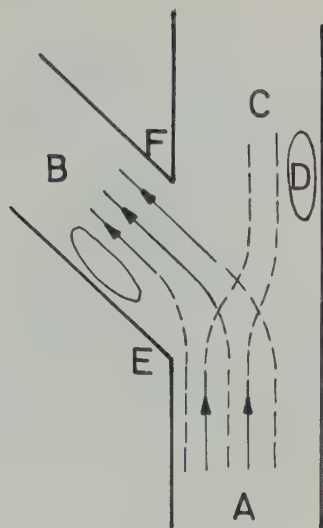


FIG. 12

spiral motion. This motion acted as a scour on the bottom and formed a continuous dune on the edge of the scour. The same action continued behind the pier leading to continuous depressions for a long distance downstream, while the spiral motion rejected the eroded material in the spaces behind the free apertures behind the obstacle, creating an inversion of the profile behind the obstacle.

*Movement of sediment at diversion.* A diversion  $B$  produces a curvature  $O_1, \rho_1$ , but along the river bank between  $A$  and  $C$ , the diversion exerts no action on the direction of the streamlines. For a line, such as  $DE$ , tangent at each point to the principal normals of the streamlines, in the vicinity of the surface, the following relation may be written (Fig. 11)

$$z_D + \frac{p_D}{\gamma} = z_E + \frac{p_E}{\gamma} - \frac{1}{g} \int_D^E \frac{v^2}{\rho_1} ds \quad (5)$$

In the vicinity of the bottom another line  $D'E'$  of the same nature gives

$$z_{D'} + \frac{p_{D'}}{\gamma} = z_{E'} + \frac{p_{E'}}{\gamma} - \frac{1}{g} \int_{D'}^{E'} \frac{v'^2}{\rho_1} ds \quad (6)$$

but also

$$z_E + \frac{p_E}{\gamma} = z_{E'} + \frac{p_{E'}}{\gamma} \quad (7)$$

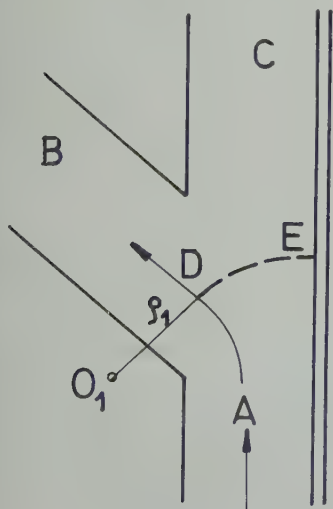


FIG. 11



FIG. 13

From these three relations

$$z_D + \frac{p_D}{\gamma} - \left( z_{D'} + \frac{p_{D'}}{\gamma} \right) = -\frac{1}{g} \left[ \int_D^E \frac{v^2}{\rho_1} ds - \int_{D'}^{E'} \frac{v'^2}{\rho_1} ds \right] \quad (8)$$

Here again the second term is negative; therefore, streamlines in the direction of the diversion will rise. In other words, the diversion will receive water coming from the vicinity of the bottom, whereas water at the surface will move straight ahead. The consequence of this distribution is that most of the bottom sediment will be moved in the direction of the diversion.

The movement of the lowest streamline toward the diversion has another consequence in that part of the upper streamlines have to dive in order to establish flow in the lower part of the section (in direction *C* of Fig. 11). Applying the same consideration described for piers to this diving motion, it is apparent that they will be the origin of curvature  $O_2$ ,  $\rho_2$ . Water in the vicinity of the right bank (in *D* of Fig. 12) will be isolated from the motion and will form an

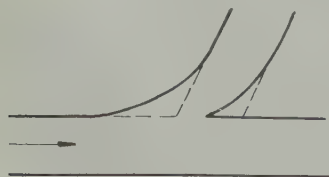


FIG. 14

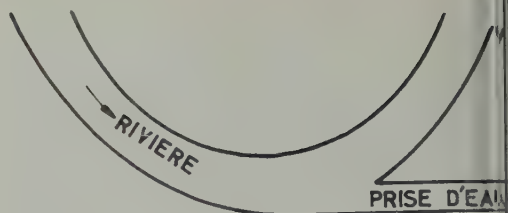


FIG. 15

elongated vertical eddy under the influence of friction. When the edge of the diversion is rounded, water between *E* and the rising motion in the direction *B* will form another vertical eddy. It would be easy to establish the fact that these two eddies have a rising motion as a result of their curvatures. The lower layers of the eddy near the edge *E* will therefore receive sediment coming from *A*, and the rising spiral motion will create a deposit which reduces the surface of the diversion entry. But the opposite edge *F* will exert the same influence as a pier; that strong erosion will occur on the two sides of this edge.

Figure 13 shows the results of such a diversion with an angle of  $60^\circ$  in the direction *AB*. From 90 to 95 per cent of the sediment is moved into the diversion *C*, when only 50 per cent of the discharge is so moved. The rounding of the edge *E*, which reduces the value of  $\rho$  in (8), will have an influence on the motion of the sediments. The part entering the diversion will be reduced by a smooth rounding of the edge. The amount of sediment entering the diversion may be reduced to 60 per cent (Fig. 14). On the other side, a reduction of the angle between *AB* and *AC* (Fig. 11) has the same influence.

The action of the diversion may be increased (Fig. 15) or reduced by the curvature of the river above the diversion. The curvature shown in Figure 15 concentrates the sediment along the left bank of the river, leading to an increase in the volume of sediment entering the diversion. Different solutions may be adopted in order to reduce this influence of the diversion, but their study is primarily a problem in hydraulics. The same theoretical reasoning can be applied to studies of scour in river bends and in the vicinity of groins.

(Manuscript received May 22, 1961.)

# The Relation between the Frequency Distributions of Sieve Diameters and Fall Velocities of Sediment Particles

JOHN F. KENNEDY<sup>1</sup> AND ROBERT C. Y. KOH

*W. M. Keck Laboratory of Hydraulics and Water Resources  
California Institute of Technology, Pasadena*

**Abstract.** A relation between the frequency distributions of sieve diameters and fall velocities is developed. The relation shows that if the sieve diameters of a sediment are log-normally distributed, the fall velocities will also have this distribution, but with a different standard deviation which can be calculated. The results of detailed measurements of the fall velocities of two different natural sands are presented, and the distributions of fall velocities are found to be in good agreement with the predicted distributions. The sedimentation diameters determined from the measured fall velocities agree very well with those predicted from the sieve diameters by the *Inter-Agency Committee on Water Resources* [1957].

## INTRODUCTION

In problems involving the transport of solids by a fluid, or the separation of solids from a transporting fluid, the most important single property of the sediment in determining its transport properties and effect on the fluid flow is the fall velocity of the sediment particles in the transporting fluid. The fall velocity of a particle is a complex function of the size, shape, and density of the particle, the properties of the fluid, the characteristics of the flow, and the concentration and distribution of other particles surrounding the particle in question. This *in situ* fall velocity usually cannot be determined; instead, the terminal fall velocities of representative individual particles falling under gravity in the transporting fluid, at rest and effectively unbounded, are used to describe the settling properties of the sediment. When the fall velocity of a particle is known, it can conveniently be described by the sedimentation diameter of the particle,  $D_s$ , which is defined as the diameter of a sphere, of the same density as the particle, which has the same fall velocity in the same quiescent fluid at the same temperature. Conversely, if the sedimentation diameter of a particle is known, its fall velocity can be computed from data on the fall velocities of spheres. Natural sediments, such as sand, are composed of particles of many sizes and shapes, and con-

sequently the frequency distributions of fall velocities and sedimentation diameters must be considered. The determination of the frequency distribution of the fall velocities of a sediment by measuring the fall velocities of individual particles of a sample of the sediment is quite tedious. Instead, a sieve analysis is usually used to determine the distribution of the sieve diameters of the particles. The sieve diameter of a particle,  $D'$ , is usually defined as the geometric mean of the openings of the last sieve through which the particle passed and the sieve on which it is retained; this is the definition that will be used here. To describe the fall velocity characteristics of a sediment, it is necessary to know the relation between the sieve diameters and the sedimentation diameters of the particles, and between the frequency distribution of sedimentation diameters and the frequency distribution of fall velocities.

The main objective of this paper is to develop a relation between the frequency distributions of sieve diameters and fall velocities. In this connection, some analytic considerations of the fall velocities of spheres outside the Stokes range are presented. The second objective is to evaluate a method which has been presented [*Inter-Agency Committee on Water Resources*, 1957] for determining sedimentation diameters from sieve diameters. The results of some careful measurements of fall velocities of two different sands are given, and these data are used to evaluate the relations derived for predicting the frequency distribution of fall velocities. The sedimentation

<sup>1</sup> Now at Hydrodynamics Laboratory, Department of Civil and Sanitary Engineering, Massachusetts Institute of Technology, Cambridge.



diameters obtained from the measurements are compared with those predicted by the Inter-Agency report. This work was done in connection with a recent investigation at California Institute of Technology on the mechanics of sediment transportation [Kennedy, 1961]. The sands used in this study of fall velocities were also used in the sedimentation study.

#### FALL VELOCITIES OF SPHERES

By equating the submerged weight of a sphere to the drag force acting on it, we can express its terminal fall velocity as

$$w^2 = \frac{4}{3} (s - 1) \frac{gD}{C_D} \quad (1)$$

where

$w$  = terminal fall velocity.

$s$  =  $\rho_f/\rho_s$ .

$\rho_f$  = mass density of the fluid.

$\rho_s$  = mass density of the sphere.

$g$  = gravitational constant.

$D$  = sphere diameter.

$C_D$  = drag coefficient =  $F/A\rho_f(w^2/2)$ .

$F$  = drag force on the sphere

= submerged weight of sphere.

$A$  = projected area of sphere.

The drag coefficient outside the Stokes range, which ends at a Reynolds number of about 0.4, must be determined experimentally and is usually expressed as a function of the Reynolds number. Graphs giving this relation, such as the one shown in Figure 1 [Rouse, 1950, p. 122], can be found in most textbooks on fluid mechanics. However, such graphs are not particularly convenient for the determination of fall velocity because a trial and error procedure is required. To make a direct determination possible, Rouse [1950, p. 781] has presented the drag coefficient-Reynolds number relation for quartz spheres in water and air as fall velocity plotted against sphere diameter with temperature as a third variable, as shown in Figure 2. This graph makes the determination of fall velocity quite convenient but does not give a closed form relation which can be used in mathematical analyses of fall velocity problems. Such a relation will now be developed.

Since  $C_D$  is a function of only the Reynolds number, (1) gives  $w$  as a function of  $D$ ,  $s$ , and the kinematic viscosity  $\nu$ . Therefore,

$$dw = \frac{\partial w}{\partial D} dD + \frac{\partial w}{\partial \nu} d\nu + \frac{\partial w}{\partial (s-1)} d(s-1)$$

The following partial derivatives can be obtained from (1):

$$2w \frac{\partial w}{\partial D} = \frac{4}{3} (s-1) \left[ \frac{g}{C_D} - \frac{gD}{C_D^2} \frac{dC_D}{d(\log C_D)} \right]$$

$$2w \frac{\partial w}{\partial \nu} = \frac{4}{3} (s-1) \left[ -\frac{gD}{C_D^2} \frac{dC_D}{d(\log C_D)} \right]$$

$$2w \frac{\partial w}{\partial (s-1)} = \frac{4}{3} gD \left[ \frac{1}{C_D} - \frac{(s-1)}{C_D^2} \frac{dC_D}{d(\log C_D)} \right]$$

where  $R$  is the Reynolds number,  $R = wD/\nu$ . The quantity  $(d(\log C_D)/d(\log R))$  is the slope of the  $C_D$ - $R$  curve on a logarithmic plot and its negative will be denoted by  $m$ .

$$m = -\frac{d(\log C_D)}{d(\log R)}$$

Substituting (1) and (6) into (3), (4), and (5) and carrying out the indicated differentiation we obtain

$$\frac{\partial w}{\partial D} = \frac{1+m}{2-m} \frac{w}{D}$$

$$\frac{\partial w}{\partial \nu} = \frac{-m}{2-m} \frac{w}{\nu}$$

and

$$\frac{\partial w}{\partial (s-1)} = \frac{1}{2-m} \frac{w}{s-1}$$

Substituting (7), (8), and (9) into (2) yields

$$\frac{dw}{w} = \frac{1+m}{2-m} \frac{dD}{D} - \frac{m}{2-m} \frac{d\nu}{\nu} + \frac{1}{2-m} \frac{d(s-1)}{s-1}$$

Values of  $m$ ,  $(1+m)/(2-m)$ ,  $m/(2-m)$ , and  $1/(2-m)$  are tabulated with Reynolds

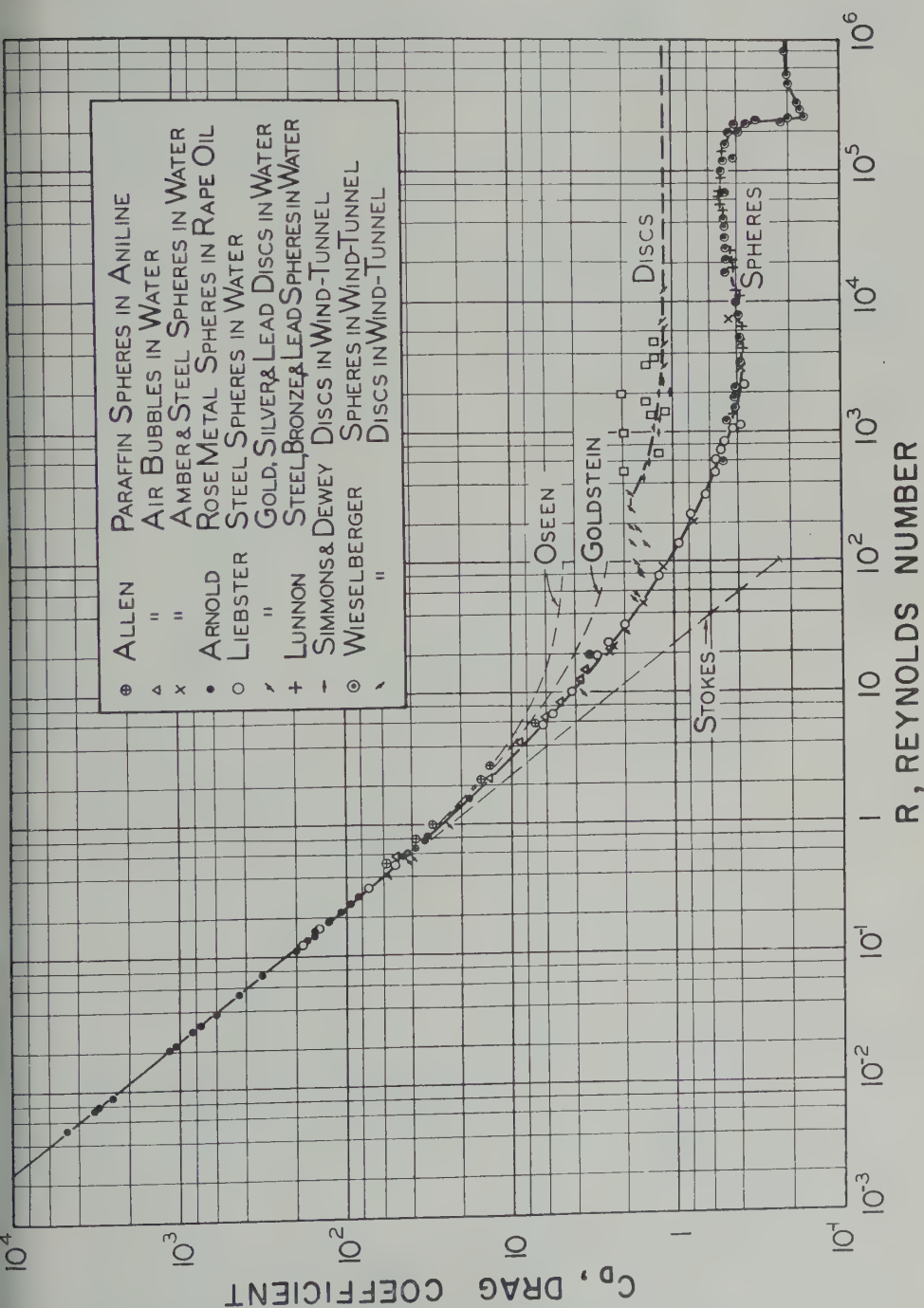


Fig. 1. Drag coefficient as a function of Reynolds number for spheres and disks.



number in Table 1 and are shown plotted against Reynolds number in Figure 3.

As can be seen in Figure 3, the relation between the Reynolds number and the three parameters appearing in (10) can be closely approximated by

$$\frac{1+m}{2-m} = 1.70R^{-0.120} \quad (11)$$

for Reynolds numbers between 1 and 1000;

$$\frac{m}{2-m} = 0.88R^{-0.220} \quad (12)$$

for  $R$  between 2 and 400; and

$$\frac{1}{2-m} = 0.90R^{-0.065} \quad (13)$$

for  $R$  between 1 and 5000. Substitution of (11), (12), and (13), into (10) yields

$$\frac{dw}{w} = 1.70R^{-0.120} \frac{dD}{D} - 0.88R^{-0.220} \frac{d\nu}{\nu} + 0.90R^{-0.065} \frac{d(s-1)}{s-1} \quad (14)$$

valid for Reynolds numbers between 2 and 400.

Equation 14 is nonlinear and cannot easily be integrated in closed form. However, the relation between  $w$  and  $D$  can be obtained for fixed values of  $\nu$  and  $s$ . In this case,  $d\nu = d(s-1) = 0$ , and (10) reduces to

$$\frac{dw}{w} = \frac{1+m}{2-m} \frac{dD}{D} \quad (15)$$

and (14) becomes

$$dw/w = 1.70R^{-0.120} dD/D$$

Substituting for  $R$  and carrying out the integration yields

$$w^{0.120} = -1.70\nu^{0.120} D^{-0.120} + C \quad (16)$$

where  $C$  is an integration constant that depends on the density and viscosity of the fluid and the density of the spheres. For quartz spheres in water at 25°C ( $s = 2.65$ ,  $\nu = 0.966 \times 10^{-6}$  cm<sup>2</sup>/sec),  $C = 1.76$ , and

$$w = [1.76 - 0.426(1/D)^{0.120}]^{1/0.120} \quad (17)$$

for Reynolds numbers between 1 and 1000.

Similarly, the relation between  $w$  and  $\nu$  for fixed  $D$  and  $s$  can be obtained by taking  $D = d(s-1) = 0$  in (14). Then

TABLE 1. Parameters for Equation 10

$R$ Reynolds Number	$\frac{m}{d(\log C_D)}$ $\frac{m}{d(\log R)}$	$\frac{1+m}{2-m}$	$\frac{m}{2-m}$	$\frac{1}{2-m}$
0.4 and less	1.000	2.000	1.000	1.000
1	0.890	1.703	0.802	0.901
2	0.835	1.575	0.717	0.858
4	0.770	1.439	0.626	0.813
10	0.685	1.281	0.521	0.760
20	0.635	1.197	0.465	0.733
40	0.570	1.098	0.399	0.699
100	0.475	0.967	0.311	0.656
200	0.417	0.895	0.263	0.632
400	0.365	0.835	0.223	0.612
800	0.300	0.765	0.176	0.588
1000	0.275	0.739	0.159	0.580
2000	0.145	0.617	0.078	0.539
5000	0	0.500	0	0.500

$$dw/w = -0.88R^{-0.220} d\nu/\nu$$

which can be integrated to yield

$$w = [k - 0.88(\nu/D)^{0.220}]^{1/0.220} \quad (18)$$

for  $R$  between 2 and 400, where  $k$  is a constant that depends on  $s$  and  $D$ .

Finally, the relation between  $w$  and  $s$  for fixed  $D$  and  $\nu$  can also be obtained from (14). Proceeding as above, we get

$$w = [p + 0.059(\nu/D)^{0.065} \ln(s-1)]^{1/0.065} \quad (19)$$

where  $p$  is a constant that depends on  $\nu$  and  $D$ . Equation 19 is valid for  $R$  between 1 and 5000.

When these relations are applied to particles other than spheres,  $D$  should be replaced by  $D_s$ .

#### RELATION BETWEEN THE FREQUENCY DISTRIBUTION OF SEDIMENTATION DIAMETERS AND THE FREQUENCY DISTRIBUTION OF FALL VELOCITIES

If the frequency distribution function of the sedimentation diameters of a sediment is known and the frequency distribution of the fall velocities is desired, the problem becomes one of determining the frequency distribution of a function of a random variable. In this case, the sedimentation diameter  $D_s$  is the random variable whose frequency distribution is known, and (15) determines the function of  $D_s$  for which the frequency distribution is desired. Let  $f(D_s)$  be



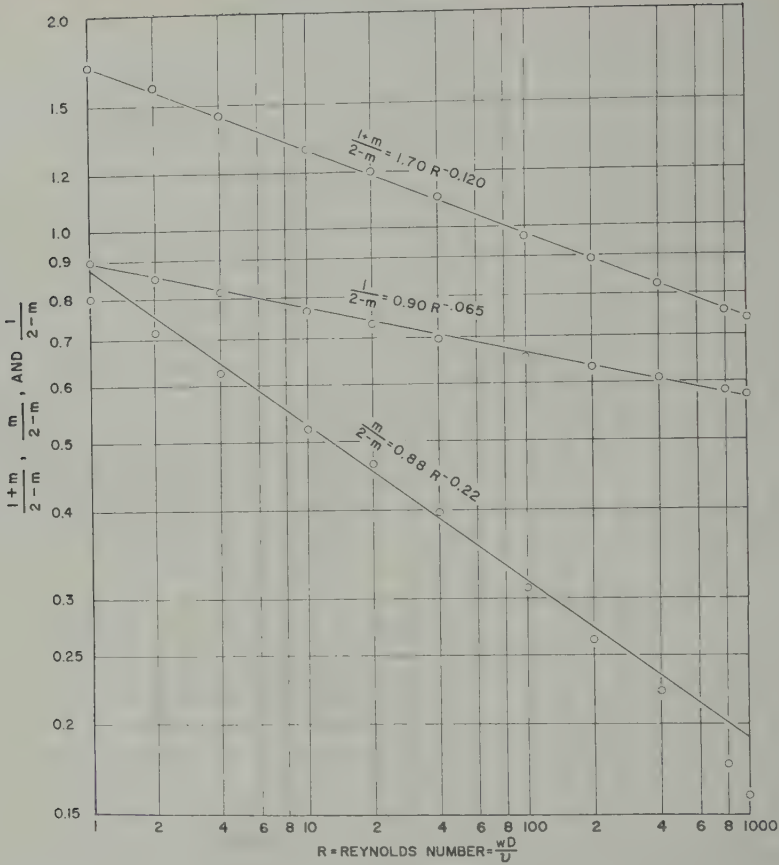


Fig. 3. Values of  $(1 + m)/(2 - m)$ ,  $m/(2 - m)$ , and  $1/(2 - m)$  as a function of Reynolds number

the frequency distribution function of the sedimentation diameters, and let  $g(w)$  be the frequency distribution function of the fall velocities. The probability that  $w$  is between  $w_0$  and  $w_0 + dw$  is the same as the probability that  $D_s$  is between  $D_{s_0}$  and  $D_{s_0} + dD_s$ , where  $D_s = D_s(w)$  is the functional relation between  $D_s$  and  $w$ , (15) or (16), and  $D_{s_0} = D_s(w_0)$ . Thus  $f(D_s) dD_s = g(w) dw$ , which can be written as

$$g(w) = f[D_s(w)] \frac{dD_s(w)}{dw} \tag{20}$$

If the frequency distribution of  $D_s$  is known or assumed, (16) can be substituted into (20) and the corresponding  $g(w)$  determined.

For natural sands and also for many particulate materials such as glass and plastic beads produced by manufacturing processes, it is observed that the logarithms of the particle sieve diameters are distributed according to the normal error law.

This distribution is called the log-normal distribution. For example, the sieve diameter distributions of the sands used in this investigation are very nearly log normal except for tails (see Fig. 5). To derive an expression for the frequency distribution of settling velocity, it will be assumed that the logarithms of sedimentation diameters are also normally distributed. Thus

$$f(\log D_s) = \frac{1}{\sigma \sqrt{2\pi}} \cdot \exp \left\{ -\frac{1}{2} \left[ \frac{\log D_s - \mu}{\sigma} \right]^2 \right\}$$

where

- $\mu$  = mean of  $\log D_s$ .
- $\sigma$  = standard deviation of  $\log D_s$ .

The frequency distribution of fall velocity

obtained by solving (16) for  $D_s$  and substituting (20) into (21):

$$f(w) = f[\log D_s(w)] \frac{d \log D_s}{dw} \exp \left\{ -\frac{1}{2} \left[ \frac{\log \nu \left( \frac{C - w^{0.120}}{1.70} \right)^{-1/0.120} - \mu}{\sigma} \right]^2 \right\} \quad (22)$$

Similarly,

$$g(w) = f[\log D_s(w)] \frac{d \log D_s}{d \log w} \exp \left\{ -\frac{1}{2} \left[ \frac{\log \nu \left( \frac{C - w^{0.120}}{1.70} \right)^{-1/0.120} - \mu}{\sigma} \right]^2 \right\} \quad (23)$$

Equations 22 and 23 show that neither  $w$  nor  $\log w$  is exactly normally distributed, since a function of  $w$  appears in the coefficients of the exponentials. However, for a sediment containing a small range of particle sizes, the logarithms of the fall velocities can be shown to be exactly normally distributed. For this case, the quantity  $(1+m)/(2-m)$  is nearly constant, and (15) can be integrated to yield

$$w = C_1 D_s^{(1+m)/(2-m)} \quad (24)$$

where  $C_1$  is a dimensional constant. Use of (24) is equivalent to replacing the part of the curve in Figure 2 covered by the sediment by a straight line segment. Substitution of (21) and (24) into (20) yields

$$g(w) = \frac{2-m}{1+m} \frac{1}{\sigma \sqrt{2\pi}} \exp \left\{ -\frac{1}{2} \left[ \frac{\log w - \frac{1+m}{2-m} \log (D_s)_{50} - \log C_1}{\frac{1+m}{2-m} \sigma} \right]^2 \right\} \quad (25)$$

where  $\sigma$  is the standard deviation of  $\log D_s$ ,

$$\begin{aligned} \sigma &= \log (D_s)_{50} - \log (D_s)_{15.9} \\ &= \log \frac{(D_s)_{50}}{(D_s)_{15.9}} \end{aligned} \quad (26)$$

where  $(D_s)_{50}$  is the sedimentation diameter such that 50 per cent by weight of the sediment has a smaller sedimentation diameter; similarly, 15.9 per cent by weight of the sediment has a sedimentation diameter smaller than  $(D_s)_{15.9}$ . The quantity  $(D_s)_{50}/(D_s)_{15.9}$  is denoted by  $\sigma_s$  and called the geometric standard deviation of the sedimentation diameters. Similarly,  $\mu = \log (D_s)_{50}$ , where  $(D_s)_{50}$  is called the geometric mean sedimentation diameter, and is the same as the median by weight. Substituting these quantities into (25) results in

$$g(w) = \frac{2-m}{1+m} \frac{1}{\log \sigma_s \sqrt{2\pi}} \exp \left\{ -\frac{1}{2} \left[ \frac{\log w - \log w_{50}}{\frac{1+m}{2-m} \log \sigma_s} \right]^2 \right\} \quad (27)$$

where

$$w_{50} = C_1 [(D_s)_{50}]^{(1+m)/(2-m)} \quad (28)$$

For a sediment with a range of particle sizes small enough so that (24) is valid, (27) shows that  $\log w$  is also normally distributed with a geometric mean of  $w_{50}$  given by (28) and a geometric standard deviation  $\sigma_w$  of

$$\sigma_w = (\sigma_s)^{(1+m)/(2-m)} \quad (29a)$$

Since  $\sigma_s$  must always be greater than unity (or equal to unity for a uniform sediment), (29a) shows that  $\sigma_w$  will be less than or greater than  $\sigma_s$  according as  $(1+m)/(2-m)$  is less than or greater than unity. From Figure 3,  $(1+m)/(2-m) = 1.0$  when  $R = 85$ . Therefore, when the Reynolds number is less than 85 for all particles of a sediment,  $\sigma_s$  will be less than  $\sigma_w$ , and the opposite will be true for sediments with  $R$  greater than 85 for all particles.

When a sediment contains significant quantities of particles with both  $R$  greater than and less than 85, no definite conclusion can be drawn, although (29) should still be qualitatively valid if the value of  $(1+m)/(2-m)$  for  $w_{50}$  is used.

Usually, only the frequency distribution of the sieve diameters is known. As discussed in section 6, if a sediment contains a limited range of particle sizes, the sieve and sedimentation diameters differ by only a nearly constant factor. Therefore, if in (24) through (29a)  $D'$  is used instead of  $D_s$ , the only difference is that a different constant coefficient must be used in (24). Since the constant does not appear in the distribution of fall velocities (equation 27), the fall velocities should be log-normally distributed if the sieve diameters have this distribution. In this case,  $\sigma_s$  is replaced by the geometric standard deviation of the sieve diameters,  $\sigma_v$ , in (27), and (29a) becomes

$$\sigma_w = (\sigma_v)^{(1+m)/(2-m)} \quad (29b)$$

#### 4. EXPERIMENTAL APPARATUS AND PROCEDURE

To obtain representative samples of the two sands from the laboratory sedimentation flumes to be used for the fall velocity measurements, a sample weighing several pounds was removed from five or six locations along each flume. Each of the two large samples was divided into successive halves with a Jones sample-splitter until a sample of approximately 30 grams of each sand remained. A sieve analysis was then made on each of these samples.

The sieve analyses were performed with a fourth-root-of-two series of 8-inch-diameter, half-depth Tyler laboratory sieves. The sieves were shaken 15 minutes on a Tyler Rotap sieve shaker. Each sieve fraction (sand contained between successive sieves) was weighed to the nearest 10 mg on an analytic balance. To obtain particles of the finer sand for the fall-velocity measurements, each sieve fraction was passed through a miniature sample-splitter until a sample of approximately 50 particles remained. For the coarser sand, exactly 50 grains were selected at random from each sieve fraction. Each of these grains was dropped into quiescent tap water, and the time required for the grain to fall a given distance between two marks on the settling column was measured with a stop watch to the nearest tenth of a second. The distances were selected to give fall times between 6.5 and 25 seconds. The particles were released under water and were allowed several inches of fall to attain their terminal velocity before reaching the first mark, where the time measurement was begun.

Two different settling columns were used: a simple glass cylinder 3.75 inches in diameter, 66 inches long, and a liter graduate 2.38 inches in diameter and 18 inches long. The column was used when the required fall distance was greater than 12 inches. At intervals of 15 minutes, the water in the column was thoroughly mixed to break up thermal gradients; the temperature was measured with an immersion thermometer. Hot or cold water was added as required to bring the temperature to the desired value, and the water was again mixed. Fall-velocity measurements were not resumed until the water again became quiescent. In any way, the temperature was kept within 1°C (in most cases within 0.5°C) of the desired value. Figure 2 indicates that a temperature variation of 1°C results in a change of less than 2 per cent in the fall velocity of even the smallest particles used (0.08 mm).

It was observed that the particles often did not fall straight down, but followed an irregular spiral path. The larger particles often had a complex rotating and oscillating motions also. Rotations and oscillations were not observed for the finer particles, although they may have been present and escaped notice.

#### SAND CHARACTERISTICS

*Sieve analyses.* Both of the sands used were predominantly quartz. They were obtained from a local foundry supply house and were given no further treatment except washing. Photomicrographs of the two sands are shown in Figure 3. Sand 1 is from the St. Peter formation and marketed commercially as 'Ottawa sand.' The finer sand, sand 2, is a Nevada sand. It is somewhat more angular than sand 1.

The cumulative distributions, by weight, of the sieve diameters of the sands are shown in Figure 5, plotted on a logarithmic-probability graph as suggested by *Otto* [1939]. The fact that the distributions plot as straight lines, especially for the tails, indicates that the logarithms of the sieve diameters do have a normal distribution; this is the distribution (21) that was assumed for the sedimentation diameters in section 6. This distribution is completely defined by the geometric mean sieve diameter  $D_g$  (which is the same as the median by weight) and the geometric standard deviation of the sieve diameters  $\sigma_v$  are given.



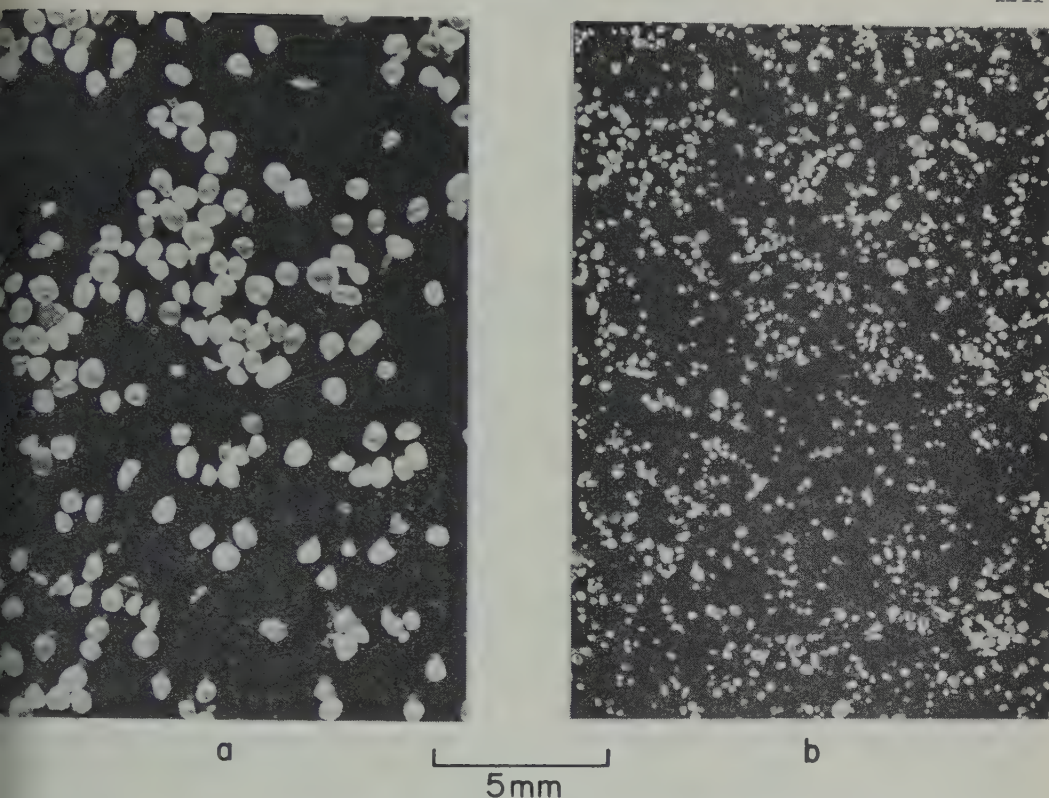


Fig. 4. Photomicrographs of sands used.

- (a) Sand 1. Geometric mean sieve diameter = 0.549 mm.  
 (b) Sand 2. Geometric mean sieve diameter = 0.233 mm.

*Fall-velocity distribution.* To determine the distribution of fall velocities, the number of terminations of fall velocities from each sieve fraction was first reduced to 50 and multiplied by a weighting factor which was the percentage, by weight, of the total sample in the sieve fraction. The number of occurrences in each velocity increment (velocity increments of 0.0050 ft/sec were used for sand 1 and 0.0020 ft/sec for sand 2) for each sieve fraction was then counted; this gave the frequency distribution for each sieve fraction. The frequency distributions for each sieve fraction were added to obtain the frequency distribution for a representative sample consisting of 5000 particles (50 particles per sieve fraction  $\times$  100 (%) weight of total sample = 5000). Thus, the total number of occurrences in the  $i$ th velocity increment,  $N_i$ , is

$$N_i = \sum_{m=1}^M \frac{50}{\gamma_m} n_{mi} p_m \quad (30)$$

where

- $n_{mi}$  = number of occurrences in the  $i$ th velocity increment for the sand in the  $m$ th sieve fraction.  
 $p_m$  = percentage, by weight, of sample retained in the  $m$ th sieve fraction.  
 $M$  = number of sieve fractions.  
 $\gamma_m$  = number of measurements of fall velocity for the  $m$ th sieve fraction.

Note that in this procedure it is assumed that weights of all the individual particles in each sieve fraction are the same. The cumulative distribution by weight of fall velocities was then calculated as the subtotal of the number of occurrences of velocities given by the frequency distribution.

The cumulative distributions of fall velocities are shown in Figure 6, plotted on an arithmetic-probability graph, and in Figure 7, plotted on a logarithmic-probability graph. These figures show



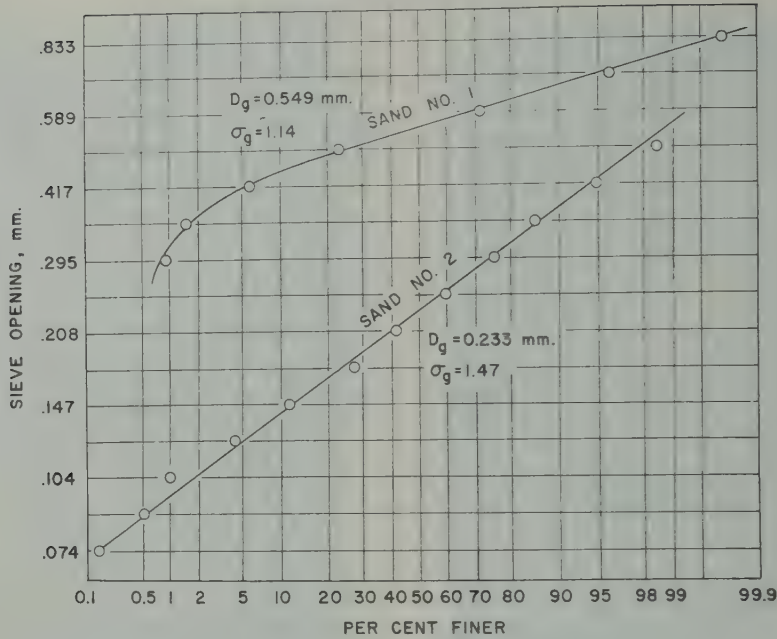


Fig. 5. Cumulative frequency distributions of sieve diameters.

that the fall velocities of sand 1 can be approximated by either a normal or a log-normal distribution. However, the latter approximation is much better if the part of the curve for velocities less than  $w_{15}$  is neglected. It is not surprising that the lower part of the distribution deviates from a log-normal distribution since, as shown in Figure 5, the sieve diameters of the

finer 15 per cent of the sediment are not normally distributed either. The fall-velocity distribution of sand 2 is very nearly log-normal except for the coarsest 5 per cent of the sediment.

In section 3, it was observed that, if the diameters of a sediment are log-normally distributed, the fall velocities will be expected to be log-normally distributed if the sediment

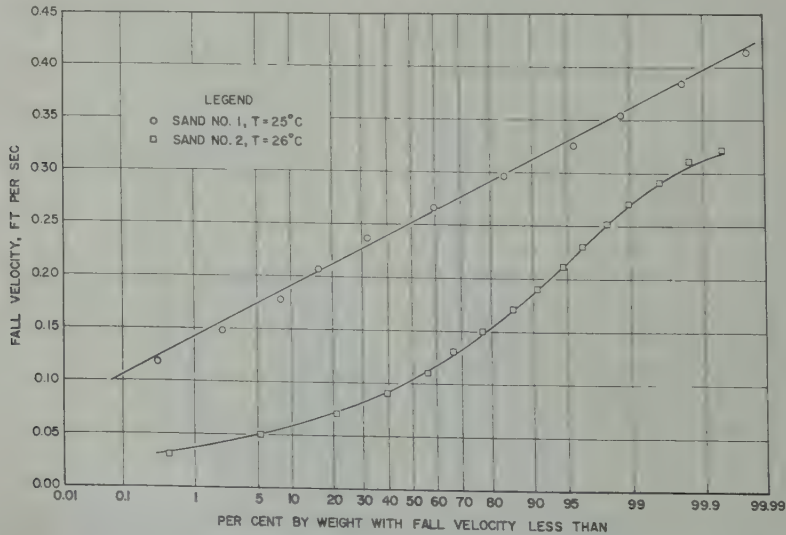


Fig. 6. Arithmetic probability plot of cumulative frequency distributions of fall velocities.

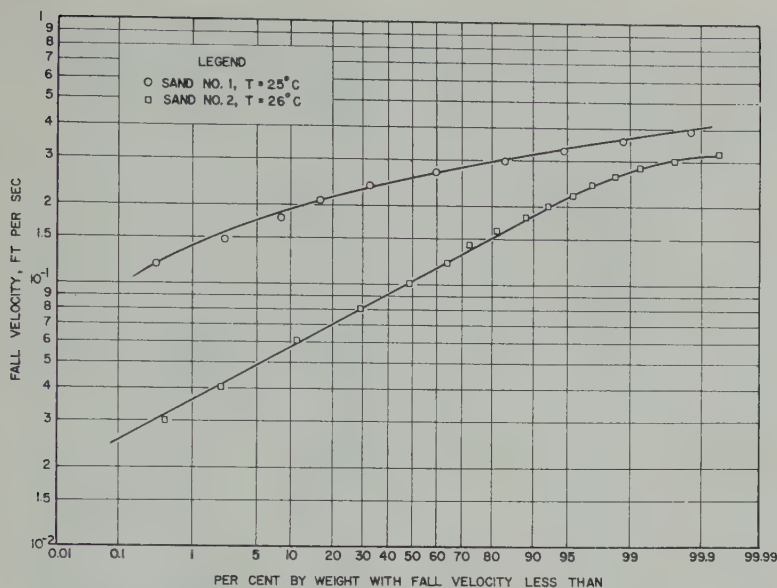


Fig. 7. Logarithmic probability plot of cumulative frequency distributions of fall velocities.

ins a limited range of particle sizes. These two  
nds tend to corroborate this observation. A  
rther discussion of the relation between the  
ve and sedimentation diameters and a summary  
of the sand characteristics are given in  
ction 6.

#### RELATION BETWEEN SIEVE DIAMETERS AND SEDIMENTATION DIAMETERS

To determine the mean sedimentation diameter  
for each sieve fraction, the distribution of  
l velocities was first plotted on arithmetic-  
probability paper. The plotting position  $P$  on  
the abscissa probability scale was that suggested  
Thomas [1948],

$$P = \frac{m}{N + 1}$$

ere

$m$  = rank of particular fall velocity  $w(m)$   
[ $m = 1, 2, \dots, N; w(m+1) > w(m)$ ]  
 $P$  = percentage of particles with fall velocities  
less than or equal to the corresponding  
value on the ordinate.

$N$  = number of measurements of fall velocity  
for the sieve fraction.

a probability plot there was some scatter of  
points, but a straight line could be drawn  
ough them quite closely. For the normal

distribution represented by this straight line,  
the mean and the median are the same and could  
be read directly from the plot. The sedimentation  
diameter corresponding to this mean diameter  
was determined from Figure 2. The standard  
deviation of the fall velocities,  $\sigma_w$ , was also  
determined from the distribution plot as

$$\sigma_w = w_{50} - w_{15.9}$$

Table 2 summarizes the data relevant to the  
distribution of fall velocities for the individual  
sieve fractions and also gives the sedimentation  
diameter for each sieve fraction. The last column  
gives the sedimentation diameter  $D_{s1}$  predicted  
by Figure 8, which was reported by the *Inter-  
Agency Committee on Water Resources* [1957].  
The sieve diameter-sedimentation diameter rela-  
tion given in Figure 8 is for a temperature of  
24°C and is based on measurements made before  
1958 by numerous investigators. The third  
variable in Figure 8, the shape factor (SF), is  
the quantity used to define particle shape; it is  
defined as  $SF = c/\sqrt{ab}$ , where  $a$ ,  $b$ ,  $c$  are,  
respectively, the longest, intermediate, and  
shortest of three mutually perpendicular axes of  
the particle. According to the Inter-Agency  
report, most natural sand particles have a shape  
factor of about 0.7, and this value was used to  
obtain the sedimentation diameters given in the  
last column of Table 2. The 1°C and 2°C tem-

TABLE 2. Summary of Fall-Velocity Measurements of Individual Sieve Fractions

Sieve Opening, mm		Geom.	No. of	Mean	Std. Dev.	$D_s$ Meas.	$D_s$ Meas.
Sieve Passing	Sieve Retaining	Mean Sieve Diameter, mm	Particles in Samples	Fall Velocity, ft/sec	of Fall Velocity, ft/sec	Sed. Diam., mm	Fine Diameter, mm
Sand 1. Temperature 25° ± 1°C							
0.990*	0.833	0.909	50	0.407	0.031	0.76	0.990
0.833	0.701	0.764	75	0.349	0.035	0.66	0.833
0.701	0.589	0.642	50	0.306	0.036	0.58	0.701
0.589	0.495	0.540	50	0.283	0.028	0.54	0.589
0.495	0.417	0.455	50	0.255	0.031	0.44	0.495
0.417	0.351	0.383	50	0.180	0.034	0.36	0.417
0.351	0.295	0.322	50	0.149	0.015	0.31	0.351
Sand 2. Temperature 26° ± 1°C							
0.589*	0.495	0.540	99	0.278	0.023	0.54	0.589
0.495	0.417	0.455	61	0.230	0.024	0.45	0.495
0.417	0.351	0.383	48	0.188	0.021	0.37	0.417
0.351	0.295	0.322	43	0.159	0.015	0.33	0.351
0.295	0.246	0.269	41	0.1305	0.0160	0.275	0.295
0.246	0.208	0.226	44	0.1024	0.0120	0.230	0.246
0.208	0.175	0.191	54	0.0866	0.0075	0.200	0.208
0.175	0.147	0.1607	33	0.0693	0.0066	0.170	0.175
0.147	0.124	0.1350	60	0.0565	0.0058	0.150	0.147
0.124	0.104	0.1135	60	0.0427	0.0061	0.127	0.124
0.104	0.088	0.0957	60	0.0339	0.0048	0.110	0.104
0.088	0.074	0.0807	57	0.0269	0.0051	0.096	0.088

\* This sieve was not actually used in the sieve analysis. It is assumed here that all the material have passed this sieve.

perature discrepancies between the present data and the temperature for Figure 8,  $T = 24^{\circ}\text{C}$ , result in differences in the sedimentation diameter of less than 2 per cent. Note that in Figure 8 the relations for the different shape factors can be replaced by lines parallel to the relation for spheres without gross error for fairly wide ranges of the diameters; then over these ranges  $D_s$  and  $D'$  differ by constant factors. This is the approximation that was used to derive (29b) and to deduce that if the sieve diameters are log-

normally distributed the fall velocities will have this distribution.

In Figure 9 the sedimentation diameters determined in this investigation are compared with the values predicted by Figure 8. With exceptions of the fractions retained on the 0.589-mm and the 0.417-mm sieves and the fraction of sand 2 retained on the 0.074-mm sieve, the agreement with the Inter-Agency values is good. The discrepancies at the first two points are due to the 0.495-mm sieve

TABLE 3. Summary of Sand Characteristics

	Geom. Mean Fall Velocity (Fig. 7)	Geom. Std. Dev. of Fall Velocities (Fig. 7)	Geom. Mean Sed. Diam. (Figs. 7 and 2)	Geom. Mean Sieve Diam. (Fig. 5)	Geom. Std. Dev. of Sieve Diam. (Fig. 5)	Geom. Mean Sed. Diam. (Fig. 8)	Reynolds Number ( $T = 25^{\circ}\text{C}$ )	$1 + m$
	$w_{50}$ , ft/sec	$\sigma_w$	$(D_s)_{50}$ , mm	$D_{50}$ , mm	$\sigma_D$	$(D_{s1})_{50}$ , mm	$R = \frac{w_{50}(D_{s1})_{50}}{\nu}$	$2 - m$ (Fig. 3)
Sand 1	0.260	1.17	0.500	0.549	1.14	0.510	45.0	1.06
Sand 2	0.103	1.63	0.238	0.233	1.47	0.238	8.52	1.31

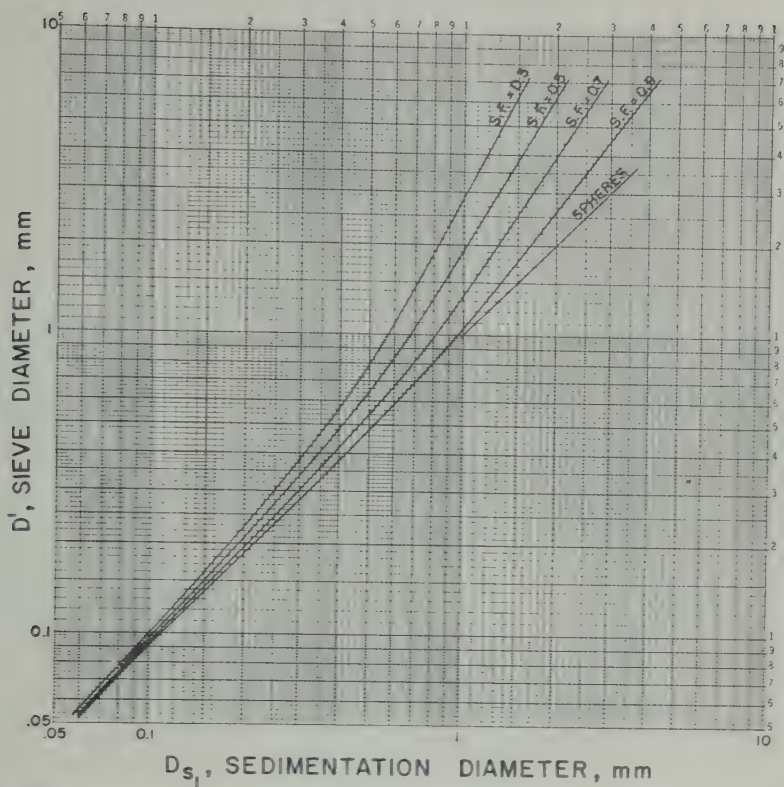


Fig. 8. Relation between sieve diameter and sedimentation diameter. (Taken from Report 12, Inter-Agency Committee on Water Resources, Subcommittee on Sedimentation, 1957.)

ality. Through use, the sieve had become etched and the openings had become enlarged. This was discovered after the fall-velocity investigation was completed and the 0.495-mm sieve which had been used was checked against a new sieve. The enlarged openings in the 0.495-mm sieve result in a large sedimentation diameter for the sieve fraction retained on it since the smaller particles were passed to the 0.417-mm sieve. The sieve fraction retained on the 0.417-mm sieve also had a sedimentation diameter which was too large since coarse particles which could have been retained on the 0.495-mm sieve were passed to it. The discrepancy for the sieve fraction of sand 2 retained on the 0.074-mm sieve cannot be explained. However, it is not surprising, since it contained the smallest particles of the sand, and less than  $\frac{1}{2}$  per cent of the weight of the sand is contained in the sieve fraction. The results of this investigation thus indicate that the relation between sieve diameters and sedimentation diameters given by the Inter-

Agency report for a shape factor of 0.7 is fairly reliable for natural sands.

A summary of the sand characteristics is given in Table 3. The values of  $(D_{s1})_{50}$  are the sedimentation diameters corresponding to  $D_{50}$  given by Figure 8. The values of  $(D_{s1})_{50}$  agree well with the experimentally determined values of the geometric mean sedimentation diameter  $(D_{s1})_{50}$ . The computed  $\sigma_w$  is obtained from (29b) by using the value of  $(1 + m)/(2 - m)$  corresponding to the Reynolds number based on  $w_{50}$  and  $(D_{s1})_{50}$ . The agreement between the experimentally determined and the computed values of  $\sigma_w$  is quite good.

*Acknowledgments.* Equations 7, 8, and 9 were first derived by Professor Norman H. Brooks of California Institute of Technology. Professor Brooks also suggested the analysis that resulted in (27). We gratefully acknowledge these contributions and also his helpful discussion and criticism. We also wish to thank Professor Vito A. Vanoni of Caltech for his many valuable suggestions.

The research reported here was supported by



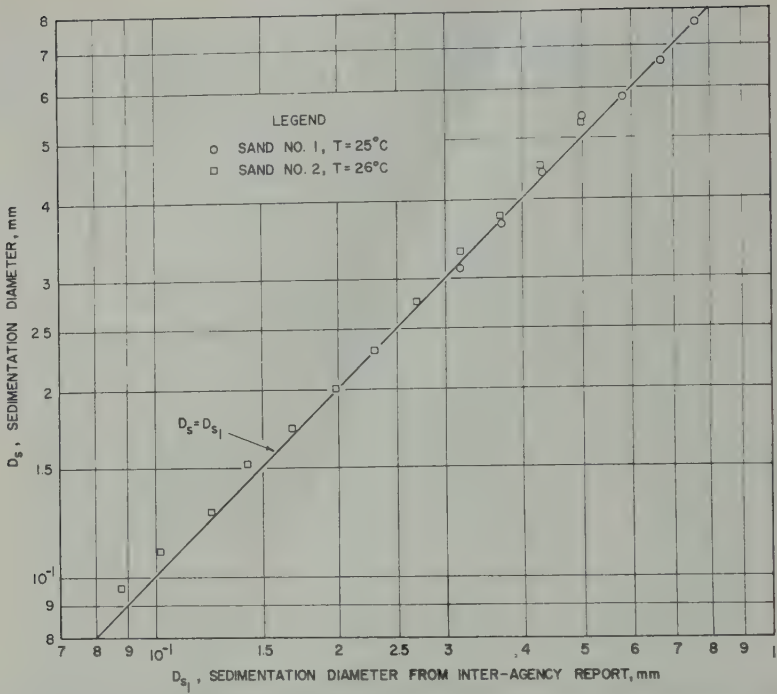


Fig. 9. Comparison of sedimentation diameters determined in this investigation and those given by the Inter-Agency Report.

funds provided by the Agricultural Research Service of the U. S. Department of Agriculture.

REFERENCES

Kennedy, John F., Stationary waves and antidunes in alluvial channels, *Rept. KH-R-2*, W. M. Keck Laboratory of Hydraulics and Water Resources, California Institute of Technology, Pasadena, California, 1961.  
Rouse, H. (editor), *Engineering Hydraulics*, John Wiley & Sons, New York, 1950.  
Otto, George H., A modified logarithmic proba-

bility graph for the interpretation of mechanical analysis of sediments, *J. Sediment. Petrol.*, 9, 329-331, 1939.  
Thomas, H. A., Jr., Frequency of minor floods, *J. Boston Soc. Civil Engrs.*, 35, 425-442, 1948.  
U. S. Inter-Agency Committee on Water Resources Subcommittee on Sedimentation, 1957, *Sedimentation fundamentals of particle size analysis*, Rept. U. S. Government Printing Office, 1957.

(Manuscript received August 28, 1961; revised October 4, 1961.)

# Head and Flow of Ground Water of Variable Density

NORBERT J. LUSCZYNSKI

*U. S. Geological Survey  
Mineola, L. I., N. Y*

**Abstract.** Fresh-water and environmental-water heads are shown to be useful in studying movement of ground water of variable density, such as in a system of fresh, diffused, and salt water. Fresh-water head at a given point in ground water of variable density is defined as the water level in a well filled with fresh water from that point to a level high enough to balance the existing pressure at the point. Fresh-water heads define hydraulic gradients along a horizontal. An environmental-water head at a given point in ground water of variable density is defined as a fresh-water head reduced by an amount corresponding to the difference of salt mass in fresh water and that in the environmental water between that point and the top of the zone of saturation. Environmental-water heads define hydraulic gradients along a vertical. Vertical and horizontal components of velocity in an anisotropic system with ground water of variable density are computed from hydraulic gradients defined by environmental-water and fresh-water heads, respectively, and from appropriate components of the permeability tensor. Equations for the component velocities are based on a particular generalized form of the Darcy equation. An equation showing a relation between the head observed in fresh water overlying diffused water and the elevation of the contact between fresh water and diffused water is given. The equation is based on the concept of environmental head. It is found to be a suitable basis for defining the specific limitations of the Ghyben-Herzberg and the Hubbert equations when they are used for fresh-diffused-salt water environments.

## INTRODUCTION

The purpose of this paper is (1) to introduce the concept of environmental-water head and to define its relation to point-water and fresh-water heads; (2) to state and illustrate equations for determining hydraulic gradients and also rates and directions of flow from environmental-water heads along the vertical and from the fresh-water heads along the horizontal in ground water of variable density; and (3) to illustrate an equation based on environmental-water heads by means of which the specific limitations of the Ghyben-Herzberg and the Hubbert equations can be defined.

The symbols are explained as they appear in the presentation. A list of all symbols used in this paper is in Appendix 1.

### 1. POINT-WATER, FRESH-WATER, AND ENVIRONMENTAL-WATER HEADS

In this section, point-water, fresh-water, and environmental-water heads are defined, and equations for determining hydraulic gradients and vector velocities by use of fresh-water and environmental-water heads are stated and illustrated.

Water at a point in ground water of variable density is called point water. Point water may be fresh, diffused, or salt. The head at any point varies with the datum and the kind of water used in the well for measuring the head.

Point-water head at a point in ground water of variable density is defined as the water level, referred to a given datum,<sup>1</sup> in a well filled sufficiently with the water of the type at the point to balance the existing pressure at the point. From this definition (Fig. 1a),

$$\rho_i H_{ip} = Z_i \rho_i + p_i / g \quad (1)$$

where

$i$  = any point in ground water of variable density.

$\rho_i$  = density of water at  $i$ .

$H_{ip}$  = point-water head at  $i$ .

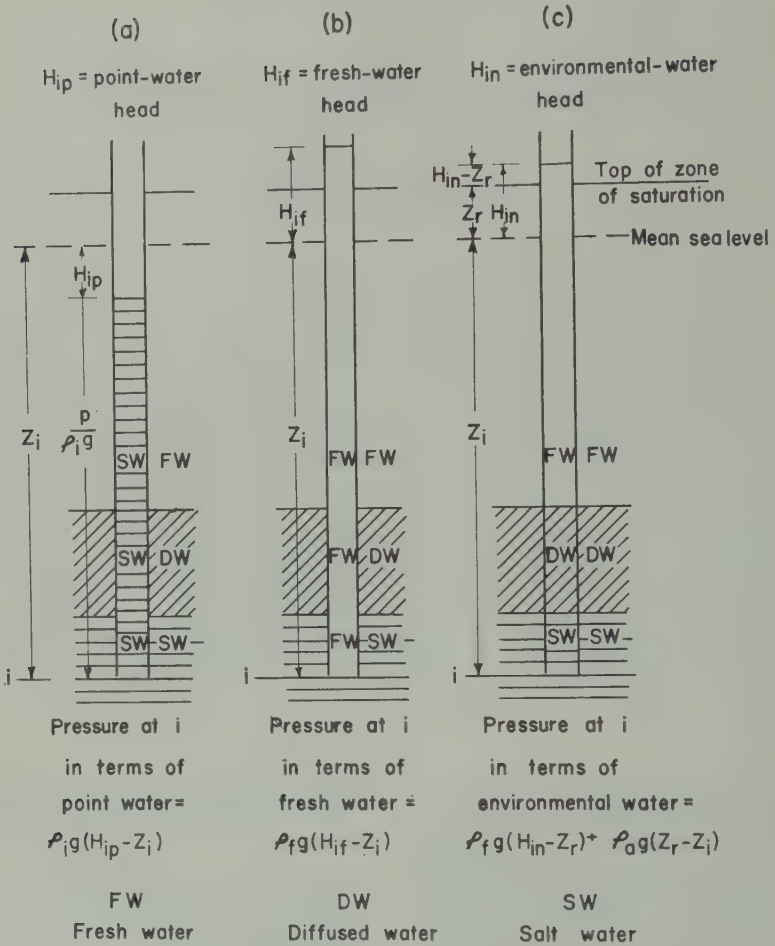
$Z_i$  = elevation of  $i$ , measured positively upward.

$p_i$  = pressure at  $i$ .

$g$  = gravitational acceleration.

The first subscript in  $H_{ip}$  refers to the point in

<sup>1</sup> All heads and elevations in this paper are referred to mean-sea-level datum.



(For other symbols, see text)

Fig. 1. Heads in ground water of variable density.

question and the second subscript signifies that the water in the well is that at the point.

Fresh-water head at any point  $i$  in ground water of variable density is defined as the water level in a well filled with fresh water from  $i$  to a level high enough to balance the existing pressure at  $i$ . The pressure at  $i$  is given by  $\rho_i g (H_{ip} - Z_i)$  when point water at  $i$  is used in the well. It is given by  $\rho_f g (H_{if} - Z_i)$  when fresh water is used (Fig. 1b). From this equality, the fresh-water head may be expressed in terms of the point-water head as

$$\rho_f H_{if} = \rho_i H_{ip} - Z_i (\rho_i - \rho_f) \tag{2}$$

where

$\rho_f$  = density of fresh water.  
 $H_{if}$  = fresh-water head at  $i$ .

Environmental water between a given  $i$  in a ground-water system and the top of zone of saturation is herein defined to be water of constant or variable density occurring in the environment along a vertical between that point and the top of the zone of saturation. Environmental-water head at a given point in ground water of variable density is defined as the fresh-water head reduced by an amount corresponding to the difference of salt mass in water and that in the environmental water between that point and the top of the zone of saturation. The reduction is occasioned

effect, by the replacement of the fresh water in the well shown in Figure 1b by the diffused water and salt water as shown in Figure 1c at depths where diffused water and salt water occur in the environment.

Environmental-water head, as determined from the equality of pressures expressed in terms of environmental water and fresh water, is

$$\rho_f H_{in} = \rho_f H_{if} - (\rho_f - \rho_a)(Z_i - Z_r) \quad (3)$$

where

$\rho_a$  = average density of water between  $Z_r$  and  $i$ , as defined by

$$\frac{1}{Z_r - Z_i} \int_{Z_i}^{Z_r} \rho \, dz.$$

$H_{in}$  = environmental-water head at  $i$ .

$Z_r$  = elevation of reference point from which the average density of water to  $i$  is determined and above which water is fresh; elevation measured positively upward.

It can also be determined from the equality of pressures expressed in terms of environmental water (Fig. 1c) and point water (Fig. 1a) as

$$\rho_f H_{in} = \rho_i H_{ip} - Z_i(\rho_i - \rho_a) - Z_r(\rho_a - \rho_f) \quad (4)$$

In (3) the relation between environmental-water head and fresh-water head is expressed. The relation between environmental-water head and point-water head is expressed in (4).

As stated,  $\rho_a$  is the average density of water between a selected reference point and the point in question. The reference point must be the top of the zone of saturation if the uppermost water body is not fresh. If the uppermost body is fresh, any reference point may be selected between the top of the zone of saturation and the first contact of fresh water with diffused water. When the reference point can be and is made coincident with the datum (mean sea level),  $Z_r = 0$ , and (3) and (4) reduce to

$$\rho_f H_{in} = \rho_f H_{if} - Z_i(\rho_f - \rho_a) \quad (3a)$$

and

$$\rho_f H_{in} = \rho_i H_{ip} - Z_i(\rho_i - \rho_a) \quad (4a)$$

In these equations,  $\rho_a$  is then the average density of water between mean sea level and point  $i$ .

The use of the contact of fresh water with the underlying diffused water as a reference point sets up (3) and (4) in a convenient form when this contact is of specific interest to the problem (see equation 9).

*Hydraulic gradients.* The gradient of (1) for any point  $i$  in ground water of variable density is

$$\nabla p_i/g + \rho_i \mathbf{k} = \nabla(\rho_i H_{ip}) - Z_i \nabla \rho_i \quad (5a)$$

where

$\nabla$  = gradient operator.

$\mathbf{k}$  = unit vector directed upward along a vertical.

Similarly, from (1) and (2) with  $H_{ip}$  eliminated, we obtain

$$\nabla p_i/g + \rho_i \mathbf{k} = \rho_f \nabla H_{if} + (\rho_i - \rho_f) \mathbf{k} \quad (5b)$$

Also from (3), keeping in mind that  $(Z_i - Z_r) \partial(\rho_a)/\partial z = (\rho_i - \rho_a)$ , we obtain

$$\begin{aligned} \rho_f \nabla H_{in} - (Z_i - Z_r) \left[ \frac{\partial(\rho_a)}{\partial x} \mathbf{i} + \frac{\partial(\rho_a)}{\partial y} \mathbf{j} \right] \\ = \rho_f \nabla H_{if} + (\rho_i - \rho_f) \mathbf{k} \end{aligned} \quad (5c)$$

where  $\mathbf{i}, \mathbf{j}$  = unit vectors normal to one another in a horizontal plane. Equations 5a to 5c represent gradients determined from point-water densities and pressures, from point-water densities and point-water heads, from fresh-water density and fresh-water heads, or from fresh-water density and environmental-water heads.

Equation 5c is of special value to this paper because of the following. Along a vertical, the left-hand side of (5c) reduces conveniently to  $\rho_f(\partial H_{in}/\partial z)$ , which is simply a product of fresh-water density and a gradient defined by environmental-water heads. Along any horizontal, the right-hand side of (5c) reduces to  $\rho_f(\partial H_{if}/\partial x)$ , which is simply a product of a fresh-water density and a gradient defined by fresh-water heads.

Because environmental-water heads define hydraulic gradients along a vertical, they are comparable along a vertical. This is evidently not the case for point-water or fresh-water heads. Also, because fresh-water heads define hydraulic gradients along a horizontal in ground water of variable density, they are comparable along a horizontal. This is not the case for point-water or environmental-water heads.

*Velocity components.* A vector velocity is the rate and direction of flow. A variation of the



Darcy equation expressing vector velocity for steady flow at a point in a ground-water system is

$$\mathbf{q}_i = -\frac{k_i}{\mu_i} g \left[ \frac{\nabla p_i}{g} + \rho_i \mathbf{k} \right] \quad (6)$$

where

$\mathbf{q}$  = vector velocity at  $i$ .

$k_i$  = permeability of the medium at  $i$ .

$\mu_i$  = dynamic viscosity at  $i$ .

The proper value of permeability depends on the medium. In an isotropic medium the permeability is constant in all directions. In an anisotropic medium the permeability varies with direction and is a tensor. The permeability tensor has three principal directional permeabilities according to the tensor theory of permeability substantiated by *Scheidegger* [1957, pp. 47-66]. He summarized the results of studies on directional permeabilities in anisotropic media made by him and other investigators. He referred to Ferrandon and Litwiniszyn, who developed more-or-less identical theories on the permeability tensor and on flow through anisotropic media. The theories state in effect that the vector velocity may be computed from (6) using a symmetric permeability tensor with components  $K_{rs}$ .

For the bracketed term in (6), any one of its equivalents in (5a-c) may be used with components  $K_{rs}$  of the permeability tensor to define velocity components in ground water of variable density. The use of (5c) in (6) is suited for the definition of specific component velocities from environmental-water and fresh-water heads as indicated in the two following paragraphs.

For the case of random orientation of coordinates in relation to the axes of principal directional permeabilities, components of velocity in (6) may be expressed in terms of the components  $K_{rs}$  of the permeability tensor and in terms of gradients of environmental-water and fresh-water heads from (5c), as follows:

$$\begin{aligned} v_x = & -K_{11} \frac{g}{\mu_i} \left[ \rho_f \frac{\partial H_{if}}{\partial x} \right] \\ & - K_{12} \frac{g}{\mu_i} \left[ \rho_f \frac{\partial H_{if}}{\partial y} \right] \\ & - K_{13} \frac{g}{\mu_i} \left[ \rho_f \frac{\partial H_{in}}{\partial z} \right] \end{aligned} \quad (7a)$$

$$\begin{aligned} v_y = & -K_{21} \frac{g}{\mu_i} \left[ \rho_f \frac{\partial H_{if}}{\partial x} \right] \\ & - K_{22} \frac{g}{\mu_i} \left[ \rho_f \frac{\partial H_{if}}{\partial y} \right] \\ & - K_{23} \frac{g}{\mu_i} \left[ \rho_f \frac{\partial H_{in}}{\partial z} \right] \end{aligned}$$

$$\begin{aligned} v_z = & -K_{31} \frac{g}{\mu_i} \left[ \rho_f \frac{\partial H_{if}}{\partial x} \right] \\ & - K_{32} \frac{g}{\mu_i} \left[ \rho_f \frac{\partial H_{if}}{\partial y} \right] \\ & - K_{33} \frac{g}{\mu_i} \left[ \rho_f \frac{\partial H_{in}}{\partial z} \right] \end{aligned}$$

where  $v_x$ ,  $v_y$ , and  $v_z$  are velocity components along the  $x$ ,  $y$ , and  $z$  coordinates, respectively, and where the  $K_{rs}$  components are as indicated in Appendix 2.

When the  $x$  and  $y$  coordinates are horizontal and the  $z$  coordinate is vertical, and when the  $x$ ,  $y$ , and  $z$  coordinates coincide with the axes of the principal directional permeabilities,

$$v_x = -K_{11} \frac{g}{\mu_i} \left[ \rho_f \frac{\partial H_{if}}{\partial x} \right]$$

$$v_y = -K_{22} \frac{g}{\mu_i} \left[ \rho_f \frac{\partial H_{if}}{\partial y} \right]$$

and

$$v_z = -K_{33} \frac{g}{\mu_i} \left[ \rho_f \frac{\partial H_{in}}{\partial z} \right]$$

where  $K_{11}$ ,  $K_{22}$ ,  $K_{33}$  are, in this case, the principal directional permeabilities in the  $x$ ,  $y$ ,  $z$  directions.

Thus, in an anisotropic medium with horizontal principal permeabilities, the components of velocity in the horizontal directions corresponding to the principal permeabilities may be computed from (8a) and (8b) by using the appropriate directional permeability, gravity, viscosity of water, density of fresh water, and the hydraulic gradient defined by fresh-water heads. The vertical component of velocity may be computed from (8c) by using the principal directional permeability along the vertical, gravity, viscosity of water, density of fresh water, and the hydraulic gradient defined by environmental-water heads.

Because the permeability in an anisotropic

medium is a tensor, the direction of flow is usually not parallel to the hydraulic gradient. The direction of flow is defined by the resultant of velocity components defined by (7a-c) or (8a-c).

*Example.* The use of environmental-water heads and fresh-water heads for defining hydraulic gradients and velocities at points in an aquifer having fresh, diffused, and salt water is to be illustrated by data furnished through the courtesy of the Government Institute of Water Supply in the Netherlands. The Institute supplied information on water levels and chloride concentrations for July 1957 at suites of wells, each screened at a different depth at each of seven observation and sampling stations in the dune area near The Hague (Fig. 2). The stations are in the general vicinity of infiltration canals and ponds by means of which imported river water is recharged to the ground-water system. Also, ground water is pumped from several nearby areas. The geologic environment consists of dune sand above sea level, a clay layer at about sea level, fine to coarse sand zones to depths of about 50 m below sea level, and then fine and silty sand interspersed with layers and lenses of clay below sea level to depths of about 100 m below sea level. These deposits are anisotropic and essentially horizontal.

The data are used in this paper only to illustrate the use of environmental-water and fresh-water heads for determining hydraulic gradients and velocities in water of variable density. Actually, the computed heads, gradients, directions, and velocities may not be precise because (a) the point-water heads and chlorides were not observed on the same day in July 1957, (b) heads are reportedly accurate only to the nearest 0.02 m, and (c) densities were computed on the basis of 1.025 g/ml for a water with 18,000 ppm chlorides. Two-dimensional steady-state flow was also assumed.

Point-water, fresh-water, and environmental-water heads are given in Figure 2. Fresh-water heads were determined by (2) and environmental-water heads by (3) or (3a).

Point-water heads in fresh water are also environmental-water heads and as such compare directly with environmental-water heads in the diffused water along the verticals. The environmental-water heads at the seven stations indicate components of flow upward at some points and

downward at other points in the fresh water as well as in the diffused water.

Point-water heads in fresh water are also fresh-water heads, and as such compare with fresh-water heads in the diffused water along the horizontals. Fresh-water heads at the seven stations indicate components of flow in a landward direction at most of the points in the fresh water as well as in the diffused water.

Consider the point at the -54-m elevation at station MN. A hydraulic gradient of about 0.001 in favor of a downward component of flow is computed from the tangent at the point in question to the environmental-water head vs. depth curve. Also a gradient of about 0.0015 in favor of a landward component of flow is computed from the tangent at the point in question to the fresh-water head vs. distance curve. (A fresh-water head of 1.12 m at the -54-m elevation at station N was used for this purpose. It was determined by (4a) from an environmental-water head interpolated between that of 1.03 m at the -47-m elevation and 1.04 m at the -56-m elevation.)

If we compare the direction of flow with that of the resultant hydraulic gradient at the -54-m elevation at station MN and assume that the horizontal and vertical permeabilities at the point are the same as the principal directional permeabilities, then the direction flow may be determined from the horizontal and vertical velocity components computed by (8a) and (8c), respectively, by using the horizontal and vertical permeabilities and the gradients defined by fresh-water and environmental-water heads. For an assumed ratio of horizontal to vertical permeability of 5, the direction of flow at the -54-m elevation at station MN would be landward and downward at an angle of 8° from the horizontal. For an assumed ratio of 10, the direction would be 4° from the horizontal. If these ratios were of the right order of magnitude, the direction of flow at the point would be landward and essentially horizontal. In comparison, the resultant hydraulic gradient was landward and downward at an angle of about 34° from the horizontal.

The horizontal permeability at the -54-m elevation is about 25 millidarcys (1 millidarcy = 0.001 cm/sec). This is estimated from the range of values furnished by the Institute. On the basis of this permeability, a horizontal gradient



of 0.0015, and a porosity of  $\frac{1}{3}$ , the component of actual velocity<sup>2</sup> along the horizontal would be landward at about 9.7 cm/day (about 0.3 ft/day) at the -54-m elevation in station MN. On the basis of a horizontal to vertical ratio of 5 to 10, a vertical gradient of 0.001, and a porosity of  $\frac{1}{3}$ , the component of actual velocity<sup>3</sup> along the vertical would be downward at about 1.3 to 0.6+ cm/day (about 0.04 to 0.02 ft/day).

## 2. EQUATION 9 VS. GHYBEN-HERZBERG AND HUBBERT EQUATIONS

In this section an equation based on the concept of environmental-water head is used for defining the specific limitations of the Ghyben-Herzberg and Hubbert equations when they are used for fresh-diffused-salt water environments.

Let  $h$  denote the difference between the environmental-water head at any point 1 in fresh water and that at any point 2 in salt water along a vertical in a ground-water system having fresh water, diffused water, and salt water (top to bottom). Actually  $h$  represents the head loss due to vertical velocities between points 1 and 2. From (4), written for points 1 and 2, we get

$$\rho_1 H_{1p} = \rho_1 h + \rho_2 H_{2p} - Z_2(\rho_2 - \rho_a) - Z_d(\rho_a - \rho_1) \quad (9)$$

where  $h = H_{1n} - H_{2n} = H_{1p} - H_{2n}$  and where  $Z_d$  is the elevation of the contact of fresh water with diffused water and also of the reference point from which  $\rho_a$  is computed. A derivation of (9) from the Darcy equation is given in Appendix 3.

Equation 9 may be interpreted as a relation between  $H_{1p}$ , a point-water or fresh-water head in fresh water, and  $Z_d$ , the elevation of the contact of fresh water with diffused water. The relation includes a term which accounts for the difference in environmental-water head between points 1 and 2, a term which accounts for the point-water head in salt water, and two terms which account for the variable density in the zone of diffusion.

Using the symbols of this paper, the Ghyben-Herzberg equation [Ghyben, 1889; Herzberg, 1901] is

$$\rho_1 H_{1p} = -Z_d'(\rho_2 - \rho_1) \quad (10)$$

where  $H_{1p}$  is the water table and  $Z_d'$  is an approximate depth to diffused water. Thus (10) is evidently a special case of (9) in which  $h = 0$  and  $\rho_a = \rho_2$ . Then  $Z_d = Z_d'$ . Therefore the depth to diffused water computed by the Ghyben-Herzberg equation is correct or approximately correct when (a) the difference in environmental-water head between points 1 and 2 is zero or relatively small, (b) the point-water head in salt water is zero or relatively small, and (c) the zone of diffusion is of zero or relatively small thickness. If only the (a) and (b) conditions are met,  $Z_d'$  is a depth to an indefinite point in the zone of diffusion.

In symbols of this paper, Hubbert's [1940] equation 189 is

$$\rho_1 H_{1p} = \rho_2 H_{2p} - Z_d''(\rho_2 - \rho_1) \quad (11)$$

This equation expresses the correct relation between  $Z_d''$ , the contact or interface between two immiscible liquids  $\rho_1$  and  $\rho_2$  (for  $\rho_2 > \rho_1$ ), and  $H_{1p}$  and  $H_{2p}$  on the  $\rho_1$ -side and  $\rho_2$ -side, respectively, of a given point on the interface of the two liquids. Equation 11 would define the contact between fresh water and salt water with a sharp interface. It was used by Perlmutter, Geraghty, and Upson [1959] for determining an elevation of such a theoretical contact of fresh water with salt water. The computed elevation was shown to be within the diffused water in an actual fresh-diffused-salt water environment. For the computations, the heads observed at points some distance apart in a vertical were used; one point was in fresh water and the other in salt water. Equation 11 is valid when the head loss due to vertical velocities between the points of observation is negligible. Then at least an approximate elevation of the theoretical contact of fresh water with salt water is determined.

The head loss between any two points in a vertical is actually the difference in environmental heads between the two points. It is defined by the  $\rho_1 h$  term in (9). When not negligible, this term should be included with (11) as in the following:

$$\rho_1 H_{1p} = \rho_1 h + \rho_2 H_{2p} - Z_d'''(\rho_2 - \rho_1) \quad (12)$$

Equation 12 is then a special case of (9) in which  $\rho_a = \rho_2$  and  $Z_d = Z_d'''$ . It may be interpreted as a relation between  $H_{1p}$ , a point-water head in fresh water, and  $Z_d'''$ , the actual eleva-

<sup>2</sup>  $v_x$  from (8a) divided by the porosity.

<sup>3</sup>  $v_z$  from (8c) divided by the porosity.



tion of the theoretical contact between fresh water and salt water.

*Examples.* Compare the  $Z_d$  elevations computed by (10-12) using the following data for two selected points at station N (Fig. 2) near The Hague in the Netherlands:

$$\rho_1 = 1.000 \text{ g/ml}$$

$$\rho_2 = 1.0205 \text{ g/ml}$$

$$H_{1p} = 1.09 \text{ m}$$

$$H_{2p} = -.21 \text{ m}$$

$$Z_1 = -17 \text{ m}$$

$$Z_2 = -80 \text{ m}$$

Sufficient information was obtained at six additional points in the vertical (Fig. 2) to define the contact between fresh water and diffused water at  $-37 \text{ m}$  and to compute  $h = +0.07 \text{ m}$  between points 1 and 2.

$Z_d' = -53 \text{ m}$  was computed by the Ghyben-Herzberg equation (10),  $Z_d'' = -64 \text{ m}$  by the Hubbert equation (11), and  $Z_d''' = -60 \text{ m}$  by (12). The difference of  $-11 \text{ m}$  between  $Z_d'$  and  $Z_d''$  is attributed to the term  $\rho_2 H_{2p}$ ; the difference of  $+4 \text{ m}$  between  $Z_d''$  and  $Z_d'''$  is due to the  $+0.07\text{-m}$  difference in environmental heads at points 1 and 2. Because the corrections in this case are small, the Ghyben-Herzberg and Hubbert equations give elevations within the zone of diffusion. Also these elevations are not appreciably different from the actual elevation of the theoretical contact,  $Z_d'''$ , between fresh water and salt water. The theoretical contact is  $23 \text{ m}$  below the contact of fresh water with diffused water.

The  $H_{1p}$  at the  $-17\text{-m}$  elevation was selected arbitrarily for the above. If, instead, the  $H_{1p} = -1.41 \text{ m}$  at the  $-2\text{-m}$  elevation (Fig. 2) is selected, then  $Z_d' = -69 \text{ m}$  from (1),  $Z_d'' = -79 \text{ m}$  from (11), and  $Z_d''' = -60 \text{ m}$  from (12). In this case  $Z_d'''$  is the same as computed previously. (In the computation,  $h = +0.39 \text{ m}$  was used.) However, the  $Z_d'$  by the Ghyben-Herzberg equation is  $9 \text{ m}$  lower than  $Z_d'''$ , and the  $Z_d''$  by the Hubbert equation is practically at point 2 in salt water.

Compare also the depths  $Z_d$ , computed from (10-12) using the following data obtained in October 1958 at two wells screened at two

different depths in the same vertical at a in Cedarhurst, L. I., N. Y.:

$$\rho_1 = 0.999 + \text{g/ml}$$

$$\rho_2 = 1.020 + \text{g/ml}$$

$$H_{1p} = 3.57 \text{ ft}$$

$$H_{2p} = -4.72 \text{ ft}$$

$$Z_1 = -167 \text{ ft}$$

$$Z_2 = -520 \text{ ft}$$

The average density at Cedarhurst in the zone of diffusion between the  $-320\text{-ft}$  and  $-490\text{-ft}$  elevations is computed to be about  $1.010 \text{ g/ml}$ . On this basis,  $h = -0.47 \text{ ft}$  is determined from (9).

$Z_d' = -170 \text{ ft}$  is obtained by the Ghyben-Herzberg equation,  $Z_d'' = -399 \text{ ft}$  by the Hubbert equation, and  $Z_d''' = -421 \text{ ft}$  by (12). The difference of  $-229 \text{ ft}$  between  $Z_d'$  and  $Z_d''$  is the result of the  $\rho_2 H_{2p}$  term. In this case, the Ghyben-Herzberg equation gives an elevation which is not even in the zone of diffusion and as much as  $150 \text{ ft}$  above it. The Hubbert equation gives a depth  $22 \text{ ft}$  shallower than the actual elevation of the theoretical contact between fresh water and salt water. The  $22 \text{ ft}$  difference indicates that every  $0.1\text{-ft}$  difference in environmental-water head between points 1 and 2 makes a difference of nearly  $5 \text{ ft}$  between the depths computed by the Hubbert equation and those computed by (12).

The theoretical contact of fresh water with salt water at Cedarhurst is about  $101 \text{ ft}$  below the contact of fresh water with diffused water as defined by electrical log to be at  $-320 \text{ ft}$ .

*Elevations computed by equations 9 to 12.*  $Z_d$  in (9) is the elevation of the contact of fresh water with diffused water. The relation between point-water head in fresh water and the depth to this contact is not simple and direct; it depends on several variables. However, the elevation of the contact can be computed if there is a suitable basis for estimating  $h$ ,  $\rho_1$ , and  $\rho_2$  for a given  $Z_2$  and  $\rho_2$ .

$Z_d'''$  in (12) is the elevation to the theoretical contact between fresh water and salt water. It can be computed from a point-water head in fresh water if there is a suitable basis for estimating  $h$  and  $H_{2p}$  for a given  $Z_2$  and  $\rho_2$ .

As shown, the  $Z_d'$  computed by the Ghyben-

erzberg equation may not necessarily be an elevation of a point in the zone of diffusion. Also as shown, the  $Z_d''$  computed by the Hubbert equation may not necessarily be an elevation of a point in the zone of diffusion. However, the Hyben-Herzberg and Hubbert equations can yield elevations of points in the zone of diffusion under conditions approximating those stated for (0) and (11).

#### APPENDIX 1. Symbols Used in This Paper

$g$  = gravitational acceleration.  
 $\mathbf{g}$  = gravitational acceleration vector.  
 $H_p, H_{if}, H_{in}$  = point-water head, fresh-water head, and environmental-water head at  $i$ , respectively.

$Z_r$  = elevation of reference point, measured positively upward.

$\rho_i$  = density of water at  $i$ .

$\rho_a$  = average density of water between depths  $Z_r$  and  $i$ .

$\rho_f$  = density of fresh water.

$\mu_i$  = viscosity of water at  $i$ .

$\partial h_{if}/\partial x$  = hydraulic gradient at  $i$  in  $x$  direction (defined by fresh water heads).

$\partial h_{if}/\partial y$  = hydraulic gradient at  $i$  in  $y$  direction (defined by fresh-water heads).

$\partial h_{in}/\partial z$  = hydraulic gradient at  $i$  and  $z$  direction (defined by environmental-water heads).

$\nabla$  = gradient operator.

#### APPENDIX 2. $K_r$ , Components of Permeability Tensor

$$\left[ \begin{array}{l} K_{11} = \left\{ \begin{array}{l} K_1 l_1 l_1 \\ + K_2 l_2 l_2 \\ + K_3 l_3 l_3 \end{array} \right\} \quad K_{12} = \left\{ \begin{array}{l} K_1 l_1 m_1 \\ + K_2 l_2 m_2 \\ + K_3 l_3 m_3 \end{array} \right\} \quad K_{13} = \left\{ \begin{array}{l} K_1 l_1 n_1 \\ + K_2 l_2 n_2 \\ + K_3 l_3 n_3 \end{array} \right\} \\ K_{21} = \left\{ \begin{array}{l} K_1 l_1 m_1 \\ + K_2 l_2 m_2 \\ + K_3 l_3 m_3 \end{array} \right\} \quad K_{22} = \left\{ \begin{array}{l} K_1 m_1 m_1 \\ + K_2 m_2 m_2 \\ + K_3 m_3 m_3 \end{array} \right\} \quad K_{23} = \left\{ \begin{array}{l} K_1 m_1 n_1 \\ + K_2 m_2 n_2 \\ + K_3 m_3 n_3 \end{array} \right\} \\ K_{31} = \left\{ \begin{array}{l} K_1 l_1 n_1 \\ + K_2 l_2 n_2 \\ + K_3 l_3 n_3 \end{array} \right\} \quad K_{32} = \left\{ \begin{array}{l} K_1 m_1 n_1 \\ + K_2 m_2 n_2 \\ + K_3 m_3 n_3 \end{array} \right\} \quad K_{33} = \left\{ \begin{array}{l} K_1 n_1 n_1 \\ + K_2 n_2 n_2 \\ + K_3 n_3 n_3 \end{array} \right\} \end{array} \right]$$

$h$  = difference in environmental-water heads at point 1 in fresh water and point 2 in diffused or salt water.

$i$  = point in variable density ground water;  
 $i = 1$ , point in fresh water;  $i = 2$ , point in diffused or salt water.

$\mathbf{i}$  = unit vector directed along a horizontal.

$k$  = permeability of the medium at  $i$ .

$\mathbf{j}$  = unit vector directed upward along a vertical.

$p$  = pressure at  $i$ .

$\mathbf{v}$  = vector velocity at  $i$ .

$v_x, v_y, v_z$  = component of velocity along axis  $x, y, z$ , respectively.

$Z_d', Z_d'', Z_d'''$  = elevation to diffused water in (9-12), respectively.

$z$  = elevation of  $i$ , measured positively upward.

where

$K_1, K_2, K_3$  = principal directional permeabilities.

$l_1, m_1, n_1$  = directional cosines between  $K_1$  and  $x, y, z$  coordinates.

$l_2, m_2, n_2$  = directional cosines between  $K_2$  and  $x, y, z$  coordinates.

$l_3, m_3, n_3$  = directional cosines between  $K_3$  and  $x, y, z$  coordinates.

#### APPENDIX 3

The introduction and use of the 'environmental-water head' is a valid interpretation of the Darcy equation. This was indicated by Professor R. Skalak, who reviewed the early draft of the paper. The following is an excerpt from his written communication:

The generalized Darcy equation in vector form is

$$\mathbf{q} = -\frac{k}{\mu}(\nabla p - \rho_i \mathbf{g}) \quad (\text{A})$$

The  $z$  component of this equation may be written as

$$v \frac{\mu}{k \rho_1 g} = -\frac{1}{\rho_1 g} \left( \frac{\partial p}{\partial z} + \rho_i g \right) \quad (\text{B})$$

where

- $v$  = vertical component of velocity.
- $\mu$  = viscosity.
- $k$  = permeability.
- $\mathbf{g}$  = gravitational acceleration vector.
- $\rho_1$  = density of fresh water.
- $p$  = pressure.
- $z$  = vertical coordinate, plus upwards.
- $\rho_i$  = density of fluid at any point.

It appears that the right-hand side of (B) is the same as the 'gradient of environmental head' that you have defined. The left-hand side is the head loss gradient in terms of velocity and is essentially the gradient of  $h$  in your equation 9. To show the equivalence of the above to your (9), integrate (B) from point 2 to point 1.

$$\int_{z_2}^{z_1} v \frac{\mu}{k \rho_1 g} dz = -\int_{z_2}^{z_1} \frac{1}{\rho_1 g} \left( \frac{\partial p}{\partial z} + \rho_i g \right) dz \quad (\text{C})$$

or

$$\int_{z_2}^{z_1} \frac{v \mu}{k g} dz = -\frac{1}{g} [p_1 - p_2] - \int_{z_2}^{z_1} \rho_i dz - \int_{z_2}^{z_1} \rho_i dz \quad (\text{D})$$

Now define  $h$  to be the head loss due to vertical velocities, i.e., such that  $-\rho_1 h$  is equal to the left-hand side of (D). Further define  $\rho_a$  such that

$$\int_{z_2}^{z_1} \rho_i dz = \rho_a (z_1 - z_2) \quad (\text{E})$$

This is the same as your  $\rho_a$ . Further note that

$$p_1 = \rho_1 g (H_{1v} - z_1)$$

and

$$p_2 = \rho_2 g (H_{2v} - z_2) \quad (\text{F})$$

Substituting in (D):

$$-\rho_1 h = -\rho_1 (H_{1v} - z_1) + \rho_2 (H_{2v} - z_2) - \rho_a (z_1 - z_2) - \rho_1 (z_1 - z_2)$$

The right-hand side of (G) is  $(-\rho_1 H_{1v} + \rho_2 H_{2v})$  where  $H_{1v}$  and  $H_{2v}$  are the environmental head defined as you have suggested. Equation (G) may be written as

$$\rho_1 H_{1v} = \rho_1 h + \rho_2 H_{2v} - z_2 (\rho_2 - \rho_a) - z_1 (\rho_a - \rho_1)$$

which is exactly your (9), when  $Z_r = Z_d$ .

**Acknowledgments.** This paper is one of the products of an investigation of salt-water encroachment in Long Island, New York. The investigation now in progress is being conducted by the Geological Survey in cooperation with the Nassau County Department of Public Works and the New York State Water Resources Commission.

I gratefully acknowledge the benefit of his comments and suggestions made by Professor Skalak, Professor H. R. Henry, and W. V. Luszczynski of the U. S. Geological Survey regarding technical material and the manuscript. I express appreciation for data furnished by the Government Institute of Water Supply in the Netherlands.

Publication authorized by the Director, Geological Survey.

## REFERENCES

- Badon Ghyben, W., Nota in verband met de genomen put boring nabij Amsterdam, *Konink. Inst. Inq. Tydschr.*, The Hague, 8-22, 1889.
- Herzberg, A., Die Wasserversorgung einiger seebäder, *J. Gasbeleucht.*, 44, Munich, 81 and 842-844, 1901.
- Hubbert, M. K., The theory of ground-water motion, *J. Geol.*, 48 (8), 864, 1940.
- Perlmutter, N. M., J. J. Geraghty, and Upson, The relation between fresh and water in southern Nassau and southern Queens Counties, Long Island, New York, *Geol.*, 54 (3), 416-435, 1959.
- Scheidegger, A. E., *The Physics of Flow through Porous Media*, The Macmillan Company, New York, pp. 47-66, 1957.

(Manuscript received March 6, 1961; revised August 11, 1961.)

## On the Theory of Leaky Aquifers

ROGER J. M. DE WIEST

*Department of Geological Engineering, Princeton University  
Princeton, New Jersey*

**Abstract.** Potential distribution is found for two cases of unsteady flow in a finite leaky aquifer, where the boundary condition at the contour of influence is time dependent and where the initial condition is one of different head in the main aquifer and in the semiconfining and quasi-impervious layer overlying it. The cases considered are a well pumped at a constant discharge and a flowing well at constant drawdown.

### INTRODUCTION

The principle of leakage into and from aquifers had been recognized some time before, but it remained for a few Dutch engineers, in the early 1880's, to formulate the problem analytically [Jacob, 1946]. This formulation, in its simplest form, was a basic contribution, but for awhile seemed that it would not attract the attention it deserved. In 1946, C. E. Jacob started his investigations of the case. In a remarkable series of contributions he and his collaborator M. S. Hantush developed the theory of the leaky aquifer as it is known today [Hantush, 1960]. The first important Russian contribution to the study of leaky aquifers seems to come from M. M. Mjatiev, who analyzed the interaction of porous strata separated by semiconfining beds [Polubarinova-Kotchikina, 1952]. These semiconfining and quasi-impervious beds are sometimes called aquicludes. Mjatiev anticipated that the discharge from one of the layers must have an influence upon the variation of the head in the other layers. He set up a system of two partial differential equations for the problem of a well penetrating two aquifers confined by three aquicludes in which the head, on the average, remains constant. Similar problems, but extended to the unsteady state and to the inclusion of the storage effect of the semipervious confining layers, have been considered by Hantush in his modified theory of leaky aquifers [Hantush, 1960].

An important part of Hantush's work deals with the study of unsteady-state phenomena in confined flow, where the occurrence of the storage coefficient  $S$  and the explicit time derivative in the differential equation are responsible for

significant transients. In cases in which the compressibility is negligible, the differential equation of confined flow can be reduced to Laplace's equation, and the time entering the boundary conditions must be considered as a parameter rather than as an independent variable. Although unsteady unconfined incompressible flow also follows Laplace's equation and occurs with negligible compressibility of the porous medium, significant transients take place because of the disturbance of the free surface [De Wiest, 1960].

The present paper is based on the hydraulic theory of aquifers and the assumption that the horizontal velocity components practically do not change with height, so that their average value over the thickness of the layer may be used. Furthermore, the assumptions made by Jacob and Hantush about the uniformity of thickness, of permeability, of compressibility, of leakage through the semiconfining bed, and of refraction of streamlines in the aquifer are also observed here.

The paper deals with two cases of unsteady flow in finite leaky aquifers when the boundary conditions are time dependent. It was motivated by the fact that the homogeneous boundary conditions of drawdown that characterize the available solutions could be relaxed in two ways. First, the initial condition of zero drawdown everywhere in the flow system can be replaced by one of constant nonzero drawdown. Second, the boundary condition of zero drawdown at the contour of influence can be replaced by one of time-dependent drawdown. These relaxations are sometimes necessary for field conditions. It is not uncommon, for example, for substantial leakage to take place before a pump-



ing test is run. On the other hand, it may happen that one has to investigate the replenishment by leakage of an aquifer that is tapped by several wells. In general, as in the case of a municipal well system, it will not be possible to shut off all the wells except one and run a pumping test on it. But it may be possible to select a well, to measure the fluctuation of available head at a certain contour of influence, and to change the pumping pattern of the surrounding wells until more or less radial flow to the test well is obtained.

The first relaxation can be deduced from Hantush's modified theory. The second one, in principle, can be taken care of by the use of Duhamel's integral. It is well known that a solution  $V(x, y, z, t)$  of Laplace's equation in a domain along which boundary the condition  $V = F(t) = 1$  exists can be transformed into a solution  $U(x, y, z, t)$  for the same problem, but with boundary condition  $V = F(t)$ , by the integral

$$U(x, y, z, t) = \int_0^t F(t - \tau) V_1(x, y, z, \tau) d\tau$$

Reference should also be made to the use of the Green's function in obtaining solutions for systems with variable initial and boundary conditions [Hantush and Jacob, 1955]. The non-steady Green's function for circular aquifers can be obtained from solutions presented by the same authors [Hantush and Jacob, 1960].

A direct solution can also be obtained by the use of the Laplace transform, a method particu-

larly suited for time-dependent boundary conditions, although the problem of taking the inverse transform may be difficult.

In the case of finite aquifers, however, it is simpler to use the method of variation of parameters. This will be illustrated for two different cases. The method works equally well for infinite aquifers, but it would lead directly to application of the Fourier integral and hence to Fourier transforms. It seems therefore that, for infinite aquifers, little can be gained by this method over the use of the Laplace transform.

### THEORY

The differential equation for the piezometric head in the case of radial flow of water to a well in a leaky elastic artesian aquifer can be written as [Jacob, 1946; Hantush, 1956]

$$\begin{aligned} (\partial^2 h / \partial r^2) + (1/r)(\partial h / \partial r) \\ = (1/a^2)(\partial h / \partial t) + (1/B^2)(h - h_c) \end{aligned}$$

where  $h(r, t)$  is the piezometric head at a distance  $r$  from the start of flow and at a point in the region of flow at a distance  $r$  from the axis of the well;  $a^2 = T/S$ ;  $S$  is the storage coefficient;  $T = Km$  is the transmissivity coefficient;  $m$  and  $m'$  (Fig. 1) are, respectively, the hydraulic conductivities and the thicknesses of the artesian aquifer and its semiconfining bed or aquiclude;  $h_c$  is the average piezometric head in the confining bed. The change of head in the aquiclude is very slow compared with the change of head in the main aquifer, and, in first approximation,  $h_c$  can be taken as the hydraulic head

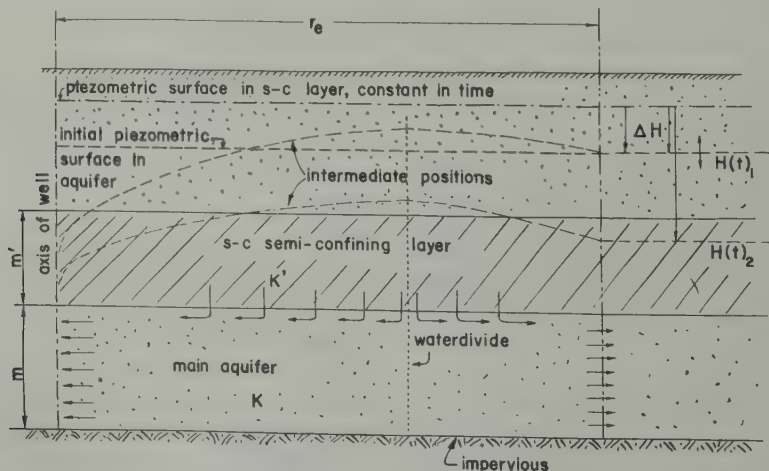


Fig. 1. Radial flow in a leaky artesian aquifer.

the top of the aquiclude;  $K'/m' = T/B^2$  is the permeance; see *Hantush and Jacob* [1955] and *Hantush* [1956] for the definition of these terms.

If one defines the drawdown  $s = h_c - h$ , then (1) can be written in the form

$$\frac{\partial^2 s}{\partial r^2} + (1/r)(\partial s / \partial r) = (1/a^2)(\partial s / \partial t) + (1/B^2)s \quad (2)$$

The drawdown  $s$  as defined in this paper is different from that defined by *Hantush and Jacob*, say  $s'$ . We have  $s = s' + \Delta H$ , where  $\Delta H = h_c - H_0$ ;  $H_0$  is the initial piezometric head. In terms of the drawdown  $s'$ , equation 2 can be written as

$$\frac{\partial^2 s'}{\partial r^2} + \frac{1}{r} \frac{\partial s'}{\partial r} = \frac{1}{a^2} \frac{\partial s'}{\partial t} + \frac{s'}{B^2} + \frac{\Delta H}{B^2} \quad (2')$$

*Finite leaky aquifer. Well pumped at constant discharge  $Q$ .* For an aquifer of radius of influence  $r_e$ , the above equations will be solved for the initial condition

$$s(r, 0) = h_c - H_0 = \Delta H \quad (3)$$

and the boundary conditions

$$s(r_e, t) = h_c - H_1(t) = H(t) \quad (4)$$

and

$$\lim_{r \rightarrow 0} r(\partial s / \partial r) = -Q/2\pi T \quad (5)$$

where  $H_0$  is the head in the aquifer at  $t = 0$ ,  $s_1(t)$  and  $H(t)$  are arbitrary functions of  $t$ . *Hantush and Jacob* [1946] solved the problem for the initial condition  $s(r, 0) = 0$  and the boundary conditions  $s(r_e, t) = 0$  and (5) in the form given above. To solve the problem, use is made herein of the method of variation of parameters. Unlike separation of variables, used by *Jacob*, this procedure does not require the knowledge of the steady-state solution;  $H(t)$  in (4) may be such that no steady-state solution develops. It is a particularly elegant method when the boundary conditions are not homogeneous and is similar to the Lagrange method for the solution of inhomogeneous ordinary differential equations. Since it may be less known to hydrologists than the method of separation of variables, it will be outlined step by step.

If the boundary condition at  $r = r_e$  were homogeneous, i.e., if  $s(r_e, t) = 0$ , then separation of variables applied to (2) would lead to the

Bessel function of order zero,  $J_0(x_n r/r_e)$  as a factor of the solution, where  $x_n$ , ( $n = 1, 2, 3, \dots$ ) are the roots of  $J_0(x) = 0$ . For simplicity of notation,  $J_0(x_n r/r_e)$  taken at  $r = r_e$  will be abbreviated as  $J_0(r_e) = 0$ . Since  $J_0$  is a fundamental solution of the homogeneous problem, one tries a Fourier-Bessel series solution in the present case:

$$s(r, t) = \sum_{n=1}^{\infty} A_n(t) J_0(x_n r/r_e) \quad (6)$$

Then

$$\begin{aligned} A_n(t) &= \frac{\int_0^{r_e} r s J_0(x_n r/r_e) dr}{\int_0^{r_e} r J_0^2(x_n r/r_e) dr} \\ &= P \int_0^{r_e} r s J_0(x_n r/r_e) dr \quad (7) \end{aligned}$$

where  $P = 2/r_e^2 J_1^2(x_n)$ . Differentiation of  $A_n(t)$  and use of (2) yields

$$\begin{aligned} dA_n/dt &= Pa^2 \int_0^{r_e} r [(\partial^2 s / \partial r^2) \\ &\quad + (1/r)(\partial s / \partial r) - (1/B^2)s] J_0(x_n r/r_e) dr \end{aligned}$$

This expression can be simplified by integration and subsequent insertion of the boundary conditions (4) and (5). Then

$$\begin{aligned} dA_n/dt &= Pa^2 \left\{ Q/2\pi T - H(t)r_e J_0'(x_n) \right. \\ &\quad \left. + \int_0^{r_e} s [\partial(r J_0') / \partial r] dr - (1/B^2) \int_0^{r_e} sr J_0 dr \right\} \quad (8) \end{aligned}$$

By use of the Bessel property  $J_0'(x_n) = -(x_n/r_e)J_1(x_n)$  and

$$\int_0^{r_e} s [\partial(r J_0') / \partial r] dr = -(x_n/r_e)^2 \int_0^{r_e} sr J_0 dr,$$

(8) reduces to

$$dA_n/dt = \frac{a^2/r_e^2 [2Q/2\pi T + H(t)x_n J_1(x_n)]}{J_1^2(x_n) - (x_n^2 + r_e^2/B^2)A_n}$$

or

$$dA_n/dt + \alpha_n A_n = \beta_n + \gamma_n H(t) \quad (9)$$

where

$$\left. \begin{aligned} \alpha_n &= a^2[(x_n/r_e)^2 + 1/B^2] \\ \beta_n &= Q/\pi S r_e^2 J_1^2(x_n) \\ \gamma_n &= 2a^2 x_n/r_e^2 J_1(x_n) \end{aligned} \right\} \quad (10)$$

The solution of (9) can be written as

$$A_n(t) = \beta_n/\alpha_n + C_n \exp(-\alpha_n t) + \gamma_n F(t) \exp(-\alpha_n t) \quad (11)$$

where  $C_n$  is the integration constant and

$$F(t) = \int_0^t H(t) \exp(\alpha_n t) dt \quad (12)$$

$C_n$  can be determined by the initial condition  $s(r, 0) = \Delta H$ .

From (7) it follows that

$$A_n(0) = 2 \Delta H/x_n J_1(x_n) \quad (13)$$

Also from (11), since  $F(0) = 0$ ,

$$A_n(0) = \beta_n/\alpha_n + C_n \quad (14)$$

It should be noted that  $F(0) = 0$  always, so that  $C_n$  does not depend upon  $H(t)$ . From (14) the integration constant is

$$C_n = 2 \Delta H/x_n J_1(x_n) - (Q/\pi T)/(\alpha_n^2 + r_e^2/B^2) J_1^2(x_n) \quad (15)$$

The integral (12) is always easy to evaluate numerically and in some cases can be worked out directly, such as for simple linear and sinusoidal time laws. A large number of fluctuations of the piezometric head in aquifers can actually be reduced to such simple laws. The computation of  $A_n$  from (11) is straightforward and the final solution can be written in the form of (6).

Special cases.

$$\begin{aligned} 1. \quad H(t) &= \Delta H + kt, \quad \text{for } 0 < t < t_f \\ &= \Delta H + kt_f, \quad \text{for } t \geq t_f \end{aligned}$$

where  $k \leq 0$ .

Then

$$\begin{aligned} F(t) &= (\Delta H/\alpha_n)[\exp(\alpha_n t_f) - 1] \\ &\quad + k[t_f/\alpha_n - 1/\alpha_n^2] \exp(\alpha_n t_f) \\ &\quad + (\Delta H/\alpha_n)[\exp(\alpha_n t) - \exp(\alpha_n t_f)] \end{aligned}$$

$$2. \quad H(t) = \Delta H + \epsilon \sin \rho t$$

$$\begin{aligned} F(t) &= (\Delta H/\alpha_n)[\exp(\alpha_n t) - 1] \\ &\quad + \epsilon(\alpha_n \sin \rho t - \rho \cos \rho t) \\ &\quad \cdot [\exp(\alpha_n t)/(\alpha_n^2 + \rho^2)] \end{aligned}$$

$$3. \quad H(t) = \Delta H, \text{ a constant.}$$

$F(t) = (\Delta H/\alpha_n)[\exp(\alpha_n t) - 1]$ , and solution can be written as

$$\begin{aligned} s(r, t) &= \sum_{n=1}^{\infty} [Q/\pi T + 2 \Delta H x_n J_1(x_n)] \\ &\quad \cdot J_0(x_n r/r_e)/(\alpha_n^2 + r_e^2/B^2) J_1^2(x_n) \\ &\quad + \sum_{n=1}^{\infty} [-Q/\pi T + 2 \Delta H r_e^2 J_1(x_n)/B^2] \\ &\quad \cdot [J_0(x_n r/r_e)] \frac{\exp[-a^2 t(x_n^2/r_e^2 + 1/\alpha_n^2)]}{(\alpha_n^2 + r_e^2/B^2) J_1^2(x_n)} \end{aligned}$$

The solution presented by Jacob [1946] can be identified in (16) for the special case  $\Delta H = 0$ . The steady-state part is given here in the form of an infinite series, where Jacob's solution is in closed form. In the case of no leakage,  $1/B^2 = 0$ , and from (16) it follows that, after some calculations [De Wiest, 1959],

$$\begin{aligned} s(r, t) &= Q \ln(r_e/r)/2\pi T \\ &\quad + \Delta H - (Q/\pi T) \sum_{n=1}^{\infty} [\exp(-a^2 t x_n^2/r_e^2) \\ &\quad \cdot J_0(x_n r/r_e)/x_n^2 J_1^2(x_n)] \end{aligned}$$

*Finite leaky aquifer. Flowing well.* The method of variation of parameters can also be used to solve this problem if one replaces the boundary condition (5) by the following:

$$\lim_{r \rightarrow 0} s_r J_0'(x_n r/r_e) = s_w r_w J_0'(x_n r_w/r_e)$$

where  $r_w$  is the well diameter and  $s_w$  is drawdown at the face of the well. Equation (16) now becomes

$$\begin{aligned} dA_n/dt &= Pa^2 \\ &\quad \cdot \left\{ -s_w r_w x_n J_1(x_n r_w/r_e)/r_e - H(t) r_e J_0'(x_n) \right. \\ &\quad \left. + \int_0^{r_e} s[\partial(r J_0')/\partial r] dr - (1/B^2) \int_0^{r_e} sr J_0 \right\} \end{aligned}$$

or

$$dA_n/dt + \alpha_n^* A_n = \beta_n^* + \gamma_n^* H(t)$$

with

$$\begin{aligned} \alpha_n^* &= \alpha_n \\ \beta_n^* &= -2x_n a^2 s_w r_w J_1(x_n r_w/r_e)/r_e^3 J_1^2(x_n) \\ \gamma_n^* &= \gamma_n \end{aligned}$$

Equation 9' can be integrated, and it follows that the integration constant  $C_n^*$  is

$$C_n^* = 2 \Delta H / x_n J_1(x_n) + \frac{2x_n s_w r_w J_1(x_n r_w / r_e)}{r_e (x_n^2 + r_e^2 / B^2) J_1^2(x_n)} \quad (15')$$

Special cases can be worked out for different values of  $H(t)$ , as in the case of the well pumped at constant discharge  $Q$ . For the case  $H(t) = \Delta H = \text{constant}$ , the solution is found to be

$$\begin{aligned} s(r, t) = & \sum_{n=1}^{\infty} [2 \Delta H x_n J_1(x_n) \\ & - 2x_n (r_w / r_e) s_w J_1(x_n r_w / r_e) \\ & \cdot J_0(x_n r / r_e) / (x_n^2 + r_e^2 / B^2) J_1^2(x_n) \\ & + \sum_{n=1}^{\infty} [2 \Delta H J_1(x_n) r_e^2 / (x_n B^2) \\ & + 2x_n (r_w / r_e) s_w J_1(x_n r_w / r_e)] J_0(x_n r / r_e) \\ & \cdot \frac{\exp \{-\alpha^2 t [(x_n / r_e)^2 + 1 / B^2]\}}{(x_n^2 + r_e^2 / B^2) J_1^2(x_n)}] \end{aligned} \quad (18)$$

The solution presented by *Hantush* [1959] can be compared with that resulting from (18) or the special case  $\Delta H = 0$ , although the steady-state part given in closed form by *Hantush* is here expanded in an infinite series.

The discharge at the face of the well is given by

$$Q = -2\pi T r_w (\partial s / \partial r)_{r=r_w}$$

**Numerical example.** Figure 2 gives curves computed from the steady-state part of (16), with  $r_e = 100,000$  ft,  $T = 20,000$  ft<sup>2</sup>/day, and  $B = 20,000$  ft. The drawdown is plotted in units of  $Q/4\pi T$  for values 0 and 1 of the param-

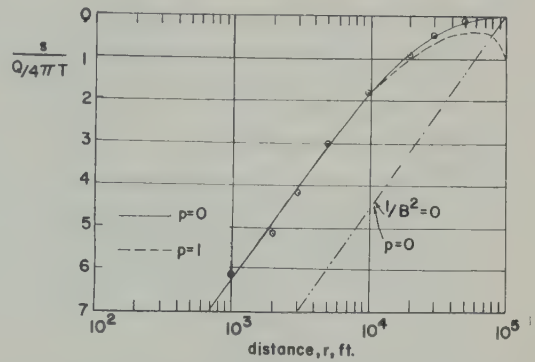


Fig. 2. Ultimate distribution of drawdown in a leaky artesian aquifer, where  $r_e = 100,000$  ft,  $T = 20,000$  ft<sup>2</sup>/day, and  $B = 20,000$  ft; for values 0 and 1 of  $p = \Delta H / (Q/4\pi T)$ .

eter  $p = \Delta H / (Q/4\pi T)$ . For  $p = 0$ , the dots on the graph represent the series solution (16) as compared with the curve obtained by *Jacob* [1946]. The dots were the results of slide-rule computations. The values of the Bessel functions were taken from the tables by *Jahnke and Emde* [1945], and calculations were carried out to the fourth place decimal. The value  $p = 1$  has been assumed for reason of clarity in the representation. It seems reasonable to assume that the value of  $p$  in general will vary between 0 and the order of 1, depending upon the discharge at which the well is pumped and the transmissivity of the aquifer. Negative values of  $p$ , for which water would penetrate into the aquiclude from the aquifer, are not excluded in this theory. The maximum in the curve for  $p \neq 0$  lies for the aquifer in question in the vicinity of  $r = 50,000$  ft and indicates the existence of a water divide in the aquifer. To the left of this divide water flows to the well; to the right of the divide water

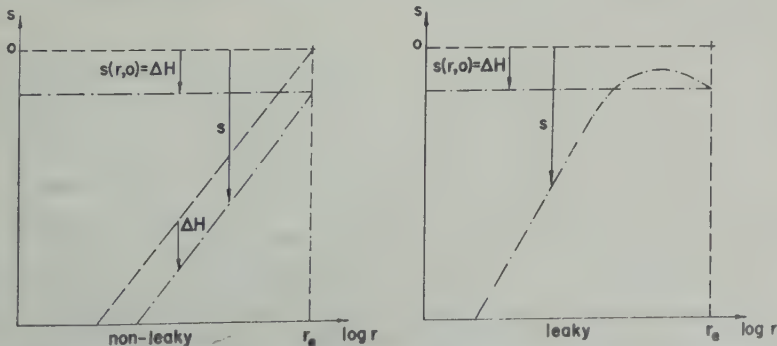


Fig. 3. Effect of initial  $\Delta H$  on ultimate drawdown in leaky and nonleaky artesian aquifer.



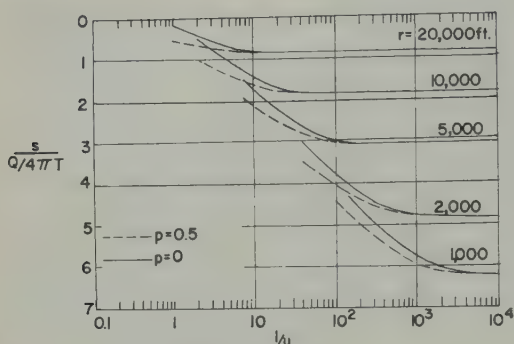


Fig. 4. Time-drawdown curves for leaky artesian aquifer with well at center discharging at rate  $Q$ ; where  $r_w = 100,000$  ft,  $T = 20,000$  ft<sup>2</sup>/day and  $B = 20,000$  ft; for values 0 and  $\frac{1}{2}$  of  $p = \Delta H / (Q / (4\pi T))$ .

flows to the mathematical contour of influence. Inasmuch as one could consider the boundary of the divide as the physical contour of influence, there is quite a difference in location with the mathematical contour. Leakage into the aquifer is responsible for the existence of the divide. In a nonleaky aquifer, such as results from (17), a  $\Delta H$  maintains itself over the entire aquifer (Fig. 3). Figure 4 gives curves for the nonsteady state as computed for  $p = 0$  and  $p = 0.5$ , for the leaky aquifer. The reciprocal of the abscissa is  $u = r^2 S / 4Tt$ . If one compares Figures 2 and 4, it appears that for the considered aquifer the existence of a  $\Delta H$  has practically no repercussion on the steady-state drawdown near the well. On the other hand,  $\Delta H$  has an effect of the same order of magnitude on the unsteady-state drawdown over the entire aquifer, although it does not affect the time at which the steady state is reached.

**Conclusion.** The advantage of the method of

variation of parameters over those indicating the introduction lies in the simplicity of the integral (12). On the other hand, the solution converges rather slowly, requiring consideration of 10 to 40 terms, and hence more time consuming than a closed form solution. Fortunately, the calculation of the terms is so simple that it can be done by slide rule. For the methods to determine the form of the constants, the reader is referred to the work of Jacob and Hantush.

#### REFERENCES

- De Wiest, R. J. M., Unsteady-state phenomena in the flow through porous media, *Tech. Rep. 1*, Civil Engineering Department, Stanford University, Stanford, 1959.
- De Wiest, R. J. M., Unsteady flow through an underdrained earth dam, *J. Fluid Mech.*, **8**, 1, 1-9, 1960.
- Hantush, M. S., Analysis of data from pump tests in leaky aquifers, *Trans. Am. Geophys. Union*, **37**, 702-714, 1956.
- Hantush, M. S., Nonsteady flow to flowing wells in leaky aquifers, *J. Geophys. Research*, **64**, 1043-1052, 1959.
- Hantush, M. S., Modification of the theory for leaky aquifers, *J. Geophys. Research*, **65**, 3713-3725, 1960.
- Hantush, M. S., and C. E. Jacob, Nonsteady radial flow in an infinite leaky aquifer, *Trans. Am. Geophys. Union*, **36**, 95-100, 1955.
- Jacob, C. E., Radial flow in a leaky artesian aquifer, *Trans. Am. Geophys. Union*, **27**, 198-200, 1946.
- Jahnke, E., and F. Emde, *Tables of Functions*, Dover Publications, New York, 1945.
- Polubarinova-Kotchina, P. Jr., *The Theory of Ground Water Movement*, State Press, Moscow, chap. 9, C. pp. 430-449, 1952. English translation available from Department of Geological Engineering, Princeton, University.

(Manuscript received June 22, 1961; revised August 25, 1961.)

## A New Borehole Thermometer

RONALD DOIG, V. A. SAULL, AND R. A. BUTLER

*Department of Geological Sciences, McGill University  
Montreal, Canada*

**Abstract.** A borehole thermometer consisting of a temperature-sensitive oscillator contained in a sealed brass probe has been designed and tested. With this device, frequency measurements are made at the surface, giving the temperature at depth. Temperature measurements are virtually independent of the type or condition of the supporting cable. The precision of the temperature measurements is better than  $0.05^{\circ}\text{C}$ . Temperatures were successfully measured with the instrument to depths greater than 2000 feet.

**Introduction.** During research on the terrestrial heat flow in the St. Lawrence lowland of Quebec, thermistor probes were used for the determination of thermal gradients after the manner described by *Misener and Thompson* [1950] and *Newstead and Beck* [1953]. Considerable dissatisfaction was experienced with the supporting cable used with these probes: it was a special steel and copper coaxial cable, and proved to be expensive, difficult to obtain, bulky, and quite stiff. In particular, it showed numerous mechanical flaws that caused electrical leakage at moderate borehole depths (if a 100,000-ohm thermistor is used a leakage resistance of 200 megohms cannot be tolerated) and made much of the cable unusable.

To circumvent these difficulties, we have designed a new borehole thermometer the operation of which is relatively independent of the nature of the supporting cable. This is described below. **Description of apparatus.** The instrument is a thermally sensitive oscillator. The oscillator, isolating amplifier, and its power supply are contained within a sealed brass probe. The alternating current output, the frequency of which is a function of the ambient temperature, is transmitted up the cable and measured at the surface.

Figure 1 is a schematic diagram of the oscillator and the amplifier. The oscillator is of the phase shift type, part of the signal being fed back from the collector to the base of the transistor ( $V_1$ ) through a phase shift network consisting of the  $R$ 's and the  $C$ 's. In this circuit the  $C$ 's are fixed and the  $R$ 's are thermistors. When the temperature changes, the value of  $R$  changes, and the frequency changes. The frequency of oscillation is also dependent on the load across the output terminals of the oscillator. For this reason the output amplifier  $V_2$  was used. This transistor is connected in the com-

mon-collector configuration, thus presenting a high impedance to the oscillator and a low impedance to the external circuit. To minimize frequency drift due to changes in the supply voltage, mercury batteries are used and the instrument is turned on a few hours before measurements are made.

At  $18^{\circ}\text{C}$ , the frequency of oscillation with the components shown is 1000 cps, and this frequency increases with temperature at a rate of about 3 per cent per degree centigrade. The circuit will oscillate over the range  $-10^{\circ}$  to  $+40^{\circ}\text{C}$ . This range can be shifted one way or the other by changing the values of  $R$  and  $C$ . To measure temperatures at great depths, transistors are available that will operate at temperatures exceeding  $200^{\circ}\text{C}$ .

The sensitivity of the measurements depends on the method used to measure the frequency output. A better evaluation of the accuracy of the temperature measurements is the short-period frequency drift. This frequency drift is equivalent to about  $0.05^{\circ}\text{C}$  over a period of a few hours and can be partly corrected by making measurements both going down and coming back up the borehole.

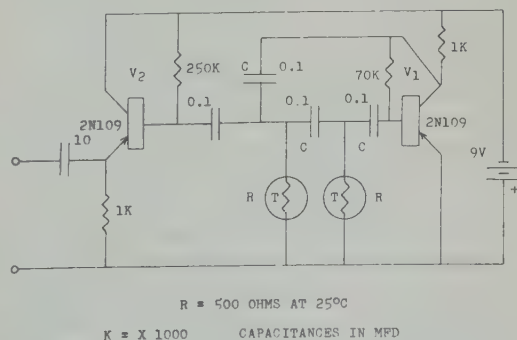


Fig. 1. Schematic diagram of the temperature-sensitive oscillator used to measure temperatures in boreholes.

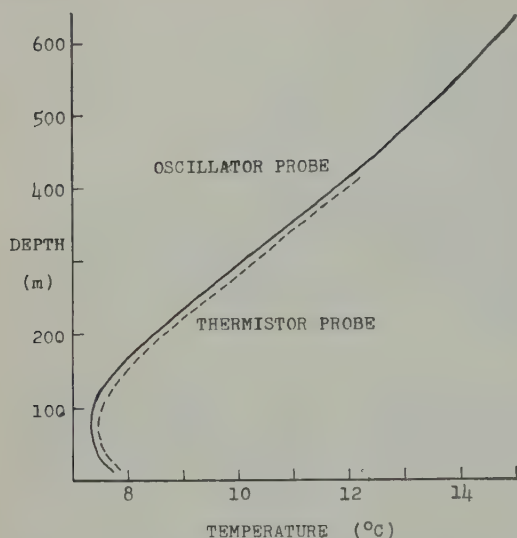


Fig. 2. Temperature-depth curves obtained in a borehole near Montreal, using both the new device and a thermistor resistance thermometer.

The time required to reach equilibrium is of the order of 3 to 4 minutes. This time constant could be substantially reduced by using lower wattage thermistors and by redesigning that part of the probe surrounding the thermistors. Heat produced by power dissipation in the thermistors and in the other components of the circuit is taken care of by calibrating the instrument under operating conditions.

Standard components are used in the whole unit including its power supply, and it fits into a brass probe 16 inches long and  $1\frac{1}{4}$  inches in outside diameter. The thermistors are contained in a narrow oil-filled section of the probe.

**Performance and testing.** The instrument was used to measure the temperature gradient in a borehole near Montreal. The frequency measurements were made by comparing the output signal from the probe to the frequency of a temperature-stabilized oscillator at the surface. Temperatures were successfully measured to the bottom of the borehole, a depth of 2200 feet. The temperature-depth curve is shown in Figure 2, along with the curve obtained using a thermistor resistance thermometer. The nearly constant deviation is considered to be due to a change in the resistance of the thermistor resistance thermometer during the 3-month interval between its calibration and its use in the borehole. The value of the heat flow obtained

using these gradient measurements, uncorrected for possible glacial effects, was  $0.81 \times 10^{-10}$  cm<sup>2</sup>/sec. This value is in strict accord with values obtained by the authors in adjacent areas using conventional equipment.

The cable used for these test measurements was selected to illustrate the lack of dependence of the measurements on the condition of the internal circuit. This cable was an army-supply lightweight telephone cable that had proved to be mechanically leaky when used with a thermistor resistance thermometer.

**Conclusions.** The nature of the instrument is such that cables with extremely poor insulation can be used, thus reducing the bulk, weight, and availability of the supporting cable. The accuracy of the temperature measurements is less than that obtained using the thermistor resistance thermometer, and for measurements in short boreholes the latter instrument is faster. For measurements in deep wells the new device can be used to advantage with lightweight, less expensive cables.

Improvements in the device are contemplated as follows:

1. Careful investigation of the frequency stability of the circuit and improvement of the stability by making suitable changes in the circuit (Fig. 1) or by using an entirely different type of electronic oscillator.
2. Further miniaturization of the instrument.
3. Reduction of the time required for the probe to reach equilibrium.
4. Development of a method of supplying power to the oscillator from the surface. This is, replacement of the internal battery with a suitable voltage regulator. This would make possible measurements to great depths without the need of removing the instrument from the borehole to change the battery and would eliminate all effects due to aging of the battery.

The authors gratefully acknowledge the support of a Geological Survey of Canada research grant awarded to V. A. Saull.

#### REFERENCES

- Doig, Ronald, unpublished M.Sc. thesis, McGill University, Montreal, 1961.  
 Misener, A. D., and L. G. D. Thompson, *Mining Met. Bull.*, 43, 542, 1950.  
 Newstead, C. N., and A. E. Beck, *Australian Phys.*, 6, 480, 1953.

(Manuscript received September 13, 1961)



## Gravity Anomalies in the Central Sierra Nevada, California

H. W. OLIVER,<sup>1</sup> L. C. PAKISER,<sup>2</sup> AND M. F. KANE<sup>3</sup>

*U. S. Geological Survey*

**Abstract.** More than 1000 measurements of gravity in the central Sierra Nevada and adjacent regions to the east show a decrease in regional Bouguer gravity values from  $-75$  mgal at the western edge of the mountains to a minimum of about  $-235$  mgal just west of the Sierra crest, a distance of only 100 km. Farther east, a positive regional gradient of about 0.6 mgal/km continues into the Inyo-White Mountains for a distance of at least 60 km. Local gravity lows are associated with Cenozoic sediments in Owens Valley, Long Valley, and Mono Basin to the east of the Sierra Nevada and with a thick, narrow deposit of Pleistocene sediments in Yosemite Valley. Local gravity highs are associated with roof pendants of metavolcanic rocks which extend down into the Sierra Nevada batholith to depths of more than 2 km. The variation in the regional Bouguer gravity values of about 160 mgal can be explained by a thickening of the earth's crust from 35 to 52 km beneath the central Sierra Nevada, combined with an eastward decrease in the density of the Sierra Nevada batholith from 2.76 to 2.64 g/cm<sup>3</sup>. Gravity data support Romney's conclusion, based on seismic evidence, that a local mountain root exists under the central and southern parts of the Sierra Nevada and not under the lower northern part, in general accordance with regional isostasy.

**Introduction.** About 3200 measurements of gravity were made in the southern half of the Sierra Nevada and adjacent regions between 1951 and 1959. The measurements include about 800 gravity stations occupied by Oliver within the Sierra Nevada and in adjacent regions of the San Joaquin Valley to the west, and about 400 stations occupied by Pakiser and Kane as part of an integrated geophysical study of the Owens Valley, Long Valley, and Mono Basin region to the east of the southern Sierra Nevada. The work in the Sierra Nevada was undertaken primarily to test isostasy in this prominent mountain range. *Byerly* [1938, 1939] and *Gutenberg* [1943] had previously shown that longitudinal waves, generated by earthquakes near the California coast and in Nevada, are significantly delayed in their passage under the Sierra Nevada, and they proposed that the delay is caused by a 'mountain root' of crustal rocks extending into the mantle of the earth to depths of 40 to 65 km below the earth's surface. Their pioneer work has been confirmed by later earthquake studies [*Chakrabarty and Richter*, 1949; *Byerly and Tuller*, 1954; *Richter*, 1955; *Romney*, 1957], by refraction studies of nuclear explosions

[*Carder and Bailey*, 1958, p. 383], and by the phase-velocity method [*Press*, 1956]. These seismic results gave strong support to the Airy mechanism of isostasy, but it remained to test specific isostatic models by comparing gravity values which could be computed from the proposed models at various points in the Sierra Nevada with direct observations of gravity at the same points.

The only published gravity observations in the Sierra Nevada were made at 12 stations along a profile across Walker Pass at the southern end [*Woollard*, 1943, Plate 3] and 8 stations across Donner Pass in the northern part [*Duerksen*, 1949, p. 36] which have been variously interpreted by *Johnston* [1940], *Tsuiji* [1956], *Thompson and Sandberg* [1958] and *Thompson and Talwani* [1959].

*Oliver* [1956, 1958, 1960] reported that Airy-Heiskanen and Pratt-Hayford isostatic models, using 'best values' of the crustal thickness  $T = 30$  km and of the depth of compensation  $D = 96$  km, respectively, yielded computed gravity values which were about 85 per cent of Bouguer gravity throughout the eastern half of the southern Sierra Nevada. It was therefore desirable to devise a system of compensation that would more accurately explain the gravity observations. In the present paper, data from

<sup>1</sup> Menlo Park, California.

<sup>2</sup> Denver, Colorado.

<sup>3</sup> Washington, D. C.





Fig. 1. Index map of California showing the area of the gravity map in Figure 2. Landforms after Raisz [1951].

about 1000 gravity stations in the northern third of the area under study are presented, and a modification of the Airy isostatic mechanism, which includes lateral variations in density within the upper part of the earth's crust, is proposed.

**Densities of surface rocks.** The location of the central Sierra Nevada is shown in Figure 1, and a combined gravity-geologic map of the area is given in Figure 2. The central Sierra Nevada is largely composed of granitic rocks of the Sierra Nevada batholith. These rocks range from quartz diorite to quartz monzonite in composition, generally becoming more felsic to the northeast. Similarly, more than 500 density measurements of surface samples made largely by Survey geologists mapping in this area (P. C. Bateman, written communication, 1960) show an average decrease in the density of these rocks from about  $2.76 \text{ g/cm}^3$  in the southwest part of the area to about  $2.64 \text{ g/cm}^3$  in the vicinity of the topographic crest. Granitic rocks continue for an unknown distance under the Cenozoic sediments of the San Joaquin Valley to the west of the Sierra Nevada and presumably underlie the basin deposits east of the Sierra Nevada. The exact locations of the east and west edges of the batholith are unknown.

The pre-Cretaceous metamorphic rocks which form roof pendants in the batholith have a variation in density from as low as  $2.5 \text{ g/cm}^3$  for slates to more than  $3.0 \text{ g/cm}^3$  for amphibolites. The density contrast between the granitic rocks and much of the metasedimentary rocks is significant, but some of the pendants contain high proportions of metavolcanic rocks. Bouguer gravity highs associated with the rocks. The average density of these greenstones, felsites, and granulites is about  $2.9 \text{ g/cm}^3$ , based on more than 100 measurements.

The average density of deposits of Cenozoic basins has been amply discussed by Pakiser, Press, and Kane [1960, p. 423] and by Kane and Pakiser [1961, p. 13]. A value of  $2.25 \text{ g/cm}^3$  was used in computing anomalies in this paper.

**Description of gravity data.** A Bouguer gravity map of the central Sierra Nevada is superimposed upon the geologic map in Figure 2. The gravity contours are based on data obtained from a network of about 1000 gravity stations shown on the map and from several hundred additional stations located beyond the western and southern limits of the map. The gravity measurements were made with a Humbley and several Worden gravity meters with scale values of 0.2 to 0.5 mgal per dial division; the entire network of stations was tied to Woollard's [1958, p. 532] gravity base at Menlo Park, California, airport. Most of the stations were located on bench marks, but the elevations of about 200 stations east of the Sierra Nevada were determined by plane-table and alidade surveying. A Bouguer reduction density of  $2.67 \text{ g/cm}^3$  was used, and the curvature and terrain corrections were computed for distances out to 100 miles from each station by the method described by Swick [1942, pp. 67-68].

Gravity ties through other surveys to Woollard's base stations at San Francisco airport, Mono Lake (J. F. Evernden, written communication, 1959) and at Las Vegas airport. Inyokern (D. R. Mabey, written communication, 1959) indicate that the over-all error in gravity measurements is less than 3 mgal. The relative accuracy of observed gravity values at stations within 40 km of each other is better than 1 mgal. The greatest source of error in Bouguer gravity values is the approximation involved in the terrain corrections, which can introduce errors up to 3 mgal in extreme cases.

The Bouguer gravity field in Figure 1 decreases from a value of about  $-75$  mgal in the southwestern corner of the map to a minimum value of about  $-235$  mgal just west of the topographic crest of the Sierra Nevada. Farther east, gravity values at stations located on pre-Cenozoic rocks increase to about  $-185$  mgal at the eastern edge of the map.

The most striking feature of the gravity field is an abrupt change in gradient at the  $-200$ -mgal contour from about  $6$  mgal/km to less than  $1$  mgal/km. This change in gradient is well established by station control; it extends throughout the length of the southern Sierra Nevada.

A series of gravity lows with closures to  $40$  mgal are superimposed upon the regional gradient. They are east of the Sierra Nevada and are clearly associated with the low-density Cenozoic rocks. These anomalies have been interpreted by *Pakiser and Kane* [1956], *Pakiser, Kane, and Kane* [1960], and *Pakiser* [in press] and are discussed in this paper only insofar as they affect regional gravity. Gravity lows are also associated with the Cenozoic sediments in the San Joaquin Valley, near the southwest

corner of the map, and with a thick, narrow deposit of Pleistocene sediments in Yosemite Valley, near  $37^{\circ}40'N$ ,  $119^{\circ}40'W$ .

The gravity highs, associated with the roof pendants of metavolcanic rocks mentioned above, distort the otherwise nearly constant gravity gradient in the western foothills of the central Sierra Nevada. For a density contrast of  $0.2$  g/cm<sup>3</sup> between the metavolcanic and granitic rocks, the minimum depth to which the roof pendants extend down into the batholith is about  $0.6$  km per  $5$  mgal of associated gravity anomaly. Because a few of the pendants have associated anomalies greater than  $15$  mgal, it is believed that these pendants extend to depths of more than  $2$  km below the earth's surface.

*Interpretation along profile A-A'.* A Bouguer gravity profile along A-A' in Figure 2 is shown in Figure 3 and denoted by 'Observed.' The profile was taken normal to the average strike of the gravity contours; it passes through several local gravity highs and through the center of the major gravity low on the east side of the Sierra Nevada.

In Figure 3, a model has been constructed of

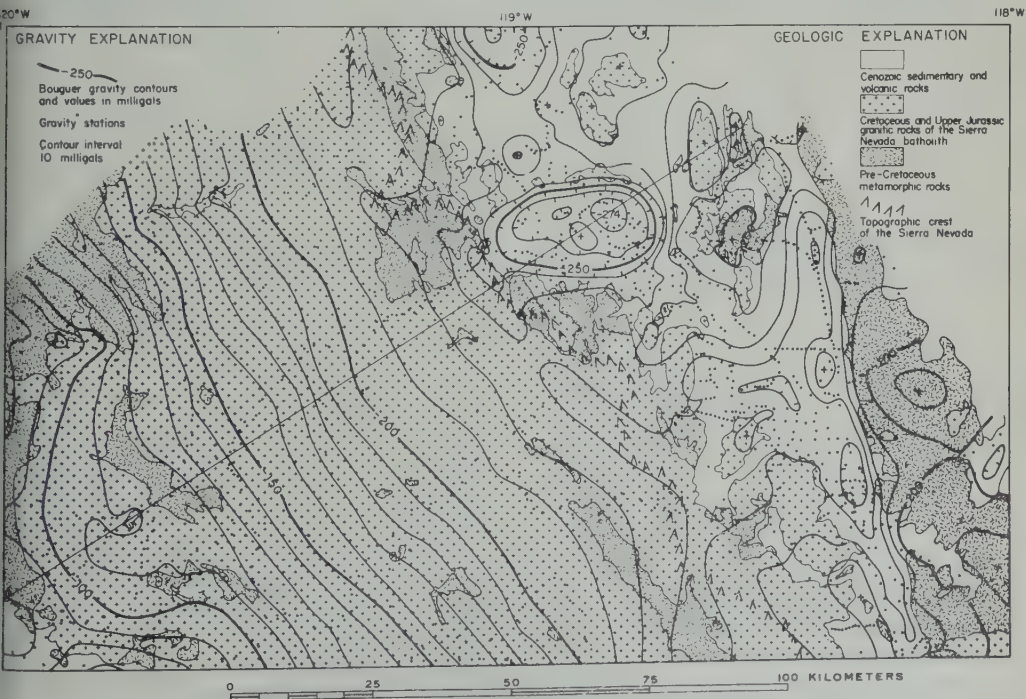


Fig. 2. Complete Bouguer gravity and geologic map of the central Sierra Nevada, California. Geology compiled by P. C. Bateman and others.

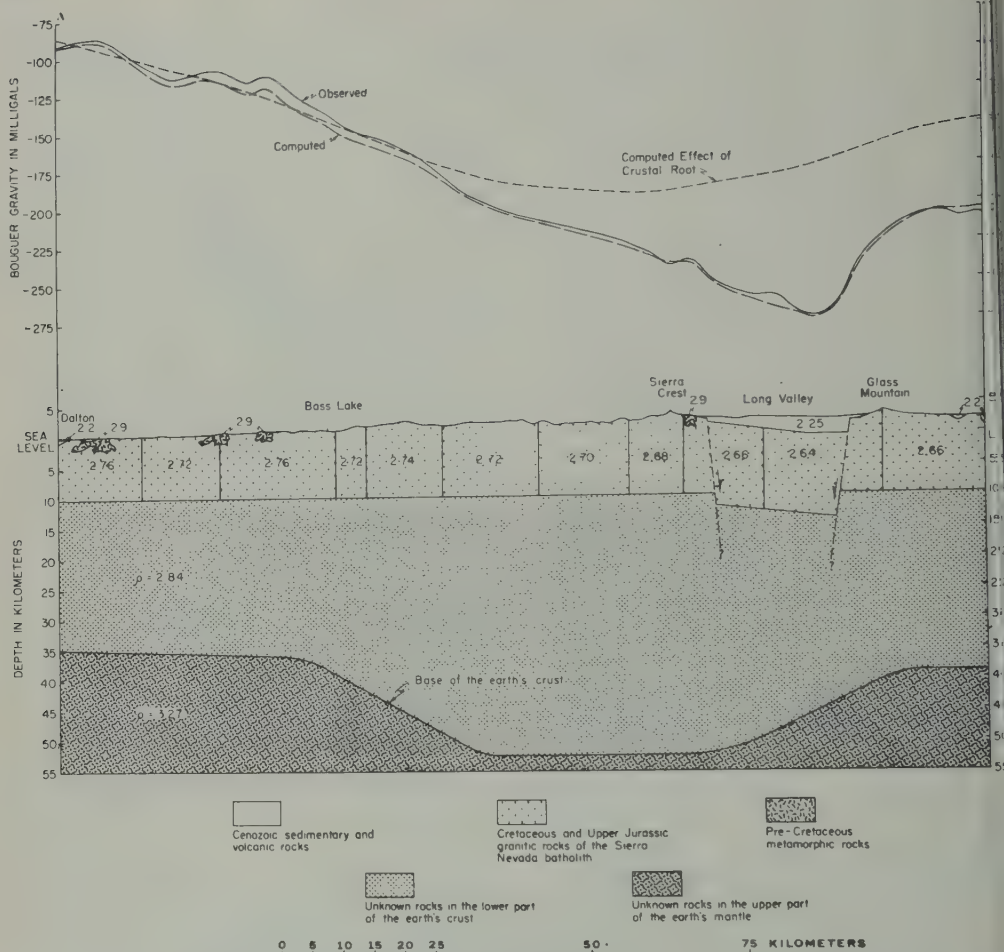


Fig. 3. Interpretation of Bouguer gravity profile along A-A'. Numbers within geologic units are the average densities of the units in  $\text{g/cm}^3$  used in the computation of the gravity profile. The average densities of the granitic rocks are based on 20 to 75 measurements in each block (taken at intervals of  $0.02 \text{ g/cm}^3$ ), and the standard deviations range from  $0.02$  to  $0.03 \text{ g/cm}^3$ .

the earth's interior below the central Sierra Nevada that yields a 'computed' gravity profile that is in close agreement with observed Bouguer gravity. The mass anomalies employed in the model are, in decreasing order of gravitational effect, (1) a thickening of the earth's crust from 35 to 52 km beneath the Sierra Nevada, (2) a horizontal variation in the density of batholithic rocks based on density measurements of surface samples collected in the vicinity of the profile, (3) low-density Cenozoic rocks in Long Valley, (4) high-density metamorphic rocks, and (5) a deep, faulted structure beneath Long Valley consistent with near-surface faults. The computed

effect of the crustal root (1) is shown separately in Figure 3; the difference between the 'computed' and 'Computed Effect of Crustal Root' curves represents the sums of the effects of anomalies (2) through (5). The value for the crustal thickness of  $35 \pm 5$  km taken at the western edge of central Sierra Nevada is based on an interpretation of available seismic data made by Press (written communication, 1959). The results of geophysical studies of crustal thicknesses in California have been summarized by Gutenberg [1959, Figure 3.11a].

Gravity interpretation in terms of these mass anomalies is not unique. For example



depth of 10 km, to which the surface density-variation of the batholith has been assumed to extend, were doubled, the depth to the base of the earth's crust under the Sierra crest would have to be decreased from 52 to 46 km. Similarly, thickening of granitic rocks under the Sierra Nevada would further reduce the size of the crustal root necessary to satisfy the gravity data, although this modification is not supported by present seismic evidence [Gutenberg, 1959, p. 57]. Other mass anomalies doubtless exist in the lower part of the earth's crust or possibly in the upper part of the earth's mantle, as shown by lateral variations in the velocity of materials at these depths [Diment, Stewart, and Roller, 1961, p. 212]. The physical model in Figure 3 is only a first-order approximation to a very complex mass distribution within the upper part of the earth's interior, but it should serve as a useful working model for future investigations. It is consistent with present geologic and seismic knowledge of the Sierra Nevada.

*Discussion of results.* The model of the earth's interior beneath the central Sierra Nevada not only accounts for the observed gravity field but provides a geologically realistic system of isostatic compensation which is nearly in hydrostatic equilibrium. This system is essentially the Airy-Heiskanen system [Heiskanen, 1938] with the following modifications:

1. The density-contrast at the base of the earth's crust of  $0.6 \text{ g/cm}^3$  assumed by Heiskanen has been changed to  $0.43 \text{ g/cm}^3$  in keeping with the recent evidence summarized by Worzel and Hurbert [1955, p. 92].
2. The system includes the effect of a horizontal variation in the density of the rocks that make up the upper part of the earth's crust. The density variation in this area is based on measured rock densities and is assumed to extend to a depth of 10 km below sea level. This modification should not be confused with the Pratt-Hayford system [Hayford and Bowie, 1912] whereby a deficiency in the density of vertical rocks was assumed to be proportional to the height of the earth's surface above sea level and the resulting horizontal density variation was assumed to extend to a depth of compensation of about 100 km.

The proposed model provides for regional compensation of the central Sierra Nevada in the sense that individual peaks and valleys are

not locally compensated. However, the model is not a regional system in the sense proposed by Vening Meinesz [1941], who assumed that the compensating mass is spread out horizontally, extending for a considerable distance beyond the physical limits of the excess topographic load on the earth's crust. It is clear from Figure 2 that the compensating masses in our model are entirely beneath the Sierra Nevada and associated fault block mountains to the east. The thickness of the earth's crust under the western foothills of the Sierra Nevada is nearly constant in our interpretation, which suggests that the strength of the crust is sufficient to support an excess load of about 600 meters of granitic rocks before bending or breaking.

Romney [1957, p. 310] has recently presented seismic evidence for the existence of a local root under only the central and southern parts of the Sierra Nevada and not beneath the lower northern part, although his earthquake data admit a general eastward increase in the thickness of the earth's crust of about 15 km throughout the length of the Sierra Nevada. If Romney's hypothesis is correct, Bouguer gravity values, corrected for near-surface effects, should increase across the eastern margin of the southern Sierra Nevada, and the amount of increase should diminish to the north. Available data east of the Sierra Nevada follow this pattern, showing an increase of 100 mgal to the east of the southern part [Oliver, 1958], at least 50 mgal to the east of the central part (Fig. 1), and only 30 mgal to the east of the northern part [Thompson and Sandberg, 1958, p. 1278]. As we have seen, a number of other explanations could be adjusted to satisfy these gravity data alone, but they would leave the seismic evidence to be accounted for by still another and possibly conflicting set of special assumptions. Both the gravity and seismic observations support a local mountain root under the southern Sierra Nevada which diminishes in size to the north in general accordance with regional isostasy.

According to our analysis, the base of the earth's crust dips toward the central Sierra crest at an angle of about  $27^\circ$  on both the west and east flanks of the Sierra Nevada. If we assume that the base of the crust coincides with the M discontinuity of seismology, the proposed crustal structure associated with the central Sierra Nevada should produce some interesting seismic



anomalies. Longitudinal waves generated by earthquakes or large explosions in Nevada and refracted along the M discontinuity ( $P_n$ ) will return to the earth's surface with a high apparent velocity in the vicinity of Bass Lake, be delayed at stations on the west side of the mountains, and have either a low apparent velocity or not arrive at all, causing a 'shadow zone' in some region west of the Sierra crest depending on the velocity of materials above and below the M discontinuity. Using  $V$  above = 7.66 km/sec and  $V$  below = 8.11 km/sec determined by Press [1960, p. 1045] for the region just south of the Sierra Nevada, the apparent velocity of  $P_n$  near Bass Lake should be about 11 km/sec, and a shadow zone for  $P_n$  should be found west of the Sierra crest. The situation will be reversed for  $P_n$  arrivals from earthquakes whose epicenters are near the California coast. Time delays in  $P_n$  have been observed for earthquakes located both east and west of the Sierra Nevada and recorded on the opposite side, but apparent velocities and amplitude variations of  $P_n$  arrivals will probably be difficult to observe because of the small amount of energy that can be expected to travel along the sloping interface shown in Figure 2, even if we ignore the likelihood that this surface is much more irregular. Some encouragement is given by limited observations of extraordinary apparent seismic velocities in the western Sierra Nevada made by Soske and Thompson [1958], who reported evidence for a 'large eastward dip at the western base of the Sierra Nevada.'

These speculations, based on the best available seismic and gravity evidence, may require modification as future, more detailed, seismic refraction data become available. The earth's gravity field associated with the Sierra Nevada is now at least as well known as that associated with any other major mountain system in the world, except possibly the Alps of Europe.

*Acknowledgments.* It is a pleasure to acknowledge the assistance of R. M. Shuler, N. H. Zickel, M. B. Duke, and G. A. Sellers of the Geological Survey in computing terrain corrections to the gravity data. We are further indebted to Francis Birch, Frank Press, P. C. Bateman, G. A. Thompson, and W. H. Diment for helpful discussions of the gravity survey. While the senior author was a graduate student the investigation was supported in part by the Committee on Experimental Geology and Geophysics, Harvard University.

## REFERENCES

- Byerly, Perry, Comment on 'The Sierra Nevada: the light of isostasy' by A. C. Lawson, *Bull. Soc. Am.*, 48, 2025-2031, 1938.
- Byerly, Perry, Near earthquakes in central California, *Bull. Seism. Soc. Am.*, 29, 427-462.
- Byerly, Perry, and B. Tuller, Sierran root (abstract), *Bull. Geol. Soc. Am.*, 65, 1335, 1954.
- Carder, D. S., and L. F. Bailey, Seismic wave times from nuclear explosions, *Bull. Seism. Soc. Am.*, 48(4), 377-398, 1958.
- Chakrabarty, S. K., and C. F. Richter, The West Pass earthquakes and structure of the southern Sierra Nevada, *Bull. Seism. Soc. Am.*, 39(2), 107, 1949.
- Diment, W. H., S. W. Stewart, and J. C. R. Crustal structure from the Nevada test site, Kingman, Arizona, from seismic and gravity observations, *J. Geophys. Research*, 66(1), 214, 1961.
- Duerksen, J. A., Pendulum gravity data in the United States, *U. S. Coast and Geodetic Survey Spec. Publ.* 244, 1949.
- Gutenberg, Beno, Seismological evidence for the structure of mountains, *Bull. Geol. Soc. Am.*, 54, 473-481, 1943.
- Gutenberg, Beno, *Physics of the Earth's Interior*, Academic Press, New York, 1959.
- Hayford, J. F., and William Bowie, The effect of topography and isostatic compensation upon the intensity of gravity, *U. S. Coast and Geodetic Survey Spec. Publ.* 10, 1912.
- Heiskanen, W. A., New isostatic tables for the reduction of gravity values calculated on the basis of Airy's hypothesis, *Intern. Assoc. Geod., static Inst. Publ.* 2, Helsinki, 1938.
- Johnston, W. D., Jr., Gravity section across the Sierra Nevada, *Bull. Geol. Soc. Am.*, 51, 1396, 1940.
- Kane, M. F., and L. C. Pakiser, Geophysical studies of subsurface structures in southern Owens Valley, California, *Geophysics*, 26(1), 12-26, 1961.
- Oliver, H. W., Isostatic compensation for the Sierra Nevada, California (Abstract), *Bull. Geol. Soc. Am.*, 67(2), 1724, 1956.
- Oliver, H. W., Gravity studies of crustal structures associated with the Sierra Nevada, California (Abstract). *Compt. rend. assoc. seism. et phys. terre*, Strasbourg, 186-188, 1958.
- Oliver, H. W., Gravity anomalies at Mount Whitney, California, *U. S. Geol. Survey Prof. Paper* 400-B, 313-315, 1960.
- Pakiser, L. C., Gravity, volcanism, and crustal formation in Long Valley, California, *U. S. Geol. Survey Prof. Paper* 424-B (in press), 1961.
- Pakiser, L. C., and M. F. Kane, Gravity studies of the structural geology of Owens and Long valleys, California (Abstract), *Bull. Geol. Soc. Am.*, 67(12), 1724, 1956.
- Pakiser, L. C., Frank Press, and M. F. Kane, A physical investigation of Mono Basin, California, *Bull. Geol. Soc. Am.*, 71, 415-448, 1960.
- Press, Frank, Determination of crustal structure

- from phase velocity of Rayleigh waves, 1, *Bull. Geol. Soc. Am.*, 67, 1647-1658, 1956.
- ess, Frank, Crustal structure in the California-Nevada region, *J. Geophys. Research*, 65(3), 1039-1051, 1960.
- isz, Erwin, *Landforms of California and Nevada*, Ginn and Company, Boston, Mass., 1951.
- chter, C. F., Foreshocks and aftershocks, *Calif. Div. Mines Bull.* 171, Pt. 2, 177-197, 1955.
- omney, Carl, Seismic waves from the Dixie Valley-Fairview Peak earthquake, *Bull. Seism. Soc. Am.*, 47, 301-319, 1957.
- ske, J. L., and G. A. Thompson, Study of crustal structure in California and Nevada by explosion seismology (Abstract), *Bull. Geol. Soc. Am.*, 69(12), 1707, 1958.
- rick, C. H., Pendulum gravity measurements and isostatic reductions, *U. S. Coast and Geodet. Survey Spec. Publ.* 232, 1942.
- ompson, G. A., and C. H. Sandberg, Structural significance of gravity surveys in the Virginia City-Mount Rose area, Nevada and California, *Bull. Geol. Soc. Am.*, 69, 1269-1282, 1958.
- Thompson, G. A., and Manik Talwani, Crustal section across California and Sierra Nevada, *Bull. Geol. Soc. Am.*, 70, 1688, 1959.
- Tsuboi, Chuji, Crustal structure in northern and middle California from gravity-pendulum data, *Bull. Geol. Soc. Am.*, 67, 1641-1646, 1956.
- Vening Meinesz, F. A., Tables for the regional and local isostatic reduction, *Publ. Netherlands Geodet. Comm.*, Drukkerij Waltman, Delft, 1941.
- Woollard, G. P., Transcontinental gravitational and magnetic profile of North America and its relation to geologic structure, *Bull. Geol. Soc. Am.*, 54, 747-790, 1943.
- Woollard, G. P., Results for a gravity control network at airports in the United States, *Geophysics*, 23(3), 520-535, 1958.
- Worzel, J. L., and G. L. Shurbet, Gravity interpretations from standard oceanic and continental crustal sections, in *Crust of the Earth*, edited by Arie Poldervaart, *Geol. Soc. Am. Spec. Paper* 62, 87-100, 1955.

(Manuscript received August 28, 1961.)



## Depth and Spacing of Tension Cracks

ARTHUR H. LACHENBRUCH

*U. S. Geological Survey, Menlo Park, California*

**Abstract.** Contraction cracks in basalt, permafrost, and mud, and crevasses in glaciers are examples of geological phenomena that might be studied by reference to a theoretical model of tension cracks in a semi-infinite solid. The effect of the crack in relieving stress at the ground surface bears on the problem of crack spacing, and the rate of energy dissipation at the advancing crack tip bears on the problem of crack depth. Even though the stresses that cause cracking develop slowly, an elastic model of the stress near a crack can be useful as long as the cracks, once initiated, propagate rapidly. Results are presented for the elastic stress perturbation caused by a crack in an infinite or semi-infinite medium in which the initial stress is a step function or a linear function of depth. Tables and graphs are presented which can be applied directly to problems in which the variation of stress with depth is arbitrary. These results, used with the modified Griffith theory of macroscopic fracture introduced by *Irwin* [1948] and *Orowan* [1950], suggest a means of predicting depth and spacing of tension cracks in terms of the stress field and measurable properties. The method is illustrated with a discussion of cooling joints in basalt, and other problems of tension fracture in geology.

### INTRODUCTION

A brittle cracking in the direction normal to the component of maximum tensile stress occurs under many conditions of geologic interest. Examples are thermal contraction cracks in cooling basalt or permafrost, desiccation cracks in mud, crevasses in glaciers, and tension cracks on the convex sides of flexures. The crack is generally initiated at a surface of great stress (often at or near the ground surface) and is propagated toward the interior of the medium where the tension diminishes and ultimately passes into compression. The depth and spacing of such tension cracks are measurable quantities which contain information about the mechanical conditions under which the cracks formed, and hence about the history of the medium in which they occur. This information can be obtained only to the extent that the physical processes responsible for the crack formation are understood. It is therefore of geologic interest to consider the cracking problem from a fundamental, quantitative point of view.

A useful physical model is provided by a modification of the Griffith theory of fracture due to *Irwin* [1948] and *Orowan* [1950] in which the surface energy considered by Griffith is replaced by the energy of plastic deformation near the advancing crack tip. Before the theory can be applied to geologic problems, however, it is necessary to have a mathematical model of stress in the cracked ground.

It is well known that most geological materials behave elastically only when deformed rapidly. Thus the geological processes which produce tension (such as thermal contraction or folding) generally must be treated by some visco-elastic relation between stress and strain. Nevertheless, the tension cracks which they produce can occur quite spontaneously and propagate at speeds approaching, in order of magnitude, those of elastic waves. Therefore an elastic model of the stress perturbation caused by cracking should give a very good approximation to the stress conditions that exist immediately after the crack has formed. Such information is often what is needed, as for example when considering the spacing of cracks that form almost simultaneously. In other problems the elastic solution is often a useful limiting case.

Hence, it should be possible to gain insight into the geologic problem by considering formal mathematical solutions for the stress perturbation caused by a crack extending from the free surface of a prestressed semi-infinite elastic medium, or from an interior surface of an infinite elastic medium. The quantity of principal importance to the problem of crack spacing is the stress perturbation in the plane in which the cracks originate, usually the free surface. The quantity of principal importance to the problem of crack depth is the stress concentration at the bottom of the crack. The geological problem is to determine how these quantities depend upon



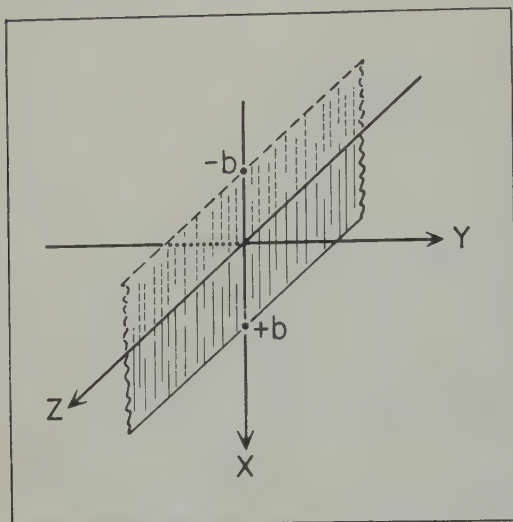


Fig. 1. Coordinate system and position of the crack.

material properties and the initial distribution of stress with depth; hence, this distribution must be treated as an arbitrary function. The first part of this paper is devoted to presenting the formal mathematical results needed. They are summarized in tables and graphs for ready application to specific problems.

The second part contains a brief description of the fracture mechanics model and illustrations of how such a model can be used with the results from the first part to approach tension-crack problems in geology.

### I. ANALYSIS OF STRESS

The purpose of this part is to present expressions to describe the elastic stress in an infinite or semi-infinite solid containing a long crack of finite depth. Before the crack appears the medium is supposed to have a nonuniform stress field with the maximum component of principal stress normal to the plane on which the crack is to form. The components of initial stress vary only in the direction of crack depth. The crack will be considered as lying in the plane  $y = 0$  in the strip  $-\infty < z < \infty$ ,  $-b < x < +b$  for the infinite medium, and  $0 < x < b$  for the semi-infinite medium,  $x > 0$  (Fig. 1). The maximum principal stress will be represented by  $\tau(x)$  which is directed parallel to the  $y$  axis and varies only with  $x$ . The  $x$  and  $z$  components of the initial stress can be assigned later, in conformity

with any particular application, as only component influences the boundary conditions at the crack walls.

The perturbation of the initial stress caused by the crack can be described in the infinite medium by the effect of normal stresses of magnitude  $-\tau(x)$ , distributed along the crack walls. This perturbation, when added to the initial stress, satisfies the condition that the crack be free of stress and hence represents the stress in the cracked medium. For the semi-infinite medium it is necessary to impose an additional condition that the stress vector vanishes on the surface  $x = 0$ .

Although several excellent discussions of a crack in an elastic medium have been published [Inglis, 1913; Westergaard, 1939; Muskhelishvili, 1953; Sneddon, 1946; Sneddon and Elliot, 1958; Knopoff, 1958], results directly applicable to the present problem do not seem to be available. In the Appendix the method of Muskhelishvili [1953] is applied to the two cases in which the initial stress in the infinite medium is an arbitrary function, or a linear function of distance from the surface  $x = 0$ . Explicit expressions for the components of stress perturbation throughout the  $xy$  plane are given. For simplicity in the present discussion it will be assumed that the maximum initial tension is attained at the surface  $x = 0$  and hence that the tension cracks originate there. The stress perturbation in  $x = 0$  will therefore be the quantity pertinent to the problem of crack spacing, and it is discussed in detail in the section that follows. In the second section of part I, corresponding results are developed for the case of the semi-infinite medium,  $x \geq 0$ , by using an iterative procedure to obtain the stress across the surface  $x = 0$ . Section 2 of part I is a discussion of the stress singularity at the crack tip in both the infinite and semi-infinite media. This quantity is fundamental to the problem of crack depth discussed in part II.

#### 1. A Tension Crack in a Totally Infinite Medium

In this section the problem of a stress perturbation caused by a crack in a totally infinite medium is considered. The results are not only useful in themselves but also form the first step in solving the more important case of the semi-infinite medium, treated in the section that follows.

*Case 1: The step function.* In this case the initial tensile stress is a constant,  $P$ , through

layer of half-width  $a$ , and the crack extends to  $\pm b$ , where  $b$  can be greater or less than  $a$ . See inset, Fig. 2.) Thus

$$\begin{aligned}\tau(x) &= P & |x| < a \\ &= 0 & |x| > a\end{aligned}$$

present interest centers about the stress perturbation in the plane  $x = 0$ , as this is the plane in which cracks are assumed to initiate. The result obtained by setting  $\theta = \pi/2$  in equations 11, A12, and A13 of the Appendix:

$$\begin{aligned}\widehat{\rho\rho}\left(\frac{\pi}{2}\right) &= -P\left\{\left[1 - \frac{2}{\pi}\theta_0\right]\left[1 - \frac{(\rho^2 - 1)^3}{(\rho^2 + 1)^3}\right] \right. \\ &\quad \left. + \frac{2}{\pi}\tan^{-1}\left(\frac{\sin 2\theta_0}{\rho^2 + \cos 2\theta_0}\right) \right. \\ &\quad \left. + \frac{4\rho^2(\rho^2 - 1)\sin 2\theta_0}{\pi(\rho^2 + 1)(\rho^4 + 2\rho^2\cos 2\theta_0 + 1)}\right\} \quad (1)\end{aligned}$$

$$\begin{aligned}\widehat{\theta\theta}\left(\frac{\pi}{2}\right) &= -P\left\{\left[1 - \frac{2}{\pi}\theta_0\right] \right. \\ &\quad \left. \cdot \left[1 - \frac{(\rho^2 - 1)[(\rho^2 + 1) + 4\rho^2]}{(\rho^2 + 1)^3}\right] \right. \\ &\quad \left. + \frac{2}{\pi}\tan^{-1}\left(\frac{\sin 2\theta_0}{\rho^2 + \cos 2\theta_0}\right) \right. \\ &\quad \left. - \frac{4\rho^2(\rho^2 - 1)\sin 2\theta_0}{\pi(\rho^2 + 1)(\rho^4 + 2\rho^2\cos 2\theta_0 + 1)}\right\} \quad (2)\end{aligned}$$

$$\widehat{\rho\theta}\left(\frac{\pi}{2}\right) = 0 \quad (3)$$

where

$$\begin{aligned}y &= \frac{1}{2}b(\rho - 1/\rho) \\ \theta_0 &= \cos^{-1} a/b\end{aligned}$$

$\widehat{\rho\rho}(\pi/2)$  represents the tangential stress in the plane  $x = 0$ , i.e. the stress directed parallel to the  $y$  axis,  $\widehat{\theta\theta}(\pi/2)$  is the normal stress (parallel to the  $x$  axis), and  $\widehat{\rho\theta}(\pi/2)$  is the shear stress in the  $xy$  plane at  $x = 0$ .

Numerical results from (1) are presented in Table 1 and Figures 2 and 3, and results from (2) in Table 2 and Figures 4 and 5.

As the crack becomes long relative to  $a$ , these solutions pass to the well-known result for stress in the half-space  $y > 0$  caused by uniform pressure  $P$  on the surface  $y = 0$  in the strip  $-a < x < +a$  [Sneddon, 1951, p. 408].

$$\begin{aligned}\widehat{\rho\rho}\left(\frac{\pi}{2}\right) &= \frac{-2P}{\pi}\left[\tan^{-1}\frac{a}{y} + \frac{ay}{a^2 + y^2}\right] \\ \widehat{\theta\theta}\left(\frac{\pi}{2}\right) &= \frac{-2P}{\pi}\left[\tan^{-1}\frac{a}{y} - \frac{ay}{a^2 + y^2}\right] \\ \widehat{\rho\theta}\left(\frac{\pi}{2}\right) &= 0\end{aligned}$$

$$\frac{a}{b} = 0, a \text{ finite}$$

The relation between these results (the case  $a/b = 0$ ) and equations 1 and 2 are illustrated

TABLE 1. Case 1, Step Function. Normalized tangential stress,  $\widehat{\rho\rho}(\pi/2)/P$ , on the surface ( $x = 0$ ) normal to the center of a crack of length  $2b$  in an infinite medium.

$y/b$	$a/b$						
	0.05	0.1	0.2	0.3	0.5	0.75	1.0
0.05	-0.82	-0.96	-1.00	-1.00	-1.00	-1.00	-1.00
0.125	-0.45	-0.74	-0.92	-0.97	-0.99	-1.00	-1.00
0.25	-0.25	-0.45	-0.73	-0.86	-0.95	-0.98	-0.99
0.5	-0.12	-0.24	-0.45	-0.61	-0.79	-0.88	-0.91
0.75	-0.080	-0.16	-0.31	-0.43	-0.61	-0.74	-0.78
1.0	-0.055	-0.11	-0.22	-0.32	-0.47	-0.59	-0.65
1.5	-0.031	-0.062	-0.12	-0.18	-0.29	-0.38	-0.42
2.0	-0.020	-0.040	-0.080	-0.11	-0.19	-0.25	-0.29
2.5	-0.014	-0.027	-0.055	-0.080	-0.13	-0.17	-0.20
3.0	-0.010	-0.019	-0.040	-0.060	-0.095	-0.13	-0.15
4.0	-0.006	-0.012	-0.023	-0.033	-0.054	-0.075	-0.087
5.0	-0.004	-0.007	-0.015	-0.022	-0.036	-0.050	-0.057
7.0	-0.002	-0.004	-0.008	-0.012	-0.019	-0.026	-0.031
10.0	-0.001	-0.002	-0.004	-0.006	-0.009	-0.013	-0.015

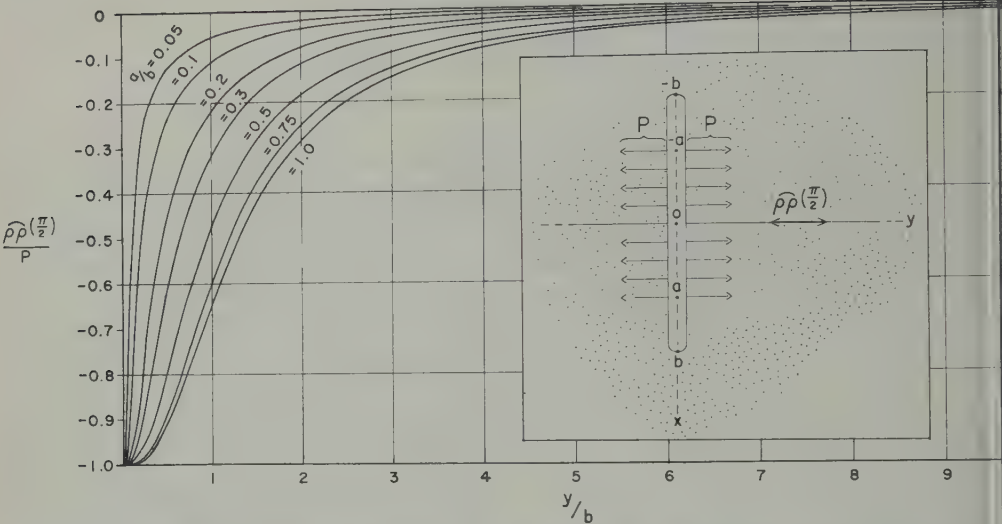


Fig. 2. Tangential stress in the plane  $x = 0$  due to a step distribution of surface pressure on the walls of a crack ( $y = 0 \pm, -b < x < +b$ ), in a totally infinite medium.

by Figures 3 and 5, respectively. They give a useful view of the effects of the constraint at the crack tips,  $x = \pm b, y = 0$ , on the stresses in the plane  $x = 0$ .

*Case 2: The linear function.* If the initial tension in the medium is a linear function of  $|x|$  (see inset, Fig. 6),

$$\tau(x) = \frac{Q}{b} |x|$$

The perturbation in the plane  $x=0$  caused by a stress-free crack extending between  $x = \pm b$

is given by setting  $\theta = \pi/2$  in equations A16, and A17 in the Appendix. Thus

$$\widehat{\rho\rho}\left(\frac{\pi}{2}\right) = -\frac{8}{\pi} Q \frac{\rho^2(\rho^2 - 1)}{(\rho^2 + 1)^3}$$

$$\widehat{\theta\theta}\left(\frac{\pi}{2}\right) = -\frac{4}{\pi} Q \frac{(\rho^2 - 1)}{(\rho^2 + 1)} \left\{ 1 + \frac{2\rho^2}{(\rho^2 + 1)} - \frac{(\rho^2 + 1)^2}{2\rho} \ln \frac{\rho^2 + 1}{\rho^2 - 1} \right\}$$

$$\widehat{\rho\theta}\left(\frac{\pi}{2}\right) = 0$$

TABLE 2. Case 1, Step Function. Normalized normal stress,  $\widehat{\theta\theta}(\pi/2)/P$ , on the surface ( $x = 0$ ) normal to the center of a crack of length  $2b$  in an infinite medium.

	$a/b$					
$y/b$	0.05	0.1	0.2	0.3	0.5	0.75
0.0	-1.00	-1.00	-1.00	-1.00	-1.00	-1.00
0.05	-0.17	-0.45	-0.69	-0.78	-0.85	-0.89
0.125	-0.020	-0.11	-0.35	-0.50	-0.72	-0.78
0.25	+0.003	-0.010	-0.095	-0.19	-0.37	-0.49
0.5	+0.011	+0.020	+0.023	+0.006	-0.065	-0.15
0.75	+0.012	+0.023	+0.042	+0.051	+0.044	+0.009
1.0	+0.011	+0.022	+0.041	+0.057	+0.074	+0.070
1.5	+0.009	+0.017	+0.032	+0.048	+0.067	+0.085
2.0	+0.005	+0.011	+0.021	+0.031	+0.050	+0.065
2.5	+0.004	+0.009	+0.016	+0.024	+0.038	+0.051
3.0	+0.003	+0.007	+0.013	+0.019	+0.028	+0.039
4.0	+0.002	+0.004	+0.007	+0.011	+0.016	+0.024
5.0	+0.001	+0.002	+0.005	+0.007	+0.012	+0.016

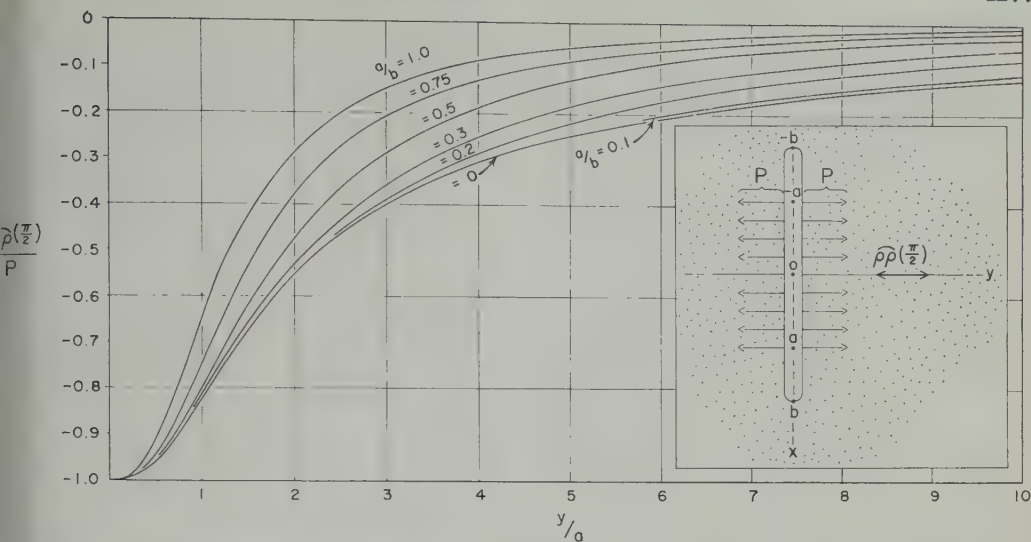


Fig. 3. The information contained in Figure 2, plotted in terms of depth of stress,  $a$ , to illustrate the relation of equation 1 to the case  $b = \infty$ , ( $a/b = 0$ ).

Numerical results from (4) and (5) are presented in Table 3 and Figure 6.

By superimposing a linear combination of solutions for case 1 it is possible to achieve an approximation of any desired accuracy to the effect of an arbitrary symmetrical distribution of normal forces on a crack of finite depth,  $2b$ , in an infinite medium under conditions of plane strain. The use of the result for case 2

simplifies the procedure if the function to be approximated is nearly linear.

In the above results, stresses less than zero are compressive; greater than zero, tensile.  $P$  and  $Q$  are positive for compressive normal stresses on the crack surfaces.

In most applications we are concerned with crack surfaces free of stress. To meet this condition the above solutions are superimposed on the stress that exists before cracking occurs.

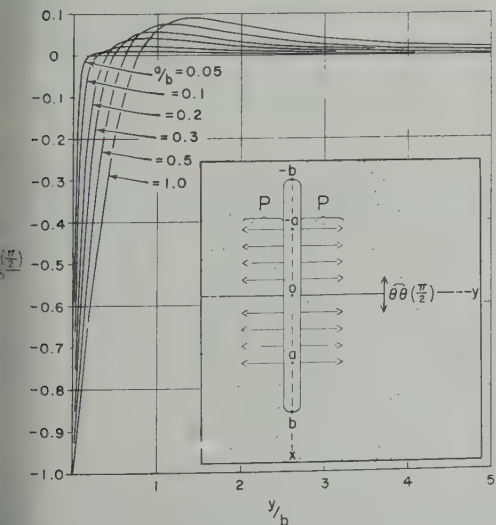


Fig. 4. Normal stress in the plane  $x = 0$  due to step distribution of surface pressure on the walls of a crack ( $y = 0 \pm$ ,  $-b < x < +b$ ) in a totally infinite medium.

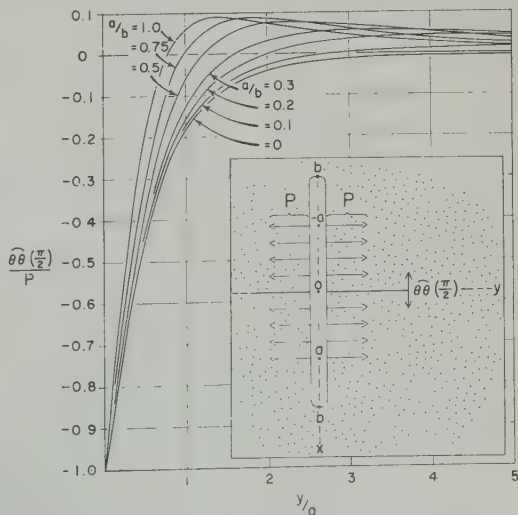


Fig. 5. The information in Figure 4 plotted in terms of depth of stress,  $a$ , to illustrate the relation of equation 2 to the case  $b = \infty$ , ( $a/b = 0$ ).



TABLE 3. Case 2, Linear Function. Normalized tangential and normal stresses,  $\widehat{\rho\rho}(\pi/2)/Q$  and  $\widehat{\theta\theta}(\pi/2)/Q$ , on the surface ( $x = 0$ ) normal to the center of a crack of length  $2b$  in an infinite medium.

$y/b$	$\widehat{\rho\rho}(\pi/2)/Q$	$\widehat{\theta\theta}(\pi/2)/Q$
0.125	-0.078	-0.20
0.25	-0.14	-0.21
0.5	-0.23	-0.12
0.75	-0.25	-0.041
1.0	-0.22	+0.003
1.5	-0.16	+0.028
2.0	-0.11	+0.027
2.5	-0.082	+0.022
3.0	-0.061	+0.018
4.0	-0.036	+0.010
5.0	-0.024	+0.008
7.0	-0.011	+0.004
10.0	-0.0063	+0.002

Thus if the horizontal stress in the  $y$  direction at the time of cracking is  $\tau(x)$ , independent of  $y$  and  $z$ , the stresses in  $xy$  plane after cracking are obtained by superimposing on  $\tau(x)$  the effect of the surface stresses,  $-\tau(x)$ , distributed over the fracture walls. A linear combination of step and linear functions are used to approximate  $-\tau(x)$ , and the above equations describe the stress perturbation it produces.

2. A Tension Crack at the Free Surface of a Semi-Infinite Medium

Many contraction cracks in extrusive rocks and those in permafrost and mud extend down-

ward from the ground surface, which can be assumed to be free of stress. For a more realistic model of these phenomena than that provided in the preceding section, it is desirable to remove the normal stresses across the surface  $x = 0$ . In the present notation, we must remove the stresses  $\widehat{\theta\theta}(\pi/2)$ . It is to be determined to what extent this process contributes to the associated tangential surface stress  $\widehat{\rho\rho}(\pi/2)$ .

To illustrate the method, we consider the reduction of the solution of case 1 to the  $xy$  space. The procedure is illustrated schematically in Figure 7. Figure 7a shows a step distribution of normal pressure,  $-\tau(x)$ , on the walls of the crack and its associated normal stresses,  $\widehat{\theta\theta}(\pi/2)$ , at  $x = 0$  as given by equation 2. To nullify the normal stress,  $\widehat{\theta\theta}(\pi/2)$ , equal and opposite pressures  $-\widehat{\theta\theta}(\pi/2)$  are applied to  $x = 0$  (Figure 7b). These pressures will have the direct effect of changing the horizontal surface stress  $\widehat{\rho\rho}(\pi/2)$  to

$$\widehat{\rho\rho}(\pi/2) - \widehat{\theta\theta}(\pi/2) \quad x = 0, \quad y > 0$$

and the indirect effect of producing new normal stresses,  $\Delta_1\tau(x)$ , at the walls of the fracture,  $y = 0 \pm, 0 < x < b$ . These new stresses,  $\Delta_1\tau(x)$ , must be removed from the fracture surface in order to maintain the initial step distribution of normal stresses there. Before this can be done, however, we must have a way of compensating  $\Delta_1\tau(x)$  from  $-\widehat{\theta\theta}(\pi/2)$ . To do this  $-\widehat{\theta\theta}(\pi/2)$

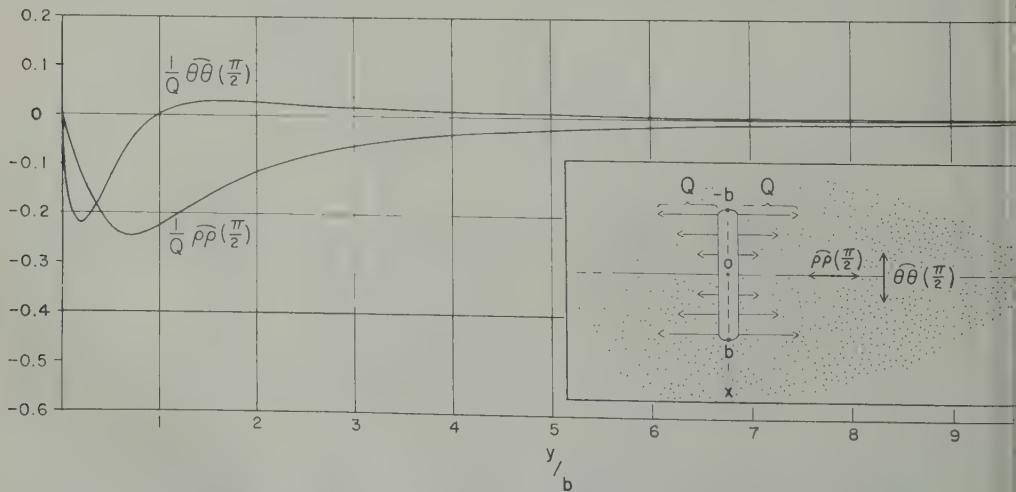


Fig. 6. Tangential and normal stress in the plane  $x = 0$  due to a symmetrical linear distribution of surface pressure on the walls of a crack ( $y = 0 \pm, -b < x < +b$ ) in a totally infinite medium.

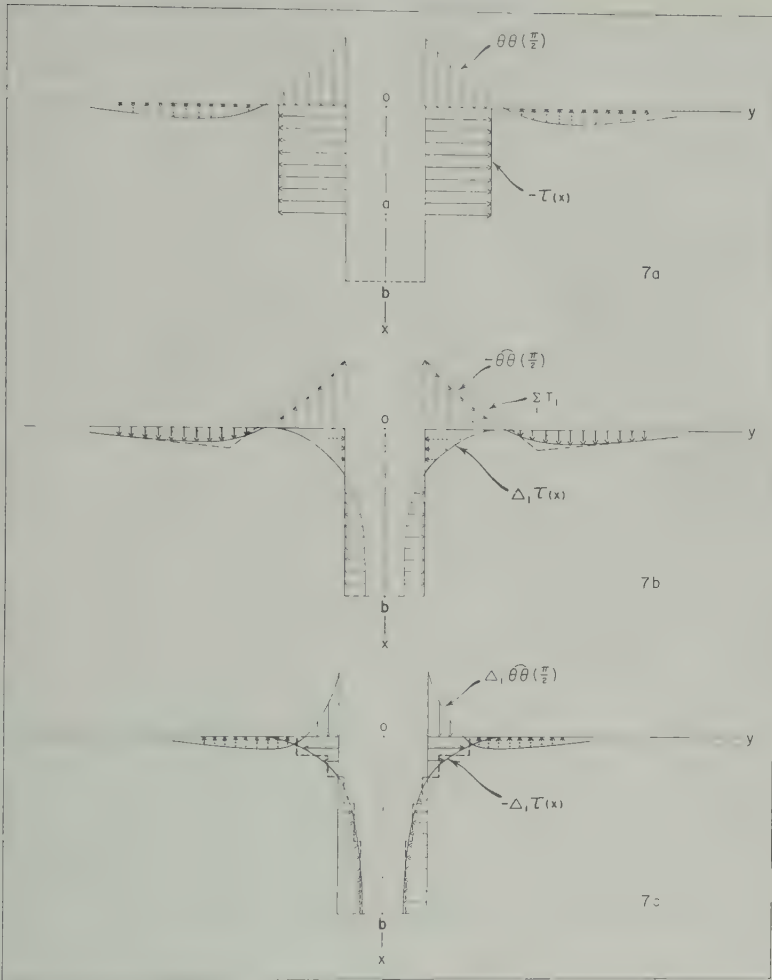


Fig. 7. Reduction of the solution for a step distribution of pressure on the walls of a crack in a totally infinite medium to the corresponding solution for a semi-infinite medium.

approximated by a continuous even function of  $y$  composed of linear segments (broken lines, Fig. 7b). Thus we can write

$$\widehat{\theta\theta}\left(\frac{\pi}{2}\right) \approx \sum_i T_i \quad (7)$$

where

$$T_i = P_i (1 - |y|/c_i) \quad |y| < c_i \\ = 0 \quad |y| > c_i$$

Each term in (7) is seen to correspond to a triangular distribution of normal pressures of half-width  $c_i$ , centered at  $y = 0$  on the plane  $x = 0$ . The corresponding new stresses at the fracture surface are therefore [Carothers, 1920]

$$\Delta_1 \tau(x) \approx -\frac{2}{\pi} \sum_i P_i \cdot \left\{ \tan^{-1} \frac{c_i}{x} - \frac{x}{c_i} \ln \left[ \frac{c_i^2}{x^2} + 1 \right] \right\} \quad (8)$$

Having calculated  $\Delta_1 \tau(x)$  we can now remove it from the fracture faces by applying normal stresses  $-\Delta_1 \tau(x)$  there. This is done by approximating  $-\Delta_1 \tau(x)$  by a step function, the effects of which can be described by a linear combination of solutions to case 1 of the preceding section (see Fig. 7c). Removal of  $\Delta_1 \tau(x)$  then results in a direct contribution  $\Delta_1 \rho \theta(\pi/2)$  to the tangential stress at  $x = 0$ . This is given by a linear combination of expressions of the form of equation 1.

TABLE 4. Case 1, Step Function. Normalized tangential stress,  $\widehat{\rho\rho}^*(\pi/2)/P$ , on the free surface ( $x = 0$ ) near a crack of depth  $b$  in a semi-infinite medium.

$y/b$	$a/b$						
	0.05	0.1	0.2	0.3	0.5	0.75	1
0.05	(-0.99)						
0.125	-0.68	(-0.98)					
0.25	-0.36	-0.68	-0.98				
0.5	-0.18	-0.36	-0.68	-0.89			
0.75	-0.12	-0.24	-0.50	-0.67	-0.87		
1.0	-0.087	-0.18	-0.37	-0.51	-0.71	-0.88	-0.99
1.5	-0.051	-0.11	-0.21	-0.31	-0.45	-0.60	-0.80
2.0	-0.033	-0.065	-0.13	-0.20	-0.31	-0.40	-0.60
2.5	-0.024	-0.050	-0.10	-0.15	-0.22	-0.29	-0.50
3.0	-0.017	-0.034	-0.075	-0.11	-0.16	-0.22	-0.40
4.0	-0.010	-0.020	-0.040	-0.059	-0.088	-0.12	-0.30
5.0	-0.006	-0.012	-0.025	-0.036	-0.061	-0.082	-0.20
7.0	-0.003	-0.006	-0.014	-0.021	-0.029	-0.042	-0.10
10.0	-0.001	-0.003	-0.005	-0.008	-0.014	-0.020	-0.05

The horizontal stress then becomes

$$\widehat{\rho\rho}\left(\frac{\pi}{2}\right) - \widehat{\theta\theta}\left(\frac{\pi}{2}\right) + \Delta_1\widehat{\rho\rho}\left(\frac{\pi}{2}\right) \quad x = 0, y > 0$$

In addition, a new normal stress  $\Delta_1\widehat{\theta\theta}(\pi/2)$  given by equation 2, appears on  $x = 0$ . However  $\Delta_1\widehat{\theta\theta}(\pi/2)$  decays much more rapidly with  $y$  than did the original normal stress  $\widehat{\theta\theta}(\pi/2)$ .

To refine the approximation,  $-\Delta_1\widehat{\theta\theta}(\pi/2)$  is represented by an expression of the form of (7),

and the entire process is repeated. All components of stress in the medium bounded by the free surface  $x = 0$  with the prescribed stress  $-\tau(x)$  on the crack surfaces  $y = 0 \pm, 0 < x < b$  may be approximated by superposition of the tensor components of the stresses resulting from the infinite medium from the surface stress  $-\tau(x)$ ,  $-\widehat{\theta\theta}(\pi/2)$ ,  $-\Delta_1\tau(x)$ ,  $-\Delta_1\widehat{\theta\theta}(\pi/2)$ , At present our interest centers on the horizontal stress at the free surface  $x = 0$ , which will be denoted by  $\widehat{\rho\rho}^*(\pi/2)$ . For  $N$  applications of

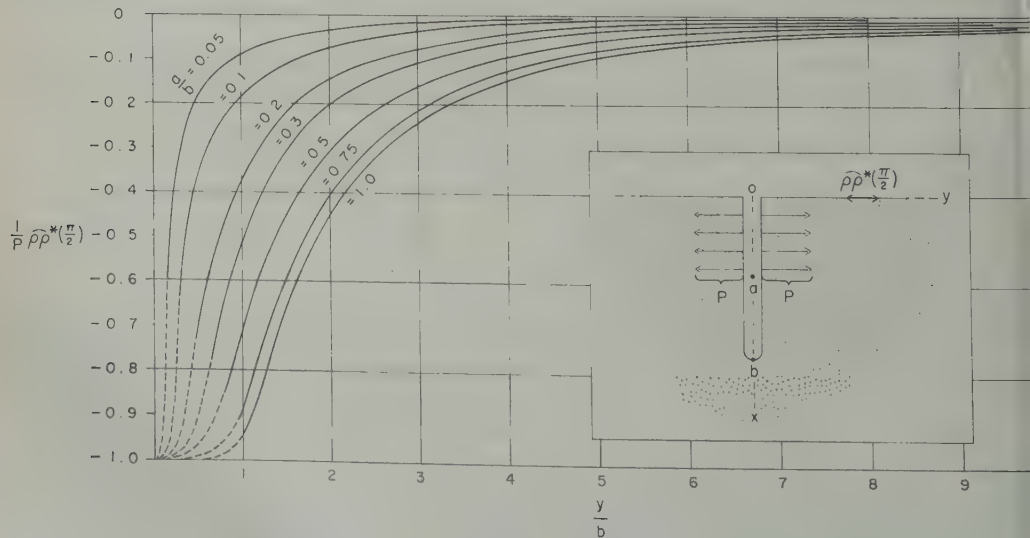


Fig. 8. Tangential stress on the free surface ( $x = 0$ ) due to a step distribution of surface pressure on the walls of a crack ( $y = 0 \pm, 0 < x < b$ ) in a semi-infinite medium.

TABLE 5. Case 2, Linear Function. Normalized tangential stress,  $\widehat{\rho\rho^*}(\pi/2)/Q$ , on the free surface ( $y = 0$ ) near a crack of depth  $b$  in a semi-infinite medium.

$y/b$	$\widehat{\rho\rho^*}(\pi/2)/Q$
0.50	-0.25
0.75	-0.30
1.0	-0.31
1.5	-0.25
2.0	-0.17
2.5	-0.13
3.0	-0.10
4.0	-0.056
5.0	-0.040
7.0	-0.018

ycle described above, it is given by

$$\widehat{\rho\rho^*}\left(\frac{\pi}{2}\right) \approx \sum_{i=0}^N \left\{ \Delta_i \widehat{\rho\rho}\left(\frac{\pi}{2}\right) - \Delta_i \widehat{\theta\theta}\left(\frac{\pi}{2}\right) \right\}$$

$$y > 0, \quad x = 0 \quad (9)$$

here

$$\widehat{\rho\rho}\left(\frac{\pi}{2}\right) = \widehat{\rho\rho}\left(\frac{\pi}{2}\right) \quad \text{and} \quad \Delta_0 \widehat{\theta\theta}\left(\frac{\pi}{2}\right) = \widehat{\theta\theta}\left(\frac{\pi}{2}\right)$$

values of  $\widehat{\rho\rho^*}(\pi/2)$  for case 1 are summarized in Table 4 and illustrated in Figure 8. For the near distribution, case 2, values of  $\widehat{\rho\rho^*}(\pi/2)$  are given by Table 5 and Figure 9. These numerical results are, of course, approximate—unlike the results of the previous section, which were derived from exact solutions.

#### Crack-Edge Stress Intensity Factor

Insofar as the fracture process is concerned, the most important quantity to be derived from

a stress analysis is the intensity of stress across the plane of fracture in the neighborhood of the apex. Under the usual mathematical idealization of a vanishingly small apical radius this stress generally becomes infinite as

$$\kappa/\sqrt{2r}$$

where  $r$  is the radial distance from the apex. The parameter  $\kappa$  depends upon the length of the crack and the stress distribution in the medium. It has been called by Irwin [1958a] the 'crack-edge stress-intensity-factor,' or simply the 'intensity factor.'

To determine  $\kappa$  for the problems under consideration it is necessary to investigate the limit of  $\widehat{\theta\theta}(\theta = 0)$  as  $\rho \rightarrow 1$ , inasmuch as  $\rho = 1$  and  $\theta = 0$ , are the coordinates of an apex.

For the step function, case 1, equation A12 yields

$$\widehat{\theta\theta}(0) \rightarrow \frac{2P}{\rho^2 - 1} \left\{ 1 - \frac{2}{\pi} \theta_0 \right\} + \text{const} \quad \rho \rightarrow 1 \quad (10)$$

From (A9) it can be shown that as  $\rho \rightarrow 1$ , and hence as  $r \rightarrow 0$ ,

$$\frac{1}{\rho^2 - 1} \rightarrow \frac{\sqrt{b}}{2} \frac{1}{\sqrt{2r}} \quad (11)$$

Hence using (28) and  $\theta_0 = \cos^{-1} a/b$ , we find that as  $\rho \rightarrow 1$

$$\widehat{\theta\theta}(0) \rightarrow P\sqrt{b} \left[ 1 - \frac{2}{\pi} \cos^{-1} \frac{a}{b} \right] \frac{1}{\sqrt{2r}} + \text{const} \quad r \rightarrow 0$$

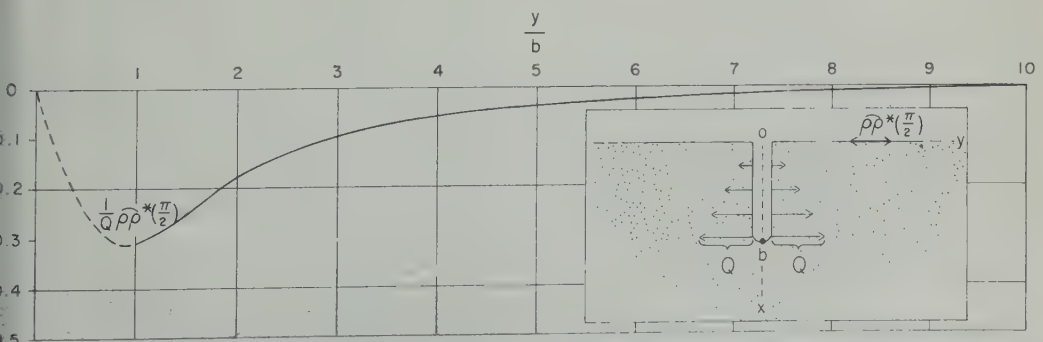


Fig. 9. Tangential stress on the free surface ( $x = 0$ ) due to a linear distribution of surface pressure on the walls of a crack ( $y = 0 \pm, 0 < x < b$ ) in a semi-infinite medium.



TABLE 6. Normalized Crack-Edge  
Stress-Intensity Factor  $\gamma$   
Step Function, Case 1

$a/b$	$\gamma(a/b) = \kappa(a/b)/P\sqrt{b}$	
	Infinite Body	Semi-Infinite Body
0.05	0.0317	0.04
0.1	0.0635	0.08
0.2	0.1285	0.16
0.3	0.1940	0.24
0.5	0.3335	0.41
0.75	0.5399	0.64
1.0	1.0000	1.1

Linear Function, Case 2

$\gamma = \kappa/Q\sqrt{b}$	
Infinite Body	Semi-Infinite Body
0.6366	0.68

and consequently for case 1

$$\kappa = P\sqrt{b} \left[ 1 - \frac{2}{\pi} \cos^{-1} \frac{a}{b} \right] \quad (12)$$

For the much studied case  $a = b$ , (12) reduces to the familiar result

$$\kappa = P\sqrt{b}$$

Similarly for case 2,

$$\theta\theta(0) \rightarrow \frac{2Q}{\pi} \frac{\rho^2 + 1}{\rho^2 - 1} + \text{const} \quad \rho \rightarrow 1$$

On application of (11) this yields

$$\kappa = Q\sqrt{b} (2/\pi) \quad (13)$$

It is interesting to note that this is the same numerical value as that obtained by *Sneddon* [1946] for a totally infinite medium containing a penny-shaped crack of radius  $b$  with constant normal pressures  $Q$  applied to the walls.

For the cases of a crack extending from the surface of a semi-infinite medium, discussed in the preceding section, it should be possible to approximate  $\kappa$  as follows:

$$\kappa \approx \kappa(-\tau) + \kappa(-\Delta_1\tau) + \kappa(-\Delta_2\tau) + \dots \quad (14)$$

where  $\kappa(-\tau)$  is the value obtained from the corresponding infinite case (equation 12 or 13)

and the other terms represent the internal factors associated with the fictitious stresses  $-\Delta_1\tau$ ,  $-\Delta_2\tau$ , etc. (equation 8). Inasmuch as the  $-\Delta_i\tau$  are approximated by step functions, each  $\kappa(-\Delta_i\tau)$  will itself be a linear combination of several terms of the form of (12). Values for the semi-infinite cases obtained from (12) are presented in normalized form in Table 6. The corresponding results for infinite cases given by (12) and (13) are also presented for comparison. For the infinite-body cases the values of  $\kappa$  are exact, but it is difficult to assess the error in the values determined for the semi-infinite cases, and they must be considered as rough approximations. It is reassuring, however, that the value of  $\kappa = 1.1$  for  $a/b = 1$  is in agreement with that recently computed by *Irwin* [1958b] for the same case by a different method.

## II. PHYSICAL APPLICATION

The results presented in part I can be used to estimate the depth and spacing of tension cracks in an infinite or semi-infinite body in which the stress is an arbitrary function of depth beneath the surface ( $x = 0$ ), insofar as the stress per unit area can be considered elastic and the material can be considered to have a well-defined tensile strength. Before this can be done, however, it is necessary to have a physical framework within which to interpret the details of the fracture process. Such a model is provided by the modified Griffith theory of macroscopic fracture introduced by *Irwin* [1948] and *Orowan* [1950]. In both the Griffith theory and the modified theory, the energy for crack extension is derived from the strain energy released by the growing crack. Only in the modified theory, however, is the energy consumption attributed principally to plastic deformation near the advancing crack tip. In most problems of macroscopic cracking, the work of plastic deformation is probably of greater importance than the surface energy considered by Griffith. Like any physical model, this one represents a simplification of the actual processes, but it rests on a substantial body of experimental information obtained with metals, plastics, glass, and concrete, and has met with success in engineering applications. In the following section this theory is outlined briefly, with no attempt made to cover the subject in detail. (For a comprehensive summary and reference to the literature see *Irwin* [1958a].) It is appli-

the results of part I, to illustrate a method of estimating crack depth in section 2, and crack spacing in section 3 of this part.

### *The Fracture Mechanics Model [Irwin, 1958a]*

To estimate the depth and spacing of tension cracks we must give some thought to the entire problem of initiation, propagation, and arresting a crack in an extended medium. The actual details of crack initiation depend upon a complex, poorly understood processes leading to the growth of small flaws under stress- and length-inhomogeneities on a microscopic scale. For brittle media it has been useful to describe crack initiation in terms of 'tensile strength,' which is the macroscopic, or average, tension under which small flaws start to grow and desce. However, when a crack assumes macroscopic size (i.e. when its length becomes large relative to the radius of the plastically deformed zone near the crack tip) it is no longer necessary or useful to view the cracking process in terms of the average stress field. In fact it has been found that the conditions for propagation of a macroscopic crack (as defined above) can be described by specifying only the crack-edge intensity factor  $\kappa$  computed formally from elasticity theory. This remarkably simple empirical result permits the application of elasticity theory to problems of macroscopic cracking. It can be viewed physically in the following way. For a long tension crack in an ideally elastic medium, the rate of release of strain energy with crack extension  $G$ , Young's modulus  $Y$ , and Poisson's ratio  $\nu$  are related to the crack-edge intensity factor  $\kappa$  by [Irwin, 1958a]

$$\kappa = \left[ \frac{YG}{\pi(1 - \nu^2)} \right]^{1/2} \quad (15)$$

Irwin has shown that this relation is approximately true for real media as long as the radius of the plastically deformed zone near the crack tip is small relative to crack length. Thus  $\kappa$  is a measure of  $G$ , which is called the 'crack extension energy' and represents the energy available to drive the crack extension process.  $\kappa$  is readily calculated for various experimental configurations from a knowledge of the ambient stress  $\sigma$  and crack depth  $b$ . As  $\kappa$  is increased to some critical value  $\kappa_c$ , characteristic of the material, the crack will begin to accelerate and propagate unstably with no further increase in applied

stress. Corresponding to  $\kappa_c$  is a value  $G_c$  which can be identified as the rate of energy consumption, principally by plastic deformation, at the advancing crack tip at the onset of rapid cracking. It has been found [ASTM Committee on Fracture Testing, 1961] that macroscopic crack extension can occur at subcritical values of  $\kappa$  but that the process is self-limiting, presumably because the incremental extension of the crack causes the plastic energy dissipation to grow faster than the crack extension force  $G$ . When  $\kappa$  attains its critical value  $\kappa_c$ , this is no longer true. Thus, subcritical or 'stable' crack growth occurs only under increasing applied load, whereas unstable propagation is spontaneous. In more brittle media, the range of  $\kappa$  over which stable propagation occurs is smaller, and the definition of  $\kappa_c$  is more precise.

Although this theory has been applied by Irwin and others to the early growth of cracks, it does not seem unreasonable to expect it to apply approximately to the problem of crack arresting as well. Thus we shall assume that a crack will continue to propagate as long as  $\kappa$  remains greater than some critical value  $\kappa_c$ . On the basis of the present model this is equivalent to the assumption that the rate of release of deformation energy with crack extension  $G$  must exceed a minimum value  $G_c$ , necessary to do the work at the advancing crack tip.  $G_c$  and  $G_0$  are expected to be of the same order of magnitude, but different symbols are adopted to acknowledge the likelihood of time-rate effects.

If the  $\kappa$  value used in equation 15 is obtained from a static elastic theory, the corresponding value of  $G$  applies strictly only to a crack that is not growing. However, as long as the rate of growth does not approach the speed of propagation of an elastic disturbance, the static result should be a good approximation for a growing crack as well. Although it is known that, before branching occurs, unstable tension cracks approach a limiting speed of about half that of elastic shear waves, it is clear that a crack must slow down before it stops. Therefore the static theory is probably adequate to describe the arresting process.

## *2. Depth of Tension Cracks*

To investigate some implied relationships between crack depth, stress distribution, and material properties, we shall consider the simple

case of a semi-infinite solid in which the stress is represented by a uniform tension  $P$  to some depth  $a$  and a superimposed gravitational compression  $-\delta g x$ . (Here  $\delta$  and  $g$  represent density and gravitational acceleration, respectively.) Many actual problems can be idealized in this way for this purpose. For a more refined treatment see *Lachenbruch* [in press].

Let  $\kappa_\theta(b)$  represent the contribution of the uniform tension to the intensity factor  $\kappa(b)$  of the deepening crack. The tension can be thought of as resulting from tectonic activity, thermal contraction, desiccation, or other geologic processes. Let  $\kappa_\delta(b)$  represent the contribution to  $\kappa(b)$  of the weight of the column of height  $b$ . The depth at which the crack stops,  $b$ , is then given implicitly by

$$\kappa_\theta(b) + \kappa_\delta(b) = \kappa_0 \quad (16)$$

Explicitly we may write

$$\kappa_\theta = \gamma(a/b)P\sqrt{b} \quad (17)$$

$$\kappa_\delta = -0.68 \delta g b^{3/2} \quad (18)$$

$$\kappa_0 = \left[ \frac{Y}{\pi(1-\nu^2)} G_0 \right]^{1/2} \quad (19)$$

where (18) is obtained by replacing  $Q$  in Table 6 by  $-\delta g b$ , and  $\gamma(a/b)$  is the normalized intensity factor for the step function in a semi-infinite medium. Introducing these expressions into (16) gives a relation between crack depth  $b$ , thickness of the layer in tension  $a$ , and material properties.

$$b + \frac{1}{0.68 \delta g} \left[ \frac{Y G_0}{\pi(1-\nu^2)} \right]^{1/2} \frac{1}{\sqrt{b}} = \frac{P}{0.68 \delta g} \gamma \left( \frac{a}{b} \right) \quad (20)$$

In general, (20) will be satisfied by two values of  $b$ . The larger value corresponds to the ultimate depth of a crack that has propagated unstably. When investigating the smaller value,  $G_0$  should be replaced by  $G_c$ , as that solution represents the critical crack depth  $b_c$  necessary for the onset of unstable propagation.

**Stable cracking—diurnal thermal stress.** For a crack penetrating a semi-infinite solid with a constant homogeneous initial stress,  $\kappa$  will increase as the square root of crack depth (the case  $a/b = 1$ , Table 6). However, inspection of Table 6 reveals that, if the tension decreases much faster with depth  $x$  than about  $x^{-1/2}$ ,  $\kappa$

will decrease for a deepening crack. Hence under the present assumption regarding stress, if  $\kappa$  does not assume the critical value  $\kappa_c$  by the time the crack reaches depth  $a$ , it never propagates and propagation will be stable and confined to the surficial layer  $x < a$ . To find the critical depth  $b_c$  necessary for unstable propagation, we take the case  $a/b = 1$  for which  $\gamma = 1.1$ . (20) becomes

$$b_c = \left[ \frac{1}{1.1P} \left\{ 0.68 \delta g b_c^{3/2} + \left( \frac{Y G_c}{\pi(1-\nu^2)} \right)^{1/2} \right\} \right]^2$$

We assume the following values, which are probably reasonable for crystalline rocks,

$$Y/\pi(1-\nu^2) \approx 3 \times 10^{11} \text{ dynes cm}^{-2}$$

$$P \approx 5 \times 10^7 \text{ dynes cm}^{-2}$$

where the value of  $P$  is selected to represent the tensile strength. The term in  $b^{3/2}$  representing weight of overburden is unimportant in this case; hence

$$b_c \approx \frac{1}{1.21P^2} \frac{Y G_c}{\pi(1-\nu^2)}$$

$$b_c \approx 10^{-4} G_c$$

Thus if  $G_c$  were  $10^4$  ergs  $\text{cm}^{-2}$ , the order of magnitude reported for glass at room temperature [*Irwin*, 1958a] and for concrete (G. Kaplan, written communication), the crack would be stable only if the layer in tension was less than 1 cm deep. If  $G_c$  were  $10^6$  ergs  $\text{cm}^{-2}$ , the surficial layer would have to be greater than 10 cm deep to induce unstable propagation. From the dependence of  $b_c$  on the applied stress  $P$ , it is seen that, if cracks were growing by fatigue under cyclic loading with amplitude  $1/2 P$ , the loaded layer would have to be greater than 40 cm deep before such cracks would propagate unstably if  $G_c = 10^6$ . Similarly if the stress layer were only  $2\frac{1}{2}$  cm deep and  $G_c = 10^6$ , applied stress would have to be greater than twice the strength  $P$  to cause unstable fracture. Thus where surficial tension in a semi-infinite solid does not penetrate to depths comparable to  $b_c$ , such tension can exceed the nominal tensile strength without producing unstable cracks.

Considerations of this kind might help explain the absence of conspicuous tension cracks



TABLE 7. Relation between Depth of Surficial Tensile Zone  $a$ , Crack Depth  $b$ , Crack-Arresting Energy  $G_0$ , and Surface Stress Relief for the Basalt-Model Discussed in Text

Stress Depth $a$ , cm	$G_0 = 10^5$ ergs cm <sup>-2</sup>				$G_0 = 10^4$ ergs cm <sup>-2</sup>				$G_0 = 0$			
	Crack Depth $b$ , cm	Stress Relief at $x = 0$ , %			Crack Depth $b$ , cm	Stress Relief at $x = 0$ , %			Crack Depth $b$ , cm	Stress Relief at $x = 0$ , %		
		$a/b$	$y = b$	$y = \frac{1}{2}b$		$a/b$	$y = b$	$y = \frac{1}{2}b$		$a/b$	$y = b$	$y = \frac{1}{2}b$
1	$\leq 1^*$				1†	1.00	94	100	141	0.007	1	2
5	$\leq 5^*$				14	0.36	67	94	316	0.016	2	5
10	10†	1.00	94	100	54	0.19	34	63	447	0.022	3	7
30	49	0.61	79	100	331	0.091	16	33	775	0.039	5	12
60	187	0.32	53	91	698	0.086	14	30	1095	0.055	6	14
90	378	0.24	42	78	978	0.092	15	31	1342	0.067	10	21
150	785	0.19	34	63	1410	0.11	18	36	1732	0.087	13	29
300	1610	0.19	33	63	2178	0.14	22	44	2450	0.12	18	38

\* Stable.

† Critical depth.

rocks exposed to extreme diurnal temperature variations. It can be shown that thermoelastic stresses in such rocks probably exceed the strength, but only in a thin surficial layer.

*Unstable cracking induced by surficial tension—cooling joints in lava.* If the crack grows to unstable depth  $b_c$  in the surficial layer  $x < a$ , it can generally be expected to propagate to some depth  $b > a$  if  $a$  is not too large. From Table 6 it is seen that, when  $b \gtrsim 2a$ ,  $\gamma \approx 0.8a/b$ . Anticipating that this condition will be satisfied in the case to be discussed, we introduce  $\gamma = 0.8a/b$  in (20) to obtain an expression for the ultimate depth of a crack propagating unstably in response to surficial tension:

$$b^2 + \frac{1}{0.68 \delta g} \left[ \frac{Y G_0}{\pi(1 - \nu^2)} \right]^{1/2} \sqrt{b} = \frac{0.8 P a}{0.68 \delta g} \quad (25)$$

It is likely that thermal contraction-crack polygons in permafrost and basalt are, for the most part, formed by tension cracks that propagate unstably in response to surficial tension. Hence, it is of some interest to examine the idealized relation (25) between the stress field described by the three parameters  $P$ ,  $a$ , and  $\delta$ ), the crack depth  $b$ , and material properties, for basalt. (Permafrost is discussed elsewhere.) Numerical results are presented in Table 7. The values chosen for the parameters were the same as those in the previous example, (22) and (23), and in addition it was assumed that  $\delta = 3$  cm $^{-2}$ . It should be emphasized that the values

of depth in Table 7 are those computed for a single crack, or one so far from its neighbors that it is unaffected by them. (This problem will be discussed further below.) It will be noted that the depth of shallower cracks is very sensitive to  $G_0$ , which is lower for more brittle, and hence cooler, media. As the depth increases, the control of crack depth passes from  $G_0$ , represented by the term in  $b^{1/2}$  (equation 25), to the effect of the compressive stress at depth, the term in  $b^2$  (equation 25). The case  $G_0 = 0$  yields an upper limit to crack depth, as it represents an ideal medium in which no energy is consumed by the crack-extension process.

It is seen that the ratio  $a/b$  passes through a minimum value which can be obtained by differentiation of (25):

$$\left( \frac{a}{b} \right)_{\min} = \frac{2.08}{P} \left\{ \delta g \frac{Y G_0}{\pi(1 - \nu^2)} \right\}^{1/3} \quad (26)$$

On the basis of the present assumptions its value is 0.086 for  $G_0 = 10^4$  and 0.18 for  $G_0 = 10^5$ . If  $G_0$  were only  $10^3$  its value would be 0.04. For ice and permafrost the individual parameters would be different, but the order of magnitude of the minimum ratio is still expected to be about 0.1. Precise significance cannot be attached to these values in the absence of specific information on  $G_0$  and tensile strength  $P$  for rocks. However, from this discussion it seems likely that the depth at which naturally occurring tension cracks arrest will not exceed the thickness of the surficial tensile zone  $a$  by more than



a factor of 10, or perhaps 20, where the actual stress is approximated by the present 3-parameter model.

*Unstable cracking induced by deep tension—tectonic forces.* It might be of interest to consider, from the present point of view, how deeply a tension crack might be expected to penetrate the earth in response to profound regional tension. We take the highly idealized view that the rock is initially unfractured and that a uniform regional tension builds up until it exceeds the strength at the surface. The crack depth is then given by the case  $a/b = 1$  by setting  $\gamma = 1.1$  in (20) and solving for the larger value of  $b$ .

For the limiting case  $G_0 = 0$ , this reduces to

$$b = \frac{1.1P}{0.68 \delta g} \quad (27)$$

Equation 27 yields the depth at which no strain energy is released by further crack extension. It therefore represents a safe upper limit to the depth of a single tension crack in a medium subjected to uniform horizontal tensile stress of magnitude  $P$ , and to hydrostatic compression from its own weight. Setting  $P = 50 \text{ kg cm}^{-2}$  and  $\delta = 3 \text{ g cm}^{-3}$  as before, we obtain from (27) a crack depth of 902 feet ( $2.75 \times 10^4 \text{ cm}$ ). It is most interesting to note that, when  $G_0 = 10^4$  and  $10^5$ , the corresponding depths given by (20) are 898 feet and 891 feet, respectively. Thus, in calculations of this kind the very simple approximation (27), which does not require knowledge of  $G_0$ , is a very good one for a wide range of media.

*Role of the neutral horizon—hypothetical tension cracks on the moon.* It is worth noting that the neutral horizon, i.e. the depth at which the initial stress  $\tau(x)$  passes from tension to compression, has practically nothing to do with crack depth in media to which the present theory applies. Tension cracks can, and often do, penetrate much deeper than the initial tension that produces them. Thus in the application of (27) above, the ambient stress passes from tension to compression at a depth of 550 feet, and hence about 40 per cent of the tension crack discussed lies below this depth in the compressional field.

A more striking example is afforded by a calculation of the depth of hypothetical tension cracks on the moon. If at some place the moon's surface might be composed of bare rock with the

properties of dense basalt, periodic thermoelastic stresses (during each 29.3-day lunation) could produce contraction cracks to a depth of 15 or 200 feet, although thermal tension would be dominated by gravitational compression at depths greater than 15 or 20 feet. Part of the great crack depth would be attained by deepening after the initial cracking occurred, as the surface thermal stress would far exceed the strength of the elastic model applies.

### 3. Spacing of Tension Cracks

The following is a simplified illustration of the method of estimating crack spacing. Suppose that the tensile stress rose rapidly so that the tensile strength was only 90 per cent of the tension at the surface. After one crack formed it would relieve the stress locally at the ground surface. A neighboring parallel crack could then form within the zone in which the stress rose, exceeding 10 per cent, for the stress would be below the strength there. It could not be farther away from the first crack than the distance between points of about 5 per cent stress relief, or otherwise a third crack would form between them. These distances can be easily computed from a knowledge of the crack depth (estimated by the method outlined above) and of the initial stress field and the information contained in Tables 4 and 5 or Figures 8 and 9. In most cases the problem is more complicated, however, and it is generally necessary to treat the tensile strength as a function of position, accounting statistically for the distribution of flaws of various sizes. This problem is discussed in another paper [Lachenbruch, in press].

*Relation between crack depth and crack spacing in cooling joints in lava.* Where cracks are closely spaced and deep, calculation of the depth of a given crack must take into account the stress perturbation caused by its pre-existing neighbors. However, when the applied stress does not change greatly during the evolution of a crack system, this complication is probably minor. (This may be the case in many cooling joints in systems in basalt.) Inasmuch as the tension stress leads to cracking builds up gradually (e.g. progressive cooling), it is unlikely that a crack will initiate in a portion of the surface stress is influenced by its neighbor; and if the influence is slight at the surface, it can generally be expected to be even less at depth.

Under these conditions it seems reasonable to apply the single-crack model described in the preceding section to the calculation of crack depth in multiple-crack systems. Hence the data of Table 7 and the discussion regarding the minimum value of  $a/b$  should also apply. The stress relief presented in Table 7 is computed from the combined effect of the simple step distribution of tension (Table 4) and the linear distribution of gravitational compression (Table 5). It is seen from Table 7 that where the stressed layer is about 2 feet (60 cm) deep the crack depth is about 23 feet (698 cm) when  $G_0 = 10^4$ . Such a crack would relieve 14 per cent of the tensile stress  $P$  at points on the surface 23 feet away ( $y = b$ ) and 30 per cent at points  $11\frac{1}{2}$  feet away ( $y = \frac{1}{2}b$ ). In the other examples in Table 7 the stress relief at a horizontal distance of 1 crack depth is even greater. The gravitational effect (Table 5) on the values of stress relief presented in Table 7 is minor, and hence the general form of the stress relief function for various values of  $a/b$  can be obtained from inspection of Figure 8. From the preceding section, the minimum value of  $a/b$  for brittle geological materials is not expected to be less than about 0.05, and generally it is expected to be greater. Hence it seems that, in naturally occurring tension-crack systems that evolve rapidly, the crack depth should be of the same order of magnitude or less than the crack spacing. If this were not true, neighboring cracks would be initiating in zones of greatly reduced tension.

*Subsequent deepening of cracks and higher-order systems—cooling lava, drying mud.* In the foregoing discussion of cracks that propagate unstably downward, the computed depth was limited by the assumed tensile strength of the material, which was set equal to  $P$ . Hence the computed depths were those that would be attained at the time of initial fracturing. The nominal applied stress could subsequently increase far beyond the tensile strength and penetrate to greater depth, and the cracks would deepen as a consequence. The ultimate crack depth could still be computed from the equations given as long as the interaction of neighboring cracks did not become appreciable.

It is well known that the final depth of cooling joints in basalt often exceeds the joint spacing by two orders of magnitude. However, on the basis of the previous discussion it seems likely

that crack systems in basalt are established initially in a relatively thin surficial layer by cracks whose depth is of the order of the crack spacing or less. Evidently the cracks deepen later, either stably or in unstable increments, during progressive cooling as the thermal stress penetrates to greater depth.

It was pointed out by Irwin (oral communication) that, after the cracks deepened enough to interact appreciably, those cracks which were by chance a little deeper might be selected for further deepening at the expense of their neighbors in a homogeneous medium. Inasmuch as basalt joints are often remarkably persistent over large depth intervals, it is possible that the deepening of the cracks follows closely the descent of the zone of solidification and that no crack could get far ahead of the others without running into a plastic zone (high  $G_0$ ) and arresting.

In other systems, however, the selective deepening of widely spaced cracks by prolonged contraction is evident, and this leads to several orders of superimposed crack systems. The deeper cracks are more widely spaced because they relieve tension over greater horizontal distances than their shallower neighbors. Such patterns are most commonly observed in drying mud, which, because of its plasticity, can be expected to conform to the present theory in only a qualitative way. Shallow, closely spaced cracks relieve surficial tension developed by rapid desiccation after a rain. Deeper cracks, more widely spaced, might represent seasonal desiccation, and profound cracks with spacing of the order of 10 to 100 feet could correspond to the draining of a marsh (George O. Gates, oral communication) or perhaps to a secular climatic trend toward aridity [Willden and Mabey, 1961].

#### CONCLUDING COMMENTS

The discussion of part II has been devoted to the problem of a crack extending from the surface of a semi-infinite medium, as this is the case that is most interesting geologically (or at least geomorphologically) and the one for which least information is available. Problems of the totally infinite medium, such as hydraulic fracturing in a nonuniform stress field, can be treated in the same way, and results applicable to such problems are presented in the first part of the paper.

It is important to emphasize that the fracture

problems here treated in a highly idealized way are actually very complex. The fracture mechanics model used is certainly not true in detail, but it represents a successful means of focusing attention on pertinent measurable quantities. The mathematical solutions used represent two-dimensional models, and the physics of the three-dimensional fracture process has been given little attention. (For a discussion of polygonal fracture patterns see *Lachenbruch* [in press].) Nevertheless, it seems that the modified Griffith theory of Irwin and Orowan, used with mathematical results of the type presented, provides a useful quantitative approach to problems of macroscopic tension fracture in geology. With analogous mathematical models for the shearing case, the same approach might yield useful information on the problem of initiation and arresting of shear faults in a nonuniform stress field under small confining pressure. Other problems of shear fracture in geology are discussed in terms of modifications of the Griffith theory in recent work by *Orowan* [1960] and *Brace* [1960].

To the extent that the present point of view is valid, the quantities  $G_c$  and  $G_0$  are properties of the medium. It is likely that a laboratory study of these quantities for geological materials would be rewarding.

#### APPENDIX

The problem of finding the stress in the interior of an elastic body under conditions of plane strain can, in the absence of body forces, be reduced to that of finding the Airy function  $U(x, y)$  such that

$$\frac{\partial^4 U}{\partial x^4} + 2 \frac{\partial^2 U}{\partial x \partial y} + \frac{\partial^4 U}{\partial y^4} = 0 \quad (\text{A1})$$

where

$$X_x = \frac{\partial^2 U}{\partial y^2}, \quad Y_y = \frac{\partial^2 U}{\partial x^2}, \quad X_y = -\frac{\partial^2 U}{\partial_x \partial_y} \quad (\text{A2})$$

and where  $U$  is to lead to the prescribed stresses on the boundary.

In the notation of *Muskhelishvili* [1953, p. 180ff.] we define the complex potentials  $\phi_1$  and  $\psi_1$  such that

$$\frac{\partial U}{\partial x} + i \frac{\partial U}{\partial y} = \phi_1(z) + z \overline{\phi_1'(z)} + \overline{\psi_1(z)}$$

throughout body (A3)

$= f(s)$  on the boundary  $L$  (A4)

Here the prime denotes differentiation with respect to  $z = x + iy$ , the complex conjugate represented by a bar, and

$$f(s) = f_1(s) + if_2(s) =$$

$$i \cdot \int_0^s (X_n + iY_n) ds \quad (\text{A5})$$

where  $X_n$  and  $Y_n$  are the  $x$  and  $y$  components of the prescribed surface stresses in the direction of the positive normal on the boundary  $L$ .

The analytic functions  $\psi_1(z)$  and  $\phi_1(z)$  are determined, respectively, to within a complex constant and a complex linear function, by the boundary relation

$$\phi_1(z) + z \overline{\phi_1'(z)} + \overline{\psi_1(z)} =$$

$$i \cdot \int_0^s (X_n + iY_n) ds \quad (\text{A6})$$

The arbitrariness in  $\phi_1$  and  $\psi_1$  as determined by (A5) represents only rigid body motion, so that (A5) completely determines the state of stress in terms of surface forces. Applying the complex transformation  $z = \omega(\zeta)$ , and setting

$$\phi_1(z) = \phi_1(\omega(\zeta)) = \phi(\zeta)$$

$$\psi_1(z) = \psi_1(\omega(\zeta)) = \psi(\zeta)$$

$$\zeta = \rho e^{i\theta}$$

we obtain for (A4)

$$\phi(\zeta) + \frac{\omega(\zeta)}{\omega'(\zeta)} \overline{\phi'(\zeta)} + \overline{\psi(\zeta)}$$

$$= i \int_0^s (X_n + iY_n) ds \quad \zeta = \sigma \quad (\text{A7})$$

where  $\sigma$  is the value of  $\zeta$  on the boundary, in the  $\zeta$  plane. By setting

$$\Phi(\zeta) = \frac{d\phi_1(z)}{dz} = \frac{\phi'(\zeta)}{\omega'(\zeta)}$$

$$\Pi(\zeta) = \frac{2\zeta^2}{\rho^2 \omega'(\zeta)} [\overline{\omega(\zeta)} \Phi'(\zeta) + \psi'(\zeta)]$$

we can write Muskhelishvili's general result for the components of stress referred to the cur-



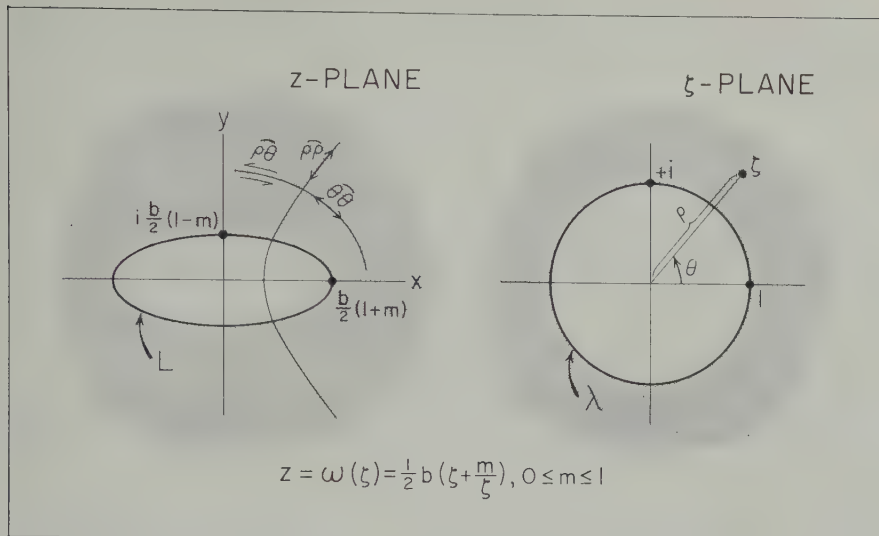


Fig. 10. The transformation mapping the exterior of an ellipse into the exterior of a unit circle.

linear coordinates of the transformation, as follows:

$$\widehat{\rho\rho} + \widehat{\theta\theta} = 4 \operatorname{Re} [\Phi(\zeta)] \quad (\text{A7a})$$

$$\widehat{\theta\theta} - \widehat{\rho\rho} + 2i\rho\theta = \Pi(\zeta) \quad (\text{A7b})$$

The components of stress are therefore given explicitly by

$$\widehat{\rho\rho} = 1/2 \{ 4 \operatorname{Re} [\Phi(\zeta)] - \operatorname{Re} [\Pi(\zeta)] \} \quad (\text{A8a})$$

$$\widehat{\theta\theta} = 1/2 \{ 4 \operatorname{Re} [\Phi(\zeta)] + \operatorname{Re} [\Pi(\zeta)] \} \quad (\text{A8b})$$

$$\widehat{\theta} = \frac{1}{2i} \operatorname{Im} [\Pi(\zeta)] \quad (\text{A8c})$$

We use the transformation [Muskhelishvili, 1953]

$$z = \omega(\zeta) = 1/2 b (\zeta + m/\zeta) \quad (\text{A9})$$

$$0 \leq m \leq 1$$

which maps the exterior of the unit circle in the  $\zeta$  plane

$$|\zeta| \geq 1$$

into the exterior of the ellipse

$$|y| \geq 1/2 b (\rho - m/\rho) \sin \theta \quad (\text{A10a})$$

$$|x| \geq 1/2 b (\rho + m/\rho) \cos \theta \quad (\text{A10b})$$

in the  $z$  plane (see Fig. 10).

Present interest centers about the degenerate case  $m = 1$ , in which the unit circle  $|\zeta| = 1$  corresponds to the double line segment  $|x| < b$ ,  $y = 0 \pm$ .

*Case 1: The step function.* We first consider the case of a step distribution of self-equilibrating surface stresses on the degenerate ellipse,  $m = 1$ ,  $\rho = 1$ . This case, which is illustrated in Figure 2 by the inset, is described by

$$\begin{aligned} Y_n &= -P & |x| < a \\ &= 0 & a < |x| < b \\ X_n &= 0 \end{aligned}$$

where  $P$  is a constant. Setting  $\zeta = \sigma$  on the boundary, and  $\theta_0 = \cos^{-1}(a/b)$ , we obtain from (A4)

$$\begin{aligned} f(s) &= f_1 + if_2 = 1/2 P b \left( \sigma + \frac{1}{\sigma} \right) \\ &\begin{cases} \theta_0 < \theta < \pi - \theta_0 \\ \pi + \theta_0 < \theta < 2\pi - \theta_0 \end{cases} \\ &= Pa & -\theta_0 < \theta < +\theta_0 \\ &= -Pa & -\theta_0 + \pi < \theta < \theta_0 + \pi \end{aligned}$$

Using equation (A6) and the general properties of analytic functions leads to



$$\phi = \frac{-Pb}{4\pi} \left\{ \frac{1}{\zeta} (2\pi - 4\theta_0) + \frac{1}{i} \left( \frac{1}{\zeta} + 2 \cos \theta_0 + \zeta \right) \cdot \ln \frac{\sigma_0 + \zeta}{\bar{\sigma}_0 + \zeta} + \frac{1}{i} \left( \frac{1}{\zeta} - 2 \cos \theta_0 + \zeta \right) \ln \frac{\sigma_0 - \zeta}{\bar{\sigma}_0 - \zeta} \right\}$$

$$\psi = \frac{-Pb}{4\pi} \left\{ \frac{2\zeta}{\zeta^2 - 1} (2\pi - 4\theta_0) + \frac{2}{i} \cos \theta_0 \left[ \ln \frac{\sigma_0 + \zeta}{\bar{\sigma}_0 + \zeta} - \ln \frac{\sigma_0 - \zeta}{\bar{\sigma}_0 - \zeta} \right] \right\}, \text{ where } \sigma_0 = e^{i\theta_0}$$

After much manipulation, the final result for the stress components is found to be

$$\widehat{\rho\rho} = P \left\{ \frac{1}{\pi} [\alpha_4 - \alpha_3 + \alpha_2 - \alpha_1] - \left[ 1 - \frac{2}{\pi} \theta_0 \right] \left[ 1 - \frac{(\rho^2 - 1)^3 (\rho^2 + 1)}{(\rho^4 - 2\rho^2 \cos 2\theta + 1)^2} \right] \right. \\ \left. + \frac{2\rho^2(\rho^4 - 1) \sin 2\theta_0 (1 - \cos 2\theta) [2\rho^2(\cos 2\theta - \cos 2\theta_0) - (\rho^2 - 1)^2]}{\pi(\rho^4 - 2\rho^2 \cos 2\theta + 1)[\rho^4 - 2\rho^2 \cos 2(\theta - \theta_0) + 1][\rho^4 - 2\rho^2 \cos 2(\theta + \theta_0) + 1]} \right\} \quad (\text{A1})$$

$$\widehat{\theta\theta} = P \left\{ \frac{1}{\pi} [\alpha_4 - \alpha_3 + \alpha_2 - \alpha_1] - \left[ 1 - \frac{2}{\pi} \theta_0 \right] \left[ 1 - \frac{(\rho^4 - 1)[(\rho^2 + 1)^2 - 4\rho^2 \cos 2\theta]}{(\rho^4 - 2\rho^2 \cos 2\theta + 1)^2} \right] \right. \\ \left. - \frac{2\rho^2(\rho^4 - 1) \sin 2\theta_0 (1 - \cos 2\theta) [2\rho^2(\cos 2\theta - \cos 2\theta_0) - (\rho^2 - 1)^2]}{\pi(\rho^4 - 2\rho^2 \cos 2\theta + 1)(\rho^4 - 2\rho^2 \cos 2(\theta - \theta_0) + 1)(\rho^4 - 2\rho^2 \cos 2(\theta + \theta_0) + 1)} \right\} \quad (\text{A2})$$

$$\widehat{\rho\theta} = P \left\{ \frac{2\rho^2(\rho^2 - 1)^2 \sin 2\theta}{\rho^4 - 2\rho^2 \cos 2\theta + 1} \left[ \frac{1 - \frac{2}{\pi} \theta_0}{\rho^4 - 2\rho^2 \cos 2\theta + 1} \right. \right. \\ \left. \left. - \frac{\sin 2\theta_0 [2\rho^2(\cos 2\theta + \cos 2\theta_0) - (\rho^2 + 1)^2]}{\pi(\rho^4 - 2\rho^2 \cos 2(\theta - \theta_0) + 1)(\rho^4 - 2\rho^2 \cos 2(\theta + \theta_0) + 1)} \right] \right\} \quad (\text{A3})$$

where

$$\alpha_1 = \tan^{-1} \left( \frac{\rho \sin \theta + \sin \theta_0}{\rho \cos \theta + \cos \theta_0} \right) \quad (\text{A14a})$$

$$\alpha_2 = \tan^{-1} \left( \frac{\rho \sin \theta - \sin \theta_0}{\rho \cos \theta + \cos \theta_0} \right) \quad (\text{A14b})$$

$$\alpha_3 = \tan^{-1} \left( \frac{\rho \sin \theta - \sin \theta_0}{\rho \cos \theta - \cos \theta_0} \right) \quad (\text{A14c})$$

$$\alpha_4 = \tan^{-1} \left( \frac{\rho \sin \theta + \sin \theta_0}{\rho \cos \theta - \cos \theta_0} \right)$$

$$Y_n = -\frac{Q}{b} x \quad x > 0$$

$$= +\frac{Q}{b} x \quad x < 0$$

$$X_n = 0$$

where  $Q$  is an intensity parameter. Setting  $\sigma = e^{i\theta}$ , we obtain from equation (A4)

$$f_1 + if_2 = +\frac{1}{8}Qb(2 + \sigma^2 + 1/\sigma^2)$$

$$-\pi/2 < \theta < +\pi$$

$$= -\frac{1}{8}Qb(2 + \sigma^2 + 1/\sigma^2)$$

$$\pi/2 < \theta < 3\pi$$

For the special case  $a = b$ , equations A11 to A13 reduce to those given by Muskhelishvili [1953, p. 340] by setting  $\theta_0 = 0$ .

**Case 2: The linear function.** We now consider the effect of a symmetrical linear distribution of normal pressures over the degenerate ellipse  $m = 1$ ,  $\rho = 1$  (see Fig. 6, insert). In this case

This leads to

$$\phi = +Qb \frac{1}{4\pi}$$

$$\cdot \left[ \zeta - \frac{1}{\zeta} + \frac{i}{2} \left( \zeta + \frac{1}{\zeta} \right)^2 \ln \frac{\zeta + i}{\zeta - i} \right]$$

$$= -Qb \frac{1}{4\pi} \left[ \frac{1}{\xi^2 - 1} \left( \xi^3 + 6\xi + \frac{1}{\xi} \right) + i \frac{(\xi^2 + 1)^2}{2\xi^2} \ln \frac{\xi + i}{\xi - i} \right]$$

and finally

$$\begin{aligned} \rho &= \frac{+Q}{\pi(\rho^4 - 2\rho^2 \cos 2\theta + 1)} \left\{ 2(\rho^4 - 1) \right. \\ &\cdot \left[ 1 - \frac{(\rho^2 + 1)^2 \sin^2 \theta + 4\rho^2 \sin^4 \theta}{\rho^4 - 2\rho^2 \cos 2\theta + 1} \right] \\ &- \frac{(\rho^2 - 1)^3}{4\rho} (\sin \theta + \sin 3\theta) \\ &\cdot \ln \left[ \frac{\rho^2 + 2\rho \sin \theta + 1}{\rho^2 - 2\rho \sin \theta + 1} \right] \\ &- \frac{1}{2\rho} [(\rho^6 + \rho^4 + \rho^2 + 1) \cos \theta \\ &- (\rho^6 - 3\rho^4 - 3\rho^2 + 1) \cos 3\theta] (\beta_1 - \beta_2) \Big\} \end{aligned} \quad (A15)$$

$$\begin{aligned} \theta &= \frac{+Q}{\pi(\rho^4 - 2\rho^2 \cos 2\theta + 1)} \left\{ 2(\rho^4 - 1) \right. \\ &\cdot \left[ 1 + \frac{(\rho^2 + 1)^2 \sin^2 \theta + 4\rho^2 \sin^4 \theta}{\rho^4 - 2\rho^2 \cos 2\theta + 1} \right] \\ &- \frac{1}{4\rho} (\rho^2 + 1)(\rho^4 - 1)[3 \sin \theta - \sin 3\theta] \\ &\cdot \ln \left[ \frac{\rho^2 + 2\rho \sin \theta + 1}{\rho^2 - 2\rho \sin \theta + 1} \right] \\ &- \frac{1}{2\rho} [(3\rho^6 - \rho^4 - \rho^2 + 3) \cos \theta \\ &- (\rho^6 + \rho^4 + \rho^2 + 1) \cos 3\theta] (\beta_1 - \beta_2) \Big\} \end{aligned} \quad (A16)$$

$$\begin{aligned} \theta &= \frac{-2Q(\rho^2 - 1) \sin \theta}{\pi(\rho^4 - 2\rho^2 \cos 2\theta + 1)} \\ &\cdot \left\{ \frac{(\rho^2 - 1) \cos \theta [(\rho^2 - 1)^2 - 4\rho^2 \cos^2 \theta]}{\rho^4 - 2\rho^2 \cos 2\theta + 1} \right. \\ &- \frac{1}{4\rho} (\rho^4 - 1) \sin 2\theta \\ &\cdot \ln \left[ \frac{\rho^2 + 2\rho \sin \theta + 1}{\rho^2 - 2\rho \sin \theta + 1} \right] \end{aligned}$$

$$- \frac{1}{2\rho} [(\rho^4 + 1) \cos 2\theta - 2\rho^2] (\beta_1 - \beta_2) \Big\} \quad (A17)$$

where

$$\beta_1 = \tan^{-1} \left( \frac{\rho \sin \theta + 1}{\rho \cos \theta} \right)$$

$$\beta_2 = \tan^{-1} \left( \frac{\rho \sin \theta - 1}{\rho \cos \theta} \right)$$

*Acknowledgment.* I am grateful to Dr. George R. Irwin and Dr. Richard Toupin of the Naval Research Laboratory for a very helpful discussion of the manuscript and for suggestions leading to substantial changes in the organization of the material presented. Professor Francis Birch also offered very valuable comments on a draft of the manuscript. Assistance with numerical calculations was provided by B. Vaughn Marshall and Gordon W. Greene.

This work is part of a continuing study by the U. S. Geological Survey of thermal problems in permafrost. It is supported in part by the Office of Naval Research, the U. S. Navy Bureau of Yards and Docks, and U. S. Air Force Cambridge Research Center.

Publication authorized by the Director, U. S. Geological Survey.

#### REFERENCES

- ASTM Committee on Fracture Testing of High-Strength Metallic Materials, The slow growth and rapid propagation of cracks, *Materials Research and Standards*, 1(5), 389-393, 1961.
- Brace, W. F., An extension of the Griffith theory of fracture to rocks, *J. Geophys. Research*, 65(10), 3477-3480, 1960.
- Carothers, S. D., Plane strain: the direct determination of stress, *Proc. Roy. Soc. London A*, 97, 110-123, 1920.
- Inglis, C. E., Stresses in a plate due to the presence of cracks and sharp corners, *Trans. Inst. Naval Architect.*, 55, 219-241, 1913.
- Irwin, G. R., Fracture dynamics, in *Fracturing of Metals*, American Society of Metals, Cleveland, Ohio, 1948.
- Irwin, G. R., Fracture, in *Handbuch der Physik*, 6, 551-590, Springer-Verlag, Berlin, 1958a.
- Irwin, G. R., The crack-extension force for a crack at a free surface boundary, *U. S. Naval Research Lab. Rept. 5120*, 10 pp., 1958b.
- Knopoff, Leon, Energy release in earthquakes, *Geophys. J.*, 1(1) 44-52, 1958.
- Lachenbruch, Arthur H., Mechanics of thermal contraction cracks and ice-wedge polygons in permafrost, *Bull. Geol. Soc. Am.*, in press, 1962.
- Muskhelishvili, N. I., *Some Basic Problems of the Mathematical Theory of Elasticity*, P. Noordhoff, Groningen, Holland, 704 pp., 1953.
- Orowan, E., Fundamentals of brittle behavior in

- metals, in *MIT Symposium on Fatigue and Fracture of Metals*, John Wiley & Sons, New York, 1950.
- Orowan, E., Mechanism of seismic faulting, in *Rock Deformation*, *Geol. Soc. Am. Mem.* 79, 323-345, 1960.
- Sneddon, I. N., The distribution of stress in the neighborhood of a crack in an elastic solid, *Proc. Roy. Soc. London A*, 187, 229-260, 1946.
- Sneddon, I. N., *Fourier Transforms*, McGraw Hill Book Co., New York, 542 pp., 1951.
- Sneddon, I. N., and H. A. Elliot, The opening Griffith crack under internal pressure, *Q. J. Appl. Math.*, 4, 262-267, 1946.
- Westergaard, H. M., Bearing pressures and cracks, *J. Appl. Mech.*, 6, A49-A53, 1939.
- Willden, Ronald, and D. R. Mabey, Giant desiccation fissures on the Black Rock and Snake Creek deserts, Nevada, *Science*, 133(3461), 1331-1360, 1961.

(Manuscript received September 22, 1961.)

# Electrostatic Erosion Mechanisms on the Moon

P. D. GRANNIS

*Center for Radiophysics and Space Research, Cornell University  
Ithaca, New York*

**Abstract.** The electrostatic processes which have been suggested by Gold as being responsible for erosion of the lunar features are evaluated. The statistics of the charge build-up on the grains of lunar dust due to the solar gas streams are considered. On the basis of the derived probability distribution for grain charge, the electrostatic hopping effect is shown to result in an erosion rate which is lower by a factor of at least  $10^2$  than that rate indicated by observations of the moon. It is found that, owing to the supporting action of the electronic space charge, positively charged dust grains may be levitated above the surface. The mass transport resulting from the 'downhill' gliding of such levitated grains may be sufficient to explain observed lunar erosion.

1. *Introduction.* It has been suggested on the basis of thermal measurements [Wesselink, 1948], polarization studies [Wright, 1927; Lyot, 1929], photometric studies [van Diggelen, 1959], and radar scattering and absorption experiments [Hey and Hughes, 1959; Senior and Siegel, 1959] that the surface of the moon is composed of dust and is smooth on the scale of centimeters. The best estimate of the size of the individual dust grain places them between 1 and 50 microns in diameter. The evidence and arguments for the dusty surface have been presented in the literature by Gold [1955; 1959; 1960; 1961] and will not be reviewed here.

Such lunar phenomena as the aging of craters and the difference in coloration of the high and low ground have been interpreted by Gold as being evidence that some erosion processes are operative on the moon. The mechanisms which he suggests for transporting the lunar dust are electrostatic in nature, depending upon random fluctuations in the electric charge of the individual dust grains.

In this paper we shall consider these electrostatic erosion mechanisms in some detail. For the purpose of this study the grains are assumed to be  $5\text{-}\mu$  spheres of silica, of density  $2.3\text{ g/cm}^3$ , and mass  $1.5 \times 10^{-10}\text{ g}$ .

2. *Charging mechanisms.* Before considering the erosion mechanisms we must examine the way in which lunar dust grains may become charged. There are several processes acting to produce a charge on a dust grain. Protons and

electrons emitted by the sun may strike a grain; although the integrated flux of the protons equals that of the electrons, local statistical variations in the particle stream may result in a net difference in the number of positive and negative charges accumulated on a grain. There are also secondary charging effects: the incident protons and electrons induce secondary electron emission, and the solar photons produce photoelectric emission. There may be variations in the number of secondary electrons ejected from a grain and in the number returning to it which result in a charge on the grain. Before calculating these various processes in detail, we shall develop a general expression for the charge probability distribution.

We can consider the solar proton bombardment, solar electron bombardment, secondary and photoelectric emission, and the return of electrons to the surface to be four independent processes. If, in a given time interval,  $n_1$  solar protons strike a grain,  $n_2$  solar electrons strike a grain,  $n_3$  secondary electrons are emitted by a grain, and  $n_4$  secondary electrons return to a grain, we can write for the charge on the grain  $q = (n_1 - n_2 + n_3 - n_4)e$ , where  $e$  is the electronic charge.

For each of these four processes the number of particles which will be considered will be large enough so that the  $n_i$  can be taken as being normally distributed with mean value  $m_i$  and variance  $\sigma_i$ . Then the distribution of  $q$  is also normal, having mean value  $m = m_1 - m_2 + m_3 - m_4$



and variance given by  $\sigma^2 = \sum_{i=1}^4 \sigma_i^2$ . The probability of a grain having charge  $q$  is then

$$p(q) = \exp [-(q - m)^2 / 2\sigma^2] / \sigma \sqrt{2\pi}$$

For all four processes involved, the variance of the probability distribution is  $\sigma_i = N_i^{1/2} = (\phi_i A t)^{1/2}$ ;  $N_i$  is the total number of particles striking or leaving the grain in the  $i$ th process;  $\phi_i$  is the flux density of these particles;  $A$  is the projected area of a grain; and  $t$  is the time interval considered. The requirement of electrical neutrality of the solar gas streams gives  $\phi_1 = \phi_2$ . Also for equilibrium between the dust surface and the electronic space charge above it,  $\phi_3 = \phi_4$ . Thus

$$\sigma^2 = 2At(\phi_1 + \phi_3)$$

The neutrality of the solar gas streams also requires that the mean value of charge striking a grain is zero; hence  $m_1 - m_2 = 0$ . Similarly it would seem that, for equilibrium between the surface and the space charge of secondary electrons,  $m_3 - m_4 = 0$ . However, establishing such an equilibrium requires that a space charge be formed by drawing electrons from the dust grains; thus a small positive charge will be left on the grains. This mean value for the charge distribution is calculated on the basis of electron density in the space charge found in section 4 to be about 2 electronic charges per grain. Inasmuch as the grain charges which will be of interest in the erosion processes are much greater than this, we may neglect this small mean charge for subsequent calculations. Thus

$$p(q) = \exp [-q^2 / 4At(\phi_1 + \phi_3)] / [4\pi At(\phi_1 + \phi_3)]^{1/2} \quad (1)$$

The parameters of (1) can now be evaluated for the lunar conditions. The projected area of a  $5\text{-}\mu$  grain is  $2 \times 10^{-7} \text{ cm}^2$ .  $\phi_1$ , the primary particle flux, is thought to be as high as  $10^{11} \text{ cm}^{-2} \text{ sec}^{-1}$  following times of solar activity.  $\phi_3$ , the flux of secondary electrons, includes three contributions: secondary electron emission induced by protons, electrons, and photons. If  $\delta$  represents the number of secondaries per incident particle or photon then  $\phi_3 = \phi_1 \delta$ ;  $\delta$  is a function of the energy of the incident radiation. We now evaluate each of the three contributions to the secondary electron flux.

The velocity of the solar gas streams is about 1000 km/sec, which corresponds to a proton energy of 5 kev. Although no data exist for the secondary yield coefficient for proton-induced emission in insulating materials, we can estimate that for this energy range the yield from silica should be from 1 to 10. This is done by roughly calculating the number of free electrons produced in  $\text{SiO}_2$  by a 5-kev proton, and considering the probability of each electron escaping from the crystal by undergoing a random walk from its place of origin. Thus

$$10^{11} \leq \phi_{3p} \leq 10^{12}$$

Pioneer V studies have set upper limits to the solar electron fluxes at the earth's orbit: for 0.1 kev,  $\phi \leq 10^7 \text{ cm}^{-2} \text{ sec}^{-1}$ ; for 1 kev,  $\phi \leq 10^8 \text{ cm}^{-2} \text{ sec}^{-1}$ . Since electrons with energy less than 0.1 kev are ineffective in producing secondary emission from silica, we can take the average flux of electrons in the energy range of interest ( $E \geq 10^2 \text{ ev}$ ) as  $\phi = 10^9 \text{ cm}^{-2} \text{ sec}^{-1}$ . The average secondary yield coefficient for electron bombardment of uncontaminated silica can be taken as 5 for electrons in this range [Salow, 1940]. Thus the secondary flux due to solar electrons is  $\phi_{3e} = 5 \times 10^9 \text{ cm}^{-2} \text{ sec}^{-1}$ .

A second source of electrons at the moon is the coronal gas, which is thought to extend beyond the earth's orbit at least on some occasions. The thermal energy of these coronal electrons is taken to be 130 ev, corresponding to a kinetic temperature of  $10^6 \text{ deg K}$ , and the flux density is taken to be  $3 \times 10^{10} \text{ cm}^{-2} \text{ sec}^{-1}$  [Parker, 1959]. The yield coefficient for the coronal electrons is about 2 [Salow, 1940]. Thus the secondary electron flux due to coronal electrons is  $\phi_{3c} = 6 \times 10^{10} \text{ cm}^{-2} \text{ sec}^{-1}$ .

To calculate the secondary electron flux due to the photoelectric effect we assume a Planckian distribution for the flux,  $\phi_\gamma(E)$ , of the solar photons corresponding to the temperature  $6000^\circ \text{K}$ . At 1 astronomical unit,

$$\phi_\gamma(E) = 2.4 \times 10^{18} E^2 / [\exp(E/kT) - 1] \quad \text{cm}^{-2} \text{ sec}^{-1}$$

Although operation of the photoelectric effect in pure silica requires quantum energies greater than 8 to 10 ev, silicates which have been irradiated with particles have an activation energy for emitting photoelectrons of only 2 to

owing to the introduction of crystal imperfections. Since photoelectric data are not available for silica, we use the data for the alkali halides, for which the activation energies are about the same and are represented approximately by [Apker and Taft, 1952]

$$\delta(E) = 10^{-11} e^{3.5E} \quad \text{for } 2.5 \leq E \leq 6 \text{ ev}$$

$$\delta(E) \rightarrow 0 \quad \text{for } E > 6 \text{ ev}$$

Bearing in mind that this is probably an upper limit for the silicate grains, we can calculate the secondary electron flux due to photons:

$$\begin{aligned} \phi_{\gamma} &= \int_{2.5 \text{ ev}}^{6 \text{ ev}} \phi_{\gamma}(E) \delta(E) dE \\ &= \int_{2.5 \text{ ev}}^{6 \text{ ev}} 2.4 \times 10^7 E^2 \frac{e^{3.5E}}{e^{E/kT} - 1} dE \\ &= 3.6 \times 10^{12} \text{ cm}^{-2} \text{ sec}^{-1} \end{aligned}$$

The combined secondary electron flux due to protons, electrons, and photons is  $\phi_s = \phi_{sp} + \phi_{se}' + \phi_{se}'' + \phi_{\gamma} \approx 4 \times 10^{12} \text{ cm}^{-2} \text{ sec}^{-1}$ . The combined flux of primary and secondary charges ( $\phi_1 + \phi_s$ ) can thus be taken to be  $4 \times 10^{12} \text{ cm}^{-2} \text{ sec}^{-1}$ .

In deriving the charge probability distribution in (1) we assumed that the probability of an electron striking a grain did not depend on the charge on that grain. However in the limiting case when the Coulomb potential energy of an electron in the neighborhood of a charged grain much exceeds its kinetic energy, there will obviously be some alteration in the charging mechanism. When highly positively charged, the grains will strongly attract electrons from the space charge; when highly negatively charged, the grains will repel electrons. Since the mean free path of space charge electrons is great compared with the height of the space charge, we can consider the perturbation due to the charged grain of the trajectory of an electron of given initial velocity and orientation with respect to the grain. This perturbation of trajectory can be related to the effective cross section for electron capture of the grain. The cross section for an electron striking a positive grain of charge  $q_0 e$  is twice that for striking a neutral grain when  $q_0 e^2(d/2)^{-1}$  equals the initial electron energy.

Thus the probability of charging a grain

above such a value is small; a similar argument holds for large negative charges on the grains. This upper limit on the charge of a grain is  $q_0 = \pm 2800e$  for electron energies of 1.6 ev, which is taken to be the average energy of the photoelectrons from silica, on the basis of the data for the alkali halides. Thus for small  $q$ , the distribution is given by (1); as  $q$  becomes greater than 2000 $e$  the distribution deviates from (1) owing to the interaction between the charge on the grain and the space charge electrons. The time required to reach an equilibrium distribution can be found approximately by calculating the interval of time needed to establish a flat distribution within the limit  $|q| \leq 2000$ . As a criterion for flatness we require that the variation of the exponential term in (1) be less than 10 per cent for charges  $|q| \leq 2000$ ; we thus find that the time needed to reach an equilibrium is of the order of 10 seconds.

**3. Electrostatic hopping.** As a result of the random charging of lunar dust grains it is possible that neighboring grains will attain the same sign of charge. In such a case it may be possible for the two grains to jump apart, perhaps lifting one of them free of the surface.<sup>1</sup> On a level surface such hopping would produce no net motion; however, if the dust layer is on a hillside, there will be a net movement down the slope. Such a process, acting over a long period of time, will result in the erosion of material from high places to low. We shall make an estimate of the upper limit to the amount of material which might be moved by this mechanism alone.

We consider the simplified case of two identical grains aligned with their line of centers perpendicular to the surface and with charges  $q_1 e$  and  $q_2 e$  such that  $q_1 q_2 = +q^2$ . The diameter of the grains is  $d$ , the mass is  $m$ , the origin of the coordinate system is at the center of the lower grain, and we assume the surface to be inclined at an angle  $\alpha$ . The hopping motion of the upper grain under the influence of electrostatic repulsion and gravity is described by

$$m \frac{d^2 y}{dt^2} = \frac{e^2 q^2}{y^2} - mg \cos \alpha$$

<sup>1</sup> It has been shown by Harwit at M.I.T. that hopping of silicate powders can be induced by bombarding them with kilovolt electrons.

With the initial conditions  $t = 0$ ,  $y = d$ , and  $dy/dt = 0$ , the solution for  $dy/dt$  is

$$\frac{1}{2} \left( \frac{dy}{dt} \right)^2 = g \cos \alpha (d - y) + \frac{e^2 q^2}{m} \left( \frac{1}{d} - \frac{1}{y} \right)$$

To find the maximum height of a hop, we set  $dy/dt = 0$ ; then

$$y_{\max} = \frac{e^2 q^2}{mdg \cos \alpha} \quad (2)$$

To get an idea of the magnitude of the charge required we evaluate (2) for a hop distance of  $d$ . Using the values  $d = 5 \times 10^{-4}$  cm,  $m = 1.5 \times 10^{-10}$  gram, and  $g = 167$  cm sec $^{-2}$ , we find  $q = 230$  for small inclinations. Since the idealized case of the grains being aligned perpendicularly to the surface is not usually realized, somewhat more than 230 electronic charges on both grains would normally be required to lift a grain 1 diameter.

To find the average displacement down a slope, we must find the time the grain spends above the surface. We take this time to be twice the time required for the grain to fall from its maximum height in the moon's gravitational field. Although the hopping grain is influenced also by the Coulomb repulsion as well as by the gravitational force, this does not significantly change the total amount of time elapsed in a hop.

Then the time above the surface is

$$t = 2(2y/g \cos \alpha)^{1/2} \quad (3)$$

for a hop of height  $y$ . Since the hop occurs on a slope of inclination angle  $\alpha$ , the lateral component of motion due to the force of gravity is

$$x = \frac{1}{2}(g \sin \alpha)t^2$$

Using (2) and (3), we find

$$x = \frac{4e^2 q^2 \sin \alpha}{mdg \cos^2 \alpha} \quad (4)$$

We can now derive a probability distribution for displacing a grain a distance  $x$  downhill. The probability of neighboring grains attaining charges  $q_1 e$  and  $q_2 e$  is  $p(q_1) p(q_2)$ , which from (1) is

$$\begin{aligned} p(q_1)p(q_2) &= \frac{\exp [-(q_1^2 + q_2^2)/4At(\phi_1 + \phi_3)]}{4\pi At(\phi_1 + \phi_3)} \\ &\quad \cdot \left[ \frac{e^2(\phi_1 + \phi_3) \sin \alpha}{g \cos^2 \alpha} \right] \end{aligned}$$

We require that  $q_1 q_2 = +q^2$ , and we integrate over all possible combinations of charges to find

the total probability of the product of charges being  $+q^2$ . Then

$$\begin{aligned} P(q^2) &= \int_{q_1=-\infty}^{q_1=+\infty} p(q_1)p(q_2) dq_1 \\ &= \exp [-q^2/2At(\phi_1 + \phi_3)]/2[\pi At(\phi_1 + \phi_3)]^{1/2} \end{aligned}$$

Because of the dependence of the distance of a hop on the charge on the grain expressed in (2) we can use (5) to find the probability of displacing a grain a distance  $x$ . This is

$$\begin{aligned} P(x) &= \frac{1}{2[\pi At(\phi_1 + \phi_3)]^{1/2}} \\ &\quad \cdot \exp \left\{ -\frac{xm dg \cos^2 \alpha}{8At(\phi_1 + \phi_3)e^2 \sin \alpha} \right\} \end{aligned}$$

To find the mass transport due to electrostatic hopping we fix a plane perpendicular to the surface and perpendicular to the maximum slope and find the mass which is carried through a centimeter length of that plane. In a given time the mass transported through a unit length of the plane is

$$M(t) = \int_0^\infty \frac{\text{number of grain pairs}}{\text{unit area}} mP(x) x dx$$

The number of pairs per unit area =  $n/2$ , where  $n$  is the number of nearest neighbors for each grain on the surface and  $A$  is the effective area of a grain. Substituting for  $P(x)$ , we find

$$\begin{aligned} M(t) &= \int_0^\infty \frac{n}{2A} m \frac{x}{2[\pi At(\phi_1 + \phi_3)]^{1/2}} \\ &\quad \cdot \exp \left[ -\frac{xm dg \cos^2 \alpha}{8At(\phi_1 + \phi_3)e^2 \sin \alpha} \right] dx \\ &= \frac{4\sqrt{\pi} ne^4 [(\phi_1 + \phi_3)At]^{3/2} \sin^2 \alpha}{mA^2 g^2 \cos^4 \alpha} \end{aligned}$$

Differentiating (6) with respect to time, we find the rate of mass transport to be

$$\begin{aligned} \frac{dM}{dt} &= \frac{6n}{m} \left[ \frac{\pi t}{A(\phi_1 + \phi_3)} \right]^{1/2} \\ &\quad \cdot \left[ \frac{e^2(\phi_1 + \phi_3) \sin \alpha}{g \cos^2 \alpha} \right] \end{aligned}$$

Evaluating this for  $5\text{-}\mu$  grains with  $n = \phi_1 + \phi_3 = 4 \times 10^{12}$  cm $^{-2}$  sec $^{-1}$ ,  $t = 10$  sec,  $\sin \alpha = 0.1$  ( $\alpha = 6^\circ$ ), and  $\cos \alpha = 1$ , we find



$dM/dt = 6 \times 10^{-10}$  g/sec. At this rate, let us see how long it would take to transport appreciable quantities of material in order for the hopping mechanism to explain the erosion of craters on the moon. Using the rate of mass transport derived above, the time required to move a 1-km depth of lunar dust of density  $1 \text{ g/cm}^3$  a distance of 10 km is about  $4 \times 10^{11}$  years, or about 100 times the supposed age of the earth-moon system.

Three primary sources of error have entered this calculation of the time for appreciable erosion which should be considered. The first is the assumption of optimum alignment of grains in calculating the height to which they jump. This perpendicular orientation is probably less likely than any other; since other alignments lead to smaller hops on the average, the calculated mass transport rate is high. The second source of error arises from the uncertainty in the value of  $(\phi_1 + \phi_s)$ , which was used in calculating the charge distribution. This is partly due to not knowing the photoelectric and secondary-emission yield coefficients for silicate materials; since the photoelectric yield coefficient used was that for the alkali halides, we might expect that our estimate for  $\phi_{sy}$  was somewhat large. The value chosen for the primary particle flux  $\phi_1$  was an upper limit; thus the estimates for the secondary emission flux densities  $\phi_{s0}$  and  $\phi_{sp}$  were also limiting values. It appears, then, that the value for the total effective flux density,  $2(\phi_1 + \phi_s)$ , was high, which again leads to a transport rate that is too great.

The third assumption made was that no adhesive forces exist between the grains which could inhibit hopping. A simple calculation shows that only about fifty spurious chemical bonds of energy 10 ev are required to keep two grains with the maximum allowable charge from hopping. For chemically clean surfaces such as would exist on the lunar dust grains a rather large number of such bonds might be expected. Thus the surface adhesion of grains may well reduce the hopping rate markedly. Only on the basis of experiments can we infer that the hopping rate is not completely negligible.

It appears, then, that the rate of mass transport calculated above represents an upper limit and that the hopping mechanism alone is therefore insufficient to explain lunar erosion.

4. *Levitation of dust grains.* It has been

shown in the preceding section that hopping in itself cannot produce appreciable erosion; however it may serve as a triggering mechanism allowing more efficient processes to be established. A process that has been suggested [Gold, 1960] is a gliding effect in which the electronic space charge above the surface serves as a cushion for positive grains, allowing them to glide freely down a slope. If the repulsive Coulomb force on a grain due to the gradient of the space charge is great enough to balance the vertical component of gravity, the horizontal component of gravity will accelerate the grain parallel to the surface and will allow large downhill displacements in one event. Termination of a glide is brought about only by discontinuities in the surface or space charge. As grains are lodged around the irregularities, the smoothness of the surface is enhanced so that subsequent gliding grains may go farther.

The process can be thought of as the fluidization of a very shallow layer of material on the surface; once electrostatic hopping or micrometeorite bombardment causes grains to leave the surface, they can move rapidly to the lowest available point. Although the length of a glide and thus the rate of mass transport is not easily calculable, we can check the possibility of levitating the grains. This depends upon the characteristics of the space charge. The density of electrons above the surface should fall off exponentially:

$$n = n_0 e^{-y/y_0}$$

The characteristic height  $y_0$  can be found from the relation

$$y_0 \sqrt{i_0} = \text{constant} = 1.9 \times 10^{-4} (\text{amp})^{1/2}$$

if the current density  $i_0$  is known. For a current density  $i_0 = e(\phi_1 + \phi_s) = 6.4 \times 10^{-7} \text{ amp/cm}^2$ , we find  $y_0 = 0.24 \text{ cm}$ . The positive potential to which the moon's surface is charged must be sufficient to keep the space charge electrons from escaping. The most energetic electrons emitted from an insulator by the photoelectric effect or secondary electron emission have kinetic energies

of 5 ev; thus we take the surface potential of the moon as  $V_0 = 5$  volts. The variation of the potential in the space charge is given by

$$V = V_0 e^{-y/y_0} \quad (7)$$



The force on a grain due to the potential gradient of the space charge is

$$F = -qe \frac{\partial V}{\partial y} = \frac{qeV_0}{y_0} e^{-y/y_0} \\ = 3.4 \times 10^{-11} qe^{-4.2y} \text{ dynes} \quad (8)$$

Actually (7) does not accurately describe the space charge for large  $y$ , owing to the interaction of the space charge electrons with the solar gas streams and corona. In fact, some of the high-energy secondary electrons will be removed from the top of the space charge. This has the effect of reducing the positive potential of the moon,  $V_0$ , and the characteristic height,  $y_0$ . The levitation effect depends only upon the gradient of the potential in the space charge near the surface, which is given by  $V_0/y_0$ . This gradient is determined almost solely by the large number of low-energy secondary electrons emitted by the grains and thus is not influenced by the effects near the top of the space charge. Thus (8) gives an accurate expression for the levitating force for small values of  $y$ . Positive grains are forced away from the surface and negative grains are returned to it. In order that a stable levitation position be found, the electrostatic force must equal the weight of the grain at the equilibrium point:

$$mg = 3.4 \times 10^{-11} qe^{-4.2y}$$

For a  $5\text{-}\mu$  grain,  $m = 1.5 \times 10^{-10}$  g, and we get for the charge required for levitation at height  $y$

$$q = 7.6 \times 10^2 e^{4.2y}$$

Thus the threshold charge for levitation is  $760e$ , which is within the limits discussed in section 2. Any grain with charge greater than this threshold value will seek a stable position in the space charge if it is in some way ejected from the surface. Even if the hopping mechanism is the only means of placing a grain in the space charge, the mass transport should be significant. At least one-tenth of all the grains made to hop should be capable of being levitated; since the average length of a glide is expected to be very much greater than 10 grain diameters, the rate of material transport should be much greater than for the hopping mechanism alone.

An interesting effect occurring for those positive grains which have been suspended above the surface is that they will continue to rise

slowly after their initial hop. This will result from an increase in their positive charge brought about because the rate of gaining electrons from the grain becomes smaller than the rate of losing electrons. The emission of secondary and photoelectrons is dependent upon the particle and photon fluxes which, of course, are independent of the height. The return of electrons, however, depends on the density of electrons, which varies exponentially with height. The ultimate limit to this charging is the same as that on the charging of surface grains because of the attraction of electrons from the space charge when the Coulomb potential energy due to the charge on a grain becomes comparable to the mean kinetic energy of the electrons.

We let  $v_1(y)$  be the number of electrons striking a grain that is levitated at height  $y$ . Then

$$v_1(y) = v_1(0)e^{-y/y_0}$$

$$v_1(0) = A(\phi_1 + \phi_2) = 8 \times 10^5 \text{ electrons/sec}$$

The number of electrons per second,  $v_2(0)$ , emitted by the grain is simply  $v_1(0)$ . The rate of increase of charge on the grain is then

$$v_2(y) - v_1(y) = v_1(0)(1 - e^{-y/y_0}) \\ = 8 \times 10^5 (1 - e^{-y/0.24})$$

For a grain levitated at  $y = y_0 = 0.24$  cm, the charging rate is  $5 \times 10^5$  electrons/sec; for a grain at a height of 1 grain diameter ( $5 \mu$ ) the charging rate is  $1.6 \times 10^5$  electrons/sec.

Another process, in addition to the hopping mechanism, which may be responsible for initiating the levitation and gliding is the stirring or agitation produced by micrometeorites. The impact of a meteorite will stir up the dusty surface causing some dust grains to be lifted to a height suitable for levitation by the space charge.

Thus we conclude that levitation and gliding may provide a potentially important mechanism for the transportation of the lunar dust layer.

#### REFERENCES

- Apker, L., and E. Taft, Studies of alkali halides by photoelectrical methods, in *Imperfections in Nearly Perfect Crystals*, John Wiley & Sons, New York, pp. 246-260, 1952.
- Gold, T., The lunar surface, *Monthly Notices R. Astron. Soc.*, **115**, 585-604, 1955.
- Gold, T., Dust on the moon, in *Vistas in Astroautics*, vol. 2, Pergamon Press, London, pp. 226-266, 1959.

- Gold, T., Processes on the lunar surface, to be published in the Report of the IAU Pulkova Conference, December 1960.
- Gold, T., The moon, in *Space Astrophysics*, edited by W. Liller, McGraw-Hill Book Co., New York, pp. 171-178, 1961.
- Hey, J. S., and V. A. Hughes, Radar observations of the moon at 10-cm wavelength, in *Paris Symposium on Radio Astronomy*, edited by R. N. Bracewell, Stanford University Press, Stanford, California, pp. 13-18, 1959.
- Liot, B., *Ann. Obs. Paris-Meudon*, 8, Fasc. I., 1929.
- Parker, E., Extension of the solar corona into interplanetary space, *J. Geophys. Research*, 64, 1675-1681, 1959.
- Salow, H., On the secondary yield of electron bombarded insulators, *Z. tech. Physik*, 21, 8-15, 1940.
- Senior, T. B. A., and K. M. Siegel, Radar reflection characteristics of the moon, in *Paris Symposium on Radio Astronomy*, edited by R. N. Bracewell, Stanford University Press, Stanford, California, pp. 29-46, 1959.
- von Diggelen, J., *Recherches Astronomiques de l'Observatoire d'Utrecht*, 14, number 2, 1959.
- Wesselink, A. J., Heat conductivity and nature of the lunar surface material, *Bull. Astron. Inst. Netherlands*, 10(390), 352-363, 1948.
- Wright, F. E., Polarization of light reflected from rough surfaces with special reference to light reflected by the moon, *Proc. Natl. Acad. Sci. U. S.*, 13, 535-540, 1927.

(Manuscript received August 5, 1961;  
revised September 28, 1961.)



# Geomagnetic and Solar Data

J. VIRGINIA LINCOLN, EDITOR

Central Radio Propagation Laboratory  
National Bureau of Standards  
Boulder, Colorado

## PRINCIPAL MAGNETIC STORMS

(Advance knowledge of the character of the records at some observatories as regards disturbances)

Observatory (Observer-in-Charge)	Greenwich date	Storm-time		Sudden commencement			C-figure, degree of activity <sup>4</sup>	Maximal activity on K-scale 0 to 9			Ranges			
		GMT of begin.	GMT of ending <sup>1</sup>	Type <sup>2</sup>	Amplitudes <sup>3</sup>			Gr. day	Gr. 3-hr. period	K-index	D	H	Z	
					D	H								Z
(1)	(2)	(3)	(4)	(5)	(6)	(7)	(8)	(9)	(10)	(11)	(12)	(13)	(14)	(15)
Wilkes (V. K. Jones)	1960	<i>h m</i>	<i>d h</i>		<i>'</i>	<i>γ</i>	<i>γ</i>					<i>'</i>	<i>γ</i>	<i>γ</i>
	Feb.	(None recorded)												
	Mar. 31	10 ..	1 22	.....	.....	.....	.....	s	1	2	8	709	1741	2009
	Apr. 2	23 13	3 12	s.c.*	-21*	-29	+74	ms	3	1	6	332	800	678
	Apr. 27	20 00	28 10	s.c.	-10	0	+25	m	28	3	5	144	533	428
	Apr. 30	01 31	1 10	s.c.	-39	-199	+101	ms	30	5	7	489	1670	1281
	May 6	17 12	7 05	.....	.....	.....	.....	ms	6	6	6	172	601	492
	May 8	04 22	9 11	s.c.*	-21*	-351*	?	s	8	2,3	8	563	1668	2040
	May 28	20 19	29 08	s.c.	-10*	+73	+24*	m	29	1	5	135	589	549
	Jun. 27	16 ..	29 12	.....	.....	.....	.....	ms	28	7	6	215	728	699
	Jun. 29	19 ..	1 10	.....	.....	.....	.....	m	30	6,7	5	145	481	735
	Jul. 14	17 02	16 08	s.c.	+19	+24	-36	m	14	7	5	200	708	853
									15	8	5			
	Aug. 14	15 10	15 09	s.c.	-7	-12	+17	m	15	2	4	111	291	213
	Aug. 16	14 09	18 11	s.c.	+11	.....	-24	m	16	7				
									17	1,2,3,4,6,7	4	193	612	484
									18	2				
	Aug. 19	16 16	22 09	s.c.	-6	.....	+17	m	20	2				
									21	2	5	21	439	368
	Aug. 29	00 22	30 12	s.c.	-31	-17	+59	m	29	2,3	5	170	514	476
	Sep. 4	02 30	6 13	s.c.	-8	-65	+20	m	4	2,3,8	5	268	826	569
									5	1,3				
									6	2				
	Oct. 4	14 ..	8 12	.....	.....	.....	.....	ms	6	8	7	312	1214	1429
	Oct. 24	14 52	1 12	s.c.*	+37*	-56*	-85*	ms	25	2	6	319	846	690
	Nov. 11	00 33	11 15	.....	.....	.....	.....	ms	11	2,3	6	393	638	955
	Nov. 12	13 48	14 14	s.c.	-20	-51	+37	s	13	4	9	856	3532	3420
	Nov. 15	13 04	16 17	s.c.	+23	+58	-72	ms	15	8	7	435	1423	2119
									16	1,2				
	Nov. 30	19 09	2 16	s.c.	-14	+41	+30	ms	1	1,3	7	570	1122	1090
	Dec. 7	18 04	8 13	.....	.....	.....	.....	ms	8	2,3	7	443	640	737
	Dec. 25	20 03	28 16	.....	.....	.....	.....	ms	27	2	6	344	778	861
									28	2				

<sup>1</sup>Approximate time of ending of storm construed as the time of cessation of reasonably marked disturbance movements in the records; more specifically, when the K-index measure diminished to 2 or less for a reasonable period.

<sup>2</sup>s.c. = sudden commencement; s.c.\* = small initial impulse followed by main impulse (the amplitude in this case is that of the main impulse only, neglecting the initial brief pulse); ... = gradual commencement.

<sup>3</sup>Signs of amplitudes of D and Z taken algebraically; D reckoned positive if towards the east and Z reckoned positive if vertically downwards.

<sup>4</sup>Storm described by three degrees of activity: m for moderate (when K-index as great as 5); ms for moderately severe (when K = 6 or 7); s for severe (when K = 8 or 9).



SELECTED GEOMAGNETIC AND SOLAR DATA

*Kp, Ci, Cp, Ap, K<sub>F</sub>, R<sub>z</sub> and Selected Days*

August 1961

Day <sup>1</sup>	Three-hour Range Indices $Kp^2$									Prel. <sup>3</sup> $Ci$	$Cp^4$	$Ap^5$	3-hr. Range Indices $K_F^6$		Pre F <sub>10.7</sub>	
	1	2	3	4	5	6	7	8	Sum				Values	Sum		
1	3o	3+	1+	1o	1o	1o	2-	3-	15o	0.5	0.5	8	4422	1113	18	39
2 D	5+	6+	6-	4+	4o	4o	3+	3o	36o	1.4	1.5	42	4654	3333	31	17
3	3-	4-	4-	3+	3+	3-	3+	4-	26+	1.0	1.0	18	3444	3233	26	24
4 D	5-	4-	4-	3+	3o	3-	3-	2-	25+	1.1	1.0	18	5442	2332	25	22
5	1+	2-	2+	3+	3-	2-	2-	2+	17o	0.7	0.5	9	2223	2222	17	1-
6	2+	1+	1+	2-	2+	2-	2-	2+	15-	0.5	0.3	7	2121	2223	15	1-
7 Q	0+	1-	0+	1-	2o	1-	2-	2o	8+	0.2	0.1	4	0110	2121	8	9
8	1o	2o	4o	4o	3o	2+	5-	1+	22+	0.8	0.9	17	1244	3242	22	27
9 Q	2-	2+	1+	0+	1o	1o	0+	0o	8o	0.1	0.1	4	3320	0010	9	51
10	2+	3-	3+	2+	4-	2o	2o	2-	20o	0.7	0.6	11	2354	3122	22	68
11 D	4-	4+	3-	3+	5-	3+	4-	4o	30-	1.2	1.1	24	4533	4333	28	92
12	2-	2o	2-	0+	1-	2-	2+	3o	13+	0.4	0.3	7	2330	1133	16	84
13 Q	2+	1o	0+	0+	0o	0o	0+	0o	4+	0.2	0.0	2	3201	0021	9	92
14	0o	0o	1o	1+	3o	4o	3-	1-	13-	0.6	0.4	8	0010	3322	11	100
15	1o	1+	4-	2-	2o	2o	1+	2-	15-	0.6	0.4	8	2242	3221	18	108
16 q	3-	2+	1o	0+	0+	1-	1-	1o	9o	0.3	0.2	5	3310	0011	9	98
17 q	1o	1o	1o	2+	1+	1-	2o	1+	11-	0.3	0.2	5	1113	1122	12	85
18 q	1o	0+	1o	2-	2o	2o	1-	1+	10o	0.3	0.2	5	2122	2212	14	64
19	2-	3+	3+	3-	2+	1+	0+	1+	16+	0.4	0.5	9	2333	2112	17	65
20	1-	1-	0o	2+	2o	3o	2+	1o	12o	0.4	0.3	6	0102	2221	10	42
21 q	2-	2-	1+	1+	1+	1+	1o	1-	10+	0.2	0.2	5	2221	2122	14	51
22 Q	1-	0+	1-	0+	0+	0+	0+	1-	4-	0.0	0.0	2	1110	0001	4	33
23 Q	0+	0+	1-	0+	1-	1-	1-	1o	5-	0.2	0.0	3	0100	0111	4	29
24 q	0o	0o	0+	1-	1o	2+	2+	2o	9-	0.3	0.1	4	0001	1233	10	33
25	2o	2-	2o	2+	3o	2-	2-	3+	18-	0.7	0.5	9	2222	3224	19	47
26	2o	2+	2o	3+	2+	1+	3o	3+	20-	0.8	0.6	11	2333	2133	20	45
27	3o	2o	3+	1o	1o	1+	1+	1o	14o	0.6	0.4	8	4232	1121	16	54
28	2+	2o	1o	1+	1o	1-	1o	1+	11-	0.2	0.2	5	3311	1012	12	36
29	2-	1-	0+	1+	1+	4-	5o	5-	19-	1.0	0.9	16	1001	1345	15	60
30 D	5-	4-	2+	4+	6o	5+	4-	5-	35-	1.4	1.4	37	5424	5424	30	62
31 D	5-	5+	5o	3-	3+	4o	3+	4-	32o	1.3	1.3	30	4553	3233	28	53
Means:										0.59	0.51	11				52
No. of days:										31	31	31				31

Notes:

<sup>1</sup> Five quiet days (Q), ten quiet days (Q or q), five disturbed days (D) selected by Committee on Characterization of Magnetic Disturbances, J. Veldkamp, Kon. Nederlandsch Meteorologisch Institut, De Bilt, Holland.

<sup>2</sup> Geomagnetic planetary three-hour-range indices *Kp* prepared by Committee on Characterization of Magnetic Disturbances, J. Bartels, Chairman, University, Göttingen, Germany.

<sup>3</sup> Preliminary magnetic character-figures, *Ci*, prepared by J. Veldkamp.

<sup>4</sup> Magnetic character-figures, *Cp*, prepared by J. Bartels.

<sup>5</sup> Average amplitudes *Ap* (unit 2γ), prepared by J. Bartels.

<sup>6</sup> Fredericksburg three-hour-range indices *K* (*K*9 = 500γ); scale-values of variometers in γ/mm: *D* = *H* = 2.5, *Z* = 3.1) prepared by Robert E. Gebhardt, Observer-in-Charge, Fredericksburg Magnetic Observatory, Corbin, Virginia.

<sup>7</sup> Provisional sunspot-numbers (dependent on observations at Zurich Observatory and its station Locarno and Arosa) prepared by M. Waldmeier, Swiss Federal Observatory, Zurich, Switzerland.

## Letters to the Editor

### Radar Reflections from the Sun at Very High Frequencies

W. G. ABEL, J. H. CHISHOLM, P. L. FLECK, AND J. C. JAMES

*Lincoln Laboratory<sup>1</sup>  
Massachusetts Institute of Technology  
Lexington, Massachusetts*

The reflection of VHF radio waves from the sun has been observed regularly over the period April 19 to July 7, 1961, in a series of radar experiments conducted by the M.I.T. Lincoln Laboratory, Lexington, Massachusetts. The VHF radar system, designed for radio studies of the solar corona and other associated propagation research, is located near El Campo, Texas, at 29.00° north latitude and 96.25° west longitude. The radar was operated at a frequency of 38.25 Mc/s with a transmitted power of 500 kw, CW. The antenna utilized in these experiments consisted of 1024 dipoles arranged in a rectangular array over a ground plane covering an area 110 ft wide in the east-west direction and 1750 ft long in the north-south direction. The effective gain of the antenna system is approximately 34 db above an isotropic radiator for beam angles near the zenith. The array produces a fan-shaped beam with half-power beam widths approximately 0.75° wide in the north-south direction and about 15° wide in the east-west direction. The narrow 0.75° beam was positioned to track the declination of the sun by means of a phasing assembly on each dipole. The beam width of 15° in the east-west direction is sufficiently wide to allow 16 minutes of transmission and 16 minutes of reception during the midday transit of the sun. Phasing adjustments were made periodically at intervals of a few days so that the beam center effectively scanned the solar corona in an angular range  $\pm 0.5^\circ$  about the center of the sun.

During the transmitting period of a solar run the frequency was alternately switched in a pseudo-random pattern between two frequencies usually offset on either side of the nominal cen-

ter frequency of 38.25 Mc/s. A frequency separation of 8 kc/s was employed for most of the radar measurements. The switching sequence was generated from an accessory timing and control system which keyed the transmitter frequency back and forth in a pseudo-random fashion with a pulse interval that ranged in length from one- to five-unit pulse periods. This system also supplied twenty successively delayed replicas of the sequence to the receiver processing system. The separation in delay of successive replicas was one unit time interval (usually 8 seconds).

The receiver consisted of a conventional superheterodyne VHF receiver followed by two final IF channels with variable bandwidth filters tuned to each of the two transmitted frequencies. The outputs of the two filters were supplied to two individual square law detectors and their voltage difference taken in a subtractor circuit. This difference voltage was then applied either directly or through an inverter (i.e., an amplifier with a gain of  $-1$ ) to each of the 20 range box integrators. The delayed sequences switched each integrator input alternately between the direct and the inverted outputs of the subtraction circuit. This system provides discrimination in range between returned signals separated by time intervals greater than the unit pulse length. The autocorrelation function of a typical pseudo-random sequence (namely, a 'maximal length' sequence of length 127) can be expressed mathematically as follows:

$$\phi(\tau) = \begin{cases} 1 - \tau & 0 \leq \tau \leq 1 \\ 1 + \tau & -1 \leq \tau \leq 0 \\ -.008 & 1 < \tau \leq 126 \end{cases}$$

where  $\tau = 1 =$  unit period.

<sup>1</sup> Operated with support from the U. S. Army, Navy, and Air Force.

Short-term variations of noise were suppressed by causing the receiver to have a voltage gain inversely proportional to the received rms noise voltage (this is the optimum method for the detection of a constant weak signal in a time varying noise background). This gain control was accomplished by driving the receiver automatic-gain-control input with a several-milliseconds-average of noise received in a separate receiver. The receiver-integrator system was calibrated by inserting weak test signals from a signal generator. The frequency of the test signals was switched in the pseudo-random sequence with an appropriate time delay to simulate a radar return in a particular range box. For a 1000-second integration period, the selected range box produced an output of about 4 standard deviations above the mean of the remaining 19 integrators for a signal -25 db with reference to the noise level in a 2 kc/s bandpass of the receiver.

A unit time length of 8 seconds was usually employed for these initial experiments. The position of the 16th range box was adjusted daily for a time delay corresponding in range to a discrete radar reflection from a point in the corona 1.5 photospheric radii toward the earth from the center of the sun. A computed delay of 2 seconds was included to allow for the slower group-velocity in the corona. For an 8-second unit pulse, radar returns distributed in range out to 8 seconds on either side of this point contribute to the integrator with progressively lower weighting because of the nature of the autocorrelation function of the sequence. The remaining 19 range boxes effectively search for radar returns over ranges from approximately 27 solar radii toward the earth to 7 solar radii beyond the center of the sun.

A summation of the results obtained for 32 radar observations using 8-second pulses during the period April 19 to July 7, 1961, is shown in Figure 1. This summation was obtained from the algebraic sum of the total integrated signal in each range box after multiplication of each daily result by a weighting function. This weighting was obtained as follows:

$$W = \frac{P_t}{500} \times \frac{1}{\int_0^{\tau} N_A dt}$$

where  $P_t$  = actual transmitted power in kw.

$$\int_0^{\tau} N_A dt$$

= integrated noise output of the square-law detector over the integration period ( $\tau$ ) for one of the two receiver IF channels.

The predominant radar return for this summation is in range box 16 with approximately 1 standard deviation above the mean of the other 19 range intervals. This range is consistent with the range of radar returns computed from theoretical models [Kerr, 1952; Bass Braude, 1957] assuming a group delay of 2 seconds in the spherically symmetric model of the ionized solar corona. It should be noted that the position of the sun as shown in Figure 1 does not include the computed 2-second radar delay, which is equal to 0.43 solar radii.

A plot of the number of standard deviations obtained in the 16th range interval versus the date of each radar measurement is shown in Figure 2(a). The bandwidth utilized for each radar observation was usually 2 kc/s, but bandwidths of 500 cps, 1 kc/s, and 4 kc/s were also used on several occasions. The bandwidths identified for each daily measurement by the adjoining legend in the upper right-hand corner of this figure. These data suggest that Doppler broadening of the received signals is 4 kc/s or greater. A large Doppler broadening was particularly evident in the preliminary spectral analysis of a magnetic tape recording obtained on June 28, 1961. It should be emphasized that the data plot in Figure 2(a) does not give an absolute measure of the strength of the solar return; it is only a statistical index from which the relative probability of a successful radar echo for each trial at this range may be derived.

The relative angular displacement of the center of the radar beam with reference to the center of the sun at the time of the meridian crossing is shown in Figure 2(b). The large angular displacement for June 11 to June 16 resulted from positioning of the antenna beam for passive recording of the Crab Nebula during its annual passage near the sun on these dates. The plot of the peak noise level due to the combination of solar and cosmic noise during the run is shown in Figure 2(c). These data exclude the periods of the numerous occurrences of solar flares with relatively short time durations that were



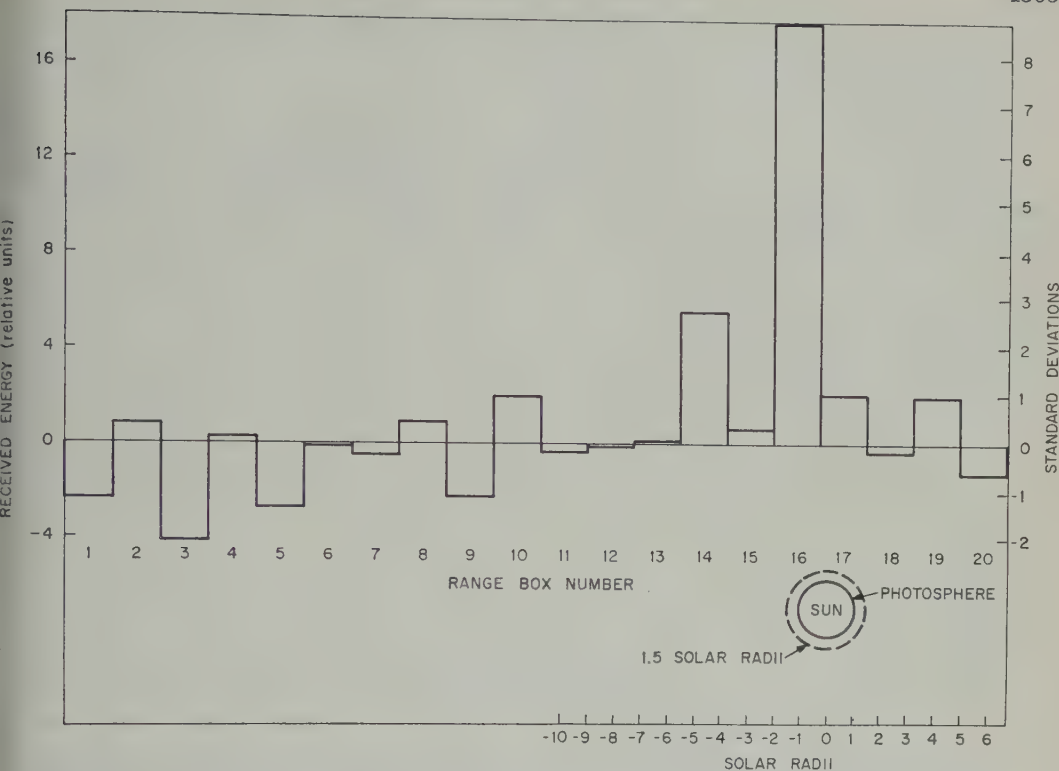


Fig. 1. Summation of the energy received in each range box relative to the position of the sun for the period April 19 to July 7, 1961.

served during some of the reception periods. The noise calibration was made at the input to the receiver with a standard noise generator and the decibel level is referred to a nominal room temperature of 290°K. The apparent temperature of the antenna is approximately 2.5 db higher than the measured temperature because of the attenuation in the transmission line feeder to the receiver (0.9 db) and other attenuation (1.6 db) in the antenna system. The data on passive noise recordings are more numerous than the radar observations since these recordings were continued with an accessory receiver which was unaffected by occasional malfunctioning of the radar transmitter and receiving system.

It appears that the effective 'average' radar cross section of the sun is roughly equal to a few hundredths of the projected area of the solar photosphere. This cross section is a rough approximation because it does not include a weighting adjustment for receiver bandwidth, solar noise background, and relative beam position with respect to the sun. In other words, the data

in Figure 2(a) do not give the strength of the echo, but only the signal-to-noise ratio. The strength of the noise is available from Figure 2(c). This cross section is 15 to 20 db below the apparent cross section observed by *Eshleman, Barthle, and Gallagher* [1960] at a lower frequency of 26 Mc/s. This cross section is also substantially less than the value computed for the 38.25 Mc/s frequency from proposed theoretical models [*Kerr, 1952; Bass and Braude, 1957*] which assume: (1) a spherically symmetric corona in which the ion density decreases radially, (2) scattering from the roughness or irregularities in the surface formed by the turning points of the family of rays entering the corona, and (3) the two-way absorption derived from the effective collision frequency for a fully ionized hydrogen atmosphere with an isothermal electron temperature of  $10^6$  degrees. It is interesting to note that the reduction of the electron temperature to  $5 \times 10^5$  degrees K in this coronal model substantially increases the two-way absorption and yields a



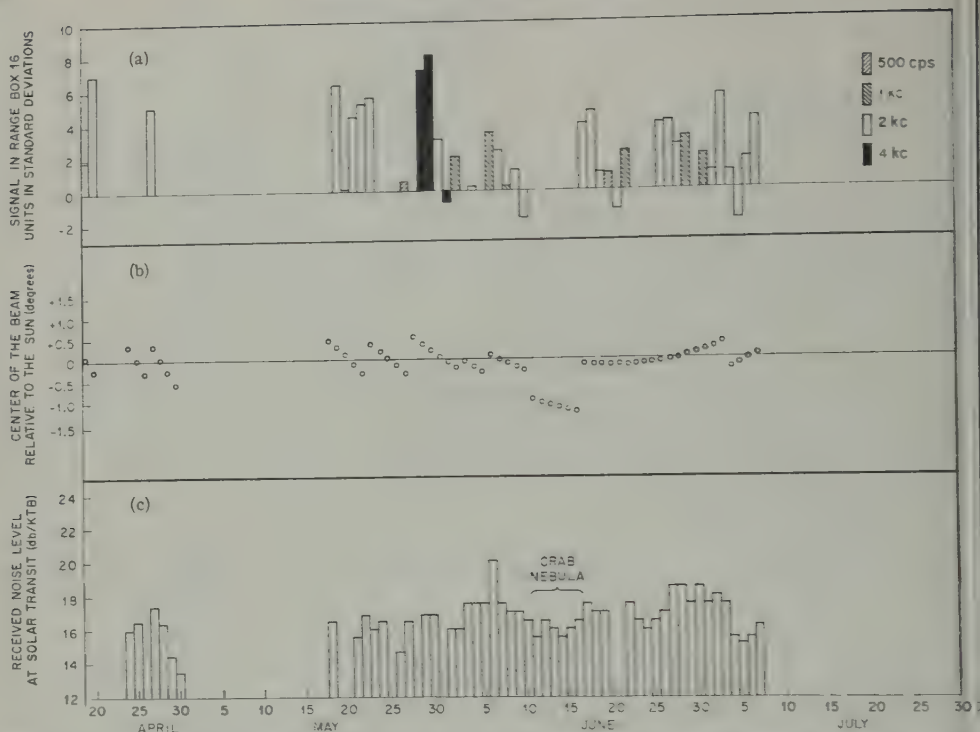


Fig. 2. Daily record of received energy in range box 16, position of the antenna beam relative to the sun, and received noise level at solar transit for the period April 19 to July 7, 1961.

reduced radar cross section approaching the experimental results. The relatively steady level of the radio noise at 38.25 Mc/s observed when the Crab Nebula was within 5 solar radii of the sun indicates that there is little absorption in the outer coronal structure (see Fig. 2 (c)).

The experimental observations are being continued with a schedule of progressively shorter pulse lengths in order to obtain increased range resolution. In addition, an experimental investigation of the extent of Doppler shift and Doppler broadening is being conducted by means of reprocessing broadband magnetic tape recordings obtained from a point in the receiver circuit before the final narrow-band filters.

The results reported here provide a measure of the system performance required to obtain systematic radar observations of the sun at 38.25 Mc/s. The pattern of the variability of the effective radar cross section over periods of days and weeks indicates a possible interesting dependence upon the level of solar activity. Unexpected small rates of Faraday rotation during the integration period may be a cause of some

of this variability since the antenna is linearly polarized. An extremely stable total electron density and homogeneous magnetic field in the outer corona and in the earth's ionosphere are required to explain a complete loss of signal. The cause of an unchanging orthogonal polarization of the returned signal over an integration period is not understood. An average loss of 3 db is expected for a large number of rotations during an integration period. These experiments also indicate that the radar returns are obtained from reflection centers within 1 solar radius of the region of the solar corona located 1.5 solar radii toward the earth, assuming a group delay of approximately 100 seconds in the outer corona.

These preliminary results obtained at 38.25 Mc/s complement the earlier results at 26 Mc/s reported by Eshleman, Barthle, and Gallagher [1960] and further demonstrate the feasibility of radar techniques for active radio investigation of the solar corona. They also emphasize the need for further systematic studies at several frequencies with improved system sensitivity, range resolution, and spectral resolution in order

to determine the range of variability of radio scattering characteristics of the corona. It is suggested that a study of the interdependence of the results of the systematic and regular radar observations of the sun with other indices of solar activity obtained by radio and optical techniques could add another dimension to the scientific understanding of coronal structure and important solar terrestrial phenomena.

*Acknowledgments.* We gratefully acknowledge the helpful interest and the many valuable contributions of Messrs. P. E. Green, Robert Price, and J. V. Evans of the M.I.T. Lincoln Laboratory, particularly in the design of the data processing equipment for the solar radar system. Further grateful acknowledgment is made to Messrs. L. J. Ricardi, M. E. Devane, and A. R. Dion of the

Antenna Group, M.I.T. Lincoln Laboratory, for their contribution in the engineering design, installation, and performance-testing of the antenna array utilized in the solar radar system.

## REFERENCES

- Kerr, F. J., On the possibility of obtaining radar echoes from the sun and planets, *Proceedings of the Institute of Radio Engineers*, 40, 660-666, 1952.
- Bass, F. G. and S. I. A. Braude, On the question of reflecting radar signals from the sun, *Ukrainian J. of Phys.*, 2, 149-163, 1957.
- Eshleman, V. R., R. C. Barthle, and P. B. Gallagher, Radar echoes from the sun, *Science*, 131, 329-332, 1960.

(Received August 17, 1961.)

## Bursts of Centimeter-Wave Emission and the Region of Origin of X Rays from Solar Flares

M. R. KUNDU

*Radio Astronomy Observatory, University of Michigan  
Ann Arbor, Michigan*

High energy ( $>20$  kev) solar X-ray emission during flares has been measured with the help of rockets and balloons by various workers [Chubb, Friedman, and Kreplin, 1960; Winckler, May, and Masley, 1961; Peterson and Winckler, 1959; Vette and Casal, 1961]. The observation of X rays in the quantum energy range 20 to 70 kev during three flares accompanied by SID's led Friedman to suggest that the presence of such X rays was characteristic of the flare process. The 20 to 70 kev X rays appeared as an extension of the high intensity flux of 2 to 10 A X rays, which are the main components responsible for flare time enhanced D-layer ionization (SID). It has been shown statistically by Dodson, Hedeman, and Covington [1954], Hachenberg and Krüger [1960], and Kawabata [1961] that centimeter-wave bursts are closely associated with SID's. Kawabata and Elwert [1961] have theoretically computed the intensity of X rays by thermal emission from very hot regions and have shown that the effective temperature of centimeter-wave bursts ( $10^7$ – $10^8$ °K) is sufficient to explain the X rays observed by Friedman during rocket flights. Peterson and Winckler [1959] first proposed a nonthermal mechanism for the production of X rays and suggested that the hard X rays originate as bremsstrahlung owing to the braking of high velocity electron jets in the flare or the photosphere. In the development of this concept De Jager [1960] predicted a close association between meter-wave type III bursts (fast frequency-drifting bursts) and flare X rays. De Jager implied that the passage of type III electron streams through the corona would be sufficient to produce the X rays. This appeared to be confirmed by subsequent observations of Winckler, May, and Masley [1961].

In view of the apparent difference of opinion regarding the production of flare X rays and the associated solar radio bursts, we have carefully examined the solar radio bursts observed in

different meter and centimeter-wave frequency ranges, simultaneously with the X rays directly measured by balloons and rockets. The details of the observed X rays and the associated radio bursts are listed in Table 1.

It appears from this table that during seven cases of flare X rays observed by balloons and rockets, there were simultaneous centimeter-wave bursts, whereas during only three cases there were meter wave bursts. Of these three cases, in only one (August 11, 1960) was there a strong group of type III bursts simultaneous with X rays; in the other two cases there were a few weak isolated type III bursts at the time of X rays, and it is questionable if the association of these type III bursts with the observed X rays (whose duration is much longer) is significant. In two of the three cases the type III bursts were followed by type II and type IV bursts during which time X rays were no longer observed. In three of the four cases where X-ray maxima were observed, the time of maximum agreed precisely with the peaks of centimeter-wave emission. In the fourth case, the maximum occurred during the 6 minutes' duration of the centimeter- $\lambda$  burst. Figures 1 and 2 show the X-ray events simultaneously with the solar radio bursts on 2800 Mc/s (Ottawa) and in the 100–580 Mc/s range (Michigan). It is seen that the second X-ray event of October 12, 1960, agreed even in fine structure detail, involving the peaks, with the centimeter-wave burst and the ratio of X-ray and centimeter- $\lambda$  intensities was nearly constant.

The centimeter-wave bursts associated with flare X rays are characterized by sharp rise time and a short impulsive phase; in one rare case (March 20, 1958) the burst source had a very large angular size (about 4' and 8' on 3 cm and 21 cm respectively) as compared with 2' and less for average bursts. Also, the spectra of the X-ray associated centimeter- $\lambda$  bursts show a ra-

TABLE 1. X-Ray Events and Associated Solar Radio Bursts

Date	X Ray		Cm- $\lambda$ Burst				Flare		Meter- $\lambda$ Burst		Start				
	Observa- tion, UT	Energy, kev	Maximum Count, UT	Start UT	End UT	Max. UT	Peak* Flux	Wave- lengths, cm	Start Max. UT	Position	Type		UT	SID	SEA
											Type	UT			
Mar. 20, 1958	1304.5-05	200-500	1304.6	1304	1309	1304.7	>850	3, 10, 15, 21	1305E	N23E29	No Event			1302	1305
Aug. 24, 1959	2247	80	—	2237	>2320	indet.	>150	10	2233	2239	N18E28	No Event		2240	2239
Aug. 31, 1959	2253	10-70	—	2236	2326	2248.8	77	3, 8, 15, 30	2235	2252	S08W46	No Event		2242	2244
Sept. 1, 1959	1700	80	—	1657.5	1713.5	1706	85	3, 10, 15	1656	1707	S11W53	No Event		1655	1656
Aug. 11, 1960	1928-32	30	1927-28	1923.5	2000	1928	1100	10, 55	1924	1928	N22E27	III	1925.9- 28.8	1927	1924
												II	1929 - 43.2		
												IV	1926 - 36		
Oct. 12, 1960	1730	20-80	1730	1725	1731	1726.5	29	10	1722	1728	S18W61	III	1725 - 30	1729	1726
Oct. 12, 1960	1747-50	20-80	1748	1745.5	1752.5	1748	83	10, 55	1745	1749	N10W23	III	1745.5- 47	1744	1747
												II	1752 - 1802		
												IV	1753 - 1800		

\* The cm- $\lambda$  peak flux corresponds to the italicized wavelength in units of  $10^{-22}$  watt m $^{-2}$  (cps) $^{-1}$ , both polarizations.



AUG 11, 1960

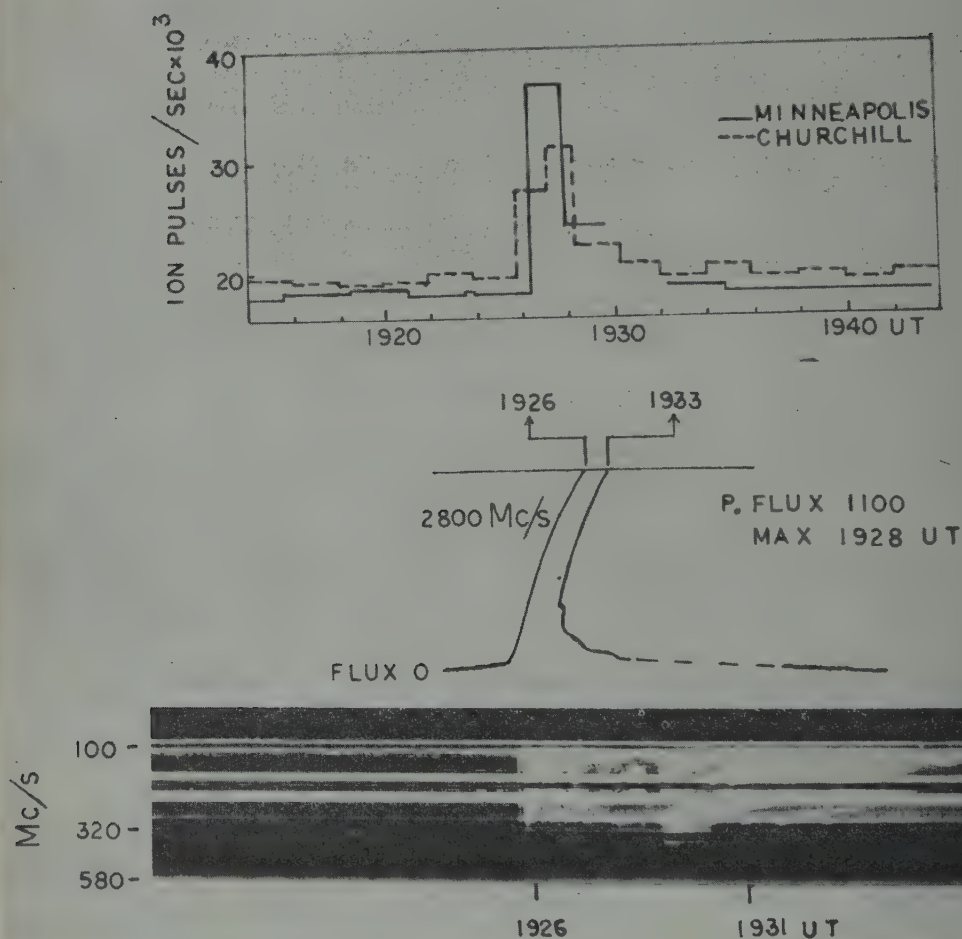


Fig. 1. Record of the X-ray event of August 11, 1960, together with the records of solar radio bursts on 2800 Mc/s (Ottawa) and in the 100 to 580 Mc/s range (Michigan). The X-ray records are reproduced from the published paper of *Winckler, May, and Masley* [1961].

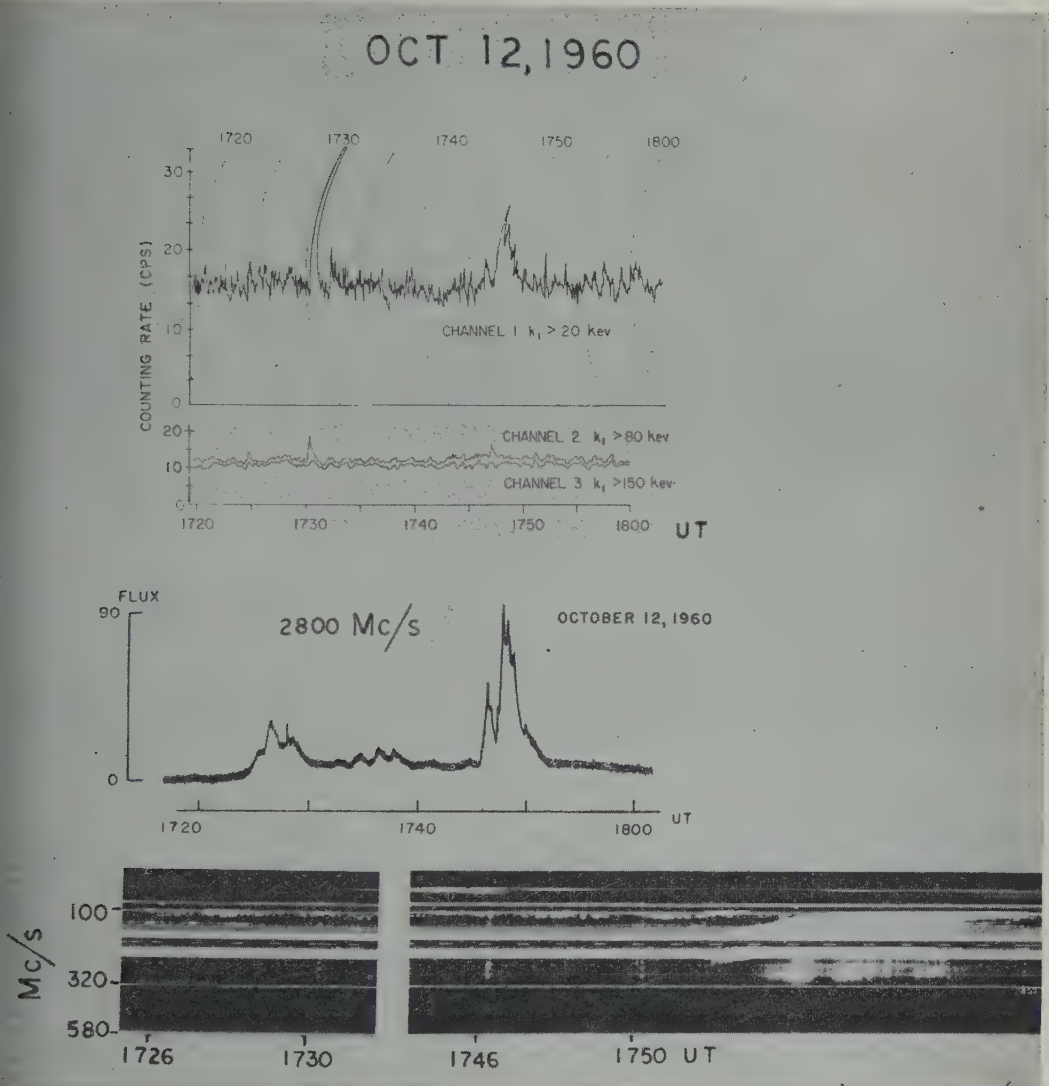


Fig. 2. Same as Figure 1 for October 12, 1960. The X-ray records are reproduced from the published paper of *Vette and Casal* [1961].

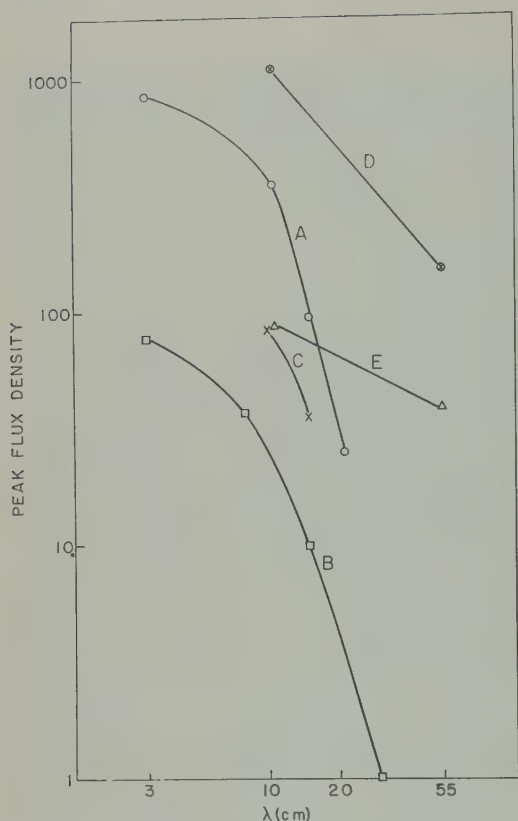


Fig. 3. The spectra of cm- $\lambda$  bursts associated with X-ray events. The curves marked A, B, C, D, and E correspond to the X-ray events of March 20, 1958; August 31, 1959; September 1, 1959; August 11, 1960; and October 12, 1960, respectively. The first three events are not associated with type III, type II, and type IV bursts on meter waves. The peak flux of cm- $\lambda$  bursts are expressed in units of  $10^{-22} \text{ W m}^{-2} (\text{c/s})^{-1}$ .

sharp low-frequency cutoff, except when they are associated with type III bursts (Fig. 3). If we assume a burst size of about  $2'$  on 3 cm, in agreement with interferometric observations [Kundu, 1959] we find a brightness temperature of about  $10^4$ – $10^7$ °K for the X-ray associated centimeter- $\lambda$  bursts which are not accompanied by any event on meter waves. These temperatures and the spectra of the centimeter- $\lambda$  bursts are consistent with thermal radiation from an isothermal plasma whose optical thickness at

centimeter wavelength is greater than unity of the long wavelength end of wavelengths between 3 and 30 cm. The spectra of the two centimeter bursts associated with meter-wave type (followed by types II and IV) bursts do show any sharp low-frequency cutoff (Fig. 3). These centimeter- $\lambda$  bursts are usually more intense and have higher temperatures ( $10^7$ – $10^8$ °K) than in the previous case. Such high temperatures of the centimeter-wave continuous bursts are probably due to an additional component of synchrotron radiation of electrons generated during the flare.

The above discussion shows that solar flare X-ray bursts are intimately associated with centimeter-wave bursts from the sun, while the relation with type III bursts is much looser. This result provides strong evidence that flare X rays of energy greater than 20 keV are generated not in the higher levels of the corona but rather in the region of origin of emission of centimeter-wave bursts, i.e., within about 10,000 to 20,000 km above the photosphere as determined by interferometric and eclipse observations.

**Acknowledgments.** I wish to thank Professor F. Haddock and Mr. J. P. Wild for many helpful discussions. This work was supported by the Office of Naval Research contract Nonr 1224 (16).

#### REFERENCES

- Chubb, T. A., H. Friedman, and R. W. Kreplin, *International Space Science Symposium*, Nice, 1960, p. 695, 1960.
- De Jager, C., *International Space Science Symposium*, Nice, p. 628, 1960.
- Dodson, H. W., E. R. Hedeman, and A. E. Coville, *Ap. J.*, **119**, 541, 1954.
- Elwert, G., *J. Geophys. Research*, **66**, 391, 1961.
- Hachenberg, O., and A. Krüger, *J. Atmospheric and Terrest. Phys.*, **17**, 20, 1960.
- Kawabata, K., paper presented at IAU Symposium on Solar Corona, Cloudercroft, 1961.
- Kundu, M. R., *Ann. d'Ap.*, **22**, 1, 1959.
- Peterson, L. E., and J. R. Winckler, *J. Geophys. Research*, **64**, 697, 1959.
- Vette, J. I., and F. G. Casal, *Phys. Rev. Letters*, **1**, 334, 1961.
- Winckler, J. R., T. C. May, and A. J. Masley, *Geophys. Research*, **66**, 316, 1961.

(Received September 20, 1961;  
revised October 3, 1961.)

Electron Temperature Measurements on the Explorer VIII Satellite

G. P. SERBU, R. E. BOURDEAU, AND J. L. DONLEY

Goddard Space Flight Center  
National Aeronautics and Space Administration  
Greenbelt, Maryland

Two of the ten experiments performed on the ionosphere direct measurements satellite (Explorer VIII) were designed to measure electron temperature. Although only a fraction of the temperature data has been processed, enough important conclusions can be drawn to warrant its publication at this time.

The Explorer VIII electron temperature experiment used to obtain data presented in this report is a simple modification of the classic Langmuir probe in that two electrodes (a grid and a collector) are used instead of one. To our knowledge it represents the first space flight of this type of device in which the effects of positive ion and photocurrents are removed experimentally. This was suggested by E. C. Whipple, Jr., because of uncertainties in correcting for these unwanted currents when interpreting the classic Langmuir probe volt-ampere curve. A detailed description of the experiment together with an evaluation of the effects which the interaction of the spacecraft and the ionized atmosphere have on electron temperature determination are described elsewhere [Bourdeau, Donley, Serbu, and Whipple, 1961; Bourdeau, 1961].

Fourteen observations selected to minimize possible effects due to solar flare activity are presented in Table 1. The experimental error spread for each value is  $\pm 150^{\circ}\text{K}$  and arises from the limited telemetry bandwidth assigned to the experiment. Any uncertainty related to the electron transparency of the grid contained in the sensor is within experimental error. This conclusion was reached by comparing results of the probe with those from other low energy plasma probes, particularly the second electron temperature experiment, carried by the satellite [Bourdeau, Donley, and Whipple, 1961].

Hanson and McKibbin [1961] obtained an ion density profile to an altitude of 750 km using an ion trap similar to the ion current monitor flown

on Explorer VIII for ion concentration determination. From this profile they concluded that the upper ionosphere is isothermal within 5 per cent at altitudes between 350 and 750 km. More recently, Jackson and Bauer [1961] reached the same conclusion for altitudes between 350 and 625 km from an electron density profile derived from a CW propagation experiment. It is assumed that the above conclusions hold up to an altitude of 1200 km, so that the electron temperatures reported here are not altitude dependent. The data tabulated above were selected entirely within the month of November 1960 and, except for one equatorial observation, were taken within the latitudes of  $24^{\circ}\text{N}$  to  $50^{\circ}\text{N}$  to minimize seasonal and latitudinal variations.

The tabulated temperatures are plotted as a function of local mean time in Figure 1. A diurnal dependency is evident. The equatorial value is separately identified. The vertical bars represent sunset and sunrise times, the spread

TABLE 1. Electron Temperatures measured on the Explorer VIII Satellite

Date Nov. 1960	Time, GM	Latitude	Altitude, km	Time, LM	$T_e$ , $^{\circ}\text{K}$
27	2259	$37^{\circ}\text{N}$	920	1747	1800
29	2355	$49^{\circ}\text{N}$	670	1923	1800
30	2041	$48^{\circ}\text{N}$	500	1945	1150
11	0311	$31^{\circ}\text{N}$	530	2203	1065
30	2238	$41^{\circ}\text{N}$	430	2210	1070
12	0339	$39^{\circ}\text{N}$	475	2231	1095
25	0528	$49^{\circ}\text{N}$	440	2304	1140
25	0531	$45^{\circ}\text{N}$	425	0011	1000
16	0916	$48^{\circ}\text{N}$	450	0152	1090
30	0751	$2^{\circ}\text{N}$	700	0223	1175
11	0902	$50^{\circ}\text{N}$	475	0226	950
18	1017	$24^{\circ}\text{N}$	740	0429	1130
10	1040	$33^{\circ}\text{N}$	845	0600	1180
5	1417	$25^{\circ}\text{N}$	1205	0805	1600



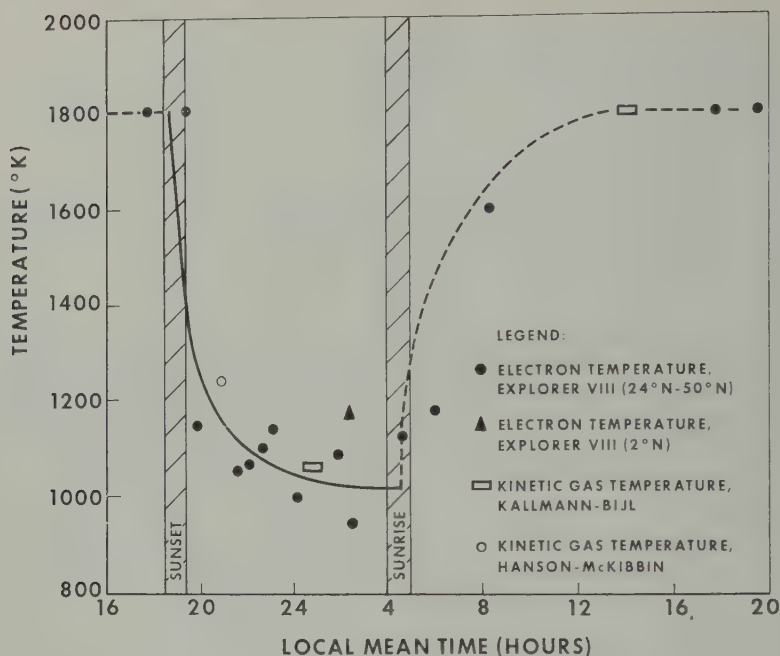


Fig. 1. Electron temperature as a function of local mean time.

being due to the different altitudes and latitudes at which the data were taken.

Our minimum values, which average about 1000°K, occur between local midnight and local daybreak. The maximum value of 1800°K (two observations) occurs in the later afternoon. These are all in good agreement with the diurnal variation of the kinetic gas temperatures reported by *Kallmann-Bijl* [1961] for this phase of the solar cycle. The agreement thus suggests thermal equilibrium between electrons and heavy particles in the upper ionosphere, in support of the conclusion reached by *Hanson and Johnson* [1961] from theoretical considerations of the ionizing radiation and the energy transfer mechanisms.

Of considerable interest is the rate of cooling of the upper atmosphere after sunset and the rate of heating after sunrise. Referring to the cooling rate, *Lowan* [1955], assuming that the principal mechanism of heat loss is by conduction downward, computes that the temperature of the upper atmosphere would decrease by about 30 per cent in the first 2½ hours after sunset. The solid curve in Figure 1 represents Lowan's cooling rate for the first 2½ hours after sunset and a best fit to the Explorer VIII

temperature data from then until sunrise. The Explorer VIII data are also in fair agreement with the kinetic gas temperature of 1240°K inferred by Hanson and McKibbin from their ion density profile which was obtained in the same month at about 3 hours after sunset. Their temperature value was computed on the assumption of thermal equilibrium and an ionic mass of 16 AMU. The identification of O<sup>+</sup> as the predominant ionic constituent at altitudes up to 100 km was previously reported from a retardation potential experiment carried on Explorer VI [Bourdeau, Donley, and Whipple, 1961]. Because of the scarcity of points in Figure 1, the rate of heating of the upper atmosphere after sunrise cannot be defined in detail at this time. Our data do, however, show a temperature increase of about 500°K three hours after sunrise.

There has been recent interest in the constancy of the temperature in the F region between the time it reaches its maximum value in the afternoon until sunset. The short active life (2 months) of the satellite, together with the nature of the real time transmissions, prevented the obtaining of data in this altitude region during the midday. *Bates* [1951] suggests that photoionization is the dominant heat source

this altitude region. *Hunt and Van Zandt* [1961] point out that if photoionization is the dominant effect, the temperature decrease would be small for large changes in solar zenith angle. Consequently, they conclude that the temperature should remain nearly constant from afternoon until sunset. If thermal equilibrium can be assumed, the conclusion of *Hunt and Van Zandt* is supported by the agreement between the 2 PM kinetic gas value ( $1800^{\circ}\text{K}$ ) reported by *Kallmann-Bijl* [1961] and the two electron temperature values obtained at sunset from Explorer VIII.

It should be noted that the Explorer VIII electron temperatures are not in agreement with all kinetic gas observations. For example, *Blamont* [1961] obtained a neutral gas value at sunset of about  $1450^{\circ}\text{K}$  from a sodium release experiment in December 1960. However, if *Blamont's* temperature value is representative of the kinetic gas temperature it would indicate a higher rate of cooling from the 2 PM value of  $1800^{\circ}\text{K}$  suggested by *Kallmann-Bijl* than that inferred by *Hunt and Van Zandt*. Also, *Jackson and Bauer* reported a neutral gas temperature of  $1640^{\circ}\text{K}$  at 3 PM from their electron density profile. However, their rocket flight took place in April 1961. The disagreement between this and the Explorer VIII electron temperature data at sunset perhaps represents more of a seasonal than a diurnal effect.

In conclusion, the model (Fig. 1) of the diurnal variation of electron temperatures in the upper ionosphere is in close agreement with those reference atmospheres obtained from satellite drag observations. The detailed time variation is consistent with the concept of heat loss by conduction downward after sunset and with photo-

ionization as the predominant heat input keeping the temperature fairly constant in the late afternoon.

## REFERENCES

- Bates, D. R., The temperature of the upper atmosphere, *Proc. Phys. London, B*, **64**, 805-821, 1951.
- Blamont, J. A., La température de l'ionosphère, Proceeding of the Second International Space Sciences Symposium, 1961.
- Bourdeau, R. E., J. L. Donley, G. P. Serbu, and E. C. Whipple, Jr., Measurements of sheath currents and equilibrium potential on the Explorer VIII Satellite, *J. Astronautical Sciences*, in press, 1961.
- Bourdeau, R. E., J. L. Donley, and E. C. Whipple, Jr., The ionosphere direct measurements satellite, National IAS-ARS Symposium, June 1961.
- Bourdeau, R. E., Ionosphere results with sounding rockets and the Explorer VIII Satellite, Proceedings of the Second International Space Sciences Symposium, 1961.
- Hanson, W. B., and F. S. Johnson, Electron temperatures in the ionosphere, *Les Congrès et Colloques de L'Université de Liège*, **20**, 390-424, 1961.
- Hanson, W. B., and D. D. McKibbin, An ion-trap measurement of the ion concentration profile above the  $F_2$  peak, *J. Geophys. Research*, **66**, 1667-1671, 1961.
- Hunt, D. C., and T. E. Van Zandt, Photoionization heating in the  $F$  region of the atmosphere, *J. Geophys. Research*, **66**, 1673-1682, 1961.
- Jackson, J. E., and Bauer, S. J., Rocket measurement of a daytime electron density profile up to 620 km, *J. Geophys. Research*, **66**, 3055-3057, 1961.
- Kallmann-Bijl, H. K., Daytime and nighttime atmospheric properties derived from rocket and satellite observations, *J. Geophys. Research*, **66**, 787-796, 1961.
- Lowan, A. N., On the cooling of the upper atmosphere after sunset, *J. Geophys. Research*, **60**, 421-429, 1955.

(Manuscript received August 7, 1961;  
revised October 2, 1961.)

## Minor PCA Events during March 1958

G. F. ROURKE

*Research and Advanced Development Division, AVCO Corporation  
Wilmington, Massachusetts*

This letter is intended to call attention to 2 polar-cap absorption (PCA) events and 2 sudden-commencement impulses during the IGY. The events occurred on March 11 and 14-15, 1958. *Hakura and Goh* [1959], *Hakura* [1960], *Hill* [1960; 1961], *Obayashi and Hakura* [1960a, b, c] and *Obayashi* [1961] have shown that the detailed pattern of polar-cap absorption possesses some definite regularities. Several hours after the beginning of a large solar flare accompanied by type IV radio noise, low-energy solar cosmic rays (10-100 Mev) enter the polar cap, causing enhanced ionization and blackout. For the larger well-developed polar-cap absorption events, enhanced ionization begins over the pole and spreads outward over the whole polar cap, indicating an isotropic direction of particle precipitation. As the regions of polar-cap absorption rotate, they manifest a strong solar control believed to be due to the greater production of electrons by photodetachment during the sunlight hours at altitudes where the collisional rate is high [*Chapman and Little*, 1957]. At high-latitude stations ( $\Phi > 75^\circ$ ) the maximum occurrence of blackout is reached in most cases just before the geomagnetic storm sudden commencement (SSC). At lower latitudes ( $\Phi = 60-75^\circ$ ) the abnormal ionization is generally weaker, spreading to the auroral zone before the SSC. An SSC almost invariably follows a PCA [*Reid and Leinbach*, 1959].

In Figure 1 the variations of  $f_{\min}$  during the PCA events of March 11 and 14-15 are shown. The solid curve indicates quarter-hour variations of  $f_{\min}$  at Thule, Resolute Bay, Fletcher's Ice Island, and Churchill, and hourly values for Arctic I and II. The dotted curve is the hourly median values at each station for March 1-10. Abnormal ionization in the D region on March 11 was of small magnitude, lasting about 18 hours. From an analysis of hourly hemispheric  $f_{\min}$  charts, it appears that the polar-cap disturbance began by 0600 GMT, March 11. The spread of

polar-cap absorption was strongly influenced by the sunrise line indicating a small flux of particles since in the majority of PCA events, the night hemisphere attains a considerable amount of ionization even though the day-night effect is still evident. An SSC was reported by Victoria ( $\Phi = 54^\circ\text{N}$ ) and Apia ( $\Phi = -16^\circ\text{S}$ ) to have occurred at 2316 GMT, March 11 [*Romañá*, 1958], and  $K_p$  was 7 during the first three intervals on March 12. Following the SSC,  $f_{\min}$  decreased to its normal value in the night hemisphere while enhanced values persisted for about 6 hours on the sunlit side.

The March 14-15 PCA, though weak, was stronger than the March 11 event with blackout being observed over the polar cap by 2000 GMT, March 14. Solar control over the  $f_{\min}$  absorption pattern was not as predominant as in the previous event. Continuous blackout observations lasting throughout the PCA were confined to stations north of  $70^\circ$  geomagnetic latitude. A sudden impulse (s.i.) in the magnetograms at nine observatories at 1000 GMT, March 15, has been reported [*Romañá*, 1958] with one observatory calling it an SSC. In the polar cap and along the auroral zone  $f_{\min}$  remained enhanced for about 10 hours after the s.i.

Both the PCA events reported here are small in magnitude compared with many others reported in the literature. However, the development of both these PCA events and the associated geomagnetic disturbances is basically no different from the development of the large disturbances. The PCA of March 11 was followed by a sudden commencement and a geomagnetic main phase storm just as with many large storms. The PCA of March 14 was followed by a sudden commencement but no geomagnetic main phase storm.

This kind of event is also typical, although is not as common as the first. Using the terminology of *Obayashi and Hakura* [1960b], the latter event may be described as a high-energy

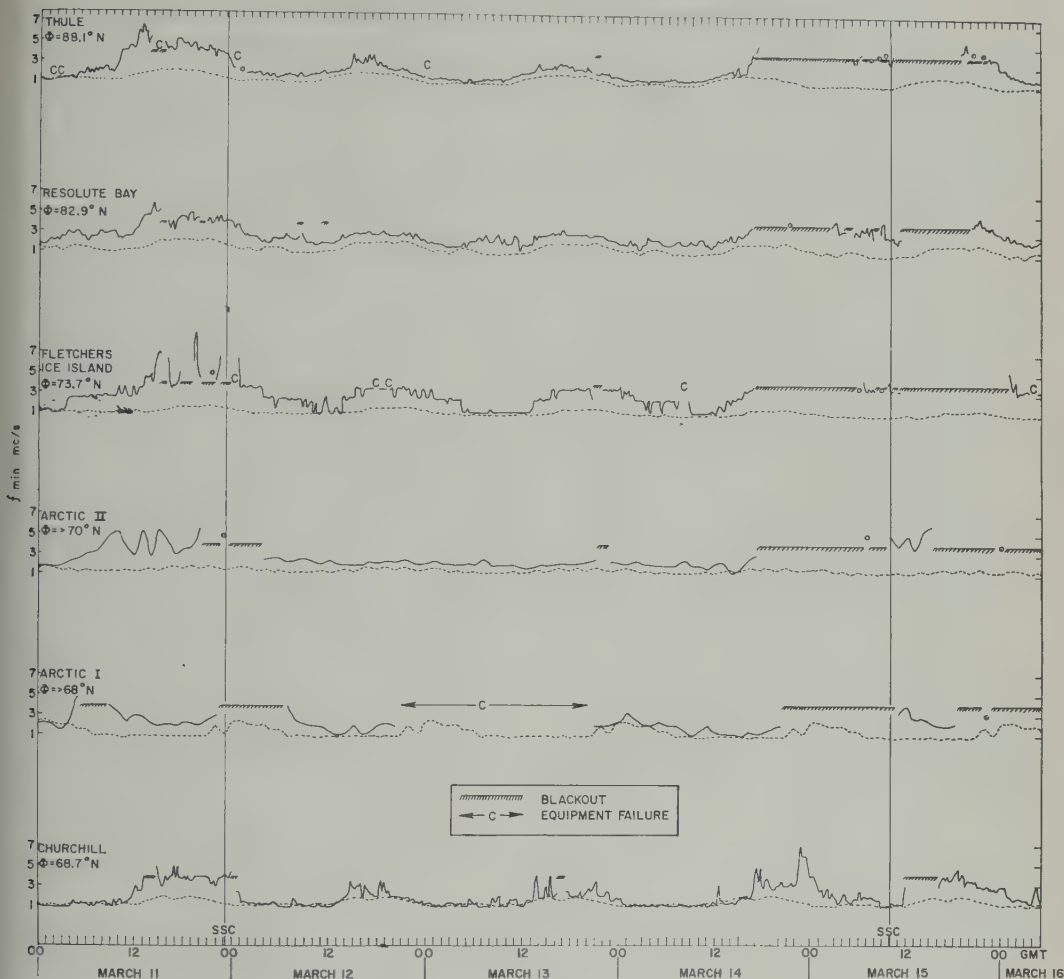


Fig. 1.  $f_{\min}$  variation for March 11-16, 1958 (solid curve), and hourly median values for March 1-10, 1958 (dotted curve).

event, and the former as a low-energy event. Thus, the relatively weak geomagnetic variations (and especially the sudden commencement) associated with these ionospheric disturbances are of similar geophysical significance as the relatively large geomagnetic variations associated with severe ionospheric storms.

**Acknowledgment.** The research in the letter was supported by Air Force Cambridge Research Laboratory under contract AF19(604)-4092.

#### REFERENCES

Chapman, S., and C. G. Little, The nondeviate absorption of high-frequency radio waves in auroral

- latitudes, *J. Atmospheric and Terrest. Phys.*, **10**, 20-31, 1957.  
 Hakura, Y., Polar cap blackout and auroral zone blackout, *J. Radio Research Lab. Japan*, **7**, 583-595, 1960.  
 Hakura, Y., and T. Goh, Pre-SC polar cap ionospheric blackout and type IV solar radio outburst, *J. Radio Research Lab. Japan*, **6**, 635-650, 1959.  
 Hill, G. E., Ionospheric disturbances following a solar flare, *J. Geophys. Research*, **65**, 3183-3207, 1960.  
 Hill, G. E., Effects of corpuscular emissions on the polar ionosphere following solar flares, *J. Geophys. Research*, **66**, 2329-2335, 1961.  
 Obayashi, T., Polar ionospheric storms and radio communication disturbances, *Arctic Inst. N. A., Research Paper No. 9*, 1961.  
 Obayashi, T., and Y. Hakura, Propagation of solar



- cosmic rays through interplanetary magnetic field, *J. Geophys. Research*, *65*, 3143-4138, 1960a.
- Obayashi, T., and Y. Hakura, Solar corpuscular radiation and polar ionospheric disturbances, *J. Geophys. Research*, *65*, 3131-3142, 1960b.
- Obayashi, T., and Y. Hakura, Enhanced ionization in the polar ionosphere associated with geomagnetic storms, *J. Atmospheric and Terrest. Phys.*, *18*, 101-122, 1960c.
- Reid, G. C., and H. Leinbach, Low-energy cosmic ray events associated with solar flares, *J. Geophys. Research*, *64*, 1801-1805, 1959.
- Romaña, A., Sudden commencements and solar flare effects, *J. Geophys. Research*, *63*, 825-828, 1958.

(Received July 21, 1961;  
revised October 5, 1961.)

# Horizontal Intensity Comparisons between the Sine Galvanometer and the Proton Vector Magnetometer

J. L. BOTTUM, R. E. GEBHARDT, AND J. B. TOWNSHEND

*U. S. Coast and Geodetic Survey  
Fredericksburg Magnetic Observatory  
Corbin, Virginia*

Observations of horizontal intensity with both the sine galvanometer and the proton vector magnetometer on a twice-weekly schedule at this Observatory permit a comparison of the two instruments, the magnetograph being used to allow for the effects of transient fluctuations. That is, each determination of the magnetograph base-line value gives new data contributing to the comparison, subject to correction for any pier difference between the positions of the two absolute instruments. Results already reported [Hurwitz and Nelson, 1960] indicated that the proton vector magnetometer gave values of horizontal intensity higher by  $2.7 \gamma$  than the sine galvanometer. This difference was called 'preliminary' pending investigation.

The sine galvanometer observations were suspended during the interval from November 1, 1959, to January 15, 1961. In this interval the instrument was dismantled and renovated, and the dimensions of its coil were redetermined [Alldredge and Hurwitz, 1960].

Since the return to service of the sine galvanometer, new comparisons have been made as shown in the accompanying table. These results indicate the sine galvanometer and the proton vector magnetometer to be now in virtual agreement; the mean difference is less than the uncertainty of  $\pm 0.5 \gamma$  which reflects the scatter of values, attributable to limitations on the accuracy of scaling a fluctuating magnetograph trace and related difficulties.

The problem remains of accounting for the  $2.7 \gamma$  reported earlier. The remeasurement of the sine galvanometer coil, which led to revision of the coil constant so as to increase the readings of the instrument by  $0.9 \gamma$ , is part of the answer. This leaves  $1.8 \gamma$  still to be accounted for. Two possible contributing factors are the following: (a) certain disturbing materials were found during the renovation of the sine galvanometer; (b) there is some unresolved uncertainty in the slight pier difference existing at the time of the earlier comparisons.

TABLE 1. Difference between Base-Line Values Determined with the Proton Vector Magnetometer and with Sine Galvanometer No. 1

Month (1961)	Number of Determinations	Mean Difference PVM minus SG, $\gamma$
Jan.	2	+0.6
Feb.	8	+1.2
Mar.	8	+0.1
Apr.	7	+0.3
May	9	-0.2
June	8	+0.1
July	4	0.0

The materials mentioned consisted of circle-illuminating lamp bulbs that were incorporated in the instrument, and a slightly magnetic spring in the tangent screw. It was not possible to obtain wholly nonmagnetic bulbs, and it was found that, by interchanging bulbs and trying different ones, changes up to  $1 \gamma$  could be produced. When the instrument was reassembled, provision was made for reading the circle by external illumination, and the offending parts were not used.

The pier difference has been redetermined by new comparisons, made through the magnetograph by using the sine galvanometer first on one pier and then on the other. Prior to this work, the piers had been partially dismantled and rebuilt (in August 1960), and we are neither prepared to specify to what extent the pier difference was altered physically nor to allocate the  $1.8 \gamma$  in detail, but it is considered that the combination of effects (a) and (b) may well suffice to account for the total.

## REFERENCES

- Hurwitz, L., and J. H. Nelson, Proton vector magnetometer, *J. Geophys. Research*, **65**, 1759-1765, 1960.  
Alldredge, L. R., and L. Hurwitz, Redetermination of coil constant of Sine Galvanometer No. 1, *J. Geophys. Research*, **65**, 2211, 1960.

(Received September 23, 1961.)

Discussion of Paper by N. D. Opdyke, 'The Paleomagnetism of the New Jersey Triassic: A Field Study of the Inclination Error in Red Sediments'

D. H. GRIFFITHS AND R. F. KING

*Department of Geology, University of Birmingham  
Birmingham, England*

Opdyke's [1961] conclusion that the Triassic sediments of the Newark group of New Jersey do not show an inclination error of the kind that we have observed in recent sediments is, of course, a valid one, but his result is to be expected if, as is commonly supposed, the remanence of red sandstones is chemical in nature rather than detrital. We take his result to be strong evidence that this particular sediment did not acquire its remanence by the alignment of magnetic particles during deposition, but we should like to point out that this may not be true of all older sediments. In particular, we should expect siltstones with a nonmagnetic cement, in which the magnetic particles are not grossly different in size from the nonmagnetic, to show deviations of the remanence quite comparable with those which have been found in varves. A field study, similar to Opdyke's, of such material would be of considerable interest.

One minor point also deserves comment. Opdyke gives as possible mechanisms for the production of an inclination error:

1. Alignment during settling of elongated particles.

2. Post-depositional compaction.

In the material we have studied, it seems likely that mechanism 1 contributes only to a minor extent to the inclination error [Griffiths, King, Rees, and Wright, 1960] and that the 'compaction' which we put forward as an alternative mechanism (and which produces an inclination error even if the particles are equidimensional) occurs at the time of deposition rather than even a short time afterwards. In other sediments, such as those laid down at high porosity in the ocean [Keen, 1960] it seems likely that compaction is important for a greater time and can be more truly called 'post-depositional.'

REFERENCES

- Griffiths, D. H., R. F. King, A. I. Rees, and A. Wright, The remanent magnetism of some recent varved sediments, *Proc. Roy. Soc. London A*, 256, 359-387, 1960.  
Keen, M. J., *Nature*, 187, 220, 1960.  
Opdyke, N. D., The paleomagnetism of the New Jersey Triassic: A field study of the inclination error in red sediments, *J. Geophys. Research*, 66, 1941-1949, 1961.

(Received August 7, 1961.)

## An Additional Measurement of the Tritium Content of Atmospheric Hydrogen of 1949

E. L. FIREMAN<sup>1</sup> AND F. S. ROWLAND<sup>2</sup>

*Brookhaven National Laboratory  
Upton, Long Island, New York*

Some recent papers have been concerned with the tritium content of atmospheric hydrogen and its steady increase since regular measurements were begun about 1953 [Gonsior, 1959; Bishop and Taylor, 1960]. Not many measurements are available for the tritium content of atmospheric hydrogen before that time [Faltings and Harteck, 1950; Harteck and Faltings, 1950], and we wish to record one additional measurement. This sample was collected on August 4, 1949, by Air Reduction Company, and it was measured for tritium activity in September 1953. This sample showed a T/H ratio of  $(5.7 \pm 1.0) \times 10^{-15}$ , corrected to the time of collection. No further details are now available concerning the conditions of collection.

The Airco sample was originally composed of 79 per cent H<sub>2</sub>, 21 per cent Ne, and 0.2 per cent N<sub>2</sub>. The hydrogen was extracted through a palladium thimble, the remaining gas containing less than 0.1 per cent H<sub>2</sub>. The hydrogen fraction was then counted in a low-level Geiger counter described previously [Fireman, 1953]. Counter fillings of 7.8- and 8.1-cm hydrogen pressure gave  $6 \pm 1$  counts/min above background, which corresponded to a T/H ratio of  $(4.5 \pm 0.8) \times 10^{-15}$ . Correction for the decay of tritium gives  $(5.7 \pm 1.0) \times 10^{-15}$  at the time of collection.

In the same apparatus and at approximately

the same time, independent measurements were made on an atmospheric hydrogen sample collected by Linde Air Products Company in the spring of 1952. A previous measurement of another aliquot of this sample showed a T/H value of  $(16.6 \pm 1.0) \times 10^{-15}$  [Grosse, Kirschenbaum, Kulp, and Broecker, 1954]. Our measurements were in excellent agreement, giving a T/H value of  $(16.7 \pm 1.2) \times 10^{-15}$  at the time of collection.

The mass spectrometer measurements of sample composition were made by Mr. A. P. Irsa; the Airco sample was furnished by Prof. T. I. Taylor. The work was done under the auspices of the Atomic Energy Commission.

### REFERENCES

- Bishop, K. F., and B. T. Taylor, Growth of the tritium content of atmospheric molecular hydrogen, *Nature*, **185**, 26, 1960.
- Faltings, V., and P. Harteck, Der Tritiumgehalt der Atmosphäre, *Z. Naturforsch.*, **5a**, 438, 1950.
- Fireman, E. L., Measurement of the (n, H<sup>3</sup>) cross section in nitrogen and its relationship to the tritium production in the atmosphere, *Phys. Rev.*, **91**, 922, 1953.
- Gonsior, B., Tritium-Anstieg im atmosphärischen Wasserstoff, *Naturwiss.*, **46**, 201, 1959.
- Grosse, A. V., A. D. Kirschenbaum, J. L. Kulp, and W. S. Broecker, The natural tritium content of atmospheric hydrogen, *Phys. Rev.*, **93**, 250, 1954.
- Harteck, P., and V. Faltings, The helium-3 problem of the atmosphere, *Nature*, **166**, 1109, 1950.

(Received August 26, 1961.)

<sup>1</sup> Present address: Smithsonian Astrophysical Observatory, Cambridge, Massachusetts.

<sup>2</sup> Present address: Department of Chemistry, University of Kansas, Lawrence, Kansas.



## The Myers Formula and Myers Rating Compared with Actual Floods

G. G. COMMONS

2601 Bridle Path  
Austin 3, Texas

The very frequent use of the Myers formula and the Myers rating for comparison of flood flows prompts an inquiry into the validity of such procedures.

The basic concept of the Myers formula [Jarvis, 1926] is that the peak flood flow varies as the square root of the drainage area and that, if the 'modified Myers maximum' flow is expressed as

$$Q = 10,000A^{0.5}$$

where  $Q$  is peak flow in  $\text{ft}^3/\text{sec}$  and  $A$  is drainage area in  $\text{mi}^2$ , the Myers rating may be expressed as a multiple or percentage of this quantity for a particular flood and drainage area.

A basic concept of flood formulas of the exponential type, such as the Myers formula, is that the flood flows vary as some power of the drainage area. To this could be added a corollary, that the flow per unit area is greater the smaller the area. This requires that the exponent be less than unity. In the Myers formula the exponent is 0.5 and, as used by Jarvis, applies to areas from 0.1 to  $10^6 \text{ mi}^2$ , and the 'modified Myers maximum' applies to the entire range.

For any flood formula to be valid, it must apply to any drainage area within its range and to subareas within the larger area. If the formula is exponential in form, a change in either the coefficient or the exponent is in itself an acknowledgment that the flood flow does not vary as that particular power of the area. In the use of the Myers formula, if the Myers rating applies to a particular area, the rating for subareas within that area must average at least as high as the rating for the larger area. If this principle is discarded, the principle that peak flood flows vary as the square root of the drainage area must also be discarded.

It must be admitted that this use of the Myers formula has been made for nearly forty years and that it is based on a number of flood records that is quite small when compared with

the (still inadequate) number available today.

For an analysis of the results obtained through an application of the Myers formula, use is made of data contained in *U. S. Geological Survey Water Supply Paper 847*, and references are to floods listed therein.

Item 224, Table 8, lists the West Nueces River, near Brackettville, Texas, with a drainage area of  $402 \text{ mi}^2$  and a peak discharge on June 14, 1935, of  $580,000 \text{ ft}^3/\text{sec}$ . The 'modified Myers maximum' formula for  $402 \text{ mi}^2$  would give a peak flow of  $200,500 \text{ ft}^3/\text{sec}$ . For an actual measured flow of  $580,000 \text{ ft}^3/\text{sec}$ , the Myers rating would be 2.89.

With the above figures as a basis on a subarea of  $4 \text{ mi}^2$ , the peak discharge would be  $57,800 \text{ ft}^3/\text{sec}$  or  $22.6 \text{ ft}^3/\text{sec}/\text{acre}$ . This is approximately equal to runoff at the rate of  $22.6 \text{ in}/\text{hr}$ . The rainfall producing this runoff must necessarily be at a greater rate and must continue for a sufficient time for runoff from the most distant point to reach the point of concentration. In view of maximum recorded rainfall records, this is a most unlikely event, and if the comparison is made on an area of  $1 \text{ mi}^2$  it becomes even more unlikely.

Tabulation of a large number of floods in Texas and similar areas has shown that, if an equation of the exponential form is used, the maximum recorded floods for areas up to about  $800 \text{ mi}^2$  may be expressed by an equation of the form

$$Q = C A^x$$

where  $Q$  is peak flow in  $\text{ft}^3/\text{sec}$ ,  $C$  is a coefficient,  $A$  is area in  $\text{mi}^2$ , and  $x$  is an exponent.

For an area of over  $30,000 \text{ mi}^2$  in and adjacent to the Balcones fault zone in Texas, which the two floods listed above and others approaching them in size have occurred, this equation has been found to be  $Q = 4326A^{0.85}$ . In addition, there is a fringe area, 2 or 3 times as large, surrounding this area in which flood flow

TABLE 1. Flood Discharges as Given by the Formula  $Q = 4326.4^{0.815}$ 

Drainage Area, mi <sup>2</sup>	Peak Discharge, ft <sup>3</sup> /sec	Peak Discharge,	
		ft <sup>3</sup> /sec/mi <sup>2</sup>	in/hr
.00156 (1 acre)	21.5	13,760	21.5
1	4,326	4,326	6.8
4.1	13,800 (measured)	3,370	5.3
100	184,540	1,845	2.9
402	580,000 (measured)	1,443	2.25
800	1,005,000	1,256	1.98

are but little less than those given by this formula. Application of this formula will give consistent results, within the range of rainfall probabilities, as shown in Table 1.

An examination of the paper by Jarvis, and particularly of Plate IX and Figure 6, will show that the line for the 'modified Myers maximum' has been drawn parallel to lines passing through the central portion of the points plotted and that, if a line were to be drawn through the highest points plotted, it would have a very distinct bend, beginning at about 800 or 1000 mi<sup>2</sup>. In Figure 6 most of the formulas plotted, with the exception of Myers', show exponents of the order of 0.7 to 0.8.

The inescapable conclusions to be drawn are (1) that the maximum recorded flood flows do

not vary as the square root of the area; (2) that the Myers formula and rating might be used to compare floods from approximately equal drainage areas, but when applied to areas differing by considerable amounts it is inapplicable and misleading; and (3) the use of the Myers formula and rating as a means of comparing flood flows should be discontinued.

#### REFERENCES

- Jarvis, C. S., Flood flow characteristics, *Trans. Am. Soc. Civil Engrs.* 89, 985-1104, 1926.  
U. S. Geological Survey, Water Supply Paper 847, Maximum discharges at stream-measurement stations through December 31, 1937.

(Received July 9, 1961; revised September 4, 1961.)

## Discussion of Paper by Ivan W. Brunk, 'Changes in the Levels of Lakes Michigan and Huron'

HARLEY F. LAWHEAD

*Corps of Engineers, Chicago, Illinois*

*Résumé.* From 10-year running averages of mean annual levels of the Great Lakes and Lake St. Clair, Brunk [1961] notes that there were peaks in the levels of most of the lakes in the 1880's and around 1950. He notes further that, for Lake Michigan-Huron, the latter peak was more than 1.5 feet lower than the peak in the 1880's. Mr. Brunk considers the difference in levels observed for the two peaks to be a lowering of the Michigan-Huron levels since 1887 that is associated solely with changes that occurred in factors other than the water-supply factors of precipitation, inflow, evaporation, and diversion.

Mr. Brunk makes an evaluation of the effects on Michigan-Huron levels of the difference in factors other than water-supply factors (evaluation of effects insofar as they bear directly on Michigan-Huron levels and differences in factors as between the periods of the two peaks) and finds the effects to be of small magnitude, except for those of changes in the natural channel for discharge from Michigan-Huron to Lake Erie.

Mr. Brunk's derivation of the effects of changes in the Michigan-Huron outlet, based on a consideration of the water balance of Lake Erie, determines the Erie net-basin-supply to be too small for the early period of the records by an amount equivalent to about 15,000 ft<sup>3</sup>/sec, and, since he takes the records of Erie storage changes and outflows as being accurate, he concludes that Michigan-Huron outflows as published for the early period by the U. S. Lake Survey are too large by about 15,000 ft<sup>3</sup>/sec. This derivation is the basis for certain quantitative results of Mr. Brunk's paper, and it leads him to the further conclusion that it is possible that practically all of the difference between Michigan-Huron levels observed for the high-water period of the 1880's and those for the high-water period of about 1950 is attributable to enlargement of the discharge capacity of the Michigan-Huron outlet.

The writer agrees that Michigan-Huron levels

of the latter peak were lower than they would have been without change in the hydraulic system of the lakes and agrees further that some of the lowering has resulted from changes in the Michigan-Huron outlet. He does not agree, however, that the amount of such lowering was more than 1.5 feet or that practically all of it has resulted from changes in the flow regimen of the Michigan-Huron outlet. This discussion is directed primarily to the following matters considered most pertinent with respect to the results of Mr. Brunk's study.

(1) *Comparison of peak levels:* Whether all of the more than 1.5-foot difference in Michigan-Huron levels from the peak of the 1880's to the peak of 1950 represents a lowering due to effects of factors other than water-supply factors;

(2) *Evaluation of factors:* Whether the list of factors or the treatment thereof is complete enough to properly narrow the field of possible causes of a lowering of Michigan-Huron levels to the single cause of changes in the lake outlet and

(3) *Outflow records:* The nature and suitability of the published Michigan-Huron and Erie outflows, particularly the early records, as a basis for a quantitative derivation of the effects on the Michigan-Huron levels of changes in the outlet of that lake.

These matters are discussed in subsequent paragraphs. Following the discussions, the writer states what he believes to be the lowering of Michigan-Huron levels that is due to changes in the lake outlet and gives the reasons therefor.

*Comparison of peak levels.* Use of the elevation difference between two peaks in the levels of one of the Great Lakes as a measure of the lowering effect caused by one or more of the factors involved implies that the peaks are comparable with respect to all other factors having bearing on the levels of that lake. It appears logical to use Lake Erie levels as a reference base in comparing two peaks in the levels of



Michigan-Huron, because, on the average, 90 per cent of the net total supply of water to Lake Erie consists of Michigan-Huron outflow and because the regimen of Lake Erie outflows has not been affected materially by changes in the Niagara River. (The writer considers that the use of Lake Erie levels as a reference base has merit, conditionally). The fact that on Lake Erie the level of the 1950 peak returned approximately to the level of the peak of the 1880's might be taken as an indication that the two peaks on Lake Michigan-Huron should be comparable with respect to water-supply factors. But to do so leads to an erroneous conclusion as explained later, and 'to see why M-H did not return to high levels of the 1880's' it is necessary to examine the several factors pertaining to lake levels of the two peaks on the lakes, including water-supply factors, to discover all differences in the factors which are pertinent to the question. Results of a further examination of the factors are discussed under the following subheading.

*Evaluation of factors.* Under conditions corresponding to the long-term average, the excess water flowing from Lake Michigan-Huron through the St. Clair-Detroit River to discharge into Lake Erie constitutes about 90 per cent of Lake Erie's net total supply, and the remaining 10 per cent is from the Lake Erie basin.<sup>1</sup> Precipitation over the Great Lakes basin, the ultimate source of the supplies, occurs in amounts which increase proceeding from northern areas of the basin to southern areas, and, under long-term average conditions, precipitation over the Michigan-Huron basin averages about 93 per cent of that over the Erie basin.

Variations from the long-term average precipitation pattern are responsible in certain instances for a considerable portion of the lack of parallelism in chronological plots comparing the levels of Michigan-Huron with those of Erie. This is true because of the storage effect of Michigan-Huron, which absorbs and modulates large variations in the lake's supplies so that corresponding variations in the lake's outflows are much

reduced in amplitude and spread over a longer period of time. An above-normal precipitation supply to the Michigan-Huron basin, that also is abnormally large with respect to concurrent precipitation supply to the Erie basin, will effect a rise in Michigan-Huron levels but cause a lesser rise in Erie levels unless the above-normal supply to Michigan-Huron persists for about 15 years, the period required for outflow-storage adjustment to a new supply condition.

During the period 1946-1955 (determining the 10-year average levels of the 1950 Michigan-Huron and Erie peaks shown on Figure 1 of Mr. Brunk's paper) precipitation was above normal by similar amounts; precipitation over the Michigan-Huron basin was about 93 per cent of that over the Erie basin, in accord with the normal precipitation pattern. During 1878-1887 (the 10-year period determining the peaks of the 1880's) precipitation over the Michigan-Huron basin was about 14 per cent above normal while that over the Erie basin was about  $5\frac{1}{2}$  per cent above normal; precipitation over the Michigan-Huron basin was about 101 per cent of that over the Erie basin. During the central five years associated with the early peak, from 1880 to 1884, precipitation over the Michigan-Huron basin was about 108 per cent of that over the Erie basin, and in 1882 and 1884 it was about 113 per cent of the Erie precipitation. Thus, in two years of the high-water period of the 1880's, the difference between Michigan-Huron and Erie precipitation was such that the Michigan-Huron precipitation was about 20 per cent greater than that of the normal distribution pattern. The difference between the precipitation patterns that prevailed during the two high-water periods is certainly a significant factor and explains a material portion of the difference in levels of the two peaks on Michigan-Huron. By routing supplies derived from the records of precipitation over the two basins for the period 1878-1887 through Michigan-Huron and Erie, it is estimated that the 10-year average effect of divergence from the normal precipitation pattern was to increase the difference between Michigan-Huron and Erie levels in the high-water period of the 1880's by an amount of the order of 0.7 foot.

The significance of deforestation was considered in connection with the estimate of the effect of divergence from the normal precipita-

<sup>1</sup> This discussion presumes some familiarity with the Great Lakes as a hydraulic system. The writer described the system in a paper on "Surface Elevations of the Great Lakes" presented at the Princeton University conference on Shipping and Navigation Problems of the Great Lakes and St. Lawrence Seaway, 19-20 January 1960.



tion pattern during the high-water period of the 1880's, as given in the preceding paragraph. The history of lumbering operations responsible for the deforestation indicates that the tendency may have been toward a larger runoff from land areas of the Michigan-Huron drainage basin during the 1880's than in the absence of deforestation. A runoff factor of 0.4 was used in the estimate. It is noted, however, that approximately one-third of the total Michigan-Huron basin consists of the lake itself and precipitation on the lake surface is a direct contribution, equal in amount to the precipitation. Any reasonable variation from the runoff factor used for the land areas would not change materially the order of magnitude of the estimate.

The significance of deforestation was considered, also, insofar as a comparison of the two peaks in Michigan-Huron levels is concerned. Lumbering operations in the Great Lakes region are reported to have had their beginnings in the 1830's, with a comparatively slow growth until after the Civil War. Shipments of lumber from the region were in large volume, commencing about 1866. The lumbering operations reached their peak about 1892 and the volume of lumber production declined rapidly after 1900. Horton (listed in Mr. Brunk's paper as reference 4) estimated that over three-quarters of Michigan's original stand of white pine had been removed by 1880. Investigators of the problem have reached different conclusions regarding the effect on lake levels of deforestation. Freeman (listed in Mr. Brunk's paper as reference 3) found 'no indication that the cutting off of the forest has had any noteworthy effect upon lake levels or upon the water yield of the higher Great Lakes drainage regions as a whole.' Horton concluded that the effect on runoff of all cultural changes (during the 75-year period from about 1850 to about 1925) had been a gradual increase in the runoff, culminating in a maximum about 1900 and followed by a reversion toward the original conditions with the use and development of the land that has prevailed subsequent to deforestation. Horton concluded also that the net effect on runoff from the land areas of the Michigan-Huron basin had been equivalent to 5 inches. Whatever the maximum effect may have been as of 1900 or the net effect may have been as of the time of Horton's study, it appears that the difference between effects on runoff pertinent to

the peaks would be considerably less. It is concluded that deforestation is not a significant factor in a comparison of the high-water levels of Michigan-Huron for the 1880's with the high water levels of around 1950.

While Mr. Brunk's evaluation of the effect of differential crustal movement is correct insofar as effect on the relationship between Michigan-Huron outflows through the lake's natural outlet and lake stages observed at the Harbor Beach gage is concerned, it is incomplete for the purpose of determining the reasons for the difference in levels of the two Michigan-Huron peaks. Crustal movement has also affected the relationship between Lake Erie outflows through the lake's natural outlet and lake stages observed at the Cleveland gage. As a result of crustal movement during the 68-year period between the two peaks, the Cleveland gage recorded levels at the time of the latter peak which were 0.26 foot higher than they would have been without the crustal movement. Thus, since in the absence of crustal movement, recorded Erie levels for the latter peak would have been 0.26 foot lower and recorded Michigan-Huron levels would have been 0.26 foot lower, this natural phenomenon is the reason for about 0.18 foot of the difference in levels of the two peaks on Michigan-Huron.

Comment is given on Mr. Brunk's evaluation of the effect of ice blockades in the Michigan-Huron outlet, although the writer does not disagree with a conclusion that any difference between the effect of ice blockades, relating to the two peaks on Michigan-Huron, is probably small. In application of his results to determining effects during the 10-year periods of the two peaks, Mr. Brunk does not recognize that the effect on Michigan-Huron levels of an ice blockade in the lake outlet is not immediately dissipated with disappearance of the blockade. If, for example, the ice retardation of outflow was average during a 10-year period which was preceded by several years with severe ice jams, the actual effect on lake levels of the 10-year period would be greater than that of an average retardation. From an inspection of the data of Mr. Brunk's analysis, it appears that the effect on levels of the two Michigan-Huron peaks was not greatly different.

The writer's interpretation of Mr. Brunk's analysis of the effect of ice blockades is that, for similar winter conditions in the early and recent

years, the retardation of Michigan-Huron outflows is of about the same magnitude. Ice jams occur frequently in the St. Clair River but seldom in the Detroit River. The occurrence of a jam in the St. Clair River materially reduces the flow into Lake St. Clair while its outflow is only slightly retarded. Generally, this produces a pronounced trough in the Lake St. Clair levels during the winter, the depth of which varies with the severity of the jam in the St. Clair River. A study of these troughs supports the showing of Mr. Brunk's analysis.

The Chicago diversion, the diversion into Lake Superior from the Albany River basin, and the Welland diversion have been considered to discover whether differences in these factors account for any material portion of the difference between Michigan-Huron levels of the peak in the 1880's and the peak of about 1950. The effect of diversions on levels of the early peak is negligible; the effect on levels of the latter peak may also be disregarded in this consideration because each of the diversions has an effect (though slightly different) on the levels of both Michigan-Huron and Erie.

*Outflow records.* The earliest reliable measurements of discharge of the Niagara and St. Clair-Detroit rivers were made by the U. S. Lake Survey in 1898 and 1899, respectively. Since those dates, an extensive series of measurements has been made in each river, extending the range in stage covered by measurements as variations in lake levels permitted and providing a basis for evaluating changes in the flow regimen.

The beds of both rivers are remarkably stable insofar as scour or silting are concerned. In the high-velocity reaches of the Niagara River, the bed is of rock, or is rocky. The bed of the St. Clair-Detroit River is of sand and gravel in the upper reach of the St. Clair River and generally of clay or a clayey mixture elsewhere, except in the lower Detroit River where the bed is rock. Maximum velocities in the St. Clair-Detroit River are much lower than those of the Niagara and, in the St. Clair-Detroit, bottom velocities are below critical values for scour. The water flowing in both rivers consists of clear, lake outflow, and therefore there is very little silting, although some sand is carried into the St. Clair River during storms on Lake Huron. In both rivers, virtually the entire flow is carried within banks, even at high river stages. On a monthly

mean basis, the stage range on the Niagara River is about 5 feet; on the St. Clair, it is about 6 feet.

There have been changes in the flow regimen of both the Niagara and the St. Clair-Detroit rivers that are attributable to known changes in the rivers. Changes in the Niagara River have had a total net effect on Lake Erie levels of about 0.1 foot. Effects of changes in the St. Clair-Detroit River are given in the following section of this discussion. The discharge records published by the Lake Survey are computed from gage records and stage-discharge relationships established, for periods of stable regimen, by the discharge measurements.

Mr. Brunk's conclusion, that the values published for Michigan-Huron outflows for the period before 1900 are too large by about 15,000 ft<sup>3</sup>/sec, involves rather absolute reliance on the accuracy of the published Erie outflows for the entire period of record and of the published Michigan-Huron outflows for the period after 1900. It is noted that the error alleged in the early Michigan-Huron outflows amounts to about 8 per cent of the average Michigan-Huron outflow or about 7 per cent of the average Erie outflow. The discharge measurements for both rivers are accepted as being of very high quality. Measurements in the St. Clair-Detroit River were made by the same agency, using the same equipment and procedures as were used in the Niagara River. Thirty-five years ago, there was some difficulty in relating discharge of the St. Clair River to stages, which since has been overcome. There is also a difficulty in obtaining stage-discharge relationships for the Niagara River, a fact which was not as well understood in 1926 as it is today. The subsequent establishment and rating of a gage in the Maid-of-the-Mist pool of the Niagara River has provided reliable data for evaluating a seasonal cycle in the regimen of Lake Erie outflows, resulting from aquatic weed growth in the upper Niagara River. The writer finds little, if any, reason in the background information pertaining to the discharge measurements and their interpretation to direct all suspicion to the early Michigan-Huron outflow records. (It is believed, however, that published values of winter outflows from Michigan-Huron may be somewhat less reliable for early periods than for later periods because there were fewer water-level gage points available in



the early periods from which to estimate ice retardation).

To the extent the published discharge values of either lake may be in error for the early period, there are other data which indicate that at least a part of the error would be found in the early Niagara records. Consider first Mr. Brunk's determination of the average Michigan-Huron outflow for 1878-1887 (shown in his Table 2) and its comparison with the average outflow for 1946-1955. Mr. Brunk makes the average flow value for the early period (194,000 ft<sup>3</sup>/sec) practically equal to the average value for the latter period (193,800 ft<sup>3</sup>/sec) in spite of the fact that precipitation over the Michigan-Huron basin was about 14 per cent above normal for the early period and about 2 per cent above normal for the latter period. Obviously, outflow for the early period should be the larger, indicating that part, at least, of any discrepancy in the early outflow records would be in the Erie outflows. Consider also a comparison of Mr. Brunk's value (about 187,000, as deduced by the writer from statements in Mr. Brunk's paper) of the average Michigan-Huron outflow for the period 1875-1899 with the average of the published values (176,000 ft<sup>3</sup>/sec) for the period 1900-1952. The value for the early period should be considerably more than 11,000 ft<sup>3</sup>/sec greater than the value for the latter period because the annual precipitation over the Michigan-Huron basin averaged 2 inches greater for the early period than for the latter period and, during the latter period, the natural supply to the Michigan-Huron outlet was reduced by about 5000 ft<sup>3</sup>/sec by diversions. (The average net value for the period 1900-1952, is equal to Chicago diversion minus Ogoki-Long Lake diversion.) The writer concludes that it is erroneous to assume that published values of the Michigan-Huron outflows for the period before 1900 should be decreased by about 15,000 ft<sup>3</sup>/sec.

*Lowering of Michigan-Huron levels.* In 1920, the Joint Board of Engineers appointed by the Governments of the United States and Canada reported on the St. Lawrence Waterway. This report is listed in Mr. Brunk's paper as reference 7. Based on detailed studies of all available records, the Board found that the levels of Lake Michigan-Huron had been lowered by changes in the lake outlet before 1926 and determined the amount of the lowering. On page 43 of

Senate Document 71, 84th Congress, 1st Session (1955), the authorizing document for the present Great Lakes Connecting Channels Project, the value of the lowering, resulting from the channel improvements made in 1934-1936, is stated. This channel improvement work is the only known change in the Michigan-Huron outlet between 1926 and 1950 whose lowering effect was not completely compensated for by the offsetting effect of other works constructed for that purpose. These lowering effects are summarized as follows:

Period of Changes in Michigan-Huron Outlet	Lowering of Michigan- Huron Levels, feet
1890-1907	0.3
1908-1925	0.3
1926-1950	0.15
1890-1950	0.75

With regard to the lowering due to the channel improvement work of 1934-1936, it is noted that the lowering is an uncompensated residual. Measures were taken to compensate for the lowering effect of that work, but largely because the amount of overdepth material removed was greater than anticipated the compensation was incomplete. Plans to compensate for the effect of the present Connecting Channels Project have included the uncompensated residual of the previous project in determining the total lowering effect to be compensated for.

The lowering of Michigan-Huron levels that resulted from channel changes in the outlet during the period 1908-1925 is considered to be attributable largely to commercial sand and gravel dredging in the upper St. Clair River. The reason for the lowering that occurred in the interval between 1890 and 1908 is not known.

By independent analysis, the details of which are indicated in this discussion, it is determined that the total lowering of Michigan-Huron levels resulting from changes in the lake's natural outlet channel is in the same order of magnitude as that determined directly from records of lake levels and outflows by the Joint Board of Engineers, updated to include uncompensated regimen change of the 1934-1936 period. Results of such independent analysis are summarized in feet of stage on Lake Michigan-Huron, as follows:

Difference between Michigan-Huron levels of 1880 and 1950 peaks (from 10-year running averages)	1.61
Portions of difference resulting from factors other than changes in St. Clair-Detroit River channel:	
From divergence of precipitation pattern	-0.7
From differential crustal movement (68 years)	-0.18
Total of these two factors	-0.88
Portion of difference resulting from channel changes	0.73

This analysis omits certain factors having only comparatively small effects (including the fact that, on the basis of 10-year running averages, the Lake Erie level of the peak of around 1950 failed to return to the Erie level of the 1880's by 0.10 foot, and thus, other things being equal, the 1950 peak on Michigan-Huron would not be expected to return quite to the level of the 1880 peak).

The writer concludes that the total lowering of Michigan-Huron levels attributable to changes in the lake's natural outlet channel is of the order of three-quarters of a foot. He further concludes that the total lowering of Michigan-Huron levels, due to channel changes and differential crustal movement during the 68-year period, is of the order of 0.9 foot. This accounts for all lowering (during the 68-year period) due to changes in factors other than water-supply factors which, by definition, include diversions since they affect supplies to the lake outlets. For periods of time longer than 68 years, the effect due to differential crustal movement would be larger than 0.18 foot.

## REFERENCE

Brunk, I. W., Changes in the levels of Lakes Michigan and Huron, *J. Geophys. Research*, 66, 3329-3335, 1961.

(Received June 30, 1961; revised August 14, 1961.)



## Author's Reply to the Preceding Discussion

IVAN W. BRUNK

*U. S. Weather Bureau, Chicago, Illinois*

The basis for the conclusion that practically all the lowering of M-H levels was due to natural and artificial changes in the outlet of M-H, was *not* because the observed drop in M-H levels between the peak in the 1880's and the peak around 1950 was more than 1.6 ft, but because the stage-discharge relationship had apparently changed by approximately 1.6 ft between the 10-year period ending 1887 and the 10-year period ending 1955 (from curve *C* to curve *B* of Fig. 2). The evaluation is also not dependent upon the choice of the two particular 10-year periods used. A similar method could be employed to determine the effect of changes between any two periods. For example, since it might appear that 10-year periods are not sufficiently long for comparison of stage-discharge relationships, a similar method was tried between a 15-year period beginning in 1875 (the year of earliest precipitation data) and a 15-year period ending in 1952 (the year of the latest computed NBS data). The indicated difference in M-H levels from the first to the second 15-year period was approximately 1.7 ft, and the computed probable effect of downcutting in the 73-year period was also approximately 1.6 ft.

It appears that changes in the stage-discharge relationship of M-H can be brought about only through (1) changes in outlet conditions, (2) ice blockades, and (3) crustal movements. Since water-supply factors of M-H are of no concern in determining the stage-discharge relationships or the change in these relationships, Mr. Lawhead's comments preceding his discussion of crustal movements would not appear to be applicable, nor would any comment on diversion at Chicago, since this is in the same category as water supply factors insofar as any effect upon the stage-discharge relationship is concerned. Likewise, the cumulative effect of ice blockades and the modulating effect of M-H, mentioned by Mr. Lawhead, do not have any effect upon the stage-discharge relationships. (The discharge values in individual years of each 10-year period were adjusted for the effect of ice, and it is only

the initial effect, not the cumulative effect, which results in any change in the stage-discharge relationship.)

The limitations of the methods used to evaluate the effect of downcutting were discussed in the original paper. If it can be demonstrated that other factors should have been included, such as the effect of crustal movements on the level of Lake Erie, it will be conceded that these should be deducted from the value derived as the probable effect of downcutting. However, it appears that these are relatively minor, since the lowering of M-H levels, by backwater effect, is equal to about 33 per cent of the lowering of Erie levels (according to Mr. Lawhead).

The only other basic problem appears to be the derivation of the stage-discharge curves. Mr. Lawhead discusses this point next, under *Outflow records*. The curve for recent times (curve *B*) is evidently not disputed, thus leaving only the early curve (curve *C*) as a possible point of contention. My argument here was that the early values (1878 to 1887) of discharge from M-H were much too large to be compatible with outflows from Lake Erie. The adjustment of these early values from a consideration of Erie outflow and precipitation yielded curve *C*. (If Erie outflows are considered correct, the conclusion in this paper must be essentially correct.)

This problem of accounting for the apparently low water yield of the Erie basin, or what happened to all the water apparently supplied to the Erie basin in the first 10-year period, has not been solved by Mr. Lawhead. For example, the average difference between the reported and computed values of M-H outflow during the 10-year period 1878 to 1887 was 20,600 ft<sup>3</sup>/sec [Brunk, 1961, Table 2]. In other words, during this period, the reported values of M-H outflow appear to be more than 10 per cent too high. A plot of reported and computed values of M-H outflow during the years 1875 to about 1900 indicates an irregular but steady decrease in the difference between the values. The problem, a result of using the difference between the Er

outflow and the water yield of the Erie basin to determine the probable M-H outflows, is whether this decrease was due to a change in the relationship between Erie precipitation and the net basin supply (NBS), or whether it was associated with progressive changes in the outlet of M-H. Available evidence, and the judgment of Horton, indicates that the effect of cultural changes in the Erie basin has *not* been in the direction of increased runoff with time. It appears to be a reasonable conclusion, therefore, that changes in the M-H outlet were primarily responsible for this difference between reported and probable values of M-H discharge. In other words, it does not appear reasonable to assume that discharge measurements made around 1898 could accurately reflect the stage-discharge relationship for the period before 1898, especially since Horton indicated that the determination of outflow from M-H before about 1898 requires special study, because changes in outlet conditions have taken place more or less progressively.

Of all the Great Lakes, the relationship between precipitation and NBS for the period 1900 to 1952 is best for Erie and poorest for M-H. (Furthermore, in using this relationship for Erie, rather than that of M-H, as was done by Mr. Lawhead, to determine the probable M-H outflows, we are working with a much smaller quantity, with correspondingly less uncertainty concerning the results obtained.) The correlation coefficients of annual values of NBS and precipitation (Lake Survey data) for two periods are as follows:

Lake	1900 to 1923	1924 to 1952
Michigan-Huron	0.42	0.78
Superior	0.69	0.72
Ontario	0.72	0.84
Erie	0.74	0.91

There is no detectable time trend in the relationship between NBS and precipitation for Erie and Ontario in the period 1900 to 1952. Computed values of NBS for Ontario for 1875 to 1899, derived from the relationship between Ontario NBS and precipitation for the years 1900 to 1952, are within 3 per cent (on the average) of reported values. Therefore, it can be assumed with at least some degree of confidence that the relationship which existed between Erie NBS and precipitation in the period 1900 to 1952 was also valid during the period 1875 to 1899.

On the other hand, the relationship between NBS and precipitation for the M-H basin is rather poor, the correlation coefficient of 0.42 indicating that only 18 per cent of the variance in the NBS is explained by the precipitation data during this period. After considerable study of the effects of deforestation and other factors on runoff, Horton concluded that, in Michigan, the effect of cultural changes had resulted in a gradual decrease in water losses, culminating in a maximum about 1900, and that the net effect on runoff had apparently been about 5 inches for the M-H region as a whole. Therefore, it appears that little significance can be given to the large values of M-H precipitation in the 1878 to 1887 period in indicating comparable large discharge values of M-H as determined by Mr. Lawhead.

Mr. Lawhead's final section shows that there is no disagreement concerning the fact that there has been a change in the M-H outlet, which has resulted in a corresponding drop in M-H levels. The only disagreement lies between the value of approximately 1.6 ft determined by the methods used in the paper and the value of 0.75 ft assumed by Mr. Lawhead.

(Received July 15, 1961.)

## Comments on Paper by V. V. Belousov, 'The Origin of Folding in the Earth's Crust'

EARL M. P. LOVEJOY

4400 Fairview Road, Reno, Nevada

Lest the impression be emplaced that silence connotes universal acceptance, may I submit to the *Journal of Geophysical Research* a comment on V. V. Belousov's article 'The Origin of Folding in the Earth's Crust' [Belousov, 1961].

I agree wholeheartedly with Belousov that crustal shrinking or contraction as a source of compression is no longer able 'to meet the demands of modern scientific observations.' But because the contraction theory is inadequate means not that compression is not causal but rather merely that a better cause of compression must be sought.

Belousov believes that vertical faulting begets folding. His submission is worthy of study and manifests original applications to the science. But, that compression could beget simultaneous faulting and folding is not disproved by his hypothesis. If one assumes compression in his Figure 6, then reverse faulting and folding could be the result, and folding need not depend solely upon vertical faulting.

I find Belousov's failure to mention the Basin Ranges of the Cordilleran interesting. Here, one has been led to believe over the decades, are the finest examples of vertical faults caused by differential movements of small blocks. Here, then, also, one would expect to find the finest examples of Belousov's folds, draped as he shows in Figures 5 and 14. I do not speak now of the older folds of thrusting but of the new folds supposedly to be formed by block faulting. Oddly, no such folds exist, nor are there any unequivocal data indicating their former presence. Where, then, is the theory of Belousov's found 'to meet the demands of modern scientific observations' in the Basin and Range. Obviously, it does not.

Concerning Belousov's remarks with respect to gravitational sliding on slight geosynclinal slopes, I must disagree. Before shales are sliding and plicating, what are the massive overlying

rocks doing? One must first assume initial movement, a starting; otherwise the system is static. The bounding competent beds would not allow sliding on shale to start. But if we assume a start then would 'thrusting' occur. With wholesale movement of the mass above a given bed there would be extremely rapid erosion by mass wasting and land sliding at the initial opening. Once large-scale movement started, jointing and fracturing would occur. Frontal breaking would follow immediately, and the rate of erosion would govern the results. If the rate of erosion were equal to that of sliding then no allocthon would result. If the rate of erosion exceeded that of sliding then a stratum would result. If the rate of erosion were lower than that of sliding then overlying beds would soon surpass the unctuous layer and friction would rapidly rise, stopping the sliding; whereupon erosion would catch up *passu*.

If Belousov believes that the underlying clay would first produce a linear bulge or diapir, a fold much like a salt bed might, his hypothesis could be tenable. As a first effort, then, one must find the elongate clay dome equivalent to a salt dome many tens of miles long. To my knowledge no such feature exists. Certainly there is no published evidence of a linear clay dome, or salt dome, whose length is measurable in tens of miles, erosion and breaching of which would have formed the opening and commenced the movement of his sliding system. Also, the mechanism does not apply to 'Laramide' thrusting in southwestern Utah, southern Nevada, or southern California.

Finally, postulating vertical fault movement is merely begging the question. What causes the vertical movements? Why would vertical faults always be parallel? Why are domes circular or elliptical, rather than rectilinear? What relationship is there between dip-slip vertical

faults and strike-slip vertical faults? Why is there generally so little folding associated with faulting?

We shall admit an admiration for Belousov's academic study and his origination of a compelling orography. But there is little in the Cordillera to convince the geologist familiar with it that Belousov's theory has been able

'to meet the demands of modern scientific observations' obtained therein.

## REFERENCE

Belousov, V. V., The origin of folding in the earth's crust, *J. Geophys. Research*, 66, 2241-2254, 1961.

(Received July 31, 1961; revised August 25, 1961.)



## Author's Reply to the Preceding Discussion

V. V. BELOUSSOV

*Institute of Physics of the Earth  
Academy of Sciences of the USSR, Moscow*

Mr. Lovejoy's remarks have convinced me that I probably did not succeed in expressing adequately enough to all the readers the idea, which I consider as major, that the problems of the origin of folding cannot be solved any longer by conjecturing abstract theories based on *schemes*. For full understanding, these problems need a detailed study of the *real* folding with all the peculiarities of its morphology, which often happens to differ greatly from those found in schemes in the textbooks on structural geology.

It was the study of real folding that brought me to my conclusions. If Mr. Lovejoy doubts my conclusions I would ask him to pay attention to actual folding and to try to analyze how folds were formed.

I did not refer to the Basin Range structures because I do not know them. They are too far from the regions of my field work, and I have had no opportunity to study them. However, in other places I have seen many block structures which did not result in folding. But if folding exists it stands in that relation to faults which I tried to show. That faults do not always follow folding can be explained by the fact that the formation of folding needs the presence of corresponding material which is not always available on the spot. The velocity of displacement along faults can also have importance. I would prefer, though, to see the actual profile across the Basin Range.

In connection with Mr. Lovejoy's doubt about gravitational folding I can only ask him to study closely the structure of Helvetic nappes in the Alps and to make an attempt to suggest some other explanation of their origin.

The salt and clay diapirs of considerable length (I have a wider term for them—'injectite folding') are rather numerous. They are found in great numbers on the foothills of the Carpathian Mountains, on the two ends of the Main Caucasus Range, in Provence, and in the Crimea. This form of structure is very common.

Mr. Lovejoy does not find examples of possible application of my ideas in the Cordilleras. However, I have just received a letter from another geologist working in the Cordilleras with quite an opposite statement.

Naturally, I do not consider that my article interprets the problem of folding. This problem can be solved only as the result of joint efforts of researchers working in different regions. The problem, though, needs *special* study, as, separately, the problems of petrology and of paleontology are studied, and not together with other tasks (for instance along with geological survey, etc.). It is necessary, moreover, to study this problem not according to schematic conceptions of folding in general, but on the basis of detailed study of the actual folding complexes.

(Received October 9, 1961.)

## Corrigendum

Dr. Michele Caputo has called attention to the following corrections to his paper 'Deformation of a Layered Earth by an Axially Symmetric Surface Mass Distribution,' which appeared in the May 1961 issue of the Journal.

In formulas 11, in the right-hand member of the third and fourth equations (lines 5, 6, 8, and 9 from the bottom of page 1480) all the signs outside the parentheses and brackets should

be changed. The same change should be made in the fourth and sixth equations of formulas 15 (lines 2 and 5 from the top of page 1481) and in the fourth and sixth equations of formulas 16 (lines 6, 7, 9, 10, 11, and 12 from the bottom of page 1481). In equation 17 and the following one (page 1482) instead of 3 there must be 1.5. In line 15 from the top of page 1483, instead of  $d$  there must be  $d/2$ .

# Information for Contributors to the *Journal of Geophysical Research*

**Manuscripts.** Send manuscripts to J. A. Peoples, Jr., Department of Geology, University of Kansas, Lawrence, Kansas. Manuscripts, including proof copies of figures, should be submitted in triplicate to expedite review and publication. Manuscripts should be in English, typewritten on heavy paper on one side of page only, double spaced (including abstracts and references), with generous margins.

Ample space should be allowed for mathematical expressions, which should be typed or very plainly written by hand. Particular attention should be given to the legibility of subscripts and superscripts and to differentiation between capital and lower-case letters. Unusual symbols and cumbersome notation should be avoided. Fractional exponents should be written in preference to root signs, and the solidus (/) should be used for fractions wherever its use will save vertical space.

Authors are urged to have their papers critically reviewed by their associates for scientific validity, manner of presentation, and use of English before submitting them for publication.

**Abstracts.** An abstract must accompany each manuscript. It should be a concise but comprehensive condensation of the essential parts of the paper, suitable for separate publication and adequate for the preparation of general indexes to geophysical literature.

**References and footnotes.** References should be indicated in the text by the insertion in brackets of the author's name and the year of publication, thus: [Faust, 1958]. If the author's name is part of the text, only the year is bracketed. If there are two or more references citing different papers published in the same year by the same author, they may be distinguished by the letters *a*, *b*, *c* after the year.

At the end of the paper references should be listed alphabetically by the author's names in the form of the references given below. (See *List of Periodicals Abstracted by Chemical Abstracts* for abbreviations of titles of journals, or write titles in full.)

Footnotes to the text should be avoided; parenthetical sentences should preferably be added to the text. If footnotes must be given they should be numbered consecutively throughout the paper.

**Tables and figures.** Material suited to tabular form should be arranged as a table and may be typewritten on a separate sheet. Tables must be numbered according to their sequence in the text, and each table should have a title. Column headings should be short and self-explanatory; more complete explanations may be given in footnotes to the table.

Figures should be prepared with the column width of this Journal in mind (a scale of 2 to 4 times that of the published figure is usually adequate). They must be drawn in India ink on white paper or tracing cloth. Coordinate paper should be avoided; if used, however, it must be blue-lined, and coordinate lines that are to show must be inked.

Titles of figures must be typewritten consecutively on a separate sheet; they are *not* to be lettered on the figure. Necessary lettering within the figure must be executed to meet competent drafting standards and should be large enough to remain legible after reduction. The ideal letter size in the reduced figure is 1/16 inch, but 1 mm is acceptable. Unnecessary blank space within the figure should be avoided.

Photographs are acceptable only if they have good intensity and contrast. They should be unmounted glossy prints.

Figure number and author's name should be written lightly in pencil on each figure. 'Top' of each figure should be indicated.

**Acknowledgments.** Acknowledgments should be made only for significant contributions by the author or professional associates. A brief closing statement will usually suffice.

## REFERENCES

- American Chemical Society, *List of Periodicals Abstracted by Chemical Abstracts*, Chemical Abstracts Service, Ohio State Univ., Columbus, 314 pp., 1956.
- American Institute of Physics, *Style Manual*, 2nd ed., American Institute of Physics, New York, 42 pp., 1959.
- Faust, L. Y., The preparation of a paper, *Geophysics*, 23, 944-952, 1958.
- Landes, K. K., A scrutiny of the abstract, *Geophysics*, 17, 645, 1952. Reprinted in *Geophysics*, 23, 942-943, 1958.
- Skillen, M. E., R. M. Gay, and others, *Words into Type*, Appleton-Century-Crofts, New York, 585 pp., 1948.
- U. S. Geological Survey, *Suggestions to Authors of the Reports of the United States Geological Survey*, 5th ed., U. S. Govt. Printing Office, Washington, 255 pp., 1958.
- William Byrd Press, *Mathematics in Type*, William Byrd Press, Richmond, 58 pp., 1954.

# Journal of GEOPHYSICAL RESEARCH

## Tables of Contents

VOLUME 66, NO. 1, JANUARY 1961

	PAGE
Mirror and Azimuthal Drift Frequencies for Geomagnetically Trapped Particles, <i>D. A. Hamlin, R. Karplus, R. C. Vik, and K. M. Watson</i> . . . . .	1
Pulsation of the Earth's Electromagnetic Field with Periods of 1 to 5 Seconds and Their Connection with Phenomena in the High Atmosphere, <i>V. A. Troitskaya</i> . . . . .	5
Spaced Observations of the Low-Frequency Radiation from the Earth's Upper Atmosphere, <i>G. R. A. Ellis</i> . . . . .	19
Ionospheric Absorption at Times of Auroral and Magnetic Pulsations, <i>Wallace H. Campbell and H. Leinbach</i> . . . . .	25
A Note on the Cause of Sudden Ionization Anomalies in Regions Remote from High-Altitude Nuclear Bursts, <i>C. M. Crain and P. Tamarkin</i> . . . . .	35
A Study of Auroral Coruscations, <i>Wallace H. Campbell and M. H. Rees</i> . . . . .	41
Observations of Cosmic Radio Noise at 18 Mc/s in Hawaii, <i>Walter R. Steiger and James W. Warwick</i> . . . . .	57
An Estimate of Electron Densities in the Exosphere by Means of Nose Whistlers, <i>Joseph H. Pope</i> . . . . .	67
On Indirect Temperature Soundings of the Stratosphere from Satellites, <i>D. Q. Wark</i> . .	77
Propagation of Planetary-Scale Disturbances from the Lower into the Upper Atmosphere, <i>J. G. Charney and P. G. Drazin</i> . . . . .	83
Sferics from Intracloud Lightning Strokes, <i>Lee R. Tepley</i> . . . . .	111
Summer Frontal Precipitation in the United States Area of Daf Climate, <i>R. D. Rudd</i> . .	125
Some Effects of Deficiencies in Upper-Level Humidity Records, <i>J. W. Hutchings</i> . . . .	131
On the Spring Maximum of Radioactive Fallout from Nuclear Test Explosions, <i>J. F. Bleichrodt, Joh. Blok, and R. H. Dekker</i> . . . . .	135
The Structure of the Pacific Equatorial Countercurrent, <i>John A. Knauss</i> . . . . .	143
Relationship between Surface Slope, Average Facet Size, and Facet Flatness Tolerance of a Wind-Disturbed Water Surface, <i>Allen H. Schooley</i> . . . . .	157
Some Nonlinear Properties of Long-Crested Periodic Waves with Lengths near 2.44 Centimeters, <i>Willard J. Pierson, Jr., and Paul Fife</i> . . . . .	163
Diffusion Theory Applied to Radiant Energy Distribution and Albedo of Snow, <i>J. C. Giddings and E. LaChapelle</i> . . . . .	181
Ultrasonic Velocity and Attenuation of Longitudinal Waves in Rocks, <i>Michel Auberger and John S. Rinehart</i> . . . . .	191
Crustal Structure from the Nevada Test Site to Kingman, Arizona, from Seismic and Gravity Observations, <i>W. H. Diment, S. W. Stewart, and J. C. Roller</i> . . . . .	201
Crustal Structure of the New York-Pennsylvania Area, <i>Jack Oliver, Robert Kovach, and James Dorman</i> . . . . .	215
The Reflected Seismic Pulse, <i>C. H. Dix</i> . . . . .	227
Elastic Pulse Reflection—Evaluation of Some Determinants, <i>C. H. Dix</i> . . . . .	235
Probing the Earth with Nuclear Explosions, <i>D. T. Griggs and Frank Press</i> . . . . .	237



	PAGE
The Thermodynamic Theory of Nonhydrostatically Stressed Solids, <i>W. Barclay Kamb</i> . . . . .	259
Variations in Radiocarbon Concentration and Sunspot Activity, <i>M. Stuiver</i> . . . . .	273
Helium, Argon, and Carbon in Some Natural Gases, <i>R. E. Zartman, G. J. Wasserburg, and J. H. Reynolds</i> . . . . .	277
Spherules from the Antarctic Ice Cap, <i>Edward Thiel and Richard A. Schmidt</i> . . . . .	307
Geomagnetic and Solar Data, <i>J. Virginia Lincoln</i> . . . . .	311
Letters to the Editor:	
Observation of a Solar Bremsstrahlung Burst at 1926 UT, August 11, 1960, <i>J. R. Winckler, T. C. May, and A. J. Masley</i> . . . . .	316
Observations of the Cosmic-Ray Equator in the Pacific Ocean Area, <i>Richard A. Hubach</i> . . . . .	321
Behavior of the 6300 O I Line at Huancayo, <i>S. M. Silberman and M. Casaverde</i> . . . . .	323
Criticism of the Theory of Magnetic Bays of Bless, Gartlein, Kimball, and Sprague, <i>K. D. Cole and F. R. Bond</i> . . . . .	327
Limitations of Radiosonde Punch-Card Records for Radiometeorological Studies, <i>B. R. Bean and B. A. Cahoon</i> . . . . .	328
A Note to the Paper by C. B. Moore, B. Vonnegut, B. A. Stein, and H. J. Survilas, 'Observation of Electrification and Lightning in Warm Clouds,' <i>Leo Alpert</i> . . . . .	332
Spiral Motion of Fluids, <i>William F. Tanner</i> . . . . .	333
On $\bar{P}$ and $L_g$ , <i>Eugene Herrin</i> . . . . .	334
International Geophysical Calendar for 1961, <i>A. H. Shapley</i> . . . . .	336
Corrigenda:	
<i>W. O. Roberts and H. Zirin</i> . . . . .	340
<i>J. Virginia Lincoln</i> . . . . .	340
<i>Mahdi S. Hantush</i> . . . . .	340

## VOLUME 66, NO. 2, FEBRUARY 1961

X Rays from Van Allen Belt Electrons, <i>J. B. Cladis and A. J. Dessler</i> . . . . .	343
Charged Particles in the Inner Van Allen Radiation Belt, <i>A. H. Armstrong, F. B. Harrison, H. H. Heckman, and L. Rosen</i> . . . . .	351
Hydromagnetic Waves and the Trapped Radiation: 1, Breakdown of the Adiabatic Invariance, <i>Donat G. Wentzel</i> . . . . .	359
Hydromagnetic Waves and the Trapped Radiation: 2, Displacements of the Mirror Points, <i>Donat G. Wentzel</i> . . . . .	363
The Distribution of Micrometeorites near the Earth, <i>A. R. Hibbs</i> . . . . .	371
VLF Phase Perturbation Associated with Meteor Shower Ionization, <i>Charles J. Chilton</i> . . . . .	379
Sources of Solar Ultraviolet Radiation, <i>R. Grant Athay</i> . . . . .	385
Theory of X-Ray Emission of the Sun, <i>G. Elwert</i> . . . . .	391
The Theory of Artificial Satellites in Terms of the Orbital True Longitude, <i>Peter Musen</i> . . . . .	403
Perpendicular Intersections with a Dipole Field, <i>Marshall H. Cohen and Martin L. Dwarkin</i> . . . . .	411
A Note on the Disposition of Daytime Auroral Ionization in Space, <i>Ray L. Leadabrand</i> . . . . .	421
Radio Wave Reflections from the Mesosphere: 1, Heights of Occurrence, <i>John B. Gregory</i> . . . . .	429
The Slant $E_s$ Echo—A High-Frequency Auroral Echo, <i>Howard F. Bates</i> . . . . .	447
Results of IGY Rocket-Grenade Experiments to Measure Temperatures and Winds above the Island of Guam, <i>W. Nordberg and W. G. Stroud</i> . . . . .	495
Observation of Infrared Cooling of a Tropical Air Mass, <i>Homer T. Mantis</i> . . . . .	465
Carbon Dioxide in the Atmosphere and in Atlantic Ocean Water, <i>Taro Takahashi</i> . . . . .	477
A Theoretical Study of Waves Breaking at an Angle with a Shore Line, <i>B. Le Méhauté</i> . . . . .	495
Direct Numerical Calculation of Wave Properties, <i>J. E. Chappellear</i> . . . . .	501
Graphical Solution and Interpretation of a New Drain-Spacing Formula, <i>Sadik Toksöz and Don Kirkham</i> . . . . .	509
The Dynamic Programming Approach to Water-Resources Development, <i>Warren A. Hall and Nathan Buras</i> . . . . .	517
The Use of a Dimensionless Unit Hydrograph to Derive Unit Hydrographs for Some Pacific Northwest Basins, <i>Donald L. Bender and John A. Roberson</i> . . . . .	521

	PAGE
Local Evaporation from a Smooth Water Surface, <i>James W. Deardorff</i> . . . . .	529
A Comparison of Computed and Measured Soil Moisture under Snap Beans, <i>W. E. Marlatt, A. V. Havens, N. A. Willits, and G. D. Brill</i> . . . . .	535
On Some Properties of Residuals and Derivatives, <i>Amalendu Roy</i> . . . . .	543
The Paleomagnetism of the Aden Volcanics, <i>E. Irving and D. H. Tarling</i> . . . . .	549
Time Variations of the Ellipticity and Preferred Direction of the $P_c$ Telluric Field, <i>S. H. Yungul</i> . . . . .	557
The Effect of the Drilling Fluid on Temperatures Measured in Bore Holes, <i>J. C. Jaeger</i> . .	563
The Theory of Heat Flux Meters, <i>J. R. Philip</i> . . . . .	571
Internal Friction in Shear and Shear Modulus of Solenhofen Limestone over a Frequency Range of $10^7$ Cycles per Second, <i>Louis Peselnick and W. F. Outerbridge</i> . . . . .	581
Sound Velocities at the Surface of Deep Sea Sediments, <i>John C. Fry and Russell W. Raft</i> . . . . .	589
Sub-Basement Seismic Reflections in Northern Utah, <i>Harry D. Narans, Jr., Joseph W. Berg, Jr., and Kenneth L. Cook</i> . . . . .	599
Excitation of the Free Oscillations of the Earth by Earthquakes, <i>Hugo Benioff, Frank Press, and Stewart Smith</i> . . . . .	605
Observations of the Free Oscillations of the Earth, <i>N. F. Ness, J. C. Harrison, and L. B. Slichter</i> . . . . .	621
Free Oscillations of the Earth Observed on Strain and Pendulum Seismographs, <i>Leonard E. Alsop, George H. Sutton, and Maurice Ewing</i> . . . . .	631
Letters to the Editor:	
An Observation of Free Oscillations of the Earth, <i>B. P. Bogert</i> . . . . .	643
Magnetic Effects of High-Altitude Nuclear Detonations, <i>A. M. Van Wijk</i> . . . . .	647
Fluctuations of the Coleman Glacier, Mt. Baker, Washington, <i>A. E. Harrison</i> . . .	649
Solar Radio Emission and Geophysical Disturbances during July 1959, <i>M. P. Hughes</i> .	651
Observed Field Strength in the Neighborhood of the Skip Distance, <i>K. C. Yeh and G. W. Swenson, Jr</i> . . . . .	654
Substitution of Small Cans for Weather Bureau Pans in Measuring Evaporation, <i>Richard B. Marston</i> . . . . .	657
Geomagnetic and Solar Data, <i>J. Virginia Lincoln</i> . . . . .	660
Corrigenda:	
<i>R. L. Smith and R. A. Helliwell</i> . . . . .	664
<i>H. K. Sen and A. A. Wyller</i> . . . . .	664

## VOLUME 66, NO. 3, MARCH 1961

Cosmic-Ray Neutron Demography, <i>W. N. Hess, E. H. Canfield, and R. E. Lingenfeller</i> . .	665
Scintillation-Counter Observations of Auroral X Rays during the Geomagnetic Storm of May 12, 1959, <i>P. D. Bhavsar</i> . . . . .	679
Effect of Hydromagnetic Waves in a Dipole Field on the Longitudinal Invariant, <i>E. N. Parker</i> . . . . .	693
Equation of a Charged Particle Shell in a Perturbed Dipole Field, <i>Ralph H. Pennington</i> . .	709
Theory of Auroral Morphology, <i>J. W. Kern and E. H. Vestine</i> . . . . .	713
The Relationship between Unique Geomagnetic and Auroral Events, <i>Y. Sobouti</i> . . . .	725
Influence of Sunspots on Geomagnetic Disturbance, <i>Fred Ward and Ralph Shapiro</i> . . .	739
Low-Latitude and High-Latitude Geomagnetic Agitation, <i>E. R. Hope</i> . . . . .	747
Some Properties of Radio Waves Reflected from the Moon and Their Relation to the Lunar Surface, <i>Tor Hagfors</i> . . . . .	777
Daytime and Nighttime Atmospheric Properties Derived from Rocket and Satellite Observations, <i>H. K. Kallmann-Bijl</i> . . . . .	787
A Subtropical Convergence Line of the South Pacific: A Case Study Using Meteorological Satellite Data, <i>Lester F. Hubert</i> . . . . .	797
Evidence of a Downward-Propagating, Annual Wind Reversal in the Equatorial Stratosphere, <i>Richard J. Reed, William J. Campbell, Lowell A. Rasmussen, and Dale G. Rogers</i> . . . . .	813

Analysis of a Falling-Sphere Experiment for Measurement of Upper-Atmosphere Density and Wind Velocity, *J. Otterman, I. J. Sattinger, and D. F. Smith* . . . . . 819

Technique for Introducing Low-Density Space Charge into the Atmosphere, *B. Vonnegut, K. Maynard, W. G. Sykes, and C. B. Moore* . . . . . 823

Calculations of Cloud Electrification Based on a General Charge-Separation Mechanism, *J. D. Sartor* . . . . . 831

Effects of Wind-Induced Advection on Sea Surface Temperature, *L. E. Eber* . . . . . 839

The Principal Factors Influencing the Seasonal Oscillation of Sea Level, *Eugenie Lisitzin and June G. Pattullo* . . . . . 845

Estimates of Vertical Motions and Meridional Heat Exchange in Gulf Stream Eddies, and a Comparison with Atmospheric Disturbances, *Chester W. Newton* . . . . . 853

Glaciological Regime at Little America Station, Antarctica, *A. P. Crary* . . . . . 871

Directional Properties and Phase Relations of the Magnetotelluric Fields at Austin, Texas, *H. W. Smith, L. D. Provazek, and F. X. Bostick, Jr.* . . . . . 879

The Record in the Meteorites: 6, On the Chronology of the Early Solar System, *Gordon G. Goles and Edward Anders* . . . . . 889

Determination of Sedimentary Thickness of the Mexican Geosyncline by Rayleigh Wave Dispersion, *D. H. Shurbet* . . . . . 899

Summary Report of Strong-Motion Measurements, Underground Nuclear Detonations, *W. M. Adams, R. G. Preston, P. L. Flanders, D. C. Sachs, and W. R. Perret* . . . . 903

A Method of Concealing Underground Nuclear Explosions, *A. L. Latter, R. E. LeLevier, E. A. Martinelli, and W. G. McMillan* . . . . . 943

Particle Motions near Explosions in Halite, *Byron F. Murphey* . . . . . 947

Use of Large Cavities to Reduce Seismic Waves from Underground Explosions, *Roland F. Herbst, Glenn C. Werth, and Donald L. Springer* . . . . . 959

Geomagnetic and Solar Data, *J. Virginia Lincoln* . . . . . 979

Letters to the Editor:

Effect of the Magnetic Field in Ionospheric Backscatter, *E. E. Salpeter* . . . . . 982

The 5577 Å Airglow Emission Mechanism, *C. A. Barth and A. F. Hildebrandt* . . . . 985

Thermal Radiation Spectrum of the Arctic Sky, *W. B. Murcray* . . . . . 987

Reply to Some Comments by Malville concerning the Midnight Auroral Maximum, *E. H. Vestine and J. W. Kern* . . . . . 989

A Note on Phase Velocity of VLF Radio Waves, *James R. Wail and Kenneth P. Spies* . . . . . 992

Discussion of Paper by J. N. Nanda, 'The Origin of Microseisms,' *M. S. Longuet-Higgins* . . . . . 994

Corrigendum: *J. H. Rosenbaum* . . . . . 994

VOLUME 66, NO. 4, APRIL 1961

The Time Variations of Solar Cosmic Rays during July 1959 at Minneapolis, *J. R. Winckler, P. D. Bhavsar, and L. Peterson* . . . . . 995

The High-Energy Cosmic-Ray Flare of May 4, 1960: 1, High-Altitude Ionization and Counter Measurements, *J. R. Winckler, A. J. Masley, and T. C. May* . . . . . 1023

The High-Energy Cosmic-Ray Flare of May 4, 1960: 2, Emulsion Measurements, *S. Biswas and P. S. Freier* . . . . . 1029

Large-Scale Electron Bombardment of the Atmosphere at the Sudden Commencement of a Geomagnetic Storm, *R. R. Brown, T. R. Hartz, B. Landmark, H. Leinbach, and J. Ortner* . . . . . 1035

The Steady State of the Chapman-Ferraro Problem in Two Dimensions, *J. W. Dungey* . . 1043

Radiation from a Current Filament above a Homogeneous Earth, with Application to Micropulsations, *P. F. Law and B. M. Fannin* . . . . . 1049

Ionospheric Electron Content and Its Variations Deduced from Satellite Observations, *K. C. Yeh and G. W. Swenson, Jr.* . . . . . 1061

A Note on 106.1-Mc/s Auroral Echoes Detected at Stanford following the Solar Event of November 12, 1960, *R. L. Leadabrand, W. E. Jaye, and R. B. Dyce* . . . . . 1069

A Local Reduction of F-Region Ionization Due to Missile Transit, *Henry G. Booker* . . 1073



	PAGE
On the Nature of Equatorial Spread <i>F</i> , <i>Robert Cohen and Kenneth L. Bowles</i> . . . . .	1081
Doppler Shifts and Faraday Rotation of Radio Signals in a Time-Varying, Inhomogeneous Ionosphere: 2, Two-Signal Case, <i>John M. Kelso</i> . . . . .	1107
Ionization Loss Rates below 90 Km, <i>Cullen M. Crain</i> . . . . .	1117
The Relationship of Low-Height Ionosonde Echoes to Auroral-Zone Absorption and VHF D Scatter, <i>Jens K. Olesen and J. W. Wright</i> . . . . .	1127
Photogrammetric Refraction Angle: Satellite Viewed from Earth, <i>B. L. Jones</i> . . . . .	1135
The Diurnal Variation of <i>K</i> Indices of Geomagnetic Activity on Quiet Days in 1940-1948, <i>Seth B. Nicholson and Oliver R. Wulf</i> . . . . .	1139
Energy Transformation and Vertical Flux Processes over the Northern Hemisphere, <i>Clayton E. Jensen</i> . . . . .	1145
An Experiment in the Study of the Structure of an Atmospheric System by Numerical Process, <i>Stanley E. Asplund</i> . . . . .	1157
On the Tensor Form of Dispersion in Porous Media, <i>Jacob Bear</i> . . . . .	1185
Capillary Pressure and Surface Discontinuity in Porous Media, <i>Rao Channapragada and Walter Rose</i> . . . . .	1199
Estimating Ground-Water Recharge from Stream Hydrographs, <i>P. Meyboom</i> . . . . .	1203
Interrelationships of Watershed Characteristics, <i>Don M. Gray</i> . . . . .	1215
Erodibility of Some California Wildland Soils Related to Their Metallic Cation Exchange Capacity, <i>James R. Wallis and Lee J. Stevan</i> . . . . .	1225
Heat Flow from a Differentiated Earth, <i>Sydney P. Clark, Jr.</i> . . . . .	1231
Paleomagnetic Study of the Sudbury Basin, <i>Peter J. Hood</i> . . . . .	1235
Earth Currents of Deep Internal Origin, <i>P. H. Roberts and F. J. Lowes</i> . . . . .	1243
Seismic Profiles in Northwestern Utah: Pilot Range and Grouse Creek Range Area, <i>Joseph W. Berg, Jr., Kenneth L. Cook, Harry D. Narans, Jr., and Richard J. Leamer</i> . . . . .	1255
Gravity Anomalies and Crustal Section across the Tonga Trench, <i>Manik Talwani, J. Lamar Worzel, and Maurice Ewing</i> . . . . .	1265
Geomagnetic and Solar Data, <i>J. Virginia Lincoln</i> . . . . .	1279
Letters to the Editor:	
Short-Term Variations in Meson and Nucleon Component of Cosmic Rays, <i>V. L. Patel and K. Maeda</i> . . . . .	1286
A Note on Solar Flare Cosmic Rays, <i>K. Maeda and V. L. Patel</i> . . . . .	1288
Solar-Stream Distortion of the Geomagnetic Field and Polar Electrojets, <i>J. W. Kern</i> . . . . .	1290
Some Results of Direct Probing in the Ionosphere, <i>W. Pfister, J. C. Ulwick, and R. P. Vancour</i> . . . . .	1293
Air Density Variations in the Mesosphere, and the Winter Anomaly in Ionospheric Absorption, <i>J. Mawdsley</i> . . . . .	1298
Determination of Cloud Altitude from a Satellite, <i>Rudolf A. Hanel</i> . . . . .	1300
Observed Magnetic Declinations in West Antarctica, <i>Ned A. Ostenso and Charles R. Bentley</i> . . . . .	1301
Photomosaic Integration of Radar Precipitation Areas, <i>F. L. Ludwig</i> . . . . .	1303
Discussion of Paper by D. M. Hershfield and M. A. Kohler, 'An Empirical Appraisal of the Gumbel Extreme-Value Procedure,' <i>Leo R. Beard</i> . . . . .	1306
Authors' Reply to Discussions by I. I. Gringorten, M. A. Benson, and L. R. Beard of the Paper, 'An Empirical Appraisal of the Gumbel Extreme-Value Procedure,' <i>D. M. Hershfield and M. A. Kohler</i> . . . . .	1308
Discussion of Paper by P. P. Rowe, 'An Equation for Estimating Transmissibility and Coefficient of Storage from River-Level Fluctuations,' <i>Mahdi S. Hantush</i> . . . . .	1310
API Nomogram, <i>Wayne J. Kammerer</i> . . . . .	1312
Seasonal Variations in Atmospheric Carbon Dioxide Concentration, <i>Eugene M. Wilkins</i> . . . . .	1314
Addendum: The Density and Mass Distribution of Meteoritic Bodies in the Neighborhood of the Earth's Orbit, <i>Harrison Brown</i> . . . . .	1316
Note on 'The Economical Net Radiometer,' <i>C. B. Tanner, J. A. Businger, and P. M. Kuhn</i> . . . . .	1318
Comment on Paper by D. G. Singleton, 'The Geomorphology of Spread <i>F</i> ,' <i>John P. Miller</i> . . . . .	1318



## Corrigenda:

<i>R. A. Duncan</i> . . . . .	1319
<i>C. B. Tanner and W. L. Pelton</i> . . . . .	1319
<i>Mahdi S. Hantush</i> . . . . .	1319

## VOLUME 66, NO. 5, MAY 1961

The Ring Current, Geomagnetic Disturbance, and the Van Allen Radiation Belts, <i>Syun-Ichi Akasofu and Sydney Chapman</i> . . . . .	1321
The Effects of Betatron Accelerations upon the Intensity and Energy Spectrum of Magnetically Trapped Particles, <i>Paul J. Coleman, Jr.</i> . . . . .	1351
Characteristics and Fine Structure of the Large Cosmic-Ray Fluctuations in November 1960, <i>J. F. Steljes, H. Carmichael, and K. G. McCracken</i> . . . . .	1363
Balloon Observations of Auroral-Zone X Rays, <i>R. R. Brown</i> . . . . .	1379
Seasonal Variations of Cosmic-Ray Intensity in Polar Regions, <i>K. Maeda and V. L. Patel</i> . . . . .	1389
The Source of Radiation from Jupiter at Decimeter Wavelengths: 3, Time Dependence of Cyclotron Radiation, <i>George B. Field</i> . . . . .	1395
The Dayglow of the Sodium D Lines, <i>J. E. Blamont and T. M. Donahue</i> . . . . .	1407
The Coupling between the Protonosphere and the Normal F Region, <i>W. B. Hanson and I. B. Ortenburger</i> . . . . .	1425
Distribution of Water Vapor in the Stratosphere, <i>H. J. Mastenbrook and J. E. Dinger</i> . . . . .	1437
Leaking Modes in the Crustal Waveguide: 1, The Oceanic PL Wave, <i>Robert A. Phinney</i> . . . . .	1445
The Reformation of Geodesy, <i>R. A. Hirvonen</i> . . . . .	1471
Deformation of a Layered Earth by an Axially Symmetric Surface Mass Distribution, <i>Michele Caputo</i> . . . . .	1479
Energy Requirements of an Expanding Earth, <i>A. E. Beck</i> . . . . .	1485
The Effect of Pressure on the Electromotive Force of a Platinum-Bismuth Thermocouple, <i>George C. Kennedy and Robert C. Newton</i> . . . . .	1491
Anomalous-Leads from Broken Hill, Australia, <i>R. D. Russell, T. J. Ulrych, and F. Kollar</i> . . . . .	1495
Rb-Sr Age Measurements on Total Rock and Separated-Mineral Fractions from the Old Granite of the Central Transvaal, <i>H. L. Allsopp</i> . . . . .	1499
Space Erosion of the Grant Meteorite, <i>David E. Fisher</i> . . . . .	1509
Cosmogenic Argon and Neon in Stone Meteorites, <i>Heinz Stauffer</i> . . . . .	1513
Thermomagnetic Properties, Natural Magnetic Moments, and Magnetic Anisotropies of Some Chondritic Meteorites, <i>F. D. Stacey, J. F. Lovering, and L. G. Parry</i> . . . . .	1523
Magnetic Disturbances and the Earth's Magnetic Field, <i>J. S. Chatterjee</i> . . . . .	1535
Abstracts of the Papers Presented at the Pacific Northwest Regional Meeting, American Geophysical Union, Moscow, Idaho, October 19-20, 1960 . . . . .	1547
Abstracts of the Papers Presented at the Pacific Southwest Regional Meeting, American Geophysical Union, Berkeley, California, January 26-27, 1961 . . . . .	1551
Geomagnetic and Solar Data, <i>J. Virginia Lincoln</i> . . . . .	1561
Letters to the Editor:	
The Effect of Faraday Rotation on Incoherent Backscatter Observations, <i>G. H. Millman, A. J. Moceyunas, A. E. Sanders, and R. F. Wyrick</i> . . . . .	1564
Solar Flare Cosmic-Ray Event of May 4, 1960, <i>K. Maeda, V. L. Patel, and S. F. Singer</i> . . . . .	1569
Dropout Phenomenon Observed in the Satellite 1958 $\delta_2$ Transmissions, <i>Ludwik Liszka</i> . . . . .	1573
Author's Reply to the Beard-Johnson Comments, <i>Philip J. Wyatt</i> . . . . .	1578
On the Extremely Low Frequency Spectrum of Earth-Ionosphere Cavity Response to Electrical Storms, <i>H. R. Raemer</i> . . . . .	1580
Magnetic Bays, Auroral Orientation, and Isochasms, <i>K. D. Cole and F. Jacka</i> . . . . .	1584
An Attempt to Observe the Day Airglow, <i>L. Wallace</i> . . . . .	1585
Simultaneous Observations of VLF Noise ('Hiss') at Hobart and Macquarie Island, <i>R. L. Dowden</i> . . . . .	1587
Discussion of a Paper by D. S. Bugnolo, 'Spread F and Multiple Scattering in the Ionosphere,' <i>Jacques Renau</i> . . . . .	1589

	PAGE
Author's Reply to the Preceding Discussion, <i>D. S. Bugnolo</i> . . . . .	1590
The Antarctic Stratospheric Vortex in 1958, <i>Clarence E. Palmer and Ronald C. Taylor</i> . . . . .	1591
Discussion of Paper by W. F. Libby and C. E. Palmer, 'Stratospheric Mixing from Radioactive Fallout,' <i>L. Machta</i> . . . . .	1592
Authors' Reply to the Preceding Discussion, <i>W. F. Libby and C. E. Palmer</i> . . . .	1593
Small-Scale Polar-Cap Absorption and Related Geomagnetic Effect, <i>G. F. Rourke</i> . .	1594
Effect of Underground Induced Polarization on ELF Propagation, <i>H. Raemer</i> . . .	1596
On the Possible Presence of Ice on the Moon, <i>Kenneth Watson, Bruce Murray, and Harrison Brown</i> . . . . .	1598
Discussion of Paper by F. Chayes, 'On Correlation between Variables of Constant Sum,' <i>A. B. Vistelius</i> . . . . .	1601

## VOLUME 66, NO. 6, JUNE 1961

Cosmic Ray Phenomena during the November 1960 Solar Disturbances, <i>J. G. Roederer, J. R. Manzana, O. R. Santochi, N. Nerurkar, O. Troncoso, R. A. R. Palmeira, and G. Schwachheim</i> . . . . .	1603
The Spectrum and Propagation of Relativistic Solar Flare Particles during July 17-18, 1959, <i>H. S. Ghielmetti</i> . . . . .	1611
Radiation Measurements to 1500 Kilometers Altitude at Equatorial Latitudes, <i>Francis E. Holly, Lew Allen, Jr., and Richard G. Johnson</i> . . . . .	1627
Effect of Hydromagnetic Waves on the Lifetime of Van Allen Radiation Protons, <i>A. J. Dragt</i> . . . . .	1641
Observations of Hydromagnetic Emissions, <i>Lee R. Tepley</i> . . . . .	1651
On the Long-Period Lunisolar Effect in the Motion of the Artificial Satellite, <i>P. Musen</i> . .	1659
An Ion-Trap Measurement of the Ion Concentration Profile above the $F_2$ Peak, <i>W. B. Hanson and D. D. McKibbin</i> . . . . .	1667
Photoionization Heating in the $F$ Region of the Atmosphere, <i>D. C. Hunt and T. E. Van Zandt</i> . . . . .	1673
Long-Distance One-Hop $F_1$ Propagation through the Auroral Zone, <i>L. H. Tveten</i> . . .	1683
Extensions of the 'Chapman' Theory of Layer Formation, <i>C. H. Cummack</i> . . . . .	1685
Density Fluctuations in a Plasma in a Magnetic Field, with Applications to the Ionosphere, <i>Tor Hagfors</i> . . . . .	1699
A Diffraction Theory for LF Sky-Wave Propagation, <i>James R. Wait</i> . . . . .	1713
A Diffraction Theory for LF Sky-Wave Propagation—An Additional Note, <i>James R. Wait and Alyce M. Conda</i> . . . . .	1725
Theory of Electrostatic Fields in the Ionosphere at Polar and Middle Geomagnetic Latitudes, <i>John R. Spreiter and Benjamin R. Briggs</i> . . . . .	1731
Atmospheric Noise Levels from 0.6 to 10 Kilocycles per Second, <i>L. H. Ginsberg and D. J. Blattner</i> . . . . .	1745
Determination of the Vertical Distribution of Ozone by Satellite Photometry, <i>S. V. Venkateswaran, James G. Moore, and Arlin J. Krueger</i> . . . . .	1751
Observations of 26.3 Mc/s Solar Radio Noise during August 1959, <i>W. C. Erickson</i> . . .	1773
A Theory of Radar Reflection from the Moon and Planets, <i>Fred B. Daniels</i> . . . . .	1781
Magnetic Variations at Conjugate Points, <i>Eugene M. Wescott</i> . . . . .	1789
An Iteration-Variation Method for Wave Propagation Problems, <i>W. J. Byatt and G. P. DeVault</i> . . . . .	1793
A Geoid and World Geodetic System Based on a Combination of Gravimetric, Astrogeodetic, and Satellite Data, <i>W. M. Kaula</i> . . . . .	1799
Improvements on the Sea Gravimeter Gss2, <i>Anton Graf and Reinhard Schulze</i> . . . . .	1813
Area-Depth Rainfall Formulas, <i>Arnold Court</i> . . . . .	1823
Surface Water Storage on Annual Ryegrass, <i>Robert A. Merriam</i> . . . . .	1833
Throughfall Variation under Tree Crowns, <i>Benjamin B. Stout and Richard J. McMahon</i> .	1839
Flow Losses in Dry Sandy Channels, <i>John H. Cornish</i> . . . . .	1845
Water Intake Rates of a Claypan Soil from Hydrograph Analyses, <i>V. C. Jamison and J. F. Thornton</i> . . . . .	1855

The Deuterium Concentration in Arctic Sea Ice, <i>Irving Friedman, Beatrice Schoen, and Joseph Harris</i> . . . . .	1861
A Study of the Free Oscillations of the Earth, <i>Gordon J. F. MacDonald and Norman F. Ness</i> . . . . .	1865
Upper Crustal Structure of Iceland, <i>Eysteinn Tryggvason and Markus Balth</i> . . . . .	1913
Treatment of Partially Stable Sedimentary Rocks Showing Planar Distribution of Directions of Magnetization, <i>E. Irving, W. A. Robertson, P. M. Stott, D. H. Tarling, and M. A. Ward</i> . . . . .	1927
Paleomagnetic Results from the Upper Triassic Lavas of Massachusetts, <i>E. Irving and M. R. Banks</i> . . . . .	1935
The Paleomagnetism of the New Jersey Triassic: A Field Study of the Inclination Error in Red Sediments, <i>N. D. Opdyke</i> . . . . .	1941
Remote Analysis of Surfaces by Neutron-Gamma-Ray Inelastic Scattering Technique, <i>C. D. Schrader and R. J. Stinner</i> . . . . .	1951
Acoustic Relaxation in Chromium, <i>Louis Peselnick and Robert Meister</i> . . . . .	1957
Geomagnetic and Solar Data, <i>J. Virginia Lincoln</i> . . . . .	1963
Letters to the Editor:	
A Relation between Solar Radio Emission and Low-Energy Solar Cosmic Rays, <i>K. Sakurai and H. Maeda</i> . . . . .	1966
Rigidity Dependence of Solar Diurnal Variation of Cosmic-Ray Intensity, <i>S. P. Duggal, K. Nagashima, and M. A. Pomerantz</i> . . . . .	1970
A Possible Explanation of the Long Duration Radar Echoes of Ionized Trails in the Upper Atmosphere, <i>C. L. Tang</i> . . . . .	1974
Two-Hop 18.6 Kc/s Whistler-Mode Echoes Received at Seattle, <i>H. R. Willard</i> . . . . .	1976
Fluctuations in a Multicomponent Plasma, <i>O. Buneman</i> . . . . .	1978
Density in a Planetary Exosphere, <i>J. Herring and L. Kyle</i> . . . . .	1980
Calibration of Pulsation Detector Coils, <i>K. Vozoff</i> . . . . .	1983
Note on the Nature of Noctilucent Clouds, <i>Eigil Hessvedt</i> . . . . .	1985
Criticism of Dr. B. Mason's Paper on 'The Origin of Meteorites,' <i>Harold C. Urey</i> . . . . .	1988
Discussion of Paper by W. A. Heiskanen, 'The Latest Achievements of Physical Geodesy,' <i>John A. O'Keefe</i> . . . . .	1992
Answer to the Discussion of Dr. O'Keefe on My Earlier Article, 'The Latest Achievements of Physical Geodesy,' <i>W. A. Heiskanen</i> . . . . .	1993
Discussion of Paper by Robert A. Merriam, 'A Note on the Interception Loss Equation,' <i>Max A. Kohler</i> . . . . .	1994
Author's Reply to the Preceding Discussion, <i>Robert A. Merriam</i> . . . . .	1995
Discussion of Paper by R. Rangarajan, 'A New Approach to Peak Flow Estimation,' <i>H. J. Ajwani</i> . . . . .	1996
Author's Reply to the Preceding Discussion, <i>R. Rangarajan</i> . . . . .	1997
Discussion of Paper by John R. Mink, 'Distribution Pattern of Rainfall in the Leeward Koolau Mountains, Oahu, Hawaii,' <i>Juergen Oelsner F. and Eduardo Basso S.</i> . . . .	1998
Corrigendum: <i>D. A. Hamlin, R. Karplus, R. C. Vik, and K. M. Watson</i> . . . . .	2001

## VOLUME 66, NO. 7, JULY 1961

The National Program for Lunar and Planetary Exploration, <i>A. R. Hibbs</i> . . . . .	2003
Characteristics of the Van Allen Radiation Zones as Measured by the Scintillation Counter on Explorer VI, <i>Alan Rosen and Thomas A. Farley</i> . . . . .	2013
Cosmic-Ray Production of Low-Energy Gamma Rays, <i>Frank C. Jones</i> . . . . .	2029
On the Interplanetary Magnetic Storm: Pioneer V, <i>P. J. Coleman, Jr., C. P. Sonett, and Leverett Davis, Jr.</i> . . . . .	2043
Energy Spectrum of Electrons Trapped in the Geomagnetic Field, <i>Martin Walt and William M. MacDonald</i> . . . . .	2047
Some Features of Magnetic Storms in High Latitudes <i>David G. Knapp</i> . . . . .	2053
Some Studies of Geomagnetic Micropulsations, <i>R. A. Duncan</i> . . . . .	2087



	PAGE
Attempt to Measure Night Helium Glow—Evidence for Metastable Molecules in the Night Ionosphere, <i>E. T. Byram, T. A. Chubb, and H. Friedman</i> . . . . .	2095
The Height and Geographical Position of the Red Auroral Arc of April 1–2, 1960, <i>James G. Moore and F. Kirk Odencrantz</i> . . . . .	2101
Some Auroral Observations Inside the Southern Auroral Zone, <i>J. V. Denholm</i> . . . . .	2105
Equatorial Spread <i>F</i> in Relation to Post-Sunset Height Changes and Magnetic Activity, <i>M. S. V. Gopal Rao and B. Ramachandra Rao</i> . . . . .	2113
Theory of Overhead Nonblanketing Sporadic <i>E</i> , <i>Jacques Renau</i> . . . . .	2121
Seasonal and Latitudinal Variations of Air Density in the Mesosphere (30 to 80 Kilometers), <i>Roderick S. Quiroz</i> . . . . .	2129
Wind and Temperature Measurements in the Mesosphere by Meteorological Rockets, <i>John E. Masterson, William E. Hubert, and Thomas R. Carr</i> . . . . .	2141
On the Deduction of the Vertical Distribution of Ozone by Ultraviolet Spectral Measurements from a Satellite, <i>Sean Twomey</i> . . . . .	2153
Stratospheric Aerosol Studies, <i>Christian E. Junge and James E. Manson</i> . . . . .	2163
Origin of Radioactive Fallout in the Northern Hemisphere after the Spring Maximum in 1959, <i>J. F. Bleichrodt, Joh. Blok, and E. R. van Abkoude</i> . . . . .	2183
Long-Range Sound Transmission in the Arctic Ocean, <i>Henry Kutschale</i> . . . . .	2189
The Velocity of Compressional Waves in Rocks to 10 Kilobars, Part 2, <i>Francis Birch</i> . . . . .	2199
The Use of Gravity Methods to Study the Underground Structure and Impact Energy of Meteorite Craters, <i>M. J. S. Innes</i> . . . . .	2225
The Origin of Folding in the Earth's Crust, <i>V. V. Beloussov</i> . . . . .	2241
Geomagnetic and Solar Data, <i>J. Virginia Lincoln</i> . . . . .	2255
Letters to the Editor:	
A Photoelectric Analyzer of All-Sky Camera Auroral Photographs, <i>Takesi Nagata and Eisuke Kaneda</i> . . . . .	2259
Ring Currents in the Region of the Van Allen Radiation Belts, <i>R. Fiebig and H. Voelcker</i> . . . . .	2262
Helium, an Important Constituent in the Lower Exosphere, <i>Marcel Nicolet</i> . . . . .	2263
Mainland Beach Changes Due to Hurricane Donna, <i>William F. Tanner</i> . . . . .	2265
Some Heat-Flow Measurements in the North Atlantic, <i>John Reitzel</i> . . . . .	2267
Anisotropic Thermal Conductivity, <i>Gene Simmons</i> . . . . .	2269
Further Statistics on the Modes of Release of Available Potential Energy, <i>Barry Saltzman and Aaron Fleisher</i> . . . . .	2271
Corrigenda:	
<i>R. L. Smith, R. A. Helliwell, and I. W. Yabroff</i> . . . . .	2274
<i>P. D. Bhavsar</i> . . . . .	2274
<i>R. R. Unterberger</i> . . . . .	2274
<i>Felix Chayes</i> . . . . .	2274

## VOLUME 66, NO. 8, AUGUST 1961

Intensity Variations in Outer Van Allen Radiation Belt, <i>S. E. Forbush, D. Venkatesan, and C. E. McIlwain</i> . . . . .	2275
Some Effects of Diamagnetic Ring Currents on Van Allen Radiation, <i>A. J. Dessler and Robert Karpus</i> . . . . .	2289
Energy Spectrum and Angular Distributions of Electrons Trapped in the Geomagnetic Field, <i>J. B. Cladis, L. F. Chase, Jr., W. L. Imhof, and D. J. Knecht</i> . . . . .	2297
The Observed Outer-Belt Electron Distribution and the Neutron Decay Hypothesis, <i>W. N. Hess, J. Killeen, C. Y. Fan, P. Meyer, and J. A. Simpson</i> . . . . .	2313
Three-Frequency Measurements of Auroral Absorption, <i>Syed Ziauddin and P. A. Forsyth</i> . . . . .	2315
The Analysis of Transient Modes of Propagation across the Auroral Zone, <i>B. J. Fulton and L. E. Petrie</i> . . . . .	2321
Effects of Corpuscular Emissions on the Polar Ionosphere following Solar Flares, <i>G. E. Hill</i> . . . . .	2329



The Latitude Dependence of Radar Meteor Shower Observations, *C. S. L. Keay and C. Ellyett* . . . . . 2337

Theory of Electrostatic Fields in the Ionosphere at Equatorial Latitudes, *John R. Spreiter and Benjamin R. Briggs* . . . . . 2345

Measurement of Ionospheric Drift by Radio-Star Observations, *Braulio Dueño* . . . . 2355

Preliminary Data on Solar Extreme Ultraviolet Radiation in the Upper Atmosphere, *H. E. Hinteregger* . . . . . 2367

Frictional Effects and the Meridional Circulation in the Mesosphere, *Bernhard Haurwitz* . 2381

Adjustable Potential-Gradient-Measuring Apparatus for Airplane Use, *B. Vonnegut, C. B. Moore, and F. J. Mallahan* . . . . . 2393

The Diurnal Variation of K Indices of Geomagnetic Activity on Disturbed Days in 1940-1948, *Seth B. Nicholson and Oliver R. Wulf* . . . . . 2399

On the Relation between the Spectrum of Turbulence and the Diabatic Wind Profile, *J. A. Businger* . . . . . 2405

Some Evidence on the Effect of Nonlinearity on the Position of the Equilibrium Range in Wind-Wave Spectra, *Blair Kinsman* . . . . . 2411

Net Precipitation in a Northern Hardwood Forest, *Raymond E. Leonard* . . . . . 2417

Projecting the Effect of Changed Stream Stages on the Water Table, *J. E. Reed and M. S. Bedinger* . . . . . 2423

Fluctuations of Ground-Water Levels Caused by Dispersion of Salts, *F. A. Kohout* . . . 2429

Ground-Water Investigations in a Saline Area of the Red River Valley, North Dakota, *Leo C. Benz, Rome H. Mickelson, Fred M. Sandoval, and Carl W. Carlson* . . . . . 2435

Some Implications of the Highly Saline Water off the Southwest Coast of Florida, *Frank Chew* . . . . . 2445

Some Experiments in Dispersion, *Jacob Bear* . . . . . 2455

In-Place Measurement of Permeability in Heterogeneous Media: 2, Experimental and Computational Considerations, *R. William Nelson* . . . . . 2469

Estimation of Electrical Conductivity from Chemical Analyses of Natural Waters, *John Logan* . . . . . 2479

Elastic Wave Interferometry—A New Tool, *I. Tolstoy* . . . . . 2485

Surface Heat Flow from a Differentiated Earth, *Gordon J. F. MacDonald* . . . . . 2489

Gravity Measurements over the Southern Rocky Mountain Trench Area of British Columbia, *G. D. Garland, E. R. Kanasewich, and Thomas L. Thompson* . . . . . 2495

Size and Mass Distribution of Cosmic Dust, *Taivo Laevastu and Otto Mellis* . . . . . 2507

Abstracts of the Papers Presented at the Forty-Second Annual Meeting, American Geophysical Union, Washington, D. C., April 18-21, 1961 . . . . . 2509

Geomagnetic and Solar Data, *J. Virginia Lincoln* . . . . . 2573

Letters to the Editor:

    Ionospheric Reflections below 50 Kilometers during Polar-Cap Absorption Events, *J. B. Gregory* . . . . . 2575

    Electron Densities in the Outer Ionosphere Deduced from Nose Whistlers, *R. L. Smith* . . . . . 2578

    Some Comments on Obtaining Electron Densities in the Exosphere Using Nose Whistlers, *Joseph H. Pope* . . . . . 2580

    Extension of Nose Whistler Analysis, *R. L. Smith and D. L. Carpenter* . . . . . 2582

    Atmospheric Ion Composition Measured above Wallops Island, Virginia, *H. A. Taylor, Jr., and H. C. Brinton* . . . . . 2587

    Comment on Paper by Henry G. Booker, 'A Local Reduction of F-Region Ionization Due to Missile Transit, *Cecil Barnes, Jr.* . . . . . 2589

    All-Sky Meteor Rates in the Southern Hemisphere, *C. Ellyett and C. S. L. Keay* . . 2590

    Remarks on the Article by A. R. Hibbs, 'The Distribution of Micrometeorites near the Earth,' *Maurice Dubin* . . . . . 2592

    Author's Reply to the Preceding Discussion on the Article, 'The Distribution of Micrometeorites near the Earth,' *A. R. Hibbs* . . . . . 2595

    Discussion on 'The Origin of Microseisms,' *J. N. Nanda* . . . . . 2597

    Discussion of Paper by W. Barclay Kamb, 'The Thermodynamic Theory of Non-hydrostatically Stressed Solids,' *G. J. F. MacDonald* . . . . . 2599

	PAGE
Discussion of Paper by W. Barclay Kamb, 'The Thermodynamic Theory of Non-hydrostatically Stressed Solids,' <i>Abraham Hoffer</i> . . . . .	2600
Factors Influencing Thickness of the Earth's Crust, <i>B. F. Howell, Jr., and R. A. Woodli</i> . . . . .	2601
Corrigendum: <i>Marshall H. Cohen and Martin L. Dwarkin</i> . . . . .	2606

## VOLUME 66, NO. 9, SEPTEMBER 1961

Dynamics and Structure of the Outer Radiation Belt, <i>C. Y. Fan, P. Meyer, and J. A. Simpson</i> . . . . .	2607
The Distribution of Trapped Particles in a Changing Magnetic Field, <i>E. N. Parker</i> . .	2641
Forbush Decrease of the Flux of Heavy Primary Nuclei of Cosmic Rays on May 12 and July 12, 1959, <i>S. Biswas</i> . . . . .	2653
Radioactivity Produced in Discoverer XVII by November 12, 1960, Solar Flare Protons, <i>John T. Wasson</i> . . . . .	2659
The Lunar Neutron Flux, <i>R. E. Lingenfelter, E. H. Canfield, and W. N. Hess</i> . . . . .	2665
Transresonant Electron Acceleration, <i>E. N. Parker</i> . . . . .	2673
A Note on Whistlers Observed above the Ionosphere, <i>Joseph C. Cain, I. R. Shapiro, J. D. Stolarik, and J. P. Heppner</i> . . . . .	2677
Drift Rate in a Dipole Field, <i>John S. Lew</i> . . . . .	2681
Rocket Measurements of the Magnetic Field above New Mexico, <i>R. Hutchinson and B. Shuman</i> . . . . .	2687
Auroral Effects on the Earth's Electric Field, <i>George D. Freier</i> . . . . .	2695
The Spectrum and the Total Intensity of Electromagnetic Waves Scattered from an Ionized Gas in Thermal Equilibrium in the Presence of a Static Quasi-Uniform Magnetic Field, <i>J. Renau, H. Camnitz, and W. Flood</i> . . . . .	2703
Prediction of VLF Diurnal Phase Changes and Solar Flare Effects, <i>W. D. Westfall</i> . . .	2733
VLF Ionospheric Reflection Coefficients—Derivation from Impedance Concepts and Values for Some Model Ionospheres, <i>Edward C. Field and Paul Tamarkin</i> . . . . .	2737
The Conductive 'Chapman' Layer, <i>C. H. Cummack</i> . . . . .	2751
Analysis of the $F_1$ - $F_2$ Transition Region, <i>G. A. M. King</i> . . . . .	2757
Effect of Electron-Ion Collisions in the $F$ Region of the Ionosphere on the Absorption of Cosmic Radio Noise at 25 Mc/s at Ahmedabad: Changes in Absorption Associated with Magnetic Storms, <i>K. R. Ramanathan, R. V. Bhonsle, and S. S. Degaonkar</i> . .	2763
Suggestion of a Second Isopycnic Level at 80 to 90 Kilometers over Churchill, Canada, <i>Allen E. Cole</i> . . . . .	2773
A Model of Solar-Flare-Induced Ionization in the $D$ Region, <i>R. C. Whitten and I. G. Poppoff</i> . . . . .	2779
Terrestrial Extremely Low Frequency Noise Spectrum in the Presence of Exponential Ionospheric Conductivity Profiles, <i>Janis Galejs</i> . . . . .	2787
Micrometeorite Measurements—Satellite and Ground-Level Data Compared, <i>W. D. Crozier</i> . . . . .	2793
On the Long-Period Lunar and Solar Effects on the Motion of an Artificial Satellite, 2, <i>Peter Musen</i> . . . . .	2797
The Aeolosphere and Atmosphere of Venus, <i>E. J. Öpik</i> . . . . .	2807
The Meteorological Rocket Network—An Analysis of the First Year of Operation, <i>Joint Scientific Advisory Group to the Meteorological Rocket Network</i> . . . . .	2821
Experimental Flight Verification of the Economical Net Radiometer, <i>R. H. Bushnell and V. E. Suomi</i> . . . . .	2843
A Method of Obtaining Detailed Wind Shear Measurements for Application to Dynamic Response Problems of Missile Systems, <i>Harold B. Tolefson and Robert M. Henry</i> . .	2849
Mean Roughness Factor as a Function of Wind Velocity, <i>Allen H. Schooley</i> . . . . .	2863
How Dry Is the Sky? <i>Murray Gutnick</i> . . . . .	2867
Lava-Sea-Air Contact Areas as Sources of Sea-Salt Particles in the Atmosphere, <i>A. H. Woodcock and A. T. Spencer</i> . . . . .	2873
A Note on the Turbulence Generated by Gravity Waves, <i>O. M. Phillips</i> . . . . .	2889

Long-Period Surface Waves from the Chilean Earthquake of May 22, 1960, Recorded on Linear Strain Seismographs, <i>James N. Brune, Hugo Benioff, and Maurice Ewing</i> . . .	2895
Measurement of <i>Q</i> for Very Long Period Free Oscillations, <i>Leonard E. Alsop, George H. Sutton, and Maurice Ewing</i> . . . . .	2911
Seismic Profiler, <i>J. I. Ewing and G. B. Tirey</i> . . . . .	2917
The Effect of Plasticity on Decoupling of Underground Explosions, <i>A. L. Latter, E. A. Martinelli, J. Matheus, and W. G. McMillan</i> . . . . .	2929
A Static Theory of the Seismic Coupling of a Contained Underground Explosion, <i>Norman A. Haskell</i> . . . . .	2937
The Seismic Head Pulse, Reflection and Pseudo-Reflection Pulses, <i>C. H. Dix</i> . . . . .	2945
Elastic Wave Propagation in Layered Anisotropic Media, <i>Don L. Anderson</i> . . . . .	2953
Phase and Group Velocities of Rayleigh Waves in a Spherical, Gravitating Earth, <i>Bruce A. Bolt and James Dorman</i> . . . . .	2965
Steady-State Calculations Bearing on Geological Implications of a Phase-Transition Mohorovicic Discontinuity, <i>G. W. Wetherill</i> . . . . .	2983
The Use of Hornblendes and Pyroxenes for K-Ar Dating, <i>Stanley R. Hart</i> . . . . .	2995
Natural Variations in Isotopic Abundances of Silicon, <i>David Tilles</i> . . . . .	3003
Variations of Silicon Isotope Ratios in a Zoned Pegmatite, <i>David Tilles</i> . . . . .	3015
Magnetic Properties of Diabase Dikes, <i>D. W. Strangway</i> . . . . .	3021
The Behavior of Volatiles on the Lunar Surface, <i>Kenneth Watson, Bruce C. Murray, and Harrison Brown</i> . . . . .	3033
Geomagnetic and Solar Data, <i>J. Virginia Lincoln</i> . . . . .	3047
Letters to the Editor:	
Radiation Measurements in the Slot between the Van Allen Belts to an Altitude of 1415 Kilometers, <i>C. A. Gurtler</i> . . . . .	3050
Rocket Measurement of a Daytime Electron-Density Profile up to 620 Kilometers, <i>J. E. Jackson and S. J. Bauer</i> . . . . .	3055
The Total Electron Content through the Entire Ionosphere by the Faraday Rotation Technique, <i>O. Burkard</i> . . . . .	3058
Some Relationships between Short-Wave Fadeouts, Magnetic Crochets, and Solar Flares, <i>Loren W. Acton</i> . . . . .	3060
Airglow and the South Atlantic Geomagnetic Anomaly, <i>K. D. Cole</i> . . . . .	3064
Possible Effects of Magnetic Field Alignment on Meteoritic Ionization, <i>Walter F. Bain</i> . . . . .	3065
A Comparison of Theory and Observation of the Echo I Satellite, <i>R. Bryant</i> . . . . .	3066
Recalculations of Cloud Electrification Based on a General Charge-Separation Mechanism, <i>J. D. Sartor</i> . . . . .	3070
Comment on Paper by B. Le Méhauté, 'A Theoretical Study of Waves Breaking at an Angle with a Shore Line,' <i>P. Groen</i> . . . . .	3072
Author's Reply to the Preceding Comment, <i>B. Le Méhauté</i> . . . . .	3072
A Note on Ocean Sediment Thickness from Surface Wave Dispersion, <i>Robert L. Kovach and Frank Press</i> . . . . .	3073
On the Geochemical Character of Iodine in Meteorites, <i>Gordon G. Goles and Edward Anders</i> . . . . .	3075
First Pulsed Radio Soundings of the Topside of the Ionosphere, <i>R. W. Knecht, T. E. Van Zandt, and S. Russell</i> . . . . .	3078
Corrigenda:	
<i>I. M. Longman</i> . . . . .	3082
<i>S. V. Venkateswaran, J. G. Moore, and A. J. Krueger</i> . . . . .	3082

## VOLUME 66, NO. 10, OCTOBER 1961

Variations of the Cosmic Radiation in November 1960, <i>J. A. Lockwood and M. A. Shea</i> . .	3083
Balloon Measurement of Solar Cosmic Rays at Fort Churchill, Canada, during July 1959, <i>James A. Earl</i> . . . . .	3095



	PAGE
The Calculation of the Electron Density in the Ionosphere from Elevation-Angle Measurements on Artificial Satellites, <i>J. E. Titheridge</i> . . . . .	3103
An HF Radar Search for Possible Effects of Earth Satellites upon the Upper Atmosphere, <i>T. A. Croft and O. G. Villard, Jr.</i> . . . . .	3109
Expected Influence of a Localized Change of Ionosphere Height on VLF Propagation, <i>James R. Wait</i> . . . . .	3119
The Interpretation and Synthesis of Certain Spread-F Configurations Appearing on Equatorial Ionograms, <i>Wynne Calvert and Robert Cohen</i> . . . . .	3125
A Waveguide Interpretation of "Temperature-Latitude Spread F" on Equatorial Ionograms, <i>M. L. V. Pitteway and Robert Cohen</i> . . . . .	3141
On the Index of Refraction in the Ionosphere, <i>Otto Theimer and Leonard S. Taylor</i> . . . . .	3157
Solar-Flare Effects on 2.5 and 5.0 Mc/s Atmospheric Radio Noise, <i>John R. Herman</i> . . . . .	3163
Infrared and Reflected Solar Radiation Measurements from the Tiros II Meteorological Satellite, <i>W. R. Bandeen, R. A. Hanel, John Licht, R. A. Stampfl, and W. G. Stroud</i> . . . . .	3169
A Statistical Study of Lower Atmospheric-Ionospheric Coupling, <i>Norman J. Macdonald and Robert W. Knecht</i> . . . . .	3187
Upper-Atmosphere Structure Measurement Made with the Pitot-Static Tube, <i>J. E. Ainsworth, D. F. Fox, and H. E. LaGow</i> . . . . .	3191
Total Atmospheric Ozone and Geomagnetic Activity, <i>S. J. Ahmed and A. Halim</i> . . . . .	3213
Airborne Filters for the Measurement of Atmospheric Space Charge, <i>C. B. Moore, B. Vonnegut, and F. J. Mallahan</i> . . . . .	3219
Natural Radioactivity in the Atmosphere, <i>Rama and M. Honda</i> . . . . .	3227
Ground-Conductivity Determinations at Low Radio Frequencies by an Analysis of the Sferic Signatures of Thunderstorms, <i>J. R. Johler and C. M. Lilley</i> . . . . .	3233
$S_q$ and Ocean, <i>Tsuneji Rikitake</i> . . . . .	3245
Backscattering of 3.21-Centimeter Radiation by Water Bubbles, <i>Louis J. Battan and Benjamin M. Herman</i> . . . . .	3255
On the Vertical Circulation of the Mediterranean Sea, <i>Georg Wüst</i> . . . . .	3261
General Theory of Dispersion in Porous Media, <i>A. E. Scheidegger</i> . . . . .	3273
Statistical Geometry of Porous Media, <i>H. D. Fara and A. E. Scheidegger</i> . . . . .	3279
Effect of Interstation Correlation on Regression Analysis, <i>Nicholas C. Matalas and Manuel A. Benson</i> . . . . .	3285
The Frequency Distribution of Near Extremes, <i>L. E. Borgman</i> . . . . .	3295
Reduction of Transpiration, <i>W. J. Roberts</i> . . . . .	3309
Average Antecedent Temperatures as a Factor in Predicting Runoff from Storm Rainfall, <i>Charles D. Hopkins, Jr., and Dale O. Hackett</i> . . . . .	3313
An Improved Statistical Model for Evaluating Parameters Affecting Water Yields of River Basins, <i>B. Harris, A. L. Sharp, A. E. Gibbs, and W. J. Owen</i> . . . . .	3319
Changes in the Levels of Lakes Michigan and Huron, <i>Ivan W. Brunk</i> . . . . .	3329
Some Aspects of the Application of the Theory of Sediment Transportation to Engineering Problems, <i>J. Bogárdi</i> . . . . .	3337
Sediment Transport of Glacier-Fed Streams in Alaska, <i>Whitney M. Borland</i> . . . . .	3347
Variation of Soil Erodibility with Geology, Geographic Zone, Elevation, and Vegetation Type in Northern California Wildlands, <i>J. E. André and H. W. Anderson</i> . . . . .	3351
Evaluating Wells and Aquifers by Analytical Methods, <i>William C. Walton and William H. Walker</i> . . . . .	3359
Cratering Symposium:	
New Evidence for the Impact Origin of the Ries Basin, Bavaria, Germany, <i>E. M. Shoemaker and E. C. T. Chao</i> . . . . .	3371
Analysis of the Formation of Meteor Crater, Arizona: A Preliminary Report, <i>R. L. Bjork</i> . . . . .	3379
High-Explosive Craters in Desert Alluvium, Tuff, and Basalt, <i>B. F. Murphey and L. J. Vortman</i> . . . . .	3389
Throwout Calculations for Explosion Craters, <i>Wilmot N. Hess and M. D. Nordyke</i> . . . . .	3405
Pacific Craters and Scaling Laws, <i>R. B. Vaile, Jr.</i> . . . . .	3413
Nuclear Craters and Preliminary Theory of the Mechanics of Explosive Crater Formation, <i>M. D. Nordyke</i> . . . . .	3439



	PAGE
A Generalized Empirical Analysis of Cratering, <i>Charles E. Violet</i> . . . . .	3461
Experimental Determination of Earthquake Fault Length and Rupture Velocity, <i>Frank Press, Ari Ben-Menahem, and M. Nafi Toksöz</i> . . . . .	3471
SH Motion from Explosions in Soil, <i>C. Kisslinger, E. J. Maleker, Jr., and T. V. McEvilly</i> .	3487
Results of the 1960 Expedition to Krakatau, <i>Robert W. Decker and Djajadi Hadikusumo</i> .	3497
Theoretical Phase Velocities for a Lunar Seismic Experiment, <i>Bruce A. Bolt</i> . . . . .	3513
Record of Cosmic-Ray Intensity in the Meteorites, <i>J. R. Arnold, M. Honda, and D. Lal</i> . .	3519
Cosmic-Ray-Induced Radioactivity in Terrestrial Materials, <i>Rama and Masatake Honda</i> .	3533
Radioactive Species Produced by Cosmic Rays in Bruderheim and Other Stone Meteorites, <i>M. Honda, S. Umemoto, and J. R. Arnold</i> . . . . .	3541
Tritium, Argon 37, and Argon 39 in the Bruderheim Meteorite, <i>E. L. Fireman and J. DeFelice</i> . . . . .	3547
On the Radioactivity of the Bruderheim Chondrite, <i>M. W. Rowe and M. A. Van Dilla</i> . .	3553
The Petrography and Chemical Composition of the Bruderheim Meteorite, <i>Michael Duke, Donald Maynes, and Harrison Brown</i> . . . . .	3557
Abstracts of the Papers Presented at a Symposium on Ground Water, Portland, Oregon, November 16-17, 1960, Sponsored by the Section of Hydrology, American Geophysical Union . . . . .	3565
Geomagnetic and Solar Data, <i>J. Virginia Lincoln</i> . . . . .	3571
Letters to the Editor:	
The Bruderheim Meteorite, <i>H. Baadsgaard, F. A. Campbell, R. E. Folinsbee, and G. L. Cumming</i> . . . . .	3574
Xenon in the Bruderheim Meteorite, <i>W. B. Clarke and H. G. Thode</i> . . . . .	3578
The Sulfur Isotope Abundances in Abee and Bruderheim Meteorites, <i>M. Shima and H. G. Thode</i> . . . . .	3580
Some Trace Element Abundances in the Bruderheim Meteorite, <i>W. D. Ehmann, A. Amiruddin, P. R. Rushbrook, and M. E. Hurst</i> . . . . .	3581
Origin of Excess Xe <sup>129</sup> in Stone Meteorites, <i>P. M. Jeffery and J. H. Reynolds</i> . . .	3582
Cosmic-Ray-Produced V <sup>50</sup> and K <sup>40</sup> in the Iron Meteorite Aroos, <i>Heinz Stauffer and Masatake Honda</i> . . . . .	3584
The Stability of the Interface between the Solar Wind and the Geomagnetic Field, <i>A. J. Dessler</i> . . . . .	3587
Note on Hydromagnetic Propagation and Geomagnetic Field Stability, <i>P. J. Coleman, Jr., and C. P. Sonett</i> . . . . .	3591
The Lifetime of Protons with Energies between 1 Kev and 1 Mev, <i>Harold Liemohn</i> . .	3593
Discussion of the Letter by R. A. Hanel, 'Determination of Cloud Altitude from a Satellite,' <i>G. Yamamoto and D. Q. Wark</i> . . . . .	3596
Evaluation of the Special World Interval Program during the IGY, <i>Martin E. Nason</i> . . . . .	3597
Magnetic Field Micropulsations and Electron Bremsstrahlung, <i>Wallace H. Campbell</i> .	3599
Short-Term Phase Perturbations Observed at 18 Kc/s, <i>C. F. Sechrist and K. D. Felperin</i> . . . . .	3601
Comments on K. Vozoff's Paper, 'Calibration of Pulsation Detector Coils,' <i>James R. Wait</i> . . . . .	3603
Note on the Autocorrelation Coefficient of K <sub>p</sub> and Its Relation to M Regions, <i>W. R. Piggott</i> . . . . .	3604
Author's Comments on the Previous Discussion, <i>Fred Ward</i> . . . . .	3605
The Earth's Free Oscillations Observed on Earth Tide Instruments at Tiefenort, East Germany, <i>W. Buchheim and S. W. Smith</i> . . . . .	3608
Discussion of Paper by John F. Mink, 'Distribution Pattern of Rainfall in the Leeward Koolau Mountains, Oahu, Hawaii,' <i>G. Reynolds</i> . . . . .	3611
Author's Reply to the Preceding Discussion, <i>John F. Mink</i> . . . . .	3612
Evaporation Reduction by Natural Surface Films, <i>James W. Deardorff</i> . . . . .	3613
Discussion of Paper by R. Rangarajan, 'A New Approach to Peak Flow Estimation,' <i>Simeon M. Berman</i> . . . . .	3615
A Note on the Accuracy of Drainage Densities Computed from Topographic Maps, <i>William J. Schneider</i> . . . . .	3617

	PAGE
Reply to Letter by W. J. Schneider, 'A Note on the Accuracy of Drainage Densities Computed from Topographic Maps,' <i>M. Morisawa</i> . . . . .	3619
Discussion of Paper by W. E. Marlatt, A. V. Havens, N. A. Willits, and G. D. Brill, 'A Comparison of Computed and Measured Soil Moisture under Snap Beans,' <i>R. M. Holmes</i> . . . . .	3620
Discussion of Paper by Jacob Bear, 'On the Tensor Form of Dispersion in Porous Media,' <i>G. de Josselin de Jong and M. J. Bossen</i> . . . . .	3623
Moiré Patterns of the Membrane Analogy for Ground-Water Movement Applied to Multiple Fluid Flow, <i>G. de Josselin de Jong</i> . . . . .	3625
Corrigendum: <i>G. de Josselin de Jong</i> . . . . .	3629

## VOLUME 66, NO. 11, NOVEMBER 1961

Formation of the Geomagnetic Storm Main-Phase Ring Current, <i>A. J. Dessler, W. B. Hanson, and E. N. Parker</i> . . . . .	3631
Spectrum of Hydromagnetic Waves in the Exosphere, <i>Gordon J. F. MacDonald</i> . . . .	3639
Spatial Distribution of Electrons from Neutron Decay in the Outer Radiation Belt, <i>W. N. Hess and J. Killeen</i> . . . . .	3671
Coordinates for Mapping the Distribution of Magnetically Trapped Particles, <i>Carl E. McIlwain</i> . . . . .	3681
A Theoretical Model of Temperature Variations at the Surface of an Orbiting Satellite, <i>Heinz H. Lettau</i> . . . . .	3693
Propagation Characteristics of Whistlers Trapped in Field-Aligned Columns of Enhanced Ionization, <i>R. L. Smith</i> . . . . .	3699
Properties of the Outer Ionosphere Deduced from Nose Whistlers, <i>R. L. Smith</i> . . . .	3709
Concerning Radiosondes, Lag Constants, and Radio Refractive Index Profiles, <i>B. R. Bean and E. J. Dutton</i> . . . . .	3717
The Solar Semidiurnal Atmospheric Oscillation, <i>K. A. Small and S. T. Butler</i> . . . .	3723
Traveling Pressure Waves Associated with Geomagnetic Activity, <i>Peter Chrzanowski, Gary Greene, K. T. Lemmon, and J. M. Young</i> . . . . .	3727
Measurements of Current Density in the Fair Weather Atmosphere, <i>J. H. Kraakevik</i> . .	3735
Atmospheric Emission and Opacity at Millimeter Wavelengths Due to Oxygen, <i>M. L. Meeks</i> . . . . .	3749
Chemical Composition of Rain Water in Kampala, Uganda, and Its Relation to Meteorological and Topographical Conditions, <i>Simon Visser</i> . . . . .	3759
Tritium Geophysics, <i>W. F. Libby</i> . . . . .	3767
Stability of Ice-Age Ice Sheets, <i>J. Weertman</i> . . . . .	3783
Depth to Sources of Magnetic Anomalies, <i>Leroy R. Alldredge and Gerald D. Van Voorhis</i> . .	3793
Effects of Moderate Stresses on Directions of Thermoremanent Magnetization, <i>John W. Kern</i> . . . . .	3801
The Effect of Stress on the Susceptibility and Magnetization of a Partially Magnetized Multidomain System, <i>John W. Kern</i> . . . . .	3807
Stress Stability of Remanent Magnetization, <i>John W. Kern</i> . . . . .	3817
Observations of Internal Waves near Hudson Canyon, <i>Roy D. Gaul</i> . . . . .	3821
Periodicity of Earthquakes and the Invariance of the Gravitational Constant, <i>W. J. Morgan, J. O. Stoner, and R. H. Dicke</i> . . . . .	3831
Some Characteristics of Surface Gravity Waves in the Sea Produced by Nuclear Explosions, <i>Wm. G. Van Dorn</i> . . . . .	3845
A Telemetering Ocean-Bottom Seismograph, <i>John Ewing and Maurice Ewing</i> . . . . .	3863
An Evaluation of a Signal-Summing Technique for Improving the Signal-to-Noise Ratios for Seismic Events, <i>L. H. Koopmans</i> . . . . .	3879
Free Oscillations of the Moon, <i>H. Takeuchi, M. Kato, and N. Kobayashi</i> . . . . .	3895
Refraction Arrivals along a Thin Elastic Plate Surrounded by a Fluid Medium, <i>J. H. Rosenbaum</i> . . . . .	3899
Energy Requirements in Terrestrial Expansion, <i>Melvin A. Cook and A. J. Eardley</i> . . .	3907
Permeability Measurements of Rock Salt, <i>Earnest F. Gloyne and Tom D. Reynolds</i> . . .	3913

The System $\text{NaAlSi}_3\text{O}_8\text{-H}_2\text{O-Argon}$ : Total Pressure and Water Pressure in Metamorphism, <i>H. J. Greenwood</i> . . . . .	3923
Geomagnetic and Solar Data, <i>J. Virginia Lincoln</i> . . . . .	3947
Letters to the Editor:	
The Primary Cosmic-Ray Electron Flux during a Forbush-Type Decrease, <i>Peter Meyer and Rochus Vogt</i> . . . . .	3950
Geomagnetic Activity and the Reception of Whistlers in Polar Regions, <i>G. McK. Allcock and M. F. Rodgers</i> . . . . .	3953
Discussion of Paper by John R. Spreiter and Benjamin R. Briggs on 'Theory of Electrostatic Fields in the Ionosphere at Polar and Middle Geomagnetic Latitudes,' <i>D. T. Farley, Jr.</i> . . . . .	3956
Increase of Ionization Associated with Geomagnetic Sudden Commencements, <i>S. Matsushita</i> . . . . .	3958
Two Methods of Detecting Ionospheric Disturbances, <i>G. A. M. King and M. D. Lawden</i> . . . . .	3962
Note on 'Vertically Traveling Shock Waves in the Ionosphere,' <i>Fred B. Daniels and Arthur K. Harris</i> . . . . .	3964
Discussion of Incoherent Backscatter Power Measurements at 440 Mc/s, <i>V. C. Pineo and H. W. Briscoe</i> . . . . .	3965
Artificial Initiation of Lightning Discharges, <i>M. Brook, G. Armstrong, R. P. H. Winder, B. Vonnegut, and C. B. Moore</i> . . . . .	3967
Interplanetary Dust Particles of Micron Size Probably Associated with the Leonid Meteor Stream, <i>W. M. Alexander, C. W. McCracken, and H. E. LaGow</i> . . . . .	3970
Some Micrometeorological Measurements in Ocean Fog, <i>Francis M. Wiener, Jay H. Ball, and Creighton M. Gogos</i> . . . . .	3974
Reply to Dr. Harold C. Urey's Criticism of the Paper by Brian Mason, 'The Origin of Meteorites,' <i>Brian Mason</i> . . . . .	3979
A Note on the Thermodynamic Theory of Nonhydrostatically Stressed Solids, <i>Mineo Kumazawa</i> . . . . .	3981
Author's Reply to Discussions of the Paper 'The Thermodynamic Theory of Nonhydrostatically Stressed Solids,' <i>W. Barclay Kamb</i> . . . . .	3985
Corrigendum: <i>Manik Talwani, J. Lamar Worzel, and Maurice Ewing</i> . . . . .	3989

VOLUME 66, NO. 12, DECEMBER 1961

Cosmic-Ray Evidence for a Ring Current, <i>P. J. Kellogg and J. R. Winckler</i> . . . . .	3991
Observations of the Van Allen Radiation Regions during August and September 1959: 2, The Capetown Anomaly and the Shape of the Outer Belt, <i>Robert A. Hoffman</i> . . . . .	4003
Cosmic-Ray Knee in 1958, <i>H. V. Neher</i> . . . . .	4007
The Magnetic Field of a Model Radiation Belt, Numerically Computed, <i>Syuh-Ichi Akasofu, Joseph C. Cain, and Sydney Chapman</i> . . . . .	4013
Geomagnetically Trapped Electrons from Cosmic-Ray Albedo Neutrons, <i>A. M. Lenchek, S. F. Singer, and R. C. Wentworth</i> . . . . .	4027
Solar Proton Impact Zones, <i>Thomas Kelsall</i> . . . . .	4047
A Study of the Enhanced Ionization Produced by Solar Protons during a Polar Cap Absorption Event, <i>G. C. Reid</i> . . . . .	4071
Evidence of Low-Frequency Hydromagnetic Waves in the Exosphere, <i>Masahisa Sugiura</i> . . . . .	4087
Hydromagnetic Interpretation of Sudden Commencements of Magnetic Storms, <i>Charles R. Wilson and Masahisa Sugiura</i> . . . . .	4097
Ionospheric Limitations on Attainable Satellite Potential, <i>David B. Beard and Francis S. Johnson</i> . . . . .	4113
Effects of the Earth's Magnetic Field on the Orbit of a Charged Satellite, <i>I. I. Shapiro and H. M. Jones</i> . . . . .	4123
A 'Layered' Exponential Model of Radar Refractivity, <i>F. L. Martin and C. G. Waldron</i> . . . . .	4129
Polar Ionospheric Spread Echoes and Radio-Frequency Properties of Ice Shelves, <i>S. Evans</i> . . . . .	4137
Solar Activity Effect and Diurnal Variation in the Upper Atmosphere, <i>W. Priestler</i> . . . . .	4143



	PAGE
The Seasonal Anomalies in the <i>F</i> Region, <i>G. A. M. King</i> . . . . .	4149
Ionospheric Currents Responsible for Sudden Commencements Observed at the Geomagnetic Equator, <i>Tadanori Ondoh</i> . . . . .	4155
A Metastable Helium Magnetometer for Observing Small Geomagnetic Fluctuations, <i>A. R. Keyser, J. A. Rice, and L. D. Schearer</i> . . . . .	4163
The Effects of Atmospheric Refraction on Angles Measured from a Satellite, <i>A. C. Holland</i> . . . . .	4171
Numerical Errors in the Time Integration of Advective Processes, <i>Joseph B. Knox</i> . . . . .	4177
Further Evidence of Hysteresis as a Factor in the Evaporation from Soils, <i>Larry G. King and Richard A. Schleusener</i> . . . . .	4187
Neutron Measurement of Surface Soil Moisture, <i>C. H. M. van Bavel</i> . . . . .	4193
An Evaluation of Uranium as a Tool for Studying the Hydrogeochemistry of the Truckee Meadows Area, Nevada, <i>Philip Cohen</i> . . . . .	4199
Laminar Flow in Rough Rectangular Channels, <i>Dah-Cheng Woo and Ernest F. Brater</i> . . . . .	4207
A Partial Duration Series for Low-Flow Analyses, <i>John B. Stall and James C. Neill</i> . . . . .	4219
Local Scour in Rivers, <i>L. J. Tison</i> . . . . .	4227
The Relation between the Frequency Distributions of Sieve Diameters and Fall Velocities of Sediment Particles, <i>John F. Kennedy and Robert C. Y. Koh</i> . . . . .	4233
Head and Flow of Ground Water of Variable Density, <i>Norbert J. Lusczynski</i> . . . . .	4247
On the Theory of Leaky Aquifers, <i>Roger J. M. De Wiest</i> . . . . .	4257
A New Borehole Thermometer, <i>Ronald Doig, V. A. Saull, and R. A. Butler</i> . . . . .	4263
Gravity Anomalies in the Central Sierra Nevada, California, <i>H. W. Oliver, L. C. Pakiser, and M. F. Kane</i> . . . . .	4265
Depth and Spacing of Tension Cracks, <i>Arthur H. Lachenbruch</i> . . . . .	4273
Electrostatic Erosion Mechanisms on the Moon, <i>P. D. Grannis</i> . . . . .	4293
Geomagnetic and Solar Data, <i>J. Virginia Lincoln</i> . . . . .	4301
Letters to the Editor:	
Radar Reflections from the Sun at Very High Frequencies, <i>W. G. Abel, J. H. Chisholm, P. L. Fleck, and J. C. James</i> . . . . .	4303
Bursts of Centimeter-Wave Emission and the Region of Origin of X Rays from Solar Flares, <i>M. R. Kundu</i> . . . . .	4308
Electron Temperature Measurements on the Explorer VIII Satellite, <i>G. P. Serbu, R. E. Bourdeau, and J. L. Donley</i> . . . . .	4313
Minor PCA Events during March 1958, <i>G. F. Rourke</i> . . . . .	4316
Horizontal Intensity Comparisons between the Sine Galvanometer and the Proton Vector Magnetometer, <i>J. L. Bottum, R. E. Gebhardt, and J. B. Townshend</i> . . . . .	4319
Discussion of Paper by N. D. Opdyke, 'The Paleomagnetism of the New Jersey Triassic: A Field Study of the Inclination Error in Red Sediments,' <i>D. H. Griffiths and R. F. King</i> . . . . .	4320
An Additional Measurement of the Tritium Content of Atmospheric Hydrogen of 1949, <i>E. L. Fireman and F. S. Rowland</i> . . . . .	4321
The Myers Formula and Myers Rating Compared with Actual Floods, <i>G. G. Commons</i> . . . . .	4322
Discussion of Paper by Ivan W. Brunk, 'Changes in the Levels of Lakes Michigan and Huron,' <i>Harley F. Lawhead</i> . . . . .	4324
Author's Reply to the Preceding Discussion, <i>Ivan W. Brunk</i> . . . . .	4330
Comments on Paper by V. V. Beloussov, 'The Origin of Folding in the Earth's Crust,' <i>Earl M. P. Lovejoy</i> . . . . .	4332
Author's Reply to the Preceding Discussion, <i>V. V. Beloussov</i> . . . . .	4334
Corrigendum: <i>Michele Caputo</i> . . . . .	4335





## Index of Names

*Journal of Geophysical Research, Volume 66**January–December 1961**Note. (a) indicates abstract; (l) indicates letter to the editor; (c) indicates corrigendum*

- Abel, W. G., 4303  
 Ackermann, William C., 1547(a)  
 Acton, Loren W., 3060(l)  
 Adams, John A. S., 2509(a)  
 Adams, Wm. Mansfield, 903, 2509(a)  
 Ahmed, S. J., 3213  
 Ainsworth, J. E., 3191  
 Ajwani, H. J., 1996(l)  
 Akasofu, Syun-Ichi, 1321, 4013  
 Albee, A. L., 2565(a)  
 Albers, H. W., 2509(a)  
 Alexander, W. M., 3970(l)  
 Allcock, G. McK., 3953(l)  
 Alldredge, Leroy R., 3793  
 Allen, Lew, Jr., 1627  
 Allsopp, H. L., 1499  
 Alpert, Leo, 332(l)  
 Alsop, Leonard E., 631, 2911  
 Amiruddin, A., 3581(l)  
 Amstutz, G. C., 2554(a), 2568(a)  
 Anders, Edward, 889, 3075(l)  
 Anderson, Don L., 2953  
 Anderson, H. W., 2510(a), 3351  
 Anderson, Keith E., 1547(a)  
 Anderson, R. Ernest, 2509(a), 2533(a)  
 André, J. E., 2510(a), 3351  
 Andre, Milo J., 2510(a)  
 Angell, J. K., 2510(a)  
 Apel, J. R., 2510(a)  
 Armstrong, A. H., 351  
 Armstrong, G., 3967(l)  
 Arnold, J. R., 1551(a), 3519, 3541  
 Arrhenius, Gustav, 2511(a)  
 Asplund, Stanley E., 1157  
 Athay, R. Grant, 385  
 Auberger, Michel, 191  
 Austin, Carl F., 2561(a)  
 Austin, George B., 2511(a)  
 Baadsgaard, H., 2518(a), 3574(l)  
 Backus, George, 2511(a)  
 Bain, Walter F., 3065(l)  
 Baker, D. R., 2550(a)  
 Ball, Jay H., 3974(l)  
 Bandeen, W. R., 3169  
 Banks, Harvey O., 1551(a)  
 Banks, M. R., 1935  
 Barnes, Cecil, Jr., 2589(l)  
 Barnes, H. L., 2511(a)  
 Barth, Charles A., 985(l), 1551(a), 2511(a)  
 Bassett, William A., 2512(a)  
 Basso S., Eduardo, 1998(l)  
 Bates, Howard F., 447  
 Bâth, Markus, 1913  
 Battan, Louis J., 3255  
 Bauer, S. J., 3055(l)  
 Bayrock, L. A., 2529(a)  
 Bean, B. R., 328(l), 1551(a), 3717  
 Bear, Jacob, 1185, 2455  
 Beard, David B., 1552(a), 4113  
 Beard, Leo R., 1306(l)  
 Beck, A. E., 1485  
 Bédient, Harold A., 2512(a)  
 Bedinger, M. S., 2423, 2554(a)  
 Behrendt, John C., 2512(a), 2512(a)  
 Belousov, V. V., 2241, 4334  
 Bender, Donald L., 521, 1547(a)  
 Benioff, Hugo, 605, 2895  
 Ben-Menahem, Ari, 2512(a), 2553(a), 3471  
 Benson, Manuel A., 3285  
 Bentley, Charles R., 1301(l)  
 Benz, Leo C., 2435, 2513(a)  
 Berg, Joseph W., Jr., 599, 1255, 2513(a)  
 Berkofsky, Louis, 2513(a)  
 Berman, Simeon M., 3615(l)  
 Berry, Fred A. F., 3565(a)  
 Bhavsar, P. D., 679, 995, 2274(c), 2513(a)  
 Bhonsle, R. V., 2763  
 Birch, Francis, 2199  
 Biswas, S., 1029, 2529(a), 2653  
 Bjork, R. L., 3379  
 Black, R. A., 2554(a)  
 Blaik, Maurice, 2514(a), 2550(a)  
 Blamont, J. E., 1407  
 Blanchard, Duncan C., 2514(a)  
 Blaney, Harry F., 1552(a)  
 Blattner, D. J., 1745  
 Bleichrodt, J. F., 135, 2183  
 Blok, Joh., 135, 2183  
 Bloomsburg, George L., 1547(a)  
 Bogárdi, J., 2514(a), 3337  
 Bogert, B. P., 643(l)  
 Bollhagen, Heins, 2561(a)  
 Bolt, Bruce A., 2514(a), 2965, 3513  
 Bond, F. R., 327(l)  
 Bonini, W. E., 2547(a)  
 Booker, Henry G., 1073  
 Books, Kenneth G., 2571(a)  
 Borgman, L. E., 1552(a), 3295  
 Borland, Whitney M., 3347  
 Bossen, M. J., 3623(l)  
 Bostick, F. X., Jr., 879, 2515(a)  
 Bottum, J. L., 4319  
 Bourdeau, R. E., 4313  
 Bowles, Kenneth L., 1081  
 Brater, Ernest D., 2570(a), 4207  
 Briggs, Benjamin R., 1731, 2345, 2563(a)  
 Brill, G. D., 535  
 Brinton, H. C., 2587(l)  
 Briscoe, H. W., 3965(l)  
 Broecker, Wallace, 2515(a)  
 Brook, M., 2515(a), 2542(a), 3967(l)  
 Brown, Harrison, 1316(l), 1598(l), 3033, 3557  
 Brown, John A., Jr., 2515(a)  
 Brown, R. M., 2515(a)  
 Brown, R. R., 1035, 1379, 2516(a), 2516(a)  
 Brune, James N., 2516(a), 2543(a), 2895  
 Brunk, Ivan W., 3329, 4330  
 Brush, Lucien M., Jr., 2517(a)  
 Bryant, R., 3066(l)  
 Buchanan, C. L., 2517(a)  
 Buchheim, W., 3608(l)  
 Buettner, K. J. K., 2517(a)  
 Bugnolo, D. S., 1590(l)  
 Bull, William B., 1552(a)  
 Buneman, O., 1978(l)  
 Buras, Nathan, 517  
 Burkard, O., 3058(l)  
 Bushnell, R. H., 2843  
 Businger, J. A., 1318(l), 2405  
 Butler, R. A., 4263

*J. Geophys. Research* 66 (1), 1–342; (2), 343–664; (3), 665–994; (4), 995–1320; (5), 1321–1602; (6), 1603–2002; (7), 2003–2274; (8), 2275–2606; (9), 2607–3082; (10), 3083–3630; (11), 3631–3990; (12), 3991–4362.

- Butler, S. T., 3723  
 Byatt, W. J., 1793  
 Byram, E. T., 2095  
  
 Cahoon, B. A., 328(l)  
 Cain, Joseph C., 2677, 4013  
 Calvert, Wynne, 3125  
 Cameron, A. G. W., 2517(a)  
 Cameron, Winifred Sawtelle, 2551(a)  
 Camnitz, H., 2555(a), 2703  
 Campbell, F. A., 2518(a), 3574(l)  
 Campbell, Wallace H., 25, 41, 2518(a), 3599(l)  
 Campbell, William J., 813  
 Canfield, E. H., 665, 2665  
 Caputo, Michele, 1479, 4335(c)  
 Carlson, Carl W., 2435, 2513(a)  
 Carlston, C. W., 2518(a)  
 Carmichael, H., 1363, 2518(a)  
 Carpenter, D. L., 2582(l)  
 Carpenter, James H., 2518(a)  
 Carr, T. D., 2561(a)  
 Carr, Thomas R., 2141  
 Carron, Maxwell K., 2520(a)  
 Carter, N. L., 2518(a)  
 Casaverde, M., 323(l)  
 Chadwick, W. B., 2519(a)  
 Chagnon, Charles W., 2540(a)  
 Chang, David B. J., 2524(a)  
 Channapragada, Rao, 1199  
 Chao, E. C. T., 3371  
 Chapman, Sydney, 1321, 2519(a), 4013  
 Chappleear, J. E., 501, 2519(a)  
 Charney, J. G., 83  
 Chase, L. F., Jr., 2297  
 Chatterjee, J. S., 1535  
 Chatterton, N. E., 2561(a)  
 Chayes, Felix, 2274(c)  
 Chernosky, Edwin J., 2519(a)  
 Chew, Frank, 2445, 2520(a), 2520(a)  
 Chilton, Charles J., 379  
 Chisholm, J. H., 4303  
 Christie, J. M., 2518(a)  
 Chrzanowski, Peter, 3727  
 Chubb, Talbot A., 1552(a), 2095  
 Cladis, J. B., 343, 1553(a), 2297  
 Clark, John F., 2520(a)  
 Clark, Sydney P., Jr., 1231  
 Clarke, W. B., 3578(l)  
 Clarke, Roy S., Jr., 2520(a)  
 Cobb, James C., 2521(a)  
 Cobb, William E., 2552(a)  
 Cochrane, John D., 2521(a)  
 Cohen, Alvin J., 2521(a), 2521(a)  
 Cohen, Marshall H., 411, 2606(c)  
 Cohen, Philip, 4199  
 Cohen, Robert, 1081, 3125, 3141  
 Colaw, K. S., 2569(a)  
  
 Cole, Allen E., 2773  
 Cole, K. D., 327(l), 1584(l), 3064(l)  
 Coleman, Paul J., Jr., 1351, 1559(a), 2043, 2521(a), 2540(a), 2541(a), 3591(l)  
 Commons, G. G., 4322  
 Conda, Alyce M., 1725  
 Convit, R., 2522(a)  
 Conway, R., 1547(a)  
 Cook, Kenneth L., 599, 1255, 2513(a), 2522(a)  
 Cook, Melvin A., 3907  
 Cooper, H. H., Jr., 2522(a)  
 Cornish, John H., 1845  
 Cotten, Donald E., 2522(a)  
 Court, Arnold, 1823  
 Cox, C. S., 1553(a)  
 Craig, H., 2537(a)  
 Crain, Cullen M., 35, 1117  
 Cram, Ira H., Jr., 2523(a)  
 Crary, A. P., 871  
 Crockett, James H., 2523(a)  
 Crockett, Curtis W., 2542(a)  
 Croft, A. R., 1553(a), 2523(a)  
 Croft, T. A., 3109  
 Crozier, W. D., 2793  
 Cummack, C. H., 1685, 2751  
 Cumming, G. L., 3574(l)  
  
 Danes, Z. F., 2523(a), 2523(a)  
 Daniels, Fred B., 1781, 3964(l)  
 D'Arcy, R. G., 2516(a)  
 Daughtry, A. C., 2524(a)  
 Davis, G. L., 2524(a)  
 Davis, Leverett, Jr., 2043, 2521(a), 2524(a)  
 Deardorff, James W., 529, 3613(l)  
 De Bremaecker, J. Cl., 2524(a)  
 Decker, Fred W., 1548(a)  
 Decker, Robert W., 3497  
 DeFelice, J., 2528(a), 3547  
 Degaonkar, S. S., 2763  
 Dehlinger, Peter, 2540(a)  
 de Josselin de Jong, G., 3623(l), 3625(l), 3629(c)  
 Dekker, R. H., 135  
 Denholm, J. V., 2105  
 Dessler, A. J., 343, 1553(a), 2289, 2525(a), 3587(l), 3631  
 Deuser, W. G., 2525(a)  
 DeVault, G. P., 1793  
 De Wiest, J. M., 4257  
 Dicke, R. H., 3831  
 Dickson, F. W., 2525(a)  
 Diment, W. H., 201  
 Dinger, J. E., 1437  
 Dix, C. H., 227, 235, 2945  
 Doe, Bruce R., 2525(a)  
 Doig, Ronald, 4263  
 Donahue, T. M., 1407  
  
 Donley, J. L., 4313  
 Donoho, Paul, 2524(a)  
 Doolittle, Robert F., 2525(a)  
 Dorman, James, 215, 2514(a), 2965  
 Dotson, W. A., 2569(a)  
 Dowden, R. L., 1587(l)  
 Dowling, George B., 2526(a)  
 Dragoun, Frank J., 2526(a)  
 Dragt, A. J., 1641, 2526(a)  
 Drazin, P. G., 83  
 Drennan, K. L., 2520(a)  
 Droessler, Earl G., 2526(a)  
 Dubin, Maurice, 2592(l)  
 Dueño, Braulio, 2355  
 Duggal, S. P., 1970(l)  
 Duke, Michael, 3557  
 Duncan, Don L., 1548(a)  
 Duncan, R. A., 1319(c), 2087  
 Dungey, J. W., 1043  
 Dutton, E. J., 3717  
 Dwarkin, Martin L., 411, 2606(c)  
 Dyce, R. B., 1069  
  
 Eardley, A. J., 3907  
 Earl, James A., 3095  
 Eber, L. E., 839  
 Ehmann, W. D., 3581(l)  
 Einstein, H. A., 2526(a)  
 Ellis, G. R. A., 19  
 Ellyett, C., 2337, 2590(l)  
 Elwert, G., 391  
 Epstein, Samuel, 2565(a)  
 Erickson, W. C., 1773  
 Ernst, W. G., 2511(a)  
 Eschner, A. R., 2555(a)  
 Evans, S., 4137  
 Ewing, John I., 2526(a), 2917, 3863  
 Ewing, Maurice, 631, 1265, 2516(a), 2564(a), 2895, 2911, 3863, 3989(c)  
  
 Fabiano, E. B., 2053  
 Fairbairn, H. W., 2538(a)  
 Fairbridge, Rhodes W., 2527(a)  
 Fan, C. Y., 2313, 2527(a), 2607  
 Fannin, B. M., 1049  
 Fara, H. D., 3279  
 Farley, D. T., Jr., 3956(l)  
 Farley, Thomas A., 2013  
 Farquhar, R. M., 2527(a)  
 Faure, G., 2527(a)  
 Felperin, K. D., 3601(l)  
 Fichtel, C. E., 2527(a)  
 Fiebig, R., 2262(l)  
 Field, Edward C., 2737  
 Field, George B., 1395  
 Fife, Paul, 163  
 Finger, Frederick G., 2532(a)

- Fireman, E. L., 2528(a), 3547, 4321  
 Fischer, Irene, 2528(a)  
 Fishel, V. C., 3565(a)  
 Fisher, David E., 1509  
 Fisher, Joel E., 2528(a)  
 Fitch, John L., 2552(a)  
 Flanders, P. L., 903  
 Fleck, P. L., 4303  
 Fleisher, Aaron, 2271(l)  
 Fletcher, J. E., 28(a)  
 Flinn, E. A., 2528(a)  
 Flood, W., 2555(a), 2703  
 Folinsbee, R. E., 2529(a), 3574(l)  
 Forbush, S. E., 2275, 2529(a)  
 Forsyth, P. A., 2315  
 Fournier, R. O., 2548(a)  
 Fox, D. F., 3191  
 Franceschini, Guy A., 2529(a)  
 Franzini, Joseph B., 1553(a), 2529(a)  
 Freden, Stanley C., 1554(a)  
 Freier, George D., 2529(a), 2695  
 Freier, Phyllis S., 1029, 2529(a)  
 Friedman, H., 2095  
 Friedman, Irving, 1861, 2530(a), 2530(a)  
 Friedman, Melvin, 2530(a)  
 Fritz, Sigmund, 2530(a), 2530(a), 2543(a), 2559(a), 2570(a)  
 Fry, John C., 589  
 Fukushima, Naoshi, 2530(a), 2530(a)  
 Fulton, B. J., 2321  
 Galejs, Janis, 2787  
 Gardner, Walter H., 3565(a)  
 Garland, G. D., 2495  
 Gaul, Roy D., 2531(a), 3821  
 Gebhardt, R. E., 4319  
 Ghielmetti, H. S., 1611  
 Gibbs, A. E., 2532(a), 2559(a), 3319  
 Giddings, J. C., 181  
 Gilbert, Freeman, 2511(a), 2531(a), 2531(a)  
 Ginsberg, L. H., 1745  
 Gloyna, Earnest F., 2555(a), 3913  
 Gogos, Creighton M., 3974(l)  
 Gold, Thomas, 2531(a), 2531(a)  
 Goldberg, Edward D., 2552(a), 2554(a)  
 Goldberg, Philip A., 2531(a)  
 Goldsmith, Julian R., 2531(a)  
 Goles, Gordon G., 889, 3075(l)  
 Gordon, L. I., 2537(a)  
 Graf, Anton, 1813  
 Graf, Donald L., 2531(a)  
 Graham, Martin, 2524(a)  
 Grannis, P. D., 4293  
 Graves, Carl D., 2525(a)  
 Gray, Don M., 1215  
 Green, J., 2568(a)  
 Greene, Gary, 3727  
 Greenwood, H. J., 3923  
 Gregory, John B., 429, 2575(l)  
 Griffiths, D. H., 4320  
 Griggs, D. T., 237, 2518(a)  
 Groen, P., 3072(l)  
 Gurtler, C. A., 3050(l)  
 Guss, D. E., 2527(a)  
 Gutnick, Murray, 2867  
 Hackett, Dale O., 3313  
 Hadikusumo, Djajadi, 3497  
 Hagfors, Tor, 777, 1699  
 Hale, Leslie C., 1554(a)  
 Halim, A., 3213  
 Hall, R. G., 2546(a)  
 Hall, Warren A., 517  
 Hamlin, D. A., 1, 2001(c)  
 Hanel, Rudolf A., 1300(l), 2532(a), 3169  
 Hanson, W. B., 1425, 1554(a), 1667, 3631  
 Hantush, Mahdi S., 340(c), 1310(l), 1319(c), 2532(a)  
 Harris, Arthur K., 3964(l)  
 Harris, B., 2532(a), 3319  
 Harris, Joseph, 1861  
 Harris, Miles F., 2532(a)  
 Harrison, A. E., 649(l)  
 Harrison, F. B., 351  
 Harrison, J. C., 621  
 Hart, Stanley R., 2533(a), 2995  
 Hartz, T. R., 1035, 2516(a)  
 Haskell, Norman A., 2937  
 Haurwitz, Bernhard, 2381, 2533(a)  
 Havard, Jesse B., 2533(a)  
 Havens, A. V., 535  
 Hays, Walter, 2509(a), 2533(a)  
 Heald, E. F., 2534(a)  
 Heard, Hugh C., 2534(a)  
 Heckman, H. H., 351  
 Hedge, Carl E., 2534(a)  
 Heezen, Bruce C., 2565(a)  
 Heiskanen, W. A., 1993(l), 2535(a)  
 Helliwell, R. A., 664(c), 2274(c)  
 Hemley, J. J., 2548(a)  
 Henriksen, S. W., 2535(a)  
 Henry, Harold R., 2535(a)  
 Henry, Robert M., 2567(a), 2849  
 Heppner, J. P., 2549(a), 2677  
 Herbst, Roland F., 959  
 Herman, Benjamin M., 3255  
 Herman, John R., 3163  
 Herrin, Eugene, 334(l)  
 Herring, J., 1980(l)  
 Hershfield, D. M., 1308(l)  
 Herzog, L. F., 2525(a)  
 Hess, Wilmot N., 665, 2313, 2665, 3405, 3671  
 Hesstvedt, Eigil, 1985(l)  
 Heymann, D., 2535(a)  
 Hibbs, A. R., 371, 1554(a), 2003, 2595(l)  
 Hildebrandt, A. F., 985(l)  
 Hill, G. E., 2329  
 Hinteregger, H. E., 2367  
 Hirvonen, R. A., 1471  
 Hirschfeld, Walter, 2537(a)  
 Hoecker, Walter H., Jr., 2536(a)  
 Hoffer, Abraham, 2600(l)  
 Hoffer, Thomas E., 2536(a)  
 Hoffman, Robert A., 4003  
 Hofmann, Walter, 1555(a)  
 Holland, A. C., 2536(a), 4171  
 Holland, Heinrich D., 2536(a)  
 Holland, Joshua Z., 2536(a)  
 Holly, Francis E., 1627  
 Holmes, R. M., 3620(l)  
 Holzer, R. E., 2536(a)  
 Honda, Masatake, 3227, 3519, 3533, 3541, 3584(l)  
 Hood, Donald W., 2550(a)  
 Hood, Peter J., 1235  
 Hope, E. R., 747  
 Hopkins, Charles D., Jr., 3313  
 Hopkins, George, Jr., 2536(a)  
 Hopkins, Walt, 1555(a)  
 Horibe, Y., 2537(a)  
 Houghton, Henry G., 2537(a)  
 Houghton, J. T., 2537(a)  
 Howell, B. F., Jr., 2601(l)  
 Hsia, Emil C., 1555(a)  
 Hubach, Richard A., 321(l)  
 Hubert, Lester F., 797  
 Hubert, William E., 2141  
 Hughes, H., 2538(a)  
 Hughes, M. P., 651(l)  
 Hume, James D., 2558(a)  
 Hunt, D. C., 1555(a), 1673  
 Hurley, James, 2537(a)  
 Hurley, P. M., 2527(a), 2538(a)  
 Hurst, M. E., 3581(l)  
 Hurwitz, Louis, 2538(a)  
 Hutchings, J. W., 131  
 Hutchinson, R., 2687  
 Imhof, W. L., 2297  
 Innes, M. J. S., 2225  
 Irvine, T. N., 2538(a)  
 Irving, E., 549, 1927, 1935  
 Isbell, A. F., 2550(a)  
 Iyer, H. M., 2538(a)  
 Izsak, Imre G., 2538(a)  
 Jacka, F., 1584(l)  
 Jackson, J. E., 3055(l)  
 Jaeger, J. C., 563  
 James, J. C., 4303  
 Jamison, V. C., 1855  
 Jaye, W. E., 1069



- Jeffery, P. M., 3582(l)  
 Jensen, Clayton E., 1145  
 Jöhler, J. R., 3233  
 Johns, Roman K. C., 2539(a)  
 Johnson, Bruce M., Jr., 1548(a), 2539(a)  
 Johnson, David S., 2539(a)  
 Johnson, Francis S., 1555(a), 2539(a), 4113  
 Johnson, H. M., 2539(a)  
 Johnson, Richard G., 1627  
 Johnston, H. Freeborn, 2539(a)  
 Joint Scientific Advisory Group to the Meteorological Rocket Network, 2821  
 Jones, B. L., 1135  
 Jones, Frank C., 2029  
 Jones, H. M., 4123  
 Jones, Paul H., 3566(a)  
 Joyner, Gerald L., 2540(a)  
 Judge, Darrell L., 2540(a), 2562(a)  
 Julian, Paul R., 2540(a)  
 Junge, Christian E., 2163, 2540(a)
- Kallmann-Bijl, H. K., 787  
 Kamb, W. Barclay, 259, 3985(l)  
 Kammerer, Wayne J., 1312(l)  
 Kanasewich, E. R., 2495  
 Kane, M. F., 4265  
 Kaneda, Eisuke, 2259(l)  
 Kao, S.-K., 2540(a)  
 Karplus, Robert, 1, 2001(c), 2289, 2525(a)  
 Kaufman, W. J., 2544(a)  
 Kaula, W. M., 1799  
 Kawano, Minoru, 2540(a), 2570(a)  
 Keay, C. S. L., 2337, 2590(l)  
 Kellogg, P. J., 3991  
 Kelsall, Thomas, 4047  
 Kelso, John M., 1107, 2541(a)  
 Kennedy, George C., 1491  
 Kennedy, John F., 4233  
 Keppel, R. V., 2541(a)  
 Kern, John W., 713, 989(l), 1290(l), 2541(a), 3801, 3807, 3817  
 Kerr, Paul F., 2512(a)  
 Kessler, Edwin, III, 2541(a)  
 Keyser, A. R., 4163  
 Killeen, J., 2313, 3671  
 King, G. A. M., 2757, 3962(l), 4149  
 King, Larry G., 4187  
 King, R. F., 4320  
 Kinsman, Blair, 2411, 2542(a)  
 Kirkham, Don, 509  
 Kirkpatrick, G. W., 1548(a)  
 Kisslinger, C., 2542(a), 3487  
 Kitagawa, N. 2515(a), 2542(a)  
 Klein, William H., 2542(a)  
 Knapp, David G., 2053
- Knauss, John A., 143  
 Knecht, D. J., 2297  
 Knecht, Robert W., 3078(l), 3187  
 Kniffen, D. A., 2542(a)  
 Knoerr, Kenneth R., 1556(a), 2543(a)  
 Knox, Joseph B., 4177  
 Knudsen, W. C., 1556(a)  
 Kobayakawa, M., 2537(a)  
 Kobayashi, N., 3895  
 Koh, C. Y., 4233  
 Kohler, Max A., 1308(l), 1994(l)  
 Kohout, F. A., 2429, 2543(a)  
 Koide, M., 2554(a)  
 Kollar, F., 1495  
 Koopmans, L. H., 3879  
 Kovach, Robert, 215, 3073(l)  
 Kozai, Yoshihide, 2538(a)  
 Kraakevik, J. H., 3735  
 Krammes, S. J., 1556(a)  
 Krebs, Oswald A., Jr., 2527(a)  
 Krone, R. B., 2526(a)  
 Krueger, A. F., Jr., 2543(a)  
 Krueger, Arlin J., 1751, 2567(a), 3082(c)  
 Kuhn, P. M., 1318(l)  
 Kumazawa, Mineo, 3981(l)  
 Kundu, M. R., 4308  
 Kuo, John T., 2516(a), 2543(a)  
 Kutschale, Henry, 2189  
 Kyle, L., 1980(l)
- LaChapelle, Edward R., 181  
 Lachenbruch, Arthur H., 4273  
 Laevastu, Taivo, 2507  
 LaFond, Eugene C., 1556(a), 2543(a), 2544(a)  
 LaGow, H. E., 3191, 3970(l)  
 Lal, D., 3519  
 Landmark, B., 1035, 2516(a)  
 Langbein, Walter B., 2544(a)  
 Laster, Stanley J., 2531(a), 2531(a)  
 Latham, Gary V., 2564(a)  
 Latter, A. L., 943, 2929  
 Lau, L. K., 2544(a)  
 Laudon, T. S., 2512(a)  
 Law, P. F., 1049  
 Lawden, M. D., 3962(l)  
 Lawhead, Harley F., 4324  
 Leadbrand, Ray L., 421, 1069  
 Leamer, Richard J., 1255, 2513(a)  
 Lees, Alan B., 2544(a)  
 Leinbach, H., 25, 1035, 2516(a)  
 LeLievier, R. E., 943  
 Le Méhauté, B., 495, 3072(l)  
 Lemmon, K. T., 3727  
 Lenchek, A. M., 4027  
 Leonard, Raymond E., 2417  
 Lettau, Heinz H., 3693  
 Lew, John S., 2681
- Lewis, Billy M., 2542(a), 2544(a)  
 Libby, W. F., 1593(l), 2544(a), 3767  
 Licht, John, 3169  
 Liemohn, Harold, 3593(l)  
 Lilley, C. M., 3233  
 Lincoln, J. Virginia, 311, 340(c), 660, 979, 1279, 1561, 1963, 2255, 2573, 3047, 3571, 3947, 4301  
 Lingenfelter, R. E., 665, 2665  
 Lisitzin, Eugenie, 345  
 Liszka, Ludwik, 1573(l)  
 Lockwood, J. A., 3083  
 Lodge, James P., 2545(a)  
 Logan, John, 2479  
 Longman, I. M., 3082(c)  
 Longuet-Higgins, M. S., 994(l)  
 Lovejoy, Earl M. P., 4332  
 Loveridge, W. D., 2568(a)  
 Lovering, J. F., 1523  
 Lowes, F. J., 1243  
 Ludwig, F. L., 1303(l)  
 Luszczynski, Norbert J., 4247  
 Luthin, James N., 1548(a), 1556(a)
- MacCarthy, Gerald R., 2545(a)  
 McCouch, G. P., 2524(a)  
 McCracken, C. W., 3970(l)  
 McCracken, K. G., 1363  
 McCullough, C. E., 2536(a)  
 MacDonald, Gordon J. F., 1865, 2489, 2599(l), 3639  
 McDonald, James E., 2545(a), 2545(a)  
 Macdonald, Norman J., 3187  
 MacDonald, William M., 2047, 2569(a)  
 McDowell, Leslie L., 2545(a)  
 McEvely, T. V., 2542(a), 3487  
 McGauhey, P. H., 1557(a)  
 McGill, David A., 2549(a)  
 McHenry, J. Roger, 2545(a)  
 McIlwain, Carl E., 2275, 2529(a), 2545(a), 3681  
 McIntyre, D. P., 2545(a)  
 McKibbin, D. D., 1667  
 McMahan, Richard J., 1839  
 McMillan, W. G., 943, 2929  
 McMurtry, R. G., 3566(a)  
 Machta, Lester, 1592(l), 2545(a)  
 Maeda, H., 1966(l)  
 Maeda, K., 1286(l), 1288(l), 1389, 1569(l)  
 Major, Maurice W., 2543(a)  
 Makela, D. R., 1549(a)  
 Mallahan, F. J., 2393, 3219  
 Malville, J. M., 2546(a)  
 Mané, Uri, 2546(a)  
 Manos, Nicholas, 2546(a)

- Manson, James E., 2163, 2540(a)  
Mantis, Homer T., 465  
Manzano, J. R., 1603  
Markowitz, Wm., 2546(a)  
Marlatt, W. E., 535  
Marston, Richard B., 657(l)  
Martin, F. L., 4129  
Martinelli, E. A., 943, 2929  
Marx, Henry P., 2546(a)  
Masch, Frank D., Jr., 2547(a)  
Masley, A. J., 316(l), 1023  
Mason, Brian, 3999(l)  
Mastenbrook, H. J., 1437  
Masterson, John E., 2141  
Matalas, Nicholas C., 3285  
Mateker, E. J., Jr., 2542(a), 3487  
Mathews, J., 2929  
Matsushita, S., 1556(a), 2547(a), 3958(l)  
Mawdsley, J., 1298(l)  
Maxwell, J. A., 2568(a)  
May, T. C., 316(l), 1023  
Maynard, K., 823  
Maynes, Donald, 3557  
Meeks, M. L., 3749  
Meister, Robert, 1957  
Mellis, Otto, 2507  
Melton, M. A., 2547(a)  
Merriam, Robert A., 1833, 1995(l)  
Meyboom, P., 1203  
Meyer, Peter, 2313, 2527(a), 2607, 3950(l)  
Meyer, R. P., 2547(a)  
Mickelson, Rome H., 2435, 2513(a)  
Miller, David H., 1548(a), 2547(a)  
Miller, Gaylord R., 2548(a)  
Miller, J. F., 2509(a)  
Miller, John P., 1318(l)  
Millman, G. H., 1564(l)  
Mink, John F., 3612(l)  
Moceyunas, A. J., 1564(l)  
Moore, C. B., 823, 2393, 3219, 3967(l)  
Moore, James G., 1751, 2101, 2567(a), 3082(c)  
Moore, Walter L., 2547(a)  
Moreton, G. E., 2546(a)  
Morey, G. W., 2548(a)  
Morgan, Robert R., 2541(a)  
Morgan, W. J., 3831  
Morisawa, M., 3619(l)  
Mundorff, M. J., 3566(a)  
Munk, Walter H., 2548(a)  
Murray, Wallace B., 987(l), 2548(a)  
Murfhey, Byron F., 947, 3389  
Murray, Bruce C., 1598(l), 2544(a), 3033  
Murthy, V. Rama, 2548(a)  
Musen, Peter, 403, 1659, 2797  
Nagashima, K., 1970(l)  
Nagata, Takesi, 2259(l)  
Nanda, J. N., 2597(l)  
Narans, Harry D., Jr., 599, 1255, 2513(a)  
Narayan, Sanker, 2548(a)  
Nason, Martin E., 3597(l)  
Naughton, J. J., 2534(a)  
Naugle, J. E., 2542(a)  
Neff, Earl L., 1548(a)  
Neher, H. V., 4007  
Neill, James C., 2563(a), 4219  
Neilon, James R., 2549(a)  
Nelson, R. William, 2469, 2549(a), 3567(a)  
Nerurkar, N., 1603  
Ness, Norman F., 621, 1865, 2549(a)  
Neumann, A. Conrad, 2549(a)  
Newton, Chester W., 853  
Newton, Robert C., 1491  
Newton, Robert R., 2550(a)  
Ney, E. P., 2550(a), 2550(a)  
Nicholson, Seth B., 1139, 2399  
Nicolet, Marcel, 2263(l)  
Noakes, John E., 2550(a)  
Nordberg, W., 455  
Nordenson, T. J., 2550(a)  
Nordyke, M. D., 3405, 3439  
Northrop, David A., 2531(a)  
Northrup, John, 2550(a)  
Obayashi, Tatsuzo, 2551(a)  
Odencrantz, F. Kirk, 2101  
Oelsner F., Juergen, 1998(l)  
Okada, J. M., 2551(a)  
O'Keefe, John A., 1992(l), 2551(a)  
Okeson, Clifford J., 1549(a)  
Olesen, Jens K., 1127  
Oliver, H. W., 4265  
Oliver, Jack E., 215, 2553(a)  
Ondoh, Tadanori, 4155  
Opdyke, N. D., 1941  
Öpik, E. J., 2551(a), 2807  
Oriard, Lewis L., 1549(a)  
Ortenburger, I. B., 1425, 1554(a)  
Ortner, J., 1035, 2516(a)  
Ostenso, Ned A., 1301(l), 2566(a), 2570(a)  
Otterman, J., 819  
Outerbridge, W. F., 581  
Owen, W. J., 2532(a), 2559(a), 3319  
Pack, D. H., 2510(a)  
Pakiser, L. C., 4265  
Palmeira, R. A. R., 1603  
Palmer, Clarence E., 1591(l), 1593(l)  
Panofsky, H. A., 2551(a)  
Parker, E. N., 693, 2641, 2673, 3631  
Parry, L. G., 1523  
Patel, V. L., 1286(l), 1288(l), 1389, 1569(l)  
Patton, Bob J., 2552(a)  
Pattullo, June G., 845, 2552(a)  
Pelton, W. L., 1319(c)  
Pennington, Ralph H., 709  
Perret, W. R., 903  
Perry, Douglas, 2524(a)  
Peselnick, Louis, 581, 1957  
Peterson, L. E., 995, 2552(a)  
Peterson, M. N. A., 2552(a)  
Petrie, L. E., 2321  
Pfister, W., 1293(l)  
Philip, J. R., 571  
Phillips, B. B., 2552(a)  
Phillips, O. M., 2889  
Phinney, Robert A., 1445  
Pierson, Willard J., Jr., 163  
Piggott, W. R., 3604(l)  
Pillsbury, Arthur F., 1555(a)  
Pineo, V. C., 3965(l)  
Pinson, W. H., 2538(a), 2553(a)  
Pitteway, M. L. V., 3141  
Pomerantz, M. A., 1970(l)  
Pomeroy, Paul W., 2553(a)  
Pooler, F., Jr., 2553(a)  
Pope, Joseph H., 67, 2580(l)  
Popham, R. W., 2569(a)  
Poppoff, I. G., 2779  
Press, Frank, 237, 605, 2553(a), 3073(l), 3471  
Preston, R. G., 903  
Priester, W., 4143  
Proctor, P. D., 2554(a)  
Provazek, L. D., 879  
Putnins, P., 2554(a)  
Quiroz, Roderick S., 2129  
Qureshy, Mohammed N., 2554(a)  
Raemer, H. R., 1580(l), 1596(l)  
Ragland, Paul C., 2509(a)  
Raitt, Russell W., 589  
Rama, 2554(a), 3227, 3533  
Ramanathan, K. R., 2763  
Rangarajan, R., 1997(l)  
Rantz, S. E., 1557(a)  
Rao, B. Ramachandra, 2113  
Rao, M. S. V. Gopal, 2113  
Rapp, R. R., 2554(a)  
Rasmussen, Lowell A., 813  
Ray, Ernest C., 2554(a)  
Redfield, Alfred C., 2530(a)  
Reed, J. E., 2423, 2554(a)  
Reed, Jack W., 1557(a)  
Reed, Richard J., 813  
Rees, M. H., 41  
Reid, G. C., 4071

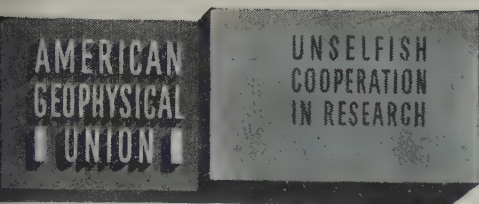
- Reinhart, K. G., 2555(a)  
 Reitzel, John, 2267(l)  
 Renau, Jacques, 1589(l), 2121,  
 2555(a), 2703  
 Renn, Charles E., 2555(a)  
 Reynolds, G., 3611(l)  
 Reynolds, J. H., 277, 3582(l)  
 Reynolds, Tom D., 2555(a), 3913  
 Rice, Donald A., 2555(a)  
 Rice, J. A., 4163  
 Rikitake, Tsuneji, 3245  
 Rinehart, John S., 191  
 Roach, F. E., 2555(a)  
 Roberson, John A., 521, 1547(a)  
 Roberts, P. H., 1243  
 Roberts, Walter O., 340(c),  
 2556(a)  
 Roberts, W. J., 2556(a), 3309  
 Robertson, W. A., 1927  
 Robinson, Margaret K., 1557(a)  
 Rockwood, David M., 3567(a)  
 Roden, Gunnar I., 1557(a)  
 Rodgers, M. F., 3953(l)  
 Rodier, J., 2556(a)  
 Roederer, J. G., 1603  
 Rogers, Dale G., 813  
 Rogers, John J. W., 2556(a)  
 Roller, J. C., 201  
 Romney, C. F., 2528(a)  
 Rorabaugh, M. I., 3567(a)  
 Rose, J. C., 2557(a), 2564(a),  
 2571(a)  
 Rose, Walter, 1199  
 Rosen, Alan, 1558(a), 2013,  
 2557(a)  
 Rosen, L., 351  
 Rosenbaum, J. H., 994(c), 3899  
 Rothacher, Jack, 1549(a)  
 Rourke, G. F., 1594(l), 4316  
 Rowe, J. J., 2548(a)  
 Rowe, M. W., 3553  
 Rowe, Paul P., 1549(a)  
 Rowland, F. S., 4321  
 Roy, Amalendu, 543  
 Rudd, R. D., 125  
 Rugg, A. M., 2528(a)  
 Rushbrook, P. R., 3581(l)  
 Russell, R. D., 1495  
 Russell, S., 3078(l)  
 Sachs, D. C., 903  
 Saito, M., 3895  
 Sakurai, K., 1966(l)  
 Salmela, Henry A., 2557(a)  
 Salpeter, E. E., 982(l)  
 Salsman, Garrett G., 2567(a),  
 2567(a)  
 Saltzman, Barry, 2271(l)  
 Sanders, A. E., 1564(l)  
 Sanders, J. E., 2557(a)  
 Sandoval, Fred M., 2435, 2513(a)  
 Santochi, O. R., 1603  
 Sartor, J. D., 831, 3070(l)  
 Sasaki, Yoshikazu, 2558(a)  
 Sattinger, I. J., 819  
 Saul, V. A., 4263  
 Saur, J. F. T., 1558(a)  
 Searce, C. S., 2549(a)  
 Schade, William J., 1559(a)  
 Schaeffer, O. A., 2535(a)  
 Schairer, J. F., 2558(a)  
 Schalk, Marshall, 2558(a)  
 Sharon, LeRoy, 2533(a)  
 Schearer, L. D., 4163  
 Scheidegger, A. E., 3273, 3279  
 Schell, I. I., 2559(a)  
 Schiff, Leonard, 3567(a)  
 Schleusener, Richard A., 4187  
 Schmidt, Milton O., 2559(a)  
 Schmidt, Richard A., 307  
 Schneider, William J., 3617(l)  
 Schnetzler, C. C., 2553(a)  
 Schoen, Beatrice, 1861  
 Schooley, Allen H., 157, 2559(a),  
 2863  
 Schrader, C. D., 1951, 2559(a)  
 Schuetz, John, 2559(a)  
 Schulze, Reinhard, 1813  
 Schwachheim, G., 1603  
 Scott, Ronald F., 1559(a)  
 Sechrist, C. F., 3601(l)  
 Sen, H. K., 664(c)  
 Serbu, G. P., 2559(a), 4313  
 Shapiro, I. I., 4123  
 Shapiro, I. R., 2677  
 Shapiro, Ralph, 739  
 Shapley, A. H., 336(l)  
 Sharp, A. L., 2532(a), 2559(a),  
 3319  
 Shea, M. A., 3083  
 Shima, M., 3580(l)  
 Shoemaker, E. M., 3371  
 Shuman, B., 2687  
 Shurbet, D. H., 899  
 Shykind, Edwin B., 2560(a)  
 Signer, Peter, 2560(a)  
 Silver, Leon T., 2560(a)  
 Silver, Samuel, 1559(a), 1559(a)  
 Silverman, S. M., 323(l)  
 Simmons, Gene, 2269(l)  
 Simpson, J. A., 2313, 2527(a),  
 2607  
 Singer, S. F., 1569(l), 2510(a),  
 2560(a), 2561(a), 4027  
 Siple, Paul A., 2561(a)  
 Skillman, T. L., 2549(a)  
 Slawson, William F., 2561(a)  
 Slichter, L. B., 621  
 Small, K. A., 3723  
 Smith, Alex G., 2561(a)  
 Smith, C. H., 2568(a)  
 Smith, D. F., 819  
 Smith, E. J., 1559(a), 2562(a)  
 Smith, H. W., 879, 2515(a)  
 Smith, L. G., 2562(a)  
 Smith, R. L., 664(c), 2274(c),  
 2578(l), 2582(l), 3699, 3709  
 Smith, Stewart W., 605, 2562(a),  
 3608(l)  
 Snidero, Mirco P., 2562(a)  
 Snodgrass, Frank E., 2548(a)  
 Snyder, Conway W., 2562(a)  
 Snyder, W. M., 2563(a)  
 Sobouti, Y., 725  
 Sodano, Emanuel M., 2563(a)  
 Sonett, C. P., 1559(a), 2043,  
 2521(a), 3591(l)  
 Spencer, A. T., 2570(a), 2873  
 Spies, Kenneth P., 992(l)  
 Spreiter, John R., 1731, 2345,  
 2563(a)  
 Springer, Donald L., 959  
 Stacey, F. D., 1523  
 Stall, John B., 2563(a), 4219  
 Stallman, R. W., 3568(a)  
 Stampf, R. A., 3169  
 Stauffer, Heinz, 1513, 2564(a),  
 3584(l)  
 Steiger, Walter R., 57  
 Stein, W., 2529(a), 2550(a)  
 Steinhart, John S., 2564(a)  
 Steljes, J. F., 1363, 2518(a)  
 Stevan, Lee J., 1225  
 Stewart, S. W., 201  
 Stinner, R. J., 1951, 2559(a)  
 Stolarik, J. D., 2677  
 Stoner, J. O., 3831  
 Stott, P. M., 1927  
 Stout, Benjamin B., 1839  
 Strangway, D. W., 3021  
 Strickholm, O. S., 2557(a),  
 2564(a)  
 Stroud, W. G., 455, 2532(a), 3169  
 Stroup, E. Dixon, 2518(a)  
 Stuiver, M., 273  
 Sugiura, Masahisa, 2564(a), 4087,  
 4097  
 Suomi, V. E., 2843  
 Sutton, George H., 631, 2564(a),  
 2911  
 Sweet, James S., 2565(a)  
 Swenson, Frank A., 3568(a)  
 Swenson, G. W., Jr., 654(l), 1061  
 Swift, L. W., Jr., 2565(a)  
 Sykes, W. G., 823  
 Takahashi, Taro, 477  
 Takeuchi, H., 3895  
 Talwani, Manik, 1265, 2565(a),  
 3989(c)  
 Tamarkin, Paul, 35, 2737  
 Tang, C. L., 1974(l)  
 Tank, W. G., 1549(a)



- Tanner, C. B., 1318(*l*), 1319(*c*)  
 Tanner, William F., 333(*l*), 2265(*l*)  
 Tarling, D. H., 549, 1927  
 Taylor, Lee R., Jr., 2587(*l*)  
 Taylor, H. P., Jr., 2565(*a*)  
 Taylor, Leonard S., 3157  
 Taylor, Ronald C., 1591(*l*)  
 Tepley, L. R., 111, 1651, 2566(*a*)  
 Teweles, Sidney, 2532(*a*)  
 Thatcher, L. L., 2566(*a*)  
 Theimer, Otto, 3157  
 Theis, C. V., 3568(*a*)  
 Thiel, Edward, 307, 2566(*a*)  
 Thode, H. G., 3578(*l*), 3580(*l*)  
 Thompson, Thomas L., 2495  
 Thornton, J. F., 1855  
 Tilles, David, 3003, 3015  
 Tilley, C. E., 2571(*a*)  
 Tilton, G. R., 2524(*a*)  
 Tinney, E. Roy, 2566(*a*)  
 Tirey, G. B., 2917  
 Tison, L. J., 2566(*a*), 4227  
 Titheridge, J. E., 3103  
 Todd, Clement J., 2567(*a*)  
 Todd, David K., 2544(*a*), 3569(*a*)  
 Toksöz, M. Nafi, 2553(*a*), 3471  
 Toksöz, Sadik, 509  
 Tolbert, William H., 2567(*a*), 2567(*a*)  
 Tolefson, Harold B., 2567(*a*), 2849  
 Tolstoy, I., 2485  
 Townshend, J. B., 4319  
 Troitskaya, V. A., 5  
 Troncoso, O., 1603  
 Tryggvason, Eysteinn, 1913  
 Tuttle, O. F., 2568(*a*)  
 Tveten, L. H., 1683  
 Twomey, Sean A., 2153, 2567(*a*)  
 Ulrych, T. J., 1495  
 Ulwick, J. C., 1293(*l*)  
 Umemoto, S., 3541  
 Underwood, J. L., 1548(*a*)  
 Unterberger, R. R., 2274(*c*)  
 Urey, Harold C., 1988(*l*)  
 Vaile, R. B., Jr., 3413  
 van Abkoude, E. R., 2183  
 van Bavel, C. H. M., 1559(*a*), 2565(*a*), 4193  
 Vancouver, R. P., 1293(*l*)  
 Van Dilla, M. A., 3553  
 Van Dorn, William G., 1560(*a*), 3845  
 Van Voorhis, Gerald D., 3793  
 van Wijk, A. M., 647(*l*)  
 Van Zandt, T. E., 1555(*a*), 1673, 3078(*l*)  
 Venkatesan, D., 2275, 2529(*a*)  
 Venkateswaran, S. V., 1751, 2567(*a*), 3082(*c*)  
 Vestine, E. H., 713, 989, 1, 2567(*a*)  
 Vik, R. C., 1, 2001(*c*)  
 Villard, O. G., Jr., 3109  
 Violet, Charles E., 3461  
 Visser, Simon, 3759  
 Vistelius, A. B., 1601(*l*)  
 Voelcker, H., 2262(*l*)  
 Vogt, Rochus, 3950(*l*)  
 von Bulow, K., 2568(*a*)  
 Vonnegut, B., 823, 2393, 3219, 3967(*l*)  
 Vortman, L. J., 3389  
 Vozoff, K., 1983(*l*)  
 Wait, James R., 992(*l*), 1713, 1725, 3119, 3603(*l*)  
 Waldron, C. G., 4129  
 Walker, E. H., 2561(*a*)  
 Walker, William H., 2568(*a*), 3359  
 Wallace, L., 1585(*l*)  
 Wallis, James R., 1225, 2568(*a*)  
 Walt, Martin, 2047  
 Walter, L. S., 2568(*a*)  
 Walton, William C., 2568(*a*), 3359  
 Wanless, R. K., 2568(*a*)  
 Ward, Fred, 739, 3605(*l*)  
 Ward, M. A., 1927  
 Wark, D. Q., 77, 2569(*a*), 3596(*l*)  
 Warwick, James W., 57  
 Wasserburg, G. J., 277  
 Wasson, John T., 2659  
 Watson, Kenneth, 1598(*l*), 3033  
 Watson, K. M., 1, 2001(*c*)  
 Webster, Ferris, 2569(*a*)  
 Weeks, Wilford F., 2509(*a*)  
 Weertman, J., 2569(*a*), 3783  
 Wennekens, M. P., 1560(*a*)  
 Wentworth, R. C., 2569(*a*), 4027  
 Wentzel, Donat G., 359, 363  
 Werth, Glenn C., 959  
 Wescott, Eugene M., 1789  
 West, Allen J., 2569(*a*)  
 Westfall, W. D., 2733  
 Wetherill, G. W., 2524(*a*), 2983  
 Wexler, Harry, 2569(*a*)  
 White, Robert M., 2569(*a*)  
 Whitney, Linwood F., Jr., 2570(*a*)  
 Whitten, R. C., 2779  
 Wiener, Francis M., 3974(*l*)  
 Wilkening, M. H., 2540(*a*), 2570(*a*)  
 Wilkins, Eugene M., 1314(*l*)  
 Willard, H. R., 1976(*l*)  
 Williams, F. U., 2536(*a*)  
 Williams, Milton, 2524(*a*)  
 Willits, N. A., 535  
 Wilson, Charles R., 4097  
 Winchester, John W., 2523(*a*)  
 Winckler, J. R., 316(*l*), 995, 1023, 3991  
 Winder, R. P. H., 3967(*l*)  
 Winston, Jay S., 2530(*a*)  
 Witters, Juanita, 2531(*a*)  
 Wold, R. J., 2512(*a*)  
 Woo, Dah-Cheng, 2570(*a*), 4207  
 Woodcock, A. H., 2570(*a*), 2873  
 Woodtli, R. A., 2601(*l*)  
 Woollard, George P., 2548(*a*), 2564(*a*), 2570(*a*), 2571(*a*)  
 Woolson, J. R., 2528(*a*)  
 Workman, E. J., 2515(*a*)  
 Worzel, J. Lamar, 1265, 2565(*a*), 3989(*c*)  
 Wright, J. W., 1127  
 Wulf, Oliver R., 1139, 2399  
 Wüst, Georg, 2571(*a*), 3261  
 Wyatt, Philip J., 1578(*l*)  
 Wyller, A. A., 664(*c*)  
 Wyllie, P. J., 2568(*a*)  
 Wyrick, R. F., 1564(*l*)  
 Yabroff, I. W., 2274(*c*)  
 Yamamoto, G., 3596(*l*)  
 Yanow, Gilbert, 2571(*a*)  
 Yeh, K. C., 654(*l*), 1061  
 Yoder, H. S., Jr., 2558(*a*), 2571(*a*)  
 Young, J. M., 3727  
 Yungul, S. H., 557  
 Zartman, R. E., 277  
 Ziauddin, Syed, 2315  
 Zietz, Isidore, 2571(*a*)  
 Zirin, H., 340(*c*)  
 Zmuda, Alfred J., 2572(*a*), 2572(*a*)







# AMERICAN GEOPHYSICAL UNION

1515 Massachusetts Avenue, N.W., Washington 5, D. C.

*Established by the National Research Council in 1919 for the development of the science of geophysics through scientific publication and the advancement of professional ideals.*

## QUALIFICATIONS FOR MEMBERSHIP

The Membership of the AGU shall consist of Members, Associate Members, Student Members, Corporation Members, and Supporting Members.

Those eligible as candidates for election to the grade of MEMBER shall be:

**MEMBER** (a) Persons who have made an active contribution to geophysical research through observation, publication, teaching, or administration. Definite evidence should be presented to the Membership Committee. "Publication" may include books, articles, unpublished manuscripts, inventions, or development of geophysical instruments.

(b) Persons who have made active practical application of geophysical research. It should be shown that the nominee's work has not been purely routine, but that it has tended to create new knowledge of, or to broaden or strengthen the application of, geophysical research. In general, the minimum qualifications for membership will be not less than three years of professional experience in some phase of geophysics.

*(Continued on next page)*

Cut along this line

## APPLICATION FOR MEMBERSHIP

Please refer to qualifications on reverse side and designate below type of membership desired:

Member (\$10) ☐

Associate (\$10) ☐

Student (\$4.50) ☐  
(1961)

Application forms for Corporation and Supporting Membership are available upon request.

1. \_\_\_\_\_  
Surname First Name Middle Name

2. \_\_\_\_\_  
Preferred mailing address for publications

\_\_\_\_\_   
Permanent address

3. \_\_\_\_\_ 4. \_\_\_\_\_  
Place Month Day Year of Birth Country of citizenship/naturalization

5. \_\_\_\_\_  
Nature of work and title and/or military rank; name and address of organization with which you are associated.

6. Check section or sections with which affiliation is desired.

- |  |   |
|--|---|
| <input type="checkbox"/> Geodesy                   | <input type="checkbox"/> Oceanography                             |
| <input type="checkbox"/> Seismology                | <input type="checkbox"/> Volcanology, Geochemistry, and Petrology |
| <input type="checkbox"/> Meteorology               | <input type="checkbox"/> Hydrology                                |
| <input type="checkbox"/> Geomagnetism and Aeronomy | <input type="checkbox"/> Tectonophysics                           |

7. **EXPERIENCE (List below, use added sheets as necessary)**

Dates: From To Name and address of organization Title, duties, nature of work

8. **EDUCATION (List Below, use added sheets as necessary)**

Dates: From To School Address Major Subject Degree, if any; year

(over)

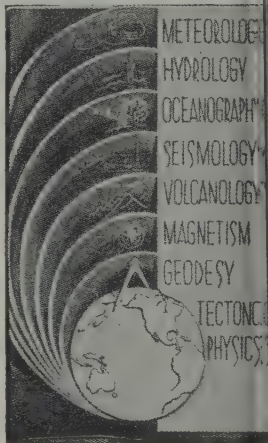
(Continued from previous page)

Those eligible as candidates for election to the grade of ASSOCIATE MEMBER shall be:

**ASSOCIATE MEMBER** Persons who have an active interest in physical processes of the Earth or technical assistance in the application of geophysics. In general, the minimum qualification for associate membership will be acceptable training or experience in some field of geophysics or allied science.

**CORPORATION AND SUPPORTING MEMBER** Corporations and other interested organizations shall be eligible as candidates for election to CORPORATION or SUPPORTING MEMBERSHIP. They shall have the privilege of designating a representative who has the rights and privileges of Members (use special form).

**STUDENT MEMBER** Those eligible as candidates for election to the grade of STUDENT MEMBER shall be persons who are graduate or undergraduate students in residence at least half-time and who are specializing in the geophysical sciences. Teaching or research assistants enrolled in more than half of a full-time academic program may also be eligible for Student Membership. Student Members shall have all the privileges of Members except that they shall not vote or hold office.



-----  
Cut along this line

\*9. References: Please list below names and addresses of two or three references; include members of the AGU or others who know you well.

\*10. Titles of technical contributions or publications, particularly those in the geophysical sciences, and where published.

\*11. Brief statement of any special interests or qualifications in the geophysical sciences.

Date \_\_\_\_\_

\_\_\_\_\_  
Written Signature

12. (STUDENT MEMBERS ONLY) The person whose signature appears above is known to me and is a student majoring in \_\_\_\_\_ (subject) at \_\_\_\_\_

(Name of college or university) expected to graduate in \_\_\_\_\_ (year) with the degree of \_\_\_\_\_

☐ He is a full-time student, or ☐ a teaching or research assistant enrolled in more than half of full-time academic program.

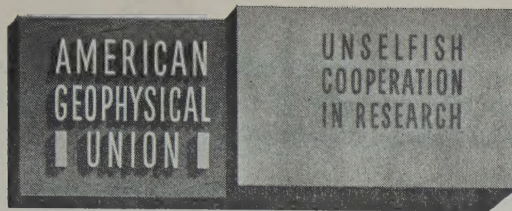
\_\_\_\_\_  
(Signature of faculty sponsor)

☐ Check here if faculty sponsor is a member of AGU and willing to act as a regular sponsor for associate membership as well.

\_\_\_\_\_  
(Typed or printed name of sponsor)

\_\_\_\_\_  
(Title)

\* Applicants for student membership may omit Questions 9, 10, and 11, but must fill in Question 12. Please return form with check or money order payable to American Geophysical Union, 1515 Massachusetts Ave., N.W., Washington 5, D. C.



## CORPORATION AND SUPPORTING MEMBERSHIPS

The American Geophysical Union is a non-profit scientific organization established by the National Research Council. Its Council is the United States National Committee of the International Union of Geodesy and Geophysics; official adherence by the United States is through the National Academy of Sciences-National Research Council.

Extracts from the Statutes:

*Article 3. Membership*—The membership of the American Geophysical Union shall be as follows:

- (e) *Corporation Members*—Corporations and other organizations interested in geophysics elected by the Council of the Union. The designated representative of each such organization shall enjoy the privileges of a Member.
- (g) *Supporting Members*—Corporations, other organizations, and individuals interested in geophysics and desirous of supporting the Union may become members under the following classifications upon election by the Council.

(Continued on next page)

Cut along this line

# American Geophysical Union

## PROPOSAL FOR \_\_\_\_\_ MEMBERSHIP

To the Council, American Geophysical Union  
1515 Massachusetts Avenue, N.W., Washington 5, D. C.

Gentlemen:

As an indication of our interest in the aims and activities of the American Geophysical Union, and to assist in maintaining and extending its program of publication and other work in the development of the geophysical sciences, the undersigned applies for \_\_\_\_\_ Membership in the AGU and, until further notice, agrees to pay annual dues at the rate established for this classification of membership, in accordance with the information set forth above and on the following page.

Company or Organization \_\_\_\_\_

By \_\_\_\_\_ Title \_\_\_\_\_

(Signature)

(over)



(Continued from previous page)

of the Union . . . : Contributing Members, . . . Sustaining Members, . . . Benefactors. . . . Each Supporting Member and the designated representative . . . shall enjoy the privileges of a Member.

Corporation Members shall pay dues of not less than \$100 for each calendar year. Dues for Supporting Members shall be as follows:

Contributing Members	\$500
Sustaining Members	\$1000
Benefactors	\$5000

Lists of Corporation Members and Supporting Members will be published in each issue of the *Transactions*, and will be included in the Membership Directory as distinct units.

By Laws provide that one copy of each issue of the *Transactions*, *Journal of Geophysical Research*, any published *List of Members and Officers*, and any other publication which may be approved for free distribution to the membership shall be sent to each Corporation and Supporting Member. Each organization in good standing may purchase any available publication of the Union at the established member discount.

### AMERICAN GEOPHYSICAL UNION

1515 Massachusetts Ave., N.W.

Washington 5, D. C.

-----  
Cut along this line

Address \_\_\_\_\_

City \_\_\_\_\_ State \_\_\_\_\_

General fields of activity \_\_\_\_\_  
\_\_\_\_\_  
\_\_\_\_\_  
\_\_\_\_\_

The following person is designated as our representative in this membership \_\_\_\_\_

\_\_\_\_\_ Title \_\_\_\_\_

Number of units of membership desired (this will be taken as one unless otherwise indicated) \_\_\_\_\_

Place \_\_\_\_\_

Date \_\_\_\_\_

# Contents

(Continued from back cover)

	PAGE
Laminar Flow in Rough Rectangular Channels. . . . . <i>Dah-Cheng Woo and Ernest F. Brater</i>	4207
A Partial Duration Series for Low-Flow Analyses. . . . . <i>John B. Stall and James C. Neill</i>	4219
Local Scour in Rivers. . . . . <i>L. J. Tison</i>	4227
The Relation between the Frequency Distributions of Sieve Diameters and Fall Velocities of Sediment Particles. . . . . <i>John F. Kennedy and Robert C. Y. Koh</i>	4233
Head and Flow of Ground Water of Variable Density. . . . . <i>Norbert J. Lusczynski</i>	4247
On the Theory of Leaky Aquifers. . . . . <i>Roger J. M. De Wiest</i>	4257
A New Borehole Thermometer. . . . . <i>Ronald Doig, V. A. Saull, and R. A. Butler</i>	4263
Gravity Anomalies in the Central Sierra Nevada, California <i>H. W. Oliver, L. C. Pakiser, and M. F. Kane</i>	4265
Depth and Spacing of Tension Cracks. . . . . <i>Arthur H. Lachenbruch</i>	4273
Electrostatic Erosion Mechanisms on the Moon. . . . . <i>P. D. Grannis</i>	4293
Geomagnetic and Solar Data. . . . . <i>J. Virginia Lincoln</i>	4301
Letters to the Editor:	
Radar Reflections from the Sun at Very High Frequencies <i>W. G. Abel, J. H. Chisholm, P. L. Fleck, and J. C. James</i>	4303
Bursts of Centimeter-Wave Emission and the Region of Origin of X Rays from Solar Flares. . . . . <i>M. R. Kundu</i>	4308
Electron Temperature Measurements on the Explorer VIII Satellite <i>G. P. Serbu, R. E. Bourdeau, and J. L. Donley</i>	4313
Minor PCA Events during March 1958. . . . . <i>G. F. Rourke</i>	4316
Horizontal Intensity Comparisons between the Sine Galvanometer and the Proton Vector Magnetometer <i>J. L. Bottum, R. E. Gebhardt, and J. B. Townshend</i>	4319
Discussion of Paper by N. D. Opdyke, 'The Paleomagnetism of the New Jersey Triassic: A Field Study of the Inclination Error in Red Sediments' <i>D. H. Griffiths and R. F. King</i>	4320
An Additional Measurement of the Tritium Content of Atmospheric Hydrogen of 1949. . . . . <i>E. L. Fireman and F. S. Rowland</i>	4321
The Myers Formula and Myers Rating Compared with Actual Floods <i>G. G. Commons</i>	4322
Discussion of Paper by Ivan W. Brunk, 'Changes in the Levels of Lakes Michigan and Huron' . . . . . <i>Harley F. Lawhead</i>	4324
Author's Reply to the Preceding Discussion. . . . . <i>Ivan W. Brunk</i>	4330
Comments on Paper by V. V. Belousov, 'The Origin of Folding in the Earth's Crust' . . . . . <i>Earl M. P. Lovejoy</i>	4332
Author's Reply to the Preceding Discussion. . . . . <i>V. V. Belousov</i>	4334
Corrigendum. . . . . <i>Michele Caputo</i>	4335
Tables of Contents for Volume 66 . . . . .	4337
Index of Names for Volume 66 . . . . .	4355



## Contents

	PAGE
Cosmic Ray Evidence for a Ring Current..... <i>P. J. Kellogg and J. R. Winckler</i>	39
Observations of the Van Allen Radiation Regions during August and September 1959. 2. The Capetown Anomaly and the Shape of the Outer Belt <i>Robert A. Hoffman</i>	40
Cosmic-Ray Knee in 1958..... <i>H. V. Neher</i>	40
The Magnetic Field of a Model Radiation Belt, Numerically Computed <i>Syun-Ichi Akasofu, Joseph C. Cain, and Sydney Chapman</i>	40
Geomagnetically Trapped Electrons from Cosmic Ray Albedo Neutrons <i>A. M. Lenchek, S. F. Singer, and R. C. Wentworth</i>	40
Solar Proton Impact Zones..... <i>Thomas Kelsall</i>	40
A Study of the Enhanced Ionization Produced by Solar Protons during a Polar Cap Absorption Event..... <i>G. C. Reid</i>	40
Evidence of Low-Frequency Hydromagnetic Waves in the Exosphere <i>Masahisa Sugiura</i>	40
Hydromagnetic Interpretation of Sudden Commencements of Magnetic Storms <i>Charles R. Wilson and Masahisa Sugiura</i>	40
Ionospheric Limitations on Attainable Satellite Potential <i>David B. Beard and Francis S. Johnson</i>	41
Effects of the Earth's Magnetic Field on the Orbit of a Charged Satellite <i>I. I. Shapiro and H. M. Jones</i>	41
A 'Layered' Exponential Model of Radar Refractivity <i>F. L. Martin and C. G. Waldron</i>	41
Polar Ionospheric Spread Echoes and Radio Frequency Properties of Ice Shelves <i>S. Evans</i>	41
Solar Activity Effect and Diurnal Variation in the Upper Atmosphere.. <i>W. Priester</i>	41
The Seasonal Anomalies in the <i>F</i> Region..... <i>G. A. M. King</i>	41
Ionospheric Currents Responsible for Sudden Commencements Observed at the Geomagnetic Equator..... <i>Tadanori Ondoh</i>	41
A Metastable Helium Magnetometer for Observing Small Geomagnetic Fluctuations..... <i>A. R. Keyser, J. A. Rice, and L. D. Schearer</i>	41
The Effects of Atmospheric Refraction on Angles Measured from a Satellite <i>A. C. Holland</i>	41
Numerical Errors in the Time Integration of Advective Processes.. <i>Joseph B. Knox</i>	41
Further Evidence of Hysteresis as a Factor in the Evaporation from Soils <i>Larry G. King and Richard A. Schleusener</i>	41
Neutron Measurement of Surface Soil Moisture..... <i>C. H. M. van Bavel</i>	41
An Evaluation of Uranium as a Tool for Studying the Hydrogeochemistry of the Truckee Meadows Area, Nevada..... <i>Philip Cohen</i>	41

(Continued inside back cover)